Evolution of Planetary Nebulae with WR-type Central Stars

Ashkbiz Danehkar

A thesis submitted to Macquarie University
in accordance with the requirements of the degree of
Doctor of Philosophy

Department of Physics and Astronomy
Faculty of Science
Macquarie University
Sydney, Australia

April 2014

Abstract

This thesis presents a study of the kinematics, physical conditions and chemical abundances for a sample of Galactic planetary nebulae (PNe) with Wolf-Rayet (WR) and weak emission-line stars (*wels*), based on optical integral field unit (IFU) spectroscopy obtained with the Wide Field Spectrograph (WiFeS) on the Australian National University 2.3 telescope at Siding Spring Observatory, and complemented by spectra from the literature. PNe surrounding WR-type stars constitute a particular study class for this study. A considerable fraction of currently well-identified central stars of PNe exhibit 'hydrogen-deficient' fast expanding atmospheres characterized by a large mass-loss rate. Most of them were classified as the carbon-sequence and a few of them as the nitrogen-sequence of the WR-type stars. What are less clear are the physical mechanisms and evolutionary paths that remove the hydrogen-rich outer layer from these degenerate cores, and transform it into a fast stellar wind. The aim of this thesis is to determine kinematic structure, density distribution, thermal structure and elemental abundances for a sample of PNe with different hydrogen-deficient central stars, which might provide clues about the origin and formation of their hydrogen-deficient stellar atmospheres.

Hα and [N II] emission features have been used to determine kinematic structures. Based on spatially resolved observations of these emission lines, combined with archival *Hubble Space Telescope* imaging for compact PNe, morphological structures of these PNe have been determined. Comparing the velocity maps from the IFU spectrograph with those provided by morpho-kinematic models allowed disentangling of the different morphological components of most PNe, apart from the compact objects. The results indicate that these PNe have axisymmetric morphologies, either bipolar or elliptical. In many cases, the associated kinematic maps for PNe around hot WR-type stars also show the

presence of so-called fast low-ionization emission regions (FLIERs).

The WiFeS observations, complemented with archival spectra from the literature, have been used to carry out plasma diagnostics and abundance analysis using both collisionally excited lines (CELs) and optical recombination lines (ORLs). ORL abundances for carbon, nitrogen and oxygen have been derived where adequate recombination lines were available. The weak physical dependence of ORLs has also been used to determine the physical properties. It is found that the ORL abundances are several times higher than the CEL abundances, whereas the temperatures derived from the He I recombination lines are typically lower than those measured from the collisionally excited nebular-to-auroral forbidden line ratios. The abundance discrepancy factors (ADFs) for doubly-ionized nitrogen and oxygen are within a range from 2 to 49, which are closely correlated with the dichotomy between temperatures derived from forbidden lines and those from He I recombination lines. The results show that the ADF and temperature dichotomy are correlated with the intrinsic nebular Hβ surface brightness, suggesting that the abundance discrepancy problem must be related to the nebular evolution.

Three-dimensional photoionization models of a carefully selected sample of Galactic PNe have been constructed, constrained by the WiFeS observations (Abell 48 and SuWt 2) and the double echelle MIKE spectroscopy from the literature (Hb 4 and PB 8). The WiFeS observations have been used to perform the empirical analysis of Abell 48 and SuWt 2. The spatially resolved velocity distributions were used to determine the kinematic structures of Hb 4 and Abell 48. The previously identified non-LTE model atmospheres of Abell 48 and PB 8 have been used as ionizing fluxes in their photoionization models. It is found that the enhancement of the [N II] emission in the FLIERs of Hb 4 is more attributed to the geometry and density distribution, while the ionization correction factor method and electron temperature used for the empirical analysis are mostly responsible for apparent inhomogeneity of nitrogen abundance.

However, the results indicate that the chemically inhomogeneous models, containing a small fraction of metal-rich inclusions (around 5 percent), provide acceptable matches to the observed ORLs in Hb 4 and PB 8. The observed nebular spectrum of Abell 48 was best produced by using a nitrogen-sequence non-LTE model atmosphere of a low-mass progenitor star rather than a massive Pop I star. For Abell 48, the helium temperature predicted by the photoionization model is higher than those empirically derived, suggesting the presence of a fraction of cold metal-rich structures inside the nebula. It is found that a dual-dust chemistry with different grain species and discrete grain sizes likely produces the nebular *Spitzer* mid-infrared continuum of PB 8. The photoionization models of SuWt 2 suggest the presence of a hot hydrogen-deficient degenerate core, compatible with what is known as a PG 1159-type star, while the nebula's age is consistent with a born-again scenario.

Declaration of Originality

This thesis is submitted in fulfillment of the requirements of the degree of Doctor of Philosophy at Macquarie University, Australia. I certify that the work in this thesis has not previously been submitted for a degree nor has it been submitted as part of requirements for a degree to any other universities or institutions, either in Australia or overseas.

I also certify that the thesis is an original piece of research and it has been written by me. Any help and assistance that I have received in my research work and the preparation of the thesis itself have been appropriately acknowledged.

In addition, I certify that all information sources and literature used are indicated in the thesis. Some of the text found within has been published in the list of refereed papers and conference proceedings found in the appendix, on which I have been the leading author.

Any views expressed in this dissertation are those of the author and do not represent those of Macquarie University.

Ashkbiz Danehkar
April 2014

Copyright Statement

Acknowledgments

Foremost I would like to thank my supervisors, Prof. Quentin Parker for his help and support throughout the past three years. There are many people I would like to thank who have contributed to this work; Prof. Barbara Ercolano of the Ludwig Maximilian University of Munich, for useful discussions and guidance in photoionization modeling; Prof. Wolfgang Steffen of the National Autonomous University of Mexico, for helping with morpho-kinematic modeling; Dr. Roger Wesson of the European Southern Observatory in Santiago, for useful discussions and guidance in chemical abundance analysis; Dr. Helge Todt of the University of Potsdam, for providing hydrogen-deficient expanding model atmospheres of Abell 48 and PB 8, and discussions in hydrogen-deficient central star; Dr. Alexei Kniazev of the Southern African Large Telescope Foundation, for providing the spectra of Abell 48; Dr. Jorge Garcia-Rojas of the University of La Laguna, for providing the spectra of PB 8; Dr. Ralf Jacob of the Leibniz Institute for Astrophysics Potsdam, for providing 1-D radiation-hydrodynamics models; Dr. Henri Plana of the State University of Santa Cruz, for providing and reducing Gemini observations; Prof. Peter Storey of the University College London, for providing his recombination line code ahead of publication; Dr. Nick Wright of the Harvard–Smithsonian Center for Astrophysics, for some discussions in photoionization models; Prof. Michael Barlow of the University College London, for some discussions in empirical analysis; Prof. Wagner Marcolino of the Federal University of Rio de Janeiro, for useful guidance in CMFGEN modeling; Dr. Graziela Keller of the University of São Paulo, for helps in CMFGEN modeling; Dr. David Frew of the Macquarie University, for astronomical lectures, initial discussions and helping in the observing proposal writing stage; Dr. Milorad Stupar of the Macquarie University, for guidance on the IRAF data reduction; A./Prof. Orsola De Marco of the Macquarie University and Dr. Jean-Claude Passy of the University of Victoria, for lectures in hydrodynamic simulations; and Drs. Wendy Noble and Maria Herke, for academic writing courses. I would also like to thank Prof. Simon Jeffery, Prof. Wolf-Rainer Hamann, Dr. Amanda Karakas, Dr. Martin Guerrero, Dr. Thomas Rauch and Nicole Reindl for for illuminating discussions and helpful comments. I would also like to thank Dr. Maria Lugaro (Monash University), Dr. Panayotis Boumis (IAASARS National Observatory of Athens) and Dr. Miriam Peña (National Autonomous University of Mexico), the examiners of my thesis for their careful review, helpful corrections and suggestions that greatly improved the final version.

I would like to thank the Macquarie University for a Macquarie University Research Excellence Scholarship (MQRES). I was also partly supported by a travel grant from the International Astronomical Union (IAU), a travel assistance from the Astronomical Society of Australia (ASA), and a Grants-in-Aid of Research (GIAR) from the National Academy of Science, administered by Sigma Xi, the Scientific Research Society. Thank the staff at the Siding Spring Observatory for their support, especially Donna Burton. I am grateful for the allocation of observing time by the Australian National University Research School of Astronomy and Astrophysics (ANU RSAA). I thank Dr. Anna Kovacevic and Dr. Lizette Guzman-Ramirez for the May 2009 ANU 2.3 m observing run, and Dr. Kyle DePew for the April 2010 ANU 2.3 m observing run. I also thank Dr. Milorad Stupar for assisting me with the 2012 February ANU 2.3 m observing run and Travis Stenborg for assisting me with the 2012 August ANU 2.3 m observing run. Thanks for computing hours awarded by the NCI National Facility at the Australian National University (ANU) and the gSTAR National Facility at Swinburne University of Technology. The NCI National Facility is supported by the Australian Commonwealth Government. The gSTAR National Facility is funded by the Australian Government's Education Investment Fund.

Contents

List of Figures

List of Tables

1

Introduction

1.1 Planetary Nebula: a historical overview

Historically, the Dumbbell nebula was the first Planetary Nebula (PN) observed by Charles Messier in 1764, and was designated as M 27 in his catalogue (now known as the Messier Catalogue; Messier 1781). The final version of Messier catalogue published in 1784 contained three other Planetary Nebulae, M 57, M 76 and M 97. The Ring Nebula (M 57) was independently discovered by Antoine Darquier and Messier in 1779. The Little Dumbbell Nebula (M 76) and the Owl Nebula (M 97) were discovered by Pierre Méchain, and have been added to the Messier Catalogue by 1782. The name *Planetary Nebula* was coined by William Herschel in the 18th century in reference to their resemblance to his recently discovered planet Uranus, while he studied thoroughly the Messier Catalogue. These PNe appeared as a resolved disc in a small telescope and the strong [O III] and Hβ emission lines visually emerge them as ghostly greenish-blue objects, similar to the planet Uranus.

The first spectroscopic observation of PNe were done by Huggins & Miller (1864), one hundred years after the first discovery. They found that the spectrum of the Cat's Eye (NGC 6543) shows a single bright emission line without any continuum emission and absorption features, which was in contrast to those stars previously observed. A year later that line was identified as a Balmer line of hydrogen (Hβ) by them, and it became apparent that two other bright lines so called "nebulium" also exist in these objects. The name was attributed to a hypothetical unknown element nebulium, which were much later found to be produced by forbidden transitions from metastable states of doubly-ionized oxygen (Bowen 1927a,b, 1928). Spectroscopic observations of other brightest planetary nebulae by others astronomers, e.g. Secchi (1867), showed that these three lines are almost common in these objects.

More observations showed the presence of other fainter lines, although Huggins & Miller were not able to correlate them with those already identified in earth laboratories. However, the emergence and development of the atomic theory in the 20th century allowed to identify many low atomic number elements in PNe, such as hydrogen, helium, nitrogen and oxygen. Russell et al. (1926) argued that the nebulium lines could be more attributed to a very abundant element of low atomic number, and might be emitted from transitions of high levels of collisional de-excitation, which cannot be produced in laboratory conditions. Bowen (1928) was the first to identify the previously unknown nebulium lines as [O III] $\lambda\lambda$4959,5007 Å oxygen emission lines, and convincingly identified other lines, namely [N II] $\lambda\lambda$6548,6583 Å (nitrogen), [O II] $\lambda\lambda$3726,3729 Å, [O II] λ4364 Å and [O II] λ7325 Å. Bowen believed that the emission lines more likely arise from the atomic transitions, which is not as dominant as on earth laboratories. Now we know that these transitions are only available in low density regions where collisional de-excitation become dominant, so we cannot observe them in laboratory conditions.

At the beginning of the 20th Century, Menzel (1926) suggested that the entire flux beyond the Lyman limit (912 Å) must be absorbed to produce the Balmer Hβ emission flux. This idea was initially coined by Herschel (1791), who postulated that PNe receive their energy from a nearby star. This idea was not taken seriously for one century, until Hubble (1922) found that the nebular diameter is closely correlated with the stellar magnitude of the central star, and argued that the nebula is probably produced by stellar continuous radiation. A method of deriving the central star temperature developed by Zanstra (1927), which can be used to determine the number of Lyman continuum photons emitted from the flux ratio of the Balmer Hβ line to the stellar continuum. However, the Zanstra temperatures of PNe were found to be significantly higher than those observed at the time. In early 20th century, it was thought that stars evolve from high to low temperatures. Therefore, high stellar temperatures of PNe were believed to be related to young stars. However, Curtis (1918) found that the velocity distributions of PNe could not be associated with young objects, so they should contain late-type stars rather than young stars.

The first step toward theoretical explanation of the origin of PN was made by Shklovsky (1956), who postulated that PNe are descendants of red giants, and their central stars are becoming white dwarfs. By comparison the nebular expansion velocities with escape velocities of red giants, Abell & Goldreich (1966) argued that PNe are the result of the ejected red giant atmospheres, and proposed a number of physical processes to eject the stellar shells. However, the transition from red giant stars to PN to white dwarfs remained poorly understood for more than a decade.

Paczyński (1971) found that the stellar temperature of a red giant star does not change until the stellar envelope is already removed. This meant that the star starts to move toward the PN phase, when the stellar envelope is ejected. Red giant stars show a typical mass loss rate of 10^{-5} M yr^{-1}, and a wind velocity around 10 km s^{-1}. However, Smith & Aller (1969) found that central stars of planetary nebulae show a higher wind velocity of ~ 1000 km s^{-1}. A wind model of the formation of planetary nebula was proposed by Kwok et al. (1978), which indicated that the nebular shell is produced by the interaction of these two winds.

1.2 Planetary Nebula: a theoretical overview

A planetary nebula (PN) is ionized circumstellar material ejected via stellar winds by the precursor asymptotic giant branch (AGB) star with initial masses between 1 and $8M_{\odot}$ (Schönberner 1981; Iben 1995). The stellar evolution of low and intermediate mass stars has been reviewed by Vassiliadis & Wood (1993); Blöcker (1995a,b). The asymptotic giant branch evolution of these stars has been discussed by Becker & Iben (1979, 1980); Iben & Renzini (1983); Schönberner (1983); Vassiliadis & Wood (1993); Iben (1995); Herwig (2005); Karakas et al. (2009, 2010, 2012). Descriptions of the thermal pulses and *s*-process nucleosynthesis have been given by Iben (1975); Iben & Renzini (1983); Iben (1995); Karakas et al. (2002); Herwig (2005). Their post-asymptotic giant branch evolution has been discussed by Schönberner (1981, 1983); Iben & Renzini (1983); Vassiliadis & Wood (1994); Blöcker (1995a,b); Iben (1995); Werner & Herwig (2006). The born-again scenario and final thermal pulse have been described by Iben et al. (1983a); Blöcker (2001); Herwig (2001); Werner (2001); Werner & Herwig (2006). In the following subsections, we briefly summarize the stellar evolution of low and intermediate-mass stars from the main sequence to the white dwarf phase.

1.2.1 From the main sequence to the red giant branch

Stars are born of molecular clouds consisting mostly of hydrogen ($\sim 75\%$) and helium ($\sim 25\%$), along with small quantities of other elements of low atomic number, namely carbon, nitrogen and oxygen, as well as a fraction of heavier elements. A star is formed in a molecular cloud when a part of it starts to collapse under its own gravity, what is now referred to as the *pre-main sequence* stage. As the molecular cloud contracts under its own weight, the gravity increases so more material is attracted. This process results in increasing temperature in the inner regions until it reaches around 10^7 K. At this point proton-burning

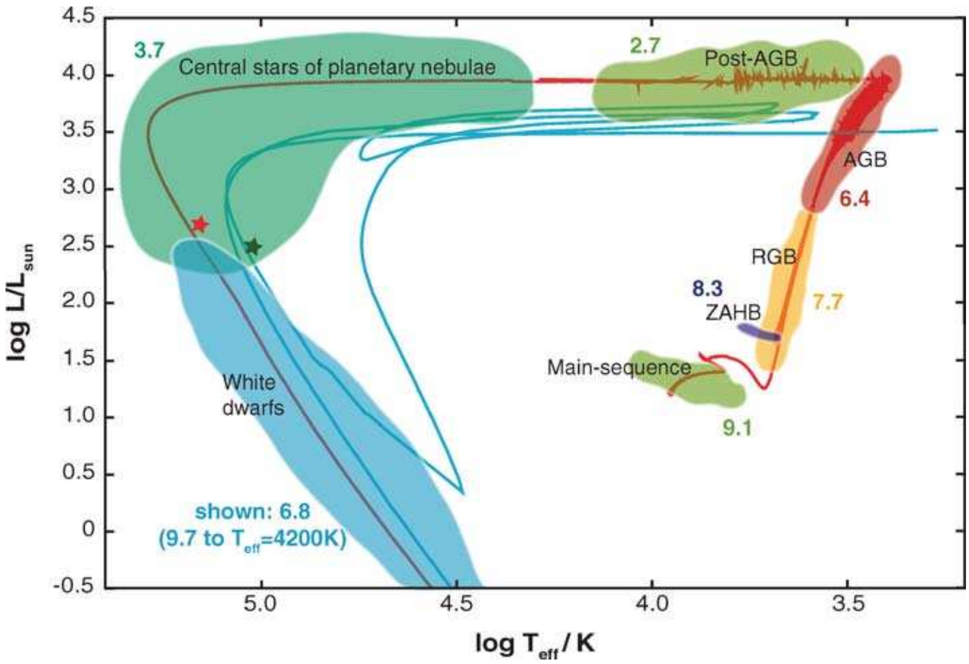

Figure 1.1: Evolutionary tracks of a progenitor star with an initial mass of $2M_{\odot}$ and solar metallicity shown in the Hertzsprung-Russell diagram. The red track shows a normal evolution phase without any late thermal pulse. The blue track shows a born-again event triggered by a very late thermal pulse. The red star shows the position of the H-deficient central stars of the planetary nebula PG 1159-035, and the green star shows the position of the H-normal central stars of the planetary nebula NGC 6853. The number labels indicates the log of the approximate duration of each evolutionary phase in units of 10^3 yr. From Herwig (2005).

reactions take place in the center, so a star is born, i.e. beginning of the main sequence.

All stars spend most of their nuclear-burning life on the *main sequence* (MS) phase, burning hydrogen in their cores (see duration in Fig. 1.1). The MS lifetime directly depends on the initial mass, i.e. low mass star has a longer life, and vice versa. In this phase, hydrogen exhaustion produces helium in the core of low to intermediate mass stars, i.e. $0.8\mathrm{M}_{\odot} < M < 8\mathrm{M}_{\odot}$. A hydrogen nuclear fusion reaction is the main source of their energy radiated by the stellar surface, and provides the radiation pressure to prevent gravitational collapse. This reaction depletes hydrogen in the core, so the helium core contracts. Following core hydrogen exhaustion, hydrogen burning begins in shells around the core and the star moves up the *red giant branch* (RGB) on the Hertzsprung-Russell (H-R) diagram and increases its radius and luminosity, as indicated in Fig. 1.1. The star now enters the first giant branch (FGB), and undergoes the *first dredge-up* (FDU), shown in Fig. 1.2, which brings the fusion products to the stellar surface. The FDU episode increases the surface abundance of ^{4}He, ^{13}C and ^{14}N. But, it decreases ^{12}C due to a part conversion to ^{13}C and ^{14}N. The surface abundance of ^{4}He is increased as hydrogen is depleted via the CN cycle. The FGB is terminated when the star now starts the ignition of helium-burning in its core, as a necessary temperature (about 10^{8} K) higher than those for hydrogen-burning is reached. High mass stars take shorter times to reach a high temperature than low mass stars, so the FGB lifetime depends on the MS mass.

The next stage depends on the progenitor mass. For low mass stars ($< 2.5\mathrm{M}_{\odot}$), the core becomes electron degenerate. This means that the pressure does not depend on the temperature if the necessary temperature for helium burning is reached, a thermonuclear runaway reactions known as the *core helium flash* takes place. Finally, after the core helium flash, increasing temperatures lift electron degeneracy, which stabilize the helium burning reactions. As a result, the stable helium burning takes place in the core while helium-burning occurs in the shell, so the star moves toward the horizontal branch. The core helium flash is short-lived, quickly resulting in stationary helium-burning in the core and a return to hydrogen-burning in the shell. For stars with masses of $\geq 2.5\mathrm{M}_{\odot}$, electron degeneracy never occurs in the core, and they can achieve the critical temperatures (10^{8} K) in the core required to ignite helium. Therefore, there is no helium flash in intermediate mass stars ($\geq 2.5\mathrm{M}_{\odot}$), as seen in

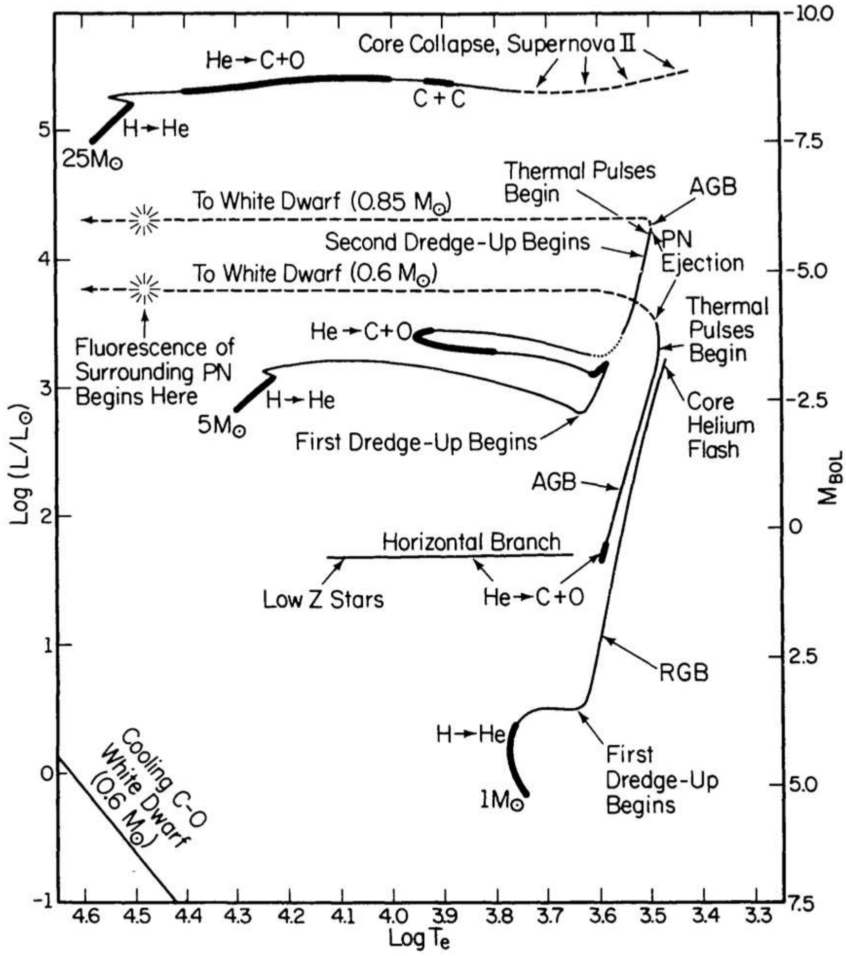

Figure 1.2: Stellar evolutionary tracks for stars with initial masses of 1, 5 and 25 $M_\odot$. The stellar luminosity unit in the solar luminosity $L_\odot$ and the effective temperature unit in Kelvine. The nuclear burning phases are labeled. From Iben (1995)

Fig. 1.2, so the hydrogen shell burns throughout.

The core helium-burning reduces the radius and luminosity of the star, resulting in a higher temperature. The hydrogen-burning continues in a shell around the helium core, while the FDU episode modifies the stellar surface composition. Following core helium exhaustion, the whole star contracts and low to intermediate mass stars move down and to the blue part (higher temperature) of the H-R diagram (see progenitor stars of 1 and 5 $M_\odot$ in Fig. 1.2).

1.2.2 The asymptotic giant branch

The Asymptotic Giant Branch (AGB) phase is the final nuclear burning phase for low- to intermediate-mass stars (Iben & Renzini 1983; Herwig 2005, and references therein). It consists of two main phases: early-AGB and thermally pulsating AGB.

As helium becomes exhausted in the core, helium burning begins in shells around the core and the star evolves towards the *early-asymptotic giant branch* (E-AGB). The carbon and oxygen contract in the inner regions, so the core becomes the electron degenerate, while the outer layer starts a new expansion phase. Fig. 1.3 shows the schematic structure of an AGB star. During the E-AGB, the star burns helium in a shell surrounding the CO core. The He-burning shell is also surrounded by a deep convective envelope of hydrogen. In the intermediate-mass stars ($> 4M_\odot$), as He-burning stopped in the core, the strong expansion extinguishes the hydrogen-burning shell, and similar enrichment to the FDU episode that takes place in the RGB (Becker & Iben 1979).

The *second dredge-up* (SDU) episode transfers the hydrogen-burning products, mainly helium and nitrogen, to the surface in the intermediate-mass stars ($4M_\odot$ to $8M_\odot$). Consequently, ^{4}He and ^{14}N are dredged-up to to the surface, while the surface abundances of ^{12}C, ^{13}C and ^{16}O are decreased. Moreover, the deep convective envelope of hydrogen moves inward in the low-mass stars ($< 4M_\odot$), but the SDU episode does not occur as the hydrogen-burning shell is not extinguished.

Following the E-AGB phase, the helium-burning shell becomes thermally unstable, so thermal pulses (TPs) take place recurrently (Schwarzschild & Härm 1965; Iben 1975; Becker & Iben 1980). This is called the *thermally-pulsing asymptotic giant branch* (TP-AGB) phase; see Fig. 1.2. These thermal pulses,

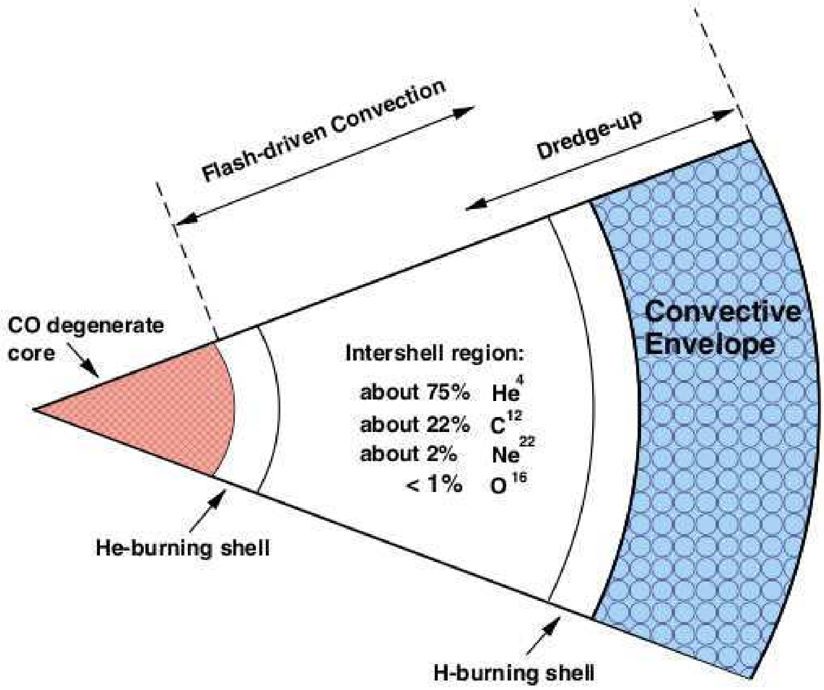

Figure 1.3: A schematic view of the layers of an AGB star, showing the degenerate CO core surrounded by a He-burning shell, a H-burning shell, and a convective envelope. From Karakas & Lugaro (2010).

which occur in both low- and intermediate mass stars, are a consequence of the thinness of the helium-burning shell. This episode causes a series of mixing and nuclear-burning episodes. The TP-AGB leads to the development of two nuclear burning shells around the CO core and the convective envelope. It develops a convection zone between the hydrogen-burning shell and the helium-burning shell. The helium-burning products, ^{12}C and some ^{16}O, are mixed throughout the helium-burning shell. During the TP-AGB phase, the convection envelope penetrates into the inter region and brings carbon and oxygen enriched material to the surface, which is known as the third dredge-up. This process is shown in Fig. 1.4.

Stars with initial masses of $> 1\mathrm{M}_{\odot}$ experience a new episode referred to

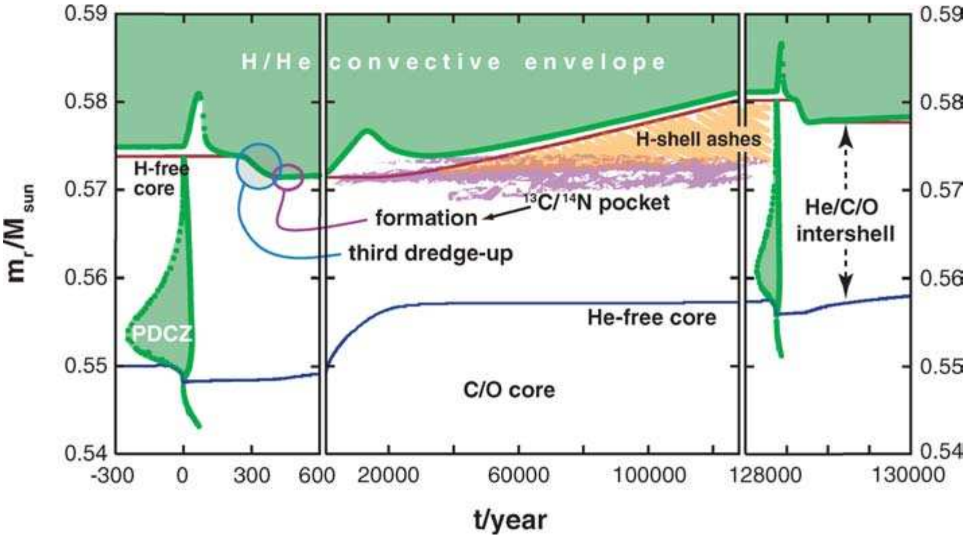

Figure 1.4: Thermal pulse episode of a AGB model of a $2M_{\odot}$ star with metallicity $Z = 0.01$. The red solid line shows the mass coordinate of the H-free core. The convective envelope is shown in green. The layers with H-shell ashes and the region of the 13 C are also shown. From Herwig (2005).

as the *third-dredge up* (TDU), which brings carbon-rich inter-shell material and *s*-process elements into the envelope, and then to the surface. Transportation of fusion products to the surface occurs in two stages; the hydrogen shell is almost extinguished, and the TDU episode bring these *s*-process elements to the surface. The *s*-process elements are produced by low-neutron capturing onto iron group elements. Thus, the TDU is responsible for the carbon and s-process overabundances in the surface. The TDU event may happen several times, which largely enrich the stellar surface.

Fig. 1.5 shows a classification of stars by progenitor mass. It is seen that stars with masses larger than $4M_{\odot}$ experience a competing phenomenon, so called *hot bottom burning* (HBB), which converts ^{12}C to into ^{13}C and then into ^{14}N via the CN-cycle (Iben 1975; Scalo et al. 1975). The initial mass required for a star to experience HBB depends on the metallicity (Karakas & Lattanzio 2007). This physical process occurs at the base of the convection envelope, which makes

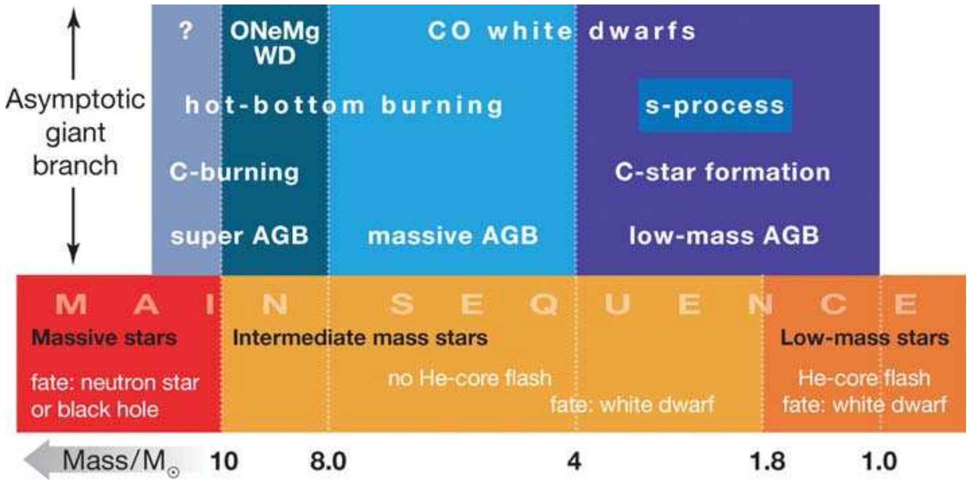

Figure 1.5: Classification of stars by progenitor mass. The lower part is for the main sequence and the upper part is for the AGB. Approximate masses delimiting the different regimes are given at the bottom. Some characterizing properties of the different regimes have been mentioned. From Herwig (2005)

a thin hot (5–8×10^7 K) layer maintaining proton-capture nucleosynthesis. It prevents the stellar surface from becoming C-rich while the TDU is also operating (Boothroyd et al. 1993). It also increases Lithium abundance (^{7}Li) via the so-called Cameron-Fowler mechanism (Cameron & Fowler 1971; Iben 1973; Sackmann et al. 1974), and aluminum (^{26}Al) via the Mg-Al cycle (Mowlavi & Meynet 2000). If the temperature is high enough, ^{16}O is destroyed to produce ^{14}N via the ON-cycle. During the HBB event, the star may also experience mass loss, which has important effects on the evolution of AGB stars.

The *slow-neutron capture process* (or *s*-process) is the capture of neutrons by nuclei in conditions of adequately low neutron densities, so the elements have enough time to decay before another neutron is captured, leading to the production of neutron-rich isotopes. It only happens in low-mass AGB stars ($< 4M_{\odot}$; see Fig. 1.5), which produces half of all elements heavier than iron such as strontium, as well as some lighter elements. After a He-shell flash, the partial mixing in the inter shell produces a pocket containing both ^{12}C and protons, and a low neutron density ($\log N_n \sim 7$ cm^{-3}). During the high temperature of the He-shell flash, the ^{22}Ne–^{25}Mg reaction takes place and produces a high neutron density ($\log N_n \sim 9$–10 cm^{-3}). These two conditions get involved in the *s*-process of low-mass stars. The TDU episode brings up the s-process elements to the surface of the star.

1.2.3 From the post-AGB phase to the white dwarf

During the AGB phase, the star has a steady mass loss with a typical rate of $\sim 10^{-7}$ M yr^{-1} and a slow wind velocity of ~ 10 km $^{-1}$s. In the latest AGB stage, the star suffers several mass loss episodes with a typical rate of $\sim 10^{-3}$ M yr^{-1}, the so-called superwind phase. This results in the removal of most of the star's envelope during a few pulses, and a *post-AGB* star is formed (also known as protoplanetary nebulae or pPNe). As a result, the inner parts of the central star are also exposed. The stellar wind is driven by the radiation pressure, which depends on the stellar temperature. Therefore, high stellar temperatures produce high radiation pressures causing the envelope of the AGB star to eject as the star leaves the AGB phase. The ultraviolet radiation emitted by the hot star ionizes the ejected envelope of the AGB star, and a planetary nebula emerges from the ionized circumstellar material. Post-AGB stars have masses in the range 0.6M$_\odot$–1M$_\odot$, and luminosities around 10^3–10^4L$_\odot$ (Blöcker 1995a).

The star leaves the post-AGB phase with a stellar effective temperature of about 5000 K (see Fig. 1.1). Although a post-AGB star emits radiation over a broad waveband, the temperature of ~ 5000 K is not enough to ionize the circumstellar matter. Leaving the post-AGB, the star moves towards higher effective temperatures of $\gtrsim 30\,000$ K, so a planetary nebula appears. As the star reaches a temperature of about 25,000 K, it can ionize the previously ejected AGB envelope, and it becomes the *central star of a planetary nebula* (CSPN).

Table 1.1: White dwarf spectral classification by McCook & Sion (1999).

Type	Characteristics
DA	Only Balmer lines; no He I or metals present
DB	He I lines; no H or metals
DC	Continuous spectrum, no lines deeper than 5% in any part of the spectrum
DO	He II strong; He I or H present
DZ	Metal lines only; no H or He lines
DQ	Carbon features, either atomic or molecular in any part of the spectrum

The effective temperatures higher than 30 000 K make considerably faster mass-loss with wind velocities up to ~ 2000 km s^{-1} due to higher radiation pressures. The superwind interacts with the previously ejected shell from the AGB phase, creating a high density shell (Kwok et al. 1978). The superwind and the interstellar medium (ISM) compress the shell on both sides, making inner and outer shock-regions. After the CSPN has reached a maximum effective temperature ($\sim 10^5$ to 2×10^5 K), it starts to cool down, resulting in a decrease in the luminosity of the planetary nebula. The planetary nebula continues to expand to larger sizes. This phase lasts around 20,000 years, a small amount of time in comparison to the whole life of the star ($\sim 10^{10}$ years). After around 30,000 to 60,000 years, the nebula has completely faded away in the ISM. The central star continues to cool as a white dwarf. The nebular material dissolves into the interstellar medium, mixing with other existing material, from where a new star may be born.

The *white dwarf* (WD) phase is the final stage of low to intermediate mass single stars. WDs are divided into two groups, namely those with hydrogen-dominated atmosphere (DA), and hydrogen-deficient atmosphere (DB). The hydrogen-dominated atmosphere WDs constitute $\sim 80\%$ of the population. Table 1.1 lists spectral classification codes for white dwarfs by McCook & Sion

(1999). This classification scheme was first introduced by Wesemael et al. (1993). DAs constituting about 80% of the known WDs show only hydrogen lines. DBs have a hydrogen-deficient atmosphere, and show just He I lines. DOs are hot enough to ionize helium, and show strong He II lines. DCs show only continuum and could be very cold helium WDs. DQs shows strong carbon lines, while DZs have strong metal lines.

1.3 Planetary Nebulae: a chemical laboratory

PNe have an important role in Galactic chemical evolution by returning significant enriched material to the ISM. Observations of PNe are used to determine the elemental abundances of the interstellar medium present in our own and other galaxies (e.g. Aller & Czyzak 1983; Kingsburgh & Barlow 1994; Stasińska et al. 1998; García-Rojas et al. 2012). Mixing processes during the progenitor's life (e.g., first and second dredge up prior to the AGB, and third dredge up and hot bottom burning during the AGB) will change the envelope composition of He, C, N and possibly O and Ne (Péquignot et al. 2000; Karakas & Lattanzio 2003; Karakas et al. 2009). Other elements such as S, Ar, and Cl are left untouched by the evolution and nucleosynthesis in low and intermediate-mass stars. For this reason PNe elemental abundances not only reflect the composition of the ISM at the time when the progenitor was born but also can be used to constrain the nucleosynthesis and mixing in AGB stars (e.g. Straniero et al. 1997; Werner & Herwig 2006; Karakas et al. 2009; Stasińska et al. 2013).

The chemical properties of a PN can be determined through plasma diagnostics and empirical analysis using key information carried by the nebular emission lines. The characteristics and evolutionary stage of its ionizing star can be identified using photoionization models, which can be used to determine the physics and time-scales of late stellar evolution of low and intermediate mass stars (e.g. Vassiliadis & Wood 1993; Blöcker 1995b; Perinotto et al. 2004;

Herwig 2005).

1.3.1 Physical conditions: temperature and density

The determination of the electron temperature is necessary for calculating the electron density and elemental abundances. Traditionally, easily observable collisionally excited lines (CELs) are used to determine the temperature. Some lines such as [O III] λ4363 and [N II] λ5755 known as 'auroral' lines depend strongly on temperature. As shown in Fig. 1.6, transition to the ^{1}S level and emission of an 'auroral' line requires more energy than transition to the ^{1}D level and emission of 'nebular' lines, namely [O III] $\lambda\lambda$4959, 5007 and [N II] $\lambda\lambda$6548, 6584. Consequently, it makes the nebular-to-auroral line ratio as a function of the electron temperature. Fig. 1.7 shows the dependence of the temperature-sensitive intensity ratios, notably [O III] $I(\lambda4959+\lambda5007)/I(\lambda4363)$ and [N II] $I(\lambda6548+\lambda6584)/I(\lambda5754)$. Therefore, the temperature weighted by each ion can be inferred by measuring the intensities of their nebular and auroral lines.

However, the temperature determination may be unreliable due to some known issues. First, the electron temperature is not uniform over the nebula. Therefore, the nebular spectra derived from an integration over the whole nebula has a large uncertainty. Table 1.2 lists the line ratios generally used for the electron temperature determination, together with their excitation zones. The temperature derived from high excitation lines such as [O III] may be an upper limit for the mean temperature, while the temperature deduced from low excitation lines such as [N II] could be a lower limit. However, collisionally excitation occurs preferentially in higher temperature regions, so the CELs yield only temperatures of hot regions of the nebula. Additionally, the critical densities of the ^{1}D levels, from which nebular lines arise, have some implications. The nebular lines are collisionally suppressed in a region with a density higher

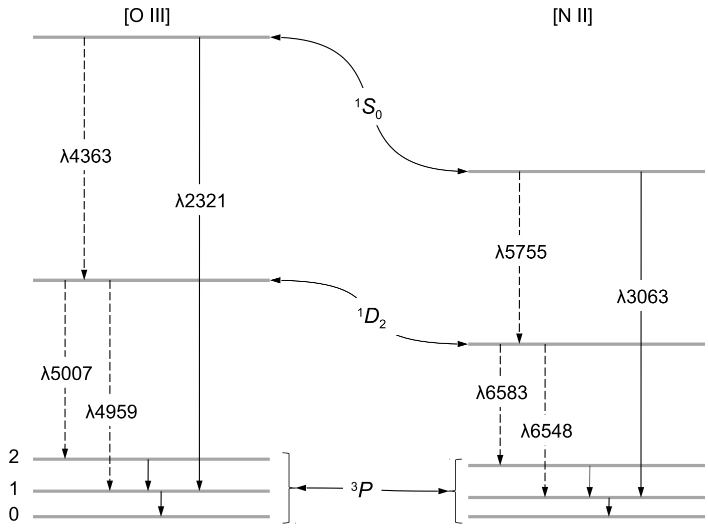

Figure 1.6: Energy-level diagrams of the 2p^3 ground configuration for the lowest terms [O III] and [N II]. From Osterbrock & Ferland (2006).

Table 1.2: Emission line ratios generally used for the electron temperature determination. From Shaw & Dufour (1995).

Ion	Intensity ratio	Excitation
O^0	[O I] $I(\lambda 6300+\lambda 6363)/I(\lambda 5577)$	Low
S^+	[S II] $I(\lambda 6716+\lambda 6731)/I(\lambda 4068+\lambda 4076)$	Low
O^+	[O II] $I(\lambda 3726+\lambda 3729)/I(\lambda 7320+\lambda 7330)$	Low
N^+	[N II] $I(\lambda 6548+\lambda 6583)/I(\lambda 5755)$	Low
Si^{+2}	Si III] $I(\lambda 1883+\lambda 1892)/I(\lambda 1206)$	Med
S^{+2}	[S III] $I(\lambda 9069+\lambda 9532)/I(\lambda 6312)$	Med
Ar^{+2}	[Ar III] $I(\lambda 7136+\lambda 7751)/I(\lambda 5192)$	Med
O^{+2}	[O III] $I(\lambda 4959+\lambda 5007)/I(\lambda 4363)$	Med
Cl^{+3}	[Cl IV] $I(\lambda 7530+\lambda 8045)/I(\lambda 5323)$	Med
Ar^{+3}	[Ar IV] $I(\lambda 4711+\lambda 4740)/I(\lambda 2854+\lambda 2868)$	Med
Ne^{+2}	[Ne III] $I(\lambda 3869+\lambda 3969)/I(\lambda 3342)$	Med
Ar^{+4}	[Ar V] $I(\lambda 6435+\lambda 7006)/I(\lambda 4626)$	High
Ne^{+4}	[Ne V] $I(\lambda 3426+\lambda 3346)/I(\lambda 2975)$	High

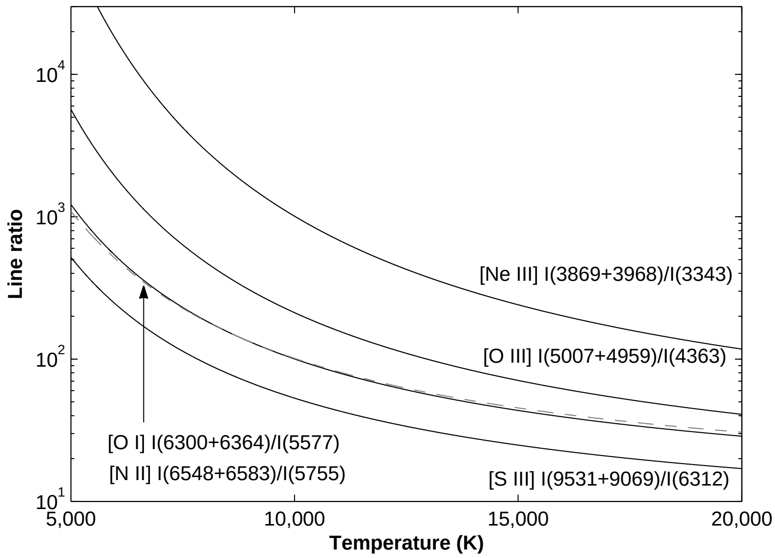

Figure 1.7: Temperature-sensitive line ratios commonly used for temperature determination. Due to similar excitation potential of [O I] (solid line) and [N II] (dashed line), their line ratios are almost coincident. Electron density $N_e = 1$ cm^{-3}. From Osterbrock & Ferland (2006).

than the critical densities. However, the auroral lines may not be suppressed, since they usually have much higher critical densities. This leads to a wrong temperature determination. Finally, the contribution of dielectronic and recombination to the auroral lines is sometime up to 70% and results in a false high temperature measurement (see Chapter 3 for more discussion). The [N II] auroral line may have a very large recombination contribution from the N^{2+} ion, but the [O III] auroral line may be less affected by recombination, as O^{3+} ion is not usually large in the nebula.

The CELs used for the electron density determination have similar excitation energies, but largely different collisional de-excitation rates. Fig. 1.8 illustrates the energy-level for the $2p^3$ ground configuration of [O II] and the $3p^3$ ground configuration of [S II]. The ratio of both lines is density dependent, so by mea-

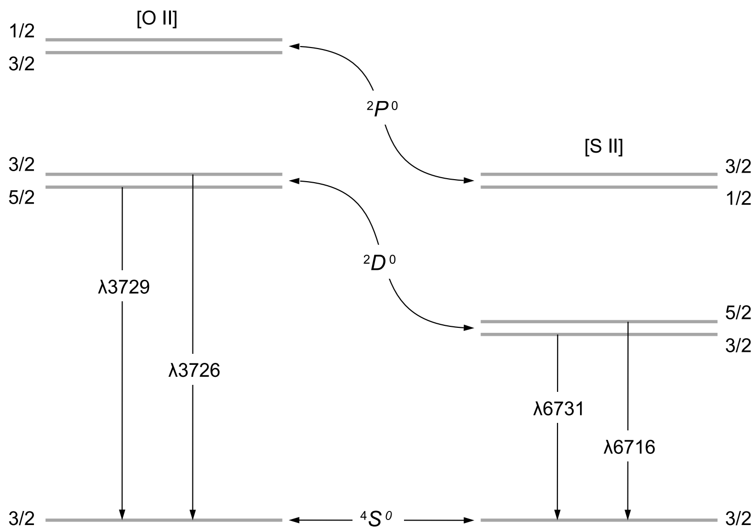

Figure 1.8: Energy-level diagrams of the $2p^3$ ground configuration of [O II] and the $3p^3$ ground configuration of [S II]. From Osterbrock & Ferland (2006).

Table 1.3: Emission line ratios generally used for the electron density determination. From Shaw & Dufour (1995).

Ion	Intensity ratio	Excitation
N^0	[N I] $I(\lambda 5200)/I(\lambda 5198)$	Low
S^+	[S II] $I(\lambda 6716)/I(\lambda 6731)$	Low
C^+	C II] $I(\lambda 2326)/I(\lambda 2328)$	Low
O^+	[O II] $I(\lambda 3729)/I(\lambda 3726)$	Low
Si^{+2}	Si III] $I(\lambda 1883)/I(\lambda 1892)$	Low
Cl^{+2}	[Cl III] $I(\lambda 5517)/I(\lambda 5537)$	Med
N^{+2}	N III] $I(\lambda 1749)/I(\lambda 1752)$	Med
Ar^{+3}	[Ar IV] $I(\lambda 4711)/I(\lambda 4740)$	Med
C^{+2}	C III] $I(\lambda 1907)/I(\lambda 1909)$	Med
O^{+3}	O IV] $I(\lambda 1401)/I(\lambda 1405)$	High
Ne^{+3}	[Ne IV] $I(\lambda 2423)/I(\lambda 2425)$	High

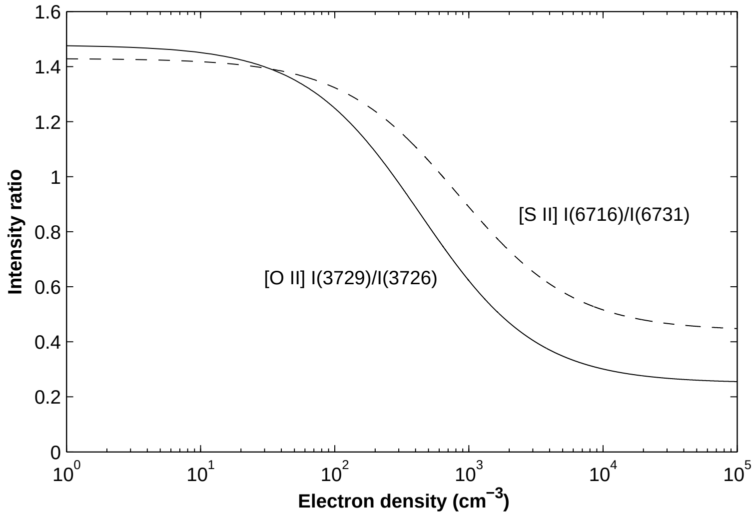

Figure 1.9: Density-sensitive line ratios commonly used for the density determination. Electron temperature $T_e = 10^4$ K. From Osterbrock & Ferland (2006).

suring them the density can be determined. Fig. 1.9 shows the dependence of the density-sensitive intensity ratios, notably [O II] $I(\lambda 3729)$ / $I(\lambda 3726)$ and [S II] $I(\lambda 6716)$ / $I(\lambda 6731)$. Table 1.3 lists the line ratios which can be used for the density temperature determination, together with their excitation zones. The intensity ratios of [O II], [S II], [Cl III] and [Ar IV] are useful density indicators.

The accuracy of the density measurement depends on the critical densities of the upper levels. The measurement may have high uncertainty in a region, where the lines are collisionally excited, but the density is significantly lower than the critical densities. The critical densities of [O II] $\lambda\lambda$3726,3729 and [S II] $\lambda\lambda$6716,6731 lines are around 10^4 cm^{-3}.

1.3.2 Chemical abundances

The intensity of an ionic line relative to a Balmer line (usually Hβ) together with the physical conditions, namely electron temperature and electron density, are used to determine the abundance of an ion, so called ionic abundance. The collisionally excited lines are very strong, so their intensities can be accurately measured. Therefore, they are commonly used for ionic abundance determination. Table 1.4 lists the collisionally excited lines generally used for estimating the ionic abundances of carbon, nitrogen, oxygen, neon, sulfur, chlorine and argon. Alternatively, recombination lines, which have a weak dependence on the nebular physical conditions, can be used for the abundance analysis. Table 1.5 also lists the recombination lines, which are used to determine the abundances of hydrogen and helium.

However, all the ionization stages of an element may not be observed, so the unseen stages of ionization must be estimated using the so-called *ionization correction factors*. The ionization correction factors can be deduced according to the ionization potential of ions (see e.g. Kingsburgh & Barlow 1994). The unseen stages of ionization can be also determined from the photo-ionization models. However, photo-ionization modeling requires a good knowledge of the central star parameters, which are often unknown. Therefore, the ionization correction factors based on similarities between the ionization potential of ions are currently the most acceptable method in the empirical abundance analysis (see e.g. Liu et al. 2001; Tsamis et al. 2003a, 2004; Wesson et al. 2003, 2005; García-Rojas et al. 2009).

1.3.3 Nebular extinction

The nebular extinction can be derived from the Balmer Hα λ6563 and Hβ λ4861 line ratio. It describes the foreground interstellar extinction. It may contain some contribution from the nebular internal dust, i.e. the remnants of

Table 1.4: Collisionally excited lines often used for the ionic abundance determination. From Shaw & Dufour (1995).

Ion	Line	Excitation
C^{+}	C II] $\lambda\lambda$2326,2328	Low
C^{+2}	C III] $\lambda\lambda$1907,1909	Med
N^{0}	[N I] $\lambda\lambda$5198,5200	Low
N^{+}	[N II] λ5755, λ6548, λ6583	Low
N^{+2}	N III] $\lambda\lambda$1749,1752	Med
O^{0}	[O I] λ6300, λ6363	Low
O^{+}	[O II] $\lambda\lambda$3726,3729, $\lambda\lambda$7320,7330	Low
O^{+2}	[O III] λ4363, λ4959, λ5007	Med
O^{+3}	O IV] $\lambda\lambda$1400,01,05,07	High
Ne^{+2}	[Ne III] λ3342, λ3869, λ3968	Med
Ne^{+3}	[Ne IV] $\lambda\lambda$2423,2425, $\lambda\lambda$4724,4725	High
Ne^{+4}	[Ne V] λ2975, λ3426, λ3346	High
S^{+}	[S II] $\lambda\lambda$4068,4076, $\lambda\lambda$6716,6731	Low
S^{+2}	[S III] λ6312, λ9069, λ9532	Med
Cl^{+}	[Cl II] λ3679, λ5807, λ9383	Low
Cl^{+2}	[Cl III] $\lambda\lambda$5517,5537	Med
Cl^{+3}	[Cl IV] λ5323, λ7531, λ8045	Med
Ar^{+2}	[Ar III] λ5192, λ7136, λ7751	Med
Ar^{+2}	[Ar III] λ5192, λ7136, λ7751	Med
Ar^{+3}	[Ar IV] $\lambda\lambda$2854,2868, λ4711, λ4740, λ7170	Med
Ar^{+4}	[Ar V] λ4626, λ6435, λ7006	High

Table 1.5: Recombination lines often used for the abundance analysis.

Ion	Line	Excitation
H^{+}	H I λ4861, λ6563	Low
He^{+}	He I λ4472, λ5876, λ6678	Low
He^{+2}	He II λ4686	Med

the AGB dust envelope.

The logarithmic extinction at Hβ, $c(\mathrm{H}\beta)$, can be obtained from the observed Balmer emission line Hα/Hβ flux ratio:

$$c(\mathrm{H}\beta)_{\mathrm{Balmer}} = \frac{\log_{10}[I(\mathrm{H}\alpha)/I(\mathrm{H}\beta)]_{\mathrm{theory}} - \log_{10}[F(\mathrm{H}\alpha)/F(\mathrm{H}\beta)]_{\mathrm{observ}}}{f(\mathrm{H}\alpha) - f(\mathrm{H}\beta)}, \tag{1.1}$$

where $I(\mathrm{H}\alpha)/I(\mathrm{H}\beta)$ is the theoretical Balmer line ratio ($I(\mathrm{H}\alpha)/I(\mathrm{H}\beta) = 2.86$ for the case B recombination, $T_{\mathrm{e}} = 10\,000$ K and $N_{\mathrm{e}} = 100$ cm^{-3}; Hummer & Storey 1987), $F(\mathrm{H}\alpha)/F(\mathrm{H}\beta)$ is the observed flux ratio, and $f(\lambda)$ is an extinction law for the given wavelength λ. For example, the Galactic extinction law for a total-to-selective extinction ratio of $R_V = 3.1$ was estimated by Howarth (1983).

Alternatively, it is possible to estimate $c(\mathrm{H}\beta)$ through a comparison of the observed radio free–free continuum radiation at 5 GHz with the measured Hβ flux. Using the formula given by Milne & Aller (1975), along with the nebular electron temperature and helium ionic abundances, the extinction $c(\mathrm{H}\beta)_{\mathrm{Radio}}$ is determined from the radio-Hβ method as follows:

$$\begin{aligned} c(\mathrm{H}\beta)_{\mathrm{Radio}} = & \log_{10}\left(\frac{3.28\times10^{-9} S_{5\mathrm{GHz}}\, t^{-0.4}}{\ln(9900 t^{3/2})[1+(1-x'')y+3.7x''y]}\right) \\ & - \log_{10}[F(\mathrm{H}\beta)] \end{aligned} \tag{1.2}$$

where $S_{5\mathrm{GHz}}$ is the observed 5 GHz flux density in Jy, $F(\mathrm{H}\beta)$ the measured Hβ flux in erg cm^{-2} s^{-1}, t is the electron temperature of the nebula in 10^4 K, $y = N(\mathrm{He})/N(\mathrm{H})$ the number abundance of helium and $x'' = N(\mathrm{He}^{++})/N(\mathrm{He})$ the fraction of doubly ionized helium atoms, assuming hydrogen is fully ionized.

1.4 Wolf-Rayet central stars of planetary nebulae

Although most central stars of PNe (CSPNe) have ‘hydrogen-rich’ surface abundances, a considerable fraction ($\lesssim 25\%$) of them show ‘hydrogen-deficient’ fast expanding atmospheres characterized by a large mass-loss rate (Tylenda et al. 1993; Leuenhagen et al. 1996; Leuenhagen & Hamann 1998; Acker & Neiner

2003). Their surface abundances exhibit helium, carbon, oxygen and neon products of the helium burning phase and a post-helium flash (Werner & Herwig 2006). Most of these CSPNe were classified as the carbon-sequence of Wolf-Rayet (or [WC]) stars, resembling those of massive Wolf–Rayet (WR) stars (van der Hucht et al. 1981; van der Hucht 2001), where the square bracket distinguishes them from massive counterparts. About half of them show very high effective temperatures, ranging from 80 000 K to 150 000 K, and are identified as the early-type ([WCE]), including spectral class [WO 1]–[WC5] (Koesterke & Hamann 1997; Peña et al. 1998). Others having surface temperatures between 20-80 kK are called the late-type ([WCL]), containing spectral class [WC 6–11] (Leuenhagen et al. 1996; Leuenhagen & Hamann 1998).

It has been suggested that [WCE] stars are the successors of the [WCL] stars, and evolve further to the [WC]-PG 1159 and then to the PG 1159 stars found in old PNe (Napiwotzki & Schoenberner 1995; Dreizler & Werner 1996; Hamann 1996; Parthasarathy et al. 1998; Werner 2001). The atmosphere of PG 1159 stars are composed mainly of helium, carbon and oxygen. Werner (2001) suggested a 'typical' surface abundance pattern of He:C:N:O = 33:50:2:15 by mass for PG 1159, which is being used for the model atmosphere fluxes of some photoionization models of PNe (e.g. Wright et al. 2011; Danehkar et al. 2013). There is a clear separation of [WC] stars having mass-loss features, but resembling the very hot PG 1159, classified as [WC]-PG 1159 such as those in Abell 30 and 78. They can be placed in a transition between the [WCE] and PG 1159 (Hamann 1996; Parthasarathy et al. 1998), but they have been also found between the [WCE] and [WCL] groups (Werner 2001).

There are a few CSPNe whose stellar emission lines are similar to those of PG 1159, but also exhibiting strong Balmer lines indicating a hydrogen-rich atmosphere such as Abell 43, NGC 7094 and Sh 2-68, the so-called 'hybrid' PG 1159-type stars (Napiwotzki & Schoenberner 1991, 1995; Napiwotzki 1999; Quirion et al. 2005). The hybrid-PG 1159 stars fit neither under hydrogen-rich nor hydrogen-deficient groups. However, they may have a relationship with the PG 1159 stars. They may be a descent from hydrogen-rich [WC] stars, which are still identified as the hydrogen-rich *wels*. Some [WC] stars such as PN G093.9-00.1 show a relatively high H abundance of 15 percent by mass, which might have a link with hybrid-PG 1159 (Werner & Herwig 2006).

These [WR] CSPNe pose challenging problems for stellar evolution theories of low- to intermediate-mass stars. Helium-burning models (Vassiliadis & Wood 1994) still have a thin hydrogen-rich outer layer, so a final helium-shell flash (Iben et al. 1983a) while the star is still in its cooling phase is necessary to remove the hydrogen outer layer, the so-called the born-again scenario. However, the radiation pressure is too small to explain the fast stellar wind and high mass-loss rate seen in both massive and non-massive WR stars (Cassinelli 1991; Dos Santos et al. 1993). Although the multiple scattering of photons (rather than single scattering) can increase the radiation pressure in the theoretical wind model (Lucy & Abbott 1993; Springmann 1994), the multiple-scattering still needs to explain acceleration at large distances far from the stars. The formation of shocks and density inhomogeneities in stellar winds, i.e. the wind clumping (Hillier 1991) add a further complication. As shown by Brown et al. (2004), wind clumps and multiple-scattering are inconsistent with each other, since clumping decreases the momentum, while multiple-scattering increases it. The angular momentum and magnetic field could have some implications for the wind theory (Poe et al. 1989; Biermann & Cassinelli 1993). The wind momentum problem is as yet unexplained in [WR] CSPNe.

The dual-dust chemistry seen in some PNe around cool [WCL] stars (Cohen et al. 1999, 2002; De Marco & Soker 2002) is more likely related to stellar evolution in a binary system. De Marco et al. (2002) suggested two binary scenarios for the formation of [WR] stars. In the first, the spiraling-in companion significantly enhances the AGB stellar mass loss rate, resulting in a hydrogen-deficient post-AGB star. The second scenario involves a merger of a low-mass stellar or planetary companion with the AGB star during the AGB phase. The presence of a circumstellar O-rich disk from a former evolutionary phase of the binary companion during the early AGB can lead to the formation of the dual dust chemistry. Recently, Górny et al. (2010) found more PNe with dual dust chemistry in the Galactic bulge, and speculated that the simultaneous presence of O-rich and C-rich dust is more likely related to the stellar evolution in a close binary system. However, we have not yet found any binary companion in [WR] central stars.

A few central stars of PNe show narrower and weaker emission lines (C IV 5805 Å and C III 5695 Å), which are not identical to those of [WR] classes. They were named weak emission-line stars (*wels*) by Tylenda et al. (1993). They are poorly studied and some of them seem to be hydrogen-rich (Méndez 1991). The number of identified *wels* is surprisingly higher towards the Galactic bulge and closer to the centre of the Galaxy, and apparently originated from different stellar populations than [WR] PNe (Górny et al. 2004, 2009). Previously, Parthasarathy et al. (1998) found that the spectra of some *wels* are very similar to PG 1159 objects, and suggested some of them could be [WC]-PG1159 stars or the transition gap between [WR] and PG 1159 (pre-)white dwarfs. However, the evolutionary link between *wels* and [WR] has not yet been confirmed.

Recently, other classes of hydrogen-deficient CSPNe have been found exhibiting spectra similar to massive WN stars, denoted by [WN] (Todt et al. 2010; Depew et al. 2011; Miszalski et al. 2012; Todt et al. 2013; Frew et al. 2014b). Todt et al. (2010) found that the atmosphere of the CSPN PB 8 contains mass fractions of 55 percent helium, 40 percent hydrogen, 1.3 percent carbon, 2 percent nitrogen, and suggested a spectral type of [WN/C]. Later, the CS of IC 4663 was found to have H:He:C:N:O:Ne = 2 : 95 : 0 : 0.8 : 0.05 : 0.2 (Miszalski et al. 2012). The CSPN Abell 48 is a hydrogen-deficient [WN] star, whose atmosphere consists of 10 percent hydrogen, 85 percent helium, < 0.3 carbon, and 3-5 percent nitrogen (Todt et al. 2013). LMC-N66 was the first PN classified as [WN] (Peña 1995; Peña et al. 2004; Hamann et al. 2003). PMR 5 was another nebula speculated as a [WN] by Morgan et al. (2003). Although [WC] stars have been supposed to be produced by the late thermal pulse (LTP) and the very late thermal pulse (VLTP), and hybrid-[WC] by the AGB final thermal pulse (AFTP) (Blöcker 2001; Herwig 2001; Koesterke 2001; Werner & Herwig 2006), the exact predecessors of [WN]-type stars are still unknown.

1.4.1 Spectral classification

The first classification of the Wolf-Rayet massive Pop I stars was developed by Beals (1938), based on line ratios and emission line features. This classification separated stars into two sequences: nitrogen and carbon. The nitrogen-sequence (WN) shows strong nitrogen lines, whereas the carbon-sequence (WC) shows strong carbon and also oxygen lines. A revised classification has been introduced by Hiltner & Schild (1966), aimed at interpreting the binary star spectra. The revised classification divided the WN sequence into two groups, WN-A and WN-B, based on the strengths and width of the emission lines, WN-A group shows narrow-weak lines and strong continuum, while WN-B group shows broad-strong emission lines. However, none of them are currently used. The line strengths among carbon and nitrogen ions leads to a numerical classification of WN3-WN8 and WC5-WC9 subtypes (Hiltner & Schild 1966; Smith 1968), which was similar to the classification for the 'normal' stars (absorption in spectra) by Morgan et al. (1943). The numerical classification reminds the words 'early-type' and 'late-type' used by Morgan et al. (1943), which are currently used to divide the WR sequence into WRE and WRL. The classification scheme of Smith (1968) has been extended by van der Hucht et al. (1981); Torres et al. (1986); Smith et al. (1990, 1994); Crowther et al. (1995); Kingsburgh et al. (1995). The recent WC classification scheme includes WO1-WO4 subtypes based on the relative strength of oxygen lines (Crowther et al. 1998;

Acker & Neiner 2003). A new WN classification scheme has been introduced by Smith et al. (1996), which is based on the helium line features, ionization, line-width and line-strength, and hydrogen oscillating Balmer/Pickering decrement. Table 1.6 summarized common criteria used to classify the WR stars.

Table 1.7 lists the WO-WC classification criteria by Crowther et al. (1998). The WO subtypes have higher ionization rather than higher oxygen abundance, so they are a higher ionization level of the WC sequence. The subclass numbers reflect an approximate indication of ionization and temperature in the stellar winds. In the WC classification, the word 'early-type' for WO1-4 and WC4-7 and 'late-type' for WC8-11 is attributed to higher ionization and low ionization stellar winds, respectively. Table 1.8 represent the classification scheme for [WR] stars introduced by Acker & Neiner (2003), based line intensities ordered by decreasing ionization potential, in agreement with Crowther et al. (1998). The square brackets distinguish them from the massive WN stars. Stellar wind temperatures and terminal velocities decrease from [WO1] to [WO4] and [WC4] to [WC11]. Acker & Neiner (2003) also denote the word *peculiar* for those [WO] subclass with abnormally wide C IV-5801/12 doublet, which may explain a high terminal wind velocity of $\sim 500\,\mathrm{km\,s^{-1}}$; higher than normal $V_{\infty} \simeq 2000$–$3000\,\mathrm{km\,s^{-1}}$ seen in normal [WO]. Table 1.9 lists the WN classification criteria by Smith et al. (1996), which defines the WN subtypes based on the He II λ5411 / He I λ5875 ratio.

Table 1.6: WR classification criteria for massive Pop I stars. From van der Hucht (2001).

Subclass	Primary	Additional Criteria
WO types	Oxygen emission lines	
WO 1	O VII $>$ O V, O VIII present	C III absent
WO 2	O VII $<$ O V	C IV $<$ O VI, C III absent
WO 3	O VII weak or absent	C IV $\simeq$ O VI, C III absent
WO 4		C IV $\gg$ O VI, C III absent
WC types	Carbon emission lines	
WC 4	C IV strong, C II weak or absent	O V moderate
WC 5	C III $\ll$ C IV	C III $<$ O V
WC 6	C III $\ll$ C IV	C III $>$ O V
WC 7	C III $<$ C IV	C III $\gg$ O V
WC 8	C III $>$ C IV	C II absent, O V weak or absent
WC 9	C III $>$ C IV	C II present, O V weak or absent
WN types	Nitrogen emission lines	
WN 2	N V weak or absent	He II strong
WN 2.5	N V present, N IV absent	
WN 3	N IV $\ll$ N V, N III weak or absent	
WN 4	N IV $\simeq$ N V, N III weak or absent	
WN 4.5	N IV $>$ N V, N III weak or absent	
WN 5	N III $\simeq$ N IV $\simeq$ N V	
WN 6	N III $\simeq$ N IV, N V present but weak	
WN 7	N III $>$ N IV, N III $<$ He II 4686	He I weak P-Cyg
WN 8	N III $\gg$ N IV, N III $\simeq$ He II 4686	He I strong P-Cyg
WN 9	N III $>$ N II, N IV absent	He I P-Cyg
WN 10	N III $\simeq$ N II	Balmer lines, He I P-Cyg
WN 11	N II $\simeq$ He II, N III weak or absent	Balmer lines, He I P-Cyg

Table 1.7: WO-WC classification scheme by Crowther et al. (1998), based on emission equivalent width ratios (W_λ) or dereddened line flux ratios (I_λ).

Subtype	FWHM(Å)	Primary	Secondary	Additional Criteria	Example PNe
	C IV λ5808	O VI λ3818/O V λ5590	O VI λ3818/C IV λ5808	O VII λ5670/O V λ5590	
		$\log W_\lambda$	$\log W_\lambda$	$\log W_\lambda$	
WO 1	40 ± 10	≥ 1.1	$\geq +0.2$	≥ 0.0	PB 6, M 3-30, NGC 2452, NGC 5189
WO 2	160 ± 20	$+0.6$ to $+1.1$	$\geq +0.2$	≤ 0.0	NGC 6905, NGC 2867, Sand 4
WO 3	90 ± 30	$+0.25$ to $+0.6$	-1 to $+0.2$	$\ll 0.0$	Hb 4, IC 1297, Hen 2-55, NGC 6369
WO 4	60 ± 30	-0.3 to $+0.25$	-1.5 to -1	$\ll 0.0$	Pe 1-1, NGC 1501, PC 14, NGC 5315
	C IV λ5808	C IV λ5808/C III λ5696	C III λ5696/O III-V λ5590	O VI λ3818/C IV λ5808	
		$\log W_\lambda$ or $\log I_\lambda$	$\log W_\lambda$ or $\log I_\lambda$	$\log W_\lambda$	
WC 4	70 ± 20	≥ 1.5	≤ -0.4	≤ -1.5	M 3-15, NGC 5315, Hen 2-86, H 1-29
WC 5	50 ± 20	$+1.1$ to $+1.5$	-0.4 to $+0.5$	≤ -1.5	M 1-25, HD165763, M 2-20
WC 6	50 ± 20	$+0.6$ to $+1.1$	$+0.0$ to $+0.7$	≤ -1.5	HD 92806
WC 7	45 ± 20	$+0.1$ to $+0.6$	≥ 0.1	≤ -1.5	HD 156327, M 2-43
	C III λ5696	C IV λ5808/C III λ5696	C IV λ5808/C II λ4267	He II λ4686/He I λ5876	
		$\log W_\lambda$ or $\log I_\lambda$	$\log W_\lambda$	$\log W_\lambda$	
WC 8	40 ± 10	-0.3 to $+0.1$	≥ 1.0	≥ 0.1	NGC 40, HD 192103
WC 9	30 ± 15	-0.7 to -0.3	-0.2 to $+1.0$	-0.8 to $+0.1$	Hen 2-142, Hen 2-99, Pe 1-7, Hen 2-459
WC 10	3 to 6	-1.2 to -0.7	-1.5 to -0.2	≤ -0.8	Hen 3-1333, Hen 2-113
WC 11	~ 3	≤ -1.2	≤ -1.5	He II λ4686 absent	K 2-16

Table 1.8: [WO]-[WC] classification scheme by Acker & Neiner (2003), based on dereddened line intensities (I_λ) relative to C IV 5806 = 100.

[WO]	FWHM(A) C IV 5808	O VIII 6068	O VII 5666	O VI 5290	O VI 3822	O V 5590	C IV 7060	C IV 4650	C IV 5470	He II 5412	He II 4686
[WO1]	33 ± 5	20 ± 8	> 25	> 80	> 1400		35 ± 20	300 ± 100	35 ± 5	45 ± 15	500 ± 200
[WO2]	32 ± 3	6 ± 1	10:	48 ± 2	1000 ± 200		18 ± 4	270 ± 60	23 ± 2	20 ± 4	300 ± 30
[WO3]	37 ± 6	2 ± 1	8 ± 6	20 ± 5	250 ± 40	27 ± 5	15 ± 4	140 ± 60	14 ± 2	15 ± 4	130 ± 30
[WO4]	52 ± 6		10:	3 ± 1	10 ± 6	9 ± 5	$3.5 \pm .5$	55 ± 10	4 ± 2	4 ± 2	25 ± 15
[WO4]$_{pec}$	80 ± 2		1.5 ± 1	3 ± 1	10 ± 6	4 ± 1	3 ± 1	35 ± 10	4 ± 2	3 ± 2	230 ± 20
[WC]	FWHM(A) C IV/III	C III 6730	C III 5696	C III 4649	C III 7037	C II 4267	C II 6461	C II 7118	C II 7058	C III 7235	C III 5696/ O III 5592
[WC4]	37 ± 8	1:	< 1	70 ± 20	< 1		< 1	2:	2:	1:	< 0.5
[WC5-6]	25 ± 3	10:	10 ± 3	210 ± 30		12:	6:	10 ± 5	13:	7 ± 5	4 ± 3
[WC7-8]	22 ± 3	35:	60 ± 30	360:	7:		4:	12:		15:	8 ± 2
[WC9]	25 ± 9	40 ± 10	260 ± 100	360 ± 60	15 ± 6	130 ± 50	10 ± 4	18 ± 2	8 ± 4	70 ± 20	25 ± 10
[WC9]$_{pec}$	80 ± 2	28	550	740	15 ± 6	100	16	10 ± 5		150	110
[WC10]	56 ± 1		850 ± 150	> 1000	200 ± 60	> 1500	270 ± 80	300:	300 ± 100	>2000	70 ± 30
[WC11]	52 ± 6		> 1000			> 1400	500:			> 3000	

Table 1.9: WN classification scheme by Smith et al. (1996).

Subclass	Primary		Secondary		Additional Criteria	
	He II 5411/He I 5875		N V 4604/N III 4640	N IV 4057/N V,III 4604-40	C IV 5808/He II 5411	C IV 5808/He I 5875
	I_λ	W_λ	I_λ	I_λ	I_λ	I_λ
WN 2	No He I	No He I	No N V	No N IV	No C IV	No C IV
WN 3	> 10	> 9	No N III	< 0.1	< 0.2	both weak
WN 4	4 to 10	3 to 9	> 2	0.6	0.2 to 0.8	2 to 10
WN 5	1.25 to 8	1 to 6	0.5 to 2	1.25 to 2.5	0.6 to 2.0	1.5 to 5
WN 6	0.65 to 1.25	1 to 3	0.2 to 0.5	0.8	0.3 to 0.6	0.5 to 1.5
WN 7	0.65 to 1.25	0.5 to 1	0.1 to 0.25	0.6	< 0.5	0.15 to 0.5
WN 8	0.1 to 0.65	0.1 to 0.5	0.05 to 0.25	0.2	< 0.4	< 0.15
WN 9	< 0.1		0.05 to 0.25	< 0.1?		

1.4.2 Evolutionary scenarios

Three thermal pulse scenarios have been proposed to describe the formation of Wolf-Rayet central stars of planetary nebulae (Blöcker 2001; Herwig 2001; Koesterke 2001; Werner 2001; Werner & Herwig 2006). Fig 1.10 depicts three different evolutionary tracks for a star with an initial mass of $2M_{\odot}$. Thermal pulses normally occur during the AGB phase, when the helium-burning shell becomes thermally unstable. However, the occurrence of the thermal pulse in the post-AGB phase can result in a hydrogen-deficient central star. The surface abundances of a hydrogen-deficient star strongly depend on the occurrence time of a thermal pulse beyond the AGB phase:

- **AFTP.** The AGB final thermal pulse (AFTP) occurs at the end of the AGB, when the envelope has a very low mass of $\sim 10^{-2}M_{\odot}$ and the central star has not yet gone through a CSPN phase. This process dilutes the surface abundance of hydrogen, while it enriches carbon and oxygen. The AFTP makes H-deficient surface abundances, but the remaining hydrogen fraction is very high (15% $>$ by mass). Therefore, it cannot explain the typical surface abundances of [WR] stars. However, it may naturally explain the relatively high hydrogen abundances in the hybrid-PG1159 stars and some [WC] stars.

- **LTP.** The late thermal pulse (LTP) occurs when the star moves from the AGB phase towards the white dwarf with constant luminosity, and the central star has recently evolved through a CSPN phase. The hydrogen surface abundance remains unchanged through the thermal pulse. A hydrogen-deficient surface is produced only when the star returns to the AGB phase, the so-called *born-again* event, and a dredge-up mixing process decreases hydrogen at the surface to a few percent ($\lesssim 5\%$) by mass.

- **VLTP.** The very late thermal pulse (VLTP) occurs when the star is on the white dwarf cooling track. The hydrogen surface abundance is completely mixed into hot inner layers during the thermal pulse, and convective hydrogen burning produces a hydrogen free star. Then, the star returns to the AGB phase, i.e. *born-again* scenario, which has been considered as the most promising explanation for the formation of WR CSPNe. The difference between LTP and VLTP is that the dredge-up mixing process decreases hydrogen in the LTP born-again scenario, whereas nuclear hydrogen burning and H-ingestion flash consume hydrogen at the surface in the VLTP scenario. Moreover, the VLTP event has two returns to the AGB; the first-return happens quickly in a few years, whereas the second-return takes longer around 10^2 yr. During the VLTP, the H-ingestion flash produces a few percent (1-4% by mass) nitrogen at the surface. The surface nitrogen abundance is typically around 0.1%, even if the star has experienced the HBB (without VLTP). Therefore, the presence of nitrogen in the stellar spectra may be an indicator of a VLTP.

Fig. 1.11 summarized all three different thermal pulse scenarios and their possible paths. Different paths have been identified by the surface abundances of hydrogen, nitrogen and carbon. DA denotes white dwarfs with H-rich surface, DB for roughly pure neutral helium surface, DO for roughly pure ionized helium surface, DOA for hydrogen-rich with a very small fraction of ionized helium, DQ for helium dominated atmosphere enriched with carbon, and DxV for variable Dx stars. O(He) stars are extremely hot H-deficient object with almost pure He absorption-line. R Coronae Borealis (RCrB) are the prototype of variable stars, having H-deficient and C-rich atmospheric abundances.

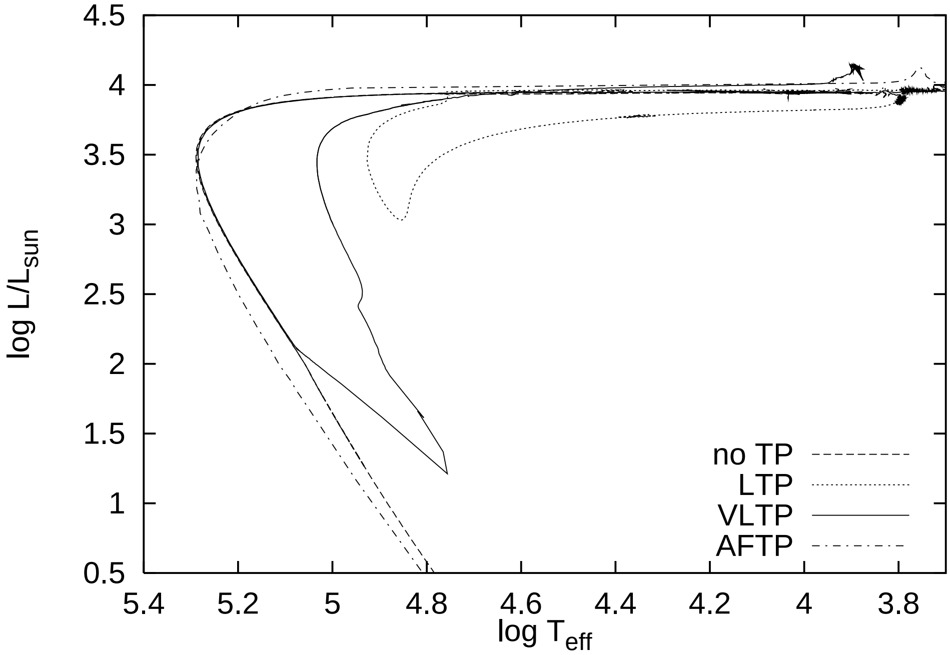

Figure 1.10: Post-AGB evolutionary tracks in the H-R diagram for a progenitor star with an initial mass of $2M_{\odot}$, and evolved through four different tracks: normal evolution phase without any late thermal pulse (dashed line), born-again event triggered by late thermal pulse (dot line) and very late thermal pulse (solid line), and final dredge-up phase, so called the AGB final thermal pulse (dot-dashed line). From Herwig (2001).

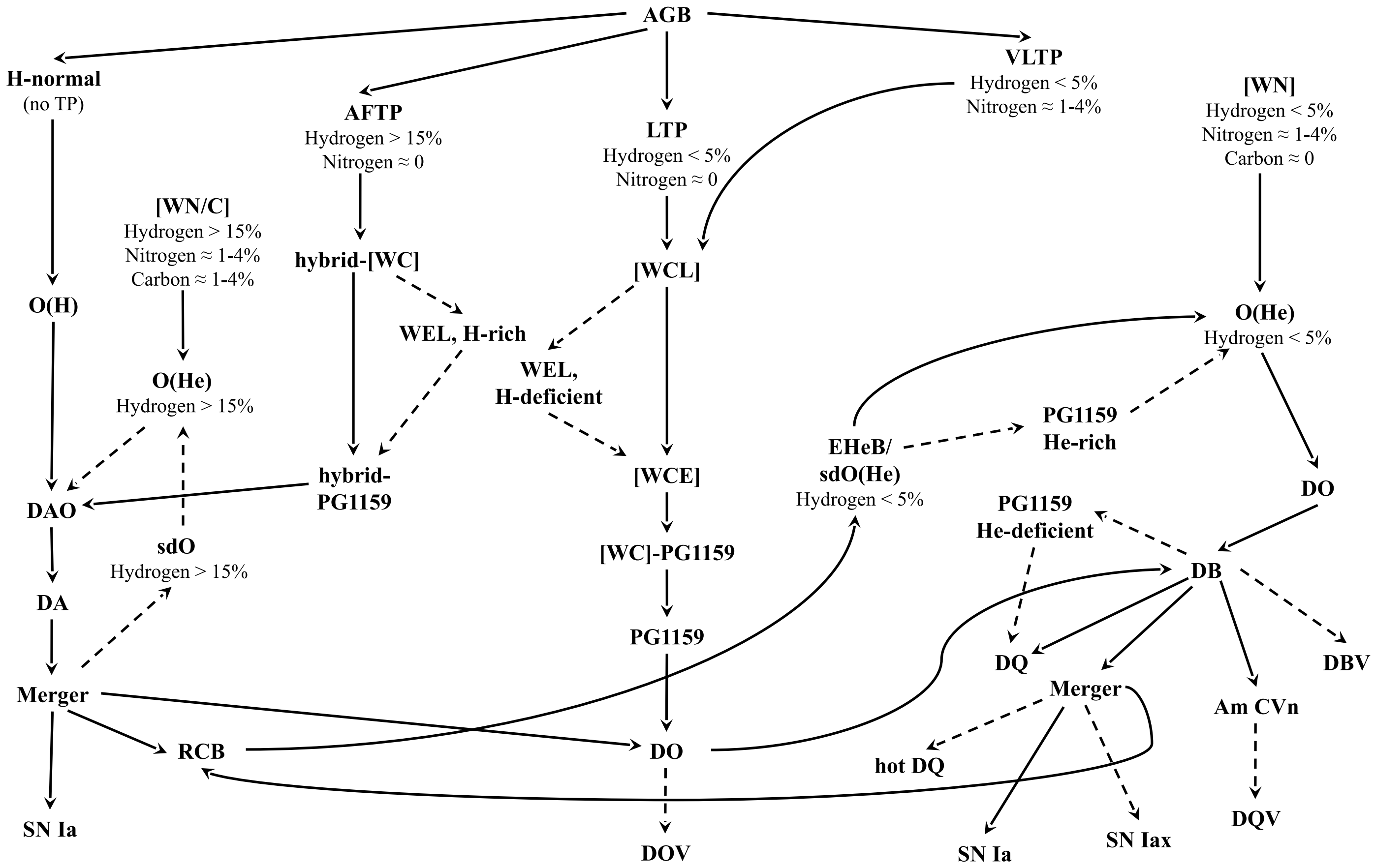

Figure 1.11: Post-AGB evolutionary paths of central stars of planetary nebulae. 'AFTP' stands for AGB final thermal pulse, 'LTP' for late thermal pulse, 'VLTP' for very late thermal pulse, [WC] for H-deficient Wolf–Rayet (WR) central star of PN with C-rich stellar atmosphere-abundances, [WN] for WR star with surface-abundances of N $\approx$ 1-4% and C $\approx$ 0, [WNC] for WR star with N $\approx$ C $\approx$ 1-4% (by mass). 'DA' white dwarfs are H-rich surface, 'DB' nearly pure neutral helium surface, 'DO' nearly pure ionized helium surface, 'DOA' hydrogen-rich with a very small fraction of ionized helium, and 'DQ' helium dominated atmosphere enriched with carbon, and 'DxV' for variable 'Dx' stars. O(He) stars are extremely hot H-deficient object with almost pure He absorption-line. R Coronae Borealis (RCB) are the prototype of variable stars, having H-deficient and C-rich atmospheric abundances. Summarized from the literature.

1.4.3 [WCE] central stars of planetary nebulae

In this subsection and the next subsection, we present a synopsis of some early- to late-type carbon-sequence WR-type CSPNe. The kinematics and chemical abundances of their PNe are studied in Chapters 2 and 3, respectively.

PB 6 (= PN G278.8+04.9). PB 6 is a very high excitation PN, ionized by an early-type hot [WR]. Tylenda et al. (1993) classified the CSPN of PB 6 as [WC 3] based on the classification scheme of van der Hucht et al. (1981) and Méndez & Niemela (1982). But, Crowther et al. (1998) suggested a [WO 1] star. The [WO] classification of [WR] stars (with subclasses [WO 1–4]) was first defined by Barlow & Hummer (1982). The oxygen-sequence of CSPNe with optical WR-like spectra was first found by Smith & Aller (1969). The O VI features of this [WR] was found by Kaler et al. (1991) earlier. Acker & Neiner (2003) estimated the stellar temperature at $T_\star = 102$ kK, while Peña et al. (1998) earlier obtained a much hotter $T_\star = 158$ kK from expanding model atmospheres and photoionization models. Previously, Sion et al. (1985) suggested that the Wolf-Rayet CSPNe with O VI features are the predecessor of PG 1159-type stars, and PB 6 with a hot [WO 1] is indeed transitioning to this type.

M 3-30 (= PN G017.9−04.8). The CSPN M 3-30 is another star with the O VI features detected by Kaler & Shaw (1984). Acker & Neiner (2003) classified it as [WO 1] following the classification scheme of Crowther et al. (1998). The stellar temperature was estimated to be $T_\star = 49$ kK by Acker & Neiner (2003). But, Kaler & Shaw (1984) first determined the He II Zanstra temperature as $T_{\rm Z}(\text{He II}) = 126$ kK, but $T_{\rm Z}(\text{H I}) = 65$ kK for the hydrogen. However, Gleizes et al. (1989) obtained $T_{\rm Z}(\text{H I}) = 34.5$ kK and $T_{\rm Z}(\text{He II}) = 58{:}$ kK. Stanghellini et al. (1993) calculated the Zanstra temperature using the fluxes and magnitudes of Tylenda et al. (1991), and gave $T_{\rm eff} = 90$ kK and the stellar luminosity of $L/{\rm L}_\odot = 9000$ at the distance $D = 4.6$ kpc. The CSPN M 3-30 is an example of the hot [WCE] that is in transition into [WC]-PG 1159, and then

PG 1159 (see e.g. Werner & Herwig 2006). Parthasarathy et al. (1998) found that some stars formerly classified as the weak emission line stars (*wels*) can fill the evolutionary gap between [WC] and PG 1159, as the [WC]-PG 1159 class.

Hb 4 (= PN G003.1+02.9). The CSPN Hb 4 was first determined as a carbon-sequence [WR] star by Aller & Keyes (1985). Tylenda et al. (1993) and Acker & Neiner (2003) classified it under [WC 3–4] and [WO 3], respectively. Preite-Martinez et al. (1989) determined $T_{\rm EB} = 85.4$ kK using the Energy-Balance (EB) method prescribed by Preite-Martinez & Pottasch (1983). Acker & Neiner (2003) adopted the same value of the stellar temperature in their classification scheme. Moreover, Stasińska & Tylenda (1990) determined $T_{\rm eff} = 89$ kK using the Zanstra method, where $T_{\rm eff} = T_{\rm z}({\rm He~II})$ if $T_{\rm z}({\rm He~II}) > T_{\rm z}({\rm H~I})$, otherwise $T_{\rm eff} = [T_{\rm z}({\rm H~I}) + T_{\rm z}({\rm He~II})]/2$. Previously, Shaw & Kaler (1989) also found $T_{\rm z}({\rm He~II}) = 89$ kK, while $T_{\rm z}({\rm H~I}) = 63.1$ kK (see Table 3 in Acker & Neiner 2003). We know that the EB method (Preite-Martinez & Pottasch 1983) presents a more reliable temperature than the Zanstra method what has an unexplained discrepancy between $T_{\rm z}({\rm H~I})$ and $T_{\rm z}({\rm He~II})$. But, the photoionization model using a black-body atmosphere by Acker et al. (2002) estimated the stellar parameters for Hb 4 as $T_{\rm eff} = 90$ kK and $L/{\rm L}_{\odot} = 3980$ at the distance of $D = 4$ kpc.

IC 1297 (= PN G358.3−21.6). The CSPN IC 1297 was classified as [WC 3] and [WO 3] by Tylenda et al. (1993) and Acker & Neiner (2003), respectively. Previously, Gleizes et al. (1989) identified its stellar spectra as [WC 4]. Shaw & Kaler (1989) determined $T_{\rm z}({\rm He~II}) = 94 \pm 5$ kK from the total Hβ and He II line fluxes, $L/{\rm L}_{\odot} = 8900 \pm 2000$ via the stellar magnitudes $B = 14.77$ and $V = 14.22$ and the Shklovsky distance $D = 4.86$ kpc. Moreover, Gleizes et al. (1989) adopted $T_{\star} = 92$ kK from $T_{\rm z}({\rm H~I}) = 86$ kK and $T_{\rm z}({\rm He~II}) = 98$ kK. Acker & Neiner (2003) calculated $T_{\rm EB} = 91.2$ kK using the same method described in Preite-Martinez et al. (1989, 1991) in conjunction with the EB method of Preite-Martinez & Pottasch (1983).

Th 2-A (= PN G306.4−00.6). Weidmann et al. (2008) classified the CSPN

Th 2-A as of type [WO 3]$_{\rm pec}$, belonging to those with a *peculiar* C IV-5801/12 doublet according to the classification scheme of Acker & Neiner (2003). Fig. 1.12 shows our observed C IV-5805 doublet line profile of the CSPN Th 2-A: it has a wide FWHM of 86 Å that is associated with a terminal velocity of $V_\infty = 5366\,{\rm km\,s^{-1}}$; according to the factor $V_\infty({\rm km/s}) = 62.4 \times FWHM({\rm \AA})$ introduced by Acker & Neiner (2003). This terminal velocity is higher than typically obtained for other [WO] stars $V_\infty \simeq 2000$–$3000\,{\rm km\,s^{-1}}$, and is similar to what measured in [WO 4]$_{\rm pec}$. We found that the PN has an excitation class of $EC = 7.2$ (EC formula of Dopita & Meatheringham 1990) associated with the effective temperature $T_{\rm eff} = 162\,{\rm kK}$ based on the $T_{\rm eff}$–EC relation of Magellanic Cloud PNe (Dopita & Meatheringham 1991). Furthermore, Preite-Martinez et al. (1989) obtained $T_{\rm EB} = 157.2\,{\rm kK}$ from the EB method. Adopting the distance of $D = 2.07\,{\rm kpc}$ (Phillips 2004) and ${\rm E}(B-V) = 0.703$, we calculated $L/{\rm L}_\odot = 5240$ for $V = 17.08\,{\rm mag}$ (Ciardullo et al. 1999) and $T_{\rm eff} = 157\,{\rm kK}$. This associates the central star with a progenitor mass of $4{\rm M}_\odot$ according to its position on the HR diagram.

Pe 1-1 (= PN G285.4+01.5). The C IV-5805 feature of CSPN Pe 1-1 was earlier found by Webster (1975), who assigned the [WR]-type spectral class. Tylenda et al. (1993) and Acker & Neiner (2003) identified it as [WC 4–5] and [WO 4], respectively. Gleizes et al. (1989) derived $T_{\rm Z}({\rm H\,I}) = 78\,{\rm kK}$, while Preite-Martinez et al. (1989) got $T_{\rm EB}({\rm H\,I}) = 85\,{\rm kK}$. Acker & Neiner (2003) adopted the temperture derived from the EB method for their stellar classification, as it is usually more reliable than the Zanstra method. The correct determination of the stellar luminosity depends on the accurate distance. Zhang (1995) determined a distance of $D = 3.75\,{\rm kpc}$ using the statistical method based on the ionized mass–radius correlation and the radio continuum surface brightness temperature–radius correlation. Phillips (2004) obtained $D = 4.16\,{\rm kpc}$ through the radio continuum 5-GHz source luminosity–surface brightness temperature correlation and the surface brightness temperature–radius correlation. How-

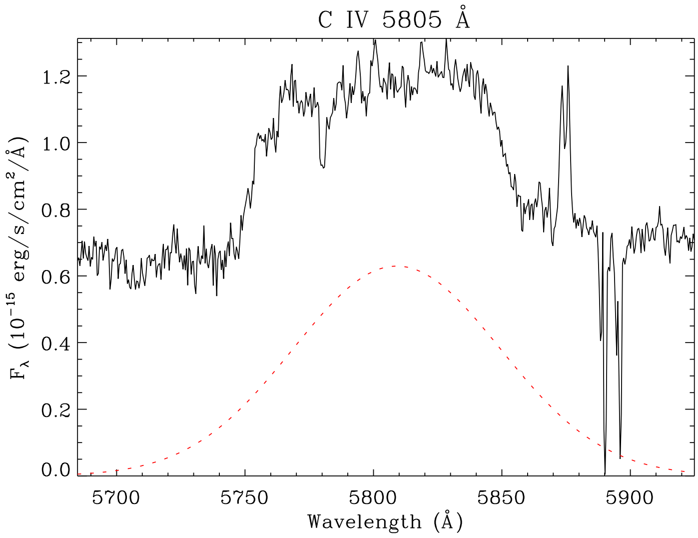

Figure 1.12: The C IV-5801/12 doublet line profile of the central star $[\mathrm{WO}\,3]_{\mathrm{pec}}$ of Th 2-A. The dotted line (red color) shows the Gaussian component that best-fits the observed line profile (black solid line).

ever, Tajitsu & Tamura (1998) reduced the distance to $D = 2$ kpc by fitting black-body curves to the IRAS four-band fluxes (12, 25, 60 and 100 μm). Adopting $T_{\mathrm{eff}} = 85$ kK and $D = 3.5$ kpc, Acker et al. (2002) derived $L/\mathrm{L}_{\odot} = 1995$ from the best photo-ionization model matched to the nebula parameters, that places it in the post-AGB evolutionary track of a progenitor mass of about 2–3$\mathrm{M}_{\odot}$ according to the HR diagram (see Fig. 2.1).

M 1-32 (= PN G285.4+01.5). Acker & Neiner (2003) classified the CSPN M 1-32 under the *peculiar* $[\mathrm{WO}\,4]_{\mathrm{pec}}$ subclass according to the wide FWHM of C IV-5801/12 doublet of 80 Å, denoting a high terminal velocity of $V_{\infty} \simeq 4900\,\mathrm{km\,s^{-1}}$; typically higher than normal $V_{\infty} \simeq 2000$–$3000\,\mathrm{km\,s^{-1}}$ observed in usual [WO] CSPNe. Previously, Tylenda et al. (1993) identified the spectra class as [WC 4–5]. The 5 GHz-radio continuum brightness temperature of $T_b = 53.2$ K corresponds to the stellar temperature of $T_{\star} = 66$ kK at the evolutionary track of 0.598$\mathrm{M}_{\odot}$ (Zhang & Kwok 1993). The peculiar terminal velocity of this [WR] is not consistent with low- to intermediate-mass progenitors and low effective temperatures, so FWHM of C IV λ5805 may have some contributions of He II or other elements. Assuming that the high terminal velocity is a real property, other mechanism must be responsible for the wind momentum, as even the multiple-scattering radiation pressure is too low to derive such high terminal velocity and mass-loss rate.

M 3-15 (= PN G006.8+04.1). The CSPN M 3-15 was first assessed as the [WR] carbon sequence by Aller & Keyes (1985). It was classified within subclasses [WC 4–6] by Tylenda et al. (1993). Aller & Keyes (1987) obtained the stellar temperature of $T_{\star} = 62.5$ kK by using the non-LTE model atmosphere by Husfeld et al. (1984). Moreover, Preite-Martinez et al. (1991) determined $T_{\rm EB} = 55.3$ kK. But, van Hoof & van de Steene (1999) and Acker et al. (2002) obtained $T_{\star} = 82.4$ kK and $L/{\rm L}_{\odot} = 4600$, and $T_{\star} = 79$ kK and $L/{\rm L}_{\odot} = 3980$ through photoionization modeling using a blackbody atmosphere, respectively. Acker & Neiner (2003) also proposed that it belongs to the subclass [WC 4] in agreement with the classification scheme of Crowther et al. (1998). Using the photoionization model, Gesicki & Zijlstra (2007) estimated a stellar black-body temperature of $T_{\star} = 79$ kK, a stellar luminosity of $L/{\rm L}_{\odot} = 6100$ and a stellar mass of $0.609{\rm M}_{\odot}$ from the H-burning evolutionary models of Blöcker (1995a). This locates M 3-15 in the evolutionary track that transitions into hot [WO] sequences.

M 1-25 (= PN G004.9+04.9). The classification scheme of Acker & Neiner (2003) places the CSPN M 1-25 in the subclasses [WC 5–6], in the transition from [WCL] to [WO] theoretically (see e.g. Werner 2001). It has been classified as [WC 6] and [WC 5] by Tylenda et al. (1993) and Crowther et al. (1998), respectively. The He II Zanstra temperature of $T_{\rm Z}({\rm He\ II}) = 73$ kK was determined by Gleizes et al. (1989), while Preite-Martinez et al. (1989) found $T_{\rm EB} = 55.9$ kK. Photoionization models done by Acker et al. (2002) and Gesicki & Zijlstra (2007) represented a stellar black-body temperature of $T_{\star} = 42$ kK and $L/{\rm L}_{\odot} = 6300$ at the distance of $D = 8$ kpc, which puts this PN in the Galactic Bulge. A mean distance of $D = 4.2$ kpc is obtained from all the distances listed in the Acker et al. (1992) catalog.

1.4.4 [WCL] central stars of planetary nebulae

Hen 2-142 (= PN G327.1−02.2). The CSPN Hen 2-142 was classified as [WC 9] (late-type [WR]) by Tylenda et al. (1993). The stellar temperature is relativity cool in comparison to early-type [WC]. The H I Zanstra temperature of $T_z(\mathrm{H\ I}) = 29.2$ kK and 44.5 kK were determined by Piliugin & Khromov (1979) and Gleizes et al. (1989), receptively. The He II Zanstra temperature of $T_z(\mathrm{He\ II}) = 36$ kK was obtained by Shaw & Kaler (1989), whereas Stanghellini et al. (1993) found $T_z(\mathrm{He\ II}) = 65$ kK. Furthermore, Preite-Martinez et al. (1989) derived $T_{\mathrm{EB}} = 25.9$ kK. However, photoionization models implemented by Acker et al. (2002) and Gesicki & Zijlstra (2007) represent $T_{\mathrm{eff}} = 26$ kK, $L/\mathrm{L}_{\odot} = 5000$ at the distance of $D = 3.5$ kpc. This positions it in the evolutionary track of a mass with the progenitor mass of 2–3$\mathrm{M}_{\odot}$ on the HR diagram (see Fig. 2.1). This star seems just to have left the AGB phase, subsequently getting hotter toward [WC 5–8]. However, the problem is that few CSPNe (12%) were identified in the [WC 5–8] range, and appears as a gap in the stellar evolutionary track (Acker & Neiner 2003). This gap represents a challenge to the theory, that requires further investigations.

Hen 3-1333 (= PN G332.9−09.9) and **Hen 2-113** (= PN G321.0+03.9). The Hen 3-1333 and Hen 2-113 were among the coolest [WR] CSPNe studied in *JHKL* bands by Webster & Glass (1974), and classified as [WC 11] (Heap 1982). Gleizes et al. (1989) derived the H I Zanstra temperature of $T_z(\mathrm{H\ I}) = 17.5$ kK and 37 kK for Hen 3-1333 and Hen 2-113, respectively. Photoionization models using Kurucz (1991) flux atmospheres by De Marco & Crowther (1998) represented $T_{\mathrm{eff}} = 25$ kK and $L/\mathrm{L}_{\odot} = 3630$ for Hen 3-1333 and $T_{\mathrm{eff}} = 29$ kK and $L/\mathrm{L}_{\odot} = 3980$ for Hen 2-113. De Marco et al. (1998) derived wind electron temperatures of 21.3 kK for Hen 3-1333 and 16.4 kK for Hen 2-113 from the empirical analysis of C II dielectronic recombination lines.

K 2-16 (= PN G352.9+11.4). The CSPN K 2-16 is the best example of late-type [WC] star with many absorption lines, classified as [WC 11] by Tylenda et al. (1993). The energy-balance temperature determined by Preite-Martinez et al. (1991) is $T_{\rm EB} = 19.6$ kK (Note it is misspelled as "He 2-16" in that paper). This makes K 2-16 the coolest star in our sample. The central star has a V-band magnitude of $V = 12.75$ (Tylenda et al. 1991). The photoionization model implemented by Acker et al. (2002) provided $T_{\rm eff} = 29$ kK and $L/{\rm L}_{\odot} = 2000$ at $D = 1$ kpc corresponding to a stellar mass of $0.524{\rm M}_{\odot}$ and the evolutionary track of the progenitor mass of $1{\rm M}_{\odot}$ (see HR diagram; Fig. 2.1). Leuenhagen et al. (1996) suggested that K 2-16 is related to V348 Sgr, which was previously classified as [WC 12] by Leuenhagen & Hamann (1994). They also noticed that its absorption feature is similar to those of extreme Helium stars. However, Crowther et al. (1998) excluded V348 Sgr from their classification due to the absence of the C III λ5696 line, and classified it under 'peculiar extreme He star'. Similarly, Acker & Neiner (2003) removed the [WC12] class from their [WR] classification scheme. Therefore, [WC 11] is the last subclass of [WR] CSPNe, which demonstrates the lowest terminal velocity and the coolest stellar temperature.

1.4.5 [WN] central stars of planetary nebulae

In this subsection, we present a synopsis of some nitrogen-sequence WR-type CSPNe. The PN Abell 48 and PB 8 are studied in Chapters 5 and 6, respectively.

Abell 48. The CSPN Abell 48 (PN G029.0+00.4) has been the subject of recent spectroscopic studies (Wachter et al. 2010; Depew et al. 2011; Todt et al. 2013; Frew et al. 2014b). It has been classified as Wolf–Rayet [WN5] (Todt et al. 2013), where the square brackets distinguish it from the massive WN stars. However, Wachter et al. (2010) described it as a spectral type of WN6 with a surrounding ring nebula. Abell 48 was first identified as a planetary nebula (PN) by Abell (1955). Recently, Todt et al. (2013) concluded from spectral analysis of the CSPN and the surrounding nebula that Abell 48 is a PN with a low-mass CSPN. A spectral analysis of the CSPN Abell 48 with the Potsdam Wolf-Rayet (PoWR) models by Todt et al. (2013) indicates that its surface composition is mainly composed of 85% helium, 10% hydrogen and 5% nitrogen by mass.

PB 8. The CSPN PB 8 has been classified as a hydrogen-rich Of-WR(H) star by Méndez (1991), [WC 5-6] by Acker & Neiner (2003), *wels* by Tylenda et al. (1993) and Gesicki et al. (2006), and hybrid nitrogen and carbon-sequence [WN/WC] star by Todt et al. (2010). A detailed spectral analysis of CSPN PB 8 with the Potsdam Wolf-Rayet (PoWR) models by Todt et al. (2010) indicates that the surface composition is hydrogen-deficient with mass fractions of 55% helium, 40% hydrogen, 1.3% carbon, 2% nitrogen and 1.3% oxygen. It resembles the rare transition class of WN/WC subtypes of massive Wolf-Rayet stars, so Todt et al. (2010) suggest a new spectral type [WN/WC] for CSPNe.

IC 4663. The stellar spectrum of IC 4663 is dominated by broad H II and N V emission lines, which was classified as a [WN3] spectral type by Miszalski et al. (2012). A spectral analysis of the CSPN IC 4663 with the CMFGEN non-LTE code by Miszalski et al. (2012) indicates that its surface composition is mainly composed of 95% helium, $< 2\%$ hydrogen and 0.8% nitrogen by mass, which is similar to the O(He) central stars, suggesting a post-AGB evolutionary sequence [WN]$\rightarrow$O(He) The stellar spectrum shows a fast wind with a terminal velocity of $V_{\infty} = 1900$ km s^{-1}. The stellar temperature of about 140 kK is hot enough to produce N VII emission.

LMC-N 66. The planetary nebula N66 (WS 35 and SMP 83) in the Large Magellanic Cloud (LMC) is known for its central star having the WR features of the nitrogen-sequence. The nebular emission lines observed during 1975-90 showed no significant variations, while the central star was invisible (Dopita et al. 1985; Peña & Ruiz 1988; Monk et al. 1988; Meatheringham & Dopita 1991). In 1990, the central star showed a brightness increase by several magnitude, and clearly depicted its [WN] spectra, but in the meantime no change in the nebular feature was observed (Torres-Peimbert et al. 1993). It showed another dramatic bright outburst at the end of 1993 and then it slowly faded. Peña et al. (1994) speculated that a very late thermal pulse may be responsible for the stellar outburst. The nebula analysis done by Dopita et al. (1993) yielded a stellar temperature of 170 kK and a luminosity of $L = 30,000 L_{\odot}$, corresponding to a stellar mass in the range 1.0–$1.2 M_{\odot}$. However, Hamann et al. (2003) determined the effective temperature of about 112 kK from non-LTE models for expanding stellar atmospheres.

1.5 Two current issues in nebular astrophysics

The main intention of this thesis is to shed light on two main problems in nebular astrophysics: nebular morphology and abundance discrepancy. PNe surrounding hydrogen-deficient stars constitute a particular study class. Only 25% of PNe currently have well-studied stars most of those that have been studied have ‘hydrogen-rich’ surface abundances. However, a considerable fraction (25%) of them exhibit ’hydrogen-deficient’ fast expanding atmospheres characterized by a large mass-loss rate. Most of them were classified as the carbon-sequence WR CSPNe or [WC], whose spectral characteristics strongly resemble those of the massive Population-I WR stars but of course have a completely different mass range, age and evolutionary history. What is less clear are the mechanisms that remove the hydrogen-rich outer layer from these degenerate cores, and transform them into a fast stellar wind. A study of the kinematics, physical conditions and chemical abundances for a sample of PNe with different hydrogen-deficient stars might provide valuable clues about the origin and formation of their hydrogen-deficient fast expanding stellar atmospheres.

1.5.1 Axisymmetric morphologies and point-symmetric jets

The majority of PNe show predominantly axisymmetric morphologies, i.e. elliptical and bipolar (e.g. Balick 1987), which have introduced considerable problems into theories of their formation and evolution. Single star evolution already describes spherical nebula, and can also explain elliptical PN if there is interaction with the interstellar medium (ISM). But, it has some difficulties in including highly axisymmetric nebulae. According to the interacting stellar winds (ISW) theory of nebular formation developed by Kwok et al. (1978), a slow dense superwind from the AGB phase is swept up by a fast tenuous wind during the PN phase, creating a compressed dense shell. Kahn & West (1985) extended this model to describe an aspherical mass distribution i.e. highly axisymmetric or bipolar nebulae. This extension later became known as the generalized interacting stellar winds (GISW) theory. However, the GISW model is not always consistent with observations and a matter of some controversy (see e.g. review by Balick & Frank 2002). Moreover, a density contrast is necessary to make an aspherical nebula in the GISW theory. More complex axisymmetric morphologies recently observed (e.g. Sahai et al. 2011) contradict the GISW theory.

A combination of rotating stellar winds and strong toroidal magnetic fields has been proposed as a mechanism for the equatorial density enhancement and the jet-like outflows (García-Segura 1997; García-Segura et al. 1999; García-Segura & López 2000; Frank & Blackman 2004). However, Soker (2006) argued that the observed magnetic fields cannot have a central role in shaping PNe, and a single star cannot supply the energy and angular momentum for complex axisymmetric PNe. It has also been suggested that axisymmetric morphologies can be produced through tidal interaction with a binary partner (Soker & Harpaz

1992; Soker & Livio 1994; Soker 2006; Nordhaus & Blackman 2006; Nordhaus et al. 2007). This binary system could consist of a white dwarf (or planet) that accretes material from an (post-) AGB star. Paczynski (1976) first suggested the binary role in shaping PNe through a common-envelope (CE) phase. Currently, there is a strong argument in favor of most aspherical PNe being shaped by this theory (Miszalski et al. 2009a,b; De Marco 2009; Nordhaus et al. 2010). Nordhaus & Blackman (2006) suggested that a binary system, consisting of a low-mass star ($< 0.3\mathrm{M}_{\odot}$) and an AGB star, undergoes a common envelope (CE) phase, which can lead to a binary-induced equatorial outflow (see Fig. 1.13). The accreted mass transfer from a AGB star to a companion forms a "common envelope" (CE) around the system. The CE phase happens when AGB mass rapidly transferred to the companion overflows the Roche lobe, and the system becomes engulfed by an envelope. Transferring energy and angular momentum from the binary system to the CE shrinks the orbital separation that causes the spiral-in process. This can unbind the CE, and if the envelope is ejected, the result is a close binary, otherwise it results in a merger. At the final stage of the spiral-in phase, axisymmetric superwind mass-loss is produced through the deposition of orbital angular momentum of the binary system, which can make a pair of diametrically opposed outflows.

The small-scale low-ionization structures (LISs) embedded or not in the global structure has been found in nearly 10% of Galactic PNe (Corradi et al. 1996; Gonçalves et al. 2001, 2009). These structures are visible in [N II] λ6584 and [S II] $\lambda\lambda$6716,6731 doublet more so than in [O III] λ5007 and Hα λ6563 emission line maps. Gonçalves et al. (2001) classified them as knots, jets and jetlike systems. *Knots*, either in pairs or isolated, are defined as those LISs with an aspect length-to-width ratio close to 1, while those with an aspect ratio much larger than 1 are classified as filaments. Highly collimated filaments appearing in opposite symmetrical pairs on the both sides of the central star, and moving with velocities much larger than the expansion velocity of the main structure, are called *jets*. Those filaments with no evidence of velocities higher than the expansion velocity of the main body are called *jetlike* structures. However, projection effects make it extremely difficult to distinguish easily between jets and jetlike systems. Around 50% of LISs are highly collimated high-velocity jets or high-velocity pairs of knots, the so-called fast, low-ionization emission regions (FLIERs; Balick et al. 1993, 1994). The FLIERs have radial velocities of 25–200 km s^{-1} with respect to the main bodies (Balick et al. 1994). We have not yet understood how the density and velocity structures of the FLIERs contrast with the main body. Soker (1990) and Soker & Harpaz (1992) hypothesized axisymmetric superwind mass-loss through a CE, tidal interaction with a low-mass companion, and angular momentum deposition of the binary system.

Fig. 1.13 summarizes a scenario of the common envelope evolution that forms the ring-shaped nebula with out point-symmetric knots. It consists of a low-mass companion ($< 0.3\mathrm{M}_{\odot}$) on the envelope made by a $3\mathrm{M}_{\odot}$ AGB star. As the CE is formed, the orbital separation reduces, making the spiral-in phase. This unbinds the CE. At the final stage of the spiral-in phase, axisymmetric superwind mass-loss is produced through the deposition of orbital angular momentum of the binary system. Nordhaus & Blackman (2006) outlined three different scenarios for the common envelope paths: (a) orbital shrinkage unbinds the CE, (b) differential rotation during the spiral-in phase makes a dynamo in the CE and unbinds the envelope, and (c) companion is shredded into an accretion disc around the core, driving an outflow and also unbinding the CE. While the first scenario can make a ring, other scenarios can result in both ring or elongated morphology with ejections along the rotation axis.

Recently, Miszalski et al. (2009b) found that nearly 30 percent, perhaps as high as 60 percent, of bipolar PNe contain post-CE binaries, suggesting the CE phase preferentially shapes aspherical PNe. The transformation of the orbital angular momentum of the binary system to the CE unbind it, shaping a nebula whose axisymmetric axis is perpendicular to the orbital plane of the binary

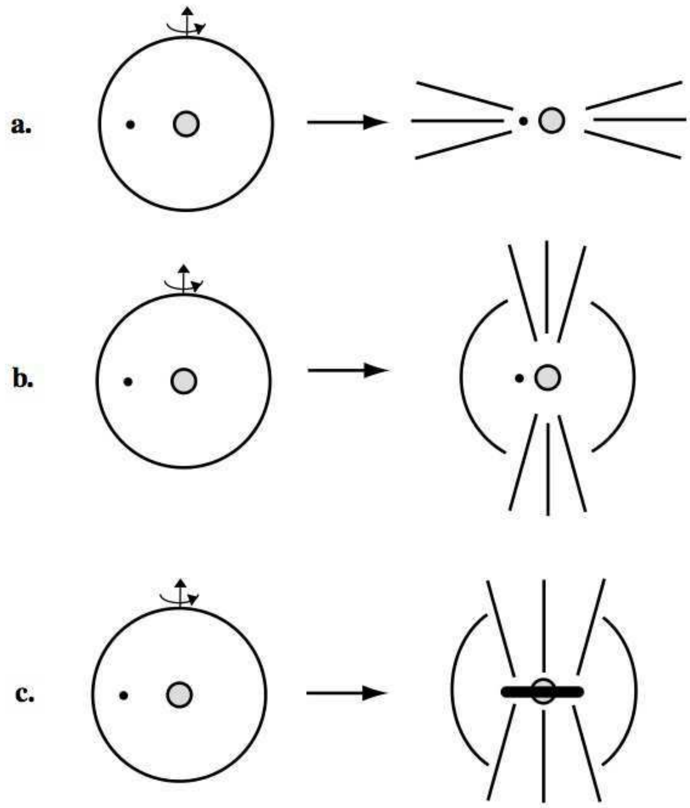

Figure 1.13: The binary-induced equatorial outflows from AGB stars (Nordhaus & Blackman 2006). (a) orbital shrinkage unbinds the envelope, (b) the spiral-in phase unbinds the envelope and (c) companion is shredded into an accretion disc around the core, the disc then drives an outflow and unbinds the envelope.

system. Recently, high resolution kinematic analysis of some PNe around post-CE CSPN have been shown to have alignments between the nebular shells and the binary orbital inclinations (see e.g. Mitchell et al. 2007; Jones et al. 2010b, 2012; Tyndall et al. 2012; Huckvale et al. 2013). With further observations of a significant sample of post-CE PNe, it should be possible to decide on whether the binary systems play a prominent role in producing the majority of the aspherical PNe.

1.5.2 Abundance discrepancy and temperature dichotomy

Until recently, bright and easy to measure optical collisionally excited lines (CELs) have been extensively used to determine heavy-element abundances of PNe (see e.g. Kingsburgh & Barlow 1994; Kwitter & Henry 2001; Tsamis et al. 2003a; Henry et al. 2004; Liu et al. 2004a; Osterbrock & Ferland 2006). However, as the method has a strong (exponential) dependence on the electron temperature ($T_{\rm e}$), any temperature variations can introduce high uncertainties (e.g. Garnett 1992; Stasińska 2005). Alternatively, optical recombination lines (ORLs) have a weak power-law dependence on the electron temperature and independent of the electron density ($N_{\rm e}$) under typical nebular conditions, thus resulting in consequently reliable analysis. But, ORLs of heavy elements are much weaker and more difficult to measure than CELs. We can detect them in nearby PNe through very deep observations, due to their extremely weak intensities relative to the hydrogen recombination line Hβ. However, the abundances of carbon, nitrogen, oxygen and neon derived from ORLs are found to be systematically higher than those derived from CELs in many PNe (Rola & Stasińska 1994; Liu et al. 1995, 2000, 2001; Luo et al. 2001; Wesson et al. 2003; Tsamis et al. 2004; Wesson & Liu 2004; Wesson et al. 2005; Tsamis et al. 2008; García-Rojas et al. 2009). This problem was already found in gaseous nebulae over seventy years ago (Wyse 1942; Aller & Menzel 1945). This is known as the abundance discrepancy problem, measured through the abundance discrepancy factor, ADF, defined as:

$$\mathrm{ADF}(\mathrm{X}^{i+}) = (\mathrm{X}^{i+}/\mathrm{H}^{+})_{\mathrm{ORLs}}/(\mathrm{X}^{i+}/\mathrm{H}^{+})_{\mathrm{CELs}}, \tag{1.3}$$

where X^{i+} is the $i+$ ionic abundance of element X and H^{+} is the abundance of ionized hydrogen. For more than 100 PNe, ADFs are typically in the range 1.6–3. However, a fraction of them (5–10 percent) have ADF of 4–80 (see review by Liu et al. 2006). For example, Abell 30, NGC 1501 and Hf 2-2, have extremely large ADF(O^{2+}) of about 700, 30 and 70, respectively (Wesson et al. 2003;

Ercolano et al. 2004; Liu et al. 2006). The origin of this discrepancy is not yet fully understood and remains one of the long-standing problems in nebular astrophysics.

The dichotomy between temperatures measured from the Balmer jump (BJ) of the H I recombination spectrum, T_e(H I), and those measured from the collisionally excited [O III] nebular-to-auroral forbidden line ratio, T_e([O III]),

$$\Delta T_{[\mathrm{O\ III}]} \equiv T_{\mathrm{e}}([\mathrm{O\ III}]) - T_{\mathrm{e}}(\mathrm{H\ I}), \tag{1.4}$$

is another long-standing problem, which may be closely related to the abundance discrepancy problem (see e.g. review by Liu 2003). Over four decades ago, Peimbert (1971) found that T_e(H I) usually tends to be lower than T_e([O III]) in three planetary nebulae and the Orion nebula. Peimbert (1971) suggested that temperature fluctuations are responsible for this problem, so the thermal structure was described by two parameters: the average temperature T_0, and the mean square temperature fluctuation t^2. Moreover, Liu & Danziger (1993) studied 14 PNe, and showed that the Balmer jump temperature is typically lower than the [O III] temperatures. The temperature fluctuations lead to overestimating the electron temperature deduced from CELs. As a result, the derived ionic abundances are underestimated. But, the analysis of temperature variations in NGC 7009 by Rubin et al. (2002) for example showed temperature fluctuation is remarkably low, but they did not rule out temperature fluctuations along the line of sight as the cause of the abundance discrepancy problem. For NGC 6543, Wesson & Liu (2004) found that the temperature fluctuations are too small to explain the discrepancy between heavy element abundances inferred from CELs compared to those derived from ORLs. Previously, Kingdon & Ferland (1995) argued that the temperature fluctuations are insufficient to solve the abundance discrepancies in the photoionization modeling. Moreover, extensive studies of several PNe by Zhang et al. (2004) showed that temperature fluctuations are so large and well beyond the predictions of any photoionization models, so they concluded that a few H-deficient materials likely exist in the nebula.

To solve the abundance discrepancy problem, Liu et al. (2000) suggested a two-phase or bi-abundance model. The model assumed that the nebula contains two components of different abundances: a cold hydrogen-deficient 'metal-rich' component, and the diffuse warm component of 'normal' abundances. The cold H-deficient inclusions embedded in the nebular gas of normal abundances dominate the emission of ORLs (Liu 2003; Liu et al. 2004a). The bi-abundance photoionization model of Abell 30 by Ercolano et al. (2003b) showed the possibility of such a scenario. Moreover, Tsamis & Péquignot (2005) used a bi-chemistry model for the abundance discrepancy in H II regions. More recently, the bi-abundance model by Yuan et al. (2011) solved the abundance discrepancy problem in NGC 6153. Previously, the analysis of the emission-line spectrum of NGC 6153 by Liu et al. (2000) pointed to a component of the ionized gas, cold and very metal-rich. The study of Abell 30 by Wesson et al. (2003) again showed the presence of H-deficient inclusions. The photoionization modeling of NGC 1501 (Ercolano et al. 2004) and Abell 48 (Danehkar et al. 2014) also suggested that some cold H-deficient inclusions may exist in the nebula. While the two-phase scenario provides a physical explanation for the temperature and abundance discrepancies, it may give a natural explanation for the temperature fluctuations. However, more detailed photoionization models are still necessary to assess the feasibility of this scenario and determine how the existence of chemical inhomogeneities affects the nebular physical conditions.

1.6 Thesis Outline

The aim of this thesis is to make a contribution to the understanding of the evolution of PNe with [WR] central stars. In particular we attempt to gain an understanding of their morphologies and chemical abundances by means of optical integral field unit (IFU) spectroscopy. We used a sample of PNe around [WR] stars as the basis for our study. The main questions that are required to be answered in the study of PNe are: 1) Which physical mechanism is responsible for shaping axisymmetric morphologies seen in most PNe? 2) How do the density and velocity structures of the so-called fast, low-ionization emission regions (FLIERs) contrast with the main body of the nebula? 3) What is the relationship between the morpho-kinematic structures and central stars? 4) What is the cause of the ORL vs. CEL abundance discrepancy and temperature dichotomy? 5) What is the origin of hydrogen-deficient inclusions which are supposed to solve the ORL vs. CEL problem? 6) Why does empirical analysis give extremely overabundant nitrogen for the FLIERs? 7) Which physical processes contribute to dual-dust chemistry seen in PNe with WR-type nuclei? However, many aspects of these questions still remain unanswered. To answer some of the questions mentioned above deeper imaging and spectroscopic observations are required. Hopefully, the work presented in this thesis will lead to a better understanding of morphological and chemical characteristics of PNe with [WR] central stars.

This thesis is divided into three parts based on different stellar spectral groups: PNe with [WC] stars, PNe with [WN] stars, and PNe with PG 1159-type stars. The first part, **Planetary Nebulae with [WC] Stars**, starts with morpho-kinematic studies of a sample of 13 Galactic PNe surrounding hydrogen-deficient Wolf-Rayet (WR) central stars and 5 Galactic PNe with weak emission-line central stars (*wels*), followed by plasma diagnostics and empirical abundance analysis, as well as photoionization models of Hb 4. The second part, **Planetary Nebulae with [WN] Stars**, presents photoionization models of Abell 48 and PB 8 whose central stars were recently classified as [WN] and [WN/WC] central stars, respectively. The third part, **Planetary Nebulae with PG 1159-type stars** presents photoionization models of SuWt 2, which was found to contain a PG 1159-type star based on the nebula's age.

This thesis is structured as follows:

- Chapter 2 presents new, integral field unit (IFU) spectroscopic observations of a sample of 13 Galactic PNe surrounding hydrogen-deficient [WR] central stars and 5 Galactic PNe with *wels* made with the Wide Field Spectrograph (WiFeS) on the ANU 2.3-m telescope at the Siding Spring Observatory. The Hα and [N II] emission features were used to measure the nebular radial velocities and velocity dispersions. Based on the spatially resolved velocity distributions of these emission lines combined with archival *Hubble Space Telescope* imaging for compact PNe, we determined their three dimensional morpho-kinematic structures. Comparing the velocity maps provided by our IFU observations with those produced by morpho-kinematic models allowed us to exclude the projection effect from the nebula's appearance and provide a more accurate morphology for most PNe in the sample, apart from the compact objects. Our results indicate that these PNe have axisymmetric morphologies, either bipolar or elliptical. In many cases the associated kinematic maps for these PNe around [WO] stars also reveal the presence of FLIERs.

- Chapter 3 presents optical integral field spectroscopic measurements of emission lines for the same sample studied in Chapter 2. The spectra, combined with archival spectra from the literature, have been used to carry out plasma diagnostics and abundance analysis using both CELs and ORLs. Nebular thermal and density structures have been derived using a variety of plasma diagnostics of CELs. The weak temperature dependence of ORLs have also been used to determine the temperature structure of the nebulae. The plasma diagnostic results are used to derive ionic and elemental abundances within the nebula from both CELs and ORLs. It is found that the ORL abundances are several times higher than the CEL abundances, whereas the temperatures derived from the He I recombination lines are typically lower than those measured from the collisionally excited nebular-to-auroral forbidden line ratios. This may point to the existence of cold, hydrogen-deficient materials embedded in the diffuse warm nebula. The abundance discrepancy factors (ADFs) for doubly-ionized N and O are within a range from 2 to 49, which are closely correlated with the dichotomy between temperatures derived from forbidden lines and those from He I recombination lines. The results show that the ADF and temperature dichotomy are correlated with the intrinsic nebular surface brightness, suggesting that the abundance discrepancy problem must be related to the nebular evolution.

- Chapter 4 presents a 3D photoionisation model of Hb 4 assuming homogeneous elemental abundances, aimed at solving a significant overabundance of nitrogen seen in FLIERs. The results indicate that the ionization correction factor method and the electron temperature used for the empirical analysis are mostly responsible for apparent enhanced nitrogen abundance. A bi-abundance model has been constructed to address the abundance discrepancy problem. It is found that the presence of the metal-rich inclusions can solve the ORL vs. CEL problem.

- Chapter 5 presents our new IFU observations and 3D photoionization modeling of Abell 48. The main aim was to investigate whether the [WN] model atmosphere from Todt et al. (2013) can produce the ionization structure of a PN with the features like Abell 48. It is found that the observed nebular line fluxes were best reproduced by using an ionizing source with temperature and luminosity corresponding to a relatively low-mass progenitor star (~ 3 M$_{\odot}$) rather than a massive Pop I star. The helium temperature predicted by the photoionization model is higher than those empirically derived, suggesting that some cold, metal-rich structures may exist in the nebula.

- Chapter 6 presents 3D photoionization modeling of PB 8, aimed at solving the ORL/CEL discrepancy by using H-deficient inclusions. The chemically homogeneous model failed to reproduce the observed ORLs of heavy elements. The bi-abundance model, containing a small fraction of hydrogen-deficient inclusions occupying ~ 6 percent of the total volume, provided acceptable matches to the observed ORLs. It is found that a dual-dust chemistry with different grain species and discrete grain sizes in the nebula likely produces the observed Spitzer infrared continuum.

- Chapter 7 presents 3D photoionization modeling of SuWt 2, aimed at uncovering the properties of the hidden hot ionizing source. It has two A-type stars, which is too cool to ionize the surrounding material. The photoionization models of SuWt 2 suggest that an ionizing source with $T_{\rm eff} \sim 150$ kK is necessary to produce the ionization structure of the nebula. However, the time-scale for the evolutionary track of a hydrogen-rich model atmosphere is inconsistent with the dynamical age obtained for the ring. This suggests that the central star has undergone a very late thermal pulse, which results in an older PN. It is found that the hidden hot star could be hydrogen-deficient and compatible with what is known as a PG 1159-type star.

- The Conclusions and future work are presented in the final Chapter 8.

Appendix A presents the spatial distribution maps of flux intensity, continuum, radial velocity and velocity dispersion of our sample and their morpho-kinematic models analyzed in Chapter 2. Appendix B presents the observed and dereddened relative nebular line fluxes of our sample analyzed in Chapter 3. Appendix C shows the observed optical nebular spectra of our sample analyzed in Chapter 3. Appendix D presents the spatial distribution maps of extinction $c(\mathrm{H}\alpha)$, electron density N_e, electron temperature T_e, ionic abundances studied in Chapter 3. Appendix E presents the observed optical stellar spectra of our sample studied in Chapters 2 and 3.

Part I

Planetary nebulae with [WC] stars

2

Spatially resolved kinematics

2.1 Introduction

Once the star leaves the AGB phase, the stellar superwind gradually changes the shape of the nebular shell. The stellar wind contributes some hydrodynamic effects into the ionized shell, thus altering the shape of the expanding shell. The photo-ionization produces the visible nebula. The emission lines emitted by the ionized gas provide valuable clues to the kinematic features of the nebular shell. Spatially resolved kinematics allows us to resolve the shape of the expanding shell. The morpho-kinematic analysis of PNe provides some insights into the AGB mass-loss processes, the transition from the post-AGB to the PN phase (see e.g. Balick 1987; Corradi & Schwarz 1995; Balick & Frank 2002; Schönberner et al. 2005a,b, 2010; Kwok 2010).

In the past decades, morpho-kinematic studies of planetary nebulae (PNe) have revealed that they frequently show axisymmetric shapes. The origin of such structures still remains as one of the important problems in the study of PNe. In this chapter, we present new, integral field unit (IFU) spectroscopic observations of a sample of 13 Galactic PNe surrounding hydrogen-deficient Wolf-Rayet (WR) central stars and 5 Galactic PNe with weak emission-line central stars (*wels*) made with the Wide Field Spectrograph (WiFeS). The Hα and [N II] emission features were used to measure the nebular radial velocities and velocity dispersions. Based on the spatially resolved velocity distributions of these emission lines combined with archival *Hubble Space Telescope* imaging for compact PNe, we determined their three dimensional morpho-kinematic structures. Comparing the velocity maps provided by our IFU observations with those produced by morpho-kinematic models allowed us to exclude the projection effect from the nebula's appearance and provide a more accurate morphology of most PNe in the sample, apart from the compact objects. Our results indicate that these PNe have axisymmetric morphologies, either bipolar or elliptical. In many cases the associated kinematic maps for these PNe around hot WR central stars also reveal the presence of so-called fast low-ionization emission regions (FLIERs).

This chapter is structured as follows. Section 2.2 describes our observational and data reduction techniques. In Section 2.3, we present the IFU kinematic results. The morpho-kinematic modeling and their results are presented in Section 2.4, followed by our conclusion in Section 2.5.

2.2 Observations

IFU observations of our sample have been conducted using the Wide Field Spectrograph (WiFeS; Dopita et al. 2007, 2010) at the Siding Spring Observatory in April 2010. WiFeS is an image-slicing Integral Field Unit (IFU) developed and built for the ANU 2.3-m telescope, feeding a double-beam spectrograph. WiFeS samples 0.5 arcsec along each of twenty five 38 arcsec $\times$ 1 arcsec slitlets, which provides a field-of-view of 25 arcsec $\times$ 38 arcsec and a spatial resolution element of 1.0 arcsec $\times$ 0.5 arcsec. The output is optimized to fit the 4096 $\times$ 4096 pixel format of the CCD detectors. Each slitlet is designed to project to 2 pixels on the detector. This yields a reconstructed point spread function (PSF) with a full width at half-maximum (FWHM) of approximately 1-2 arcsec. The spectrograph uses volume phase holographic gratings to provide a spectral resolution of $R = 3000$ (100 km s^{-1} FWHM) and $R = 7000$ (45 km s^{-1} FWHM).

All targets were observed with the spectral resolution of $R \sim 7000$ in the 4415–7070 Å range. Each spectrum is 4096 pixels long, resulting in a linear wavelength dispersion per pixel of 0.36 Å for the blue and 0.45 Å for the red at $R \sim 7000$. This spectral resolution gives a mean FWHM instrumental resolution of 45 km s^{-1} per spaxel, so we can measure the radial velocity variation of $\delta v \sim$ 5 km s^{-1}. The typical seeing of $\delta x \sim 2$ arcsec enables us to identify morphologies of PNe with angular diameters larger than 10 arcsec. Although this spatial resolution is not ideal for study of micro-structures and compact PNe, it could resolve inclination angles of compact PNe. All targets were observed in the classical data accumulation mode. We also acquired series of bias, dome flat-field frames, twilight sky flats, arc lamp exposures, and wire frames for data reduction, flat-fielding and wavelength & spatial calibrations.

2.2.1 Sample selection

We selected a sample of 13 Galactic PNe with [WR] central stars (Crowther et al. 1998; Acker & Neiner 2003; Weidmann et al. 2008), and 5 Galactic PNe with *wels* from the literature (Tylenda et al. 1991, 1993; Gorny et al. 1997; Górny et al. 2004). These well-known [WR] PNe with a range from early- to late-type and many with available *HST* imaging allowed us to identify morphologies seen in different stages of post-AGB stellar evolution. But, [WCL] PNe are usually very compact, since they are too young in comparison to [WCE] PNe, so we cannot see significant details of their morphologies.

Current details of the CSPNe are presented in Table 2.1. The usual PN names, spectral classes of the central stars (primarily from Crowther et al. 1998; Acker & Neiner 2003), the PNG numbers (from Acker et al. 1992) are given in Columns 1–3, respectively. Acker & Neiner (2003) classified the CSPN M 1-32 under the *peculiar* $[\mathrm{WO\,4}]_{\mathrm{pec}}$ subclass according to the wide FWHM of C IV-5801/12 doublet, corresponding to a terminal velocity of $V_{\infty} \simeq 4900\,\mathrm{km\,s^{-1}}$; typically higher than $V_{\infty} \simeq 2000$–$3000\,\mathrm{km\,s^{-1}}$ observed in normal [WO] CSPNe. Similarly, Weidmann et al. (2008) classified the CSPN Th 2-A as of type $[\mathrm{WO\,3}]_{\mathrm{pec}}$, belonging to those with a *peculiar* C IV-5801/12 doublet, corresponding to a terminal velocity of $V_{\infty} \simeq 5300\,\mathrm{km\,s^{-1}}$. The effective temperature and stellar luminosity, together with their references, are given in Columns 4–6. Most stellar luminosities have been chosen from the literature (Kaler et al. 1991; De Marco & Crowther 1998; Acker et al. 2002; Gesicki & Zijlstra 2007). For M 3-30 and IC 1297, we derived the stellar luminosity from the evolutionary tracks for helium-burning models by Blöcker (1995a) and the relation between terminal velocity (V_{∞}), effective temperature (T_{eff}) and stellar mass ($M_{\star}$) given by Pauldrach et al. (1988). For Th 2-A, we obtained the stellar luminosity through the standard bolometric correction method (Vacca et al. 1996; Massey et al. 2001) for a V-band magnitude of $V = 17.08$ (Ciardullo et al. 1999) and distance of $D = 2500$ pc (Stanghellini & Haywood 2010). For M 1-32, we used $V = 17$ mag (Peña et al. 2001) and $D = 4796$ pc (Stanghellini & Haywood 2010). For M 2-42, we adopted $V = 17$ mag and $D = 4.4$ kpc (Tajitsu & Tamura 1998). For the Galactic bulge PN Sa 3-107, we assumed $D = 6$ kpc and used $V = 16.4$ mag (Lasker et al. 2008). The terminal velocity together with the reference are presented in Columns 7 and 8. The mass-loss rates (Column 9) were calculated using the formula given by Nugis & Lamers (2000), and given stellar luminosities, and adopting the typical [WR] chemical composition of $Y = 0.43$ and $Z = 0.56$. Columns 10 presents the stellar mass determined from the helium-burning evolutionary models by Blöcker (1995a). The exposure time used for each PN is given in Column 11. Fig. 2.1 shows positions of the CSPNe of our sample on the Hertzsprung–Russell (HR) diagram for hydrogen-burning models (Vassiliadis & Wood 1994) and helium-burning models (Blöcker 1995a). We notice that all

CSPNe are located between the evolutionary tracks for the progenitor mass of $1M_{\odot}$ and $4M_{\odot}$.

2.2.2 Data reduction

Data reduction was performed using the newly developed IRAF pipeline wifes.[1] The reduction procedure consists of the following steps:

(i) *Sensitivity correction*. Each CCD pixel has a slightly different sensitivity, which makes pixel-to-pixel variations in the spectral direction. We corrected this effect using the ground flat-field frames taken with exposures of a quartz iodine (QI) lamp. All bias frames are combined to create a medium-average bias frame, which is subtracted from each of the calibration frames. The flat-field frames from QI lamp exposures are combined to create a master flat-field frame. The final master flat-field frame is used to remove pixel-to-pixel sensitivity variations from the science data.

(ii) *Wavelength calibration*. We performed the wavelength calibration using Cu–Ar arc exposures taken at the beginning of the night. For each slitlet the corresponding arc spectrum is extracted, and then wavelength solutions for each slitlet are obtained from the extracted arc lamp spectra using low-order polynomials. The IRAF fitcoords task applies the identified arc-line positions to the science data. The poor quality of the Cu–Ar arc exposures taken with the blue arm did not allow us to use the blue spectra for our kinematic analysis.

[1] IRAF is distributed by NOAO, which is operated by AURA, Inc., under contract to the National Science Foundation.

Table 2.1: PNe with [WC] central stars observed with the ANU 2.3-m Telescope. References are as follows: A92 – Acker et al. (1992); A02 – Acker et al. (2002); A03 – Acker & Neiner (2003); B95 – Blöcker (1995a); D98 – De Marco & Crowther (1998); D11 – Depew et al. (2011); G97 – Gorny et al. (1997); G07 – Gesicki & Zijlstra (2007); K91 – Kaler et al. (1991); N00 – Nugis & Lamers (2000); P89 – Preite-Martinez et al. (1989); S89 – Shaw & Kaler (1989); T91 – Tylenda et al. (1991); T93 – Tylenda et al. (1993).

Name	CSPN	PNG A92	$T_{\rm eff}$ [a] (kK)	$\log(L)$ [a] ($L_\odot$)	Ref. [a] ($T_{\rm eff}, L$)	V_∞ [b] (km s^{-1})	Ref. [b] (V_∞)	$\log \dot{M}$ [c] ($M_\odot$/yr)	$M_\star$ [d] ($M_\odot$)	ExpTime (sec)
PB 6	[WO 1]	278.8+04.9	103	3.57	K91	2496	A03	−7.15	0.60	1200
M 3-30	[WO 1]	017.9−04.8	49	3.3 [d]	A03	2059	A03	−7.50	0.56	1200
Hb 4	[WO 3]	003.1+02.9	85	3.6	A03,A02	2059	A03	−7.11	0.60	300,1200
IC 1297	[WO 3]	358.3−21.6	91	3.7 [d]	A03	2933	A03	−6.98	0.62	60,1200
Th 2-A	[WO 3]pec [f]	306.4−00.6	157 [f]	3.88 [f]	P89	5300 [f]	–	−6.75	0.70	1200
Pe 1-1	[WO 4]	285.4+01.5	85	3.3	A02	2870	A03	−7.50	0.55	60,1200
M 1-32	[WO 4]pec	011.9+04.2	50 [e]	3.6 [d]	–	4867	A03	−7.11	0.60	1200

Remarks:

[a] References to stellar luminosity and effective temperature given in column 6. [b] References to terminal velocity given in column 8. [c] The mass-loss rates calculated using the formula given by Nugis & Lamers (2000). [d] Evolutionary tracks of helium-burning model by Blöcker (1995a). [e] This work, statistically from the nebular excitation class. [f] The spectral class given by Weidmann et al. (2008). Here we estimated the luminosity using the standard bolometric correction method, the effective temperature from Preite-Martinez et al. (1989) and also statistically from the nebular excitation class, and terminal velocity from the C IV-5801/12 doublet line profile of the central star. [g] Stellar luminosity from the standard bolometric correction method.

Table 2.1: (continued)

Name	CSPN	PN G A92	$T_{\rm eff}$ [a] (kK)	$\log(L)$ [a] ($L_\odot$)	Ref. [a] ($T_{\rm eff}$, L)	V_∞ [b] (km s^{-1})	Ref. [b] (V_∞)	$\log \dot{M}$ [c] ($M_\odot$/yr) N00	$M_\star$ [d] ($M_\odot$) B95	ExpTime (sec)
M 3-15	[WC 4]	006.8+04.1	55	3.6	A03,A02	1872	A03	−7.11	0.59	60,1200
M 1-25	[WC 5-6]	004.9+04.9	56	3.8	A03,A02	1747	A03	−6.85	0.62	60,1200
Hen 2-142	[WC 9]	327.1−02.2	35	3.7	A03,G07	884	A03	−6.98	0.60	60,1200
Hen 3-1333	[WC 10]	332.9−09.9	30	3.7	D98	312	A03	−6.98	0.60	1200
Hen 2-113	[WC 10]	321.0+03.9	30	3.7	D98	260	A03	−6.98	0.60	60,1200
K 2-16	[WC 11]	352.9+11.4	19	3.3	A03,A02	260	A03	−7.50	0.52	1200
NGC 6578	*wels*	010.8−01.8	63	< 4.03	S89	1498	T93	< -6.55	< 0.68	60,1200
M 2-42	*wels*	008.2−04.8	62	3.31 [g]	T91	1560	D11	−7.48	0.55	1200
NGC 6567	*wels*	011.7−00.6	47	3.62	G97	1747	T93	−7.08	0.60	60,1200
NGC 6629	*wels*	009.4−05.0	35	3.53	G97	1747	T93	−7.20	0.56	60,1200
Sa 3-107	*wels*	358.0−04.6	45 [e]	$\lesssim 4.0$ [g]	–	874	D11	$\lesssim -6.60$	$\lesssim 0.70$	1200

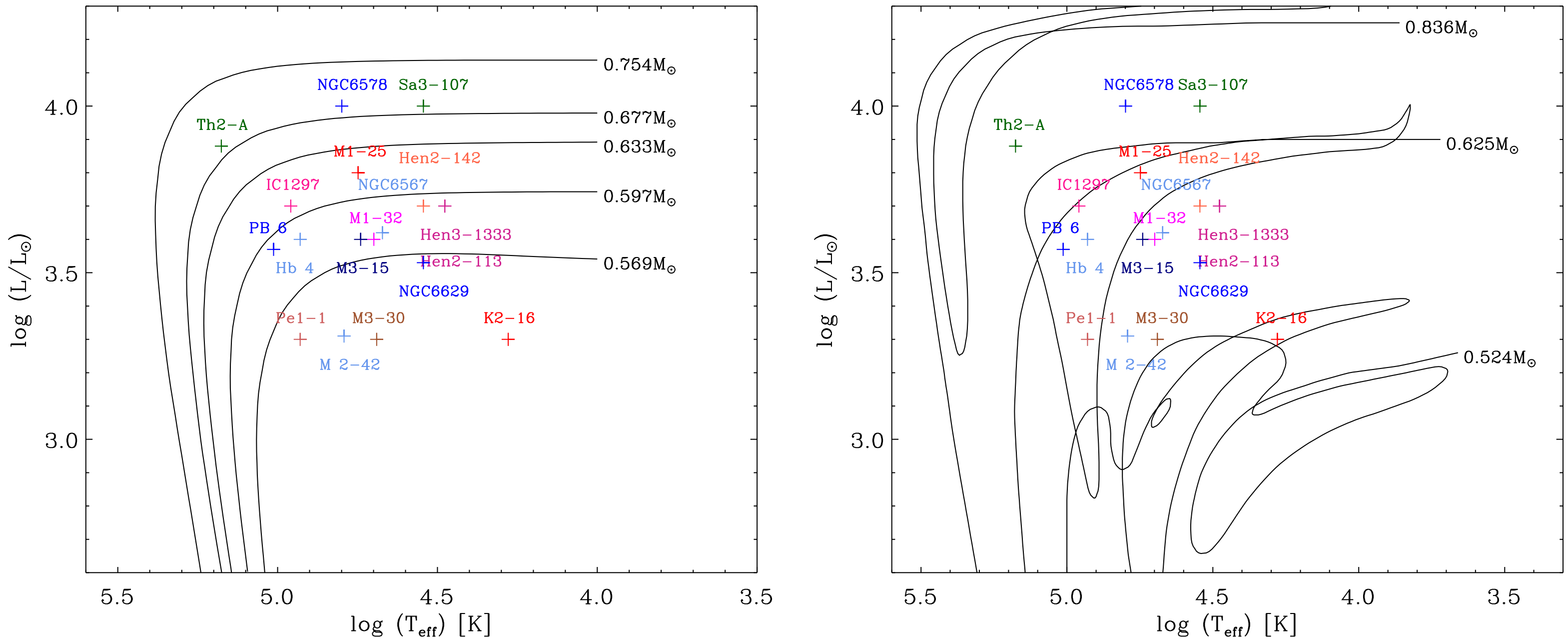

Figure 2.1: Left panel: Positions of the central stars of our sample on the HR diagram for hydrogen-burning models with $(M_{\rm ZAMS}, M_\star) = (1\mathrm{M}_\odot, 0.569\mathrm{M}_\odot)$, $(1.5\mathrm{M}_\odot, 0.597\mathrm{M}_\odot)$, $(2\mathrm{M}_\odot, 0.633\mathrm{M}_\odot)$, $(2.5\mathrm{M}_\odot, 0.677\mathrm{M}_\odot)$ and $(3\mathrm{M}_\odot, 0.754\mathrm{M}_\odot)$ and metallicity $Z = 0.016$ from Vassiliadis & Wood (1994). Right panel: Evolutionary tracks for helium-burning models with $(M_{\rm ZAMS}, M_\star) = (1\mathrm{M}_\odot, 0.524\mathrm{M}_\odot)$, $(3\mathrm{M}_\odot, 0.625\mathrm{M}_\odot)$ and $(5\mathrm{M}_\odot, 0.836\mathrm{M}_\odot)$ from Blöcker (1995a). $M_{\rm ZAMS}$ is the zero-age main sequence (ZAMS) mass and $M_\star$ the final post-AGB mass of the central star.

(iii) *Spatial calibration*. We accomplished the spatial calibration by using so called 'wire' frames obtained by diffuse illumination of the coronagraphic aperture with a QI lamp. This procedure locates only the center of each slitlet, since small spatial distortions by the spectrograph are corrected by the WiFeS cameras. The IRAF autoidentify task determine the spatial solutions for aligning the spatial scales along each slitlet.

(iv) *Cosmic-ray and bad pixel removal*. Cosmic rays and bad pixels were removed from the rawdata set before the sky subtraction. We used the IRAF task lacos_im (LA-Cosmic package; van Dokkum 2001) to remove cosmic rays from the rawdata files. The IRAF/STSDAS task imedit was used to manually remove bad pixels and any remaining cosmic rays.

(v) *Background subtraction*. A suitable sky window was selected from the science data for the sky subtraction purpose.

(vi) *Flux calibration*. We calibrated the science data to absolute flux units using observations of the spectrophotometric standard star EG 274 and LTT 3864. After manually removing absorption features, an absolute calibration curve was fitted to the integrated spectrum using a third-order polynomial. The flux calibration curve was then applied to the object data using the standard IRAF flux-calibration tasks to convert to an absolute flux scale.

(vii) *Differential atmospheric refraction correction*. The refraction of light by the Earth's atmosphere varies at different wavelengths and optical path length through Earth's atmosphere. To correct it, the IRAF task wfreduce uses the zenith distance, parallactic angle, and local hour angle at the time of observation, and creates a table of atmospheric refraction. This is used to adjust each datacube wavelength slice and relocates each slice in x and y to its exact spatial position by using the IRAF/STSDAS task imshift. The absolute flux scale is then corrected for the atmospheric extinction.

(viii) *Interpolation*. A linear interpolation technique was used to minimize sampling noise due to image-slicing IFU sampling technique and to reconstruct smooth surfaces in 2-D. Residual cosmic rays were identified by finding pixels with values that significantly exceed the neighborhood.

2.2.3 Archival imaging data

To perform our analysis for compact PNe, we obtained *Hubble Space Telescope* (HST) broad- or narrow-band images of PB 6, Hb 4, Pe 1-1, M 3-15, M 1-25, Hen 2-142, Hen 3-1333, Hen 2-113, NGC 6578, NGC 6567 and NGC 6629 from the *HST* archive. These images are listed in Table 2.2, together with the corresponding programme IDs. We used the IRAF task lacos_im to remove cosmic rays from them.

Fig. 2.2 show the *HST* images of these objects. The short exposure time and the MIRVIS long-pass filter used for PB 6 is not suitable for study of the morphology. Similarly, the F350LP and F555W place some limitations as they are not suitable for identifying any FLIERs. The *HST* image taken by the F350LP filter shows the aspherical morphology of Pe 1-1. The F656N narrow-band filter used for M 3-15, M 1-25 and Hen 2-142 clearly show the elliptical morphology. Hen 3-1333 and Hen 2-113 are young and compact, and it is difficult to determine their morphology using the *HST* images. For compact bipolar PNe, we can only determine their orientation from our IFU kinematic maps.

Fig. 2.3 shows the narrow band Hα+[N II] images of other objects, taken with the 3.5-m ESO New Technology Telescope (NTT) by Schwarz et al. (1992), which can be compared with the IFU maps. Three of them, M 3-30, IC 1297 and M 1-32, have elliptical (ring) morphologies. K 2-16 apparently has a spherical morphology. However, our IFU kinematic maps points to an aspherical morphology.

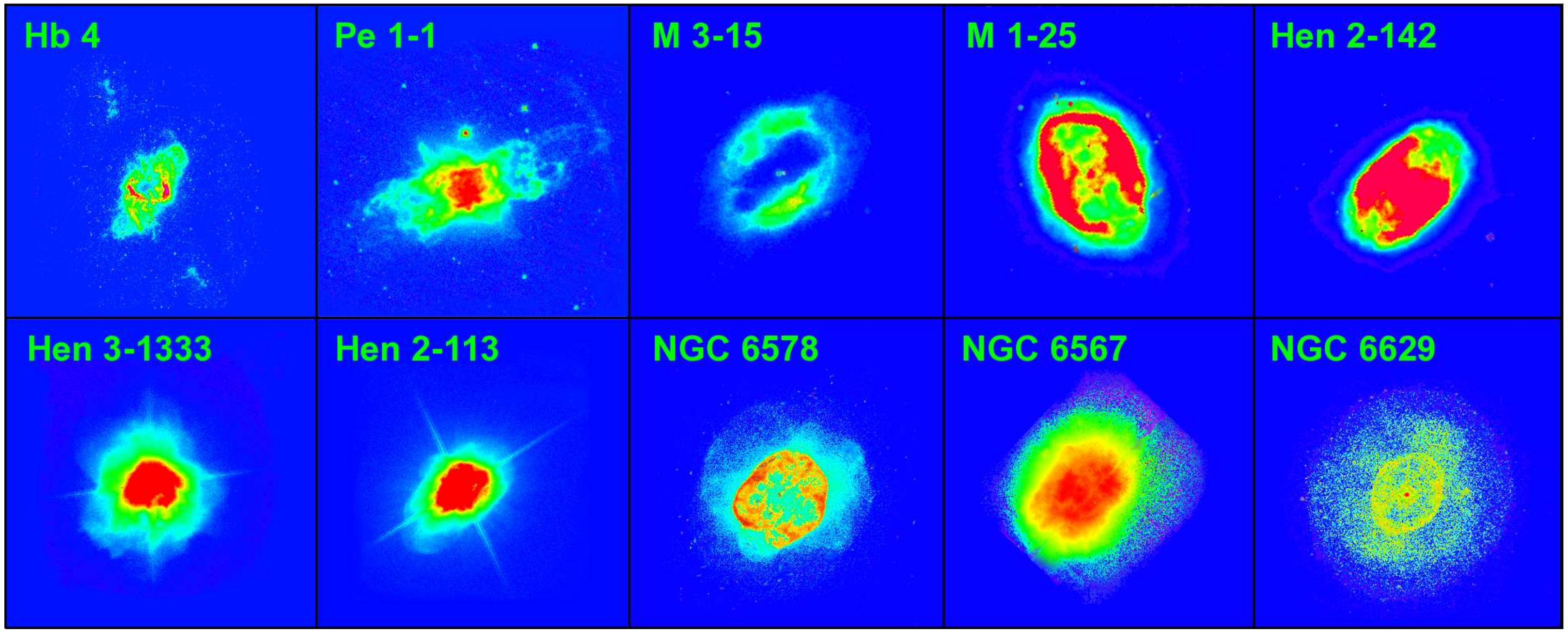

Figure 2.2: *HST* images of Hb 4, Pe 1-1, M 3-15, M 1-25, Hen 2-142, Hen 3-1333, Hen 2-113, NGC 6578, NGC 6567 and NGC 6629. North is up and east is toward the left-hand side. For more detail about the instrument and filter/grating used in each image, see Table 2.2.

Table 2.2: Archival *HST* images of our sample.

Name	Instrument	Aperture	Filters/ Gratings	Wavelength range (Å)	Plate scale (arcsec/pix)	Exp.Time (sec)	Programme ID	PI
PB 6	STIS	F28X50LP	MIRVIS	4950–9450	0.050	22	12600	R. Dufour
Hb 4	WFPC2	PC	F658N	6570–6598	0.045	400	6347	K. Borkowski
Pe 1-1	WFC3	UVIS	F350LP	3467–8225	0.039	136	11657	L. Stanghellini
M 3-15	WFPC2	PC	F656N	6552–6570	0.045	100	9356	A. Zijlstra
M 1-25	WFPC2	PC	F656N	6552–6570	0.045	300	8345	R. Sahai
Hen 2-142	WFPC2	PC	F656N	6552–6570	0.045	400	6353	R. Sahai
Hen 3-1333	ACS	HRC	F606W	4796–6978	0.026	34	9463	R. Sahai
Hen 2-113	ACS	HRC	F606W	4796–6978	0.026	60	9463	R. Sahai
NGC 6578	WFPC2	PC	F502N	4995–5050	0.045	160	11122	B. Balick
NGC 6567	NICMOS	NIC	F108N	10797–10836	0.043	384	7837	S. Pottasch
NGC 6629	WFPC2	PC	F555W	4789–6025	0.045	10	6119	H. Bond

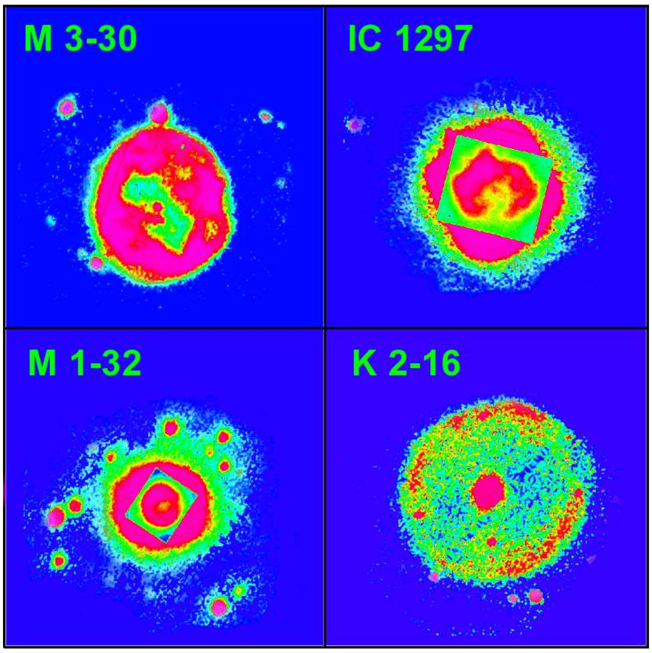

Figure 2.3: Narrow band Hα+[N II] images of M 3-30, IC 1297, M 1-32 and K 2-16 taken with the 3.5-m ESO New Technology Telescope (NTT) by Schwarz et al. (1992). North is up and east is toward the left-hand side.

2.3 Observational results

2.3.1 Systemic and expansion velocities

Table 2.3 lists our velocity results for different emission lines of the integrated spectrum of each PN. Column 2 presents the local standard of rest (LSR) systemic velocity ($v_{\rm sys}$) derived from the Hα emission line, corresponding to the mean LSR velocity of the whole nebula, which is compared with the previously published value from Durand et al. (1998) in Column 3. The LSR velocity is defined as the line of sight radial velocity, transferred to the local standard of rest by correcting for the motions of the Earth and Sun. Our expansion velocities ($v_{\rm exp}$) derived from the half width at half maximum (HWHM) for Hα λ6563, [N II] $\lambda\lambda$6548,6584 and [S II] $\lambda\lambda$6716,6731, and average HWHM values are presented in columns 4–7, respectively. Column 8 provides the expansion velocity from the reference given in Column 9. The IFU data and moprho-kinematic models enable us to determine the PN morphology more clearly (see Section 2.4), which are summarized in Columns 10 and 11; the primary morphological classification and the secondary descriptors, giving details about other characteristics according to the classification codes introduced by Sahai et al. (2011). This classification has four primary classes: bipolar (*B*), elliptical (*E*), multipolar (*M*), and irregular (*I*). The *B* class is defined by objects having two primary, diametrically opposed lobes, centered on its expected location. The *E* class represents objects which are elliptical along a specific axis. The *M* class defines objects showing more than one primary lobe pairs whose axes are not aligned. The *I* class is defined by objects do not display any geometrical symmetry. The structure may be open or closed at their outer ends, which denoted by '*o*' or '*c*', respectively. The secondary descriptors describe other structural features in the *B*, *E* and *M* classes. The point symmetry is denoted by *ps*: due to two or more pairs of diametrically opposed lobes by *ps(m)*, diametrically opposed ansae by *ps(an)* and overall shape of the lobes by *ps(s)*. Rings projected on lobes is denoted by *rg*. The central region with a toroidal structure is defined by '*t*'.

We corrected the observed radial velocity $v_{\rm obs}$ for the radial velocities induced by the motions of the Earth and Sun at the time of our observation by using the IRAF/ASTUTIL task rvcorrect, that represents the LSR radial velocity. We also corrected the measured velocity dispersion ($\sigma_{\rm obs}$) for the instrumental width and the thermal broadening according to $\sigma_{\rm true} = (\sigma^2_{\rm obs} - \sigma^2_{\rm ins} - \sigma^2_{\rm th} - \sigma^2_{\rm fs})^{1/2}$. The instrumental width $\sigma_{\rm ins}$ is derived from the [O I] λ5577 and λ6300 night sky lines, which is typically $\sigma_{\rm ins} \approx 18\,{\rm km\,s^{-1}}$ for the WiFeS at the chosen spectral resolution of $R \sim 7000$. The thermal broadening $\sigma_{\rm th}$ is obtained through the Boltzmann's equation $\sigma^2_{\rm th} = 8.3\,T_e[{\rm kK}]/Z$ [${\rm km\,s^{-1}}$], where Z is the atomic weight of the atom or ion. The observed velocity dispersion $\sigma_{\rm obs}$ should be also corrected for the fine structure broadening $\sigma_{\rm fs}$ in the hydrogen recombination lines, that is typically $\sigma_{\rm fs} \approx 3$ ${\rm km\,s^{-1}}$ for Hα (Clegg et al. 1999). The expansion velocities were obtained through the observed true HWHM of the integrated flux across the whole nebula, i.e. $V_{\rm HWHM} = (8\ln(2))^{1/2}\sigma_{\rm true}/2$ [km s^{-1}].

Measuring the expansion velocity by means of the HWHM method is not very fruitful for more detailed kinematic studies. The radiation-hydrodynamics models by Schönberner et al. (2010) showed that the HWHM velocities of volume-integrated line profiles always underestimate the true expansion velocity. They also found that the HWHM method is suitable for slowly expanding objects, but it does not reflects real expansion velocities of larger spatially resolved objects. For the Magellanic Cloud PNe, Dopita et al. (1985, 1988) assumed that $v_{\rm exp} = 1.82\,V_{\rm HWHM}$, nearly twice the more widespread use of the HWHM velocity. This definition measures the maximum gas velocity behind the outer shock. It may not represent the expansion velocity of the nebular shell. Here, we however assumed $v_{\rm exp} = V_{\rm HWHM}$, which measures the expansion of a spherical gaseous shell. In Section 2.4, we see that the HWHM velocities overestimate the true expansion velocity of some nebular shell: M 3-30, IC 1297 and M 1-32. These errors can be due to the contribution of FLIERs embedded in the main structure.

Table 2.3: LSR systemic velocities, expansion velocities and morphological classification for PNe. References are as follows: A76 – Acker (1976); A02 – Acker et al. (2002); A12 – Akras & López (2012); D97 – De Marco et al. (1997); D98 – Durand et al. (1998); G96 – Gesicki & Acker (1996); G07 – Gesicki & Zijlstra (2007); G09 – García-Rojas et al. (2009); L97 – Lopez et al. (1997); M88 – Meatheringham et al. (1988); M06 – Medina et al. (2006); P01 – Peña et al. (2001); R09 – Richer et al. (2009); W89 – Weinberger (1989).

Name	v_{sys}(Hα)	v_{sys}(km s^{-1})	V_{HWHM}(km s^{-1})				v_{exp} [a]	Ref. [a]	Morphology[b]	
	(km s^{-1})	D98	Hα	[N II]	[S II]	Mean	(km s^{-1})	(v_{exp})	P	S
PB 6	52.1	45.9 ± 1.3	35.5	32.5	30.6	32.9 ± 2.4	38 ± 4	G09	E/I?	ps(m)?
M 3-30	79.2	67.3 ± 14.0	31.6	41.9	35.0	36.2 ± 5.1	37.31 ± 5	M06	E,o	rg,ps(an)
Hb 4	−45.9	-48.5 ± 1.5	23.2	24.0	22.4	23.2 ± 0.8	21.5	L97	E,o	rg,ps(an)
IC 1297	12.6	16.6 ± 1.5	31.8	31.7	30.1	31.2 ± 0.8	32.7 ± 1.7	A76	E,o	ps(an)?
Th 2-A	−52.9	-51.3 ± 18.0	39.7	30.0	34.4	34.7 ± 4.8	35	M88	E,o	rg,ps(an)
Pe 1-1	7.1	8.0 ± 0.5	21.7	24.3	24.3	23.4 ± 1.3	24	G96	E,o	ps(an)
M 1-32	−73.8	-76.8 ± 7.6	33.7	32.0	27.9	31.2 ± 2.9	14:	P01	E,o	rg,ps(an)
M 3-15	111.3	109.7 ± 0.7	23.7	22.3	17.8	21.2 ± 3.0	18.2	R09	E,o	rg,ps(an)

Remarks:

[a] References to expansion velocities given in column 9. [b] Morphological classification codes by Sahai et al. (2011).

Table 2.3: (continued)

Name	$v_{\rm sys}$(Hα)	$v_{\rm sys}$(km s^{-1})	$V_{\rm HWHM}$(km s^{-1})				$v_{\rm exp}$ [a]	Ref. [a]	Morphology[b]	
	(km s^{-1})	D98	Hα	[N II]	[S II]	Mean	(km s^{-1})	Ref. [a]	P	S
M 1-25	25.8	26.3 ± 2.0	27.4	28.3	24.2	26.6 ± 2.0	23	M06	E,o	
Hen 2-142	-92.5	-94.5 ± 0.3	22.1	21.6	17.5	20.4 ± 2.3	20	A02,G07	E,o	
Hen 3-1333	-62.2	-64.8 ± 12.0	31.6	37.2	30.6	33.1 ± 3.3	30	D97	B/M	t?
Hen 2-113	-56.7	-58.0 ± 0.3	22.5	22.3	20.1	21.6 ± 1.2	19	D97	B/M	t?
K 2-16	23.4	14.9 ± 12.0	31.0	34.1	28.5	31.2 ± 2.8	34	A02	E	rg,ps(an)
NGC 6578	19.3	17.1 ± 1.8	18.7	23.5	23.6	21.9 ± 3.0	17.2 ± 1.4	M06	E,c	
M 2-42	122.9	133.1 ± 13.3	14.5	21.5	18.9	18.3 ± 3.5	15	A12	E	rg,ps(an)
NGC 6567	136.7	132.4 ± 0.7	24.2	38.9	37.5	33.5 ± 8.0	19	W89	E,c	
NGC 6629	25.0	26.5 ± 1.3	16.5	20.8	23.7	20.3 ± 3.6	16.3 ± 2.5	M06	E,c	
Sa 3-107	-132.9	–	17.0	16.9	14.5	16.1 ± 1.6	–	–	B/E?	

2.3.2 Flux and velocity maps

A spatially resolved emission line profile contains the information of flux intensity, continuum offset, radial velocity and velocity dispersion. As a first step, we extracted this information from a chosen emission line profile (Hα and [N II] in the present study) for each spaxel of the datacube by fitting Gaussian functions using an IDL-based routine MPFIT developed by Markwardt (2009) for the non-linear least-squares minimization problem. The emission line profile is resolved if its width is wider than the instrumental width ($\sigma_{\rm ins}$).

By fitting Gaussian profiles to the emission line Hα and [N II] for all spaxels across the IFU field, we mapped the flux intensity, continuum, LSR velocity, and velocity dispersion of each object, as shown in Fig. 2.4 for [WR] PNe M 3-30, Hb 4, IC 1297, Th 2-A and K 2-16 (for all PNe see Appendix A). Contour lines in the figure depict the 2-D distribution of the Hα emission obtained from the SuperCOSMOS Hα Sky Survey (SHS; Parker et al. 2005), which can aid us in distinguishing the nebular borders. We also smoothed the extracted map spatially using interpolation between 2 spaxels, in order to increase the signal-to-noise (S/N) ratio.

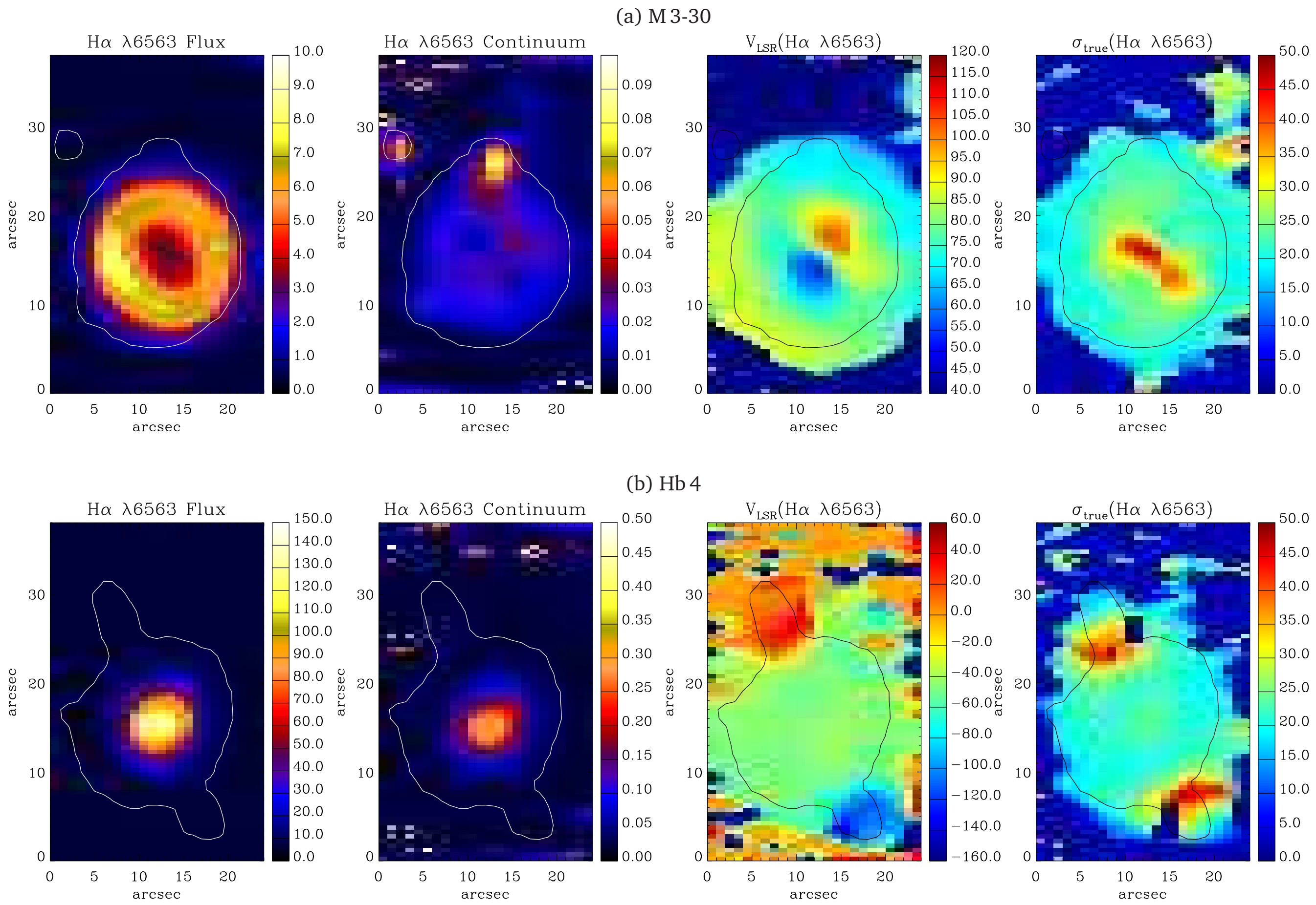

Figure 2.4: From left to right, spatial distribution maps of flux intensity, continuum, LSR velocity and velocity dispersion of Hα λ6563 emission line profile for M 3-30, Hb 4, IC 1297, Th 2-A and K 2-16. Flux unit is in 10^{-15} erg s^{-1} cm^{-2} spaxel^{-1} and velocity unit in km s^{-1}.

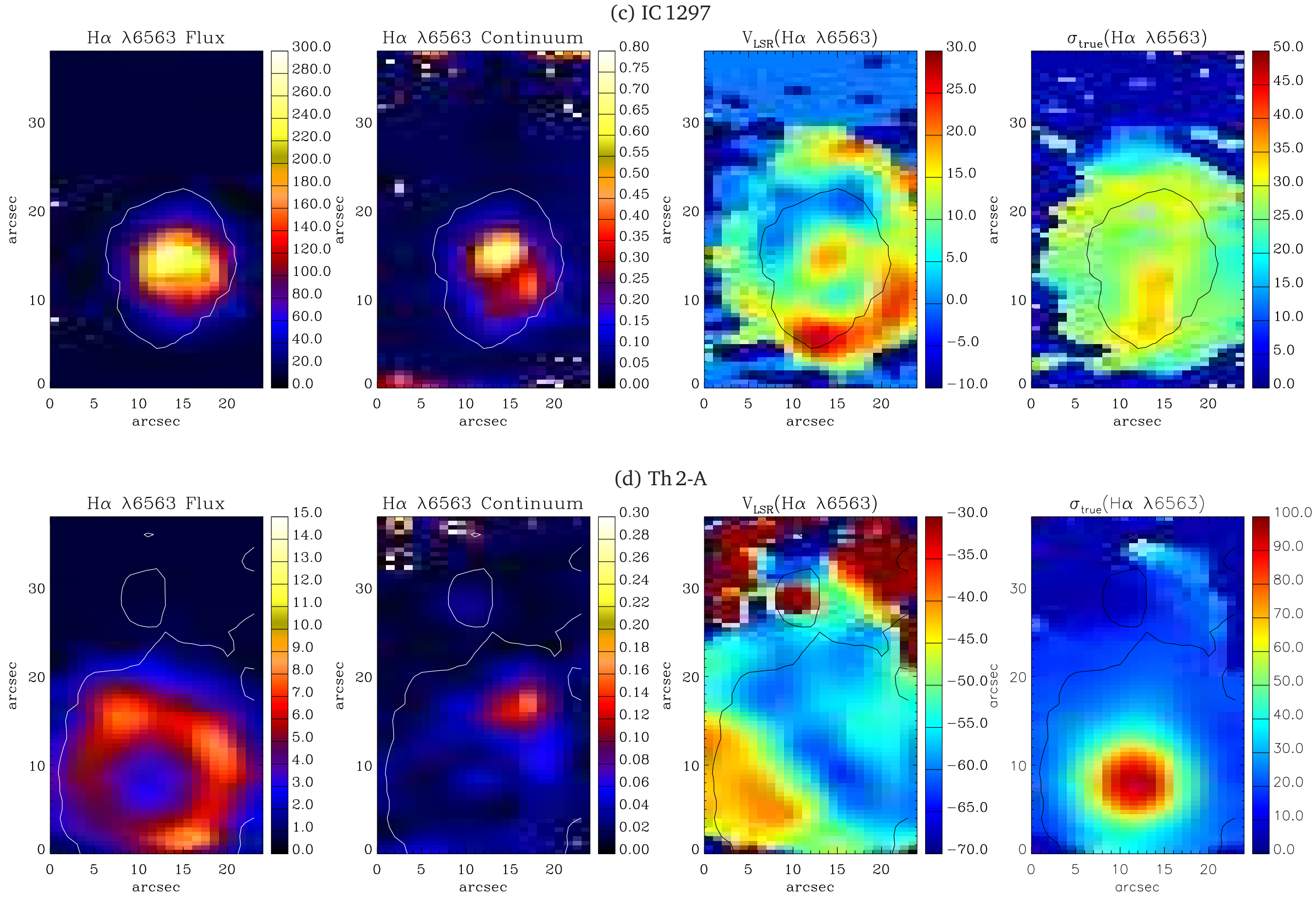

Figure 2.4: (continued)

(e) K 2-16

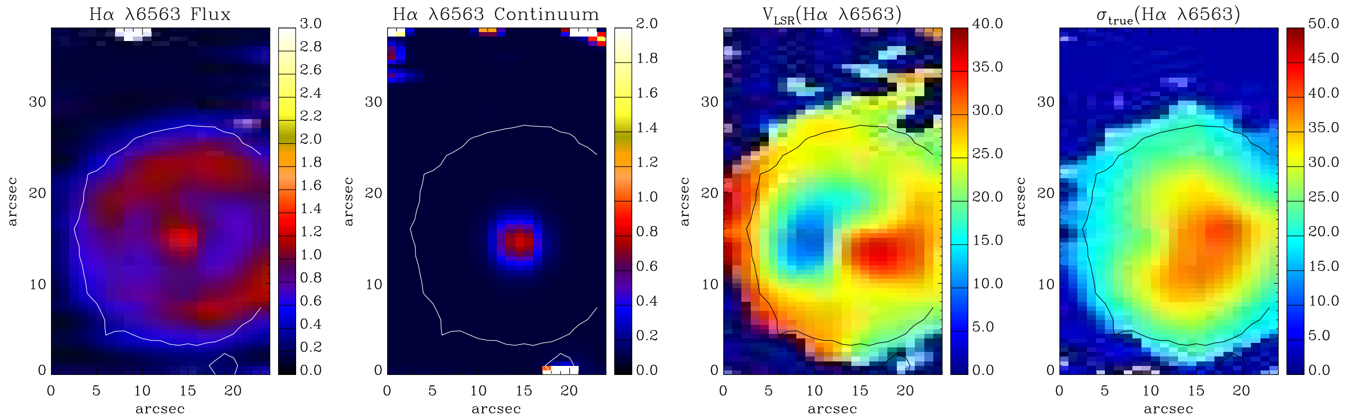

Figure 2.4: (continued)

2.3.3 Results of individual objects

PB 6. As seen in the *HST* image (Fig. A1 b), PB 6 has a highly filamentary structure and several knots inside and outside the main shell. However, the short exposure time ($t = 22$ sec) and the MIRVIS long-pass filter (4950–9450 Å) did not reveal much detail of the nebula structure. Our IFU velocity map (Fig. A1 a) taken with a longer exposure time ($t = 1200$ sec) depicts that two groups of ionized gas are moving in opposite directions on the both sides of the CSPN, which presumably are LISs. We estimated the LSR systemic velocity at $v_{\rm sys} = 52\,{\rm km\,s^{-1}}$. For this object, we obtained a mean expansion velocity of $V_{\rm HWHM} = 32.9 \pm 2.4$ ${\rm km\,s^{-1}}$ from Hα, [N II] and [S II] emission lines. García-Rojas et al. (2009) obtained $v_{\rm exp} = 38 \pm 4$ from the [O III] line.

M 3-30. From Hα, [N II] and [S II] emission-line profiles, we estimated the expansion velocity as $36.2 \pm 5.1\,{\rm km\,s^{-1}}$ for the whole structure. Our derived expansion velocity from [N II] emission, $V_{\rm HWHM} = 41.9\,{\rm km\,s^{-1}}$, is in agreement with $v_{\rm exp}([\rm N\ II]) = 37.3 \pm 5\,{\rm km\,s^{-1}}$ found by Medina et al. (2006). Previously, Stanghellini et al. (1993) also identified the morphology as the elliptical with inner knots or filaments. The kinematics maps (Fig. 2.4a) also show a pair of FLIERs embedded in the main structure moving with the radial velocity of $\pm 54 \pm 10\,{\rm km\,s^{-1}}$ with respect to the main body, much larger than the expansion velocity of the whole nebula. These FLIERS are also visible in the narrow-band Hα+[N II] image taken with the 3.5 m ESO NTT (Schwarz et al. 1992); see Fig. 2.3. The velocity dispersion is much higher in the center between the two FLIERS.

Hb 4. As shown in Fig. 2.4b, the radial velocity maps of HB 4 indicates the presence of two FLIERs outside of the main body. The *HST* image of Hb 4 (see Fig. 2.2) also depicts that the main shell has indeed a torus morphology. This ring structure is not noticeable in the IFU flux and velocity maps due to the low spatial resolution. The FLIERs have low-ionization and very low brightness, as we cannot easily see them in the IFU flux intensity map, while we notice them in the radial velocity and velocity dispersion maps. We determined $v_{\rm jet} = \pm 150 \pm 10\,{\rm km\,s}^{-1}$ with respect to the LSR systemic radial velocity of $-45.9 \pm 4\,{\rm km\,s}^{-1}$ at the inclination angle of $i = 40^{\circ}$, which is similar to the value found by Lopez et al. (1997) from the Echelle long-slit spectra. These FLIERs were previously found by Corradi et al. (1996) in the (Hα+[N II])/[O III] image. Our velocity dispersion map also shows a high value of $45 \pm 10\,{\rm km\,s}^{-1}$ in the locations of FLIERs. Excluding FLIERs, we determined $V_{\rm HWHM} = 23.2 \pm 0.8\,{\rm km\,s}^{-1}$ for the main shell of Hb 4 from Hα, [N II] and [S II] emission line profiles. Our value is in excellent agreement with what found by Robinson et al. (1982) and Lopez et al. (1997). However, Acker et al. (2002) obtained expansion and turbulence velocities of 16 and 14 km s^{-1}, respectively. Similarly, Medina et al. (2006) found $v_{\rm exp} = 16\,{\rm km\,s}^{-1}$ for Hβ, but 23 km s^{-1} for He II λ4686.

IC 1297. The velocity map in Fig. 2.4c points out that IC 1297 has a ring-shaped morphology. Zuckerman & Aller (1986) described it as a broken ring. But, Stanghellini et al. (1993) classified it under the irregular nebulae, as it was difficult to recognize any morphology from the Hα and [O III] narrow band image (see Fig. 2.3) taken with the 3.5-m ESO New NTT (Schwarz et al. 1992). The Hα, [N II] and [S II] emission lines yield a mean $V_{\rm HWHM} = 31.2 \pm 1\,{\rm km\,s}^{-1}$, which is in good agreement with $v_{\rm exp}({\rm H}\alpha) = 31\,{\rm km\,s}^{-1}$ and $v_{\rm exp}([{\rm N\ II}]) = 34.5\,{\rm km\,s}^{-1}$ reported by Acker (1976) (see Table I in Weinberger 1989); though Gesicki & Zijlstra (2000) derived a lower value of 22 km s^{-1} from HWHM of the asymmetric [O III] emission line. Corradi et al. (1996) earlier suggested the presence of 1 isolated knot, which was later rejected by Gonçalves et al. (2001), and turned out to be a field star. But, our IFU kinematic maps reveal the presence of a pair of FLIERs embedded in the main shell.

Th 2-A. The ring-like morphology of Th 2-A is visible in the Hα image (see Fig. A5) of Górny et al. (1999). As seen in Fig. 2.4d, our radial velocity and velocity dispersion maps show a toroidal structure. Furthermore, we notice high velocity dispersion in the center. This may point at FLIERs, and requires further investigations. The Hα, [N II] and [S II] emission lines represent a mean expansion velocity of $V_{\rm HWHM} = 34.7 \pm 4.8\,{\rm km\,s^{-1}}$, in agreement with $v_{\rm exp}([{\rm O\ III}]) = 35\,{\rm km\,s^{-1}}$ by Meatheringham et al. (1988).

Pe 1-1. As shown in Fig. 2.2, the *HST* image taken via the F350LP filter shows that Pe 1-1 has a barrel morphology with open ends. We can see two bipolar outflows on the both sides of the central star. Our radial velocity map taken with the WiFeS (Fig. A6 a) depicts the same bipolar orientation on the sky plane, as seen in the *HST* images. Additionally, our velocity dispersion shows two FLIERs having a high velocity dispersion of $\sigma_{\rm true} = 35 \pm 10\,{\rm km\,s^{-1}}$ on both sides. The whole structure has a $\sigma_{\rm true} = 19.9 \pm 1.4\,{\rm km\,s^{-1}}$ and expands with $V_{\rm HWHM} = 23.4 \pm 1.7\,{\rm km\,s^{-1}}$. This is in good agreement with $v_{\rm exp} = 24\,{\rm km\,s^{-1}}$ derived by Gesicki & Acker (1996) from Hβ emission line profile, whereas they also estimated a macroturbulence of $10\,{\rm km\,s^{-1}}$.

M 1-32. A narrow-band Hα+[N II] image of M 1-32 taken with the 3.5 m ESO NTT by Schwarz et al. (1992) reveals a compact torus morphology (see Fig. 2.3). We cannot distinguish it in our IFU field (Fig. A7 a). But, the radial velocity map aids us in determining the orientation of this nebula projected onto the plane of the sky. We estimated an expansion velocity of $V_{\rm HWHM} = 31.2 \pm 2.9\,{\rm km\,s^{-1}}$, which is much higher than $v_{\rm exp} = 14$ and $\leq 13\,{\rm km\,s^{-1}}$ found by Peña et al. (2001) and Medina et al. (2006), respectively. It seems that we also measured some contributions of FLIERs. Peña et al. (2001) found profile wings that extend to about $\pm 100\,{\rm km\,s^{-1}}$, which may be associated with a high velocity bipolar or multipolar ejection.

M 3-15. As seen in Fig. 2.2, the *HST* image reveals that M 3-15 has a torus morphology with a radius of $\simeq 2''$ from its center to the tube center. The spatial resolution of our IFU field is not enough to show it. Using the *HST* image, Sahai et al. (2011) describes it as an object having collimated lobe pair, and the lobes are closed at ends. For M 3-15, we estimated the expansion velocity of

$V_{\rm HWHM} = 23.0\,{\rm km\,s^{-1}}$ from Hα and [N II] emission lines, though we got $V_{\rm exp} = 17.8\,{\rm km\,s^{-1}}$ from [S II] emission line. Using [O III], Hα and [N II] lines, Gesicki & Acker (1996) determined the expansion velocity and macroturbulence of 16 and $17\,{\rm km\,s^{-1}}$, respectively. Recently, Richer et al. (2009) also derived $V_{\rm exp} = 18.2\,{\rm km\,s^{-1}}$ from [O III] λ5007.

M 1-25. Fig. 2.2 shows the *HST* images of M 1-25 taken via the F656N filter. Sahai et al. (2011) described it as an elliptical structure with lobes closed at the ends. We determined an expansion velocity of $V_{\rm HWHM} = 26.6 \pm 2\,{\rm km\,s^{-1}}$, which is in the range of the values previously found: Gesicki & Acker (1996) obtained an expansion velocity of $30\,{\rm km\,s^{-1}}$ and a macroturbulence of $12\,{\rm km\,s^{-1}}$, while Medina et al. (2006) derived $v_{\rm exp} = 23\,{\rm km\,s^{-1}}$.

Hen 2-142. The *HST* image (Fig. 2.2) shows that Hen 2-142 has a bipolar morphology with two lobes emanating at the main nebula. Sahai & Trauger (1998) described them as long filaments, probably jetlike outflows, on opposite sides of the nebula. The jetlike structure, filaments with no evidence of velocities higher than the expansion velocity of the main nebula (Gonçalves et al. 2001), have been observed in several young PNe (e.g. Sahai & Trauger 1998). It is unclear how these jetlike structures are produced in young PNe. The typical seeing of $\delta x \sim 2$ arcsec is not enough to disclose the kinematic structure of this compact PN. However, we determined an expansion velocity of $V_{\rm HWHM} = 20.4 \pm 2\,{\rm km\,s^{-1}}$ from Hα, [N II] and [S II] emission line profiles. This in full agreement with $v_{\rm exp} = 20\,{\rm km\,s^{-1}}$ by Acker et al. (2002) and Gesicki & Zijlstra (2007); they also found a turbulence velocity of $7\,{\rm km\,s^{-1}}$.

Hen 3-1333. The *HST* image (Fig. 2.2) shows a compact dusty disk or torus structure in Hen 3-1333 (De Marco & Soker 2002; Chesneau et al. 2006). The *HST* images studied by Chesneau et al. (2006) depict a complex external structure including several lobes and an internal structure i.e. two dark lanes, in addition to the compact carbon disk; previously determined by De Marco & Soker (2002). Our observation for the Hα emission line profile gives

$V_{\rm HWHM} = 31.6\,{\rm km\,s^{-1}}$, in agreement with $v_{\rm exp} = 30\,{\rm km\,s^{-1}}$ derived by De Marco et al. (1997).

Hen 3-113. The *HST* image (Fig. 2.2) shows two ringlike structures in Hen 2-113, described as the projection of a hourglass-shaped geometrical model by Lagadec et al. (2006). Our observation for the Hα emission line profile presents $V_{\rm HWHM} = 22.5\,{\rm km\,s^{-1}}$. This is in agreement with $v_{\rm exp} = 19\,{\rm km\,s^{-1}}$ derived by De Marco et al. (1997). Additionally, Gesicki et al. (2006) derived expansion and turbulence velocities of 18 and $15\,{\rm km\,s^{-1}}$, respectively.

K 2-16. K 2-16 is a faint, circular nebula with a diameter of 23″. Kohoutek (1977) suggested that it is probably a large and old PN. As seen in Fig. 2.3, the image taken with the 3.5 m ESO NTT, using EFOSC2, through a narrow Hα+[N II] filter shows a faint circular morphology. We took an IFU field of this PN with exposure time of 20 minutes. As seen in Fig. 2.4e, the velocity structure is more likely associated with a toroidal nebula with inner FLIERs. We determined an expansion velocity of $V_{\rm HWHM} = 31.2 \pm 2.8\,{\rm km\,s^{-1}}$ from Hα, [N II] and [S II] emission line across the whole nebula. Our value of the expansion velocity obtained here is in good agreement with $v_{\rm exp} = 34\,{\rm km\,s^{-1}}$ derived by Acker et al. (2002); while they also obtained a turbulence velocity of $12\,{\rm km\,s^{-1}}$.

NGC 6578. The *HST* image, Fig. 2.2 shows a barrel with closed ends (Sahai et al. 2011). Previously, Stanghellini et al. (1993) described it as elliptical with inner filamentary structure. The Hα emission line yields a HWHM velocity of $V_{\rm HWHM} = 18.7\,{\rm km\,s^{-1}}$, which is in agreement with $v_{\rm exp} = 17.2\,{\rm km\,s^{-1}}$ derived from Hβ, [O III] and [N II] by Medina et al. (2006). Our derived LSR systemic radial velocity of $v_{\rm sys} = 19.3\,{\rm km\,s^{-1}}$ is also in agreement with $v_{\rm LSR} = 17.1 \pm 1.8\,{\rm km\,s^{-1}}$ by Durand et al. (1998).

M 2-42. The radial velocity map combined with the Hα image obtained from the SuperCOSMOS Sky Survey (Fig. A15; Parker et al. 2005) shows an elliptical shape with two point-symmetric knots. The Hα HWHM velocity yields $V_{\rm HWHM} = 14.5\,{\rm km\,s^{-1}}$ for the shell, in agreement with $v_{\rm exp} = 15\,{\rm km\,s^{-1}}$ derived by

Akras & López (2012). As seen in Table 2.3, the HWHM velocities determined from [S II] and [N II] are slightly higher than the value given by the Hα profile. This may indicate that low ionization zones (N^+ and S^+) have been formed far from the ionizing source.

NGC 6567. NGC 6567 has been classified as elliptical by several authors (e.g. Zuckerman & Aller 1986; Stanghellini et al. 1993; Gorny et al. 1997). As seen in Table 2.3, our derived velocities from [S II] and [N II] emission lines are much higher than the value $V_{\rm HWHM} = 24.3\,{\rm km\,s^{-1}}$ deduced from Hα profile and previous published results: $v_{\rm exp} = 18\,{\rm km\,s^{-1}}$ (Zuckerman & Aller 1986) and $19\,{\rm km\,s^{-1}}$ (Weinberger 1989). Recently, Medina et al. (2006) got $v_{\rm exp} = 17\,{\rm km\,s^{-1}}$ and $27\,{\rm km\,s^{-1}}$ from [O III] and [N II] profiles, respectively. They are probably from two different ionization zones. Emission lines from high excitation zones usually have a lower expansion velocity, since they are closer to the central star.

NGC 6629. The *HST* image of NGC 6629 (see Fig. 2.2) depicts an elliptical-shaped with closed ends, and also multiple halos, as previously identified by Stanghellini et al. (1993). The derived explanation velocity $V_{\rm HWHM}({\rm H}\alpha) = 16.5\,{\rm km\,s^{-1}}$ is in excellent agreement with $v_{\rm exp}({\rm H}\beta) = 16.5\,{\rm km\,s^{-1}}$ found by Medina et al. (2006). The LSR systemic velocity, $v_{\rm sys} = 25\,{\rm km\,s^{-1}}$ is also in good agreement with the result found earlier, $v_{\rm LSR} = 26.6\,{\rm km\,s^{-1}}$ (Schneider et al. 1983; Maciel & Dutra 1992).

Sa 3-107. Although the SuperCOSMOS Sky Survey (Fig. A18; Parker et al. 2005) shows an round shape, our radial velocity maps correspond to a bipolar morphology. For this object, we obtained a mean expansion velocity of $V_{\rm HWHM} = 16.1 \pm 1.6\ {\rm km\,s^{-1}}$ from Hα, [N II] and [S II] emission lines. We also obtained the LSR systemic velocity of $v_{\rm sys} = -132.9\,{\rm km\,s^{-1}}$.

2.4 Morpho-kinematic modeling

We have used the three-dimensional morpho-kinematic modeling program SHAPE (version 4.5) to study the kinematic structure of our sample. The program has been used to model a number of PNe, for example NGC 6337 (García-Díaz et al. 2009), Abell 41 (Jones et al. 2010b), Hb 5 (López et al. 2012), HaTr 4 (Tyndall et al. 2012), NGC 7026 (Clark et al. 2013) and Abell 65 (Huckvale et al. 2013). The program, described in detail by Steffen & López (2006) and Steffen et al. (2011), uses interactively molded geometrical polygon meshes to generate the three-dimensional structure of gaseous nebulae. It constructs a cell grid, each cell representing a volume, and uses a ray-casting algorithm to perform radiative transfer through these cells. For the present study, the three-dimensional structure has then been transferred to a regular cell grid, together with the physical emission properties, including the velocity that, in our case, has been define as radially outwards from the nebular center with a linear function of magnitude, which increases uniformly with distance from the nebular center, commonly known as a homologous flow (Steffen et al. 2009). The program produces several outputs that can be directly compared with long slit or IFU observations, namely the position-velocity (P-V) diagram, the two-dimensional velocity tomography (or channels) and appearance of the object on the sky (projected three-dimensional emissivity). The P-V diagrams are used for multiple long slit spectra. The velocity map (or channels) can be used to interpret the IFU velocity map. The two-dimensional appearance can be compared with the nebula image, but ionization stratification of each ion makes different morphologies in different emission lines. The program does not include explicit photo-ionization modeling, such that under such conditions the emissivity distribution for each spectral line is modeled ad-hoc based on the observations of the corresponding emission line.

The modeling procedure consists of defining the geometry (e.g. torus, sphere and cylinder and their modification), assigning emissivity distribution and defining a velocity law as a function of position. For best comparison with our IFU maps, the 3D emission and velocity information has then been exported and processed in the same way. The inclination (θ), the position angle '*PA*' in the plane of the sky, and the model parameters are modified in an iterative process until the qualitatively fitting solution is produced. The Hα and [N II] radial velocity maps were used to determine the morphology and its orientation for each PN. We adopted a 3D model, and then modified its geometric parameters and inclination to conform to the observations.

To determine the inclination of the system to the line-of-sight, we require to iteratively adjust the inclination angle, and compare 2-D velocity maps produced by morpho-kinematic models with IFU velocity maps. The inclination angle can also be used to examine whether its morphology is linked to the orbital inclination of its possible binary system (see e.g. Mitchell et al. 2007; Tyndall et al. 2012). For example, Fig. 2.5 shows the 2-D line-of-sight velocity map and the projected 3-D emissivity on the sky at the inclination of 45° for two different models, toroidal with inner FLIERs, and with outer FLIERs. It is difficult to identify FLIERs due to the projection effects at the inclination of $i = 0°$ and 90°. But, 2-D velocity maps allow us to easily determine FLIERs inside or outside the global structure at other inclination angles.

2.4.1 Modeling results

Table 2.4 lists the key parameters and results of the best-fitting morpho-kinematic models, which have been obtained by comparing the IFU maps and the archival images with the results produced by the models. Columns 4–6 present the position angle (PA), the Galactic position angle (GPA), and the inclination (θ) in the sky plane, respectively. The PA is the position angle of the nebular symmetry axis projected onto the plane of the sky, and measured from the north towards

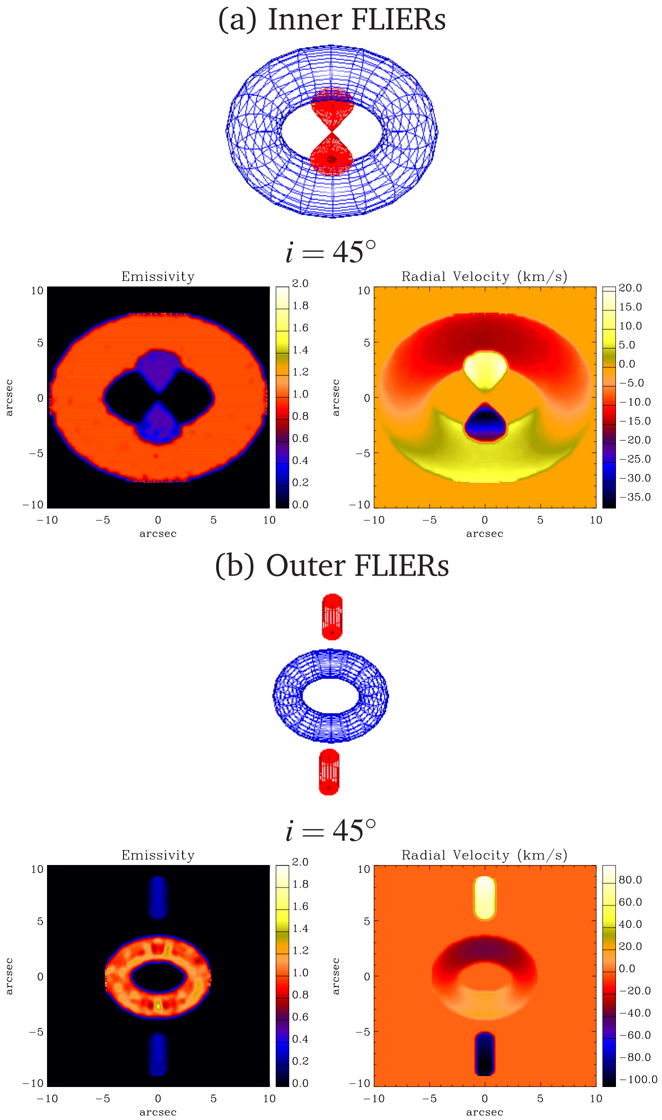

Figure 2.5: The SHAPE mesh models of (a) torus with inner FLIERs and (b) torus with outer FLIERs. The derived 2-D line-of-sight velocity map and the projected 3-D emissivity on the plane of the sky at the inclination of 45°.

the east in the equatorial coordinate system (ECS). The GPA is the position angle projected onto the sky plane, measured from the North Galactic Pole (NGP) towards the Galactic east. Comparison between observed and model velocity components yields the LSR systemic velocity ($v_{\rm sys}$) and the expansion velocity ($v_{\rm exp}$) given in Columns 7 and 8, respectively. But, we were not able to determine $v_{\rm exp}$ of most PNe from their radial velocity maps. Column 9 gives the

HWHM velocities for comparison with the results (Column 8) from spatially resolved methods. We notice that the HWHM velocities overestimate the true expansion velocity of M 3-30, IC 1297 and M 1-32 because of the effects of FLIERs embedded in the nebula. The velocity of the FLIERs ($v_{\rm jet}$), together with its reference, are given in Columns 10 and 11.

The SHAPE mesh models before rendering are shown in Fig. 2.6 at their best-fitting inclinations to the line of sight. The results of the rendered models are shown in Fig. 2.7. More detail of the models and IFU kinematic maps are shown in Figs. A1–A18 (see Appendix A).

2.4.2 Notes on individual objects

M 3-30. A SHAPE model has been constructed for M 3-30, which is consistent with the nebular Hα emission features. As shown in Fig. 2.6, the model was built with a torus and inner bi-conical structure for its two FLIERs. The rendered representation of M 3-30 in Fig. 2.7 displays the similar appearance seen in the narrow band Hα+[N II] image taken by Schwarz et al. (1992) (Fig. 2.3). From the model, we derived a position angle of $-44^{\circ} \pm 5^{\circ}$ and an inclination of $34^{\circ} \pm 5^{\circ}$ relative to the line of sight. The maximum observed velocity between redshifted and blueshifted of the torus in the velocity map (Fig. 2.4a) corresponds to the expansion velocity of ~ 27 km s^{-1} at the inclination of the PN. This expansion velocity is lower than the value of ~ 36 km s^{-1} derived from the HWHM of the integrated line flux. This error can be explained by two FLIERs embedded in the main body. Similarly, we derived $v_{\rm jet} = \pm 54$ km s^{-1} with respect to $v_{\rm sys} = 67$ km s^{-1}, from the maximum observed velocity measured in the bi-conical structure. The morpho-kinematic model shows that the ring likely expands at a lower velocity similar to that of the ring in Hb 4.

Table 2.4: The key parameters and results of the best-fitting morpho-kinematic models. References are as follows: A12 – Akras & López (2012): D13 – this work.

Name	CSPN	PNG	PA (°)	GPA (°)	θ (°)	v_{sys} (km s^{-1})	v_{exp} [a] (km s^{-1})	V_{HWHM} (km s^{-1})	v_{jet} (km s^{-1})	Ref. (v_{jet})
M 3-30	[WO 1]	G017.9−04.8	−44.0	19.2	34.0	67.0	27.0	36.2	±54.0	D13
M 1-32	[WO 4]$_{\mathrm{pec}}$	G011.9+04.2	−17.0	43.1	15.0	−77.0	15.0	31.2	±200.0	A12
NGC 6567	*wels*	G011.7−00.6	−40.0	21.4	−46.0	135.0	–	33.5	–	–
NGC 6578	*wels*	G010.8−01.8	−48.0	13.6	35.0	19.0	–	21.9	–	–
NGC 6629	*wels*	G009.4−05.0	−40.0	22.6	−50.0	26.0	–	20.3	–	–
M 2-42	*wels*	G008.2−04.8	40.0	102.4	77.0	120.0	–	18.3	±70.0	A12
M 3-15	[WC 4]	G006.8+04.1	40.0	98.8	45.0	110.0	–	21.2	±100.0	A12
M 1-25	[WC 5-6]	G004.9+04.9	31.0	89.0	140.0	26.0	–	26.6	–	–

Remarks:

[a] Possible FLIERs, need to be observed further.

Table 2.4: (continued)

Name	CSPN	PNG	PA (°)	GPA (°)	θ (°)	$v_{\rm sys}$ (km s^{-1})	$v_{\rm exp}$ [a] (km s^{-1})	$V_{\rm HWHM}$ (km s^{-1})	$v_{\rm jet}$ (km s^{-1})	Ref. ($v_{\rm jet}$)
Hb 4	[WO 3]	G003.1+02.9	25.0	83.3	40.0	−46.0	–	23.2	±150.0	D13
IC 1297	[WO 3]	G358.3−21.6	32.0	104.0	−160.0	16.0	26.0	31.2	? [b]	–
Sa 3-107	*wels*	G358.0−04.6	41.0	101.5	50.0	−133.0	–	16.1	–	–
K 2-16	[WC 11]	G352.9+11.4	80.0	130.6	−20.0	23.0	–	31.2	±58.0	D13
Hen 3-1333	[WC 10]	G332.9−09.9	−2.0	52.6	30.0	−64.0	–	33.1	–	–
Hen 2-142	[WC 9]	G327.1−02.2	−45.0	−4.3	60.0	−95.0	–	20.4	–	–
Hen 2-113	[WC 11]	G321.0+03.9	60.0	88.3	129.0	−58.0	–	21.6	–	–
Th 2-A	[WO 3]$_{\rm pec}$	G306.4−00.6	−24.0	−17.1	−17.0	−53.0	34.0	34.7	$>\pm$120.0	D13
Pe 1-1	[WO 4]	G285.4+01.5	−75.0	−104.2	−70.0	7.0	–	23.4	? [b]	–

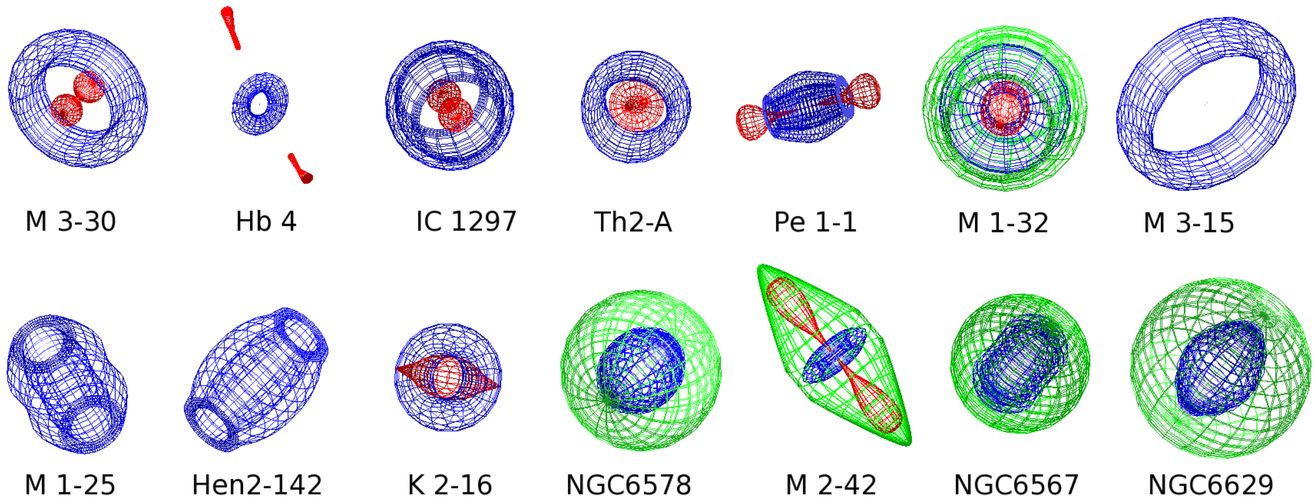

Figure 2.6: SHAPE mesh models of the PNe: M 3-30, Hb 4, IC 1297, Th 2-A, Pe 1-1, M,1-32, M 3-15 (first row), M 1-25, Hen 2-142, K 2-16, MGC 6578, M 2-42, NGC 6567 and NGC 6629 (second row), before rendering at the best-fitting inclination.

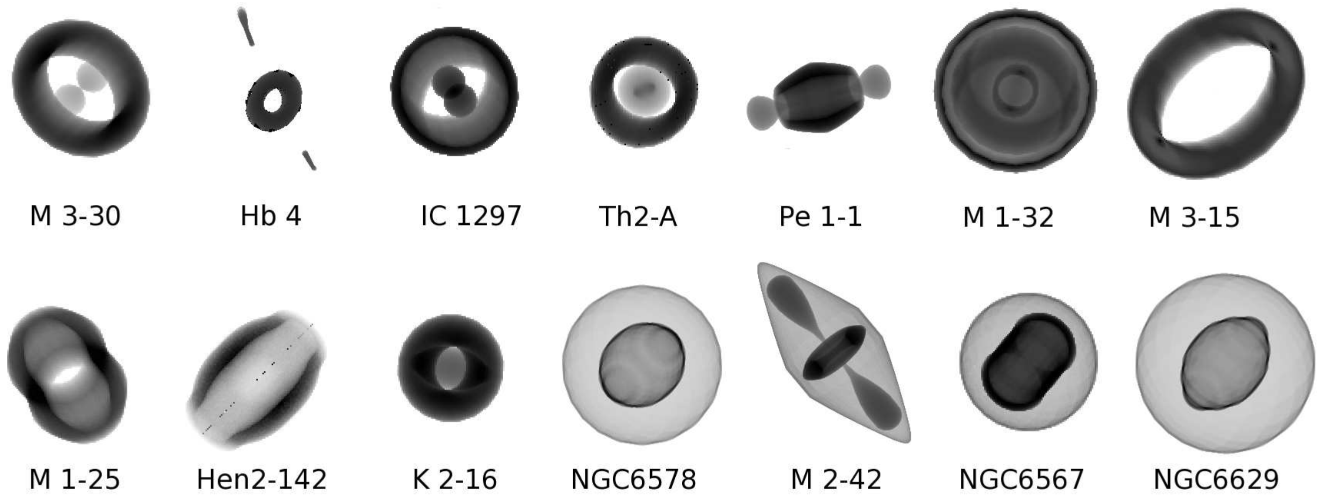

Figure 2.7: Rendered SHAPE models of the PNe: M 3-30, Hb 4, IC 1297, Th 2-A, Pe 1-1, M,1-32, M 3-15 (first row), M 1-25, Hen 2-142, K 2-16, MGC 6578, M 2-42, NGC 6567 and NGC 6629 (second row) at the best-fitting inclination.

Hb 4. Close inspection of the *HST* images (see Fig. 2.2) reveals that the central shell of Hb 4 has a ring-like structure. It also indicates the presence of two FLIERs located furthest away from the ring shell. We also notice that the ring shell is deformed, most likely as a result of the motion of the nebula, with respect to the ISM. The FLIERs are not exactly aligned vertically, which could be because of interaction with the ISM. Fig. 2.6 shows a deformed SHAPE model consisting of a ring and two point-symmetric knots. It does not include the outer faint halo. The WiFeS spectral resolution is not ideal for determining the expansion velocity of the ring from the line-of-sight redial velocity map. But, the HWHM gives a rough estimate of the expansion velocity, $V_{\rm HWHM} = 23\,{\rm km\,s^{-1}}$, measured from an aperture 10×10 arcsec^2 located on the inner shell. The HWHM method usually underestimates the true expansion velocity, but suitable for slowly expanding objects (Schönberner et al. 2010). From Fig. 2.4b, it is clear that the northern FLIER is redshifted, whereas the southern FLIER is blueshifted with respect to $v_{\rm sys} = -46\,{\rm km\,s^{-1}}$. The maximum observed velocity between them corresponds to the velocity of $v_{\rm jet} = \pm 150$ ${\rm km\,s^{-1}}$ at the inclination of $40^{\circ} \pm 5^{\circ}$. The point-symmetric structure has a position angle of $25^{\circ} \pm 10^{\circ}$ with respect to the plane of the sky. As seen in Fig. 2.4b, the FLIERs show higher values of the velocity dispersion due to their relatively high velocities and interaction with the local ISM.

IC 1297. A morpho-kinematic model of IC 1297 was built from an elongated cylinder. It has an inclination of $-160^{\circ} \pm 10^{\circ}$ relative to the line of sight. The model velocity component produced at this spatial orientation was compared by eye to the velocity map provided by the IFU observation (Fig. 2.4c). It looks nearly as a twin of M 3-30. It has more likely a torus structure with two inner knots at a different inclination. The narrow band Hα+[N II] image taken by Schwarz et al. (1992) probably shows the same structure, but it also shows an outer halo surrounding the central ring. A much deeper observation is necessary to confirm this structure. From the SHAPE model, we found the maximum expansion velocity of $v_{\rm exp} = 26 \pm 5\,{\rm km\,s^{-1}}$.

Th 2-A. The roughly rectangular shape seen in Th 2-A (see Fig. A5) might be related to interaction with the ISM, as the nebula is moving through the ISM. The asymmetric brightness seen in the observed [N II] flux map, Fig. 2.4d, could also be due to the interaction. In this situation, the nebula shell is deformed, tending in some cases to a rectangular shape. As shown in Fig. 2.6, we adopted a torus surrounding a prolate ellipsoid (jets) for the morpho-kinematic study of this object. From the radial velocity map (Fig. 2.4d), the expansion velocity of the shell relative to the nebula center was found to be $v_{\rm exp} = 34 \pm 10\,{\rm km\,s^{-1}}$ at the inclination of $-17^{\circ} \pm 4^{\circ}$ to the line of sight, in agreement with the HWHM velocity found in Section 2.3. Furthermore, the high velocity dispersion and large blueshift in the center are likely related to the FLIERs seen pole-on. The velocity dispersion in the center corresponds to a jet velocity of $v_{\rm jet} > v_{\rm HWHM} = 120\ {\rm km\,s^{-1}}$.

Pe 1-1. The spatial resolution of our observation is not ideal for Pe 1-1. However, the derived radial velocity map combined with *HST* imaging and a SHAPE model have allowed us to get a better understanding of its morpho-kinematic structure. We used a cylindrical structure including bipolar lobes located its outside. The velocity dispersion map of this PN (see Fig. A6) is similar to what we got for Hb 4. Therefore, this PN may also have some FLIERs or bipolar collimated outflows. But, the long-pass filter (F350LP) is not ideal for identifying any FLIERs, as they are visible in [N II] and [S II] more so than in other emission lines.

M 1-32. A ring-like SHAPE model successfully reproduces the blueshifted and redshifted components seen in the radial velocity maps of M 1-32 (see Fig. A7). The model is composed of a thick torus, a inner prolate ellipsoid (bipolar outflows) and outer thin halo. The velocity dispersion maps show a bright center attributed to the FLIERs. Akras & López (2012) recently modeled this PN using a similar morpho-kinematic structure. The maximum observed velocity between components in the IFU maps corresponds to $v_{\rm exp} = 15\,{\rm km\,s^{-1}}$ at the derived inclination, which is roughly in agreement with the value found by Akras & López (2012). However, it is much lower than the measured HWHM velocity of $31\,{\rm km\,s^{-1}}$. This error could be due to the contribution of the fast collimated bipolar outflows as previously noted by Medina et al. (2006). We derived an inclination angle of $15^{\circ} \pm 10^{\circ}$, which is in decent agreement with 5° found by Akras & López (2012). Moreover, Akras & López (2012) estimated that bipolar jets (FLIERs) reaches $v_{\rm jet} = \pm 200$ ${\rm km\,s^{-1}}$. The velocity dispersion in the center of the IFU map is also associated with a jet velocity of $v_{\rm jet} > v_{\rm HWHM} =$ 60 ${\rm km\,s^{-1}}$.

M 3-15. The *HST* image of M 3-15 combined with the IFU radial velocity map shows the orientation of this PN. The SHAPE model was built with a ring based on the appearance in the *HST* image. This is much simpler than the model adopted by Akras & López (2012), being composed of a torus, a inner prolate ellipsoid and outer halo. The low spatial resolution did not allow us to identify any jet structure. Akras & López (2012) also identified FLIERs, which move with equal and opposite supersonic velocities of $v_{\rm jet} = \pm 100$ ${\rm km\,s^{-1}}$. Our derived inclination angle of $45^{\circ} \pm 10^{\circ}$ constrained by the *HST* image is different from 5° of the SHAPE model only constrained by the long-slit spectra (Akras & López 2012). The two velocity components seen in the IFU maps indicates that the ring oriented with its symmetry axis to the line of sight such that the northern wall on the near side and the southern wall on the far side.

M 1-25 and Hen 2-142. The spatial resolution of our IFU observation cannot resolve any structure of M 1-25 and Hen 2-142. But, the archival *HST* imaging allowed us to adopt a elongated cylinder model for them. The results of the rendered model are shown in Fig. 2.7, which are comparable to their *HST* images (see Fig. 2.2). We also notice large faint outer halos in both PNe, which are visible in the velocity maps. But, we did not include them in the SHAPE models.

K 2-16. The radial velocity maps of K 2-16 indicate that this PN cannot have a circular structure seen in the Hα+[N II] narrow band image (Fig. 2.3). Aspherical morphologies, either toroidal or cylindrical structure, can only be associated with the observed velocity maps. The wire-frame model of K 2-16, before rendering, is shown in Fig. 2.6. The basic model was a elliptical structure surrounding a thin prolate ellipsoid. This morpho-kinematic model reproduces the two velocity components seen in the velocity maps (Fig. A13). Taking the inclination of 20° found by the best-fitting morpho-kinematic model, we derived a velocity of $v_{\rm jet} = \pm 58\,{\rm km\,s^{-1}}$ from the difference between velocity components in the IFU maps.

NGC 6578, NGC 6567 and NGC 6629. To model these PNe, we used their *HST* images (Fig. 2.2). But, the radial velocity maps helped us to determine their orientations. Our model was built with a modified ellipsoid surrounded by a outer faint spherical halo. The main shell was modified in order to provide a reasonable match with the *HST* images. As seen in Fig. 2.7, the rendered images produced by the SHAPE models successfully show the nebula's inherent shapes seen in the *HST* images.

M 2-42. The IFU kinematic maps of M 2-42 combined with the SuperCOSMOS Hα Sky Survey (Fig. A15; SHS; Parker et al. 2005) reveals that the presence of FLIERs in opposite symmetrical pairs. These FLIERs are not easily visible in the IFU flux maps. But, we notice them in the IFU velocity maps. We therefore adopted a morpho-kinematic model consisting of a inner torus (central shell), a prolate ellipsoid (outer halo) and two point-symmetric knots, similar to the model used by Akras & López (2012). Fig. 2.6 shows the mesh model of M 2-42, before rendering. The model successfully reproduces the synthetic intensity map similar to what seen in the SHS Hα image. It also reproduces the two velocity components of FLIERs moving in opposite directions on both sides of the central star. The inclination of $77^\circ \pm 10^\circ$ derived by the best-fitting model is in agreement with what found by Akras & López (2012). Taking this inclination, we derived a velocity of $v_{\rm jet} = \pm 70 \pm 10\,{\rm km\,s^{-1}}$ with respect to the core, similar to the value given by Akras & López (2012).

2.5 Conclusion

Our aim in this chapter was to determine morphological features of a sample of Galactic PNe surrounding hydrogen-deficient [WR] central stars. The capabilities of the IFU observations, coupled with *HST* or other imaging, have allowed us to identify their three-dimensional morpho-kinematic structures. The overall results indicates that these PNe have axisymmetric morphologies, either bipolar or elliptical. Some of them show elliptical shapes with FLIERS (e.g. M 3-30 and Hb 4). Recently, Akras & López (2012) also identified other [WR] PNe having axisymmetric shapes and fast bipolar outflows. Moreover, the recent *Chandra X-Ray Observatory* survey of PNe (Kastner et al. 2012) indicates that most elliptical PNe with FLIERs display "diffuse X-ray" sources. Diffuse X-ray sources and "hot bubbles" were also found in some aspherical PNe around [WR] stars, e.g. NGC 40 (Montez et al. 2005) and NGC 5315 (Kastner et al. 2008), which could be evidence for collimated jets and wind-wind shocks. The "hard X-ray" emission may suggest the presence of a binary companion, whereas soft, diffuse X-ray emission is more likely related to shocks (Kastner et al. 2012). Nordhaus & Blackman (2006) suggested that a binary system consisting of a low-mass star ($< 0.3{\rm M}_{\odot}$) and an AGB star undergoes a common envelope (CE) phase, which can lead to binary-induced equatorial outflow and nebular aspherical morphology. While no binary companion has been found in the [WR] PNe of our sample, the merger scenario of a low-mass companion with an AGB star during the AGB phase may explain their typical aspherical morphologies.

The picture that emerges from this work is that all [WR] PNe of our sample show axisymmetric morphologies, apart from PB 6 (see Fig. 2.6). This could imply a possible link between PNe with their WR-type nuclei. But, the expansion velocities presented in Tables 2.3 and 2.4 do not show any specific link with the stellar parameters given in Table 2.1. As can be seen in Fig. 2.8 (top), the HWHM velocity plotted against the [WC]-[WO] evolutionary sequence, there is no general trend between them. Moreover, Fig. 2.8 (bottom) shows no explicit dependence of $V_{\rm HWHM}$ on $T_{\rm eff}$. But, the theoretical evolutionary models by Schönberner et al. (2005a,b) predicted that the expansion velocity increases as the nebula evolves and the central star becomes hotter. However, we did not see any link between the nebular kinematics and stellar characteristics. Some PNe with hot stars, such as Pe 1-1, Hb 4 and M 1-32, have low expansion velocities, wheres some PNe around cool stars, such as Hen 3-1333 and K 2-16, show high expansion velocities. This tendency cannot be explained by single star evolution. Table 2.5 also presents nebular kinematic age (Column 8) calculated using adopted distance (Column 6), nebular size, and expansion velocity (Column 4). We defined the kinematic age as the radius divided by the expansion velocity. Column 10 gives the kinematic ages obtained by Gesicki & Zijlstra (2007). We see that the compact PN Hen 3-1333 and Hen 2-113 are very young, whereas some evolved ring PNe (e.g. M 3-30, Th 2-A and K 2-16) are old. We note that both Hen 3-1333 and Hen 2-113 have the same age and stellar parameters, but they show different expansion velocities. Therefore, their nebular kinematics are somehow unrelated to their assumed stellar parameters. Moreover, the point-symmetric fast knots or jets moving in opposite directions were found in other PNe around hot [WR] stars, Hb 4, M 3-30, M 3-15 and M 1-32. Their velocities were found to be in the range 60–200 km s^{-1} with respect to the main bodies, which seem inconsistent with the GISW theory.

The method used here presents only a first-order description of the nebular morphology, the inclination with respect to the line of sight, the orientation on the sky plane, and a rough estimate of the expansion velocity. Our method was designed to easily determine any morphologies at different inclinations from the IFU velocity maps. But, the lack of high spatial and spectral resolution (WiFeS spectrograph) means that we cannot perform a detailed morpho-kinematic modeling of our sample. Notwithstanding its limitations, this study may offer some insight into their overall three-dimensional structures. This approach is time-saving, so it is ideal for study of a large sample of PNe, where precise detail is not important. More detailed morpho-kinematic analysis and further high-resolution observations will expand our knowledge on their kinematic structures.

We believe future deep imaging and kinematic observations of PNe with [WR] central stars are necessary to investigate possible mechanisms, which shape their aspherical morphologies. Deeper observations of the central engine will lead to a better understanding of this issue. The presence of binary companions should be inspected. But, it is extremely difficult to detect a low-mass star or a planet, which could also influence the shaping of its nebula. In-depth studies of [WR] CSPNe are also required to unravel the puzzle of the mechanism responsible for shaping [WR] PNe, which as yet remains unanswered.

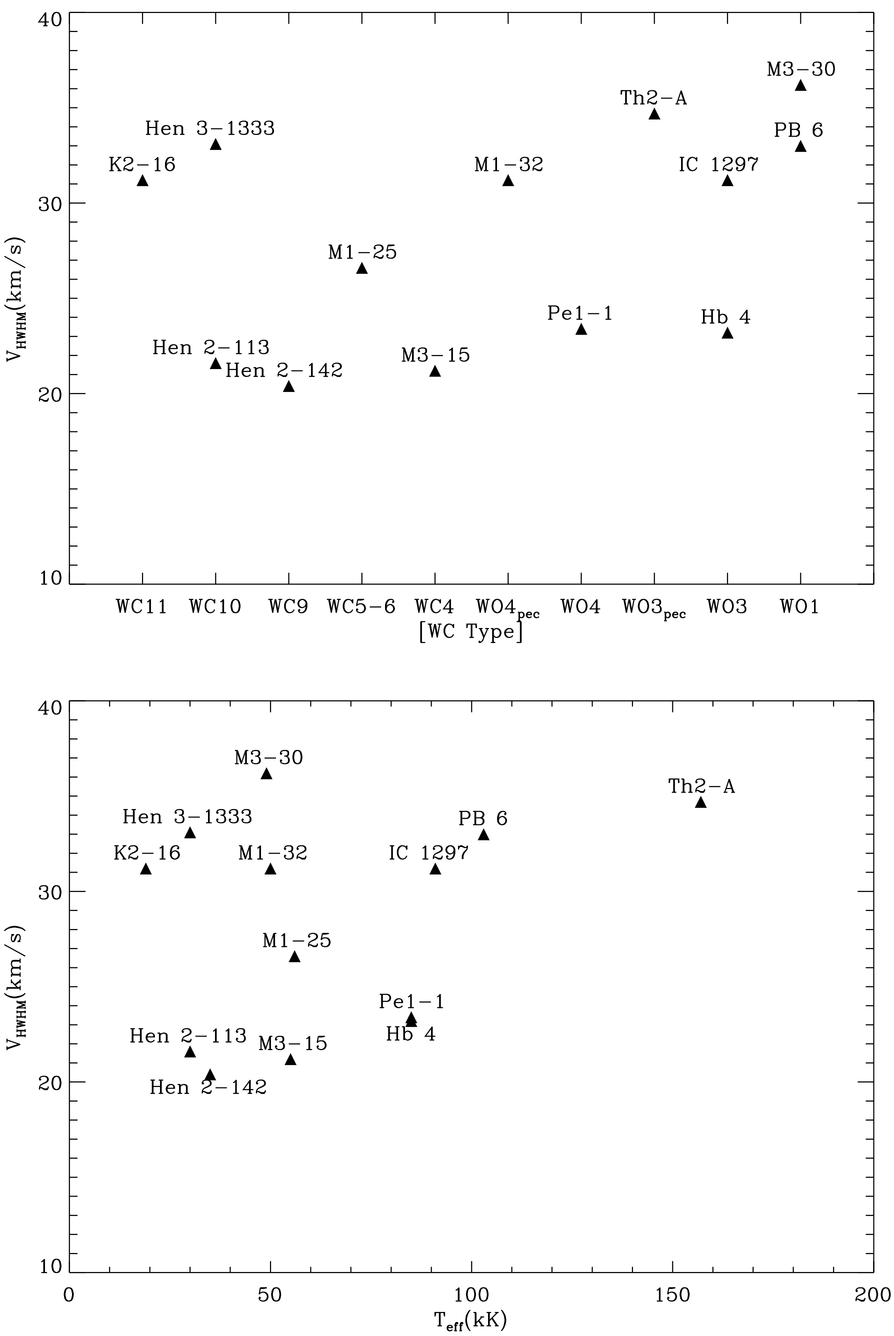

Figure 2.8: Top panel: variation of the HWHM velocity ($V_{\rm HWHM}$) along the spectral sequence. Bottom panel: variation of the HWHM velocity along the stellar effective temperature ($T_{\rm eff}$).

Table 2.5: Nebular kinematic age obtained from adopted distance, nebular size and expansion velocity. References are as follows: A92 – Acker et al. (1992); D97 – De Marco et al. (1997); G07 – Gesicki & Zijlstra (2007); S10 – Stanghellini & Haywood (2010); T98 – Tajitsu & Tamura (1998); T03 – Tylenda et al. (2003); Z95 – Zhang (1995).

Name	Ang.Diam.[a] (arcsec)	Ref.[a]	$v_{\rm exp}$ (km s^{-1})	$v_{\rm jet}$ (km s^{-1})	Distance[b] (pc)	Ref.[b]	$t_{\rm shell}$ (yr)	$t_{\rm jet}$ (yr)	$t_{\rm kin}$(yr) G07
PB 6	11.0	A92	33	–	4471	S10	3533	–	3555
M 3-30	19.2×18.5	T03	27	54	4536	S10	7486	3743	–
Hb 4	11.4×7.4	T03	23	150	5096	S10	5051	2416	3911
IC 1297	10.9×9.9	T03	26	–	4100	T98	3887	–	–
Th 2-A	27.7×25.2	T03	34	120	2500	S10	4601	1955	–
Pe 1-1	3.0	A92	23	–	6569	S10	2031	–	2300
M 1-32	9.4×8.3	T03	15	200	4796	S10	6669	1700	–
M 3-15	4.2	A92	21	100	6825	S10	3235	1941	3611
M 1-25	4.6	A92	27	–	6682	S10	2698	–	2347

Remarks:

[a] References to angular dimensions given in column 3. [b] References to distances given in column 7.

Table 2.5: (continued)

Name	Ang.Diam.[a] (arcsec)	Ref.[a]	$v_{\rm exp}$ (km s^{-1})	$v_{\rm jet}$ (km s^{-1})	Distance[b] (pc)	Ref.[b]	$t_{\rm shell}$ (yr)	$t_{\rm jet}$ (yr)	$t_{\rm kin}$ (yr) G07
Hen 2-142	4.4×3.5	T03	20	–	4620	Z95	2190	–	1565
Hen 3-1333	3.6×3.4	T03	33	–	1350	D97	330	–	–
Hen 2-113	3.5	–	22	–	1500	D97	582	–	559
K 2-16	26.6×24.3	T03	31	58	2200	T98	4273	4567	1778
NGC 6578	12.1×11.8	T03	22	–	3680	S10	4738	–	–
M 2-42	22.0×14.0	–	18	70	4400	T98	8112	3278	–
NGC 6567	8.1×6.4	T03	34	–	3652	S10	1833	–	–
NGC 6629	16.6×15.5	T03	20	–	2399	S10	4561	–	–
Sa 2-107	11.0×10.0	–	16	–	6000	–	9322	–	–

3

Physical conditions and chemical abundances

The contents of this chapter are being prepared for publication in the Monthly Notices of the Royal Astronomical Society.

3.1 Introduction

Historically, strong and easy to measure collisionally excited lines (CELs) provided the reliable chemical tracers, which have extensively been used to derive the abundances of heavy elements such as N, O, Ne, Ar and S relative to H (see e.g. Kingsburgh & Barlow 1994; Kwitter & Henry 2001; Tsamis et al. 2003a; Henry et al. 2004; Liu et al. 2004a). But, CEL calculation depends exponentially on the electron temperature, so temperature variations introduce uncertainties to our results (e.g. Garnett 1992; Stasińska 2005). On the other hand, optical recombination lines (ORLs) have a much weaker dependence on temperature and density, thus resulting in reliable abundance analysis. The ORLs from heavy element ions are observable in nearby PNe through deeper observations, since they are extremely weak relative to Hβ. But, they are easily detectable in bright H II regions (e.g. Tsamis et al. 2003b; Peimbert et al. 2005; García-Rojas et al. 2007; López-Sánchez et al. 2007; Peña-Guerrero et al. 2012). However, the recent studies of ORLs indicated that the abundances derived using the ORL method are systematically higher than those derived from CELs in many PNe (Liu et al. 2000, 2001; Luo et al. 2001; Wesson et al. 2003; Tsamis et al. 2004; Wesson & Liu 2004; Wesson et al. 2005; Tsamis et al. 2008; García-Rojas et al. 2009). Such discrepancies are commonly described using the so-called abundance discrepancy factor (ADF): ADF(X^{i+}) = $(X^{i+}/H^{+})_{ORLs}$ / $(X^{i+}/H^{+})_{CELs}$, where X^{i+} is the $i+$ ionic abundance of element X and H^{+} is the abundance of ionized hydrogen. For the majority of more than 100 PNe, the ADFs are typically in the range 1.6–3, about 5–10 per cent of them however the ADFs are in the 4–80 range (see review by Liu et al. 2006). For example, NGC 6153 is a typical PN having a large ADF $\sim$10 (Liu et al. 2000), but some PNe such as Abell 30, NGC 1501 and Hf 2-2, showing extremely large ADF(O^{2+}) of about 700, 30 and 70, respectively (Wesson et al. 2003; Ercolano et al. 2004; Liu et al. 2006). The exact causes of the CEL/ORL abundance discrepancies are not fully understood and remain the main open problem in the astrophysics of these objects. This problem was already found in gaseous nebulae over seventy years ago (Wyse 1942; Aller & Menzel 1945). It is also seen in H II regions (e.g. García-Rojas et al. 2007). This is known as the abundance discrepancy problem.

The dichotomy between electron temperatures measured from ORLs and those measured from CELs is another long-standing problem in the study of planetary nebulae, which may be closely linked to the abundance discrepancy problem. Over four decades ago, Peimbert (1967, 1971) found that the dichotomy between [O III] CEL and H I Balmer jump (BJ) temperatures, $T_{\rm e}$([O III]) $>$ $T_{\rm e}$(BJ), in H II regions and planetary nebulae, and suggested the presence of significant temperature fluctuations, characterized by two parameters: the average temperature, T_0, and the mean square temperature fluctuation t^2. It can have different weights in the high and low ionization regions, e.g. $T_{0,\mathrm{H}}$ and t^2_{H} for [O III] and $T_{0,\mathrm{L}}$ and t^2_{L} for [N II]. The temperature fluctuations lead to overestimating the electron temperature deduced from CELs, as a result, the derived ionic abundances are underestimated (Peimbert 1967). However, the detailed analysis of NGC 6543 by Wesson & Liu (2004) for example showed that the temperature fluctuations are too small to explain the abundance discrepancy problem. Recently, Wesson et al. (2005) found that the derived temperatures mostly follow the relation $T_{\mathrm{e}}([\mathrm{O\,III}]) > T_{\mathrm{e}}(\mathrm{BJ}) > T_{\mathrm{e}}(\mathrm{He\,I}) > T_{\mathrm{e}}(\mathrm{O\,II})$. This relation was predicted by the two-phase models (Liu 2003; Liu et al. 2004a), containing some cold ($T_{\mathrm{e}} \sim 10^3$ K) hydrogen-deficient small-scale structures, highly enriched in helium and heavy elements, embedded in the diffuse warm ($T_{\mathrm{e}} \sim 10^4$ K) nebular gas of normal abundances. The existence and origin of such inclusions are still unknown. The study of Abell 30 by Wesson et al. (2003) pointed to the presence of cold ionized material in its hydrogen-deficient knots. Furthermore, Ercolano et al. (2003b) showed the feasibility of such scenario by implementing a bi-abundance photoionization model of Abell 30. Previously, Parthasarathy et al. (1998) identified the central star of Abell 30 as [WC]-PG1159 type. Additionally, Yuan et al. (2011) used a bi-abundance model to solve the abundance discrepancy problem in NGC 6153, whose central star was classified as a [WC]-PG 1159 star by Liu et al. (2000). The photoionization modeling of the planetary nebula NGC 1501 containing a [WO 4] star by Ercolano et al. (2004) indicated the presence of cold ionized hydrogen-deficient material within the nebula. It is unclear whether there is any link between the assumed hydrogen-deficient inclusions in PNe and their hydrogen-deficient central stars.

In this chapter, we present medium-resolution ($R \sim 7000$) integral field unit (IFU) spectra in the 4415–7070 Å range for 13 PNe containing Wolf-Rayet [WC] central stars and 5 Galactic PNe with weak emission-line stars (*wels*). The spectra, combined with archival spectra from the literature, have been used to carry out plasma diagnostics and abundance analysis using both collisionally excited lines (CELs) and optical recombination lines (ORLs) from heavy element ions. Nebular thermal and density structures have been derived using a variety of plasma diagnostics of CELs. The weak temperature dependence of ORLs have also been used to further investigate the temperature structure of the nebulae. The plasma diagnostic results are used to derive ionic and elemental abundances within the nebula from both CELs and ORLs.

This chapter is structured as follows. In Section 3.2, we describe briefly our observations and present our optical emission line fluxes obtained with the 2.3-m ANU telescope. In Section 3.3, we describe the corrections for interstellar extinction, and present nebular electron temperatures and densities derived from the CELs and the ORLs. In Section 3.4, we present ionic abundances and elemental abundances, followed by a discussion of individual PN in Section 3.5. In Section 3.6, we discuss the implication of our observations for the AGB stellar models and the cause of the abundance discrepancy and temperature dichotomy

3.2 Observations

The optical integral field unit (IFU) spectra of PNe analyzed in this work were obtained at Siding Spring Observatory, Australia, using the Wide Field Spectrograph (WiFeS; Dopita et al. 2007, 2010) mounted on the 2.3-m ANU telescope in 2010 and 2012. An observational journal is presented in Table 3.1, including spectral classes of the central stars (column 3), the stellar effective temperature (column 4), the absolute total flux of Hβ (column 5), the radio flux densities at 5 GHz (column 6), the nebular angular-dimensions measured in the optical and in the radio observations (columns 7 and 8) and the exposure time used for each PN (column 9).

Our observations were carried out with the B7000/R7000 grating combination and the RT 560 dichroic using the classical mode, which covers $\lambda\lambda$4415–5589 Å in the blue channel and $\lambda\lambda$5222–7070 Å in the red channel. Exposure times ranged from 60–1200 sec depend on the Hβ surface brightness. Spectroscopic standard stars were observed for the flux calibration purposes notably EG 274 and LTT 3864. We also acquired series of bias, dome flat-field frames, twilight sky flats, arc lamp exposures, and wire frames for data reduction, flat-fielding, wavelength calibration and spatial calibration. The suitable sky window has been selected from the science data for the sky subtraction purpose.

The spectra were reduced using the IRAF pipeline wifes.[1] The reduction involves flat-fielding, wavelength calibration, spatial calibration, sky subtraction and flux calibration (fully described in Chapter 2). The dome flat-field frames were used to preform the flat-fielding, i.e. correcting pixel-to-pixel sensitivity variations. Wavelength calibration was carried out using Cu–Ar arc exposures and reference arc. Spatial calibration was done by relocating the center of each slitlet using wire frames. The science data was calibrated to absolute flux units using observations of spectrophotometric standard stars and the IRAF flux-calibration tasks.

The top and bottom panels of Figs. C1-C18 (Appendix C) show the blue and red spectra of our sample extracted from apertures over the whole nebulae, normalized such that $F(\mathrm{H}\beta) = 100$. As seen, some recombination lines from heavy element ions have been observed in each PN.

To extract flux intensity and formal 1-σ errors, we applied a single Gaussian profile to each line and excluded the stellar continuum offset from the final flux. The emission line profiles are resolved if their width are wider than the instrumental width.

[1]IRAF is distributed by NOAO, which is operated by AURA, Inc., under contract to the National Science Foundation.

Table 3.1: Journal of observations. References are as follows: A92 – Acker et al. (1992); A03 – Acker & Neiner (2003); C92 – Cahn et al. (1992); C98 – Condon & Kaplan (1998); C99 – Condon et al. (1999); D11 – Depew et al. (2011); F13 – Frew et al. (2013a); P82 – Purton et al. (1982); S10 – Stanghellini & Haywood (2010); T93 – Tylenda et al. (1993); T03 – Tylenda et al. (2003); W08 – Weidmann et al. (2008).

Name	PN G (A92)	CSPN (A03)	$\log F(\mathrm{H}\beta)$ (C92) ($\mathrm{erg\,cm^{-2}\,s^{-1}}$)	F(1.4 GHz) (C98) (mJy)	F(5 GHz) (S10) (mJy)	Angular diameter (arcsec) (optical)	(radio)	Exp.Time (sec)
PB 6	278.8+04.9	[WO 1]	−11.87	–	30.0	11.0(A92)	–	1200
M 3-30	017.9−04.8	[WO 1]	−12.29	8.6	7.3	19.2 × 18.5(T03)	22.0(A92)	1200
Hb 4	003.1+02.9	[WO 3]	−11.96	158.0	166.0	11.4 × 7.4(T03)	7.5(A92)	300,1200
IC 1297	358.3−21.6	[WO 3]	−10.95	59.9	69.0	10.9 × 9.9(T03)	–	60,1200
Th 2-A	306.4−00.6	[WO3]pec(W08)	−12.80(A92)	–	0.060	27.7 × 25.2(T03)	–	1200
Pe 1-1	285.4+01.5	[WO 4]	−12.26	–	125.3	3.0(A92)	–	60,1200
M 1-32	011.9+04.2	[WO 4]pec	−12.20(A92)	70.5	64.0	9.4 × 8.3(T03)	9.0(A92)	1200
M 3-15	006.8+04.1	[WC 4]	−12.45(A92)	48.4	65.0	4.2(A92)	5.0(A92)	60,1200
M 1-25	004.9+04.9	[WC 5-6]	−11.90	40.3	55.0	4.6(A92)	3.2(A92)	60,1200
Hen 2-142	327.1−02.2	[WC 9]	−11.85	–	65.0	4.4 × 3.5(T03)	–	60,1200
Hen 3-1333	332.9−09.9	[WC 10]	−12.15	–	26.0(P82)	3.6 × 3.4(T03)	–	1200
Hen 2-113	321.0+03.9	[WC 10]	−11.82	–	115.0(P82)	3.5	–	60,1200
K 2-16	352.9+11.4	[WC 11]	−12.77(F13) [a]	2.5	–	26.6 × 24.3(T03)	–	1200

[a] Calculated from the observed intensity of Hα using the logarithmic extinction formula.

Table 3.1: (continued)

Name	PN G (A92)	CSPN (A03)	$\log F(\mathrm{H}\beta)$ (C92) (erg cm^{-2} s^{-1})	F(1.4 GHz) (C98) (mJy)	F(5 GHz) (S10) (mJy)	Angular diameter (arcsec) (optical)	(radio)	Exp.Time (sec)
NGC 6578	010.8−01.8	*wels*(T93)	−11.57	162.4	166.0	12.1 × 11.8(T03)	–	60,1200
M 2-42	008.2−04.8	*wels*(D11)	−12.12	9.8	14.0	22.0 × 14.0	–	1200
NGC 6567	011.7−00.6	*wels*(T93)	−10.95	163.3	161.0	8.1 × 6.4(T03)	–	60,1200
NGC 6629	009.4−05.0	*wels*(T93)	−10.93	264.0	265.8	16.6 × 15.5(T03)	–	60,1200
Sa 3-107	358.0−04.6	*wels*(D11)	−12.95(F13) [a]	5.2(C99)	–	11.0 × 10.0	–	1200

3.3 Nebular analysis

3.3.1 Line intensities and interstellar reddening

Table B1-B18 (Appendix B) represents a full list of observed lines and their measured fluxes. The emission line identification, laboratory wavelength, and multiplet number, are given in columns 1–3, respectively. Columns 4–6 present the observed fluxes, and the fluxes after correction for interstellar extinction and the formal 1σ errors associated with the line fluxes with respect to Hβ (flux calibration error estimated to be about 5%). All fluxes are given relative to Hβ, on a scale where H$\beta = 100$. Figs. C1–C11 (Appendix C) show the observed optical spectra of our objects, from 4415 Å to 7060 Å. The spectra normalized such that $F(\mathrm{H}\beta) = 100$.

The logarithmic extinction at Hβ, $c(\mathrm{H}\beta)$, was obtained from the observed Balmer emission line Hα/Hβ flux ratio and its theoretical line ratio of the case B recombination (Storey & Hummer 1995, based on the physical conditions derived in § 3.3). Each flux intensity was then dereddened using the formula, $I(\lambda) = 10^{c(\mathrm{H}\beta)[1+f(\lambda)]}F(\lambda)$, where $F(\lambda)$ and $I(\lambda)$ are the observed and intrinsic line flux, respectively, and $f(\lambda)$ is the standard Galactic extinction law of $R_V =$ 3.1 (Howarth 1983) normalized such that $f(\mathrm{H}\beta) = 0$.

Table 3.2 compares $c(\mathrm{H}\beta)$ derived from the Balmer flux ratio Hα/Hβ (column 2) with those from the radio-Hβ method (column 3) and the literature (column 4). There is a generally good agreement between them for most PNe, except M 3-30, M 1-25 and Hen 2-142. We denote $c(\mathrm{H}\beta)_{\mathrm{radio}}$ for the extinction derived from the radio-Hβ method, which is estimated through a comparison of the observed radio free–free continuum radiation at 5 GHz with the measured Hβ flux. We used the formula given by Milne & Aller (1975), along with the electron temperature of the nebula derived in Section 3.3, the helium ionic abundances derived in Section 3.4, the measured Hβ flux, and the observed 5

Table 3.2: Comparison between our derived $c(\mathrm{H}\beta)$ from the Balmer flux ratio $\mathrm{H}\alpha/\mathrm{H}\beta$, and those from the radio-Hβ method and the literature. References are as follows: A91 – Acker et al. (1991a); A03 – Acker & Neiner (2003); K03 – Kwitter et al. (2003); M02 – Milingo et al. (2002); P11 – Pottasch et al. (2011).

Name	Balmer	Radio	Literature
PB 6	0.60	0.70	0.52(A03)
M 3-30	0.96	0.61	1.30(A03)
Hb 4	1.86	1.67	1.99(A03)
IC 1297	0.23	0.27	0.19(A03)
Th 2-A	1.11	1.03	0.93(M02)
Pe 1-1	1.96	1.85	1.87(A03)
M 1-32	1.40	1.54	1.59(A03)
M 3-15	2.27	1.83	2.10(A03)
M 1-25	1.60	1.19	1.46(A03)
Hen 2-142	1.55	1.23	1.73(A03)
Hen 3-1333	1.06	–	1.00(A03)
Hen 2-113	1.31	–	1.48(A03)
K 2-16	0.56	–	0.97(A03)
NGC 6578	1.53	1.30	1.39(K03)
M 2-42	0.99	0.77	1.03(A91)
NGC 6567	0.78	0.64	0.70(K03)
NGC 6629	0.98	0.90	0.90(P11)

GHz flux density in Jy from the literature (see Table 3.1). We assumed that hydrogen is fully ionized.

Fig. 3.1 (top panel) compares our derived $c(\mathrm{H}\beta)$ with those from the literature. They are generally in good agreement with the previous values. However, we see significant differences in the derived $c(\mathrm{H}\beta)$ for M 3-30 and K 2-16, which could be due to the uncertainties in the flux measurement and flux calibration, or contribution of the stellar emission to the nebula spectrum in PNe with late-type [WC] stars. As shown in Fig. 3.1 (bottom panel), there is a generally good agreement between our derived $c(\mathrm{H}\beta)$ and from Balmer line Hα/Hβ and those from the radio-Hβ method. However, there are some large differences in values found for M 3-30, M 3-15, M 1-25 and Hen 2-142, which can be explained by the uncertainties in our measured values of $F(\mathrm{H}\beta)$, derived electron temperatures, helium ionic abundances and the observed 5-GHz continuum fluxes.

The $c(\mathrm{H}\beta)$ extinction maps have been derived from the Hα and Hβ ratio. We adopted the Case B theoretical values (Storey & Hummer 1995), the standard dust extinction law for the Milky Way ($R_V = 3.1$), the mean electron density and temperature obtained for each object. Assuming that the contribution of the interstellar extinction is uniform over the entire PN, inhomogeneous extinction maps of a PN may be related to the internal dust contribution. Thus, $c(\mathrm{H}\beta)$ extinction maps can be used to explore the dust distribution of PNe. Fig. 3.2 presents the extinction maps $c(\mathrm{H}\beta)$ for PB 6, M 3-30, Hb 4, IC 1297, Th 2-A and K 2-16 (for all PNe see Appendix D), showing the contributions of the interstellar medium and the nebular internal dust. The extinction map of PB 6, Fig. 3.2(a), shows a shell structure, with the central peak brighter than the surrounding. It is likely the remnants of the AGB dust envelopes rather than the foreground interstellar extinction. As shown in Fig. 3.2(b), the extinction map of M 3-30 is higher in the region of the nebular ring structure, while it is low in the central region. It seems that it points out the presence of dust grains in the nebula shell, which descended from the star during the AGB phase. The extinction map of IC 1297, Fig. 3.2(d), indicates that the shell has more dust extinction, so they may be related to its internal dust distribution. The extinction map of Th 2-A, Fig. 3.2(e), depicts a homogeneous extinction map, which can be the foreground interstellar extinction. As shown in Fig. 3.2(f), the extinction map of K 2-16 shows a similar structure to a ring seen in the narrow band Hα+[N II] image taken by Schwarz et al. (1992) (see Chapter 2). This may suggest that the ionized gas and the dust have a similar distribution.

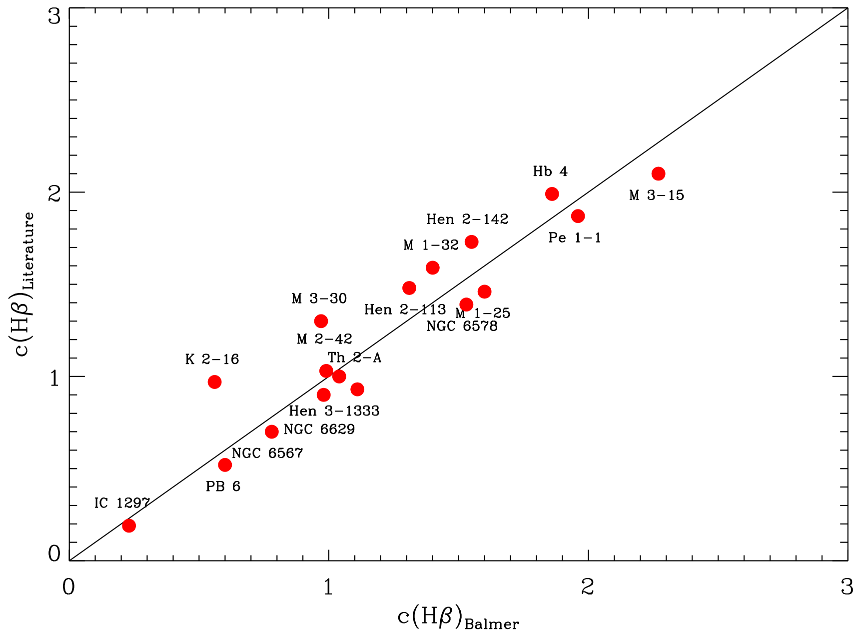

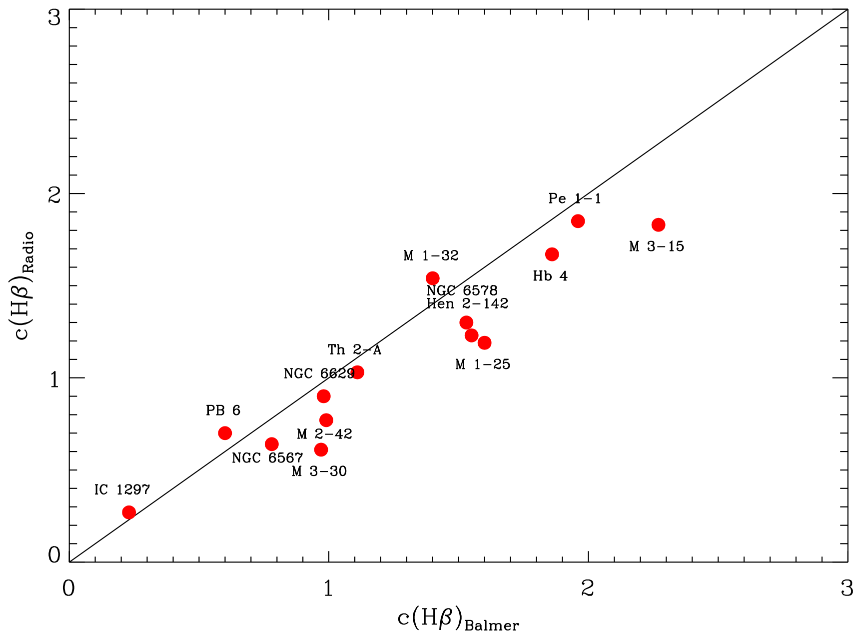

Figure 3.1: Top panel: comparison between our $c(\mathrm{H}\beta)$ derived from the Balmer flux ratio $\mathrm{H}\alpha/\mathrm{H}\beta$ and those from the literature (see Table 3.2). There is a generally good agreement, except few data. Bottom panel: comparison between our derived $c(\mathrm{H}\beta)$ derived from the Balmer flux ratio $\mathrm{H}\alpha/\mathrm{H}\beta$ and those from the radio-$\mathrm{H}\beta$ method. There is a generally good agreement, except some data.

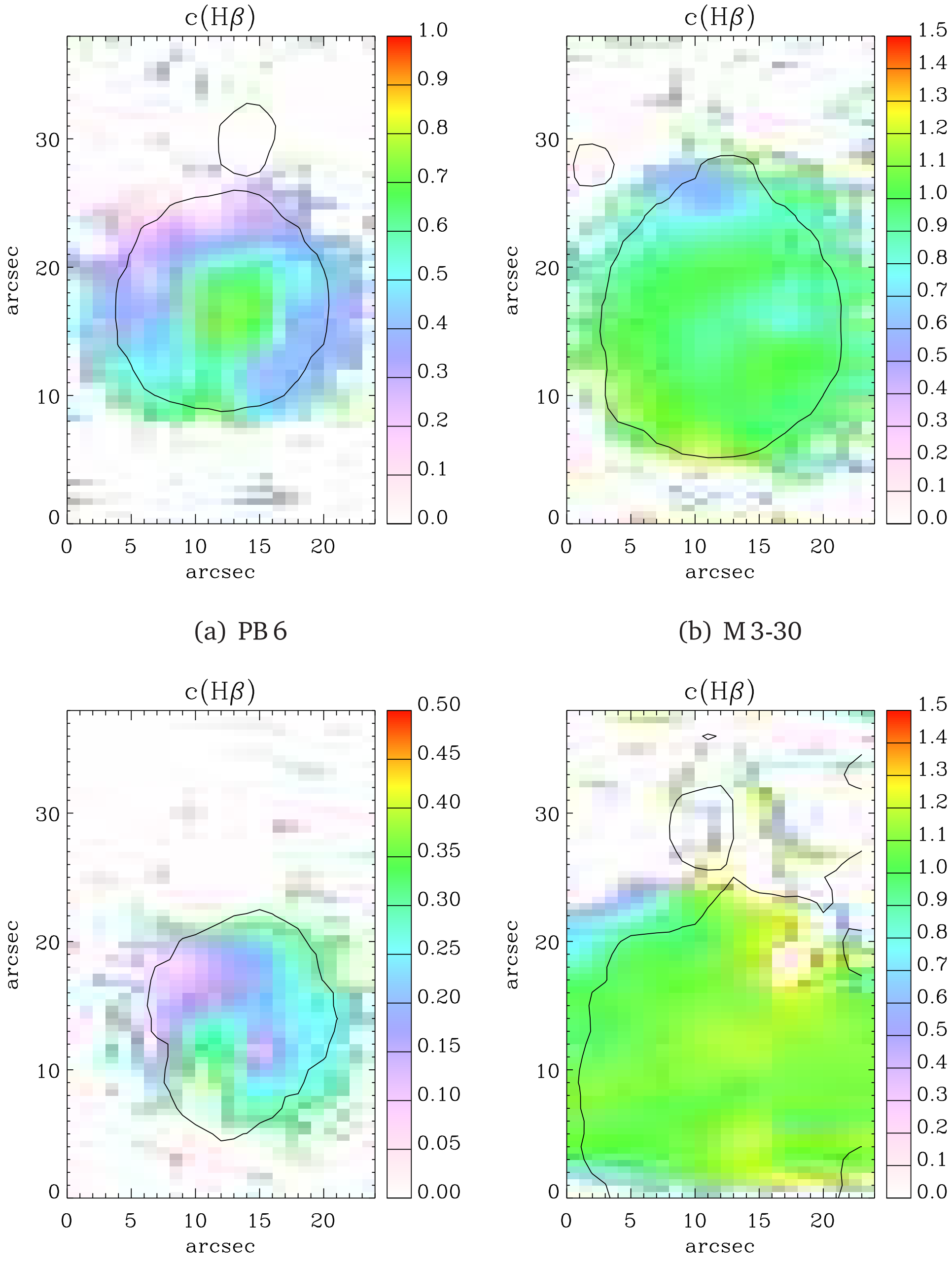

(a) PB 6 (b) M 3-30

(c) Hb 4 (d) IC 1297

Figure 3.2: Spatial distribution maps of extinction $c(\mathrm{H}\alpha)$ from the flux ratio Hα/Hβ. From left to right, and top to bottom: PB 6, M 3-30, IC 1297, Th 2-A and K 2-16. North is up and east is toward the left-hand side. The black contour lines show the distribution of the narrow-band emission of Hα in arbitrary unit obtained from the SuperCOSMOS Sky Hα Survey (SHS; Parker et al. 2005).

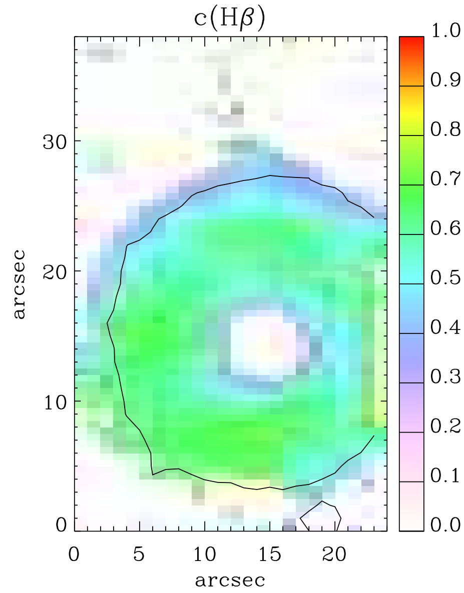

(e) Th 2-A

Figure 3.2: (continued)

3.3.2 CEL plasma diagnostics

The nebular electron temperatures $T_{\rm e}$ and densities $N_{\rm e}$ have been obtained from the intrinsic intensities of CELs by solving level populations for an n-level ($\geqslant 5$) atomic model using the EQUIB code (Howarth & Adams 1981; Wesson et al. 2012, part of the NEAT code). The following diagnostic ratios were used:

$T_{\rm e}$([N II]): $I(\lambda6548 + \lambda6584)/I(\lambda5755)$

$T_{\rm e}$([O III]): $I(\lambda4959 + \lambda5007)/I(\lambda4363)$

$T_{\rm e}$([S III]): $I(\lambda9069)/I(\lambda6312)$

$N_{\rm e}$([S II]): $I(\lambda6717)/I(\lambda6731)$

$N_{\rm e}$([O II]): $I(\lambda3729)/I(\lambda3726)$

$N_{\rm e}$([Ar IV]): $I(\lambda4711)/I(\lambda4740)$

$N_{\rm e}$([Cl III]): $I(\lambda5538/I(\lambda5518)$

The atomic data sets used for our plasma diagnostics from collisionally excited lines (CELs), as well as for abundances derived from CELs, are given in Table 3.3. The diagnostics procedure was done in an iterative way to provide self-consistent results for $N_{\rm e}$([S II]) and $T_{\rm e}$([N II]), i.e., a representative initial $T_{\rm e}$([N II]) was assumed to calculate $N_{\rm e}$; then $T_{\rm e}$ was derived in conjunction with the derived $N_{\rm e}$([S II]), and were iterated to provide self-consistent results. We then used the temperature $T_{\rm e}$([N II]) to derive $N_{\rm e}$([O II]), $N_{\rm e}$([Ar IV]) and $N_{\rm e}$([Cl III]) where adequate lines were available. The density $N_{\rm e}$([S II]) was also used to derive $T_{\rm e}$([O III]) and $T_{\rm e}$([S III]).

The derived electron temperatures and densities for our sample of PNe are presented in Table 3.4. The ion, diagnostic lines, and ionization potential required to reach the ionization stage, are given in columns 1–3, respectively. The derived value of $T_{\rm e}$ or $N_{\rm e}$ are given for each PN. For all PNe, we deduced $T_{\rm e}$ and $N_{\rm e}$ from [N II] (λ6548+λ6584)/λ5755 and [S II] λ6717)/λ6731, respectively. We were able to drive $N_{\rm e}$ using [Cl III] λ5538/λ5518 for PB 6, M 3-30, Hb 4, IC 1297, M 1-32, M 3-15, NGC 6578, M 2-42, NGC 6567 and NGC 6629; [Ar IV] λ4711/λ4740 for the same PNe and Th 2-A, except M 1-32 and NGC 6629; [O II] λ3729/λ3726 for M 3-30, Hb 4, Pe 1-1, M 1-32, M 3-15, M 1-25 and K 2-16. We also obtained $T_{\rm e}$ using [O III] $\lambda\lambda$4959,5007/λ4363 for all PNe, apart from Hen 2-42, Heb 3-1333, Hen 2-113, K 2-16 and Sa 3-107. The large difference in wavelength between [S III] λ9069 and λ6312 lines and different critical densities could make this diagnostic ratio very sensitive to errors such reddening correction and flux calibration.

Electron densities

The electron densities deduced from various CEL diagnostic ratios, [S II], [O II], [Ar IV] and [Cl III], are presented in Table 3.4. The ionization potential of S^{+} and O^{+}, 10.4 and 13.6 eV, are bellow those of Cl^{2+} and Ar^{3+}, 23.8 and 40.7 eV, respectively. The emission lines emitted from dissimilar ionization zones, so un-

Table 3.3: References for CEL atomic data.

Ion	Transition probabilities	Collision strengths
N^{+}	Bell et al. (1995)	Stafford et al. (1994)
O^{+}	Zeippen (1987)	Pradhan et al. (2006)
O^{2+}	Storey & Zeippen (2000)	Lennon & Burke (1994)
Ne^{2+}	Landi & Bhatia (2005)	McLaughlin & Bell (2000)
S^{+}	Mendoza & Zeippen (1982)	Ramsbottom et al. (1996)
S^{2+}	Mendoza & Zeippen (1982)	Tayal & Gupta (1999)
	Huang (1985)	
Ar^{2+}	Biémont & Hansen (1986)	Galavis et al. (1995)
Ar^{3+}	Mendoza & Zeippen (1982)	Ramsbottom et al. (1997)
Ar^{4+}	Biemont & Bromage (1983)	Galavis et al. (1995)
Cl^{2+}	Mendoza & Zeippen (1982)	Butler & Zeippen (1989)

like densities derived from different ions may point to the presence of density inhomogeneities within the nebula. For PB 6, the electron density derived from [Ar IV] is 690 cm^{-3} lower than those from [Cl III], while all lines arise from similar ionization regions. M 3-30 has a low electron density of about 300 cm^{-3}. We see that $N_{\rm e}$([Cl III]) is about 170 cm^{-3} lower than $N_{\rm e}$([Ar IV]), which can be due to some systematic errors such as the reddening correction and the flux calibration. For the ring-like shell of Hb 4, the [S II], [Cl III] and [Ar IV] doublets yield slightly similar density. However, the density derived from [O II] doublet is by a factor of 2 lower than those from other doublets. This may be explained by a measurement error in the blended [O II] $\lambda\lambda$ 3726,3729 doublet. Alternatively, it may be explained by the differences between the O^{+} collision strengths calculated by Pradhan et al. (2006) and Kisielius et al. (2009). IC 1297 does not seems to have any density variation, since densities from different ions are the same. For Th 2-A, [S II] doublet yields a density which is by a factor of 2 higher than given by the [Ar IV], which may suggests the presence of inhomogeneous condensations. However, we notice that the [Ar IV] $\lambda\lambda$4711, 4740 doublet lines have the highest critical densities among all the density-diagnostic lines.[2] With the relatively low densities prevailing in PB 6, M 3-30, IC 1297 and Th 2-A, the λ4711/λ4740 flux ratios are less sensitive to density, so small errors in the measurement of those lines make very high uncertainties in the derived densities. For Pe 1-1, M 1-32 and M 3-15, the densities derived from the [S II] and [O II] are different by a factor around 2, while they are emitted from similar ionization zone. This could be due to poor qualities of the [O II] $\lambda\lambda$ 3726,3729 emission lines measured from the blue end of the spectrum or inaccurate atomic data (see e.g. Kisielius et al. 2009). For M 1-32, the density derived from [Cl III] diagnostic line ratios is by a factor of 1.8 higher than those from the value from [S II] doublet. The [Cl III] diagnostic lines with higher critical densities could preferentially be emitted from the higher density medium. It is also possible that [Cl III] diagnostic lines arise from higher ionization zones; whereas [S II] diagnostic lines from low ionization zones. This behavior is consistent with the presence of strong density variations in the nebulae and the high excitation regions are likely more dense than low excitation regions in M 1-32. For M 3-15, NGC 6578, M 2-42, NGC 6567 and NGC 6629, the densities derived from different ionization zones does not show a large variation

Apart from the density inhomogeneities, we see some variations in the density distribution. Fig. 3.3 shows the density distribution maps derived from the density-sensitive [S II] $\lambda\lambda$6717,6731 doublet for PB 6, M 3-30, IC 1297, Th 2-A and K 2-16. There are large-scale variations in the density distribution in some PNe. The diagnostic N_e map of PB 6 shows that the density increases largely towards northwest. M 3-30 seems to have a uniform density distribution. We

[2] [S II] $\lambda\lambda$6717, 6731, $N_{cr} = 1400, 3600$ cm^{-3}; [O II] $\lambda\lambda$3726, 3729, $N_{cr} = 4500, 1000$ cm^{-3}; [Ar IV] $\lambda\lambda$4711, 4740, $N_{cr} = 16300, 101000$ cm^{-3}; [Cl III] $\lambda\lambda$5518, 5538, $N_{cr} = 7400, 24000$ cm^{-3} respectively.

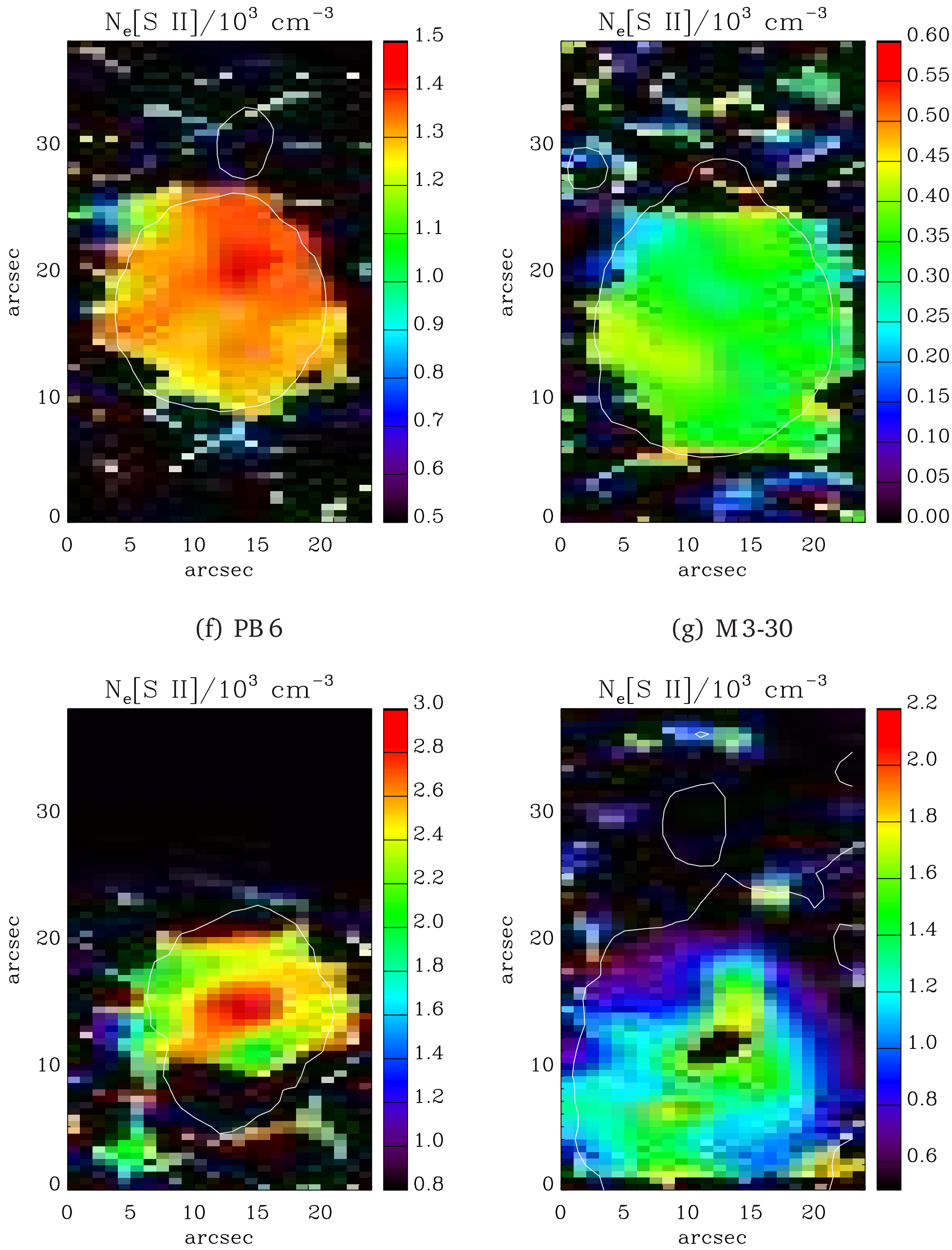

(f) PB 6

(g) M 3-30

(h) Hb 4

(i) IC 1297

Figure 3.3: As Figure 3.2 but for spatial distribution maps of electron density $N_{\rm e}/10^3$ (cm^{-3}) from the flux ratio [S II] 6717/6731. The white contour lines show the distribution of the narrow-band emission of Hα in arbitrary unit obtained from the SHS.

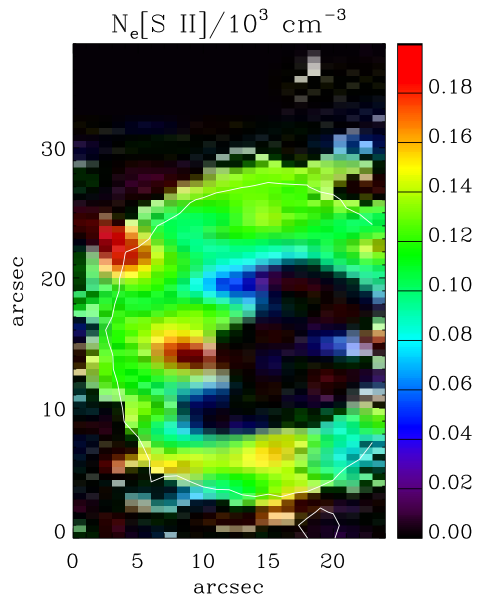

(e) Th 2-A

Figure 3.3: (continued)

see that the density increases in the central regions of both IC 1297 and Th 2-A. For the low-density PN K 2-16, density cannot be determined for the central regions, as [S II] emission is faint.

Fig. 3.4 (top) plots the electron density (N_e) versus the [WR] spectral sequence. After excluding K 2-16, we see that the electron density decreases as the star evolves, assuming (hot) [WCE] is a successor of (cool) [WCL] (e.g. Napiwotzki & Schoenberner 1995). K 2-16 is quite exceptional due to its cool central star and high half width at half maximum (HWHM) velocity of 34 km s^{-1} derived from [N II] line (see Chapter 2). Using the stellar parameters $T_\mathrm{eff} = 29$ kK and $\log L/\mathrm{L}_\odot = 3.3$ found by Acker et al. (2002), it may have a post-AGB age of around 8000 yr. Therefore, the evolutionary time-scale of a 1M$_\odot$ star may explain its typically low density of $N_\mathrm{e} \sim 100\,\mathrm{cm}^{-3}$.

Fig. 3.4 (bottom) shows the logarithmic electron density $\log N_\mathrm{e}$([S II]) plotted against the stellar effective temperature T_eff from Table 3.1. The relation between N_e and T_eff for the 18 PNe (Fig. 3.4, bottom, dotted line) can be fitted

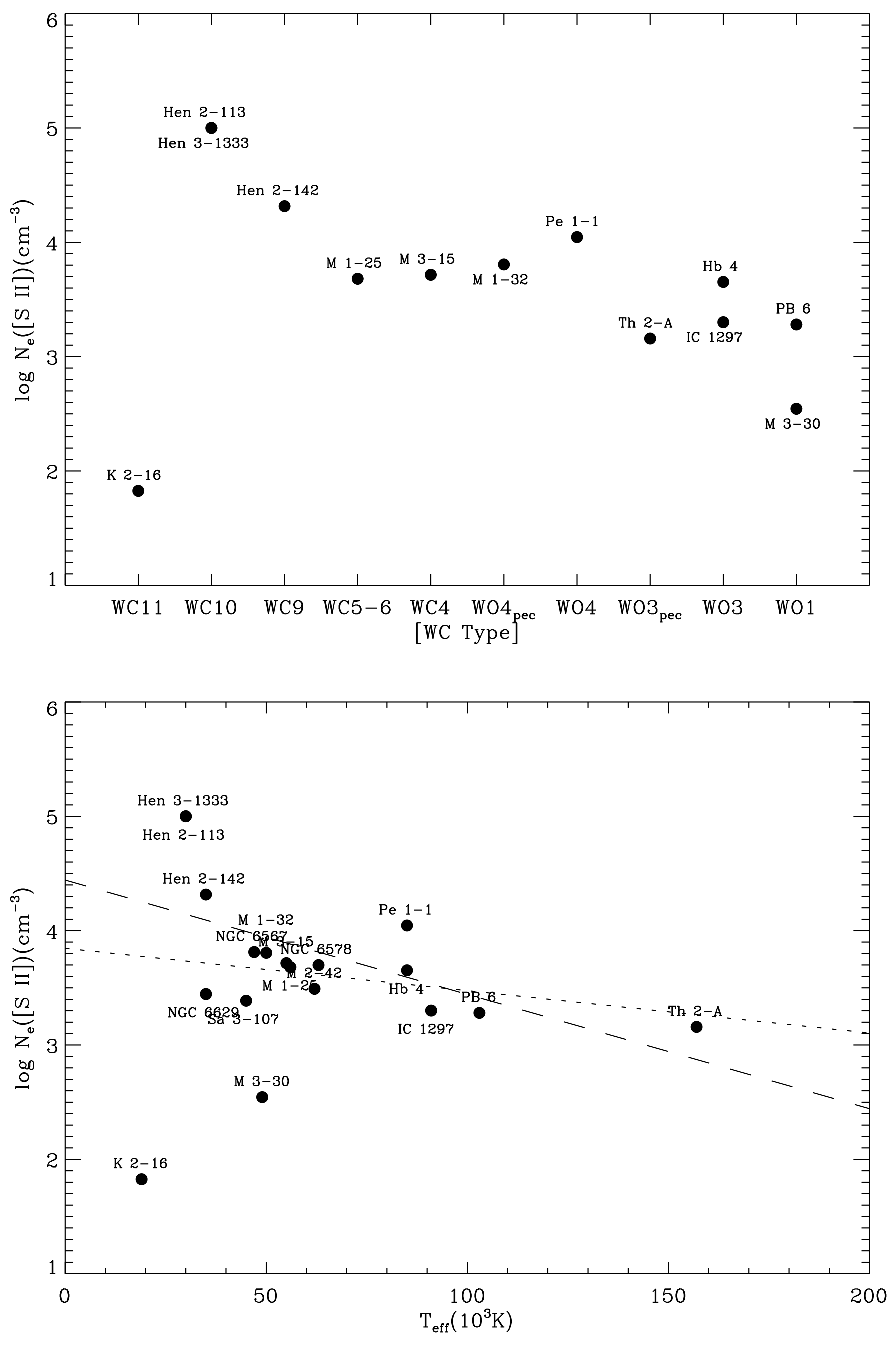

Figure 3.4: Top panel: variation of the logarithmic electron density $\log N_{\rm e}([\mathrm{S\,II}])(\mathrm{cm}^{-3})$ along the spectral sequence. Bottom panel: variation of the logarithmic electron density $\log N_{\rm e}([\mathrm{S\,II}])(\mathrm{cm}^{-3})$ along the stellar effective temperature $T_{\rm eff}(10^3\,\mathrm{K})$. The dotted line is a linear fit to $\log N_{\rm e}([\mathrm{S\,II}])$ as a function of $T_{\rm eff}$. The dashed line is a similar linear fit found after excluding K 2-16 and M 3-30, discussed in the text.

by

$$\log N_{\rm e}([\mathrm{S\,II}]) = (3.846 \pm 0.381) - (3.71 \pm 5.53) \times 10^{-6} T_{\rm eff}(\mathrm{K}), \qquad (3.1)$$

which has a weak linear (Pearson) correlation coefficient of -0.17 (one is a perfect fit and zero represents no correlation; negative shows anti-correlation), while a linear fit to the 15 PNe, after excluding K 2-16 and M 3-30, yields a better correlation:

$$\log N_{\rm e}([\mathrm{S\,II}]) = (4.443 \pm 0.253) - (9.99 \pm 3.52) \times 10^{-6} T_{\rm eff}(\mathrm{K}). \qquad (3.2)$$

with a linear correlation coefficient of -0.60. The fit is shown as a dashed line in Fig. 3.4 (bottom). Both K 2-16 and M 3-30 might have a low-mass central star, so their low nebular densities could be related to their evolutionary parameters. The nebula density decreases as the nebula evolves, so it is typical as high as 10^5 cm^{-3} in young compact PNe, while it is reduced to less than 100 cm^{-3} in old PNe (e.g. see SuWt 2 in Chapter 7, Danehkar et al. 2013).

Fig. 3.5 shows the logarithmic electron density $\log N_{\rm e}([\mathrm{S\,II}])$ plotted against the logarithmic intrinsic nebular Hβ surface brightness. The dashed line represents a linear fit to the 18 PNe, which has a strong linear correlation coefficient of 0.77:

$$\log N_{\rm e}([\mathrm{S\,II}]) = (4.592 \pm 0.234) + (0.514 \pm 0.107) \log S(\mathrm{H}\beta), \qquad (3.3)$$

where the dereddened nebular Hβ surface brightness is defined as the integrated Hβ flux divided by the nebular area, $S(\mathrm{H}\beta) = I(\mathrm{H}\beta)/(\pi r^2)$, in unit of erg cm^{-2} s^{-1} sr^{-1}, the intrinsic Hβ flux $I(\mathrm{H}\beta) = 10^{c(\mathrm{H}\beta)} F(\mathrm{H}\beta)$, and r is the nebular optical angular radius (see Table 3.1). Eq. (3.3) indicates that $S(\mathrm{H}\beta) \propto N_{\rm e}^{1.95}$, which is in agreement with the theoretical relation approximated by O'Dell (1962), $S(\mathrm{H}\beta) \propto \varepsilon\, r N_{\rm e}^2 \propto \varepsilon^{2/3} M^{1/3} N_{\rm e}^{5/3}$, where M is the total mass of the nebula and ε is the filling factor.

As seen in Fig. 3.5, there is a strong correlation between the electron density and the nebular Hβ surface brightness, but Fig. 3.4 (bottom) depicts a weak

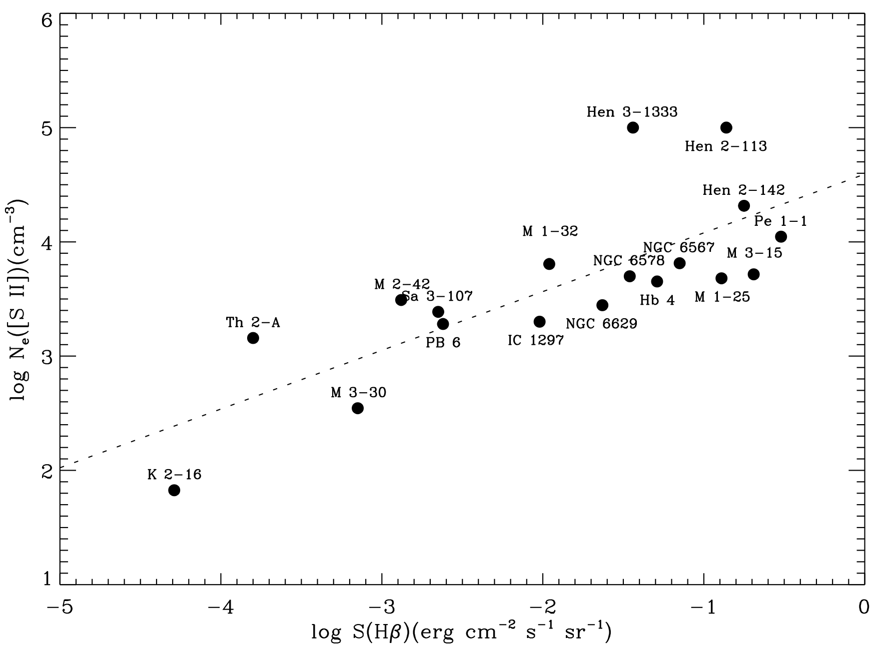

Figure 3.5: The logarithmic electron density $\log N_{\rm e}([\mathrm{S\,II}])(\mathrm{cm}^{-3})$ plotted against the logarithmic intrinsic nebular Hβ surface brightness $\log S(\mathrm{H}\beta)(\mathrm{erg\,cm^{-2}\,s^{-1}\,sr^{-1}})$. The dotted line is a linear fit to $\log N_{\rm e}([\mathrm{S\,II}])$ as a function of $\log S(\mathrm{H}\beta)$, discussed in the text.

correlation between the electron density and the stellar effective temperature. In an extensive study of Magellanic Cloud PNe, Stanghellini et al. (2002, 2003, 2008) found that the nebular surface brightness declines with radii in most emission lines. The nebular Hβ surface brightness can represent an evolutionary indicator of the nebula because of strong correlations with both the nebular density and radius. The nebular surface brightness decreases due to the expansion of the nebula, as the density drops. But, this evolutionary parameter is not only related to the gaseous evolution but is also a function of the ionizing source.

Electron temperatures

The electron temperatures deduced from the ratios of the nebular lines to auroral lines are presented in Table 3.4. We adopted N_e([S II]) to derive T_e([N II]), and iterated until convergence. We also used N_e([S II]) to determine T_e([O III]) and T_e([S III]) where adequate CELs were available. Table 3.4 lists T_e([N II]) and T_e([O III]) derived before and after correcting for recombination contributions to the auroral lines.

The recombination excitation can also make some major contributions to the [N II] λ5755 auroral line, the [O II] $\lambda\lambda$3726,3729 nebular lines, and the [O II] $\lambda\lambda$7320,7330 auroral lines; but small contribution to the [O III] λ4363 auroral line. The recombination contribution can lead to apparently high temperatures deduced from the [N II] (λ6548+λ6584)/λ5755 ratio in the nebula containing a fraction of cold, metal-rich inclusions. Furthermore, it can also lead to over-estimated temperatures in the nebula containing inhomogeneous condensations, whose density is higher than the critical densities of the nebular lines, while the auroral lines emitted from the lower density medium (Viegas & Clegg 1994). Owing to the relatively low critical densities of the [N II] nebular lines[3] , the presence of density inhomogeneities lead to apparently high electron temperatures. However, because of the fairly low critical densities of the [O II] $\lambda\lambda$3726,3729 nebular lines, their recombination emissivities depend also on electron density, in addition to electron temperature and abundance, so the derived density is not affected by the recombination excitation.

The recombination contribution to the [N II] λ5755 auroral line can be estimated by the formula given by Liu et al. (2000):

$$\frac{I_R(\lambda 5755)}{I(\mathrm{H}\beta)} = 3.19\, t^{0.30} \left(\frac{\mathrm{N}^{2+}}{\mathrm{H}^{+}}\right)_{\mathrm{ORLs}}, \qquad (3.4)$$

where $t \equiv T_e(\mathrm{He\,I})/10^4$ is the ORL electron temperature in 10^4 K and $\mathrm{N}^{2+}/\mathrm{H}^{+}$ is

[3] [N II] $\lambda\lambda$5755, 6584, $N_{cr} = 1.3 \times 10^7$, 8.6×10^4 cm^{-3}; [O III] $\lambda\lambda$4363, 5007, $N_{cr} = 2.4 \times 10^7$, 6.9×10^5 cm^{-3}; [S III] $\lambda\lambda$6312, 9069, $N_{cr} = 1.4 \times 10^7$, 8.0×10^5 cm^{-3} respectively.

derived from the N II ORLs (see Table 3.10).

We estimated the recombination contribution to the [O III] λ4363 auroral line using the following formula by Liu et al. (2000):

$$\frac{I_{\rm R}(\lambda 4363)}{I({\rm H}\beta)} = 12.4\, t^{0.79} \left(\frac{{\rm O}^{3+}}{{\rm H}^{+}}\right)_{\rm ORLs}, \tag{3.5}$$

where the $\mathrm{O}^{3+}/\mathrm{H}^{+}$ ratio is computed using

$$\mathrm{O}^{3+}/\mathrm{H}^{+} = [(\mathrm{He}/\mathrm{H}^{+})^{2/3} - 1] \times (\mathrm{O}^{+}/\mathrm{H}^{+} + \mathrm{O}^{2+}/\mathrm{H}^{+}). \tag{3.6}$$

The $\mathrm{O}^{2+}/\mathrm{H}^{+}$ ratio is taken from Table 3.10, while the $\mathrm{O}^{+}/\mathrm{H}^{+}$ ratio is excluded.

For PB 6, which has $T_{\rm e}$[N II] $= 11480$ K, the observed lines of N II 5932, 5952, 5452 yield $\mathrm{N}^{2+}/\mathrm{H}^{+} = 6.57 \times 10^{-3}$, for $T_{\rm e}$(He I)$= 5100$ K and $N_{\rm e} = 2000\,{\rm cm}^{-3}$ (Table 3.8). Inserting them into equation (3.4), we have $I_{\rm R}(\lambda 5754)/I({\rm H}\beta) = 0.017$, or 37 per cent of the observed intensity of the λ5755 line. After subtracting the recombination contribution from the observed intensity, the [N II] line ratio yields $T_{\rm e}$[N II]$= 9400$ K, i.e. 2080 K lower than the value derived before the correction. Applying the same procedure to M 3-30, which has $T_{\rm e}$[N II] $= 9020K$, we obtain from $\mathrm{N}^{2+}/\mathrm{H}^{+} = 7.57 \times 10^{-4}$ and $T_{\rm e}$(He I)$= 2500$ K, as given by the ORLs, a corrected nebular to auroral line ratio which yields $T_{\rm e}$[N II]$= 7510$ K. Similarly, for Hb 4 the corrected [N II] nebular to auroral line ratio results in $T_{\rm e}$[N II] $=$ 9920 K, using $\mathrm{N}^{2+}/\mathrm{H}^{+} = 6.6 \times 10^{-4}$ and $T_{\rm e}$(He I)$= 4200$ K as given by ORLs. For IC 1297, using $\mathrm{N}^{2+}/\mathrm{H}^{+} = 7.9 \times 10^{-4}$ and $T_{\rm e}$(He I)$= 4500$ K one gets $I_{\rm R}(\lambda 5754)/I({\rm H}\beta) = 0.002$, which is about 31 per cent of the observed value. After correcting for the recombination contribution, the temperature is 1260 lower. For Th 2-A, we get the recombination contribution about 45 per cent of the observed value, resulting in a temperature, which is 2040 K lower than the value derived before the correction. The contribution of recombination excitation to the observed [N II] λ5755 nebular intensities are estimated to be 8, 13 and 23 per cent for Pe 1-1, M 1-32 and M 3-15, respectively, which have a negligible effect on the derived temperature. We summarize our findings for all objects in Table 3.4.

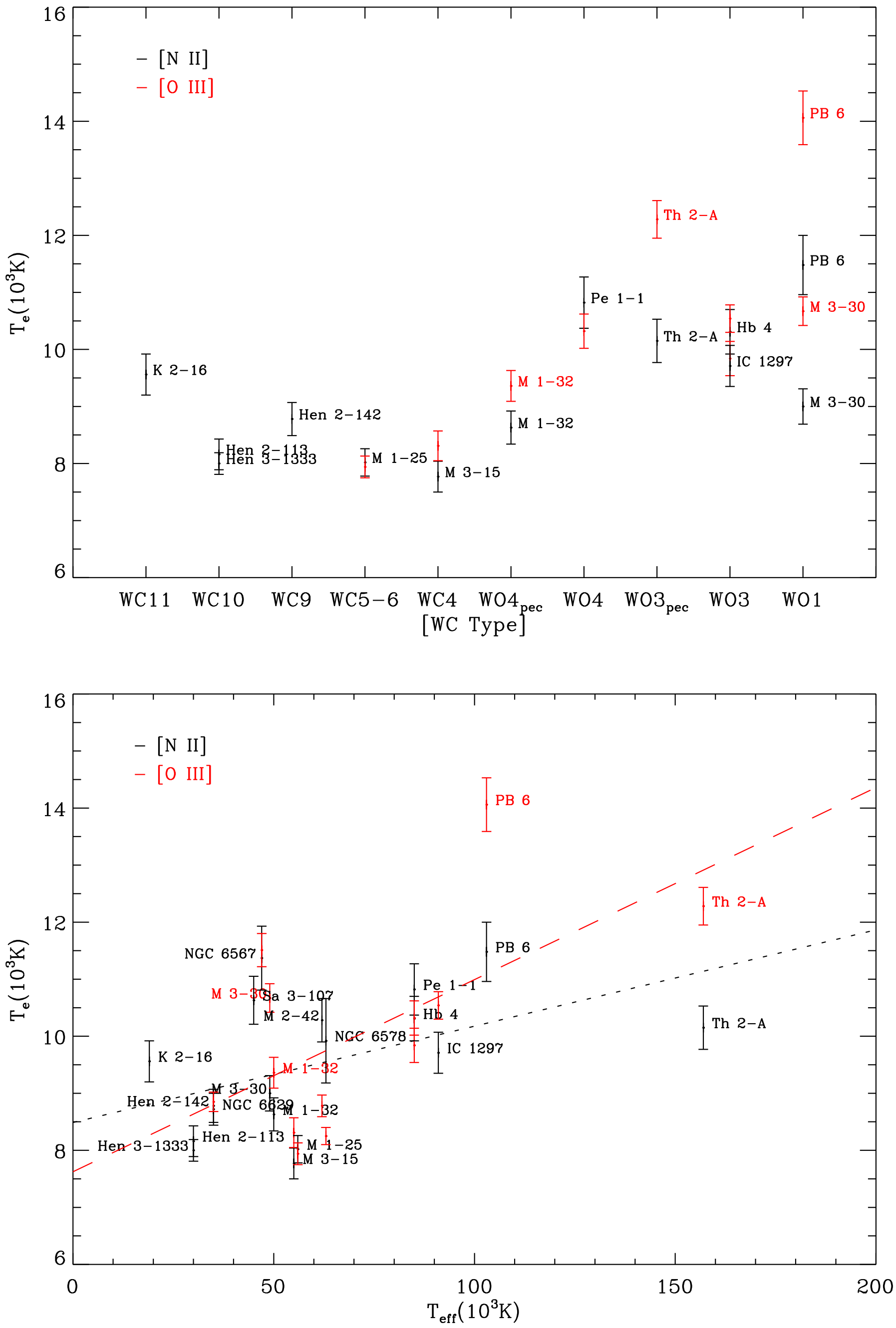

Figure 3.6: Top panel: variation of the electron temperature $T_e(10^3\,\mathrm{K})$ along the spectral sequence. Bottom panel: variation of the electron temperature $T_e(10^3\,\mathrm{K})$ along the stellar effective temperature $T_{\mathrm{eff}}(10^3\,\mathrm{K})$. The electron temperature derived from [N II] (black line) and [O III] diagnostic ratios (red line). The dotted and dashed lines are respectively linear fits to T_e([N II]) and T_e([O III]) as functions of T_{eff}, discussed in the text.

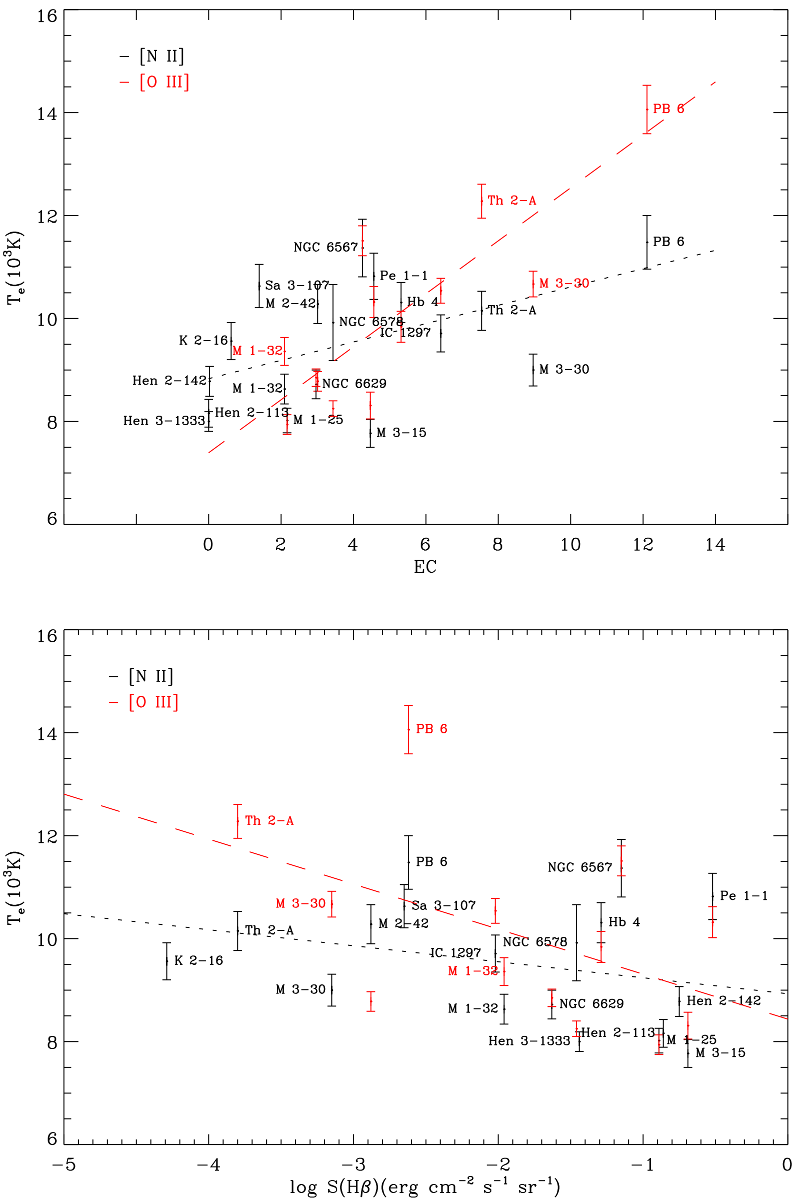

Figure 3.7: Top panel: variation of the electron temperature $T_e(10^3\,\mathrm{K})$ along the excitation class (EC). The electron temperature derived from [N II] (black line) and [O III] diagnostic ratios (red line). The dotted and dashed lines are respectively linear fits to T_e([N II]) and T_e([O III]) as functions of EC, discussed in the text. Bottom panel: the electron temperature $T_e(10^3\,\mathrm{K})$ plotted against the logarithmic intrinsic nebular Hβ surface brightness $\log S(\mathrm{H}\beta)(\mathrm{erg\,cm^{-2}\,s^{-1}\,sr^{-1}})$. The electron temperature derived from [N II] (black line) and [O III] diagnostic ratios (red line). The dotted and dashed lines are respectively linear fits to T_e([N II]) and T_e([O III]) as functions of $\log S(\mathrm{H}\beta)$, discussed in the text.

We obtained a recombination contribution of about 5–60% for different PNe. However, N^{2+}/H^{+} ionic abundances derived from N II ORLs are very uncertain. As the ORLs tend to be among the weakest lines, their ionic abundances are highly sensitive to errors in the measurement of lines, and flux calibration. The exact value of the [N II] electron temperature requires detailed knowledge of the ORL electron temperature and N^{2+}/H^{+} abundances. Meanwhile, collisional de-excitation of the metastable levels populated by recombination also adds a further complication, which we did not consider. The recombination contribution to [N II] auroral lines may be correctly estimated for low-density uniform nebular media. However, the observed [N II] auroral lines can be more difficult to evaluate in the present of inhomogeneous condensations. The dense clumps in the nebula whose density is larger than the lower density medium, from which the $\lambda\lambda$6548,6584 nebular lines originate, make likely larger diagnostic temperatures as derived from the [N II] nebular to auroral ratios, since collisional de-excitation of the high density region suppresses the nebular lines, but not the auroral lines (Viegas & Clegg 1994). The presence of inhomogeneous condensations can lead to overestimated temperatures, but this effect is more difficult to quantify. Therefore, in the CEL abundance analysis that follows in Section 3.4, we have not considered the corrected $T_{\rm e}$[N II]. However, the [N II] temperature diagnostic values are probably poor indicators of temperature in the low-ionization regions, so we have carefully adopted $T_{\rm e}$ based on our diagnostic results and those found in the previous studies listed in Table 3.7.

Fig. 3.6 (top) plots the electron temperature $T_{\rm e}$ (before correcting for the recombination excitation) versus the spectral sequence. We see that the electron temperature increases as the star evolves from cool [WCL] to hot [WO] sequences. Fig. 3.6 (bottom) shows the electron temperature $T_{\rm e}$ plotted against the stellar effective temperature $T_{\rm eff}$. It is seen that $T_{\rm e}$ increases with an increase in $T_{\rm eff}$. The relation between $T_{\rm e}$([N II]) and $T_{\rm eff}$ for the 18 PNe can be fitted by

$$T_{\rm e}([\mathrm{N\,II}]) = (8489 \pm 538) + (16.880 \pm 7.796)\,T_{\rm eff}(\mathrm{K})/10^3, \tag{3.7}$$

with a linear correlation coefficient of 0.48 (dotted line in Fig. 3.6). Similarly, a linear fit (dashed line in Fig. 3.6) between $T_{\rm e}$([O III]) and $T_{\rm eff}$ for the 13 PNe yields

$$T_{\rm e}([\mathrm{O\,III}]) = (7624 \pm 1030) + (33.683 \pm 13.111)\,T_{\rm eff}(\mathrm{K})/10^3, \tag{3.8}$$

which has a linear correlation coefficient of 0.61.

Fig. 3.6 (top) plots the electron temperature $T_{\rm e}$ (before correcting for the recombination excitation) versus the spectral sequence. We see that the electron temperature increases as the star evolves from cool [WCL] to hot [WO] sequences. Fig. 3.6 (bottom) shows the electron temperature $T_{\rm e}$ plotted against the stellar effective temperature $T_{\rm eff}$. It is seen that $T_{\rm e}$ increases with an increase in $T_{\rm eff}$. The relation between $T_{\rm e}$([N II]) and $T_{\rm eff}$ for the 18 PNe can be fitted by

$$T_{\rm e}([\mathrm{N\,II}]) = (8489 \pm 538) + (16.880 \pm 7.796)\,T_{\rm eff}(\mathrm{K})/10^3, \tag{3.9}$$

with a linear correlation coefficient of 0.48 (dotted line in Fig. 3.6). Similarly, a linear fit (dashed line in Fig. 3.6) between $T_{\rm e}$([O III]) and $T_{\rm eff}$ for the 13 PNe yields

$$T_{\rm e}([\mathrm{O\,III}]) = (7624 \pm 1030) + (33.683 \pm 13.111)\,T_{\rm eff}(\mathrm{K})/10^3, \tag{3.10}$$

which has a linear correlation coefficient of 0.61.

Fig. 3.7(top) plots $T_{\rm e}$ versus the excitation class (EC; Dopita & Meatheringham 1990). A trend of increasing $T_{\rm e}$ with increasing EC is seen. A linear fit (dotted line) to $T_{\rm e}$([N II]) and as a function of EC for the 18 PNe plotted in Fig. 3.7 (top) yields

$$T_{\rm e}([\mathrm{N\,II}]) = (8831 \pm 388) + (178.12 \pm 77.34)\,\mathrm{EC}, \tag{3.11}$$

with a linear correlation coefficient of 0.50, while a linear fit (dashed line) to $T_{\rm e}$([O III]) as a function of EC for the 13 PNe yields

$$T_{\rm e}([\mathrm{O\,III}]) = (7391 \pm 583) + (514.64 \pm 98.96)\,\mathrm{EC}, \quad (3.12)$$

which has a strong linear correlation coefficient of 0.84. Fig. 3.7(bottom) shows the electron temperature $T_{\rm e}$(10^3 K) plotted against the logarithmic intrinsic nebular Hβ surface brightness $\log S(\mathrm{H}\beta)$. The dashed line in the figure represents a linear fit to the $T_{\rm e}$([N II]) data for the 18 PNe, with

$$T_{\rm e}([\mathrm{N\,II}]) = (8929 \pm 552) - (310.85 \pm 253.02)\,\log S(\mathrm{H}\beta), \quad (3.13)$$

The linear correlation coefficient is -0.29, while a linear fit to the $T_{\rm e}$([O III]) data for the 13 PNe yields

$$T_{\rm e}([\mathrm{O\,III}]) = (8437 \pm 967) - (874.09 \pm 462.99)\,\log S(\mathrm{H}\beta), \quad (3.14)$$

which has a linear correlation coefficient of -0.49.

As seen in Fig. 3.7, the correlation between $T_{\rm e}$([O III]) and EC is much stronger than the $T_{\rm e}$–S(Hβ) correlation. The electron temperatures of high-excitation PNe are typically higher than low-excitation PNe, which can be explained by the radiations from the central stars. Although elemental abundances and dust are involved in heating and cooling mechanisms of the nebula, the ionizing photons can make major contribution to the thermal properties of the gas.

3.3.3 ORL plasma diagnostics

An alternative method of plasma diagnostics is to use the ORLs. The emissivities of heavy element ORLs relative to a hydrogen recombination line weakly depend on the electron temperature and density. However, emissivities of CELs relative to a hydrogen recombination line increase exponentially with the electron temperature. Because the sensitivity of ORLs to the electron density is very

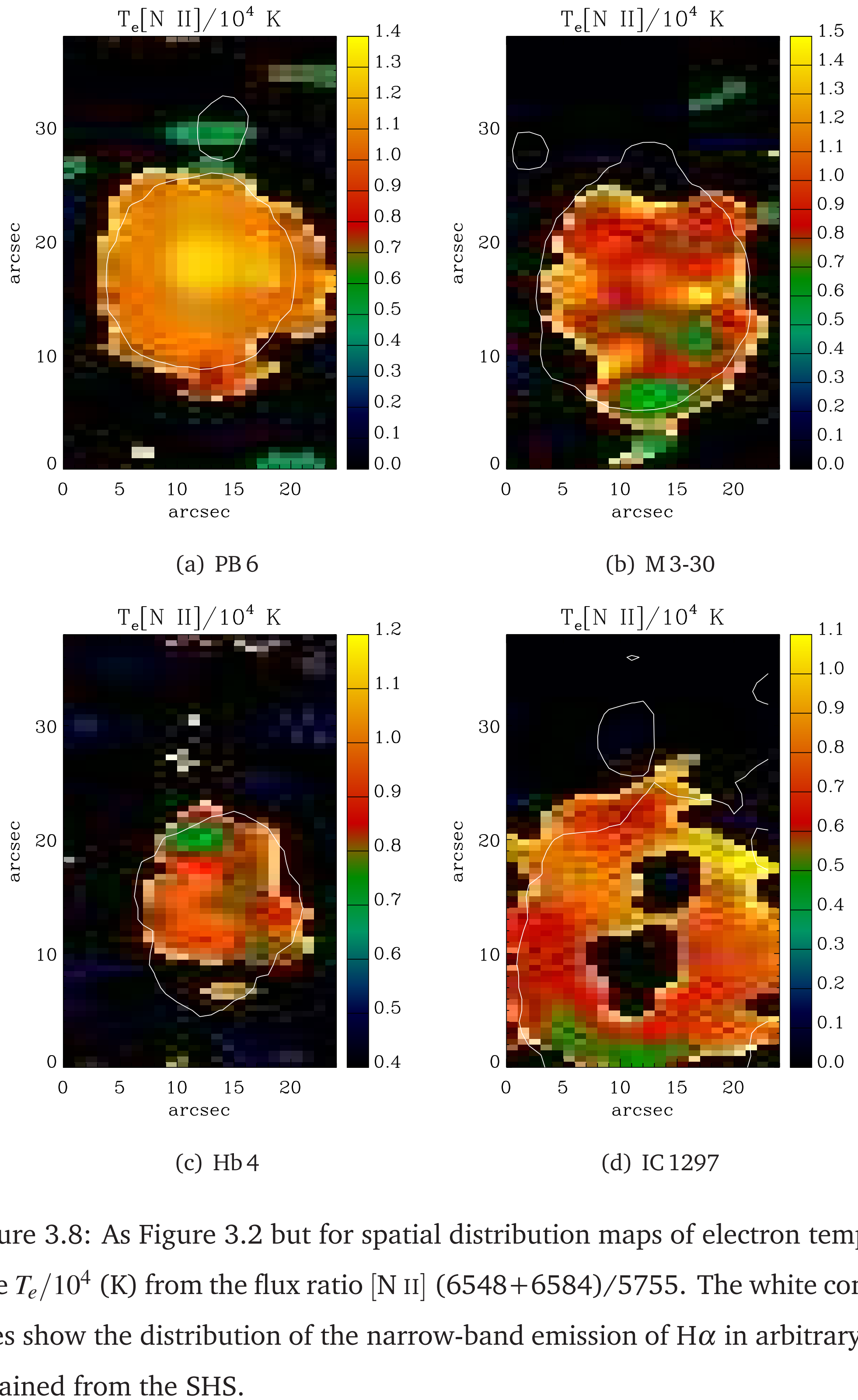

Figure 3.8: As Figure 3.2 but for spatial distribution maps of electron temperature $T_e/10^4$ (K) from the flux ratio [N II] (6548+6584)/5755. The white contour lines show the distribution of the narrow-band emission of Hα in arbitrary unit obtained from the SHS.

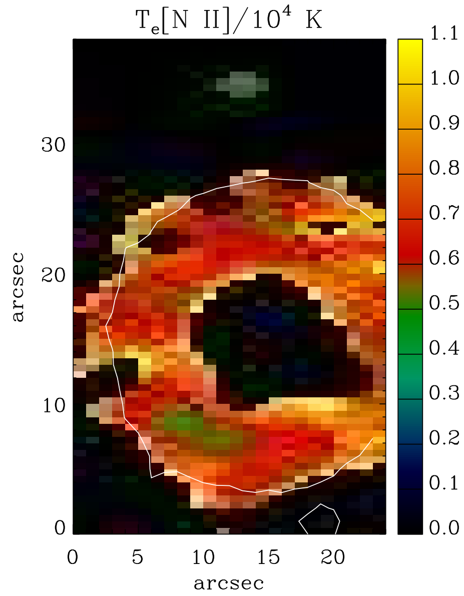

(e) Th 2-A

Figure 3.8: (continued)

weak, the abundances deduced from ORLs should in theory be more reliable than those from CELs.

Using the fact that emissivities of heavy element ORLs have a relatively weak, power-law dependence on the electron temperature, the relative intensities of ORLs can be used to determine electron temperatures (see e.g. McNabb et al. 2013; Storey & Sochi 2013). However, the plasma diagnostics based on ORLs generally have larger uncertainties, since the dependence of the line fluxes on the physical conditions is so weak. The heavy element ORLs are very weak compared to the CELs, so deeper spectroscopic surveys are required to measure them accurately. Despite all our efforts to measure them in PNe (see e.g. Liu et al. 2004b; Tsamis et al. 2003a; Wesson et al. 2003, 2005, 2008; Wang & Liu 2007; Fang & Liu 2013) and H II regions (see e.g. Tsamis et al. 2003b; Peimbert et al. 2004; García-Rojas et al. 2005, 2006, 2007), the ORL measurements still have low signal-to-noise ratios or line blending.

The plasma diagnostics based on the flux intensity ratio of two different

ORLs is the most common way to determine electron temperature (see e.g. Liu et al. 2004b; Tsamis et al. 2003a; Wesson et al. 2003, 2005). However, strong flux intensities are necessary to get a reliable result. The least squares minimization, relying on a number of lines, can be used as an alternative method for the electron temperature determination of ORLs (McNabb et al. 2013; Storey & Sochi 2013). This method is based on minimizing difference between the normalized intrinsic line flux intensities and the normalized values calculated by the theoretical model.

To derive the electron temperature from ORLs, we used the effective recombination coefficients $\alpha_{\rm eff}$ of ions from the references listed in Table 3.5 in their valid temperature range. The electron temperature is identified at the minimum value of the following least-squares equation for each ion:

$$\chi^2 = \frac{1}{N}\sum_{i=1}^{N} \frac{\left[\left(I_i/\sum_{j=1}^{N} I_j\right)_{\rm obs} - \left(I_i/\sum_{j=1}^{N} I_j\right)_{\rm mod}\right]^2}{\left(I_i/\sum_{j=1}^{N} I_j\right)^2_{\rm mod}} \tag{3.15}$$

where $(I_i)_{\rm mod} = \alpha_{\rm eff}(\lambda_i)/\lambda_i$ is the theoretical model quantity of line i calculated for given $T_{\rm e}$ and $N_{\rm e}$, and $(I_i)_{\rm obs}$ the measured intrinsic line flux of line i with wavelength λ_i.

In the least squares minimization method, a single fitting parameter is used, the electron temperature or density. The theoretical model quantity of each line is normalized to the total theoretical model quantity of all the lines involved in the procedure, while the measured intrinsic line flux of that line is normalized to the total intrinsic line flux of these lines. Accordingly, the fitting parameter ($T_{\rm e}$ or $N_{\rm e}$) is determined from its value at $\chi^2_{\rm min}$.

Similarly, we used the least-squares minimization method and the effective recombination coefficients of ions to determine the electron density from ORLs. The electron temperature derived from ORLs using the least-squares minimization was used to calculate the electron density in order to provide a self-consistent result.

Table 3.4: Plasma diagnostics.

Ion	Diagnostic	I.P.	PB 6	M 3-30	Hb 4 (shell)	Hb 4 (N-knot)	Hb 4 (S-knot)	IC 1297	Th 2-A	Pe 1-1	M 1-32	M 3-15
		(eV)	Electron Temperature, T_e(K)									
[N II]	$\frac{\lambda6548+\lambda6584}{\lambda5755}$	14.53	11480 ± 520	9020 ± 310	10310 ± 390	11400 ± 610	...	9710 ± 360	10150 ± 380	10820 ± 450	8630 ± 290	7780 ± 270
[N II] [a]	$\frac{\lambda6548+\lambda6584}{\lambda5755}$	14.53	9400 ± 350	7510 ± 210	9920 ± 300	...	...	8450 ± 280	8110 ± 240	10430 ± 430	8220 ± 270	7160 ± 230
[O III]	$\frac{\lambda4959+\lambda5007}{\lambda4363^b}$	35.12	14060 ± 470	10670 ± 250	9900 ± 300	...	...	10540 ± 240	12280 ± 330	10320 ± 300	9360 ± 270	8310 ± 260
[O III] [a]	$\frac{\lambda4959+\lambda5007}{\lambda4363^b}$	35.12	...	10030 ± 220	9840 ± 300	...	...	10480 ± 240	11800 ± 310	...	...	...
[S III]	$\frac{\lambda9069^b}{\lambda6312}$	23.34	...	...	7560 ± 530	...	...	8860 ± 180	...	7750 ± 400	6534 ± 374	6920 ± 420
He I	$\frac{\lambda5876}{\lambda4472}$	24.59	5160 ± 370	1630 ± 120	2400 ± 170	...	...	3370 ± 240	1730 ± 130	4880 ± 380	1540 ± 120	...
He I	$\frac{\lambda6678}{\lambda4472}$	24.59	...	2340 ± 180	4150 ± 300	...	...	4540 ± 330	3640 ± 260	9300 ± 730	2270 ± 170	...
He I	$\frac{\lambda7281^b}{\lambda5876}$	24.59	...	...	5940 ± 880	...	...	4540 ± 230	...	9390 ± 1050	...	...
He I	$\frac{\lambda7281^b}{\lambda6678}$	24.59	...	...	7050 ± 1050	...	...	5030 ± 260	...	...	...	...
			Electron Density, N_e(cm^{-3})									
[S II]	$\frac{\lambda6717}{\lambda6731}$	10.36	2000 ± 480	350:	6700 ± 1890	830 ± 510	890 ± 250	2000 ± 850	1400 ± 420	11100 ± 9960	6400 ± 3260	5200 ± 2670
[O II]	$\frac{\lambda3729^b}{\lambda3726^b}$	13.62	...	100:	3470 ± 1887	...	...	...	...	6270 ± 3210	3440 ± 1710	3940:
[Ar IV]	$\frac{\lambda4711}{\lambda4740}$	40.74	1730 ± 810	300:	6760 ± 1340	...	...	2140 ± 790	630:	...	...	5970:
[Cl III]	$\frac{\lambda5538}{\lambda5518}$	23.81	2420 ± 590	170:	7170 ± 1280	...	...	2080 ± 580	...	...	11490 ± 3010	7490 ± 2030

Notes: Uncertain (errors of 50 per cent) and very uncertain (greater than a factor of 2) values are followed by ':' and '::', respectively.

[a] Corrected for recombination contribution to the auroral line [N II] $\lambda5755$ and [O III] $\lambda4363$.

[b] Fluxes adopted from the literature as follows: PB 6, Kaler et al. (1991); M 3-30 and K 2-16, Peña et al. (2001); IC 1297 and NGC 6629, Milingo et al. (2002); Th 2-A, Kingsburgh & Barlow (1994); Hb 4, Pe 1-1, M 1-32, M 3-15 and M 1-25, García-Rojas et al. (2012); Hen 2-142, Girard et al. (2007); Hen 3-1333 and Hen 2-113, De Marco et al. (1997). NGC 6578 and NGC 6567, Kwitter et al. (2003); M 2-42, Wang & Liu (2007).

Table 3.4: (continued)

Ion	Diagnostic	I.P. (eV)	M 1-25	Hen 2-142	Hen 3-1333	Hen 2-113	K 2-16	NGC 6578	M 2-42	NGC 6567	NGC 6629	Sa 3-107
			Electron Temperature, $T_{\rm e}$(K)									
[N II]	$\frac{\lambda6548+\lambda6584}{\lambda5755}$	14.53	8020 ± 240	8780 ± 290	6670::	8160 ± 270	9560 ± 360	9920 ± 740	10280 ± 380	11370 ± 560	8720 ± 280	10630 ± 420
[O III]	$\frac{\lambda4959+\lambda5007}{\lambda4363^{\rm b}}$	35.12	7940 ± 190	...	...	...	...	8250 ± 150	8780 ± 190	11510 ± 290	8850 ± 170	...
[S III]	$\frac{\lambda9069^{\rm b}}{\lambda6312}$	23.34	6570:	...	...	7140:	...	6520:	...	9220:	7500:	...
He I	$\frac{\lambda5876}{\lambda4472}$	24.59	2350 ± 210	...	...	...	...	3600 ± 260	...	4630 ± 330	4470 ± 320	3120 ± 230
He I	$\frac{\lambda6678}{\lambda4472}$	24.59	2410 ± 180	1750 ± 140	...	...	...	5080 ± 370	...	9260 ± 660	5590 ± 400	4520 ± 330
He I	$\frac{\lambda7281^{\rm b}}{\lambda5876}$	24.59	5310 ± 650	...	...	...	...	4890 ± 250	2710 ± 140	9920 ± 500	...	...
He I	$\frac{\lambda7281^{\rm b}}{\lambda6678}$	24.59	5280 ± 590	...	...	...	...	5490 ± 280	3320 ± 170	...	...	...
			Electron Density, $N_{\rm e}$(cm^{-3})									
[S II]	$\frac{\lambda6717}{\lambda6731}$	10.36	4800 ± 2480	20700:	10^5:	10^5:	100::	5000 ± 1530	3100 ± 760	6500 ± 2500	2790 ± 690	2440 ± 580
[O II]	$\frac{\lambda3729^{\rm b}}{\lambda3726^{\rm b}}$	13.62	3940 ± 1590	...	...	...	80::	...	...	...	...	...
[Ar IV]	$\frac{\lambda4711}{\lambda4740}$	40.74	...	...	...	...	...	4070 ± 2740	4230 ± 690	6140 ± 3430	...	...
[Cl III]	$\frac{\lambda5538}{\lambda5518}$	23.81	...	...	...	...	...	4260:	3030:	5920 ± 2950	2530 ± 1610	...

Table 3.5: References for ORL atomic data.

Ion	Effective recombination coefficients	Case
H^{+}	Storey & Hummer (1995)	B
He^{+}	Porter et al. (2013)	B [a]
He^{+}	Smits (1996)	A, B [b]
He^{2+}	Storey & Hummer (1995)	B
C^{2+}	Davey et al. (2000)	A, B
N^{2+}	Escalante & Victor (1990)	A, B
N^{3+}	Pequignot et al. (1991)	A
O^{2+}	Storey (1994)	B
	Liu et al. (1995)	A

Table 3.6 represents the electron temperatures ($T_{\rm e}$) and densities ($N_{\rm e}$) derived from the C II, N II and O II ORLs for those PNe where adequate recombination lines were available. Using Eq. (3.15), the temperature (or density) is identified from its value at the minimum χ^2. The uncertainty was determined using the formal errors associated with the ORLs. It shows that the C II, N II and O II ORLs are emitted from ionized regions having temperatures much colder than the regions, from which [N II] and [O III] CELs originate.

In the following subsection we discuss the electron temperatures derived from He I, C II, N II and O II ORLs for those objects where there were sufficient adequate observations.

Electron temperature from He I ORLs

Apart from temperatures derived from the CEL [N II] ratios, Table 3.4 also presents helium temperatures derived from the flux ratio He I $\lambda\lambda$5876/4472, $\lambda\lambda$6678/4472, $\lambda\lambda$7281/5876 and $\lambda\lambda$7281/6678. The uncertainties were estimated based on the formal errors associated with the line fluxes. To derive the

Table 3.6: Electron temperatures and densities derived from ORLs.

Nebula	Ion	Lines	T_e (K)	N_e (cm^{-3})
IC 1297	C II	6151, 6462, 5060	3300 ± 310	2400 ± 220
Pe 1-1	C II	6151, 6462	2400 ± 180	7400 ± 540
NGC 6567	C II	6151, 6462	6800 ± 480	2500 ± 180
PB 6	N II	5932, 5952	2300 ± 190	5200 ± 430
Hb 4	N II	5680, 5932, 5940, 6482	5700 ± 680	6900 ± 830
M 3-15	N II	5667, 5680	2600 ± 270	2500 ± 260
M 1-25	N II	5667, 5680, 5686, 5711	4200 ± 490	3500 ± 410
M 2-42	N II	5667, 5680	3500 ± 300	2300 ± 200
NGC 6629	N II	4803, 5932	4100 ± 290	2200 ± 160
M 3-30	O II	4649, 4662, 4676	4000 ± 400	4700 ± 480
IC 1297	O II	4649, 4676	3600 ± 580	2800 ± 450
NGC 6578	O II	4649, 4662	7700 ± 760	10400 ± 1030
M 2-42	O II	4649, 4676 4609	2800 ± 310	11600 ± 1270
NGC 6567	O II	4649, 4676	5100 ± 1000	3100 ± 610
NGC 6629	O II	4649, 4676	3600 ± 290	2800 ± 230
Sa 3-107	O II	4907, 4891	5000 ± 400	2400 ± 192

electron temperature from the helium line ratios, we used the analytic formula given for the emissivities of He I lines by Benjamin et al. (1999) and new fitting parameters calculated by Zhang et al. (2005). The method by Benjamin et al. (1999) was valid for the temperature 5000–20,000 K. However, Zhang et al. (2005) combined the He I recombination model of Smits (1996) and the collisional excitation rates for the $2s^3S$ and $2s^1S$ meta-stable levels by Sawey & Berrington (1993), and provided a new electron temperature diagnostics based on the method developed by Benjamin et al. (1999), but the temperature range of $T_e < 5000$ K was also included. We notice that the He I temperatures are typically much lower than the forbidden-line temperature.

Electron temperature and density from C II ORLs

At typical nebular conditions, emissivities of carbon recombination lines vary weakly with electron temperature and density (Davey et al. 2000; Storey & Sochi 2013). This dependence can be used to determine T_e and N_e. Table 3.6 lists that the C II lines detected in IC 1297 and Pe 1-1. Both PNe have the multiplet V17.04 (λ6462; 6g–4f) and V16.04 (λ6151; 6f–4d). Additionally, C II λ5060 line (3p–2p) was measured in IC 1297. The λ6462 line is the strongest C II recombination line which was detected in these two PNe. The least-squares minimization method in IC 1297 yielded an electron temperature of 3300 K and an electron density of 2400 cm^{-3}. For Pe 1-1, we derived $T_e = 2400$ K and $N_e = 7400$ cm^{-3}. Similarly, we determined an electron temperature of 6800 K and an electron density of 2500 cm^{-3} from the λ6151 and λ6462 lines in NGC 6567. We used the Case A effective recombination for λ6462, and the Case B for λ6151 and λ5060 from the atomic data of Davey et al. (2000), which is valid from 500 to 20 000 K. The Case A effective recombination for λ6462 differs from its Case B value by only 2 per cent. We assumed that the contribution from the blended N II λ6150.75 (4p–3d) line is negligible.

Electron temperature and density from N II and O II ORLs

N II and O II ORLs are weakly temperature- and density-sensitive (McNabb et al. 2013). They are faint but fairly well detected in some PNe, with the flux errors of less than 10 per cent. The effective recombination coefficients of N II calculated by Escalante & Victor (1990) are in the range from 500 to 20 000 K, which allows us to identify any cold ionized regions. The effective recombination coefficients by Storey (1994) were used for the plasma diagnostics of the O II ORLs.

Table 3.6 lists the electron temperatures and densities derived from N II ORLs for six PNe. The well-detected λ5932 and λ5952 lines in PB 6 are likely to provide the most reliable temperature and density as these two lines can only be produced by recombination from the $3p\,^3P$–$3d\,^3D^\circ$ level of N^{2+} and the V28 multiplet. Using all lines from the similar multiplet reduces the effects of any errors caused by atomic data. The least-squares minimization technique for these lines yielded an electron temperature of 2300 K and an electron density of 5200 cm^{-3}. This temperature suggests the existence of a cold component within the nebular gas of PB 6. This nebula has indeed a highly filamentary structure and several knots inside and outside the main shell (*HST* image, ID 12600, P.I. Dufour; see Chapter 2). Similarly, we determined $T_e = 2600$ K and $N_e = 2500$ cm^{-3} from the well-detected λ5667 and λ5680 lines in M 3-15. Both lines are produced by recombination from the $3p\,^3D$–$3s\,^3P^\circ$ level of N^{2+} and the V28 multiplet. A linear least-squares fit to four N II ORLs from different multiplets yielded an electron temperature of 5700 K and an electron density of 6900 cm^{-3} for Hb 4. The λ5680 line from the V3 multiplet ($3p\,^3D$–$3s\,^3P^\circ$) is the strongest N II recombination line detected in Hb 4, whereas λ5940 (V28) and λ6482 (V8) are relatively very weak. For M 1-25, we measured $T_e = 4200$ K and $N_e = 3500$ cm^{-3} from $\lambda\lambda$5686,5711 lines produced by recombination from the $3p\,^3D$–$3s\,^3P^\circ$ level of N^{2+} and the V3 multiplet, and $\lambda\lambda$5667,5680 lines from the

V28 multiplet. The $\lambda\lambda$5667,5680 ORLs from the V28 multiplet are by a factor of ~ 5 stronger than those from the V3 multiplet ($\lambda\lambda$5686,5711) in the spectra of M 1-25. For M 2-42, we determined an electron temperature of 3500 K and an electron density of 2300 cm^{-3} using the well-detected λ5667 and λ5680 lines from the V3 multiplet. However, N II ORLs from different multiplets were used to derive $T_{\rm e} = 4100$ K and $N_{\rm e} = 2200$ cm^{-3} for NGC 6629.

Table 3.6 also lists the electron temperatures and densities deduced from O II ORLs for seven PNe. The recombination lines from the V1 multiplet (3p^{4}D$^\circ$–3s^{4}P), here λ4649, λ4662 and λ4676, are likely to provide the reliable temperature diagnostics (see e.g. Wesson et al. 2005; McNabb et al. 2013). For M 3-30, the least-squares minimization method for O II ORLs yielded an electron temperature of 4000 K and an electron density of 4700 cm^{-3}. For IC 1297, we derived $T_{\rm e} = 3600$ K and $N_{\rm e} = 2800$ cm^{-3} from the O II $\lambda\lambda$4649,4676 ORLs, which are in fair agreement with $T_{\rm e} = 3300$ K and $N_{\rm e} = 2400$ cm^{-3} deduced from the C II ORLs. For NGC 6578, we measured $T_{\rm e} = 7700$ K and $N_{\rm e} = 10400$ cm^{-3} from λ4649 abd λ4662 lines produced by recombination from the 3p^{4}D$^\circ$–3s^{4}P level of O^{2+} and the V1 multiplet. For M 2-42, the least-squares minimization method for O II ORLs yielded $T_{\rm e} = 2800$ K and $N_{\rm e} = 11600$ cm^{-3}. Using the O II $\lambda\lambda$4649,4676 ORLs from the V1 multiplet, we determined $T_{\rm e} = 5100$ K and $N_{\rm e} = 3100$ cm^{-3} for NGC 6567; and $T_{\rm e} = 3600$ K and $N_{\rm e} = 2800$ cm^{-3} for NGC 6629. For NGC 6567, the values derived from the O II ORLs are in decent agreement with $T_{\rm e} = 6800$ K and $N_{\rm e} = 2500$ cm^{-3} deduced from the C II ORLs. For NGC 6629, the values derived from the O II ORLs are in decent agreement with $T_{\rm e} = 4100$ K and $N_{\rm e} = 2200$ cm^{-3} deduced from the N II ORLs. For Sa 3-107, we derived $T_{\rm e} = 5000$ K and $N_{\rm e} = 2400$ cm^{-3} from the O II $\lambda\lambda$4907,4891 ORLs (V28 multiplet).

Using the ORLs from the same multiplet reduces any effects of deviation from local thermodynamic equilibrium (LTE) at low densities. Tsamis et al. (2003b) found that the relative intensities of O II V1 multiplet components deviate from LTE predictions for those nebulae having electron densities lower than than 1000 cm^{-3}. For example, the V1 ORLs from the dense PNe such as IC 4191 ($N_{\rm e} = 10700\,{\rm cm}^{-3}$) and NGC 5315 ($N_{\rm e} = 14100\,{\rm cm}^{-3}$) are in good agreement with theory, but they show abnormal values in NGC 3132 having a low mean electron density of $N_{\rm e} = 600\,{\rm cm}^{-3}$ (Tsamis et al. 2003a). It is the same in H II regions (Tsamis et al. 2003b). This effect can be reduced by using all the lines from the V1 multiplet (e.g. Wesson et al. 2005).

3.3.4 Comparison with previous results

Table 3.7 lists the physical conditions of our sample derived in this study alongside the values obtained previously. We can compare densities and temperature derived from CELs and ORLs with those given in the literature. We also present $T_{\rm e}$([N II]) and $T_{\rm e}$([O III]) before and after correcting for the effects of recombination excitation, when we can estimate them using Eqs. (3.4) and (3.17). We also compare $T_{\rm e}$(He I) derived from He I lines with the values determined previously. We have chose the maximum value of $T_{\rm e}$(He I) derived from He I $\lambda\lambda$5876/4472 and $\lambda\lambda$6678/4472; or $\lambda\lambda$7281/5876 and $\lambda\lambda$7281/6678 if the He I λ4472 line was not measured correctly. We also present $T_{\rm e}$ and $N_{\rm e}$ weighted by heavy elements from C II, N II and O II lines for some PNe.

Table 3.7: Comparison of extinctions, electron temperatures and densities derived here from ORLs and CELs with those found in previous studies. In the column T_e[N II], values before and after '/' are temperatures derived before and after correcting for the effects of recombination excitation, respectively. References are as follows: A87, Aller & Keyes (1987); C96, Costa et al. (1996); C09, Chiappini et al. (2009); D97, De Marco et al. (1997); G07, Girard et al. (2007); G09, García-Rojas et al. (2009); G12, García-Rojas et al. (2012); H96, Henry et al. (1996); H04, Henry et al. (2004) and Milingo et al. (2002); K86, Kaler (1986); K91, Kaler et al. (1991); K94, Kingsburgh & Barlow (1994); K03, Kwitter et al. (2003); M96, McKenna et al. (1996); M13, McNabb et al. (2013); P01, Peña et al. (2001) and Peña et al. (1998); P11, Pottasch et al. (2011); R97, Ratag et al. (1997); S98, Stasińska et al. (1998); T77, Torres-Peimbert & Peimbert (1977); W04, Wang et al. (2004); Z05, Zhang et al. (2005): D13, this chapter.

Nebula	Ref.	c(Hβ)	T_e(BJ) ORL	T_e(He I) ORL	T_e(C II) ORL	T_e(N II) ORL	T_e(O II) ORL	T_e[N II] CEL	T_e[O II] CEL	T_e[S II] CEL	T_e[O III] CEL	T_e[S III] CEL	N_e(C II) ORL	N_e(N II) ORL	N_e(O II) ORL	N_e[S II] CEL	N_e[O II] CEL	N_e[Ar IV] CEL	N_e[Cl III] CEL
PB 6	D13	0.60		5160		2300		11480/9400			14060			5200		2000		1730	2420
	G09	0.50		13250				12575			15525					2100	2125	1700	
	G07	0.57						11300			15800					2890			
	H04							9800	7600		14600	16300				2200			
	P01	0.40						11300	13000		14800					2700			
	H96	0.48									15560					2800			
	M96							10410			12220								
	K91	0.54						11000			14600					2100		2500	
	K86							11920			14370								
	T77	0.55						11900			14000					2000			
M 3-30	D13	0.96		2340			4000	9020/7510			10670/10030				4700	350		300	170
	G07	0.52						10000			10000					340			
	P01	0.80						11567			10333					528	1012	2004	
Hb 4	D13	1.86		4150		5700		10310/9920			9900/9840	7560		6900		6700	3470	6760	7170
	G12	1.81	7560	7660				8600	12950	10000	9950	9350				5760	4900	7400	7360
	G07	1.76						10400			9600					6710			
	P01	2.30						11700			9617					4720	1683	5878	
	C96	1.77									9250					5026			
	A87							10500								5600			
IC 1297	D13	0.23		4540	3300		3600	9710/8450			10540/10480	8860	2400		2800	2000		2140	2080
	G07	0.18						10100			10100					2800			
	Z05		10000	5100															
	H04	0.07						8900	8100		9900	11000				2400			
	KA91																		
	K86							8340			10820								

Table 3.7: (continued)

Nebula	Ref.	$c(\mathrm{H}\beta)$ ORL	T_e(BJ) ORL	T_e(He I) ORL	T_e(C II) ORL	T_e(N II) ORL	T_e(O II) ORL	T_e[N II] CEL	T_e[O II] CEL	T_e[S II] CEL	T_e[O III] CEL	T_e[S III] CEL	N_e(C II) ORL	N_e(N II) ORL	N_e(O II) ORL	N_e[S II] CEL	N_e[O II] CEL	N_e[Ar IV] CEL	N_e[Cl III] CEL
Th 2-A	D13	1.11		3640				10150/8110			12280/11800					1400		630	
	H04	0.93						11700	5900		11600					1200			
	K94	1.07						12100			12500					1220		8240	
Pe 1-1	D13	1.96		9300	2400			10820/10430			10320	7750	7400			11100	6270		
	G12	1.80	10300	9000				10100	9640	6700	9980	9620				14000	13160	40950	31360
	G07	2.16						11600			9700					18310			
M 1-32	D13	1.40		2270				8630/8220			9360	6534				6400	3440		11490
	G12	1.30	8000	8530				8350	9700	6300	9430	8270				8350	5370		14800
	G07	1.30						8600			10900					9250			
	P01	1.90						9720			9990					6857	2370		
M 3-15	D13	2.27				2600		7780/7160			8310	6920		2500		5200	3940	5970	7490
	G12	2.09	9800	7320				9500		8100	8350	8630				5660	7470	7680	10250
	C09							10644			8431					5400			
	G07	2.08						11100			11000					5560			
	H04	1.85						10400	10800	9000	8000	10500				3700			
	P01	2.30						11140			8743						3903		
	S98							9623			8251					9450			
	R97	2.12						9400			8400					10600			
	A87							11200								2500			
M 1-25	D13	1.60		2410		4200		8020			7940	6570:		3500		4800	3940		
	G12	1.41	7750	5830				7720	7300	5750	7800	7900				7740	6650		15100
	C09							8672			8058					4850			
	G07	1.46						8100			7900					8000			
	H04	1.34						8200	7900	9100	8400	9300				4300			
	P01	1.00						8340			7957					12267	4187		
	S98							7175			7948					17200			
Hen 2-142	D13	1.55		1750				8780								20700			
	G07	2.11						7500								20000			
Hen 3-1333	D13	1.06						6670								10^5:			
	D97	0.99						8800									$10^{4.8}$:		
Hen 2-113	D13	1.31						8160				7140:				10^5:			
	D97	1.44						8400									$10^{4.8}$:		
K 2-16	D13	0.56						9560								100::	80::		
	P01	0.40						11700								514	104		

Table 3.7: (continued)

Nebula	Ref.	$c(\mathrm{H}\beta)$ ORL	T_e(BJ) ORL	T_e(He I) ORL	T_e(C II) ORL	T_e(N II) ORL	T_e(O II) ORL	T_e[N II] CEL	T_e[O II] CEL	T_e[S II] CEL	T_e[O III] CEL	T_e[S III] CEL	N_e(C II) ORL	N_e(N II) ORL	N_e(O II) ORL	N_e[S II] CEL	N_e[O II] CEL	N_e[Ar IV] CEL	N_e[Cl III] CEL
NGC 6578	D13	1.53		5080			7700	9920			8250	6520:			10400	5000		4070	4260:
	W04															3470		4070	2140
	H04	1.39						10000	9000		7800	9300				2400			
	P01	1.3						14200			7900					2300	890	3320	
M 2-42	D13	0.99				3500	2800	10280			8780			2300	11600	3100		4230	3030:
	W07	1.06	14000	5650				9350	11860		8470					3240		4170	2880
	W04					15850	399									3550			2630
NGC 6567	D13	0.78		9260	6800		5100	11370			11510	9200:	2500		3100	6500		6140	5920
	W07	0.9	14000	6260				10016	14360		10580					7080	8510	9120	7760
	H04							12600	11800	16300	11000	14500				6700			
	W04					19950	631									6030	8320	7940	10970
	Z05	0.67	12000	7060							11400								
	K03	0.7						14000	11800	16300	11000	14500				6700			
	P01	0.6						9350			9490					4460	5540	4730	
NGC 6629	D13	0.98		5590		4100	3600	8720			8850	7500:		2200	2800	2790			2530
	P11	0.9									8700	8700				1600	2400		1400
	H04							10300	6500		8500	9200				1100			
	P01	0.6									8380					3660	1120		

3.4 Ionic and elemental abundances

3.4.1 Ionic abundances from CELs

We determined abundances for ionic species of N, O, Ne, S, Ar and Cl from CELs. To deduce ionic abundances, we solve the statistical equilibrium equations for each ion using the EQUIB code, giving level population and line sensitivities for specified $T_{\rm e}$ and $N_{\rm e}$. The accurate determination depends on the physical conditions, namely $T_{\rm e}$ and $N_{\rm e}$. Once the level population are solved, the ionic abundances, $\mathrm{X}^{i+}/\mathrm{H}^{+}$, can be derived from the intrinsic intensities of CELs as follows:

$$\frac{N(\mathrm{X}^{i+})}{N(\mathrm{H}^{+})}=\frac{I(\lambda_{ij})}{I(\mathrm{H}\beta)}\frac{\lambda_{ij}(\mathrm{\AA})}{4861}\frac{\alpha_{\rm eff}(\mathrm{H}\beta)}{A_{ij}}\frac{N_{\rm e}}{n_i}, \tag{3.16}$$

where $I(\lambda_{ij})$ is the dereddened flux of the emission line λ_{ij} emitted by ion X^{i+} following the transition from the upper level i to the lower level j, $I(\mathrm{H}\beta)$ the dereddened flux of Hβ, $\alpha_{\rm eff}(\mathrm{H}\beta)$ the effective recombination coefficient of Hβ, A_{ij} the Einstein spontaneous transition probability of the transition, n_i the fractional population of the upper level i, and $N_{\rm e}$ is the electron density.

The derived abundances are presented in Table 3.9. The atomic data references used for the calculations are listed in Table 3.3. For the CEL abundance analysis of each object, we adopted the density and temperature based on the results from our CEL plasma diagnostics in Section 3.3 and those found in previous studies (see Table 3.7), as listed in Table 3.8. Following Kingsburgh & Barlow (1994), we used $T_{\rm e}$[N II] for singly ionized species and $T_{\rm e}$[O III] for ions of higher excitation ions in the abundance calculations. For the CEL abundance analysis, we adopted $T_{\rm e}$[N II] from our plasma diagnosis and previous studies, whereas $T_{\rm e}$[O III] were used instead for all ionic species other than those singly ionized species in PB 6, M 3-30, IC 1297 and Th 2-A. However, electron temperatures derived from the [N II] $\lambda\lambda$6548+6584/λ5755 line ratio is unreliable due to contamination of the [N II] λ5755 auroral lines by recombination contribution. This could overestimate temperatures in ways that result in inaccurate abundances. The electron temperature $T_{\rm e}$[N II] corrected for the recombination excitation could be used, but its reliability depends on ORL N^{2+} and $T_{\rm e}$(He I). High uncertainties of ORLs result in inaccurate estimation of the recombination excitation.

The forbidden lines of [O III] $\lambda\lambda$4959,5007 were used to derived O^{2+}/H^{+} ionic ratios. For O^{+}/H^{+} ionic abundances, we adopted the observed flux intensities of [O II] λ3727 doublet from the literature (see Remarks in Table 3.9). However, [O II] flux intensities are usually less reliable due to the recombination contribution. We did not use the [O II] $\lambda\lambda$7320,7330 lines for the O^{+}/H^{+} ratio, since the abundances derived from them are usually higher than those from λ3727 doublet. This may be attributed to errors in the atomic data (see e.g. Kisielius et al. 2009). However, this could be due to the recombination excitation and/or the fact that they are biased towards higher density regions ($N_{\rm cr} = 3.3\text{-}4.9 \times 10^{6}\,{\rm cm}^{-3}$). We can estimate the recombination contribution to the [O II] $\lambda\lambda$7320,7330 lines using the formula given by Liu et al. (2000):

$$\frac{I_{\rm R}(\lambda\lambda 7320,7330)}{I({\rm H}\beta)} = 9.36\,t^{0.44}\left(\frac{{\rm O}^{2+}}{{\rm H}^{+}}\right)_{\rm ORLs}, \tag{3.17}$$

where $t \equiv T_{\rm e}({\rm He\,I})/10^{4}$ is the ORL electron temperature t in 10^{4} K and O^{2+}/H^{+} is derived from the O II ORLs (see Table 3.10).

Table 3.9 also lists the O^{+}/H^{+} ratios derived from the [O II] $\lambda\lambda$7320,7330 lines before and after correcting for recombination contributions. However, the O^{+}/H^{+} abundance ratio derived from the [O II] λ3727 doublet are more reliable than the [O II] $\lambda\lambda$7320,7330 lines. But, they may give only upper limits due to recombination contributions.

The N^{+}/H^{+} abundance ratio was derived from the [N II] λ6548 and λ6584 lines. We did not use the weak auroral line [N II] λ5755 due to its high uncertainty and the recombination contribution from N^{2+}. For the most PNe, we determined the S^{+}/H^{+} and S^{2+}/H^{+} abundance ratios from [S II] $\lambda\lambda$6716,6731 doublet and [S III] λ6312 line, respectively. Table 3.9 also lists the S^+/H^+ ratios derived from the [S II] $\lambda\lambda$4068,4076 lines. But, we did not consider them for S^+/H^+, as they are generally weak and affected by recombination processes and density effects. For the most PNe, we were able to determine the Ar^{2+}/H^+ abundance ratio from the [Ar III] λ4711 and λ4740 lines and the Ar^{3+}/H^+ abundance ratio from the [Ar IV] $\lambda\lambda$4711,4740 doublet. For some PNe with [WO] central stars, we also derived the Ar^{4+}/H^+ abundance ratio from the [Ar V] λ6435 and λ7005 lines. Furthermore, we derived the Cl^{2+}/H^+ abundance ratio from the [Cl III] $\lambda\lambda$5518,5538 doublet in the most PNe. We determined the Ne^{2+}/H^+ abundance ratio from [Ne III] $\lambda\lambda$3869,3967 line fluxes adopted from the literature.

For Sa 3-107, where O^{2+} but not O^+ is observed, the O^+/H^+ ionic ratio was estimated by using a correlation derived from O^{2+}/O^+ plotted against S^{2+}/S^+, as shown in Fig. 3.9. A linear fit to the 12 PNe plotted in Fig. 3.9 yields

$$\frac{S^{2+}}{S^+} = (6.507 \pm 2.227) + (0.460 \pm 0.166)\left(\frac{O^{2+}}{O^+}\right), \tag{3.18}$$

which has a linear correlation coefficient of 0.66. This equation can be used to estimated O^+ from S^{2+}/S^+ when only O^{2+} is available. Previously, Kingsburgh & Barlow (1994) obtained $S^{2+}/S^+ = 4.677 + (O^{2+}/O^+)^{0.433}$ using a least-squares fit to the 22 PNe, which was then used to estimate S^{2+} when only S^+ was observed, and vice versa.

Fig. 3.10 shows the spatial distribution of ionic abundance ratio He^+/H^+, H^{2+}/H^+, N^+/H^+, O^{2+}/H^+ and S^+/H^+ for the four PNe surrounding [WO] central stars, namely PB 6, M 3-30, IC 1297 and Th 2-A (for all PNe see Appendix D). The spatially-resolved ionic abundance maps were produced by assuming T_e and N_e given in Table 3.8. We notice that both O^{2+}/H^+ and He^{2+}/H^+ are very high in inner regions near to the central stars, while He^+/H^+, N^+/H^+ and S^+/H^+ are mostly higher at the edges of the nebula. It obviously demonstrates the ionic stratification layers, which have been produced in the inner

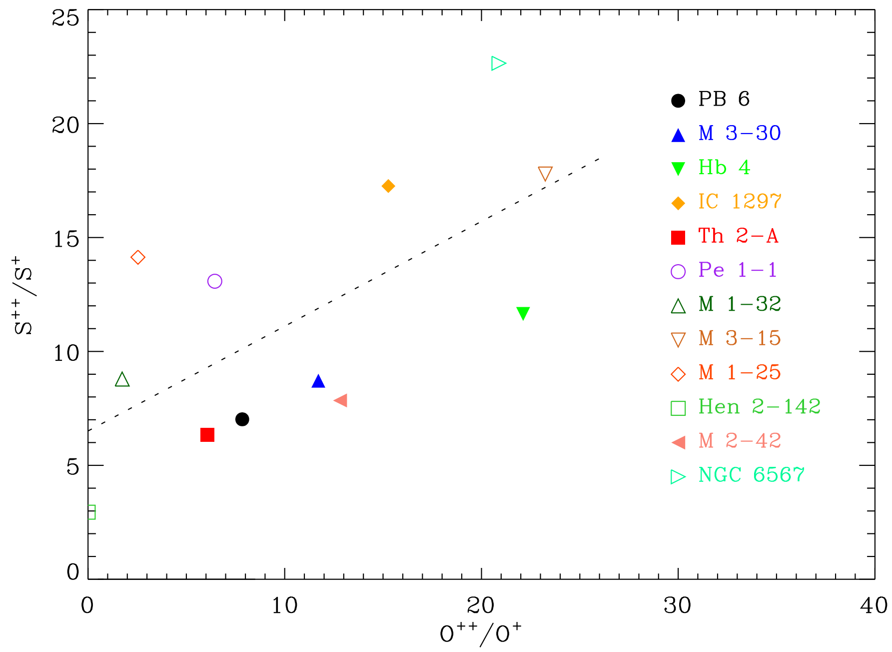

Figure 3.9: S^{2+}/S^{+} versus O^{2+}/O^{+}. The dotted line is a linear fit to S^{2+}/S^{+} as a function of O^{2+}/O^{+}, discussed in the text.

high-excitation and the outer low excitation zones.

Table 3.8: Adopted electron densities and temperature for the CEL and ORL abundance analysis.

Nebula	$N_e\,(\mathrm{cm}^{-3})$ CEL	$T_e\,(\mathrm{K})$ CEL(Low)	$T_e\,(\mathrm{K})$ CEL(High)	$T_e\,(\mathrm{K})$ ORL
PB 6	2000	11500	14000	5100
M 3-30	350	9000	10000	2500
Hb 4	6700	10000	10000	4200
IC 1297	2000	9700	10000	4500
Th 2-A	1400	10000	12000	3600
Pe 1-1	11100	10000	10000	9300
M 1-32	6400	8600	8600	2300
M 3-15	5200	8000	8000	7300
M 1-25	4800	8000	8000	2400
Hen 2-142	20700	8500	8500	1800
Hen 3-1333	100000	8800	8800	8800
Hen 2-113	100000	8200	8200	8200
K 2-16	100	10000	10000	10000
NGC 6578	5000	10000	10000	5100
M 2-42	3100	10300	10300	5600
NGC 6567	6500	11400	11400	9260
NGC 6629	2800	8700	8700	5600
Sa 3-107	2400	10000	10000	4500

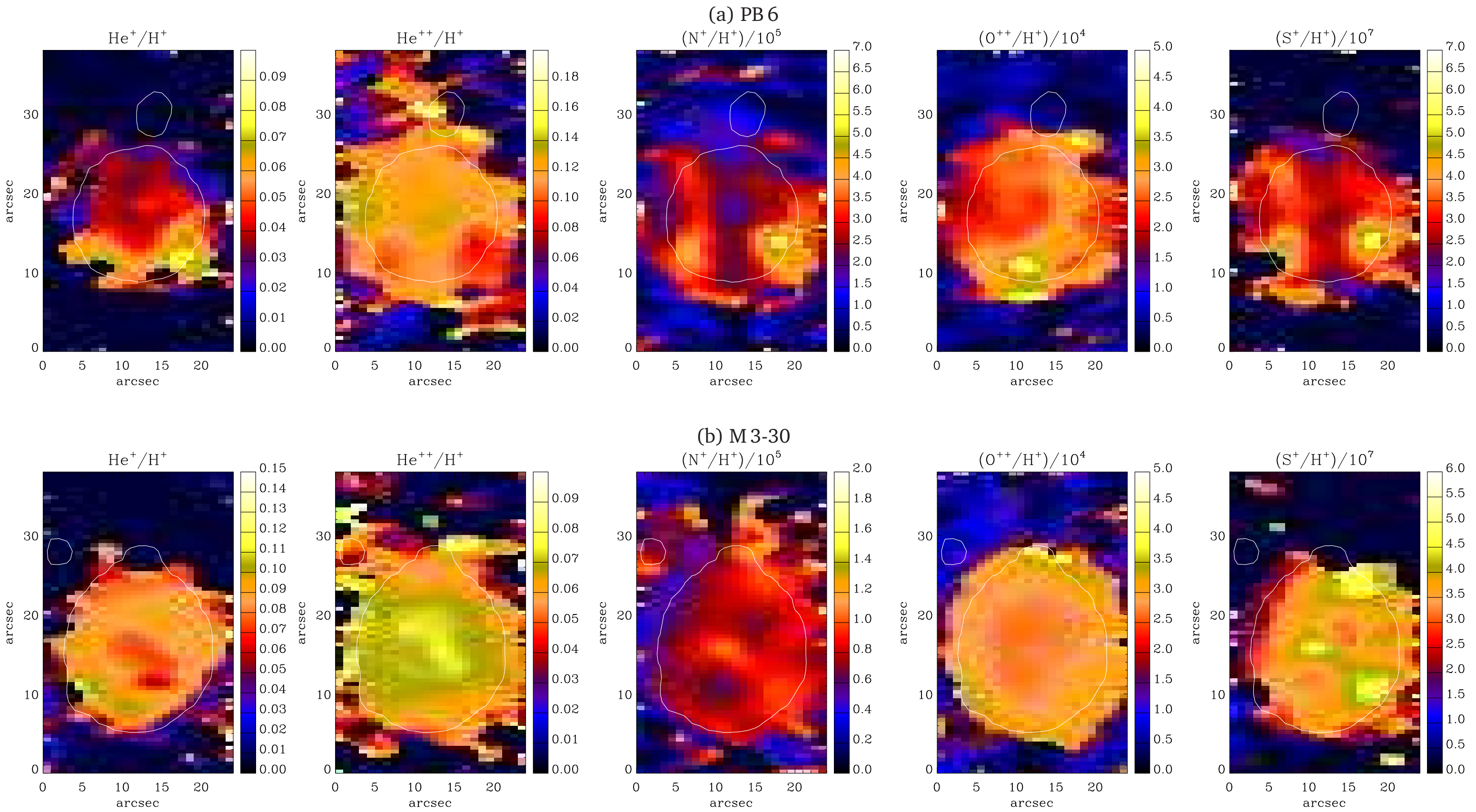

Figure 3.10: Spatial distribution maps of ionic abundance maps. From top to bottom: PB 6, M 3-30, IC 1297 and Th 2-A. From left to right, spatial distribution maps of He^{+}/H^{+}, H^{2+}/H^{+}, N^{+}/H^{+} ($\times10^{-5}$), O^{2+}/H^{+} ($\times10^{-4}$) and S^{+}/H^{+} ($\times10^{-7}$). North is up and east is toward the left-hand side. The white contour lines show the distribution of the narrow-band emission of Hα in arbitrary unit obtained from the SHS.

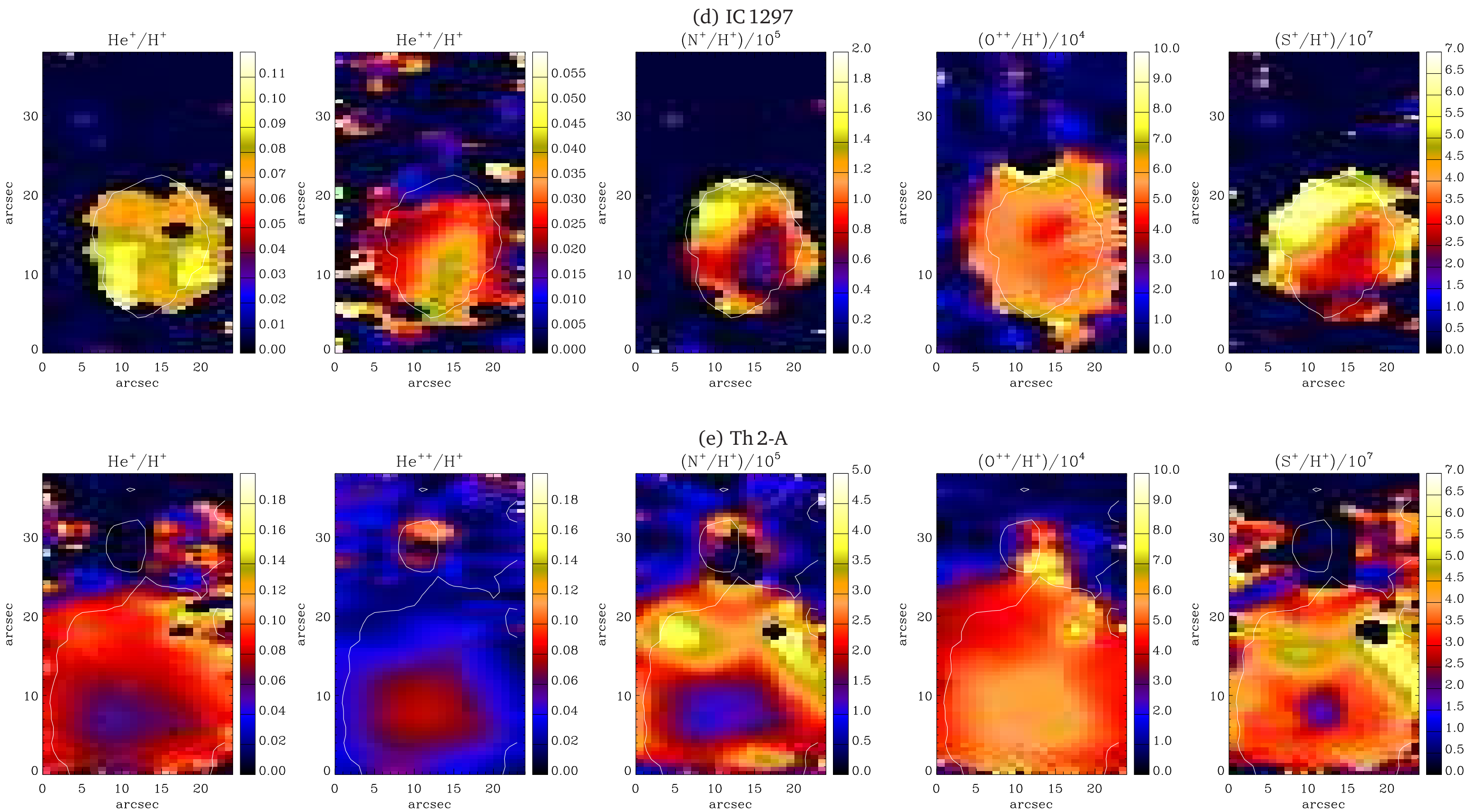

Figure 3.10: (continued)

Table 3.9: Ionic and elemental abundances for helium relative to hydrogen, derived from ORLs, and those for heavy elements, derived from CELs.

Ion	λ_0 (Å)	PB 6	M 3-30	Hb 4			IC 1297	Th 2-A	Pe 1-1
				(shell)	(N-knot)	(S-knot)			
He^{+}/H^{+}	4471.50	0.045	0.064	0.091	...	...	0.077	0.056	0.106
	5875.66	0.044	0.069	0.100	0.069	0.060	0.081	0.063	0.107
	6678.16	0.037	0.065	0.092	0.043	0.032	0.077	0.057	0.103
	Average	0.043	0.067	0.096	0.063	0.053	0.079	0.060	0.106
He^{++}/H^{+}	4685.68	0.105	0.055	0.010	...	...	0.028	0.041	...
	icf(He)	1.000	1.000	1.000	1.000	1.000	1.000	1.000	1.000
He/H		0.148	0.122	0.107	0.063	0.053	0.107	0.101	0.106
N^{+}/H^{+}	6548.10	2.676(−5)	7.388(−6)	1.882(−5)	3.802(−5)	3.519(−5)	8.264(−6)	2.260(−5)	2.141(−5)
	6583.50	2.694(−5)	7.624(−6)	1.922(−5)	4.008(−5)	3.956(−5)	8.455(−6)	2.302(−5)	2.240(−5)
	Average	2.685(−5)	7.506(−6)	1.902(−5)	3.905(−5)	3.737(−5)	8.359(−6)	2.281(−5)	2.190(−5)
	icf(N)	20.142	18.929	24.762	29.150	25.613	19.827	9.991	7.439
N/H		5.408(−4)	1.421(−4)	4.710(−4)	1.138(−3)	9.572(−4)	1.657(−4)	2.278(−4)	1.629(−4)

[a] Fluxes adopted from the literature as follows: PB 6, Kaler et al. (1991); K 2-16, Peña et al. (2001); IC 1297 and NGC 6629, Milingo et al. (2002); Th 2-A, Kingsburgh & Barlow (1994); Hb 4, Pe 1-1, M 1-32, M 3-15 and M 1-25, García-Rojas et al. (2012); M 3-30 and Hen 2-142, Girard et al. (2007); Hen 3-1333 and Hen 2-113, De Marco et al. (1997). NGC 6578 and NGC 6567, Kwitter et al. (2003); M 2-42, Wang & Liu (2007).

[b] Fluxes adopted from the literature as follows: M 3-30, Peña et al. (2001); Th 2-A, Milingo et al. (2002).

[c] Corrected for recombination contribution to the auroral line [O II] $\lambda\lambda$7320,7330.

Notes: [ ] values in square brackets are not adopted for mean values. ( ) values in parentheses are exponents of base 10.

Table 3.9: (continued)

Ion	λ_0 (Å)	PB 6	M 3-30	Hb 4 (shell)	Hb 4 (N-knot)	Hb 4 (S-knot)	IC 1297	Th 2-A	Pe 1-1
O^{+}/H^{+}	3727.43 [*]	1.902(−5)	1.583(−5)	1.843(−5)	1.170(−5)	1.072(−5)	2.983(−5)	4.893(−5)	5.428(−5)
	7324.83 [a]	[2.217(−5)]	...	[3.115(−5)]	...	...	[4.217(−5)]	...	[1.079(−4)]
	Adopted	1.902(−5)	1.583(−5)	1.843(−5)	1.170(−5)	1.072(−5)	2.983(−5)	4.893(−5)	5.428(−5)
O^{++}/H^{+}	4958.91	1.427(−4)	1.849(−4)	4.076(−4)	3.278(−4)	2.512(−4)	4.648(−4)	2.968(−4)	3.474(−4)
	5006.84	1.560(−4)	1.859(−4)	4.073(−4)	3.311(−4)	2.766(−4)	4.453(−4)	2.980(−4)	3.516(−4)
	Average	1.494(−4)	1.854(−4)	4.075(−4)	3.295(−4)	2.639(−4)	4.551(−4)	2.974(−4)	3.495(−4)
	icf(O)	2.275	1.489	1.071	1.000	1.000	1.220	1.411	1.000
O/H		3.832(−4)	2.996(−4)	4.563(−4)	3.412(−4)	2.746(−4)	5.915(−4)	4.888(−4)	4.038(−4)
Ne^{2+}/H^{+}	3868.75 [a]	3.809(−5)	6.279(−5)	1.202(−4)	...	...	1.344(−4)	1.109(−4)	9.544(−5)
	3967.46 [a]	4.509(−5)	...	1.236(−4)	...	...	2.054(−4)	1.047(−4)	8.879(−5)
	Average	4.159(−5)	6.279(−5)	1.219(−4)	...	...	1.699(−4)	1.078(−4)	9.211(−5)
	icf(Ne)	2.565	1.616	1.120	...	...	1.300	1.644	1.155
Ne/H		1.067(−4)	1.015(−4)	1.365(−4)	...	...	2.209(−4)	1.772(−4)	1.064(−4)
S^{+}/H^{+}	6716.44	2.939(−7)	3.494(−7)	7.474(−7)	9.908(−7)	9.864(−7)	3.504(−7)	3.754(−7)	3.957(−7)
	6730.82	2.900(−7)	3.507(−7)	6.781(−7)	9.816(−7)	9.869(−7)	3.488(−7)	3.787(−7)	3.945(−7)
	4072.48 [a]	[5.130(−7)]	...	[5.082(−7)]	...	...	[6.740(−7)]	[1.984(−6)]	[6.680(−7)]
	Average	2.919(−7)	3.500(−7)	7.127(−7)	9.862(−7)	9.867(−7)	3.496(−7)	3.770(−7)	3.951(−7)
S^{++}/H^{+}	6312.10	2.051(−6)	3.051(−6)	5.329(−6)	...	...	5.160(−6)	2.386(−6)	3.507(−6)
	9068.60 [a]	...	...	1.127(−5)	...	...	6.923(−6)	4.602(−6) [b]	6.846(−6)
	Average	2.051(−6)	3.051(−6)	8.302(−6)	...	...	6.037(−6)	3.494(−6)	5.176(−6)
	icf(S)	1.918	1.881	2.049	2.159	2.071	1.909	1.545	1.417
S/H		4.494(−6)	6.397(−6)	1.847(−5)	2.129(−6)	2.043(−6)	1.219e(−5)	5.980(−6)	7.895(−6)

Table 3.9: (continued)

Ion	λ_0 (Å)	PB 6	M 3-30	Hb 4			IC 1297	Th 2-A	Pe 1-1
				(shell)	(N-knot)	(S-knot)			
Ar^{2+}/H^{+}	7135.80 [a]	5.158(−7)	1.267(−6) [b]	1.973(−6)	...	...	1.324(−6)	1.416(−6) [b]	
	7751.43 [a]	...	...	1.913(−6)	...	...	1.124(−6)	1.149(−6) [b]	
	Average	5.158(−7)	1.267(−6)	1.943(−6)	...	...	1.224(−6)	1.283(−6)	1.674(−6)
Ar^{3+}/H^{+}	4711.37	1.029(−6)	5.184(−7)	7.031(−7)	...	...	5.604(−7)	4.335(−7)	2.115(−8)
	4740.17	1.004(−6)	5.151(−7)	7.006(−7)	...	...	5.697(−7)	3.981(−7)	4.493(−8)
	Average	1.016(−6)	5.167(−7)	7.018(−7)	...	...	5.650(−7)	4.158(−7)	3.304(−8)
Ar^{4+}/H^{+}	4624.92	7.244(−7)	...	...	...	...	...	...	...
	6434.73	3.540(−7)	...	8.374(−9)	...	...	3.793(−8)	...	...
	7005.40	5.581(−7)	...	8.455(−9)	...	...	...	...	...
	Average	5.455(−7)	...	8.414(−9)	...	...	3.793(−8)	...	...
	icf(Ar)	1.052	1.056	1.042	...	...	1.053	1.111	1.155
Ar/H		2.186(−6)	1.883(−6)	2.765(−6)	...	...	1.924(−6)	1.887(−6)	1.972(−6)
Cl^{++}/H^{+}	5517.66	3.794(−8)	7.836(−8)	1.062(−7)	...	...	8.652(−8)	...	5.390(−8)
	5537.60	4.060(−8)	7.458(−8)	1.088(−7)	...	...	8.771(−8)	...	7.439(−8)
	Average	3.927(−8)	7.647(−8)	1.075(−7)	...	...	8.712(−8)	...	6.415(−8)
	icf(Cl)	2.191	2.097	2.224	...	...	2.019	...	1.525
Cl/H		8.605(−8)	1.603(−7)	2.391(−7)	...	...	1.759(−7)	...	9.783(−8)

Table 3.9: (continued)

Ion	λ_0 (Å)	M 1-32	M 3-15	M 1-25	Hen 2-142	Hen 3-1333	Hen 2-113	K 2-16
He^{+}/H^{+}	4471.50	0.097	0.119	0.101	0.018	...	...	...
	5875.66	0.104	0.111	0.103	...	...	...	...
	6678.16	0.099	0.095	0.103	0.019	...	...	...
	Average	0.102	0.107	0.103	0.018	...	...	...
He^{++}/H^{+}	4685.68	...	...	...	...	...	...	...
	icf(He)	1.000	1.000	1.000	1.340	...	...	...
He/H		0.102	0.109	0.103	0.025	...	...	...
N^{+}/H^{+}	6548.10	1.395(−4)	1.738(−5)	7.234(−5)	9.624(−5)	1.697(−4)	1.004(−4)	3.334(−5)
	6583.50	1.415(−4)	1.743(−5)	7.371(−5)	9.697(−5)	2.587(−4)	1.100(−4)	4.973(−5)
	Average	1.405(−4)	1.741(−5)	7.302(−5	9.660(−5)	2.142(−4)	1.052(−4)	4.153(−5)
	icf(N)	2.738	24.196	3.538	1.009	1.000	1.000	1.412
N/H		3.846(−4)	4.212(−4)	2.584(−4)	9.744(−5)	2.142(−4)	1.052(−4)	5.863(−5)
O^{+}/H^{+}	3727.43 *	1.600(−4)	3.366(−5)	1.502(−4)	3.504(−4)	8.493(−4)	3.973(−4)	1.083(−4
	7324.83 [a]	[3.661(−4)]	[9.532(−5)]	[2.582(−4)]	[6.708(−5)]	[3.290(−4)]	[4.912(−4)]	...
	Adopted	1.600(−4)	3.366(−5)	1.502(−4)	3.504(−4)	8.493(−4)	3.973(−4)	1.083(−4
O^{++}/H^{+}	4958.91	2.778(−4)	7.703(−4)	3.788(−4)	2.691(−6)	...	...	4.106(−5)
	5006.84	2.782(−4)	7.912(−4)	3.837(−4)	3.397(−6)	...	...	4.817(−5)
	Average	2.780(−4)	7.807(−4)	3.812(−4)	3.044(−6)	...	...	4.461(−5)
	icf(O)	1.000	1.000	1.000	1.000	1.000	1.000	1.000
O/H		4.380(−4)	8.144(−4)	5.314(−4)	3.535(−4)	8.493(−4)	3.973(−4)	1.530(−4)

Table 3.9: (continued)

Ion	λ_0 (Å)	M 1-32	M 3-15	M 1-25	Hen 2-142	Hen 3-1333	Hen 2-113	K 2-16
Ne^{2+}/H^+	3868.75 [a]	2.566(−5)	1.873(−4)	3.556(−5)	...	...	...	...
	3967.46 [a]	2.880(−5)	1.102(−4)	2.420(−5)	...	...	...	...
	Average	2.723(−5)	1.488(−4)	2.988(−5)	...	...	...	...
	icf(Ne)	1.575	1.043	1.394	...	...	...	...
Ne/H		4.291(−5)	1.552(−4)	4.166(−5)	...	...	...	...
S^+/H^+	6716.44	2.140(−6)	5.271(−7)	1.043(−6)	9.358(−7)	1.865(−5)	3.939(−6)	2.307(−6)
	6730.82	2.141(−6)	5.285(−7)	1.045(−6)	9.351(−7)	2.602(−5)	5.731(−6)	2.258(−6)
	4072.48 [a]	[3.036(−6)]	[7.463(−7)]	[1.946(−6)]	...	...	...	...
	Average	2.140(−6)	5.278(−7)	1.044(−6)	9.354(−7)	2.234(−5)	4.834(−6)	2.282(−6)
S^{++}/H^+	6312.10	1.122(−5)	7.293(−6)	1.021(−5)	2.755(−6)	...	2.374(−6)	...
	9068.60 [a]	2.632(−5)	1.148(−5)	1.917(−5)	...	7.917(−7)	3.580(−6)	...
	Average	1.877(−5)	9.387(−6)	1.469(−5)	...	7.917(−7)	2.977(−6)	...
	icf(S)	1.103	2.033	1.166	1.000	1.000	1.000	1.008
S/H		2.308(−5)	2.016(−5)	1.835(−5)	3.690(−6)	2.313(−5)	7.812(−6)	2.302(−6)
Ar^{2+}/H^+	7135.80 [a]	3.829(−6)	2.357(−6)	3.433(−6)	...	...	...	...
	7751.43 [a]	3.632(−6)	2.172(−6)	3.144(−6)	...	...	...	...
	Average	3.730(−6)	2.265(−6)	3.288(−6)	...	...	...	...
Ar^{3+}/H^+	4711.37	...	5.719(−7)	...	...	...	...	...
	4740.17	3.987(−8)	6.068(−7)	...	...	...	...	...
	Average	3.987(−8)	5.894(−7)	...	...	...	...	...

Table 3.9: (continued)

Ion	λ_0 (Å)	M 1-32	M 3-15	M 1-25	Hen 2-142	Hen 3-1333	Hen 2-113	K 2-16
Ar^{4+}/H^+	4624.92	...	...	...	...	...	...	...
	6434.73	...	...	...	...	...	...	...
	7005.40	...	...	...	...	...	...	...
	Average	...	...	...	...	...	...	...
	icf(Ar)	1.575	1.043	1.394	...	...	...	...
Ar/H		5.940(−6)	2.977(−6)	4.584(−6)	...	...	...	...
Cl^{2+}/H^+	5517.66	1.560(−7)	1.303(−7)	1.330(−7)	1.290(−7)	...	...	...
	5537.60	2.022(−7)	1.536(−7)	1.965(−7)	1.327(−7)	...	...	...
	Average	1.791(−7)	1.420(−7)	1.647(−7)	1.308(−7)	...	...	...
	icf(Cl)	1.229	2.148	1.249	1.340	...	...	...
Cl/H		2.202(−7)	3.049(−7)	2.057(−7)	1.753(−7)	...	...	...

Table 3.9: (continued)

Ion	λ_0 (Å)	NGC 6578	M 2-42	NGC 6567	NGC 6629	Sa 3-107
He^{+}	4471.50	0.106	0.109	0.101	0.093	0.110
	5875.66	0.111	0.097	0.104	0.095	0.117
	6678.16	0.107	0.091	0.099	0.093	0.111
	Average	0.109	0.098	0.102	0.094	0.114
He^{2+}	4685.68	0.0005	0.000	0.001	0.0005	0.002
	icf(He)	1.000	1.000	1.000	1.000	1.000
He/H		0.110	0.098	0.103	0.095	0.116
N^{+}	6548.10	2.199(−6)	6.247(−6)	1.908(−6)	2.049(−6)	1.806(−6)
	6583.50	2.305(−6)	6.223(−6)	1.915(−6)	2.143(−6)	1.991(−6)
	Average	2.252(−6)	6.235(−6)	1.911(−6	2.096(−6)	1.899(−6)
	icf(N)	23.807	13.809	22.125	11.335	32.233
N/H		5.361(−5)	8.610(−5)	4.228(−5)	2.376(−5)	6.120(−5)
O^{+}	3727.43 [a]	1.154(−5)	1.599(−5)	1.005(−5)	3.654(−5)	3.436(−6) [d]
	7324.83 [a]	[1.411(−5)]	[2.281(−5)]	[1.385(−5)]	[3.325(−5)]	...
	7324.83 [a.c]	...	[1.827(−5)]	[1.270(−5)]	[1.680(−5)]	...
	Adopted	1.154(−5)	1.599(−5)	1.005(−5)	3.654(−5)	3.436(−6)
O^{2+}	4958.91	2.620(−4)	2.006(−4)	2.103(−4)	3.771(−4)	1.060(−4)
	5006.84	2.629(−4)	2.083(−4)	2.125(−4)	3.761(−4)	1.067(−4)
	Average	2.624(−4)	2.045(−4)	2.114(−4)	3.766(−4)	1.063(−4)
	icf(O)	1.003	1.002	1.004	1.002	1.009
O/H		2.747(−4)	2.208(−4)	2.224(−4)	4.141(−4)	1.108(−4)

[d] O^{+}/H^{+} ionic abundance ratio estimated from Eq. (3.18).

Table 3.9: (continued)

Ion	λ_0 (Å)	NGC 6578	M 2-42	NGC 6567	NGC 6629	Sa 3-107
Ne^{2+}	3868.75 [a]	7.481(−5)	4.758(−5)	4.313(−5)	8.697(−5)	...
	3967.46 [a]	1.431(−4)	2.952(−5)	5.430(−5)	1.987(−4)	...
	Average	1.090(−4)	3.855(−5)	4.871(−5)	1.428(−4)	...
	icf(Ne)	1.047	1.080	1.052	1.100	...
Ne/H		1.140(−4)	4.164(−5)	5.126(−5)	1.571(−4)	...
S^{+}	6716.44	8.000(−8)	2.875(−7)	5.735(−8)	4.855(−8)	4.080(−8)
	6730.82	8.000(−8)	2.877(−7)	5.753(−8)	4.850(−8)	4.066(−8)
	4072.48 [a]	[2.712(−7)]	[4.907(−7)]	[1.208(−7)]	...	...
	Average	8.000(−8)	2.876(−7)	5.744(−8)	4.852(−8)	4.073(−8)
S^{2+}	6312.10	1.665(−6)	2.263(−6)	9.951(−7)	2.254(−6)	8.440(−7)
	9068.60 [a]	5.711(−6)	...	1.599(−6)	3.447(−6)	...
	Average	3.688(−6)	2.263(−6)	1.297(−6)	2.851(−6)	8.440(−7)
	icf(S)	2.023	1.705	1.976	1.605	2.230
S/H		7.623(−6)	4.348(−6)	2.676(−6)	4.652(−6)	1.973(−6)

Table 3.9: (continued)

Ion	λ_0 (Å)	NGC 6578	M 2-42	NGC 6567	NGC 6629	Sa 3-107
Ar^{2+}	7135.80 [a]	1.422(−6)	8.056(−7)	3.744(−7)	1.529(−6)	...
	7751.43 [a]	1.288(−6)	...	3.410(−7)	...	...
	Average	1.355(−6)	8.056(−7)	3.577(−7)	1.529(−6)	...
Ar^{3+}	4711.37	3.336(−7)	2.633(−7)	1.904(−7)	...	...
	4740.17	3.118(−7)	2.883(−7)	1.865(−7)	1.075(−7)	...
	Average	3.227(−7)	2.758(−7)	1.885(−7)	1.075(−7)	...
	icf(Ar)	1.044	1.078	1.047	1.097	...
Ar/H		1.751(−6)	1.166(−6)	5.720(−7)	1.795(−6)	...
Cl^{2+}	5517.66	5.933(−8)	6.893(−8)	3.892(−8)	7.166(−8)	...
	5537.60	5.557(−8)	6.840(−8)	3.740(−8)	6.927(−8)	...
	Average	5.745(−8)	6.866(−8)	3.816(−8)	7.046(−8)	...
	icf(Cl)	2.067	1.921	2.064	1.632	...
Cl/H		1.187(−7)	1.319(−7)	7.876(−8)	1.150(−7)	...

3.4.2 Ionic abundances from ORLs

We determined abundances for ionic species of He, C, N and O from ORLs for our sample where possible. In our calculation, we adopted the ORL electron temperature and the CEL electron density listed in Table 3.8. The atomic data sets used for the effective recombination coefficients of ORLs are given in Table 3.5. Using the effective recombination coefficients, we determine ionic abundances from the measured intensities of optical recombination lines (ORLs) as follows:

$$\frac{\mathrm{X}^{i+}}{\mathrm{H}^{+}} = \frac{I_{\lambda}}{I_{\mathrm{H}\beta}} \frac{\lambda(\mathrm{\AA})}{4861} \frac{\alpha_{\mathrm{eff}}(\mathrm{H}\beta)}{\alpha_{\mathrm{eff}}(\lambda)}, \tag{3.19}$$

where $I(\lambda)$ is the intrinsic line flux of the emission line λ emitted by ion X^{i+}, $I(\mathrm{H}\beta)$ is the intrinsic line flux of Hβ, $\alpha_{\mathrm{eff}}(\mathrm{H}\beta)$ the effective recombination coefficient of Hβ, and $\alpha_{\mathrm{eff}}(\lambda)$ the effective recombination coefficient for the emission line λ.

$\mathrm{He}^{+}/\mathrm{H}^{+}$ and $\mathrm{He}^{2+}/\mathrm{H}^{+}$

The total and ionic helium abundances derived from the He I and He II ORLs are given in Table 3.9. For the He I lines, we have used case B recombination coefficients of Porter et al. (2012, 2013) for the temperature $T_{\mathrm{e}}(\mathrm{He\,I}) > 5\,000$, and Smits (1996) for $T_{\mathrm{e}}(\mathrm{He\,I}) < 5\,000$. To obtain the $\mathrm{He}^{+}/\mathrm{H}^{+}$ ionic abundance, the ionic abundances derived from the λ4472, λ5876 and λ6678 ORLs were averaged with weights of 1:3:1, roughly the intrinsic intensity ratios of the three lines. The $\mathrm{He}^{2+}/\mathrm{H}^{+}$ ionic abundance was derived from the He II λ4686 line, using the case B recombination coefficient from Storey & Hummer (1995). The total He abundance relative to H is often obtained by simply taking the sum of $\mathrm{He}^{+}/\mathrm{H}^{+}$ and $\mathrm{He}^{2+}/\mathrm{H}^{+}$ ionic abundances. However, we used the ionization correction factor given by Zhang & Liu (2003) for the low excitation PN Hen 2-142:

$$\frac{\mathrm{He}}{\mathrm{H}} = \left(\frac{\mathrm{He}^{+}}{\mathrm{H}^{+}}\right)\left(1+\frac{\mathrm{S}^{+}}{\mathrm{S}^{2+}}\right)_{\mathrm{CELs}}. \tag{3.20}$$

The neutral helium has an ionization potential of 24.5 eV, so singly ionized sulfur S^{+} having the value of 23.3 eV can be used to correct the total helium abundances.

As seen in Table 3.9, we notice that the He^{+}/H^{+} abundances derived from the triplet λ5876 are usually higher than those determined from other He I lines. The value deduced from the triplet λ4472 are usually lower. This discrepancy can be explained by the fact that the intrinsic intensity of the He I λ5876 line is about three times other lines, and there are some errors in recording weak lines, namely the He I $\lambda\lambda$4472,6678 ORLs. It may be also due to other systematic errors, such as the reddening correction, the flux calibration and the collisional excitation contribution.

C^{2+}/H^{+}

The C^{2+}/H^{+} ionic abundances derived for different PNe are presented in Table 3.10. The C^{2+}/H^{+} ratios were derived from some high-excitation C II ORLs, including the 4f–6g 6462 line for PB 6, M 3-30, Hb 4, IC 1297, Th 2-A, Pe 1-1, M 1-32, M 3-15, M 1-25, NGC 6578, M 2-42, NGC 6567, NGC 6629 and Sa 3-107; the 4d–6f 6151 line for IC 1297, Pe 1-1, M 3-15 and NGC 6567; and the 2p–3p 5060 line for IC 1297 using the case B recombination coefficients of Davey et al. (2000). Temperature $T_{\rm e}$ from He I ORLs and density $N_{\rm e}$ from CELs were adopted in the calculation.

Following Kingsburgh & Barlow (1994), the total carbon are derived, correcting for the unseen stages of ionization using:

$$\frac{\rm C}{\rm H} = \left(\frac{\rm C^{2+}}{\rm H^{+}}\right)\left(\frac{\rm O}{\rm O^{2+}}\right)_{\rm CELs} \tag{3.21}$$

Total C/H abundances derived from ORLs are given in Table 3.10. However, carbon ionic ratios derived from ORLs are generally not equal to those derived from CELs (Tsamis et al. 2003a, 2004). Therefore, oxygen ionic abundances derived from CELs may not be suitable choices for the ionization correction scheme of carbon ORLs.

N^{2+}/H^{+} and N^{3+}/H^{+}

We have detected a number of N II multiplets in most PNe. They were used to calculate ORL N^{2+}/H^{+} ionic ratios, as presented in Table 3.10. We used effective recombination coefficient from Escalante & Victor (1990), assuming case A for singlets and case B for triplets. The multiplet V3 lines are more reliable due to less sensitive to optical depth effect, and have been detected in M 3-30, Hb 4, IC 1297, Pe 1-1, M 1-25, M 2-42, NGC 6567, NGC 6629 and Sa 3-107. Other multiplets are extremely case-sensitive, and also quick weak, with large flux uncertainties, so they are less reliable. We detected the extremely case-senstive multiplet V28 in many PNe, which sometime has a departure from the case B approximation for the triplets, so its calculated N^{2+}/H^{+} ionic ratio is usually unreliable.

For nitrogen, when only N^{2+} was measurable, the unobserved ionization stage are corrected for by assuming $N/N^{2+} = O/O^{2+}$, so

$$\frac{\mathrm{N}}{\mathrm{H}} = \left(\frac{\mathrm{N}^{2+}}{\mathrm{H}^{+}}\right)\left(\frac{\mathrm{O}}{\mathrm{O}^{2+}}\right)_{\mathrm{CELs}} \tag{3.22}$$

When both N^{2+} and N^{3+} were measured, the total elemental abundance was derived assuming $N/N^{+} = O/O^{+}$, with N/H then given by

$$\frac{\mathrm{N}}{\mathrm{H}} = \left(\frac{\mathrm{N}^{2+}}{\mathrm{H}^{+}} + \frac{\mathrm{N}^{3+}}{\mathrm{H}^{+}}\right)\left[1 - \left(\frac{\mathrm{O}^{+}}{\mathrm{O}}\right)_{\mathrm{CELs}}\right]^{-1} \tag{3.23}$$

In the case of M 3-30, IC 1297, NGC 6567 and Sa 2-107, the λ4641 (V2) N III recombination line was detected, so N^{3+} abundance is available, and Eq. (3.23) is applied. The effective radiative and dielectric recombination coefficients of Pequignot et al. (1991) were used to calculate ORL N^{3+}/H^{+} ionic ratios presented in Table 3.10. However, the λ4641 N III recombination line is usually affected by continuum fluorescence (Ferland 1992). Therefore, the ionic ratio derived from this line can largely contain fluorescence contribution, and it is unreliable.

Total N/H abundances derived from ORLs thus are presented in Table 3.10.

O^{2+}/H^{+}

Table 3.10 lists the ORL O^{2+}/H^{+} ionic ratios calculated from the O II lines of mostly multiplet V1 and some multiplet V28. The abundances from the quartet-quartet transition of multiplet V1 is less case-sensitive, and it has only 4 per cent difference between case A and B. However, multiplet V28 is extremely case-sensitive, and their case B effective recombination coefficient is 20 times the case A values. Therefore, the ORL O^{2+}/H^{+} ionic ratio derived from the case-sensitive multiplet V28 is higher than those from multiplet V1. The faint O II lines of multiplet V28 with high flux uncertainties makes the derived ionic abundances quickly unreliable. Furthermore, a departure from case B towards case A can also overestimate the calculated O^{2+}/H^{+} ionic ratios.

The ionization correction factor for O is $(\mathrm{He}/\mathrm{He}^{+})^{2/3}$ (Kingsburgh & Barlow 1994). However, only O^{2+} is measured from ORLs. Following Wesson et al. (2005), we assume that O^{+}/O^{2+} derived from CELs is applicable to ORLs, so instead the total elemental abundance is derived using

$$\frac{\mathrm{O}}{\mathrm{H}} = \left(\frac{\mathrm{O}^{2+}}{\mathrm{H}^{+}}\right)\left(\frac{\mathrm{He}}{\mathrm{He}^{+}}\right)^{2/3}\left[1+\left(\frac{\mathrm{O}^{+}}{\mathrm{O}^{2+}}\right)_{\mathrm{CELs}}\right] \tag{3.24}$$

Total O/H abundances derived from ORLs thus are given in Table 3.10.

3.4.3 Elemental abundances

Total elemental abundances listed in Tables 3.9 and 3.10 for the studied PN sample are derived using the ionization correction factor (*icf*) scheme of Kingsburgh & Barlow (1994), except *icf*(Cl) from Liu et al. (2000) and *icf*(ORLs) from Wang & Liu (2007).

Table 3.10: Ionic and elemental abundances for carbon, nitrogen and oxygen derived from ORLs.

Ion	λ_0 (Å)	Mult	X^{i+}/H^+
		PB 6	
C^{2+}	6461.95	V17.04	3.724(−4)
	icf(C)		2.565
C/H			9.554(−4)
N^{2+}	5931.78	V28	3.244(−3)
	5940.24	V28	9.342(−3)
	5452.08	V29	7.137(−3)
	Average		6.574(−3)
	ADF(N^{2+})		31.183
	icf(N)		2.565
N/H			1.686(−2)
		M 3-30	
C^{2+}	6461.95	V17.04	1.421(−3)
	icf(C)		1.616
C/H			2.297(−3)
N^{2+}	5666.63	V3	7.568(−4)
	ADF(N^{2+})		8.608
N^{3+}	4640.64	V2	8.527(−4)
	icf(N)		1.056
N/H			1.699(−3)
O^{2+}	4649.13	V1	3.481(−3)
	4661.63	V1	4.009(−3)
	4676.23	V1	2.676(−3)
	4906.83	V28	4.751(−3)
	Average		3.729(−3)
	ADF(O^{2+})		20.115
	icf(O)		1.616
O/H			6.027(−3)

The total O/H abundance ratio is calculated from the O^+/H^+ and O^{2+}/H^+ ratios, correcting for the unseen O^{3+}/H^+ using,

$$\frac{\mathrm{O}}{\mathrm{H}} = \left(\frac{\mathrm{O}^+}{\mathrm{H}^+} + \frac{\mathrm{O}^{2+}}{\mathrm{H}^+}\right)\left(\frac{\mathrm{He}}{\mathrm{He}^+}\right)^{2/3}_{\mathrm{ORLs}} \tag{3.25}$$

where the He^+ and He abundances are derived from ORLs in Section 3.4.2.

The total N/H abundance ratio is calculated from the N^+/H^+ ratio, correct-

Table 3.10: (continued)

		Hb 4	
C^{2+}	6461.95	V17.04	3.392(−4)
	icf(C)		1.120
C/H			3.798(−4)
N^{2+}	5679.56	V3	4.409(−4)
	5931.78	V28	5.404(−4)
	5940.24	V28	8.072(−4)
	6482.05	V8	8.566(−4)
	Average		6.613(−4)
	ADF(N^{2+})		1.572
	icf(N)		1.120
N/H			7.405(−4)
O^{2+}	4649.13	V1	1.373(−3)
	6641.05	V4	2.997(−3)
	4609.44	V92a	6.906(−4)
	Average		1.687(−3)
	ADF(O^{2+})		4.140
	icf(O)		1.120
O/H			1.889(−3)

ing for the unseen N^{2+}/H^+ and N^{3+}/H^+ using,

$$\frac{N}{H} = \left(\frac{N^+}{H^+}\right)\left(\frac{O}{O^+}\right) \tag{3.26}$$

Similarly, the unseen Ne^+/H^+ is corrected for, using

$$\frac{Ne}{H} = \left(\frac{Ne^{2+}}{H^+}\right)\left(\frac{O}{O^{2+}}\right) \tag{3.27}$$

For sulfur, we have the S^+/H^+ and S^{2+}/H^+ ratios. The total S/H abundance is derived using

$$\frac{S}{H} = \left(\frac{S^+}{H^+} + \frac{S^{2+}}{H^+}\right)\left[1 - \left(1 - \frac{O^+}{O}\right)^3\right]^{-1/3} \tag{3.28}$$

The total Ar/H abundance ratio is derived using the following equation, assuming $Ar^+/Ar = N^+/N$:

$$\frac{Ar}{H} = \left(\frac{Ar^{2+}}{H^+} + \frac{Ar^{3+}}{H^+} + \frac{Ar^{4+}}{H^+}\right)\left(1 - \frac{N^+}{N}\right)^{-1} \tag{3.29}$$

Table 3.10: (continued)

	IC 1297		
C^{2+}	6151.43	V16.04	5.902(−4)
	6461.95	V17.04	4.049(−4)
	5060.00		2.925(−4)
	Average		4.292(−4)
	icf(C)		1.300
C/H			5.579(−4)
N^{2+}	5679.56	V3	2.057(−4)
	5931.78	V28	7.821(−4)
	4552.53	V58a	1.410(−3)
	Average		7.993(−4)
	ADF(N^{2+})		6.268
N^{3+}	4640.64	V2	4.630(−4)
	icf(N)		1.053
N/H			1.329(−3)
O^{2+}	4649.13	V1	1.425(−3)
	4676.23	V1	6.732(−4)
	4491.23	V86a	2.341(−3)
	4609.44	V92a	7.369(−4)
	Average		1.294(−3)
	ADF(O^{2+})		2.844
	icf(O)		1.300
O/H			1.682(−3)
	Th 2-A		
C^{2+}	6461.95	V17.04	1.001(−3)
	icf(C)		1.644
C/H			1.646(−3)
N^{2+}	4788.13	V20	4.046(−3)
	ADF(N^{2+})		29.189
	icf(N)		1.644
N/H			6.651(−3)
O^{2+}	4906.83	V28	8.247(−3)
Ion	λ_0 (Å)	Mult	X^{i+}/H^+
	ADF(O^{2+})		27.730
	icf(O)		1.644
O/H			1.356(−2)

Table 3.10: (continued)

	Pe 1-1		
C^{2+}	6151.43	V16.04	7.055(−4)
	6461.95	V17.04	9.345(−4)
	Average		8.200(−4)
	icf(C)		1.155
C/H			9.473(−4)
N^{2+}	5679.56	V3	1.637(−4)
	5931.78	V28	7.265(−4)
	5941.65	V28	1.056(−4)
	5495.67	V29	1.664(−3)
	Average		6.650(−4)
	ADF(N^{2+})		4.715
	icf(N)		1.155
N/H			7.682(−4)
O^{2+}	4906.83	V28	3.842(−3)
	4649.13	V1	5.605(−4)
	Average		2.201(−3)
	ADF(O^{2+})		6.298
	icf(O)		1.155
O/H			2.543(−3)
	M 1-32		
C^{2+}	6461.95	V17.04	1.269(−3)
	icf(C)		1.575
C/H			2.000(−3)
N^{2+}	5710.77	V28	2.417(−3)
	6170.17	V58a	5.146(−3)
	Average		3.781(−3)
	ADF(N^{2+})		15.488
	icf(N)		1.575
N/H			5.957(−3)

We used the following equation given by Liu et al. (2000) according to the ionization potential of Cl and S ion stages:

$$\frac{\mathrm{Cl}}{\mathrm{H}} = \left(\frac{\mathrm{Cl}^{2+}}{\mathrm{H}^{+}}\right)\left(\frac{\mathrm{S}}{\mathrm{S}^{2+}}\right) \tag{3.30}$$

Table 3.11 compares total elemental abundances by number with results determined previously, for He, C, N, O, Ne, S, Ar and Cl for the 17 PNe analyzed in this work, given in logarithmic units relative to hydrogen where $\log N(\mathrm{H}) = 12$.

Table 3.10: (continued)

	M 3-15		
C^{2+}	6151.43	V16.04	8.157(−4)
	6461.95	V17.04	6.047(−4)
	Average		7.102(−4)
	icf(C)		1.043
C/H			7.408(−4)
N^{2+}	5666.63	V28	3.124(−4)
	5679.56	V28	3.814(−4)
	Average		3.469(−4)
	ADF(N^{2+})		0.859
	icf(N)		1.043
N/H			3.619(−4)
O^{2+}	4650.84	V1	9.522(−3)
	ADF(O^{2+})		12.197
	icf(O)		1.043
O/H			9.932(−3)

The element abundances of He and C are derived from the ORLs analysis, and N, O, Ne, S, Ar, and Cl from the empirical method based on CEL analysis. The results obtained in this work are generally in decent agreement with previous determinations. Large discrepancies with previous studies from some elements are likely attributed to old atomic data and different physical conditions assumed for the calculations.

3.4.4 ORL/CEL discrepancy correlations

It has been shown that the ORL/CEL abundance discrepancy is closely correlated with the dichotomy of temperature derived from forbidden lines and from recombination lines, while they are also correlated with various nebular physical quantities such as surface brightness, diameter, metallicity, density and excitation class (Liu et al. 2001; Tsamis et al. 2004; Liu et al. 2004a; Zhang et al. 2004; Wesson et al. 2005; Wang & Liu 2007; Tsamis et al. 2008; García-Rojas et al. 2013). Here, we explore these correlations for our sample.

Table 3.10: (continued)

	M 1-25		
C^{2+}	6461.95	V17.04	4.436(−4)
	icf(C)		1.394
C/H			6.183(−4)
N^{2+}	5686.21	V3	6.757(−4)
	5710.77	V3	1.202(−3)
	5666.63	V28	9.995(−4)
	5679.56	V28	7.984(−4)
	Average		9.188(−4)
	ADF(N^{2+})		4.958
	icf(N)		1.394
N/H			1.281(−3)
O^{2+}	4649.13	V1	9.726(−4)
	4906.83	V28	2.548(−3)
	4491.23	V86a	1.386(−3)
	Average		1.636(−3)
	ADF(O^{2+})		4.292
	icf(O)		1.394
O/H			2.280(−3)
	NGC 6578		
C^{2+}	6461.95	V17.04	1.026(−3)
	icf(C)		1.047
C/H			1.074(−3)
O^{2+}	4649.13	V1	1.395(−3)
	4661.63	V1	1.852(−3)
	4890.86	V28	4.115(−3)
	Average		2.454(−3)
	ADF(O^{2+})		9.351
	icf(O)		1.047
Ion	λ_0 (Å)	Mult	X^{i+}/H^+
O/H			2.568(−3)

Fig. 3.11 (top) shows the logarithmic abundance discrepancy factor for O^{2+}, defined as

$$\log \mathrm{ADF}(O^{2+}) \equiv \log(O^{2+}/H^+)_{\mathrm{ORL}} - \log(O^{2+}/H^+)_{\mathrm{CEL}}, \tag{3.31}$$

plotted against the difference $\Delta T_{[\mathrm{N\,II}]}$ between the [N II] forbidden-line and the

Table 3.10: (continued)

	M 2-42		
C^{2+}	6461.95	V17.04	4.969(−4)
	icf(C)		1.080
C/H			5.367(−4)
N^{2+}	5666.63	V3	3.291(−4)
	5679.56	V3	3.223(−4)
	Average		3.257(−4)
	ADF(N^{2+})		4.086
	icf(N)		1.080
N/H			3.518(−4)
O^{2+}	4649.13	V1	7.909(−4)
	4676.23	V1	8.194(−4)
	4906.83	V28	1.541(−3)
	4609.44	V92a	8.718(−4)
	Average		1.006(−3)
	ADF(O^{2+})		4.920
	icf(O)		1.080
O/H			1.086(−3)
	NGC 6567		
C^{2+}	6151.43	V16.04	1.135(−3)
	6461.95	V17.04	1.172(−3)
	Average		1.154(−3)
	icf(C)		1.052
C/H			1.214(−3)
N^{2+}	5679.56	V3	5.947(−5)
	4803.29	V20	9.188(−4)
	5927.81	V28	5.442(−4)
	Average		3.040(−4)
	ADF(N^{2+})		7.566
N^{3+}	4640.64	V2	9.978(−5)
	icf(N)		1.047
N/H			4.229(−4)
O^{2+}	4649.13	V1	8.847(−4)
	4661.63	V1	2.478(−4)
	4676.23	V1	2.931(−4)
	4906.83	V28	3.956(−4)
	4609.44	V92a	4.697(−4)
	Average		4.582(−4)
	ADF(O^{2+})		2.167
	icf(O)		1.052
O/H			4.821(−4)

Table 3.10: (continued)

	NGC 6629		
C^{2+}	6461.95	V17.04	5.003(−4)
	icf(C)		1.100
C/H			5.502(−4)
N^{2+}	5679.56	V3	2.647(−4)
	5710.77	V3	2.453(−4)
	4803.29	V20	9.170(−4)
	5931.78	V28	2.150(−4)
	Average		4.105(−4)
	ADF(N^{2+})		19.000
	icf(N)		1.100
N/H			4.514(−4)
O^{2+}	4649.13	V1	6.504(−4)
	4676.23	V1	5.115(−4)
	4906.83	V28	3.083(−3)
	4890.86	V28	4.164(−3)
	4491.23	V86a	1.452(−3)
	Average		1.972(−3)
	ADF(O^{2+})		5.237
	icf(O)		1.100
O/H			2.169(−3)
	Sa 3-107		
C^{2+}	6461.95	V17.04	5.629(−4)
	icf(C)		1.042
C/H			5.864(−4)
N^{2+}	5710.77	V3	2.677(−3)
	5931.78	V28	1.307(−3)
	Average		1.992(−3)
	ADF(N^{2+})		33.912
N^{3+}	4640.64	V2	1.151(−4)
	icf(N)		1.032
N/H			2.175(−3)
O^{2+}	4906.83	V28	3.004(−3)
	4890.86	V28	7.344(−3)
	Average		5.174(−3)
	ADF(O^{2+})		48.657
	icf(O)		1.042
O/H			5.389(−3)

Table 3.11: Comparison of elemental abundances derived here from ORLs and CELs with those found in previous studies, on a logarithmic scale where H = 12. References: A86, Aller et al. (1986); A87, Aller & Keyes (1987); C96, Costa et al. (1996); C09, Chiappini et al. (2009); D97, De Marco et al. (1997); G07, Girard et al. (2007); G09, García-Rojas et al. (2009); G13, García-Rojas et al. (2013); H90, Henry (1990); H96, Henry et al. (1996); H04, Henry et al. (2004) and Milingo et al. (2002); K91, Kaler et al. (1991); KA91, Koeppen et al. (1991); K94, Kingsburgh & Barlow (1994); P01, Peña et al. (2001) and Peña et al. (1998); P11, Pottasch et al. (2011); R97, Ratag et al. (1997); S98, Stasińska et al. (1998); T77, Torres-Peimbert & Peimbert (1977); W88, Webster (1988); W07, Wang & Liu (2007): D13, this chapter.

Nebula	Ref.	He	C	N	O	Ne	S	Ar	Cl
		ORL	ORL	CEL	CEL	CEL	CEL	CEL	CEL
PB 6	D13	11.17	8.98	8.73	8.58	8.03	6.65	6.34	4.93
	G09	11.26	9.51	8.70	8.55	8.04	6.50	6.20	5.51
	G07	11.16		8.94	8.79	8.23	6.82	6.12	
	H04	11.23		8.88	8.83	8.06	6.31	6.77	5.26
	P01	11.24		8.74	8.59	8.02			
	H96	11.30		8.43	8.80	8.05			
	K91	11.23	8.85	8.67	8.59	8.02	6.64	5.97	
	T77	11.26		8.94	8.72	8.08			
M 3-30	D13	11.09	9.36	8.15	8.48	8.01	6.81	6.27	5.20
	G07	11.09		7.02	8.48		6.91	6.53	
	P01	11.23		8.29	8.45	7.87			
Hb 4	D13	11.03	8.58	8.67	8.66	8.14	7.27	6.44	5.38
	G13	11.06	9.07	8.55	8.79	8.17	7.01	6.73	5.37
	G07	11.02		8.60	8.72	8.16	7.08	6.49	5.17
	P01	11.14		8.23	8.73	8.33			
	C96	11.13		8.10	8.89	8.28	7.30	6.73	
	KA91	11.01		8.37	8.92		7.16	6.62	
	H90	11.11		8.46	8.77	8.03			
	A87	11.10		8.34	8.68	8.10	6.89	6.26	
IC 1297	D13	11.03	8.75	8.22	8.77	8.34	7.09	6.28	5.25
	G07	11.05		8.37	8.77	8.10	7.10	6.27	5.37
	H04	11.11		8.35	8.86	8.24	6.86	6.42	5.29
	KA91	11.05		8.42	8.89		7.02	6.28	
	A86	11.05		8.46	8.77	8.14	7.07	6.23	

Table 3.11: (continued)

Nebula	Ref.	He ORL	C ORL	N CEL	O CEL	Ne CEL	S CEL	Ar CEL	Cl CEL
Th 2-A	D13	11.00	9.22	8.36	8.69	8.25	6.78	6.28	
	H04	11.11		8.48	8.79	8.29	6.64	6.51	4.87
	K94	10.96		8.27	8.67	8.17	6.54	5.93	
Pe 1-1	D13	11.03	8.98	8.21	8.61	8.03	6.90	6.29	4.99
	G13	11.02	9.13	8.06	8.67	8.03	6.81	6.43	5.14
	G07	10.99		8.15	8.62	8.02	6.62	6.34	4.91
	KA91	10.95		8.10	8.75		6.84	6.28	5.89
M 1-32	D13	11.01	9.30	8.59	8.64	7.63	7.36	6.77	5.34
	G13	11.10	9.75	8.44	8.74	7.69	7.17	6.99	5.47
	G07	11.07		8.35	8.66	7.58	7.34	6.89	4.93
	P01	11.10		8.37	8.34	8.91			
M 3-15	D13	11.04	8.87	8.62	8.91	8.19	7.32	6.47	5.48
	G13	11.03	8.85	8.33	8.81	8.02	7.21	6.49	5.30
	C09	11.12		8.55	8.81		7.25	6.61	6.83
	G07	10.99		8.01	8.36	7.68	6.72	6.14	4.77
	H04	11.11		8.44	8.88	8.18	6.92	6.50	5.40
	P01	11.15		8.48	8.74	7.84			
	S98	11.05		8.32	8.89	8.36			
	R97	11.03		8.14	8.74	7.86	6.86	6.53	
	H90	11.01		6.72	8.51	7.62			
	A87	11.03		8.08	8.41	7.48	6.70	6.50	
M 1-25	D13	11.01	8.79	8.41	8.73	7.62	7.26	6.66	5.31
	G13	11.09	8.96	8.40	8.87	7.71	7.22	6.92	5.50
	C09	11.17		8.45	8.68	7.49	7.17	6.77	6.37
	G07	11.09		8.41	8.75	7.47	7.26	6.66	5.31
	H04	11.18		8.34	8.70	7.55	6.96	6.52	5.30
	P01	11.13		8.60	8.70	7.23			
	S98	11.10		8.25	9.09				
	R97	11.10		8.82	9.08	8.41	7.47	6.92	5.99
	KA91	11.07		8.32	8.99		7.33	6.67	5.48
	W88	11.11		8.19	8.94				

Table 3.11: (continued)

Nebula	Ref.	He ORL	C ORL	N CEL	O CEL	Ne CEL	S CEL	Ar CEL	Cl CEL
Hen 2-142	D13	10.40		7.99	8.55		6.57		5.24
	G07	10.67		8.22	8.95		6.90	5.40	5.12
Hen 3-1333	D13			8.33	8.93		7.36		
	D97			7.92	8.68		7.00		
Hen 2-113	D13			8.02	8.60		6.89		
	D97			7.82	8.68		6.59		
K 2-16	D13			7.77	8.18		6.36		
	P01			7.58	7.90				
NGC 6578	D13	11.04	9.03	7.73	8.44	8.06	6.88	6.24	5.07
	H04	11.08		8.36	8.87	8.35	6.91	6.50	5.27
	P01	11.19		8.64	8.82	8.11			
	A87	11.04		8.04	8.75	8.18	6.98	6.50	5.41
M 2-42	D13	10.99	8.73	7.93	8.34	7.62	6.64	6.07	5.12
	W07	11.03	8.90	8.26	8.75	8.10	7.11	6.23	5.43
NGC 6567	D13	11.01	9.08	7.63	8.35	7.71	6.43	5.76	4.90
	W07	11.01	9.95	8.56	8.46	7.69	6.46	5.70	4.87
	H04	11.00		7.79	8.43	7.68	6.20	5.75	4.68
	P01	10.94		7.91	8.63	7.73			
	A87	11.03		7.78	8.50	7.78	6.76	5.90	5.00
NGC 6629	D13	10.98	8.74	7.38	8.62	8.20	6.67	6.25	5.06
	P11	10.98		7.65	8.68	7.92	6.34	6.30	5.08
	H04	11.04		7.80	8.65	7.95	6.50	6.28	4.98
	P01	10.97		7.57	8.62	7.75			
	A87	10.94		7.76	8.60	7.77	6.55	6.60	
Sa 3-107	D13	11.06	8.77	7.79	8.04		6.30		

He I recombination-line temperatures

$$\Delta T_{[\mathrm{N\,II}]} \equiv T_{\mathrm{e}}([\mathrm{N\,II}]) - T_{\mathrm{e}}(\mathrm{He\,I}). \tag{3.32}$$

The relation between ADF(O^{2+}) and $\Delta T_{[\mathrm{N\,II}]}$ for the 11 objects plotted in Fig. 3.11 (top) can be fitted by,

$$\begin{aligned}\log \mathrm{ADF}(\mathrm{O}^{2+}) =& (0.364 \pm 0.355) + (10.305 \pm 6.700) \times 10^{-5} \\ & \times \Delta T_{[\mathrm{N\,II}]}(\mathrm{K}),\end{aligned} \tag{3.33}$$

with a linear correlation coefficient of 0.45.

Fig. 3.11 (bottom) shows $\Delta T_{[\mathrm{O\,III}]} \equiv T_{\mathrm{e}}([\mathrm{O\,III}]) - T_{\mathrm{e}}(\mathrm{He\,I})$ plotted against ADF (O^{2+}). A linear fit to the 10 PNe plotted in the figure yields

$$\begin{aligned}\log \mathrm{ADF}(\mathrm{O}^{2+}) =& (0.399 \pm 0.224) + (8.050 \pm 4.084) \times 10^{-5} \\ & \times \Delta T_{[\mathrm{O\,III}]}(\mathrm{K}),\end{aligned} \tag{3.34}$$

with a linear correlation coefficient of 0.57.

Previously, Liu et al. (2001) found that ADF(O^{2+}) is strongly correlated with the difference between the [O III] forbidden-line and H I Balmer jump electron temperatures:

$$\log \mathrm{ADF}(\mathrm{O}^{2+}) = (0.21 \pm 0.09) + (20.1 \pm 3.3) \times 10^{-5} \Delta T(\mathrm{K}), \tag{3.35}$$

where $\Delta T \equiv T_{\mathrm{e}}([\mathrm{O\,III}]) - T_{\mathrm{e}}(\mathrm{BJ})$. Moreover, Tsamis et al. (2004) also derived a similar correlation for a sample of 16 PNe. As seen in Fig. 3.11, the ORL/CEL ADF for O^{2+} is correlated with the difference between the nebular to auroral forbidden-line temperature and the H I temperature. We see that higher values of ADF associates with higher CEL-ORL temperature discrepancies. Both correlations indicate that there is an intimate connection between the nebular thermal structure and the ORL/CEL abundance discrepancy.

In Fig. 3.12 we plot the O^{2+}/H^{+} ADF (top) and the N^{2+}/H^{+} ADF (bottom) as a function of the intrinsic nebular Hβ surface brightness $\log S(\mathrm{H}\beta)$. A linear

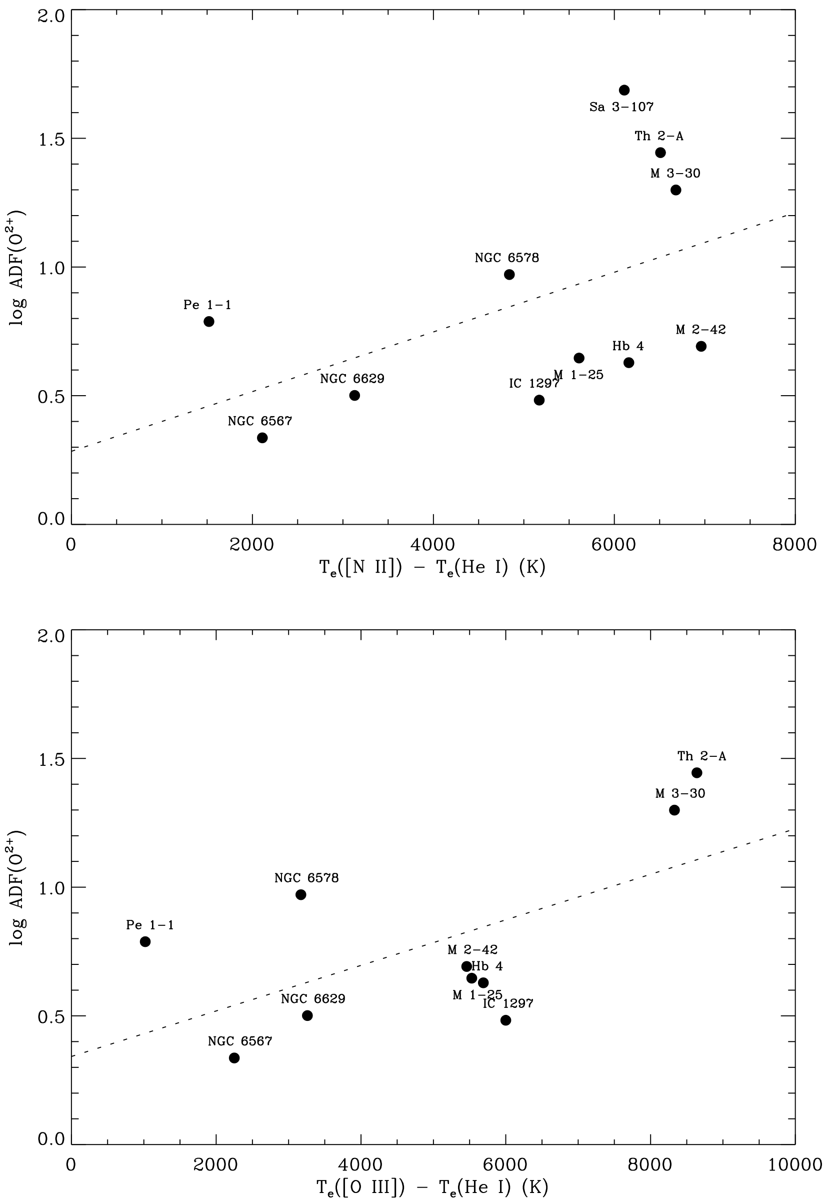

Figure 3.11: Top panel: The difference $\Delta T_{[\mathrm{N\,II}]}$(K) between the nebular electron temperatures derived from the [N II] CELs, T_{e}([N II]), and from the He I ORLs, T_{e}(He I), plotted against the ORL/CEL ionic ADF for O^{2+}. Bottom panel: the difference $\Delta T_{[\mathrm{O\,III}]}$(K) between the nebular [O III] electron temperatures, T_{e}([O III]), and the He I temperatures, T_{e}(He I), plotted against the ORL/CEL ionic ADF for O^{2+}. The dotted line is a linear fit to ΔT_{e} as a function of ADF(O^{2+}), discussed in the text.

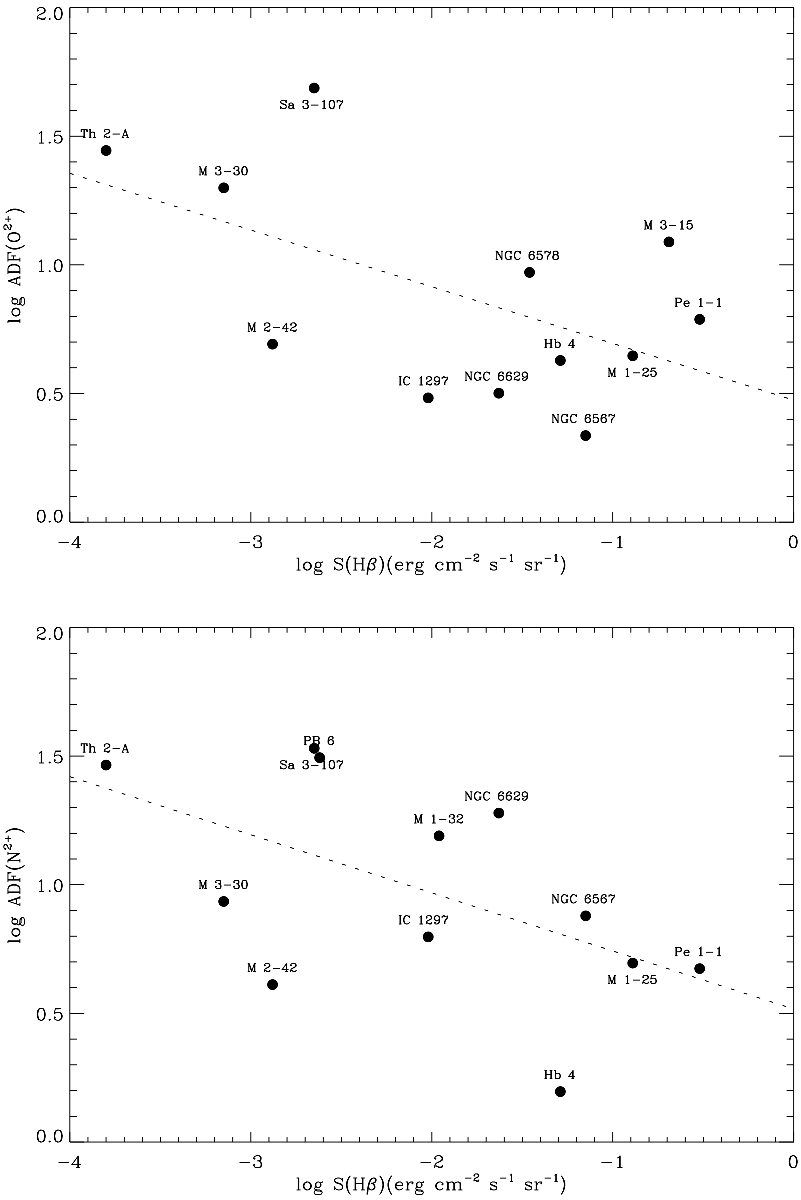

Figure 3.12: The ORL/CEL ionic ADF for O^{2+} (top) and N^{2+} (bottom) plotted against the logarithmic intrinsic nebular Hβ surface brightness. The dotted line is a linear fit to ADF(O^{2+}) as a function of $\log S(\mathrm{H}\beta)$, discussed in the text.

fit to the 12 PNe plotted in Fig. 3.12 (top) yields

$$\log \mathrm{ADF}(\mathrm{O}^{2+}) = (0.494 \pm 0.216) - (0.217 \pm 0.103) \log S(\mathrm{H}\beta), \tag{3.36}$$

with a linear correlation coefficient of -0.56.

We also see that a negative linear correlation exists between ADF($\mathrm{N}^{2+}/\mathrm{H}^{+}$) and the nebular H$\beta$ surface brightness for 12 PNe (Fig. 3.12, bottom), which can be fitted by

$$\log \mathrm{ADF}(\mathrm{N}^{2+}) = (0.517 \pm 0.251) - (0.226 \pm 0.111) \log S(\mathrm{H}\beta), \tag{3.37}$$

with a linear correlation coefficient of -0.54.

Similarly, we found that $\Delta T_{[\mathrm{N\,II}]}$ and $\Delta T_{[\mathrm{O\,III}]}$ are strongly correlated with decreasing nebular surface brightness (see Fig. 3.13) as follows

$$\Delta T_{[\mathrm{N\,II}]}(\mathrm{K}) = (2561 \pm 881) - (1313.72 \pm 399.02) \log S(\mathrm{H}\beta), \tag{3.38}$$

$$\Delta T_{[\mathrm{O\,III}]}(\mathrm{K}) = (1429 \pm 1095) - (2061.95 \pm 505.43) \log S(\mathrm{H}\beta), \tag{3.39}$$

with linear correlation coefficients of -0.70 and -0.79, respectively. We see that the ADFs and ORL-CEL temperature dichotomies ΔT are closely correlated with decreasing nebular surface brightness. The nebular surface brightness is an indicator of the nebula evolution, since it decreases due to the expansion of the nebula, as the density drops. Therefore, the ORL/CEL abundance discrepancy likely is a function of nebular evolution. Furthermore, the temperature dichotomies is closely related to the ADFs.

As seen in Fig. 3.14, it seems that our data does not show any clear correlation between the $\mathrm{O}^{2+}/\mathrm{H}^{+}$ and the excitation class (EC), which is in disagreement with the strong correlation found by Liu et al. (2004a). We see a very weak correlation with a large scatter for the 12 PNe plotted in Fig. 3.14 (dotted line):

$$\log \mathrm{ADF}(\mathrm{O}^{2+}) = (0.795 \pm 0.292) - (0.022 \pm 0.058)\,\mathrm{EC}, \tag{3.40}$$

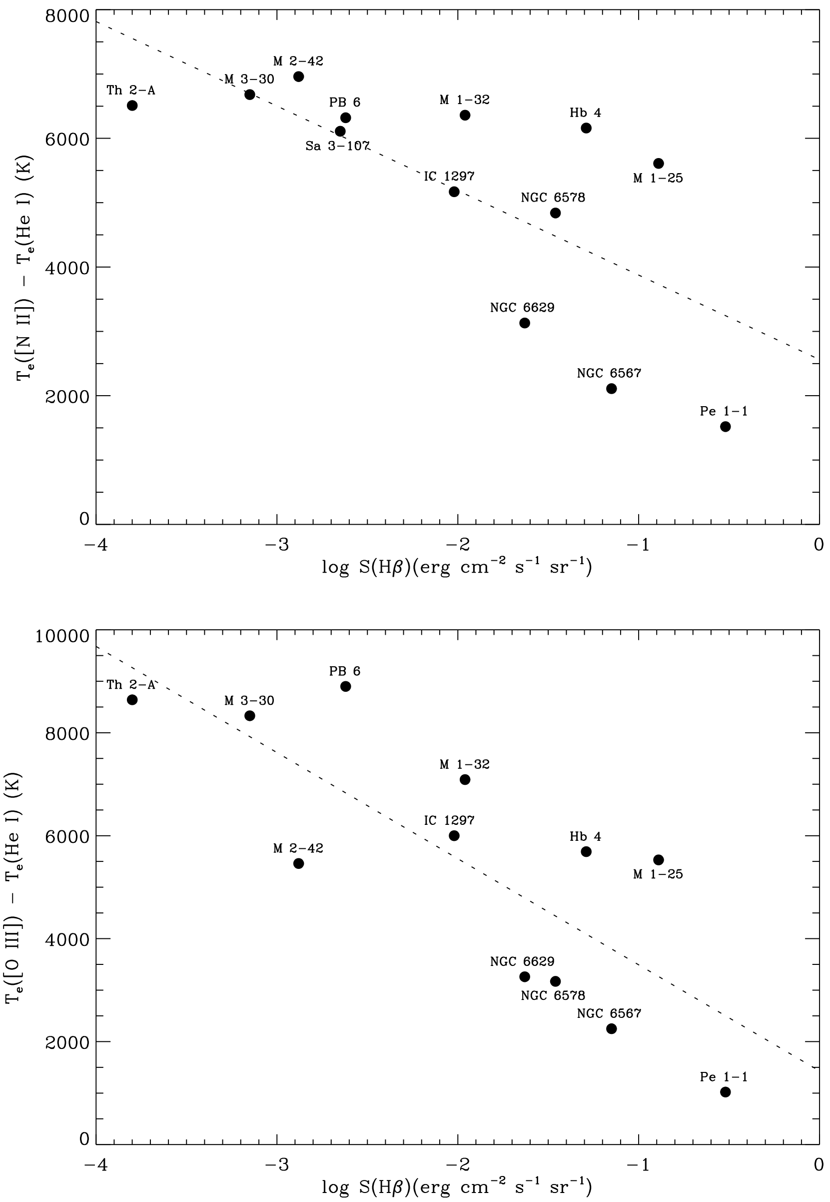

Figure 3.13: Top panel: the difference $\Delta T_{[\mathrm{N\,II}]}$(K) between the nebular electron temperatures derived from the [N II] CELs, T_e([N II]), and from the He I ORLs, T_e(He I), plotted against the logarithmic intrinsic nebular Hβ surface brightness $\log S(\mathrm{H}\beta)$(erg cm^{-2} s^{-1} sr^{-1}). The dotted line is a linear fit to $\Delta T_{[\mathrm{N\,II}]}$ as a function of $\log S(\mathrm{H}\beta)$. Bottom panel: the difference $\Delta T_{[\mathrm{O\,III}]}$(K) between the nebular [O III] electron temperatures, T_e([O III]), and the He I temperatures, T_e(He I), plotted against $\log S(\mathrm{H}\beta)$. The dotted line is a linear fit to ΔT as a function of $\log S(\mathrm{H}\beta)$, discussed in the text.

which has a linear correlation coefficient of 0.12, while a linear fit to the 10 PNe, after excluding M 3-30 and Th 2-A, yields a better correlation:

$$\log \mathrm{ADF}(\mathrm{O}^{2+}) = (1.356 \pm 0.298) - (0.147 \pm 0.074)\,\mathrm{EC}, \tag{3.41}$$

with a linear correlation coefficient of −0.58. The fit shown as a dashed line in Fig. 3.14 is in agreement with Liu et al. (2004a). Both M 3-30 and Th 2-A contain [WO] stars with effective temperature of 49 kK and 157 kK, respectively.

Similarly, we derived the following weak correlations between the dichotomy of temperature ($\Delta T_{[\mathrm{N\,II}]}$ and $\Delta T_{[\mathrm{O\,III}]}$) and the EC (see Fig. 3.15, dotted line),

$$\Delta T_{[\mathrm{N\,II}]}(\mathrm{K}) = (4558 \pm 986) + (128.21 \pm 170.93)\,\mathrm{EC}, \tag{3.42}$$

$$\Delta T_{[\mathrm{O\,III}]}(\mathrm{K}) = (2760 \pm 1279) + (512.98 \pm 213.54)\,\mathrm{EC}, \tag{3.43}$$

which have linear correlation coefficients of 0.22 and 0.61, respectively. We also obtained the following correlations, after excluding the high-excitation PN PB 6, M 3-30 and Th 2-A (see Fig. 3.15, dashed line),

$$\Delta T_{[\mathrm{N\,II}]}(\mathrm{K}) = (6106 \pm 1568) + (-367.68 \pm 406.36)\,\mathrm{EC}, \tag{3.44}$$

$$\Delta T_{[\mathrm{O\,III}]}(\mathrm{K}) = (5120 \pm 2102) + (-193.23 \pm 520.31)\,\mathrm{EC}, \tag{3.45}$$

with linear correlation coefficients of −0.30 and −0.14. It is known that the EC is closely related to the ionizing source. From the relations (3.40)–(3.45), it is obvious that the abundance discrepancy and temperature dichotomy do not have any clear correlation with the excitation class or ionizing radiations.

We find that the correlation between ADFs and $S(\mathrm{H}\beta)$ is much stronger than the ADF-EC correlation. This suggests that the abundance discrepancy problem is related to the nebular evolution rather than the radiation fields. The discrepancy is higher in old evolved PNe.

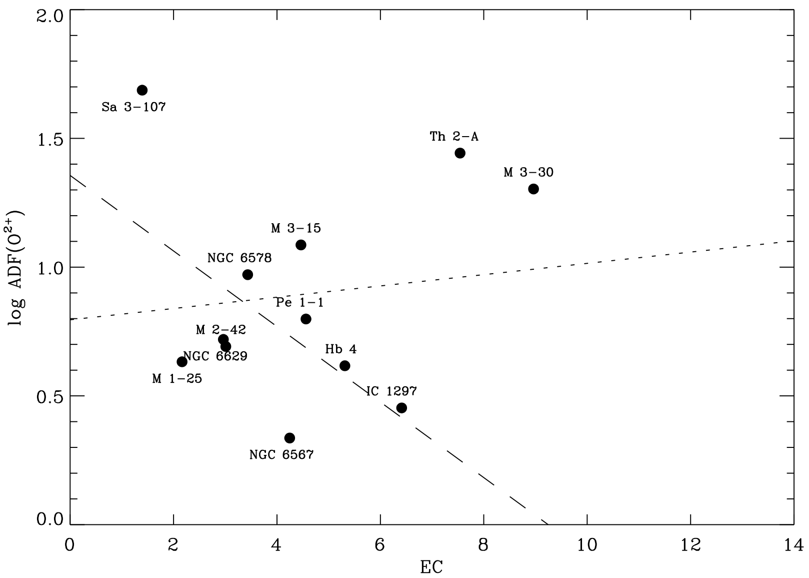

Figure 3.14: The ORL/CEL ionic ADF for O^{2+} plotted against the excitation class (EC). The dotted line is a linear fit to ADF(O^{2+}) as a function of EC. The dashed line is a similar linear fit found after excluding M 3-30 and Th 2-A, discussed in the text.

3.5 Discussion of individual objects

PB 6 (= PN G278.8+04.9). This object is a PN with extremely filamentary structure (*HST* image, ID 12600; see Chapter 2). It is classified as a Type I PN based on an N/O ratio exceeding 0.8 (Kingsburgh & Barlow 1994). Previously, it has been also classified as of Type I by Peimbert & Torres-Peimbert (1983), with He/H $\geqslant 0.125$ and $\log$ N/O $\geqslant -0.3$, belonging to He and N rich PNe. PB 6 was extensively studied by García-Rojas et al. (2009), who utilized high-resolution optical spectra from the Magellan telescope (MIKE spectrograph). We see that nebular spectrum to be of extremely high excitation, where $I(4686) = 141$, on a scale where $I(\mathrm{H}\beta) = 100$. The excitation class (E.C.) scheme proposed by Dopita & Meatheringham (1990) yields E.C. = 11.65 cor-

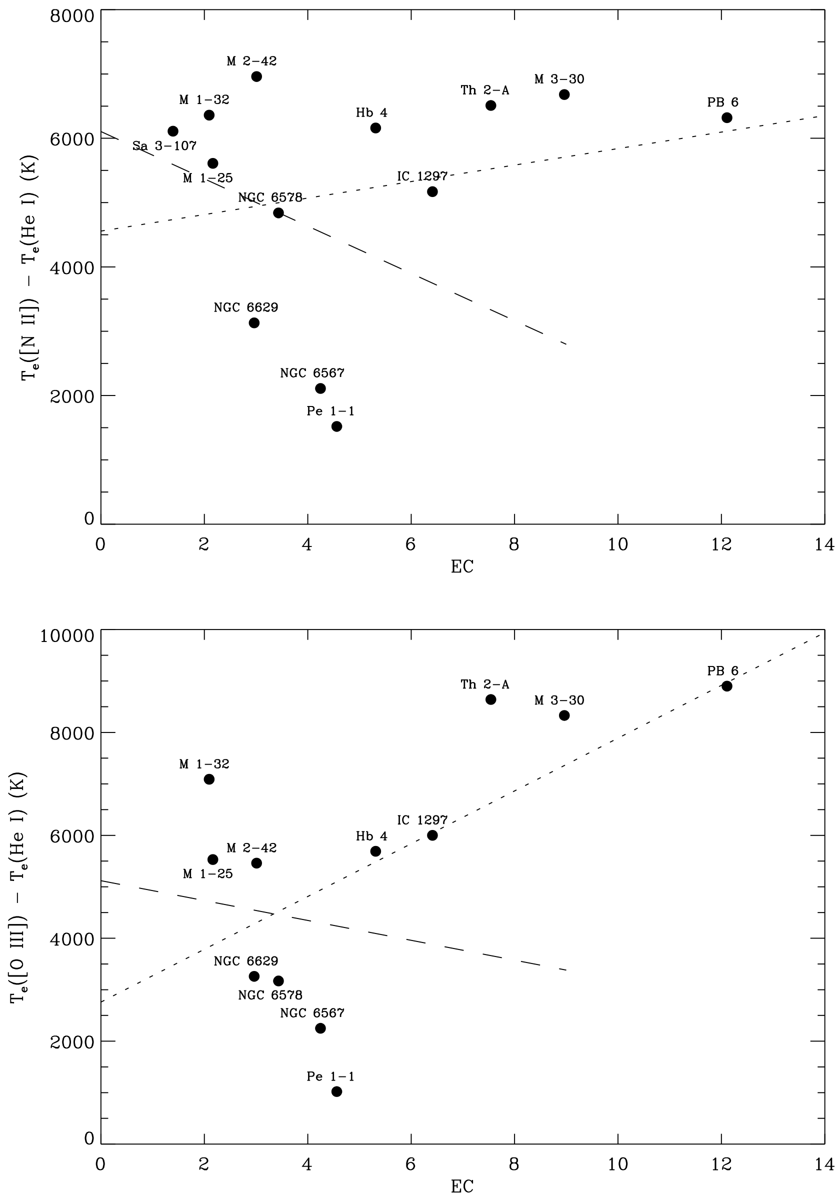

Figure 3.15: Top panel: the difference $\Delta T_{\rm e}$(K) between the nebular electron temperatures derived from the [N II] CELs, $T_{\rm e}$([N II]), and from the He I ORLs, $T_{\rm e}$(He I), plotted against the excitation class (EC). Bottom panel: the difference $\Delta T_{\rm [O\,III]}$(K) between the nebular [O III] electron temperatures, $T_{\rm e}$([O III]), and the He I temperatures, $T_{\rm e}$(He I), plotted against the EC. The dotted line is a linear fit to $\Delta T_{\rm e}$ as a function of EC. The dashed line is a similar linear fit found after excluding PB 6, M 3-30 and Th 2-A, discussed in the text.

responding to $T_{\rm eff} = 360$ kK (Dopita & Meatheringham 1991). However, the stellar temperature of $T_{\rm eff} = 102$ kK was estimated from spectral analysis of the central star by Acker & Neiner (2003), who also identified its central star as Wolf-Rayet [WO1]. From our spectrum and the recent He I atomic data (Porter et al. 2013), we derive He/H = 0.148 in agreement with Girard et al. (2007), whereas other studies derived higher overall He/H ratio of 0.17-0.18 (Torres-Peimbert & Peimbert 1977; Kaler et al. 1991; Peña et al. 2001; Henry et al. 2004; García-Rojas et al. 2009). We obtain N/O = 1.4 similar to Girard et al. (2007), Peña et al. (2001) and García-Rojas et al. (2009). Although García-Rojas et al. (2009) derived a very high $\rm C_{ORL}/O_{CEL}$ ratio of 9.1 from the C II λ4267 ORL and oxygen CELs, we find $\rm C_{ORL}/O_{CEL}$ = 2.5 in decent agreement with Kaler et al. (1991) and Henry et al. (1996). The high C/O and N/O ratios are consistent with the third dredge-up (TDU) and the hot bottom burning (HBB) in progenitor stars with initial masses $\gtrsim 4 M_{\odot}$ (Karakas & Lattanzio 2007; Karakas et al. 2009). It is found that the oxygen and argon abundances are slightly below solar abundance by -0.11 and -0.06 dex, in agreement with [O/H] = -0.14 and [Ar/H] = -0.20 by García-Rojas et al. (2009). However, our sulfur and chlorine abundances may be unreliable due to measurement errors and inaccurate ionization correction factor.

We derive $N_{\rm e}$(S II) = 2000 cm^{-3} similar to the values found by Henry et al. (2004) and García-Rojas et al. (2009). An electron temperature of 11480 K was derived from the [N II] nebular $\lambda\lambda$6548,6584 doublet and auroral λ5755 line, in agreement with Peña et al. (2001) and Henry et al. (2004). We derived $T_{\rm e}$(N II) = 9400 K by correcting for the recombination contribution with $\rm N^{2+}/H^{+} = 6.57 \times 10^{-3}$ and $T_{\rm e}$(He I) = 5100 K. For the CEL abundance calculation of all singly ionized species, we have adopted $T_{\rm e}$ = 11500 K, which is no different from those found by the previous studies (see Table 3.7). For ionic species other than singly ionized species, we have used $T_{\rm e}$(O III) = 14000 K, in decent agreement with $T_{\rm e}$(O III) = 14600 K by Henry et al. (2004). As our observation did not cover the [O III] λ4363 line, we have adopted the measured flux from Kaler et al. (1991). Moreover, Henry et al. (2004) obtained T_e(S III) = 16300 K from the [S III] nebular $\lambda\lambda$9069,9532 doublet and auroral λ6312 line. For the ORL abundance calculation, we have used T_e(He I) = 5100 K.

M 3-30 (= PN G017.9−04.8). This object is an elliptical PN shell (Schwarz et al. 1992) with two symmetric FLIERs located inside the shell (see Chapter 2) either side of a [WO1] central star (Acker & Neiner 2003). It is of high excitation, E.C. = 8.5 (Dopita & Meatheringham 1990) or E.C. = 9.1 (Reid & Parker 2010), which is associated with $T_{\rm eff} = 210$ kK (Dopita & Meatheringham 1991). However, Gleizes et al. (1989) derived Zanstra temperatures $T_{\rm z}({\rm H\ I}) = 34.5$ kK and $T_{\rm z}({\rm He\ II}) = 58$: kK, which is inconsistent with the nebular high-excitation He II $I(4686) = 84$, on a scale where $I({\rm H}\beta) = 100$. We find He/H = 0.12, identical to Girard et al. (2007). However, Peña et al. (2001) derived He/H = 0.17 due to different atomic data used in their analysis (recombination coefficients by Pequignot et al. 1991). We obtain O/H = 3×10^{-4}, in generally good agreement with Peña et al. (2001) and Girard et al. (2007). M 3-30 is an extremely carbon-rich PN with $C_{\rm ORL}/O_{\rm CEL}$ = 7.7, though N/O = 0.5 (non-Type I). This indicates that the progenitor was a low-mass carbon-rich AGB star with initial masses $\lesssim 2M_{\odot}$ (Karakas et al. 2009). We see that the metallicity of M 3-30 is sub-solar based on [O/H] = -0.2, [S/H] = [Cl/H] = -0.3, and [Ar/H] = -0.13. The argon abundance is not expected to change during AGB nucleosynthesis, but it may be inaccurate because of measurement errors. We adopted the [Ar III] λ7136 flux from Girard et al. (2007).

We used N_e(S II) = 350 cm^{-3}, similar to Girard et al. (2007), to derive the abundances for several ions. We used the value of T_e(N II) = 9000 K for singly ionized species, whereas T_e(O III) = 10000 K derived by Girard et al. (2007) was used for other ionic species in the CEL abundance analysis. We also derived T_e(O III) = 10670 K by adopting the [O III] λ4363 line from Peña et al. (2001). We derived T_e(O III) = 10030 K by correcting for the recombination contribution with O^{3+}/H^+ derived from O^{2+}/H^+ and He^+/He, ignoring O^+/H^+, while $T_e = T_e$(He I). The value of T_e(He I) = 2500 K was used for the ORL abundance calculation.

Hb 4 (= PN G003.1+02.9). This object is quite a heavily reddened PN, $c(\mathrm{H}\beta) = 1.86$ derived from the Balmer emission line $\mathrm{H}\alpha/\mathrm{H}\beta$ flux ratio, in agreement with García-Rojas et al. (2012). It is an aspherical PN with two FLIERs located outside the ring-like shell (*HST* image, ID 6347, P.I. Borkowski). We find that Hb 4 has an excitation class of E.C. = 5.0 based on the scheme proposed by Dopita & Meatheringham (1990). This E.C. corresponds to $T_{\mathrm{eff}} = 131$ kK (Dopita & Meatheringham 1991), inconsistent with a [WO3] central star with $T_{\mathrm{eff}} = 85$ kK derived by Acker & Neiner (2003). We find N/O = 1.03 (Type I PN), higher than N/O = 0.76 by Girard et al. (2007) and N/O = 0.58 (non-Type I PN) by García-Rojas et al. (2012). We find He/H = 0.11, in good agreement with Girard et al. (2007) and García-Rojas et al. (2013). Our derived $\mathrm{C_{ORL}/O_{CEL}} = 0.8$ is less than the value of $\mathrm{C_{ORL}/O_{CEL}} = 1.95$ by García-Rojas et al. (2013). The nitrogen enrichment and low C/O associate it with an intermediate-mass AGB star, which has experienced HBB, converting dredged-up ^{12}C to ^{14}N. The oxygen and argon abundances indicate that it has a solar metallicity, so the progenitor star must have an initial mass of $\gtrsim 5M_{\odot}$ in order to undergo the HBB phase, based on the predicted AGB models (Karakas & Lattanzio 2007).

We derived a temperature of $T_e = 10310$ K from the [N II] nebular to auroral line ratio, in agreement with Girard et al. (2007). The value of T_e(N II) = 9960 K is obtained by excluding the recombination contribution calculated by $N^{2+}/H^+ = 6.61 \times 10^{-4}$ and T_e(He I) = 4200 K. We also derived T_e(O III) = 9900 K in good agreement with García-Rojas et al. (2012). We obtained N_e(N II) = 6700 cm^{-3}, N_e(Ar IV) = 6760 cm^{-3} and N_e(Cl III) = 7170 cm^{-3}, in generally good agreement with García-Rojas et al. (2012).

IC 1297 (= PN G358.3−21.6). This PN, excited by a [WO3] type star (Acker

& Neiner 2003), has an elliptical morphology (Zuckerman & Aller 1986). We find N/O = 0.3 (non-Type I), in agreement with Koeppen et al. (1991) and Henry et al. (2004). We derive He/H = 0.11 similar to Aller et al. (1986), Koeppen et al. (1991) and Girard et al. (2007), but Henry et al. (2004) derived He/H = 0.13, which is attributed to different He I recombination coefficients (Pequignot et al. 1991). We obtain O/H = 5.9×10^{-4}, in generally good agreement with Aller et al. (1986) and Girard et al. (2007). It is found that the oxygen abundance is slightly above solar abundance by 0.08 dex. The argon and chlorine abundances are not expected to change during AGB nucleosynthesis; we see [Ar/H] = −0.12 in good agreement with [Ar/H] = [Cl/H] = −0.13 by Girard et al. (2007). Oxygen is assumed to be unchanged by AGB nucleosynthesis, but oxygen can be produced in a few special cases, such as metal-poor progenitor stars (e.g. Dinerstein et al. 2003). This PN may not be produced by an intermediate-mass AGB star, since HBB makes a high nitrogen abundance. Moreover, HBB depletes oxygen when the base of the convective envelope is at a temperature higher than 8×10^7 K (Karakas et al. 2009). We also see C/H = 0.94. The progenitor could be a low-mass star with an initial mass less than $4M_{\odot}$.

Th 2-A (= PN G306.4−00.6). This PN, ionized by a [WO3]pec (Weidmann et al. 2008), has a rink-like morphology (Górny et al. 1999). The elemental abundances of Th 2-A has been studied by Kingsburgh & Barlow (1994) and Henry et al. (2004). Weidmann et al. (2008) classified the central star of Th 2-A as of type [WO 3]pec, those with *peculiar* C IV-5801/12 doublets (Acker & Neiner 2003). We find our nebular spectrum to be of relatively high excitation of E.C. = 7.6 (Dopita & Meatheringham 1990), related to $T_{\rm eff} = 160$ kK (Dopita & Meatheringham 1991). We derive $c({\rm H}\beta)$ = 1.12 from the Hα/Hβ ratio, in good agreement with the value of $c({\rm H}\beta)$ = 1.03 from the radio-Hβ method, $c({\rm H}\beta)$ = 0.93 by Henry et al. (2004) and $c({\rm H}\beta)$ = 1.07 by Kingsburgh & Barlow (1994). Our spectrum, however, shows $I(4686) = 58$, slightly higher than

$I(4686) = 50$ by Kingsburgh & Barlow (1994) and Milingo et al. (2002), on a scale where $I(\mathrm{H}\beta) = 100$. We derive $T_{\mathrm{e}}(\mathrm{N\,II}) = 10150\,\mathrm{K}$ slightly lower than $T_{\mathrm{e}}(\mathrm{N\,II}) = 11700\,\mathrm{K}$ by Henry et al. (2004) and $T_{\mathrm{e}}(\mathrm{N\,II}) = 12100\,\mathrm{K}$ by Kingsburgh & Barlow (1994). Nonetheless, we find $T_{\mathrm{e}}(\mathrm{O\,III}) = 12280\,\mathrm{K}$, in generally good agreement with $T_{\mathrm{e}}(\mathrm{O\,III}) = 11600\,\mathrm{K}$ (Henry et al. 2004) and $T_{\mathrm{e}}(\mathrm{O\,III}) = 12500\,\mathrm{K}$ (Kingsburgh & Barlow 1994). Moreover, we find roughly the same density; $N_{\mathrm{e}}(\mathrm{S\,II}) = 1400\,\mathrm{cm}^{-3}$ similar to $N_{\mathrm{e}}(\mathrm{S\,II}) = 1200\,\mathrm{cm}^{-3}$ by Henry et al. (2004) and $N_{\mathrm{e}}(\mathrm{S\,II}) = 1220\,\mathrm{cm}^{-3}$ by Kingsburgh & Barlow (1994). For the CEL abundance analysis, we have used $T_{\mathrm{e}} = 10000\,\mathrm{K}$ for all singly ionized species, but we have adopted $T_{\mathrm{e}} = 12000\,\mathrm{K}$ for ions other than singly ionized species. For the ORL abundance analysis, we have used $T_{\mathrm{e}}(\mathrm{He\,I}) = 3600\,\mathrm{K}$.

We find a He/H ratio of 0.10, whereas Henry et al. (2004) found He/H= 0.13. Henry et al. (2004) adopted electron temperatures derived from CELs, and used the effective recombination coefficients from Pequignot et al. (1991). However, Kingsburgh & Barlow (1994) got a different value of He/H = 0.09 using the effective recombination coefficients from Brocklehurst (1971) and Hummer & Storey (1987). Nonetheless, we find N/O = 0.47 similar to N/O = 0.49 (Henry et al. 2004) and N/O = 0.40 (Kingsburgh & Barlow 1994). We also find that Th 2-A is a carbon-rich PN with $\mathrm{C_{ORL}/O_{CEL}} = 3.4$. Our calculated oxygen abundance ratio of O/H $= 4.9 \times 10^{-4}$ is related to a solar metallicity, in good agreement with the value found by Kingsburgh & Barlow (1994). Based on N/O and C/O ratios, Th 2-A could be produced by an AGB star with an initial mass less $4M_{\odot}$ (Karakas & Lattanzio 2007).

Pe 1-1 (= PN G285.4+01.5). Pe 1-1 is a heavily reddened object; $c(\mathrm{H}\beta)_{\mathrm{Balmer}} = 1.96$ and $c(\mathrm{H}\beta)_{\mathrm{Radio}} = 1.85$, and shows a bipolar PN with point-symmetric jets (*HST* images, ID 11657, P.I. Stanghellini). The density of $N_{\mathrm{e}} = 10^4\,\mathrm{cm}^{-3}$ derived from [S II)] ratio associates it with a relatively high-density PN. The [N II] temperature diagnostic ratio presents $T_{\mathrm{e}}(\mathrm{N\,II}) = 10820\,\mathrm{K}$. We find $T_{\mathrm{e}}(\mathrm{N\,II}) = 10430\,\mathrm{K}$ corrected for the recombination contribution, which is no different from $T_{\mathrm{e}}(\mathrm{O\,III}) =$

10320 K. Additionally, an electron temperature of 9300 K was derived from the He I λ6678/λ4472 ratio, which does not show a high departure from CEL temperatures. As seen in Table 3.7, our derived density and temperatures are in good agreement with García-Rojas et al. (2012).

We find N/O = 0.4 (non-Type I), whereas N/O = 0.25 found by García-Rojas et al. (2013) and N/O = 0.34 by Girard et al. (2007). We find a oxygen abundance of O/H = 4.04×10^{-4} lower than O/H = 4.68×10^{-4} by García-Rojas et al. (2013), and a nitrogen abundance of N/H = 1.63×10^{-4} higher than O/H = 1.15×10^{-4} by García-Rojas et al. (2013). This can be due to different atomic data and physical conditions adopted for the abundance calculations. It is found that our value of the oxygen abundance is slightly below solar abundance by -0.08 dex, while [Ar/H] = [Cl/H] = -0.11 and [S/H] = -0.22. Moreover, we find C_{ORL}/O_{CEL} = 2.35, in decent agreement with C_{ORL}/O_{CEL} = 2.78 derived by García-Rojas et al. (2013). The abundance pattern indicates that Pe 1-1 probably evolved from a low-mass carbon-rich AGB star ($\lesssim 2M_{\odot}$) with a sub-solar metallicity by about -0.1 dex.

M 1-32 (= PN G285.4+01.5). Acker & Neiner (2003) classified the central star of M 1-32 as of type [WO 4]pec, whose C IV-5801/12 doublet shows a *peculiar* terminal velocity of about 5000 km s^{-1}. Our observations indicate that this object could be a Type I PN with N/O = 0.88. However, N/O = 0.5 was derived by Girard et al. (2007) and García-Rojas et al. (2013), whereas Peña et al. (2001) obtained N/O = 1.09. We find C_{ORL}/O_{CEL} = 4.57, lower than C_{ORL}/O_{CEL} = 10.19 by García-Rojas et al. (2013). Moreover, we find a He/H ratio of 0.10, which is lower than previous published values (see Table 3.11). The high value C/O ratio can be related to the third dredge-up (TDU), while the high value N/O ratio is usually produced by the HBB phase (Karakas et al. 2009). The oxygen abundance indicates that it has roughly solar metallicity, in agreement with García-Rojas et al. (2013). According to the AGB models (Karakas & Lattanzio 2007), this PN must have a progenitor star with an initial mass more than $5M_{\odot}$ to undergo the HBB phase.

We find a reasonable agreement between physical conditions derived from CELs and those of García-Rojas et al. (2012). We derive T_e(N II) = 8630 K, similar to T_e(N II) = 8600 K by Girard et al. (2007) and T_e(N II) = 8350 K by García-Rojas et al. (2012). An electron temperature of 9360 K was derived from the [O III] nebular $\lambda\lambda$4959,5007/λ4363 ratio (auroral line flux adopted from García-Rojas et al. 2012), in agreement with T_e(O III) = 9430 K by García-Rojas et al. (2012). We derive N_e(S II) =6400 cm^{-3}, in agreement with N_e(S II) =6857 cm^{-3} derived by Peña et al. (2001).

M 3-15 (= PN G006.8+04.1). M 3-15 is the most reddened object in our sample, a value of c(Hβ) = 2.27 derived from the Hα/Hβ flux ratio, similar to c(Hβ) = 2.10 given by Acker & Neiner (2003). We derived a temperature of T_e(N II) = 7780 K, lower than the values found by other authors, listed in Table 3.7. We believe that the low temperature results from an error in the [N II] λ5755 measurement. Adopting the [O III] λ4363 flux from García-Rojas et al. (2012), we obtained T_e(O III) = 8310 K, identical to Ratag et al. (1997), Stasińska et al. (1998), Chiappini et al. (2009) and García-Rojas et al. (2012). We derived N_e(S II) = 5200 K cm^{-3}, in agreement with Girard et al. (2007), Chiappini et al. (2009) and García-Rojas et al. (2012). For the CEL abundance analysis, we have used T_e = 8000 K and N_e = 5200 K cm^{-3}. For the ORL abundance analysis, we have adopted T_e(He I) = 7300 K from García-Rojas et al. (2012). The abundances listed in Table 3.11 for M 3-15 can be compared with the values presented in the literature. We find a N/O ratio of 0.52 similar to Peña et al. (2001) and Chiappini et al. (2009), but higher than N/O = 0.33 by García-Rojas et al. (2013). We derive C_{ORL}/O_{CEL} = 0.91, roughly the same as C_{ORL}/O_{CEL} = 1.1 derived by García-Rojas et al. (2013). We see that the oxygen and sulfur abundances are above solar abundance by 0.2 dex.

M 1-25 (= PN G004.9+04.9). M 1-25 is an extreme bipolar PN with a [WC5-6] central star (Acker & Neiner 2003). Only a few PNe were found to possess

[WC5-8] stars, which could be related to a possibly rapid transition through this stage, assuming [WCL]$\rightarrow$[WO] (e.g. Werner 2001). An electron temperature of 8000 K was derived from the [N II] and [O III] temperature diagnostic ratios, which is similar to those found previously; see Table 3.7. We derived N_e(S II) = 4800 cm^{-3}, identical to the value found by Chiappini et al. (2009), but lower than N_e(S II) $\approx$ 8000 cm^{-3} by Girard et al. (2007) and García-Rojas et al. (2012). For M 1-25, we got c(Hβ) = 1.6 from the Hα/Hβ flux ratio, higher than c(Hβ) = 1.46 by Girard et al. (2007) and c(Hβ) = 1.4 by García-Rojas et al. (2012), which could be due to systematic errors in the flux calibration.

We find a He/H ratio of 0.103, whereas García-Rojas et al. (2013) found He/H = 0.123, which is related to the values of the electron temperature assumed for the ORL abundance analysis. However, we find N/0 = 0.49 and C_{ORL}/O_{CEL} = 1.16, in decent agreement with N/0 = 0.34 and C_{ORL}/O_{CEL} = 1.23 by García-Rojas et al. (2013). We see that the oxygen abundance is slightly above solar abundance, [O/H] = 0.04, while the sulfur and argon abundances are above solar abundance by 0.14 and 0.26 dex, respectively. Based on the abundance pastern, M 1-25 can be associated with an AGB star with an initial mass about $3.5 M_{\odot}$ (stellar models by Karakas et al. 2009).

Hen 2-142 (= PN G327.1$-$02.2). Hen 2-142 has been studied by Girard et al. (2007), who obtained N/O = 0.19 and O/H = 8.91×10^4, although we got N/O = 0.28 and O/H = 3.54×10^4. The central star of Hen 2-142 is classified as of type [WC9] and has an effective temperature of 35 kK (Acker & Neiner 2003). Therefore, the helium gas is not fully ionized as we got a He/H ratio of 0.025. Hen 2-142 is an extreme bipolar PN with a high density of 2×10^4 cm^{-3}, and a temperature of about 8800 K. We find c(Hβ) = 1.55 from the Balmer emission line Hα/Hβ flux ratio, which is lower than c(Hβ) = 1.73 by Acker & Neiner (2003) and c(Hβ) = 2.11 by Girard et al. (2007). This could be because of some errors in measurements and/or flux calibration. However, we derived

$c(\mathrm{H}\beta)_{\mathrm{Radio}} = 1.23$ from the radio-Hβ method.

Hen 3-1333 (= PN G332.9−09.9). This object is a quite young, high-density PN with an early-type [WC10] central star (Acker & Neiner 2003), and has been studied by De Marco et al. (1997). The central star is very cool, and has a Zanstra temperature of $T_{\mathrm{Z}}(\mathrm{H\,I}) = 17$ kK (Acker & Neiner 2003), which cannot produce He I lines. We find a N/O ratio of 0.25, as low as N/O = 0.17 by De Marco et al. (1997). However, we derive O/H = 8.5×10^{-4}, twice the value found by De Marco et al. (1997). Additionally, De Marco et al. (1997) derived a very large carbon abundance of $(\mathrm{C/O})_{\mathrm{CEL}} = 13.13$. We see that the abundance pattern of Hen 2-113 is predicted by the AGB models with progenitor masses less than $2.5 M_{\odot}$ (Karakas et al. 2009).

Hen 2-113 (= PN G321.0+03.9). This young, high-density PN with [WC10] star (Acker & Neiner 2003) looks nearly as a twin of Hen 3-1333, and has been also studied by De Marco et al. (1997). Its cool central star shows a Zanstra temperature of $T_{\mathrm{Z}}(\mathrm{H\,I}) = 21$ kK (Acker & Neiner 2003), which cannot ionize helium in the nebula. We derive a N/O ratio of 0.26, but N/O = 0.14 was found by De Marco et al. (1997). We also find O/H = 3.97×10^{-4}, in reasonable agreement with O/H = 4.8×10^{-4} by De Marco et al. (1997). The extreme carbon-rich feature of Hen 2-113 found by De Marco et al. (1997), $(\mathrm{C/O})_{\mathrm{CEL}} = 10.42$, is predicted by the AGB models of progenitor stars with initial masses less than $2.5 M_{\odot}$ (Karakas et al. 2009).

K 2-16 (= PN G352.9+11.4). K 2-16 is a presumably old, large PN with an early-type [WC11] central star (Acker & Neiner 2003), and has been studied by Peña et al. (2001). We find a temperature of $T_{\mathrm{e}}(\mathrm{N\,II}) = 9560$ K and $N_{\mathrm{e}}(\mathrm{S\,II}) \approx 100{::}\,\mathrm{cm}^{-3}$, while Peña et al. (2001) derived $T_{\mathrm{e}}(\mathrm{N\,II}) = 11700$ K and $N_{\mathrm{e}}(\mathrm{S\,II}) = 514\,\mathrm{cm}^{-3}$. Adopting the [O II] λ3726,3729 doublet from Peña et al. (2001), we derived a O/H ratio of 1.53×10^{-4} much higher than O/H = 7.89×10^{-5} calculated by Peña et al. (2001). The high oxygen abundance can be explained by different temperature and atomic data. Similarly, we derive N/H = $5.86 \times$

10^{-5} higher than N/H = 3.83×10^{-5} by Peña et al. (2001). We did not identify any He I lines, since the central star has a low temperature, $T_{\rm eb}$(H I)= 19 kK (Acker & Neiner 2003) and is not enough to ionize the helium gas. It is found that K 2-16 has a sub-solar metallicity with [O/H] = −0.51 and [S/H] = −0.76.

NGC 6578 (= PN G010.8−01.8). NGC 6578 has been studied by Henry et al. (2004), who derived the abundance ratios of N/O = 0.31 and He/H = 0.12. Similarly, we obtained N/O = 0.2 and He/H = 0.11. However, we derived a O/H ratio of 2.75×10^{-4} much lower than O/H = 7.42×10^{-4} calculated by Henry et al. (2004). The low oxygen abundance may result from adopting an unreliable [N II] temperature, as the measured auroral line is very weak and uncertain. This object has also been studied by Aller & Keyes (1987), who derived N/O and He/H similar to our results, but they found O/H = 5.62×10^{-4}. We find a density of $N_{\rm e}$(S II) = 5000 cm^{-3}, which is almost double the values found by Peña et al. (2001) and Henry et al. (2004). The carbon ration of $\rm C_{ORL}/O_{CEL}$ = 5.46 indicates that NGC 6578 is a carbon-rich PN. The oxygen abundance is below solar abundance by −0.25 dex, so NGC 6578 could be produced by a metal-poor progenitor star. Comparing N/O and He/H with values predicted by the stellar models (Karakas et al. 2009), this PN probably evolved from a AGB star with an initial mass of about $2.5M_{\odot}$.

M 2-42 (= PN G008.2−04.8). This PN has an extremely bipolar morphology (Akras & López 2012) (see also Chapter 2). We find N/O = 0.39 and He/H = 2.43, in reasonable agreement with N/O = 0.32 and He/H = 1.42 by Wang & Liu (2007). But, Wang & Liu (2007) derived O/H = 5.62×10^{-4}, which is almost twice our value of O/H = 2.21×10^{-4}. This can be explained by the electron temperature adopted for the abundance analysis. Wang & Liu (2007) derived a temperature of $T_{\rm e}$(N II) = 9350 K, which has been used for their abundance calculations. However, we adopted $T_{\rm e}$ = 10300 K derived from the [N II] (λ6548+λ6584)/λ5755 diagnostic ratio.

NGC 6567 (= PN G011.7−00.6). NGC 6567 has a very high $\rm C_{ORL}/O_{CEL}$ ratio of 5.46. We find N/O = 0.19, in generally good agreement with Aller & Keyes (1987), Peña et al. (2001) and Henry et al. (2004). A density of N_e = 6500 cm^{-3} was derived from the [S II] μ6731/λ6717 flux ratio, which is almost the same as the value found by Kwitter et al. (2003) and Wang et al. (2004).

NGC 6629 (= PN G009.4−05.0). Our abundance analysis presents N/O = 0.09 and He/H = 0.095, in good agreement with the most values from the literature, as listed in Table 3.11. We derived C_{ORL}/O_{CEL} = 1.24, which is higher than C/O = 0.44 given by Pottasch et al. (2011). We obtained an oxygen abundance of O/H = 4.14×10^{-4}, which is the same as Peña et al. (2001), but Pottasch et al. (2011) found O/H = 4.80×10^{-4}. We see that our oxygen abundance is below solar abundance by −0.07.

Sa 3-107 (= PN G358.0−04.6). The central star of the Galactic bulge PN Sa 3-107 has been classified as of *wels* by Depew et al. (2011), although its nebula has never been analyzed. We find a He/H ratio of 0.116. We, unfortunately, do not have any [O II] line within our wavelength coverage, so we have adopted O^+ estimated using Eq. (3.18) from S^{2+}/S^+ ratio. We find a N/O ratio of 0.55 (non-Type I) and a very high C_{ORL}/O_{CEL} ratio of 5.29. We notice that the oxygen and sulfur abundances are largely below solar values, [O/H] = −0.65 and [S/H] = −0.82 dex. The abundance pattern suggested that Sa 3-107 probably evolved from a low-mass, low-metallicity star ($\lesssim 2M_\odot$)

3.6 Discussions and conclusion

3.6.1 Comparison with AGB nucleosynthesis models

The elemental abundances of planetary nebulae represent the products of the nucleosynthesis and mixing processes that occurred during previous evolutionary phases. The richest nucleosynthesis occurs during the AGB, where TDU mixes carbon and other helium burning products to the surface. HBB also occurs in intermediate-mass AGB stars with masses $\geq 5M_{\odot}$. Although we have a good qualitative picture of the evolution of low and intermediate-mass stars, the details of the mixing and nucleosynthesis during the AGB are uncertain (e.g. Busso et al. 1999; Herwig 2005). Elemental abundances from PNe are an invaluable tool to help constrain these uncertain mixing processes, and to gain insight into non-standard physics such as rotation (e.g. Charbonnel & Lagarde 2010).

In Table 3.12, we present the new yields for PNe originating from different AGB models with progenitor masses $M_{\rm int}/{\rm M}_{\odot} = 1.75$–6.0 and metallicities $Z = 0.008$–0.02. The PN yields were obtained from the AGB stellar models using the Mount Stromlo Stellar Structure Code calculating the structure (Lattanzio 1986) and a post-processing code performing nucleosynthesis calculations where abundances for many species are obtained (described in detail by Karakas et al. 2002; Karakas & Lattanzio 2007; Karakas 2010). The parameters were chosen to reflect the elemental abundances of most of the PNe in our sample, while oxygen is used as a metallicity indicator. We computed models with $Z = 0.02$ and $Z = 0.008$ using scaled solar abundances from Anders & Grevesse (1989), and $Z = 0.01$ using the revised solar elemental abundances from Asplund et al. (2005). These models were described in Karakas (2010) for $Z = 0.008$, Karakas et al. (2010) for $Z = 0.01$, and Karakas et al. (2012) for $Z = 0.02$. The models with 1.75M$_{\odot}$ and 3M$_{\odot}$, $Z = 0.02$ were not presented in Karakas et al. (2012), here calculated using the same parameters (mass loss and initial abundances). As the AGB stars with > 6.5M$_{\odot}$ likely evolve too quickly to form observable PNe, we consider models with masses between 1.5 and 6.5 M$_{\odot}$. As noted in Table 3.12, this mass range includes all major AGB nucleosynthetic events, namely the core helium flash (CHe), TDU and HBB. Only high-mass models with HBB would evolve into Type I PNe, whereas low-mass models with CHe tend to produce carbon-rich PNe (Karakas et al. 2009).

Table 3.12: PN yields by number, on a logarithmic scale where H = 12, obtained from the AGB stellar models with initial mass $M_{\rm int}$ and metallicity Z. The current core mass $M_{\rm core}$ is also given (the new AGB nucleosynthesis calculations were received from A. Karakas).

$M_{\rm int}/{\rm M}_{\odot}$	$M_{\rm core}/{\rm M}_{\odot}$	He/H	C/H	N/H	O/H	Ne/H	Ar/H	Cl/H	Experience [a]
$Z = 0.02$									
1.75	0.610	11.05	8.83	8.25	8.76	8.08	6.45	5.26	CHe
3.0	0.678	11.08	9.08	8.33	8.73	8.24	6.46	5.28	TDU
4.0	0.764	11.06	9.06	8.34	8.71	8.16	6.45	5.27	TDU
4.5	0.849	11.06	8.90	8.37	8.71	8.08	6.45	5.26	TDU
5.0	0.867	11.08	8.74	8.70	8.71	8.08	6.46	5.27	TDU,HBB
6.0	0.908	11.12	8.25	8.94	8.68	8.08	6.47	5.28	TDU,HBB
$Z = 0.01$									
1.8	0.585	11.04	9.04	8.10	8.61	8.04	6.29	5.11	CHe,TDU
3.0	0.683	11.04	9.05	8.15	8.57	8.14	6.29	5.11	TDU
6.0	0.923	11.11	8.18	8.84	8.51	7.90	6.31	5.13	TDU,HBB
$Z = 0.008$									
2.5	0.663	11.03	9.16	8.04	8.54	8.42	–	–	TDU
4.0	0.836	10.99	8.91	8.05	8.52	7.82	–	–	TDU,HBB
4.5	0.861	11.04	8.39	9.04	8.51	7.91	–	–	TDU,HBB
6.0	0.948	11.11	8.12	9.04	8.35	7.82	–	–	TDU,HBB

[a] The models experience the core He-flash (CHe), the third dredge-up (TDU), and the hot bottom burning (HBB)

Elemental abundances predicted by the AGB stellar models can be compared to the observations presented in Table 3.11. We see that about half of the sample have nearly solar metallicity, 2 PNe showing super-solar metallicity (M 3-15 and Hen 3-1333) and the remaining PNe having half-solar to LMC metallicities. We can compare predictions for the models with $Z = 0.01$, 0.02 and 0.008 to our observations. But, we do not have any calculated model for super-solar metallicity. For example, we see that an AGB model with $Z = 0.02$ and $3{\rm M}_{\odot}$

can likely produce the abundance pattern of Th 2-A. Similarly, a model with $Z = 0.01$ and 3M$_{\odot}$ likely makes Pe 1-1, and a model with $Z = 0.02$ and 4.5M$_{\odot}$ may produce M 1-25. We note that AGB modeling parameters, namely mass loss and convection, are very uncertain, so variations in either would alter the predicted elemental yields of C, N, O and Ne, but not Ar and Cl. For example, higher mass loss will lead to a shorter AGB lifetime and less TDU episodes, so a smaller C/O ratio is produced from a model with $\sim$3M$_{\odot}$ (Marigo 2002; Stancliffe & Jeffery 2007; Karakas 2010). More efficient convection would lead to hotter temperatures during HBB, so it makes a lower C/O ratio and a larger N/O ratio (e.g. Ventura & D'Antona 2005; Ventura et al. 2013).

We notice that the AGB models that make C-rich PNe, defined to have $\mathrm{C/O} > 1$, never produce N-rich PNe, $\mathrm{N/O} > 0.5$ except for the model with 5M$_{\odot}$ and 6M$_{\odot}$, $Z = 0.02$. Even in the massive model with $Z = 0.02$, the C/O ratio is just above unity. However, two Type I PNe in our sample, PB 6 and M 1-32, are extremely C-rich with $\mathrm{C/O} > 1$. HBB would destroy carbon, so they cannot have simultaneously very high C/O ratios and high N/O based on our AGB stellar models. Moreover, the post-AGB lifetimes for intermediate-mass AGB stars with HBB are likely so short (50-100 years), which unlikely make observable PNe (e.g. Blöcker 1995a). Therefore, alternative ways must make high N/O in those PNe (see discussions by Karakas et al. 2009). Rapid rotation on the main sequence can lead to higher N/O (and He/H) ratios after the first dredge-up, which carries through to the AGB phase (Charbonnel & Lagarde 2010; Ekström et al. 2012; Stasińska et al. 2013). The stellar rotation can be sped by a binary companion, leading to higher N/O ratios.

Fig. 3.16 shows the elemental abundances for the PNe of our sample with respect to the solar abundances taken from the recent compilation by Asplund et al. (2009). The oxygen abundance can be used as a metallicity indicator. We notice that the oxygen abundance is about the solar value for nearly half of the PNe. Assuming that these PNe evolved from the progenitor stars with solar metallicity, elements are destroyed or produced should lie below or above. We see that all PNe show large C and N enhancement and a small He enhancement. The carbon is dredged from the He-burning shell to the envelope by TDU during the AGB. The helium is also brought to the surface during different dredge-up episodes. The nitrogen enhancement could be attributed to HBB or alternative ways such as stellar rotation or/and binarity. The Ne is not expected to be altered during the AGB. Karakas et al. (2009) found that the neon abundance can be enhanced in lower mass AGB models (2.5 and $3M_{\odot}$) via the partial mixing of protons, but Ne is mildly increased (by ~ 0.3 dex) through HBB and dredge-up in the metal-poor AGB star models ($Z = 0.004$ and 0.008) with initial masses of 5 and $6M_{\odot}$. The S, Cl and Ar abundances are generally supposed to be unchanged by AGB nucleosynthesis. The argon abundance is about solar except two PNe, although S and Cl abundances show a departure from solar, as seen in Fig. 3.16. This is more likely the observational errors. However, neutron captures mildly increase chlorine abundance in the metal-poor massive ($\gtrsim 3M_{\odot}$) AGB models (Karakas et al. 2009). However, we see that chlorine is below in comparison to the oxygen metallicity, which may be because of some measurement errors and/or *icf* methods. We notice that sulfur abundance is less than the metallicity given by oxygen in many PNe, which could be due to the depletion of S into dust (Pottasch & Bernard-Salas 2006).

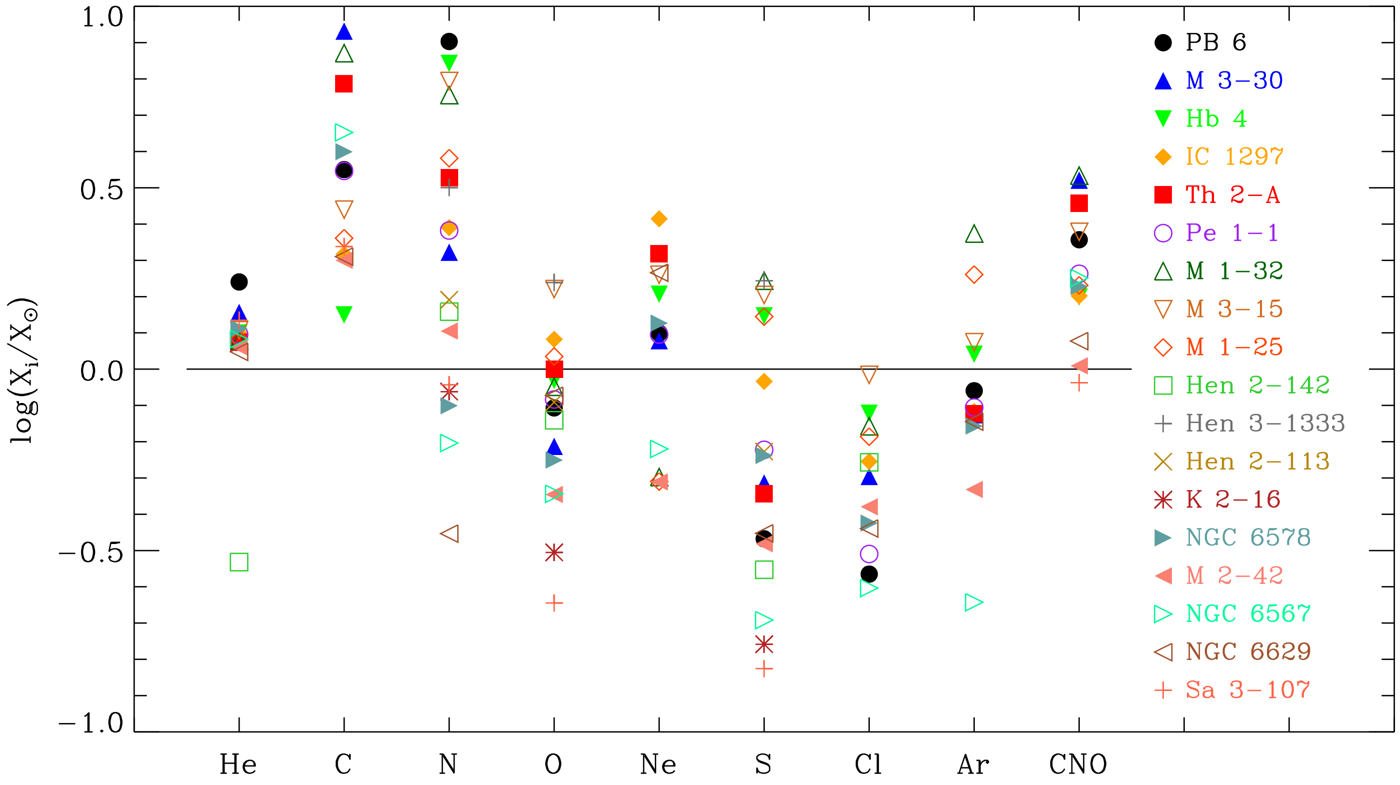

Figure 3.16: Elemental abundances with respect to solar abundances. Helium and carbon derived from ORLs, and other elements derived from CELs. Abundances at the solid line are equal to solar abundances.

3.6.2 Abundance discrepancy and temperature dichotomy

In Section 3.4.4, it was found that there is a dependence of the nebular ORL/CEL ADFs upon the dichotomy between temperatures derived from forbidden lines and those from He I recombination lines, $T_{\rm e}({\rm CELs}) - T_{\rm e}({\rm He\,I})$, and the intrinsic nebular surface brightness, $\log S({\rm H}\beta)$. It has been known that the ORL/CEL ADFs are closely correlated with the difference between $T_e([{\rm O\,III}])$ and $T_e({\rm BJ})$ (Liu et al. 2001, 2004a; Tsamis et al. 2004; Wesson et al. 2005; Wang & Liu 2007). These correlations suggests that the observed ORLs possibly originate from cold ionized gas located in metal-rich clumps inside the nebulae. The correlation between the nebular ADFs and the intrinsic Hβ surface brightness found here is consistent with previous results (Liu et al. 2004a; Tsamis et al. 2004). Moreover, Wang & Liu (2007) found that the ADFs increase with decreasing the nebular 6-cm radio surface brightness. Nebular surface brightness decreases as PN evolves and expands, and its density drops, so it could be a parameter describing the PN evolution. We see that the ADFs are larger for lower surface brightness objects, i.e. old evolved PNe.

The correlation between the ORL/CEL ADFs and the temperature dichotomy has been predicted by the bi-abundance nebular model first proposed by Liu et al. (2000), but the origin of such material is as yet unknown. The born-again scenario (Iben & Renzini 1983; Iben et al. 1983b) is one possibility, whereby H-deficient material would have been ejected from the stellar surface during the (very-) late thermal pulse. The detailed analysis of the 'born-again' planetary nebula Abell 58, surrounding V605 Aql described as an older twin of Sakurai's object, by Wesson et al. (2008) supported the idea that its hydrogen-deficient knot contains some very cold ionized material. But, the knot of Abell 58 is found to be oxygen-rich whereas the central star is carbon-rich, which was not predicted by the single-star born-again theory. Alternatively, Liu (2003) suggested that H-deficient material could be introduced by the evaporation and destruction of planets of stars. The implications of these two scenarios need more observations and detailed abundance analysis of a large sample of PNe.

Previously, Peimbert (1971) proposed that the temperature dichotomy must be related to the abundance discrepancy. Torres-Peimbert et al. (1980) also suggested that the abundance discrepancy is produced by spatial temperature fluctuations. However, Liu et al. (2000) found that temperature fluctuations cannot explain the ionic abundances derived from infrared (IR) fine-structure CELs. IR fine-structure CELs are insensitive to electron temperature (and temperature fluctuations), thus resulting in reliable ionic abundances. Liu et al. (2004a) also showed that temperature fluctuations cannot explain the large ADFs. As argued by (Tsamis et al. 2004) there is no correlation between the ADFs and the excitation energy of the UV, optical or IR CEL transition, suggesting temperature fluctuations cannot be not the main cause of the abundance discrepancy in a chemically homogeneous medium. The abundance analysis of 22 PNe by Wesson et al. (2005) showed no correlation between the temperature dichotomy and temperature fluctuations, implying other mechanism made ORLs. Spatial-resolved abundance analysis by Tsamis et al. (2008) also showed small temperature fluctuations, indicating the existence of a distinct metal-rich component inside the nebula.

Recently, Nicholls et al. (2012, 2013) proposed the κ-distribution of electron energies to explain the abundance discrepancy and temperature dichotomy, which might be a potential explanation. In this scenario, the electrons in the gas have a non-thermal equilibrium energy distribution whose departure from the Maxwell-Boltzmann distribution characterized by a κ index. Dopita et al. (2013) conclude that κ-distributions with $\kappa \sim 20$, or somewhat larger, are able to predict the abundance discrepancy and the temperature dichotomy in H II Regions. Zhang et al. (2014) found that both the scenarios, bi-abundance models and κ-distributed electrons, are adequately consistent with observations of four PNe with very large ADFs, and concluded the spectra are emitted from cold and low-κ plasmas rather than a single Maxwell-Boltzmann electron energy distribution. It is unclear whether chemically inhomogeneous plasmas introduce non-Maxwell-Boltzmann equilibrium electrons to the nebula. The relations between both the scenarios should be evaluated further.

In conclusion, our detailed abundance analysis of PNe with WR-type stars has allowed us to correlate the abundance discrepancy, temperature dichotomy, and nebular surface brightness with each other. In Section 3.4.4, we saw that that the ADF is closely related to the nebular surface brightness, and it is larger in old evolved nebulae. However, it has no correlation with the stellar characteristics. The new correlations have put forward a resolution of the ORL/CEL problem, which appears to be explained by a hitherto unknown component within the nebula. More deeper high-resolution spectroscopy and further investigation will no doubt lead to a better understanding of the ORL versus CEL problem.

4

Hb 4: a planetary nebula with FLIERs

The contents of this chapter were submitted for publication in the Monthly Notices of the Royal Astronomical Society. The authors were A. Danehkar, B. Ercolano, R. Wesson, W. Steffen and Q. A. Parker. The 6.5-m Magellan telescope observation and the emission line fluxes used in this chapter are from García-Rojas et al. (2012).

4.1 Introduction

The high-excitation planetary nebula Hb 4 (PN G003.1+02.9) belongs to the particular class of planetary nebulae (PNe) with low-ionization structures (LISs). The central star of Hb 4 has been classified as Wolf-Rayet [WO3] (Acker & Neiner 2003). This object has been the subject of some kinematic studies (Lopez et al. 1997) (see Chapter 2) and recent abundance analysis (García-Rojas et al. 2012, 2013). The images of Hb 4 taken by the *HST* (programme ID 6347) show that the inner shell has a bright ring-like morphology with angular dimensions of about 7.2 arcsec $\times$ 5.7 arcsec. It is seen that Hb 4 possesses a tenuous halo with a diameter of about 17 arcsec. A pair of point-symmetric LISs are located at the distance about 10 arcsec from the central star of Hb 4. The long-slit spectra analyzed by Lopez et al. (1997) associated these point-symmetric LISs with relatively high velocities of ±150 km s^{-1} with respect to the main body. These highly collimated outbursts have been found in other PNe, the so-called fast, low-ionization emission regions (FLIERs; Balick et al. 1993, 1994, 1998). It has been found that the strength of the [N II] λ6584 line with respect to Hα in the FLIERs of Hb 4 is typically larger than its shell (Hajian et al. 1997). Previously, Balick et al. (1994) claimed the presence of nitrogen enrichment by factors of 2–5 in the FLIERs of some PNe. However, Hajian et al. (1997) challenged these conclusions. Gonçalves et al. (2003, 2006) suggested that empirically derived N overabundance seen in FLIERs are a result of inaccurate ionization correction factors (*icf*s) applied in the empirical analysis. Gonçalves et al. (2006) constructed a chemically homogeneous photoionization model of NGC 7009, which can reproduce the spectroscopic characteristics of different regions, including the shell and the FLIERs.

Hb 4 shows a moderate abundance discrepancy factor of ADF(O^{2+}) = O$^{2+}_{\rm ORLs}$ / O$^{2+}_{\rm CELs}$ $\simeq 4$ (García-Rojas et al. 2013) (see Chapter 3). Additionally, we notice that electron temperatures measured from He I lines are much lower than those measured from CELs. The abundance discrepancies have been seen in many PNe in the range 1.6–3 (e.g. Liu et al. 2000, 2001; Tsamis et al. 2004; Liu et al. 2004a; Wesson & Liu 2004; Wesson et al. 2005; Tsamis et al. 2008). However, a small fraction (5–10%) of them have ADFs of 4–80 (see review by Liu et al. 2006). Few PNe show extremely large ADFs, for example Abell 30 (ADF = 700; Wesson et al. 2003; Ercolano et al. 2003b). Temperature fluctuations have been proposed to solve the problem (Peimbert 1967, 1971). However, temperature fluctuations were found to be very small in some PNe, which show large abundance discrepancies (e.g. Rubin et al. 2002; Wesson & Liu 2004). To solve the problem, Liu et al. (2000) suggested a bi-abundance model, containing some cold hydrogen-deficient small-scale structures, highly enriched in helium and heavy elements, embedded in the diffuse warm nebular gas of normal abundances. Wesson et al. (2005) found that most PNe follow the relation

T_e(CELs) $>$ T_e(He I) $>$ T_e(O II ORLs), already predicted by the bi-abundance model. The feasibility of the bi-chemistry model has been evaluated in photoionization models of Abell 30 (Ercolano et al. 2003b) and NGC 6153 (Yuan et al. 2011).

The objective of the present study is to assess how photoionization effects may enhance [N II] emission in the FLIERs, assuming chemically homogeneous abundances. In addition, we examine whether a bi-abundance model can explain the observed ORLs. We conduct this study by using the Monte Carlo three-dimensional radiative transfer code MOCASSIN by Ercolano et al. (2003a, 2005, 2008). Our observations, kinematic structure, and empirical results are described in Sections 4.2. Our first photoionization model is described in Section 4.3, aimed at solving overabundance of nitrogen in the FLIERs. In Section 4.4, we use a bi-abundance model to predict the ORLs. Our final conclusions are given in Section 4.5.

4.2 Observations

The observations used to constrain the photoionisation model of Hb 4 are listed in Table 4.1. The integral field unit (IFU) observations (see Chapter 2) were carried out at the Siding Spring Observatory, using the 2.3-m ANU telescope and the Wide Field Spectrograph (WiFeS; Dopita et al. 2007, 2010). The gratings used were the B7000/R7000 grating combination and the RT 560 dichroic, giving wavelength coverage from 4415-5589 Å in the blue and 5222-7070 Å in the red, and mean spectral resolution of 0.83 Å full width at half-maximum (FWHM) in the blue and 1.03 Å FWHM in the red. The WiFeS has a field-of-view (FOV) of $25'' \times 38''$ and spatial resolution of $1''.0 \times 0''.5$. The spectral resolution of $R(=\lambda/\Delta\lambda) \sim 7000$ corresponds to a FWHM of ~ 45 km s^{-1}. We used the classical data accumulation mode, so a suitable sky window has been selected from the science data for the sky subtraction purpose. We also acquired

Table 4.1: Journal of the Observations for Hb 4.

Date (UT)	λ-range(Å)	FWHM(Å)	Spect.	Exp.Time (s)
		ANU 2.3-m		
2010/04/21	4415–5589	0.83	WiFeS	300, 1200
	5222–7070	1.03	WiFeS	300, 1200
		Magellan 6.5-m		
2010/06/05	3350–5050	0.15	MIKE	60, 1500
	4950–9400	0.25	MIKE	60, 1500

biases, dome flat frames, Cu-Ar arc exposures, wire frames, and the standard star EG 274 and LTT 3864 for the data reduction process. We reduced the data using the IRAF pipeline wifes and the same reduction procedure described in detail in Chapter 2. The deep optical observations were obtained from García-Rojas et al. (2012, 2013), which were carried out at Las Campanas Observatory, using the 6.5-m Magellan telescope and the double echelle MIKE spectrograph. The standard grating settings yield wavelength coverage from 3350-5050 Å in the blue and 4950-9400 Å in the red; the mean spectral resolution is 0.15 Å FWHM in the blue and 0.25 Å FWHM in the red.

4.2.1 Kinematic structure

Fig. 4.1(a) shows the spatially resolved flux intensity and radial velocity map produced by fitting Gaussian profiles to the emission line Hα for spaxels across the IFU field. We obtained the F658N narrow-band image from the *HST* archive, as shown in Fig. 4.1(b). The radial velocity map shows the outer pair of FLIERs. The *HST* image depicts that the main shell has a torus morphology, which is not noticeable in the IFU maps due to the low spatial resolution. We also notice that the torus shell is deformed and the FLIERs are not exactly aligned vertically, which could be because of interaction with the interstellar medium (ISM). Fig. 4.1(c) shows the morpho-kinematic model implemented using the 3D modeling program SHAPE (Steffen & López 2006; Steffen et al. 2011). For best comparison with our IFU maps, the emissivity and velocity grids have then been exported from the SHAPE model and processed in the same way as the IFU data (described in detail in Chapter 2). The model consists of a thick torus, two point-symmetric thin knots, inner thin halo, and outer tenuous halo. We assumed that the structures follow a Hubble-type velocity law (Steffen et al. 2009), where the expansion velocity increases uniformly with distance from the center. Taking the inclination of $40^{\circ} \pm 5^{\circ}$ found by the best-fitting model, we derived a velocity of $V_{\rm FLIER} = \pm 150 \pm 10$ km s^{-1} for the FLIERs, similar to the value found by Lopez et al. (1997). We also measured an expansion velocity of $V_{\rm exp} = 23 \pm 4$ km s^{-1} by means of the half width at half maximum (HWHM) method from an aperture with a diameter of 6.5 arcsec located on the inner shell, in agreement with what found by Robinson et al. (1982) and Lopez et al. (1997). We assumed $V_{\rm exp} = V_{\rm HWHM}$, although Schönberner et al. (2010) found that the HWHM method underestimates the true values of high velocities, but suitable for slowly expanding objects.

Fig. 4.2 shows high resolution long-slit spectra of Hb 4 obtained with the Manchester Échelle Spectrometer (MES) on the 2.1-m telescope at the San Pedro Martír Observatory (SPM Kinematic Catalogue; López et al. 2012). Using high-resolution long-slit spectroscopy obtained with MES-SPM, we get a better understanding of the structure of Hb 4 analogous to the IFU observations. Long-slits a and c together with deep imagery shows the symmetry axis of the nebula. The morpho-kinematic model that best reproduces the features of the longslit spectra has an inclination of $40^{\circ} \pm 10^{\circ}$, similar to the results of the IFU observation. However, the kinematic feature of the inner shell is clear in the [N II] emission, which shows a expanding torus structure corresponding to $V_{\rm exp} = 25 \pm 5$ km s^{-1}, in agreement with the HWHM method. The inner shell

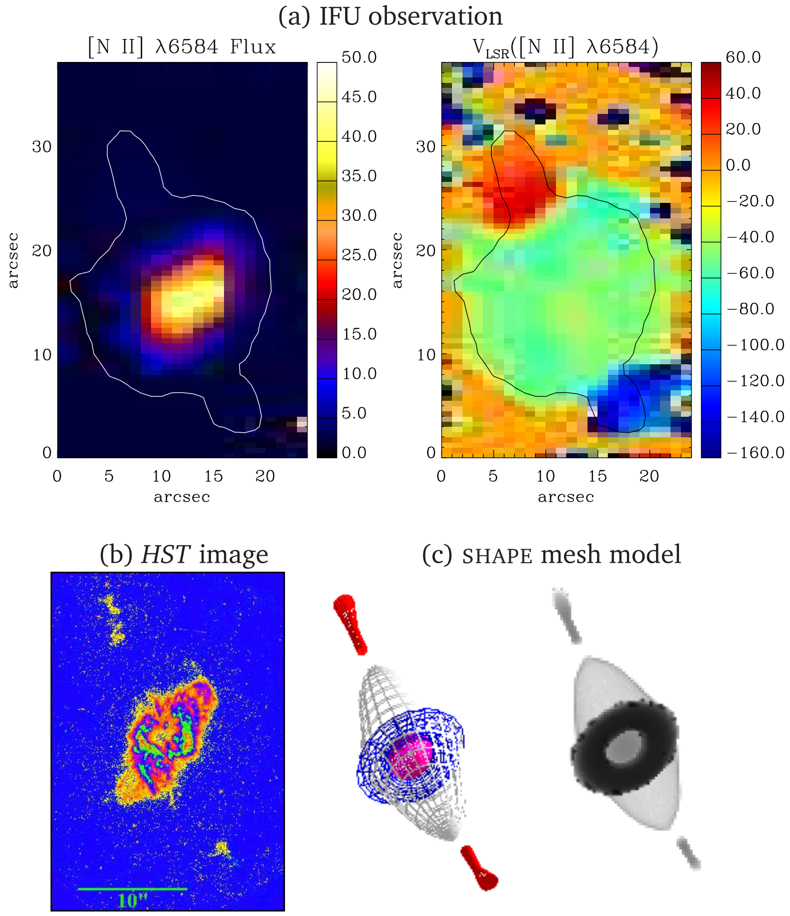

Figure 4.1: (a) IFU maps of Hb 4 in Hα λ6563 Å (bottom). From left to right: spatial distribution maps of flux intensity on a logarithmic scale and local standard of rest (LSR) radial velocity. Flux unit is in 10^{-15} erg s^{-1} cm^{-2} spaxel^{-1} and velocity in km s^{-1}. North is up and east is toward the left-hand side. White/black contour lines show the distribution of the narrow-band emission of Hα in arbitrary unit obtained from the SuperCOSMOS Hα Sky Survey (Parker et al. 2005). (b) The *HST* image on a logarithmic scale taken by the F658N filter (Observing program 6347; PI. Borkowski, 1996). (c) The SHAPE mesh model before rendering at the best-fitting inclination and corresponding rendered model.

probably is the only element that has a memory of mass-loss at the end of the AGB phase. The long-slit observation also indicates that the point-symmetric structures travel at a maximum velocity of $150 \pm 10\,\mathrm{km\,s^{-1}}$ with respect to the center of the nebula.

4.2.2 Nebular empirical analysis

A list of observed lines and their measured fluxes is presented in Table 4.6. All line fluxes were measured using Gaussian curve fitting. The emission line identification, laboratory wavelength, and multiplet number, are given in columns 1–3, respectively. Columns 4–6 present the observed fluxes of the inner shell (MIKE spectra), northern FLIER and southern FLIER (WiFeS spectra), corrected for interstellar extinction, according to the logarithmic formula $I(\lambda) = F(\lambda) \times 10^{c(\mathrm{H}\beta)[1+f(\lambda)]}$, where $F(\lambda)$ and $I(\lambda)$ are the observed and intrinsic line flux, respectively, and $f(\lambda)$ is the standard Galactic extinction law of Howarth (1983) for a total-to-selective extinction ratio of $R_V = A(V)/E(B-V) = 3.1$, and normalized such that $f(\mathrm{H}\beta) = 0$. The Balmer emission lines were used to derive the logarithmic extinction at Hβ for the theoretical line ratio of the case B recombination ($T_{\mathrm{e}} = 10\,000\,\mathrm{K}$ and $N_{\mathrm{e}} = 7000\,\mathrm{cm^{-3}}$; Hummer & Storey 1987). All fluxes in columns 4–6 are given relative to Hβ, on a scale where H$\beta = 100$. Fig. 4.3 shows flux maps for emission lines emitted from different ionization zones, namely [N II] and [O III] with respect to Hα. It indicates the [N II] emission is higher at the FLIERs and the outer edge of the inner shell. We also notice that the [O III] emission fluxes at the inner shell and outer tenuous halo are much higher than what observed at the FLIERs.

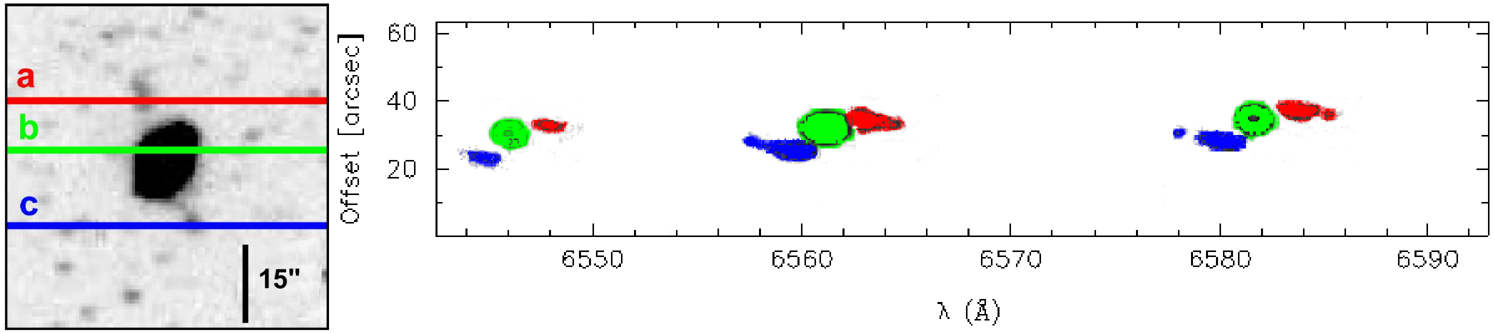

Figure 4.2: Left panel: Deep Hα+[N II] imagery of Hb 4 obtained with MES-SPM and the positions of the three SPM long-slits. Right panel: Long-slit Hα+[N II] spectra of Hb 4 acquired with MES-SPM for slits a (red), b (green) and c (blue).

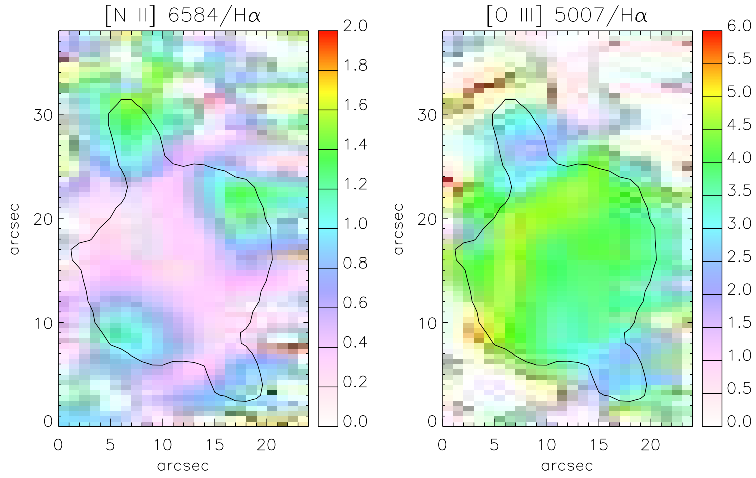

(a) (b)

Figure 4.3: Flux maps of (a) [N II] λ 6584 Å and (b) [O III] λ 5007 Å with respect to the Hα recombination line emission. All fluxes dereddened using the logarithmic extinction $c(\mathrm{H}\beta) = 1.8$ and the case B recombination theoretical model ($T_{\mathrm{e}} = 10\,000$ K and $N_{\mathrm{e}} = 7000\,\mathrm{cm}^{-3}$).

The results derived from the plasma diagnostics are listed in Table 4.2, for the emission lines measured from the MIKE spectra. We obtained the electron temperatures (T_{e}) and densities (N_{e}) from temperature-sensitive and density-sensitive emission lines by solving the equilibrium equations of level populations for multilevel (≥ 5) atomic models using the EQUIB code (see the NEAT code by Wesson et al. 2012). The atomic data sets used for the plasma diagnostics and abundance analysis include the improved He I emissivities by Porter et al. (2013), and those used by Danehkar et al. (2014), and the remaining atomic data the same as Wesson et al. (2012). For the plasma diagnostics, we assumed a representative electron temperature of 10 000 K to derive N_{e} from density-sensitive emission line ratios; and an electron density of 7000 cm^{-3} to derive T_{e} from temperature-sensitive emission line ratios. The recombination contributions to nebular auroral lines are estimated using the formulas given by Liu et al. (2000). From the values given in Table 4.4 and $T_{\rm e}$(He I)= 7400 K, the contribution of recombination excitation of N^{2+}, O^{2+} , O^{3+} to the observed fluxes of [N II] λ5755, [O II] $\lambda\lambda$7320,7330 and [O III] λ4363 are estimated to be 14, 25 and 3 percent, respectively; where the O^{3+}/H^{+} ratio is estimated using $O^{3+}/H^{+} = [(He/H^{+})^{2/3} - 1] \times (O^{+}/H^{+} + O^{2+}/H^{+})$ and assuming the O^{+}/H^{+} ratio is negligible. The high temperature derived from the [O II] lines may be attributed to the differences between the collision strengths calculated by Pradhan et al. (2006) and Kisielius et al. (2009). To determine the electron temperature from the He I lines, we used analytic formulae given for the emissivities of He I lines by Benjamin et al. (1999) and new fitting parameters by Zhang et al. (2005). The correct choice of electron densities and temperatures is important for the abundance analysis.

Table 4.3 presents the empirical ionic abundances derived from the observed CELs of the inner shell, respectively (MIKE spectra). The results for the FLIERs were measured in Chapter 3), although our observations did not cover [O II] lines, so we assumed the [O II] lines measured by García-Rojas et al. (2012). We determined abundances for ionic species of N, O, Ne, S, Cl and Ar from the observed CELs. In our determination, we adopted $T_{\rm e} = 10$ kK and $N_{\rm e} = 7000\,{\rm cm}^{-3}$ based on the plasma diagnostics. Solving the equilibrium equations, using the EQUIB code, yields level populations and line sensitivities for given $T_{\rm e}$ and $N_{\rm e}$. Once the level populations are solved, the ionic abundances, X^{i+}/H^{+}, can be derived from the observed CELs. We did not use the [O II] $\lambda\lambda$7320,7330 lines for the O^{+}/H^{+} ratio, since the abundances derived from them are usually higher than those from λ3727 doublet, see Table 4.3. This could be attributed to errors in the atomic data (see Kisielius et al. 2009). The total elemental abundances listed in Table 4.5 were calculated using the *icf* formulae (Tabel 13 in Wang & Liu 2007).

Several heavy element ORLs of the inner shell are well detected by the MIKE spectra. Using the effective recombination coefficients, we determined abun-

Table 4.2: Plasma diagnostics.

Ion	Lines	Result
		N_e (cm^{-3}) [a]
[S II]	$I(\lambda6731)/I(\lambda6716)$	7010 ± 3460
[O II]	$I(\lambda3729)/I(\lambda3726)$	3400 ± 1850
[Cl III]	$I(\lambda5538)/I(\lambda5518)$	5930 ± 1460
[S III]	$I(\lambda9069)/I(\lambda6312)$	7237 ± 537
[Ar IV]	$I(\lambda4740)/I(\lambda4711)$	7990 ± 1420
		T_e (K) [b]
[N II]	$I(\lambda6548+\lambda6584)/I(\lambda5755)$	9800 ± 780
[N II] [c]	$I(\lambda6548+\lambda6584)/I(\lambda5755)$	9230 ± 690
[O II]	$I(\lambda3728)/I(\lambda7325)$	17980 ± 3290
[O II] [c]	$I(\lambda3728)/I(\lambda7325)$	13340 ± 2890
[O III]	$I(\lambda4959+\lambda5007)/I(\lambda4363)$	10020 ± 300
[O III] [c]	$I(\lambda4959+\lambda5007)/I(\lambda4363)$	9910 ± 310
He I	$I(\lambda5876)/I(\lambda4471)$	3980 ± 430
He I	$I(\lambda6678)/I(\lambda4471)$	7570 ± 1020
He I	$I(\lambda7281)/I(\lambda6678)$	8090 ± 1350
He I	$I(\lambda7281)/I(\lambda5876)$	9940 ± 1830

[a] Assuming $T_e = 10\,000$ K;

[b] Assuming $N_e = 7000\,\mathrm{cm}^{-3}$;

[c] Corrected for recombination contribution to the auroral lines.

dances for ionic species of He, C, N and O from the observed ORLs, as listed in Table 4.4. In our calculation, we adopted the mean He I temperature of 7.4 kK, which is expected to be the temperature of the cold metal-rich inclusions embedded in the nebula (Liu et al. 2000). The He^{+}/H^{+} abundance was derived from the intensities of the λ4471, λ5876 and λ6678 He I lines, weighted 1:3:1 according to their approximate intensity ratios. The He^{2+}/H^{+} abundance was derived from the He II λ4686 line. Our derived ORL total abundances for C, N

Table 4.3: Empirical ionic abundances of the inner shell derived from CELs.

X^{i+}/H^+	Lines	$N_{X^{i+}}/N_{H^+}$ Ring [a]	N-FLIER [b]
N^+	[N II] $\lambda\lambda$6548, 6584	1.53(−5)	3.91(−5)
O^+	[O II] $\lambda\lambda$3726, 3729	1.81(−5)	1.20(−5) [d]
O^+	[O II] $\lambda\lambda$7320, 7330	[3.27(−5)]	–
O^+ [c]	[O II] $\lambda\lambda$7320, 7330	[2.46(−5)]	–
O^{2+}	[O III] $\lambda\lambda$4959, 5007	3.82(−4)	3.29(−4)
Ne^{2+}	[Ne III]$\lambda\lambda$3868, 3967	1.18(−4)	–
S^+	[S II] $\lambda\lambda$6716, 6731	4.24(−7)	1.01(−6)
S^{2+}	[S III] $\lambda\lambda$6312, 9069	8.69(−6)	–
Cl^{2+}	[Cl III] $\lambda\lambda$5517,5537	9.94(−8)	–
Ar^{2+}	[Ar III] λ5191, λ7135, λ7751	1.75(−6)	–
Ar^{3+}	[Ar IV] $\lambda\lambda$4711,4740	1.07(−6)	–
Ar^{4+}	[Ar V] $\lambda\lambda$6435,7005	2.11(−8)	–

[a] Assuming $T_e = 10\,000$ K and $N_e = 7000\,\mathrm{cm}^{-3}$.

[b] Assuming $T_e = 10\,000$ K and $N_e = 1000\,\mathrm{cm}^{-3}$.

[c] Corrected for recombination contribution.

[d] Adopting the [O II] line fluxes from García-Rojas et al. (2012).

Notes: [ ] values in square brackets are not used for our analysis.

and O are calculated using the mean of the ionic abundances derived from the observed ORLs, listed in Table 4.5, and the *icf* formulae given by Wang & Liu (2007).

According to the strength of He II λ4686 relative to Hβ, the Hb 4 is classified as the intermediate excitation class with EC = 5.8 (Dopita & Meatheringham 1990). This intermediate excitation class is associated with $T_{\rm eff} = 113$ kK according to the transformation given by Dopita & Meatheringham (1991) for Magel-

Table 4.4: Empirical ionic abundances derived from ORLs.

X^{i+}/H^{+}	λ (Å)	Mult	$N_{X^{i+}}/N_{H^{+}}$ [a]
He^{+}	4471.50	V14	0.094
	5876.66	V11	0.101
	6678.16	V46	0.093
	Average		0.097
He^{2+}	4685.68	3.4	0.020
He/H			0.117
C^{2+}	4267.15	V6	6.87(−4)
	6151.43	V16.04	5.64(−4)
	6461.95	V17.04	7.16(−4)
	5342.38	V17.06	4.48(−4)
	Average		6.04(−4)
C^{3+}	4647.42	V1	3.94(−4)
	4651.47	V1	3.66(−4)
	Average		3.80(−4)
N^{2+}	5666.63	V3	4.93(−4)
	5676.02	V3	5.10(−4)
	5679.56	V3	5.69(−4)
	5686.21	V3	5.41(−4)
	5710.77	V3	7.66(−4)
	4607.16	V5	9.97(−4)
	4630.54	V5	6.85(−4)
	Average		6.52(−4)
N^{3+}	4379.11	V18	2.08(−4)
	Adopted		2.08(−4)

[a] Assuming $T_{\rm e} = 7\,400$ K and $N_{\rm e} = 7000\,{\rm cm}^{-3}$.

Table 4.4: (continued)

X^{i+}/H^{+}	λ (Å)	Mult	$N_{X^{i+}}/N_{H^{+}}$ [a]
O^{2+}	4638.85	V1	1.17(−3)
	4641.81	V1	3.11(−3)
	4649.13	V1	1.50(−3)
	4661.63	V1	1.43(−3)
	4676.23	V1	1.06(−3)
	4317.14	V2	1.00(−3)
	4349.43	V2	9.38(−4)
	4366.89	V2	1.97(−3)
	4416.97	V5	3.29(−3)
	4075.86	V10	3.44(−3)
	4072.16	V10	1.24(−3)
	4119.21	V20	1.53(−3)
	4275.55	V67a	1.23(−3)
	4609.44	V92a	1.66(−3)
	Average		1.75(−3)

lanic Cloud PNe. We notice that He II λ4686 emission line is also predicted by a blackbody model with $T_{\rm eff} = 110$ kK. This could be attributed to either unknown properties of the H-deficient ionizing flux or an undetected ionizing companion (see e.g. SuWt 2, Danehkar et al. 2013). However, He II λ4686 emission line can be reproduced using a H-rich non-local thermodynamic equilibrium (NLTE) model atmosphere with $T_{\rm eff} = 90$ kK (see Section 4.3), in agreement with the stellar temperature found by the spectral analysis of the [WO3] central star of Hb 4 (Acker & Neiner 2003).

4.3 Chemically homogeneous model

The modeling is undertaken using the fully 3D Monte Carlo photoionization code MOCASSIN (version 2.02.70), described in detail by Ercolano et al. (2003a, 2005, 2008) in which the 3D radiative transfer of the stellar and diffuse field is self-consistently computed in an iterative way in a completely arbitrary distribution of gas density and chemical abundances. It allows us to study the nebula with an inhomogeneous density distribution, as well as including chemical inhomogeneities. The models were run on the VAYU computer cluster at Australian National University, consisting of 1492 nodes in SUN X6275 blades with 2 quad-core 2 930-MHz Intel Nehalem processors and 24 GB of memory each. The gas density distribution was constructed in $20 \times 20 \times 80$ cubic grids with the same size corresponding to 32 000 cubic cells of length 1.0×10^{16} cm each (assuming a distance of 3700 pc). The ionizing source was placed in a corner in order to take advantage of the axisymmetric morphology used. The nebular and stellar input parameters for the model (MC1) described in this section and the next section (MC2) are listed in Table 4.5. The atomic data sets used for the modeling include opacities from Verner et al. (1993) and Verner & Yakovlev (1995), hydrogen and helium free–bound coefficients of Ercolano & Storey (2006), and energy levels, collision strengths and transition probabilities from Version 7.0 of the CHIANTI database (Landi et al. 2012, and references therein).

4.3.1 Modeling strategy

The fundamental parameters for photoionization modeling are the hydrogen density in the ionized region, the nebular geometry, the nebula chemistry and the central star properties. The derived densities are listed in Table 4.2. The ionization potentials of S^{+} and O^{+}, respectively 10.4 and 13.6 eV, are bellow those of Cl^{2+} and Ar^{3+}, 23.8 and 40.7 eV, respectively. The [Cl III] and [Ar IV] doublets yield densities, which respectively are by a factor of 1.7 and 2.4 higher than the the value derived from [O II]. So, the emission lines emitted from different ionization zones may point to a moderate density inhomogeneity. It is likely that a slow dense superwind from the AGB phase created an inner compressed dense shell surrounded by a thin shell during the PN phase, as predicted by the generalized interacting stellar winds (GISW) theory (Kahn & West 1985). We adopted a nebular geometry according to the archival *HST* images and the morpho-kinematic model derived from the spatially resolved kinematics (see Section 4.2). But, distance adds a further complication to the geometry. Photoionization modeling could be better constrained by adopting a known distance. Once the distances are ascertained, other nebular parameters can be easily found. A method was developed by Tajitsu & Tamura (1998) gave a distance of $D = 2.3$ kpc for Hb 4, by fitting blackbody curves to *IRAS* fluxes. However, Stanghellini & Haywood (2010) statistically found $D = 5096$ pc for HB 4, by calibrating to few known distances of Galactic PNe. Moreover, Gesicki & Zijlstra (2007) derived a distance of 4 kpc using a photoionization model. In this chapter, we aimed to calibrate the distance by matching the Hβ luminosity $L(\mathrm{H}\beta)$ of the inner shell. We found that a blackbody model with stellar luminosity $L_{\star} = 4950\,\mathrm{L}_{\odot}$ and effective temperature $T_{\mathrm{eff}} = 110$ kK well produces the observed Hβ absolute flux of the nebula at a distance of 3.7 kpc. We initially tested a blackbody model with $T_{\mathrm{eff}} = 90$ kK and $L_{\star} = 4000\,\mathrm{L}_{\odot}$ derived by Acker et al. (2002). We then increased the effective temperature by 20 percent to produce the ionic helium abundance ratio $\mathrm{He}^{2+}/\mathrm{He}^{+}$ derived from the empirical analysis and the intrinsic flux of He II λ4686 emission line. However, we were able to match the He II λ4686 emission line flux by using a NLTE model atmosphere with $T_{\mathrm{eff}} = 90$ kK. We also adjusted the stellar luminosity to match the intrinsic fluxes of [N II] and [O III] emission lines. We initially adopted the elemental abundances derived from empirical analysis, but they were iteratively adjusted until the best emission-line spectrum was reproduced.

The first model referred to in this chapter as MC1 aimed at solving the problem of nitrogen overabundance in the FLIERs. The following steps were used to constrain the model MC1:

1. The dense torus was developed from the kinematic model, the *HST* images and the plasma diagnostics. The torus has a radius of $D(\mathrm{pc}) \times 3.8 \times 10^{13}$ cm from the center of the tube to its center, where D is the distance in pc. The radius of the tube is $D(\mathrm{pc}) \times 1.6 \times 10^{13}$ cm. The H number density of the torus was initially taken to be homogeneous and equal to $N_{\mathrm{H}} = 7000$ cm^{-3}.

2. The model was assumed to have a homogeneous abundance distribution. The element abundances derived from the empirical analysis were used for the initial model.

3. The distance to the nebula and the central star properties (T_{eff} and $L_{\star}$) were determined through comparison of the Hβ luminosity $L(\mathrm{H}\beta) = 4\pi \times D^2 \times I(\mathrm{H}\beta)$ (where D is the distance) with the intrinsic flux of $I_{\mathrm{H}\beta} = 20.4 \times 10^{-12}$ erg cm^{-2} s^{-1} measured from an aperture with a diameter of 6.5 arcsec located on the inner shell (in agreement with Acker et al. 1989, 1991b), and comparison of the predicted $\mathrm{He}^{2+}/\mathrm{He}^{+}$ with the empirical result. The distance of 3.7 kpc yielded the best match to the observed Hβ luminosity and it is also in agreement with 4 kpc found by Acker et al. (2002) and Gesicki & Zijlstra (2007).

4. The element abundances were adjusted to produce the best flux intensities of important emission lines, relative to Hβ (such as [N II] and [O III]) and the temperatures of the gas weighted by ionic species.

5. We developed an inhomogeneous density distribution for the torus to better match other emission lines (such as [O II]) and ionization structure. The density distribution of the torus was chosen to follow a power-law dependence on radius $N_{\mathrm{H}} \propto r^{-\alpha}$. The radial density dependence ($\alpha = 1 \ldots 2$) was iteratively changed until the nebula spectrum and thermal structure yield the best match to the observation and plasma diagnostics.

6. To match the flux intensities of [N II] and [O III] in the FLIERs, a larger

Table 4.5: Physical properties and model parameters.

	Empirical analysis				Models				
	Ring		N-FLIER		MC1			MC2 (Ring)	
Parameter	CEL	ORL	CEL	ORL	Ring	FLIER	Halo	H-poor	Normal
$T_{\rm eff}$ (kK)	90				90			90	
$L_\star$ ($L_\odot$)	4000				4950			4950	
Filling factor	–		–		1.00	1.00	1.00	0.053	1.00
$\langle N(H^+)\rangle$ (cm^{-3})	–		–		6508	2000	1250	10000	5942
$\langle N_e\rangle$ (cm^{-3})	$\sim$7000	–	$\sim$1000:	–	7315	2179	1520	10768	6748
Hβ fraction	0.996		0.004		0.908	0.007	0.085	0.188	0.812
Ionized mass ($M_\odot$)	–		–		0.085	0.003	0.080	0.005	0.075
He/H	–	0.117	–	0.071	0.11	0.11	0.11	0.30	0.11
C/H ($\times10^5$)	–	103.0	–	–	130.0	130.0	130.0	130.0	130.0
N/H ($\times10^5$)	38.08	89.61	111.1	–	12.7	12.7	12.7	225.0	11.0
O/H ($\times10^5$)	45.22	207.20	34.11	–	25.0	25.0	25.0	800.0	20.5
Ne/H ($\times10^5$)	13.97	–	–	–	6.2	6.2	6.2	100.0	6.8
S/H ($\times10^7$)	187.1	–	21.62	–	100.0	100.0	100.0	200.0	100.0
Cl/H ($\times10^7$)	2.14	–	–	–	1.4	1.4	1.4	2.5	1.64
Ar/H ($\times10^7$)	29.6	–	–	–	10.0	10.0	10.0	20.0	10.0

density model was developed, which also incorporates the torus previously constrained. The initial H number density of the FLIERs was taken to be $N_{\rm H} = 1000$ cm^{-3} derived from the plasma diagnostics, but it was adjusted to match the emission-line spectrum.

The density distribution

The three-dimensional density distribution grid was developed from the kinematic analysis and the *HST* images. The density distribution is a difficult input to constrain, so a model directly deduced from the plasma diagnostics is also favorable. We described the inner shell with a torus having a radius of 1.4×10^{17} cm from its center to the tube center, and a tube radius of 6.0×10^{16} cm. The *HST* imaging shows a variation of the Hα emission with radius, which led us to describe the density distribution of the torus by a power-law dependence on radius $N_{\rm H} = N_0 + N_1 (r/r_{\rm in})^{-\alpha}$, peaking to $N_{\rm H} = 8800$ cm^{-3} in the inner radius and decreasing to a minimum value of $N_{\rm H} = 7000$ cm^{-3} in the outer radius. We adopted the characteristic densities of $N_0 = 6600\,{\rm cm}^{-3}$ and $N_1 = 2200\,{\rm cm}^{-3}$, the radial density dependence of $\alpha = 1.85$. The inner radius is equal to $r_{\rm in} = 8.0 \times 10^{16}$ cm. The characteristic densities were adjusted to fit the intrinsic flux of the Hβ emission line. From the *HST* images and SPM long-slit of the Hα emission, we could describe the inside of the shell by a rim and inner caps. To have a lower computation time, we only used a sphere of radius 8.0×10^{16} cm and homogeneous density of 2000 cm^{-3}. The Hα *HST* imaging and the SuperCOSMOS Hα Sky Survey (Parker et al. 2005) also indicate that the nebula is surrounded by a outer faint halo. We modeled the halo using a ellipsoid with homogeneous, low density of 1250 cm^{-3}, a semimajor axis of 6.0×10^{17} cm and a semiminor axis of 1.5×10^{17} cm. A cylinder, used to describe the FLIER, has a radius of 5×10^{16} cm and a length of 1.0×10^{17} cm, and is located at a distance of 7.0×10^{17} cm from the central star, along the axis of the torus and the ellipsoid. The H number density in the FLIER is taken to be homogeneous and equal to 2000 cm^{-3}.

The MOCASSIN code allowed us to integrate the predicted emission-line fluxes emitted from different regions: Ring (shell, rim and inner caps), FLIER (point-symmetric knot), and (outer faint) Halo. They can be directly compared with the observations, as we show in Table 4.6.

The nebular elemental abundances

The homogeneous elemental abundances used for the model MC1 are listed in Table 4.5 (Columns 6-8), where they are given by number with respect to hydrogen. As seen, we chose the same abundance values for all different regions: Ring, FLIER and Halo. Our model used 9 elements, including all major contributors to the thermal balance of the gas, as well as those producing temperature-sensitive and density-sensitive emission lines. The initial guesses

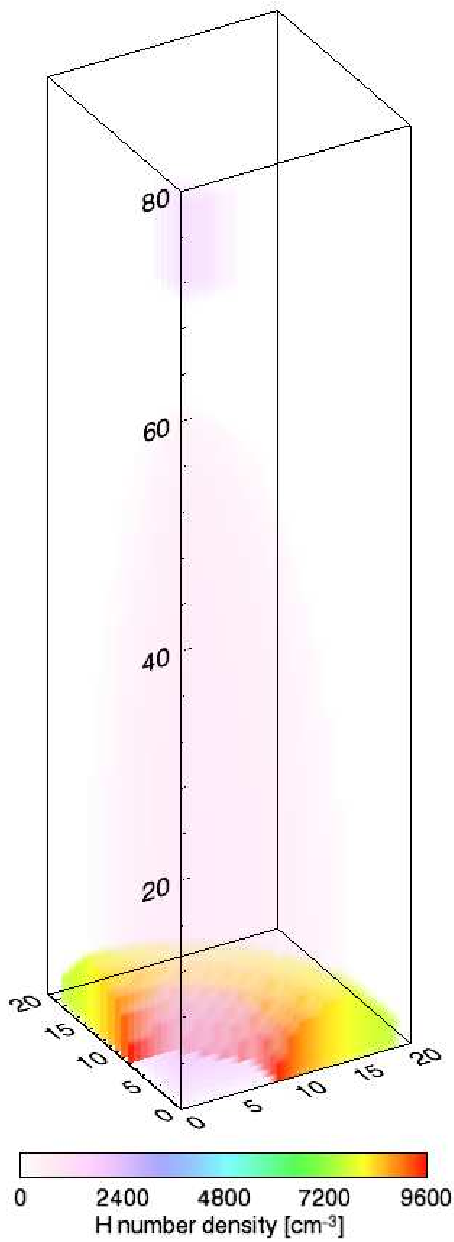

Figure 4.4: The density distribution constructed in $20 \times 20 \times 80$ cubic grids adopted for photoionization modeling of Hb 4. Each cubic cell has a length of 1.0×10^{16} cm. The torus has a power-law density distribution, a radius of 1.4×10^{17} cm from its center to the tube center, and a tube radius of 6.0×10^{16} cm. The FLIER is a cylinder with a radius of 5×10^{16} cm and a length of 1.0×10^{17} cm, and is located at the distance of 7.0×10^{17} cm from the center of the torus. The outer halo is an ellipsoid with a semimajor axis of 6.0×10^{17} cm and a semiminor axis of 1.5×10^{17} cm. The ionizing source is placed in the corner (0,0,0).

at the elemental abundances were taken from the empirical analysis, see Table 4.5 (Columns 2 and 3). The starting values of N, O, Ne, S, Cl and Ar were taken from the CEL abundance analysis, while those of He and C were chosen from the ORL abundance analysis. We adopted the initial abundances while the density structure and the central star properties were varied to fit the emission-line fluxes from each element. The elemental abundances were successively modified to get the best fit of the emission-line spectrum.

The ionizing spectrum

Adopting the density distribution model, the effective temperature and luminosity of the central star were varied to make an ionizing flux that could reproduce the He^{2+}/He^{+} ionic abundance ratio, the He II λ4686, [N II] and [O III] emission lines. A blackbody model with $T_{\rm eff} = 110$ kK and $L_{\star} = 4950\,{\rm L}_{\odot}$ resulted in the best fit of the emission-line spectrum of the inner shell. However, the assumption of a blackbody may not be quite correct (Rauch 2003). The NLTE model atmosphere has a major departure at energies higher than 54 eV, which could have an impact on the predicted nebular spectrum.

It is more realistic to use NLTE model atmosphere rather than blackbody. We have examined various models of hydrogen-deficient NLTE stellar atmospheres (Gräfener et al. 2002; Rauch 2003). However, after H-deficient NLTE model atmosphere did not provide a good match, we used a NLTE stellar atmosphere with an abundance ratio of H : He = 8 : 2 by mass, $\log g = 5$ (cgs), $T_{\rm eff} = 90$ kK and $L_{\star} = 4950\,{\rm L}_{\odot}$ from the NLTE Tübingen Model-Atmosphere Fluxes Package[1] (TMAF; Rauch 2003). Comparing the stellar parameters with stellar evolutionary tracks by Blöcker (1995a), one gets a stellar mass of $0.6{\rm M}_{\odot}$ and a progenitor mass of $3{\rm M}_{\odot}$.

[1] Website: http://astro.uni-tuebingen.de/∼rauch/TMAF/TMAF.html

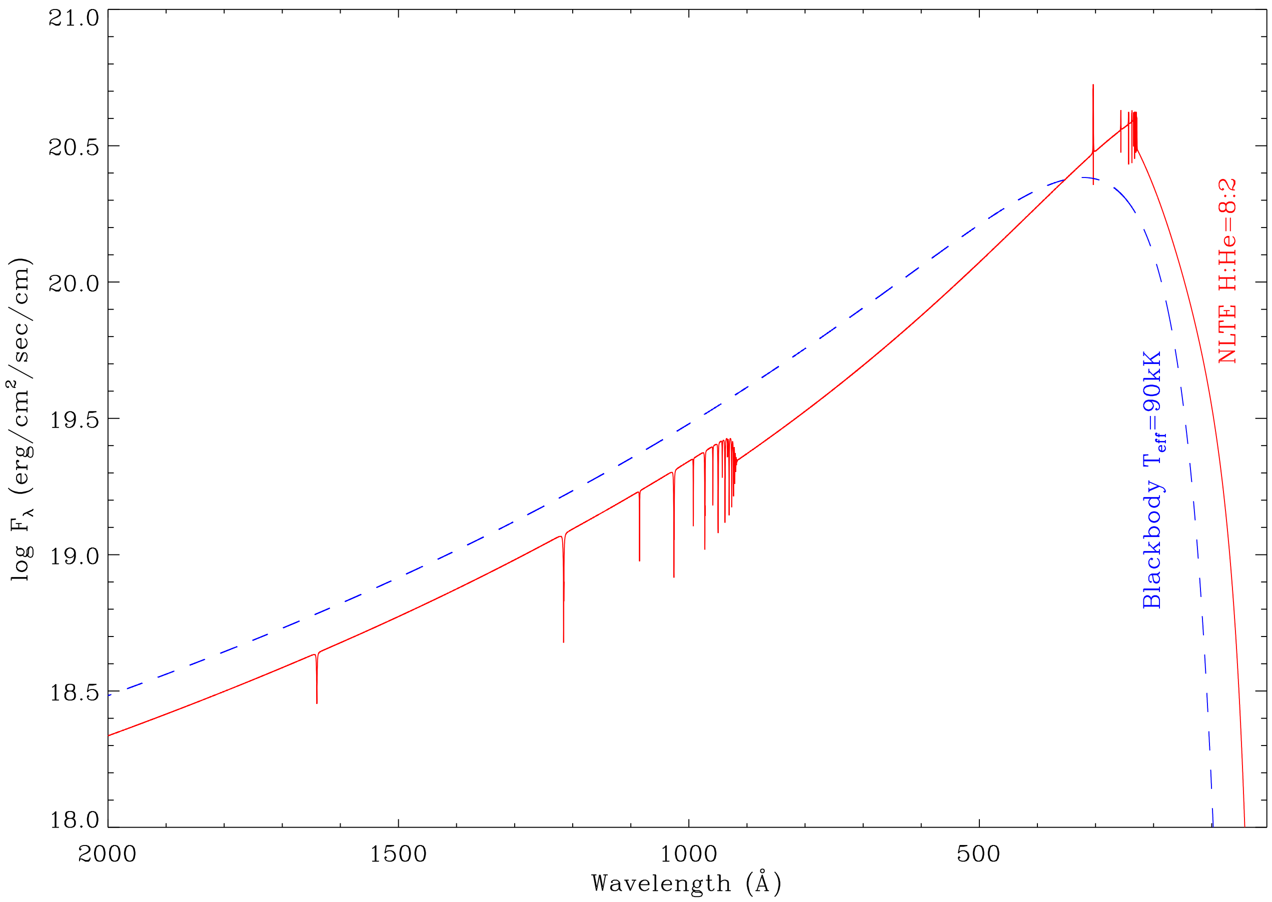

Figure 4.5: H-rich NLTE model atmosphere flux (Rauch 2003) used as an ionizing source in the photoionization model, compared with a blackbody model. Red line: NLTE model atmosphere with an abundance ratio of $\mathrm{H:He} = 8:2$ by mass, $\log g = 5$ (cgs) and $T_{\rm eff} = 90$ kK. Dashed blue line: the flux of a blackbody with $T_{\rm eff} = 90$ kK.

Fig. 4.5 compares the adopted NTLE model atmosphere with a blackbody flux with $T_{\rm eff} = 90$ kK. As seen, there is a significant difference between a blackbody flux and a NTLE model atmosphere at energies higher than 13.6 eV and 54.4 eV, resulting in large differences in predicted emission lines.

4.3.2 Model results

Emission-line spectrum

The ratios of predicted over observed values from the best-fitting model MC1 are presented in Columns 7 and 8 of Table 4.6 for Ring and FLIER, respectively. Columns 4–6 present the observed fluxes for the Ring, northern FLIER and southern FLIER, relative to Hβ on a scale where H$\beta = 100$. Most predicted CELs are in fair agreement with the observed values, except temperature-sensitive auroral lines ([N II] and [O III]) and those lines much sensitive to hydrogen-deficient ionizing flux. The majority of the H I lines are in good agreement with the observations, although discrepancies within 15-29% are seen in those lines towards the blue end of the emission-line spectrum (3734–3970Å). This may be due to line blending or/and measurement errors. Alternatively, the presence of inhomogeneous condensations and high density clumps can enhance the strengths of the higher order Balmer lines. All He I lines of the inner shell are in excellent agreement with the observations, with fits to within 12%, apart from the He I λ7281 (51%) dramatically blended with near telluric lines. The He I λ5876 and λ6678 lines in the FLIER also show discrepancies of 41% and 115%, respectively, which could be due to either low signal-to-noise ratios of the FLIER spectrum or ionization stratification. The He I λ5876 and λ6678 lines in the southern FLIER was measured 13% lower and 27% higher than the northern FLIER, respectively. Although high uncertainty could contribute to discrepancies, possible metal-rich inclusions may have some implications. However, the Hβ intrinsic fluxes of the FLIERS are 0.3–0.4% of the inner shell, which introduce high uncertainties to the faint lines. The [N II] and [O III] CELs are in excellent agreement with the observations, discrepancies within 3.5%, except the auroral lines. We notice that the auroral line [N II] λ5755 and [O III] λ4363 in the inner shell show discrepancies of 53% and 69%, respectively. The predicted [N II] λ5755 line in the FLIER is by a factor of near 3 larger than the observation. Nonetheless, the low signal-to-noise ratios of the faint lines can make inaccurate results for the FLIERs. The recombination contributions could make large discrepancies in the auroral lines (see e.g. Liu et al. 2000), though the thermal balance of the gas has some major impacts on them. Metal-rich inclusions can also largely affect both thermal structures and auroral lines of the nebula (Liu et al. 2004a). The sulfur CELs have discrepancies within 16%, apart from the [S III] λ9069. The [S III] λ9069 line may be problematic due to flux calibration or/and uncertain atomic data (see e.g. improved atomic data by Grieve et al. 2014). While [S II] λ4069 and [S III] λ6312 are in reasonable agreement (16-17%) with the observations, the predicted [S II] $\lambda\lambda$6716,6731 doublet perfectly matches the observations. The observed $\lambda\lambda$6716,6731 doublet in the the FLIERs may be enhanced by shock excitation. The high velocity of $V_{\rm FLIER} = \pm 150\,{\rm km\,s}^{-1}$ derived for the FLIERs and interaction with the photodissociation region could enhance the [S II] $\lambda\lambda$6716,6731 doublet in the FLIERs, but they show discrepancies less than 10% with the observations. Finally, the model underestimates [Ar III] $\lambda\lambda$7136,7751 by factors larger than 7, which appears to be blended with telluric emission lines. However, the predicted [Ar III] λ5192 is by a factor of 2 lower than the observed flux. Moreover, the [Ar IV] lines show discrepancies within 20%. They could be attributed to uncertainties of the atomic data of Ar and the effect of dielectronic recombination (e.g. see discussion by Morisset et al. 2004). We notice that the model overestimates [Ar V] $\lambda\lambda$6435,7005 by factors of 7. Hydrogen-rich ionizing flux has a departure from hydrogen-deficient model atmosphere, which contributes to the lines emitted from ions with ionization energies higher than about 54 eV, thus resulting in [Ar V] lines largely higher than the observations.

The [N II] λ6583 and [O III] λ5007 lines predicted by the FLIER model are in excellent agreement with the observations. However, the H number density of 2000 cm^{-3} used in the model is twice the value determined by the empirical analysis of the [S II] λ6725 double. As the $\lambda\lambda$6716,6731 doublet is largely affected by shock excitation in the FLIERs, it is not possible to determine the electron density accurately. Furthermore, the photo-dissociation regions (PDRs) can also significantly cool the nebula down through the far-infrared (FIR) fine structure lines of [O I] and [C II], which results in [O I] λ6300 and [S II] λ6731 emission lines (Hollenbach & Tielens 1997).

There are large discrepancies between the prediction of the fluxes for the ORLs and the observations. The O II ORLs are mostly underestimated by a factor around 7. The N II ORLs show lower discrepancies, and they are underestimated by a factor around 4. The C II ORLs show much lower discrepancies within 3-31%, except C II λ6578 and λ7236 lines. Most of the ORLs could be affected by fluorescence lines (see e.g. Escalante & Morisset 2005; Escalante et al. 2012). However, fluorescence excitation has a considerable effect in relatively low ionization or low density plasma, so its contribution to the recombination lines must be negligible in the inner shell of Hb 4. Therefore, the large discrepancies in the ORLs must be attributed to physical conditions and chemistry of regions where recombination processes occur. In Section 4.4, we attempt to solve this problem by including a small fraction of metal-rich structures in the nebula of normal abundances.

Table 4.6: Comparison of predictions from models MC1 and MC2 and the observations. The observed, dereddened intensities are in units such that $I(\mathrm{H}\beta) = 100$. Columns (7)–(11) give the ratios of predicted over observed values in each case.

			Observed			MC1		MC2 (Ring)		
Line	λ_0(Å)	Mult	Ring	N-FLIER	S-FLIER	Ring	N-FLIER	H-poor	Normal	Total
			H, He recombination lines							
$\mathrm{H}\beta/10^{-12}$ erg cm^{-2} s^{-1}			20.42	0.08	0.06	0.94	1.44	0.16	0.75	0.91
Hβ	4861.33	H4	100.00	100.00	100.00	1.000	1.000	1.000	1.000	1.000
Hα	6562.82	H3	285.33	286.00	286.00	0.986	0.988	1.039	0.986	0.995
Hγ	4340.47	H5	48.83	–	–	0.965	–	0.946	0.966	0.962
Hδ	4101.74	H6	25.09	–	–	1.041	–	1.013	1.041	1.036
H I	3970.07	H7	13.71	–	–	1.171	–	1.137	1.171	1.165
H I	3835.39	H9	6.29	–	–	1.174	–	1.143	1.174	1.168
H I	3770.63	H11	3.15	–	–	1.275	–	1.253	1.275	1.271
H I	3750.15	H12	2.40	–	–	1.290	–	1.276	1.289	1.287
H I	3734.37	H13	2.12	–	–	1.152	–	1.149	1.151	1.151
He I	7065.28	10	5.75	–	–	0.945	–	1.323	0.885	0.965
He I	5875.64	11	14.86	11.48	9.94	1.024	1.411	3.129	0.983	1.373
He I	4471.47	14	4.87	–	–	1.062	–	3.261	1.026	1.432
He I	4026.21	18	2.42	–	–	0.878	–	3.045	0.853	1.251
He I	7281.35	45	0.71	–	–	1.505	–	2.957	1.433	1.710
He I	6678.15	46	3.88	2.06	2.62	0.970	2.147	3.481	0.936	1.399

Table 4.6: (continued)

			Observed			MC1		MC2 (Ring)		
Line	λ_0(Å)	Mult	Ring	N-FLIER	S-FLIER	Ring	N-FLIER	H-poor	Normal	Total
He II	4685.68	3.4	24.86	–	–	1.043	–	0.744	1.159	1.084
He II	5411.52	4.7	1.92	–	–	1.024	–	0.731	1.139	1.065
				Heavy-element recombination lines						
C II	6578.05	2	0.24	–	–	1.732	–	1.957	1.657	1.712
C II	7236.42	3	0.26	–	–	2.132	–	2.758	2.035	2.167
C II	4267.15	6	0.76	–	–	0.974	–	1.433	0.927	1.019
C II	6151.43	16.04	0.03	–	–	1.087	–	1.383	1.037	1.100
C II	6461.95	17.04	0.08	–	–	0.946	–	1.401	0.900	0.991
C II	5342.38	17.06	0.03	–	–	1.317	–	1.875	1.254	1.366
N II	5666.64	3	0.06	–	–	0.257	–	5.690	0.213	1.208
N II	5676.02	3	0.03	–	–	0.228	–	5.049	0.189	1.072
N II	5679.56	3	0.13	–	–	0.221	–	4.891	0.183	1.039
N II	5686.21	3	0.02	–	–	0.256	–	5.668	0.212	1.204
N II	5710.77	3	0.02	–	–	0.170	–	3.767	0.141	0.800
N II	4630.54	5	0.08	–	–	0.196	–	4.121	0.162	0.882
O II	4638.86	1	0.12	–	–	0.176	–	6.382	0.141	1.275
O II	4641.81	1	0.80	–	–	0.067	–	2.415	0.053	0.482
O II	4649.13	1	0.73	–	–	0.139	–	5.032	0.111	1.005
O II	4661.63	1	0.19	–	–	0.142	–	5.149	0.113	1.028

Table 4.6: (continued)

			Observed			MC1		MC2 (Ring)		
Line	λ_0(Å)	Mult	Ring	N-FLIER	S-FLIER	Ring	N-FLIER	H-poor	Normal	Total
O II	4676.24	1	0.12	–	–	0.189	–	6.848	0.151	1.368
O II	4317.14	2	0.07	–	–	0.217	–	8.056	0.172	1.605
O II	4345.56	2	0.05	–	–	0.301	–	11.205	0.240	2.232
O II	4349.43	2	0.17	–	–	0.223	–	8.298	0.178	1.653
O II	4366.89	2	0.16	–	–	0.101	–	3.765	0.081	0.750
O II	4069.62	10	0.42	–	–	0.047	–	1.781	0.037	0.354
O II	4072.15	10	0.30	–	–	0.158	–	6.026	0.126	1.198
O II	4075.86	10	1.19	–	–	0.058	–	2.195	0.046	0.436
O II	4153.30	19	0.05	–	–	0.306	–	11.863	0.244	2.355
O II	4119.22	20	0.14	–	–	0.124	–	4.803	0.099	0.954
O II	4275.55	67a	0.08	–	–	0.141	–	6.005	0.113	1.183
Collisionally excited lines										
[N II]	5754.64	3F	1.35	1.56	1.41	1.533	3.141	0.207	1.239	1.051
[N II]	6548.03	1F	27.40	73.30	67.78	0.966	1.023	1.461	0.828	0.943
[N II]	6583.41	1F	82.30	235.94	232.71	0.983	0.971	1.485	0.842	0.959
[O II]	3726.03	1F	17.15	–	–	2.253	–	0.925	1.794	1.636
[O II]	3728.82	1F	7.91	–	–	1.844	–	0.731	1.497	1.358
[O II]	7318.92	2F	3.11	–	–	1.730	–	0.163	1.255	1.057
[O II]	7319.99	2F	*	*	*	*	*	*	*	*
[O II]	7329.66	2F	2.66	–	–	1.665	–	0.157	1.207	1.016
[O II]	7330.73	2F	*	*	*	*	*	*	*	*

Table 4.6: (continued)

			Observed			MC1		MC2 (Ring)		
Line	λ_0(Å)	Mult	Ring	N-FLIER	S-FLIER	Ring	N-FLIER	H-poor	Normal	Total
[O III]	4363.21	2F	7.26	–	–	1.685	–	0.174	1.441	1.211
[O III]	4958.91	1F	370.19	317.60	243.44	0.966	1.010	1.853	0.800	0.991
[O III]	5006.84	1F	1108.39	956.98	799.84	0.963	1.001	1.847	0.797	0.988
[Ne III]	3868.75	1F	106.55	–	–	0.998	–	0.454	1.105	0.986
[Ne III]	3967.46	1F	33.10	–	–	0.968	–	0.440	1.071	0.956
[S II]	4068.60	1F	2.24	–	–	1.171	–	0.144	1.184	0.995
[S II]	6716.47	2F	3.64	19.10	18.68	0.882	0.744	0.512	0.988	0.902
[S II]	6730.85	2F	6.36	20.07	20.21	0.989	0.980	0.531	1.085	0.985
[S III]	6312.10	3F	2.33	–	–	1.163	–	0.053	1.109	0.917
[S III]	9068.60	1F	43.34	–	–	0.751	–	0.295	0.711	0.635
[Cl III]	5517.71	1F	0.53	–	–	0.844	–	0.122	1.020	0.857
[Cl III]	5537.88	1F	0.80	–	–	1.011	–	0.189	1.173	0.994
[Ar III]	7135.78	1F	23.12	–	–	0.149	–	0.065	0.146	0.131
[Ar III]	7751.10	2F	5.43	–	–	0.152	–	0.066	0.149	0.134
[Ar III]	5191.82	3F	0.09	–	–	0.455	–	0.016	0.446	0.368
[Ar IV]	4711.37	1F	2.93	–	–	1.163	–	0.085	1.204	1.001
[Ar IV]	4740.17	1F	4.11	–	–	1.207	–	0.122	1.199	1.004
[Ar V]	6434.73	1F	0.05	–	–	6.838	–	0.211	7.960	6.552
[Ar V]	7005.40	10F	0.11	–	–	6.605	–	0.203	7.689	6.329

Ionic and thermal structure

Table 4.7 lists the ionization structures for the two regions predicted by the photoionization model MC1. The upper entries in each row are for the Ring and the lower entries are for the FLIER. Hydrogen is fully singly-ionized in Ring and FLIER. We see that helium is fully singly-ionized in FLIER, while it is 79 percent singly ionized and 20 percent doubly ionized in Ring, in agreement with the empirical results of Table 4.4. The predicted ionic fractions of N^{+} in Ring and FLIER are twice the empirical result. But, we see that the *icf* of nitrogen is overestimated by the empirical scheme, $icf(\mathrm{N}) = 28.4$, while the model predicted $icf(\mathrm{N}) = 4.9$ for FLIER. This results in the empirical elemental abundances of nitrogen, which is higher by a factor of three in the FLIERs in comparison to the inner shell. Empirical analysis relies on the *icf* method to correct the unseen ionization stages (e.g. Kingsburgh & Barlow 1994). However, the *icf* method can have some high uncertainties due to poor qualities of emission lines measured from the blue end of the spectrum, e.g. [O II] $\lambda\lambda$3726,3729 lines. Very low surface-brightness of FLIERs also adds further uncertainty. We see that the predicted ionic fraction of O^{+} in Ring twice the empirical value, but it is by a factor of seven larger than the empirical result in FLIER. This must introduce errors in the empirical determination of elemental abundances. We notice that the FLIER model predicts the intrinsic fluxes of $I([\mathrm{O\,II}]\lambda3726) = 155$ and $I([\mathrm{O\,II}]\lambda3729) = 86$ on a scale where $I(\mathrm{H}\beta) = 100$. These predicted values should be checked by future observations, as we currently do not have any separately measurement of [O II] lines from the FLIERs. The empirical ionic fractions of S^{+} and S^{2+} are 23% and 71% higher than the predicted values. The large discrepancies seen in the Ar ionic fractions can be explained by a departure of the H-deficient ionizing flux at higher energies.

Table 4.7: Fractional ionic abundances obtained from the photoionization model MC1. For each element the first row is for the ring and the second row is for the FLIER.

	Ion						
Element	I	II	III	IV	V	VI	VII
H	1.17(−2)	9.88(−1)					
	2.20(−2)	9.78(−1)					
He	4.52(−3)	7.92(−1)	2.03(−1)				
	9.26(−3)	9.90(−1)	7.91(−4)				
C	1.17(−4)	5.63(−2)	5.54(−1)	3.68(−1)	2.14(−2)	2.97(−15)	1.00(−20)
	8.18(−4)	1.45(−1)	7.88(−1)	6.60(−2)	3.31(−6)	6.78(−19)	1.00(−20)
N	1.27(−3)	7.38(−2)	5.22(−1)	3.75(−1)	2.28(−2)	5.44(−3)	1.20(−15)
	1.38(−3)	2.03(−1)	7.16(−1)	7.89(−2)	1.49(−5)	4.05(−9)	1.00(−20)
O	8.56(−3)	7.78(−2)	7.72(−1)	1.17(−1)	2.03(−2)	4.20(−3)	5.89(−4)
	1.38(−2)	2.33(−1)	7.53(−1)	1.91(−4)	7.00(−8)	4.44(−11)	1.06(−14)
Ne	8.25(−5)	1.70(−2)	8.71(−1)	8.66(−2)	2.22(−2)	2.98(−3)	4.21(−5)
	1.06(−4)	4.42(−2)	9.55(−1)	3.19(−4)	1.99(−7)	9.39(−11)	3.10(−15)
S	1.46(−5)	2.80(−2)	2.71(−1)	4.23(−1)	2.47(−1)	2.48(−2)	6.65(−3)
	1.05(−4)	6.61(−2)	7.24(−1)	2.03(−1)	6.81(−3)	2.70(−6)	4.63(−10)
Cl	6.60(−5)	4.47(−2)	3.72(−1)	5.27(−1)	3.87(−2)	1.15(−2)	6.73(−3)
	5.01(−4)	1.15(−1)	6.39(−1)	2.44(−1)	1.36(−3)	2.40(−7)	8.59(−11)
Ar	1.31(−4)	5.55(−3)	1.98(−1)	6.68(−1)	7.94(−2)	3.55(−2)	1.41(−2)
	4.26(−5)	9.69(−3)	5.34(−1)	4.56(−1)	2.24(−4)	4.17(−7)	3.88(−10)

Table 4.8 lists the mean temperatures weighted by ionic species for the two regions calculated by the photoionization model MC1. Once again, the upper entries for each element are for the Ring and the lower entries are for the FLIER. The value of T_e(O II) = 11,806 K predicted by the Ring model is lower than the value of T_e(O II) = 13,340 K empirically derived from CELs after correcting for recombination contribution to the auroral lines. The predicted temperature of [O III] is 12,004 is about 1,980 higher than the empirical value of the inner shell before the recombination correction. Similarly, the temperature of T_e(N II) = 11,722 predicted by the Ring model is about 1,920 K higher the value empirically derived from CELs before the recombination correction. Moreover, the predicted He I temperature of 11,940 K is much larger than the mean He I temperature of 7,400 K derived from ORLs. While temperature-sensitive CELs are emitted from different ionization stratification layers, inhomogeneous density distribution can make moderate discrepancy in temperatures determined from those lines. Moderate discrepancy between temperatures derived from CELs of low and high ionization zones is more attributed to inhomogeneous condensations, but it cannot explain very large discrepancy between the predicted He I temperature and observation. Liu et al. (2000) suggested that a bi-abudance model containing some cold, hydrogen-deficient inclusion embedded in the diffuse warm nebular gas of normal abundances can solve this problem. In Section 4.4, we exam the feasibility of this scenario.

CEL abundance analysis depends exponentially on the assumed electron temperature. As a result, temperature variations introduce uncertainties in empirical results. Assuming T_e = 12,000 K, we derived the N^+/H^+ ionic abundance ratio of 2.5×10^{-5}, which is lower than the value given in Table 4.3. Both temperature and density variations result in errors on empirically derived ionic abundances. While the *icf* method is mostly responsible for apparent enhancement of nitrogen abundance in the FLIERs, the electron temperature and density used for the empirical analysis also have some partial contributions.

Table 4.8: Mean electron temperatures (K) weighted by ionic species for Hb 4 obtained from the photoionization model MC1. For each element the first row is for the ring and the second row is for the FLIER.

	Ion						
El	I	II	III	IV	V	VI	VII
H	11515	12165					
	11569	11631					
He	11495	11940	13019				
	11572	11630	11584				
C	11659	11740	12011	12279	14924	15740	12157
	11520	11591	11640	11598	11527	11527	11630
N	10926	11722	12026	12243	14143	16603	16903
	11477	11564	11652	11600	11525	11500	11630
O	11174	11806	12004	12900	14352	16530	18792
	11484	11582	11647	11547	11514	11496	11501
Ne	10845	11710	12011	12937	14532	17035	19652
	11511	11593	11632	11554	11501	11499	11495
S	11578	11583	11986	12000	12378	13995	16479
	11503	11567	11645	11599	11536	11502	11485
Cl	11617	11674	12006	12129	12948	14944	16621
	11507	11577	11637	11636	11618	11550	11517
Ar	10629	11272	11920	12014	12804	13456	15681
	11462	11537	11630	11632	11532	11508	11493

Finally, Figure 4.6 shows spatial distributions of electron temperature, electron density and ionic fractions of He^{+}, He^{2+}, N^{+}. N^{2+}, O^{+}, O^{2+} and S^{+} along the equatorial direction. The stellar ionizing radiation is coming from the corner (0,0,0). As seen, the large temperature variations exist in the nebula. Furthermore, N^{+} ionic fraction is significantly high in the FLIER, in agreement with the observation.

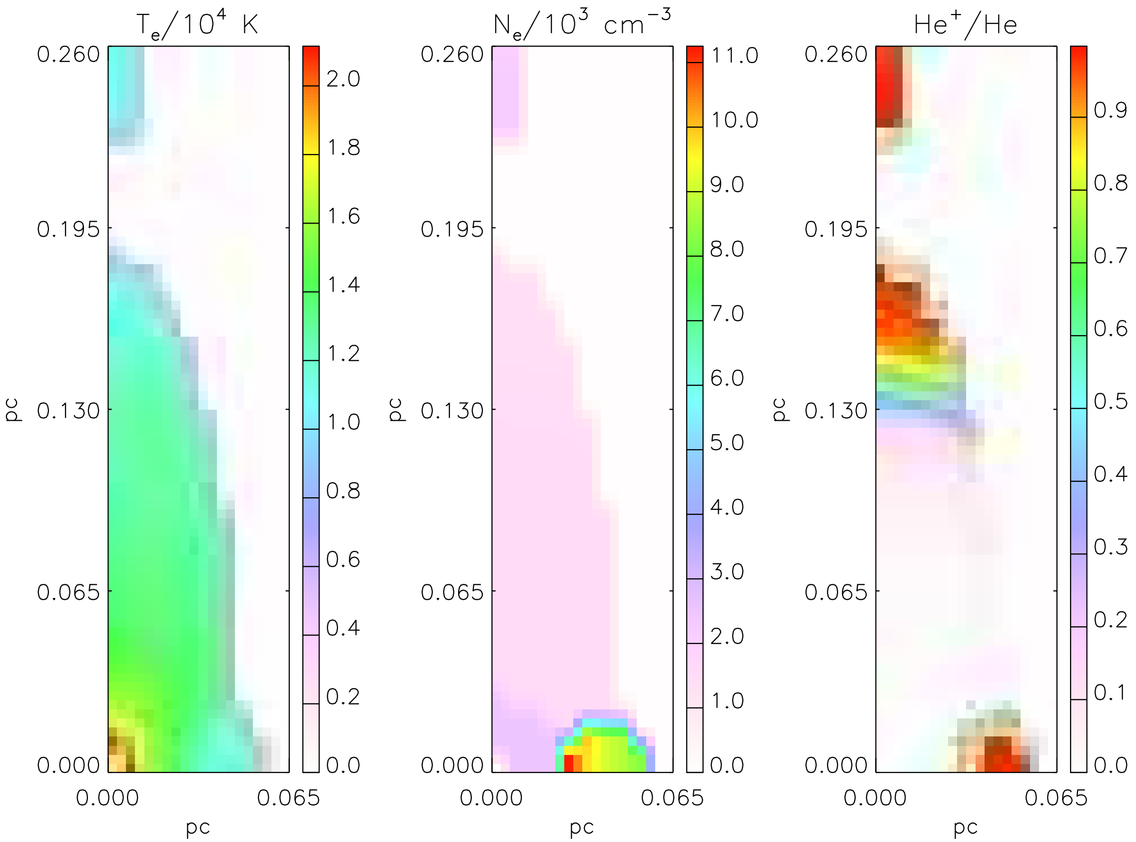

Figure 4.6: Spatial distributions of electron temperature, electron density and ionic fractions from the photoionization MC1. Ionic fractions are shown for He^+, He^{2+}, N^+. N^{2+}, O^+, O^{2+} and S^+. The ionizing source is placed in the corner (0,0,0).

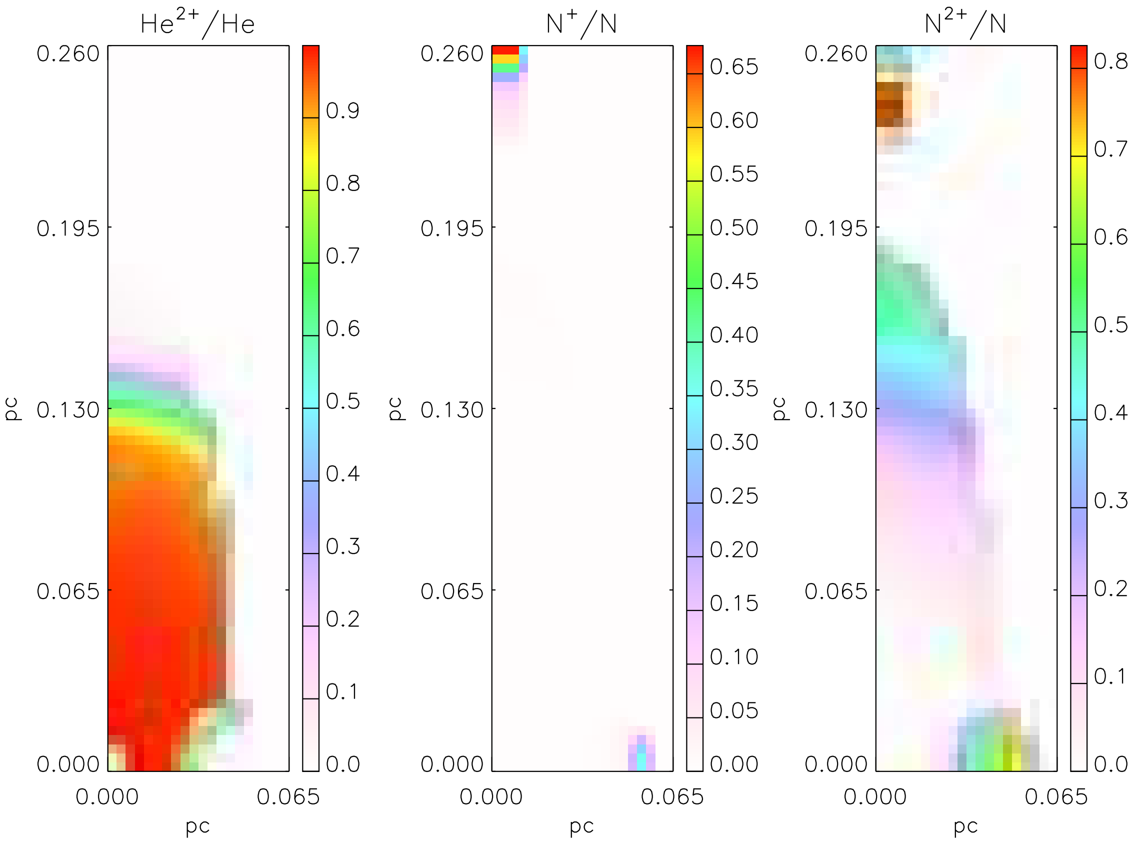

Figure 4.6: (continued)

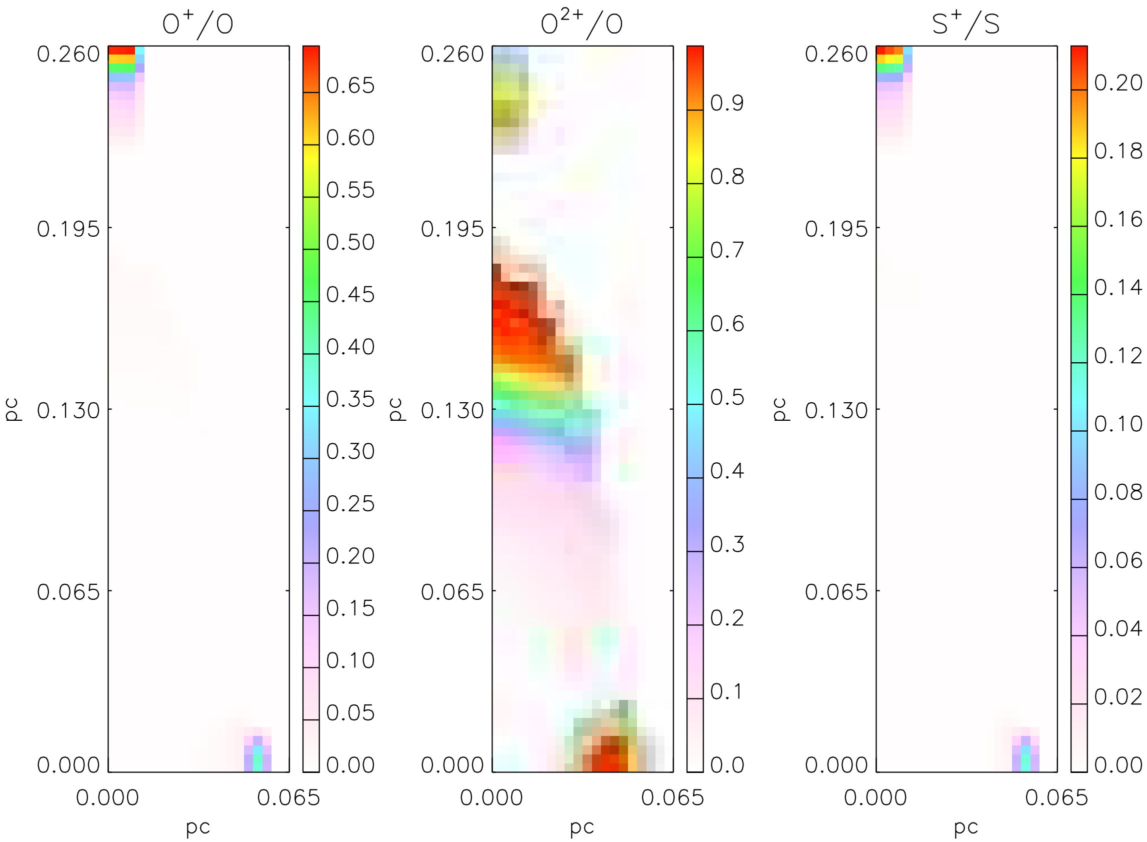

Figure 4.6: (continued)

4.4 Bi-abundance model

In the model MC1, the elemental abundances in the nebula were assumed to be homogeneous. Fits to the CELs are acceptable, and some issues can be explained by inhomogeneous condensations. However, the model still shows major discrepancies between the predicted ORLs and the observations, which are not associated with density inhomogeneity. Additionally, we see major discrepancy between electron temperatures determined from the observed He I ORLs and those from the observed CELs. A second attempt to reproduce the emission-line spectrum of Hb 4 was done using a bi-chemistry model, which consists of the diffuse warm nebular gas of normal abundances surrounding a small fraction of cold H-deficient small-scale structures, highly enriched in helium and heavy elements.

The second model referred to in this chapter as MC2 aimed at solving the observed ORL-CEL discrepancies. The following procedures were used to constrain the model MC2:

1. We adopted the density model and chemistry of the inner shell and the central star properties ($T_{\rm eff}$ and $L_{\star}$) found from MC1.

2. We added some metal-rich cells with a small filling factor ($\varepsilon \sim 0.05$; 0.005 M$_{\odot}$) mixed with the normal-abundances shell (0.075 M$_{\odot}$) . The elemental abundances of He, C, N and O derived from the ORL empirical analysis were used for the initial abundances of the metal-rich inclusions, assuming a H number density of $N_{\rm H}$ = 10,000 cm^{-3}.

3. We adjusted the elemental abundances and the filling factor of the metal-rich inclusions to reproduce the observed N II and O II ORLs and the mean He I temperature.

4. As the CELs were also affected by the metal-rich inclusions, the characteristic densities (N_0 and N_1) of the normal shell were adjusted to match the

nebular emission-line spectrum.

4.4.1 Model inputs

Table 4.5 presents the parameters of the 'metal-rich' inclusions (column 9) and the 'normal' plasma (column 10) for the best fitting model MC2. In this model, we assumed N_{H} = 10,000 cm^{-3} for the 'metal-rich' inclusions, while higher values yield lower abundances of metal-rich inclusion and corresponds to a lower filling factor. The filling factor was found to be $\varepsilon = 0.053$. To balance the thermal and ionic structure, we also changed the characteristic densities of the normal shell, $N_0 = 6040\,\mathrm{cm}^{-3}$ and $N_1 = 2010\,\mathrm{cm}^{-3}$. The normal mean density of MC2 is slightly lower (92%) than MC1 to account for the presence of the metal-rich, dense cells embedded in the normal plasma.

For the model MC2, the abundances of nitrogen and oxygen were adopted to be 20 and 39 times larger in the metal-rich component than in the normal one; these enrichment factors are able to reproduce the observed N II and O II ORLs. The neon abundance was chosen to be 15 times higher in the metal-rich component than in the normal one in order to reproduce the ionic structure of the whole nebula, although we did not observe any reliable Ne II lines to constrain our model. The abundances of other elements (S, Cl and Ar) in the metal-rich component were chosen to be roughly twice their abundances in the normal component, as they often remain unaffected by nucleosynthesis and other processes.

4.4.2 Model results

ORL spectrum

The ORL intensities predicted by model MC2 are compared to the observed values in Table 4.6. The agreement between the predictions from MC2 and the observations is better than MC1. In addition, the model yields a better fit to the measured fluxes of the auroral [N II] λ5755 and [O III] λ4363 lines, which is overestimated by MC1. This is due to the fact that the cold metal-rich inclusions reduce the temperature of the diffuse nebular gas. The majority of the O II lines are in good agreement with the observations, with fits to within 30%, except λ4069.6, λ4075.9, λ4153.3 λ4317.1, λ4345.6, λ4349.4 and λ4641.8. The O II line λ4069.6 could be blended with the O II 4069.9 and also the [S II] 4068.6. Similarly, the O II λ4075.9 line may have some contribution of the [S II] 4076.3. The extremely low intensities of the O II line λ4153.3, λ4317.1, λ4345.6 and λ4349.4 lines yield very low signal-to-noise ratios, while the O II λ4317.1 and λ4345.6 lines could be also blended with near O II ORLs such as λ4317.7 and λ4345.5, respectively. The O II λ4641.8 line could be mixed with the N III λ4640.6 line. The N II lines are also in good agreement with the observations, discrepancies less than 20%. The predicted C II ORLs show lower discrepancies within 40%, apart from C II λ6578 and λ7236 lines. In particular, the C II λ4267.2 line is much stronger than any nearby O II ORLs, so it could not be blended with them. As seen in Table 4.4, the abundances from the λ6151, λ6462 and λ5342 lines are in pretty good agreement with the λ4267 line, and their lower energy level is the upper level of the λ4267 line, so no other process besides recombination produces the line flux. The C II λ6578 and λ7236 lines have unreliable measurements and could be blended with nearby lines.

Ionic and thermal structure

Table 4.9 presents the volume-averaged fractional ionic abundances for the ring, which can be compared with the first row of Table 4.7. As seen, the predicted ionic fractions of the important ions are generally in agreement with MC1. Once again, hydrogen is fully ionized and helium is 78 percent singly ionized and 21 percent doubly ionized, in good agreement with MC1. It can be seen that the general ionization structure in MC2 is in agreement with MC1.

For example, the predicted ionic fraction of N^+, O^+, N^{2+} and O^{2+} are about the values calculated by MC1. The S^+ ionic fraction predicted by MC2 is 1.4 times the predication of MC1, while S^{2+} and S^{3+} are roughly similar.

Results for the mean temperatures weighted by ionic species are shown in Table 4.10. The first entries for each element are for the H-poor inclusion, the second entries are for the normal plasma, and the third entries are for the total structure. The value of T_e(O II) = 10,699 K predicted by the whole structure is about 2,600 K lower than the empirical result of T_e(O II) = 13,340 K. However, the temperatures of T_e(N II) = 10,628 K predicted by the Ring model is in decent agreement with the value of T_e(O II) = 9,800 K empirically derived from CELs. The predicted value of [O III] is 11,354 K, which is about 1,300 K higher than the empirical result T_e(O III) = 10,020 K. The temperature of 5,693 K weighted by He I in the H-poor component is about 1,700 K lower than than the mean He I temperature of 7,400 K derived from ORLs. It is also worth noticing that the mean temperatures predicted by MC2 is lower than those from MC1. This is due to the cooling effects of the H-poor inclusions. We take no account of the interaction between the two regions, which could lead to temperature variations. We assumed a uniform distribution ($\varepsilon = 0.05$) for the H-poor structures, but positions of individual H-poor cells can dramatically affect both ionization and thermal structure. As the inner shell is dense ($N_H \sim$ 7000 cm^{-3}) and optically thick, the transition region between photoionization and PDR regions does not have much thermal effects.

4.5 Conclusions

In this chapter, we have intended to address the problem of the apparent nitrogen overabundance in the outer FLIERs of a nebula with geometry and spectroscopic features like Hb 4. We have constructed a 3D photoionization model assuming chemically homogeneous abundances, without the need of chemical

Table 4.9: Fractional ionic abundances for the ring obtained from the photoionization model MC2.

Element	Ion I	II	III	IV	V	VI	VII
H	1.97(−2)	9.80(−1)					
He	1.20(−2)	7.82(−1)	2.06(−1)				
C	1.42(−4)	7.35(−2)	5.41(−1)	3.61(−1)	2.47(−2)	3.42(−15)	1.00(−20)
N	4.74(−3)	7.55(−2)	5.16(−1)	3.72(−1)	2.60(−2)	6.20(−3)	1.36(−15)
O	1.23(−2)	7.73(−2)	7.61(−1)	1.20(−1)	2.35(−2)	4.83(−3)	6.65(−4)
Ne	2.73(−3)	2.74(−2)	8.49(−1)	9.18(−2)	2.58(−2)	3.40(−3)	4.67(−5)
S	1.69(−5)	3.78(−2)	2.54(−1)	4.18(−1)	2.54(−1)	2.85(−2)	7.63(−3)
Cl	8.31(−5)	5.95(−2)	3.75(−1)	5.02(−1)	4.20(−2)	1.35(−2)	7.66(−3)
Ar	2.22(−3)	1.32(−2)	2.07(−1)	6.39(−1)	8.12(−2)	4.11(−2)	1.65(−2)

inhomogeneity. The density distribution of the model plays a crucial role in reproducing the emission-line spectrum. The density model consists of a dense torus where densities reach 8,800 cm^{-3} at the inner edge, an outer tenuous halo with a constant density of 1250 cm^{-3}, and an inner bubble and a pair of outer FLIERs with a constant density of 2000 cm^{-3}. This combination was required to resemble the morphological features seen in the *HST* images, as well as the kinematic analysis. Although H-deficient NLTE model atmospheres did not provide a good match to the observations of the nebular spectrum, a NLTE model atmosphere with an abundance ratio of H : He = 8 : 2 (by mass), temperature $T_{\rm eff} = 90\,$kK and luminosity $L_\star = 4950\,{\rm L}_\odot$ can predict the ionization structure and the nebular spectrum of the shell. This ionizing source provided the best fit of the observed Hβ luminosity and the He^{2+}/He^{+} abundance ratio derived empirically. The model reproduced the majority of emission lines from two different regions of Hb 4, the inner shell and the outer FLIER. But, some discrepancies still remain, which could be due to much complex inhomoge-

Table 4.10: Mean electron temperatures (K) weighted by ionic species for the ring obtained from the photoionization model MC2. For each element the first row is for the H-poor fraction, the second row is for the normal part and the third row is for the total.

	Ion						
El	I	II	III	IV	V	VI	VII
H	4697	5725					
	11331	12327					
	8396	11634					
He	4678	5693	6119				
	11317	12056	13216				
	7263	11246	13047				
C	5223	5172	5720	5896	6120	6120	5645
	11429	11569	12142	12476	14961	15727	12315
	9575	9745	11276	12154	14950	15724	11570
N	4572	5012	5704	5864	6116	6121	6024
	10868	11476	12176	12438	14231	16591	16904
	6471	10628	11256	11995	14202	16590	16904
O	4573	5049	5734	6117	6121	6121	6121
	10975	11601	12162	13061	14403	16511	18804
	9396	10699	11354	12928	14398	16511	18804
Ne	4573	5017	5736	6115	6121	6121	6121
	10829	11566	12140	13089	14564	17022	19681
	4832	9076	11402	13022	14561	17022	19681
S	4817	4758	5665	5749	5874	6117	6121
	11317	11337	12039	12172	12559	14078	16457
	9505	9404	11304	11302	12176	14063	16457
Cl	5060	5063	5693	5835	6046	6121	6121
	11361	11463	12117	12309	13128	14918	16613
	9371	9617	11152	11825	13041	14916	16613
Ar	4570	4662	5644	5780	6113	6121	6121
	10733	11080	11902	12178	12949	13561	15639
	4910	7629	10800	11529	12854	13557	15639

neous condensations throughout the nebula and the major difference between the H-deficient and blackbody spectral energy distribution.

Following Gonçalves et al. (2003, 2006), we have examined ways in which the [N II] λ6584 emission could be significantly enhanced with respect to Hβ in the FLIERs in comparison to the inner shell. Our findings show that the large strength of the [N II] λ6584 emission in the FLIERs is more likely attributed to geometry and inhomogeneous density distributions rather than chemical inhomogeneity. It has been demonstrated that the [N II] features of the inner shell and outer FLIERs can be reproduced in a chemically homogeneous model. We notice that the *icf*(N) predicted by our models, 13.6 and 4.9 for the inner shell and the FLIER, respectively, are not identical. Although the empirical analysis shows twice the predicted value for the inner shell, the empirical *icf*(N) of the FLIER is about six time higher than the prediction. This could be due to the uncertainties in the flux measurement and flux calibration of some emission lines, such as the [O II] lines. The (N^+/N)/(O^+/O) predicted by the model MC1 are 0.95 and 0.87 for the inner shell and the FLIER, respectively. It is clear that with the typical $N^+/N = O^+/O$ assumption of the *icf* method, we cannot accurately determine the elemental abundance of nitrogen. Since the CEL method depends exponentially on temperature, inaccurate values of electron temperature result in misleading abundance results (e.g. Garnett 1992; Stasińska 2005). Therefore, inaccurate values of T_e and N_e in addition to the *icf* method, without doubt, contribute to the apparent overabundance of nitrogen.

Our first photoionization model was not able to predict the observed ORLs from heavy element ions. We intended to solve this issue through a bi-abundance model (Liu et al. 2000). We have assumed that the nebula contains two different chemical components, namely cold 'metal-rich' and diffuse warm 'normal' abundance. The ORLs are predominately emitted from the cold 'metal-rich regions embedded in the warm 'diffuse' plasma of normal abundances. The results indicate that the bi-abundance model may provide a physical explanation for large discrepancies between ORL and CEL abundances empirically derived. It may also give a natural explanation for the helium temperatures, which are typically lower than the temperatures derived from the CELs. While H-deficient, metal-rich inclusions in the nebula are able to solve the ORL-CEL problem, the origin of such structures is as yet unknown. One might expect a link between them and hydrogen-deficient central stars. It is possible that they were ejected from the stellar surface during the born-again scenario. They could also be produced by the evaporation and destruction of the planetary system of the progenitor star (Liu 2003). Further work is required to investigate any link between the metal-rich inclusions in the planetary nebulae and their H-deficient central stars.

Part II

Planetary nebulae with [WN] stars

5

Abell 48 with a [WN]-type star

The contents of this chapter were published in the Monthly Notices of the Royal Astronomical Society, Vol. 439, Pages 3605–3615, 2014. The authors were A. Danehkar, H. Todt, B. Ercolano and A. Y. Kniazev. Some small modifications have been made, and a section on the evolutionary status (§5.6.3) has been also included. The non-LTE hydrogen-deficient model atmosphere used in this chapter was determined by Todt et al. (2013).

5.1 Introduction

The highly reddened planetary nebula Abell 48 (PN G029.0+00.4) and its central star (CS) have been the subject of recent spectroscopic studies (Wachter et al. 2010; Depew et al. 2011; Todt et al. 2013; Frew et al. 2014b). The CS of Abell 48 has been classified as Wolf–Rayet [WN5] (Todt et al. 2013), where the square brackets distinguish it from the massive WN stars. Abell 48 was first identified as a planetary nebula (PN) by Abell (1955). However, its nature remains a source of controversy whether it is a massive ring nebula or a PN as previously identified. Recently, Wachter et al. (2010) described it as a spectral type of WN6 with a surrounding ring nebula. But, Todt et al. (2013) concluded from spectral analysis of the CS and the surrounding nebula that

Abell 48 is rather a PN with a low-mass CS than a massive (Pop I) WN star. Previously, Todt et al. (2010) also associated the CS of PB 8 with [WN/C] class. Furthermore, IC 4663 is another PN found to possess a [WN] star (Miszalski et al. 2012).

A narrow-band Hα+[N II] image of Abell 48 obtained by Jewitt et al. (1986) first showed its faint double-ring morphology. Zuckerman & Aller (1986) identified it as a member of the elliptical morphological class. The Hα image obtained from the SuperCOSMOS Sky Hα Survey (Parker et al. 2005) shows that the angular dimensions of the shell are about $46'' \times 38''$, and are used throughout this chapter. The first integral field spectroscopy of Abell 48 shows the same structure in the Hα emission-line profile. But, a pair of bright point-symmetric regions is seen in [N II] (see Fig. 5.2), which could be because of the N^+ stratification layer produced by the photoionization process. A detailed study of the kinematic and ionization structure has not yet been carried out to date. This could be due to the absence of spatially resolved observations.

The main aim of this chapter is to investigate whether the [WN] model atmosphere from Todt et al. (2013) of a low-mass star can reproduce the ionization structure of a planetary nebula with the features like Abell 48. We present integral field unit (IFU) observations and a three-dimensional photoionization model of the ionized gas in Abell 48. The chapter is organized as follows. Section 5.2 presents our new observational data. In Section 5.3 we describe the morpho-kinematic structure, followed by an empirical analysis in Section 5.4. We describe our photoionization model and the derived results in Sections 5.5 and 5.6, respectively. Our final conclusion is stated in Section 5.7.

5.2 Observations and data reduction

Integral field spectra listed in Table 5.1 were obtained in 2010 and 2012 with the 2.3-m ANU telescope using the Wide Field Spectrograph (WiFeS; Dopita

Table 5.1: Journal of the IFU observations of Abell 48 with the ANU 2.3-m Telescope.

PN	Date (UT)	λ range (Å)	R	Exp.(s)
Abell 48	2010/04/22	4415–5589	7000	1200
		5222–7070	7000	1200
	2012/08/23	3295–5906	3000	1200
		5462–9326	3000	1200

et al. 2007, 2010). The observations were done with a spectral resolution of $R \sim 7000$ in the 441.5–707.0 nm range in 2010 and $R \sim 3000$ in the 329.5–932.6 nm range in 2012. The WiFeS has a field-of-view of $25'' \times 38''$ and each spatial resolution element of $1\farcs0 \times 0\farcs5$ (or $1'' \times 1''$). The spectral resolution of $R (= \lambda/\Delta\lambda) \sim 3000$ and $R \sim 7000$ corresponds to a full width at half-maximum (FWHM) of ~ 100 and 45 km s^{-1}, respectively. We used the classical data accumulation mode, so a suitable sky window has been selected from the science data for the sky subtraction purpose.

The positions observed on the PN are shown in Fig. 5.1(a). The centre of the IFU was placed in two different positions in 2010 and 2012. The exposure time of 20 min yields a signal-to-noise ratio of $S/N \gtrsim 10$ for the [O III] emission line. Multiple spectroscopic standard stars were observed for the flux calibration purposes, notably Feige 110 and EG 274. As usual, series of bias, flat-field frames, arc lamp exposures, and wire frames were acquired for data reduction, flat-fielding, wavelength calibration and spatial calibration.

Data reductions were carried out using the IRAF pipeline WIFES (version 2.0; 2011 Nov 21).[1] The reduction involves three main tasks: WFTABLE, WFCAL and WFREDUCE. The IRAF task WFTABLE converts the raw data files with

[1]IRAF is distributed by NOAO, which is operated by AURA, Inc., under contract to the National Science Foundation.

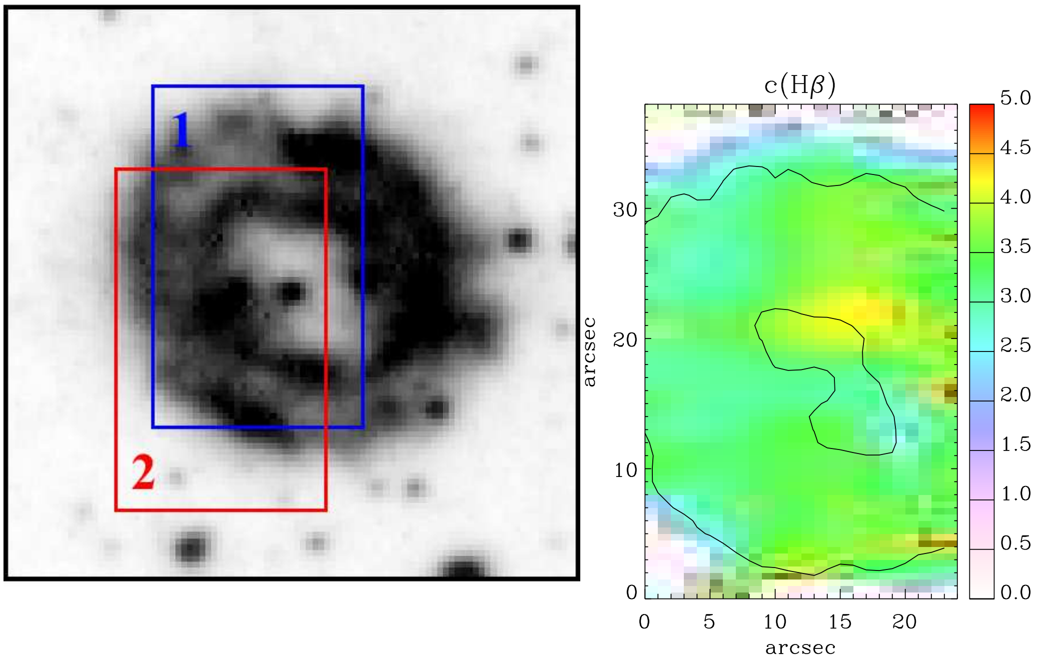

(a) (b)

Figure 5.1: From left to right: (a) narrow-band filter image of PN Abell 48 in Hα obtained from the SuperCOSMOS Sky Hα Survey (SHS; Parker et al. 2005). The rectangles correspond the 25×38-arcsec^2 IFU: 1 (blue) and 2 (red) taken in 2010 April and 2012 August, respectively. Image dimension is 60×60 arcsec^2. (b) Extinction $c(\mathrm{H}\beta)$ map of Abell 48 calculated from the flux ratio Hα/Hβ from fields. Black contour lines show the distribution of the narrow-band emission of Hα in arbitrary unit obtained from the SHS. North is up and east is towards the left-hand side.

the single-extension Flexible Image Transport System (FITS) file format to the Multi-Extension FITS file format, edits FITS file key headers, and makes file lists for reduction purposes. The IRAF task WFCAL extracts calibration solutions, namely the master bias, the master flat-field frame (from QI lamp exposures), the wavelength calibration (from Ne–Ar or Cu–Ar arc exposures and reference arc) and the spatial calibration (from wire frames). The IRAF task WFREDUCE applies the calibration solutions to science data, subtracts sky spectra, corrects for differential atmospheric refraction, and applies the flux calibration using observations of spectrophotometric standard stars.

A complete list of observed emission lines and their flux intensities are given in Table 5.2 on a scale where Hβ = 100. All fluxes were corrected for reddening using $I(\lambda)_{\rm corr} = F(\lambda)_{\rm obs} 10^{c({\rm H}\beta)[1+f(\lambda)]}$. The logarithmic $c({\rm H}\beta)$ value of the interstellar extinction for the case B recombination ($T_{\rm e} = 10\,000$ K and $N_{\rm e} = 1000\,{\rm cm}^{-3}$; Storey & Hummer 1995) has been obtained from the Hα and Hβ Balmer fluxes. We used the Galactic extinction law $f(\lambda)$ of Howarth (1983) for $R_V = A(V)/E(B-V) = 3.1$, and normalized such that $f({\rm H}\beta) = 0$. We obtained an extinction of $c({\rm H}\beta) = 3.1$ for the total fluxes (see Table 5.2). Our derived nebular extinction is in excellent agreement with the value derived by Todt et al. (2013) from the stellar spectral energy (SED). The same method was applied to create $c({\rm H}\beta)$ maps using the flux ratio Hα/Hβ, as shown in Fig. 5.1(b). Assuming that the foreground interstellar extinction is uniformly distributed over the nebula, an inhomogeneous extinction map may be related to some internal dust contributions. As seen, the extinction map of Abell 48 depicts that the shell is brighter than other regions, and it may contain the asymptotic giant branch (AGB) dust remnants.

5.3 Kinematics

Fig. 5.2 shows the spatial distribution maps of the flux intensity, continuum, radial velocity and velocity dispersion of Hα λ6563 and [N II] λ6584 for Abell 48. The white contour lines in the figures depict the distribution of the emission of Hα obtained from the SHS (Parker et al. 2005), which can aid us in distinguishing the nebular borders from the outside or the inside. The observed velocity $v_{\rm obs}$ was transferred to the local standard of rest (LSR) radial velocity $v_{\rm LSR}$ by correcting for the radial velocities induced by the motions of the Earth and Sun at the time of our observation. The transformation from the measured velocity dispersion $\sigma_{\rm obs}$ to the true line-of-sight velocity dispersion $\sigma_{\rm true}$ was done by $\sigma_{\rm true} = \sqrt{\sigma_{\rm obs}^2 - \sigma_{\rm ins}^2 - \sigma_{\rm th}^2}$, i.e. correcting for the instrumental width (typically

Table 5.2: Observed and dereddened relative line fluxes of the PN Abell 48, on a scale where Hβ = 100. Uncertain and very uncertain values are followed by ':' and '::', respectively. The symbol '*' denotes blended emission lines.

$\lambda_{\rm lab}$(Å)	ID	Mult	$F(\lambda)$	$I(\lambda)$	Err(%)
3726.03	[O II]	F1	20.72:	128.96:	25.7
3728.82	[O II]	F1	*	*	*
3868.75	[Ne III]	F1	7.52	38.96	9.4
4340.47	H I 5-2	H5	21.97	54.28:	17.4
4471.50	He I	V14	3.76:	7.42:	12.0
4861.33	H I 4-2	H4	100.00	100.00	6.2
4958.91	[O III]	F1	117.78	99.28	5.3
5006.84	[O III]	F1	411.98	319.35	5.2
5754.60	[N II]	F3	1.73::	0.43::	40.8
5875.66	He I	V11	87.70	18.97	5.3
6312.10	[S III]	F3	4.47::	0.60::	46.9
6461.95	C II	V17.04	3.36:	0.38:	26.2
6548.10	[N II]	F1	252.25	26.09	5.2
6562.77	H I 3-2	H3	2806.94	286.00	5.1
6583.50	[N II]	F1	874.83	87.28	5.3
6678.16	He I	V46	55.90	5.07	5.3
6716.44	[S II]	F2	85.16	7.44	5.1
6730.82	[S II]	F2	92.67	7.99	5.5
7135.80	[Ar III]	F1	183.86	10.88	5.2
7236.42	C II	V3	29.96:	1.63:	20.7
7281.35	He I	V45	11.08::	0.58::	41.3
7751.43	[Ar III]	F1	111.83::	4.00::	34.5
9068.60	[S III]	F1	1236.22	19.08	5.3
c(Hβ)				3.10 ± 0.04	
Hβ/10^{-13} $\frac{\rm erg}{\rm cm^2 s}$			1.076 ± 0.067	1354.6 ± 154.2	

$\sigma_{\rm ins} \approx 42$ km/s for $R \sim 3000$ and $\sigma_{\rm ins} \approx 18$ km/s for $R \sim 7000$) and the thermal broadening ($\sigma_{\rm th}^2 = 8.3\,T_{\rm e}[{\rm kK}]/Z$, where Z is the atomic weight of the atom or ion).

We have used the three-dimensional morpho-kinematic modelling program SHAPE (version 4.5) to study the kinematic structure. The program described in detail by Steffen & López (2006) and Steffen et al. (2011), uses interactively moulded geometrical polygon meshes to generate the 3D structure of objects. The modelling procedure consists of defining the geometry, emissivity distribution and velocity law as a function of position. The program produces several outputs that can be directly compared with long slit or IFU observations, namely the position–velocity (P–V) diagram, the 2-D line-of-sight velocity map on the sky and the projected 3-D emissivity on the plane of the sky. The 2-D line-of-sight velocity map on the sky can be used to interpret the IFU velocity maps. For best comparison with the IFU maps, the inclination (i), the position angle '*PA*' in the plane of the sky, and the model parameters are modified in an iterative process until the qualitatively fitting 3D emission and velocity information are produced. We adopted a model, and then modified the geometry and inclination to conform to the observed Hα and [N II] intensity and radial velocity maps. For this chapter, the three-dimensional structure has then been transferred to a regular cell grid, together with the physical emission properties, including the velocity that, in our case, has been defined as radially outwards from the nebular centre with a linear function of magnitude, commonly known as a Hubble-type flow (see e.g. Steffen et al. 2009).

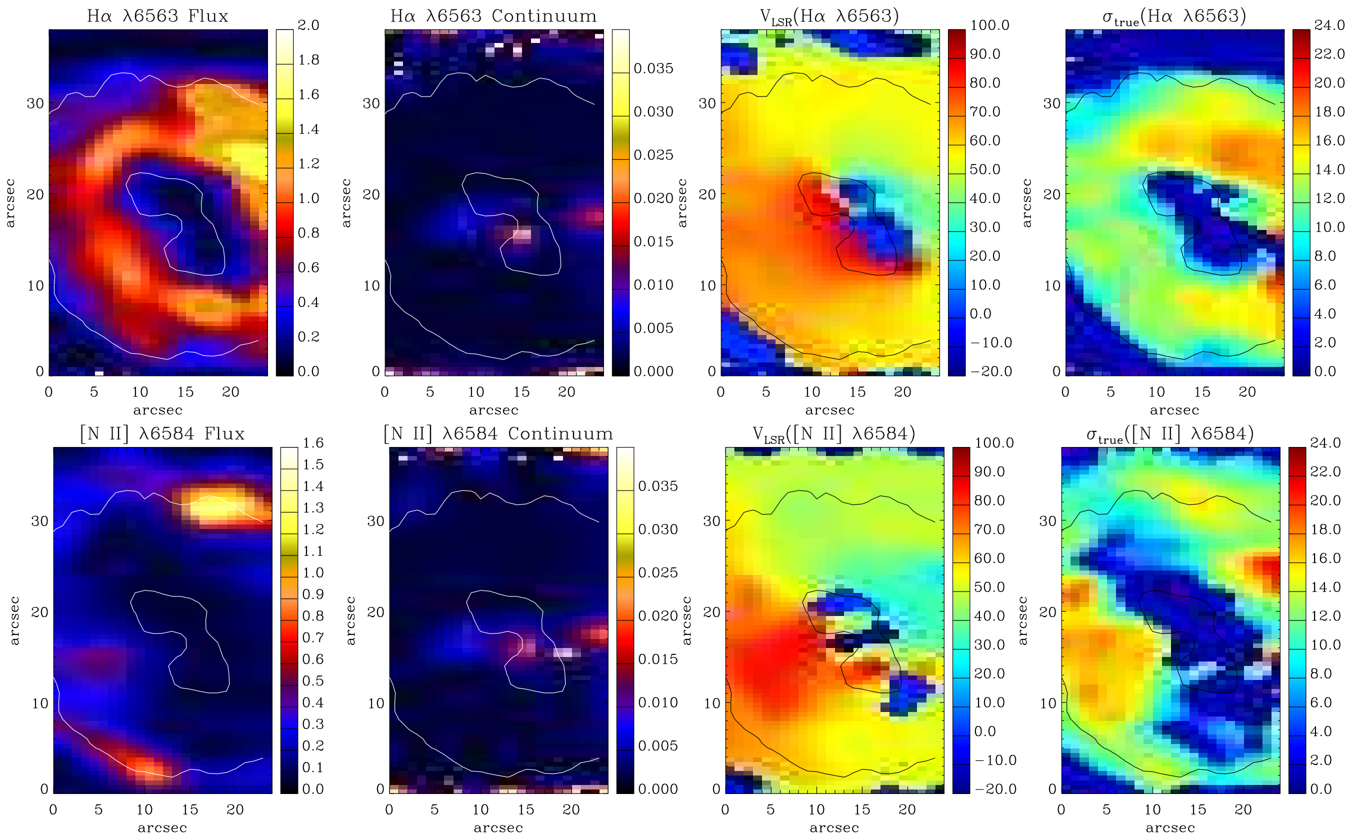

Figure 5.2: Maps of the PN Abell 48 in Hα λ6563 Å (top) and [N II] λ6584 Å (bottom) from the IFU (PA = 0°) taken in 2010 April. From left to right: spatial distribution maps of flux intensity, continuum, LSR velocity and velocity dispersion. Flux unit is in 10^{-15} erg s^{-1} cm^{-2} spaxel^{-1}, continuum in 10^{-15} erg s^{-1} cm^{-2} Å^{-1} spaxel^{-1}, and velocities in km s^{-1}. North is up and east is towards the left-hand side. The white/black contour lines show the distribution of the narrow-band emission of Hα in arbitrary unit obtained from the SHS.

The morpho-kinematic model of Abell 48 is shown in Fig. 5.3(a), which consists of a modified torus, the nebular shell, surrounded by a modified hollow cylinder and the faint outer halo. The shell has an inner radius of 10″ and an outer radius of 23″ and a height of 23″. We found an expansion velocity of $v_{\rm exp} = 35 \pm 5\,{\rm km\,s^{-1}}$ and a LSR systemic velocity of $v_{\rm sys} = 65 \pm 5\,{\rm km\,s^{-1}}$. Our value of the LSR systemic velocity is in good agreement with the heliocentric systemic velocity of $v_{\rm hel} = 50.4 \pm 4.2\,{\rm km\,s^{-1}}$ found by Todt et al. (2013). Following Dopita et al. (1996), we estimated the nebula's age around 1.5 of the dynamical age, so the star left the top of the AGB around 8880 years ago.

Fig. 5.3 shows the orientation of Abell 48 on to the plane of the sky. The nebula has an inclination of $i = -35^{\circ}$ between the line of sight and the nebular symmetry axis. The symmetry axis has a position angle of PA $= 135^{\circ}$ projected on to the plane of the sky, measured from the north towards the east in the equatorial coordinate system (ECS). The PA in the ECS can be transferred into the Galactic position angle (GPA) in the Galactic coordinate system (GCS), measured from the north Galactic pole (NGP; GPA $= 0^{\circ}$) towards the Galactic east (GPA $= 90^{\circ}$). Note that GPA $= 90^{\circ}$ describes an alignment with the Galactic plane, while GPA $= 0^{\circ}$ is perpendicular to the Galactic plane. As seen in Table 5.3, Abell 48 has a GPA of $197\overset{\circ}{.}8$, meaning that the symmetry axis is approximately perpendicular to the Galactic plane.

Based on the systemic velocity, Abell 48 must be located at less than 2 kpc, since higher distances result in very high peculiar velocities ($v_{\rm pec} > 189\,{\rm km\,s^{-1}}$; $v_{\rm pec} = 170\,{\rm km\,s^{-1}}$ found in few PNe in the Galactic halo by Maciel & Dutra 1992). However, it cannot be less than 1.5 kpc due to the large interstellar extinction. Using the infrared dust maps[2] of Schlegel et al. (1998), we found a mean reddening value of $E(B-V) = 11.39 \pm 0.64$ for an aperture of 10′ in diameter in the Galactic latitudes and longitude of $(l,b) = (29.0, 0.4)$, which is within a line-of-sight depth of $\lesssim 20$ kpc of the Galaxy. Therefore, Abell 48 with $E(B-V) \simeq 2.14$

[2]Website: `http://www.astro.princeton.edu/~schlegel/dust`

(a) SHAPE mesh model

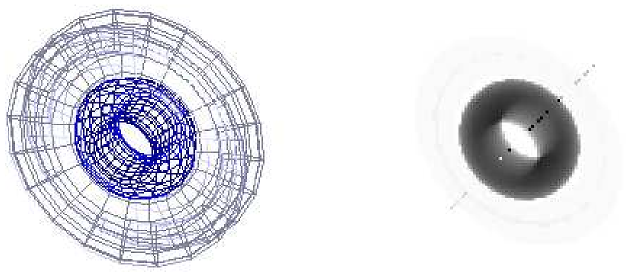

(b) SHAPE model results

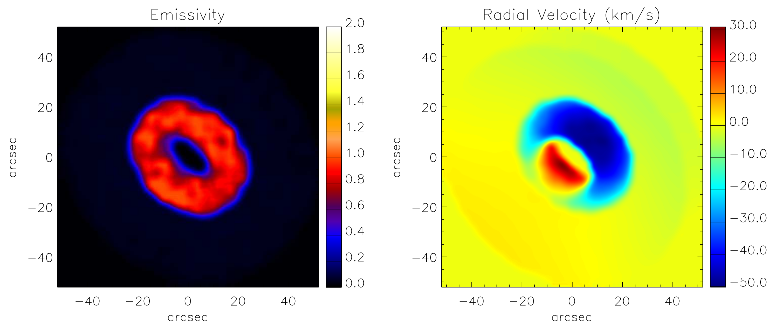

Figure 5.3: (a) The SHAPE mesh model before rendering at the best-fitting inclination and corresponding rendered model. (b) The normalized synthetic intensity map and the radial velocity map at the inclination of $-35°$ and the position angle of 135°, derived from the model ($v_{\rm sys} = 0$), which can be compared directly with Fig. 5.2.

Table 5.3: Kinematic results obtained for Abell 48 based on the morpho-kinematic model matched to the observed 2-D radial velocity map.

Parameter	Value
$r_{\rm out}$ (arcsec)	23 ± 4
δr (arcsec)	13 ± 2
h (arcsec)	23 ± 4
i	$-35° \pm 2°$
PA	$135° \pm 2°$
GPA	$197°48' \pm 2°$
$v_{\rm sys}$ (km s−1)	65 ± 5
$v_{\rm exp}$ (km s−1)	35 ± 5

must have a distance of less than 3.3 kpc. Considering the fact that the Galactic bulge absorbs photons overall 1.9 times more than the Galactic disc (Driver et al. 2007), the distance of Abell 48 should be around 2 kpc, as it is located at the dusty Galactic disc.

5.4 Nebular empirical analysis

5.4.1 Plasma diagnostics

The derived electron temperatures ($T_{\rm e}$) and densities ($N_{\rm e}$) are listed in Table 5.5, together with the ionization potential required to create the emitting ions. We obtained $T_{\rm e}$ and $N_{\rm e}$ from temperature-sensitive and density-sensitive emission lines by solving the equilibrium equations of level populations for a multilevel atomic model using EQUIB code (Howarth & Adams 1981). The atomic data sets used for our plasma diagnostics from collisionally excited lines (CELs), as well as for abundances derived from CELs, are given in Table 5.4. The diagnostics procedure to determine temperatures and densities from CELs is as follows: we assume a representative initial electron temperature of 10 000 K in order to derive $N_{\rm e}$ from [S II] line ratio; then $T_{\rm e}$ is derived from [N II] line ratio in conjunction with the mean density derived from the previous step. The calculations are iterated to give self-consistent results for $N_{\rm e}$ and $T_{\rm e}$. The correct choice of electron density and temperature is important for the abundance determination.

We see that the PN Abell 48 has a mean temperature of $T_{\rm e}$([N II]) $= 6980 \pm 930$ K, and a mean electron density of $N_{\rm e}$([S II]) $= 750 \pm 200$ cm^{-3}, which are in reasonable agreement with $T_{\rm e}$([N II]) $= 7\,200 \pm 750$ K and $N_{\rm e}$([S II]) $= 1000 \pm 130$ cm^{-3} found by Todt et al. (2013). The uncertainty on $T_{\rm e}$([N II]) is order of 40 percent or more, due to the weak flux intensity of [N II] λ5755, the recombination contribution, and high interstellar extinction. Therefore, we adopted the mean electron temperature from our photoionization model for our CEL

Table 5.4: References for atomic data.

Ion	Transition probabilities	Collision strengths
N^{+}	Bell et al. (1995)	Stafford et al. (1994)
O^{+}	Zeippen (1987)	Pradhan et al. (2006)
O^{2+}	Storey & Zeippen (2000)	Lennon & Burke (1994)
Ne^{2+}	Landi & Bhatia (2005)	McLaughlin & Bell (2000)
S^{+}	Mendoza & Zeippen (1982)	Ramsbottom et al. (1996)
S^{2+}	Mendoza & Zeippen (1982)	Tayal & Gupta (1999)
	Huang (1985)	
Ar^{2+}	Biémont & Hansen (1986)	Galavis et al. (1995)
Ion	Recombination coefficient	Case
H^{+}	Storey & Hummer (1995)	B
He^{+}	Porter et al. (2013)	B
C^{2+}	Davey et al. (2000)	B

abundance analysis.

Table 5.5 also lists the derived He I temperatures, which are lower than the CEL temperatures, known as the ORL-CEL temperature discrepancy problem in PNe (see e.g. Liu et al. 2000, 2004b). To determine the electron temperature from the He I $\lambda\lambda$5876, 6678 and 7281 lines, we used the emissivities of He I lines by Smits (1996), which also include the temperature range of $T_{\rm e} < 5000$ K. We derived electron temperatures of $T_{\rm e}$(He I) $= 5110$ K and $T_{\rm e}$(He I) $= 4360$ K from the flux ratio He I $\lambda\lambda$7281/5876 and $\lambda\lambda$7281/6678, respectively. Similarly, we got $T_{\rm e}$(He I) $= 6960$ K for He I $\lambda\lambda$7281/5876 and $T_{\rm e}$(He I) $= 7510$ K for $\lambda\lambda$7281/6678 from the measured nebular spectrum by Todt et al. (2013).

Table 5.5: Diagnostics for the electron temperature, T_e and the electron density, N_e. References: D13 – this work; T13 – Todt et al. (2013).

Ion	Diagnostic	I.P.(eV)	T_e(K)	Ref.
[N II]	$\frac{\lambda6548+\lambda6584}{\lambda5755}$	14.53	6980 ± 930	D13
			7200 ± 750	T13
[O III]	$\frac{\lambda4959+\lambda5007}{\lambda4363}$	35.12	11870 ± 1640	T13
He I	$\frac{\lambda7281}{\lambda5876}$	24.59	5110 ± 2320	D13
			6960 ± 450	T13
He I	$\frac{\lambda7281}{\lambda6678}$	24.59	4360 ± 1820	D13
			7510 ± 4800	T13
			N_e(cm^{-3})	
[S II]	$\frac{\lambda6717}{\lambda6731}$	10.36	750 ± 200	D13
			1000 ± 130	T13

5.4.2 Ionic and total abundances from ORLs

Using the effective recombination coefficients (given in Table 5.4), we determine ionic abundances, X^{i+}/H^+, from the measured intensities of optical recombination lines (ORLs) as follows:

$$\frac{N(X^{i+})}{N(H^+)} = \frac{I(\lambda)}{I(H\beta)}\frac{\lambda(\text{Å})}{4861}\frac{\alpha_{\rm eff}(H\beta)}{\alpha_{\rm eff}(\lambda)}, \tag{5.1}$$

where $I(\lambda)$ is the intrinsic line flux of the emission line λ emitted by ion X^{i+}, $I(H\beta)$ is the intrinsic line flux of Hβ, $\alpha_{\rm eff}(H\beta)$ the effective recombination coefficient of Hβ, and $\alpha_{\rm eff}(\lambda)$ the effective recombination coefficient for the emission line λ.

Abundances of helium and carbon from ORLs are given in Table 5.6. We derived the ionic and total helium abundances from He I $\lambda4471$, $\lambda5876$ and $\lambda6678$ lines. We assumed the Case B recombination for the He I lines (Porter et al. 2012, 2013). We adopted an electron temperature of $T_e = 5\,000$ K from

Table 5.6: Empirical ionic abundances derived from ORLs.

Ion	λ(Å)	Mult	Value [a]
He^{+}	4471.50	V14	0.141
	5876.66	V11	0.121
	6678.16	V46	0.115
	Mean		0.124
He^{2+}	4685.68	3.4	0.0
He/H			0.124
C^{2+}	6461.95	V17.40	3.068(−3)
	7236.42	V3	1.254(−3)
	Mean		2.161(−3)

[a] Assuming $T_{\rm e} = 5\,000$ K and $N_{\rm e} = 1000\,{\rm cm}^{-3}$.

He I lines, and an electron density of $N_{\rm e} = 1000$ cm^{-3}. We averaged the He^{+}/H^{+} ionic abundances from the He I λ4471, λ5876 and λ6678 lines with weights of 1:3:1, roughly the intrinsic intensity ratios of these three lines. The total He/H abundance ratio is obtained by simply taking the sum of He^{+}/H^{+} and He^{2+}/H^{+}. However, He^{2+}/H^{+} is equal to zero, since He II λ4686 is not present. The C^{2+} ionic abundance is obtained from C II λ6462 and λ7236 lines.

5.4.3 Ionic and total abundances from CELs

We determined abundances for ionic species of N, O, Ne, S and Ar from CELs. To deduce ionic abundances, we solve the statistical equilibrium equations for each ion using EQUIB code, giving level population and line sensitivities for specified $N_{\rm e} = 1000$ cm^{-3} and $T_{\rm e} = 10\,000$ K adopted according to our photoionization modelling. Once the equations for the population numbers are solved, the ionic abundances, X^{i+}/H^{+}, can be derived from the observed line intensities of CELs as follows:

$$\frac{N(\mathrm{X}^{i+})}{N(\mathrm{H}^{+})} = \frac{I(\lambda_{ij})}{I(\mathrm{H}\beta)} \frac{\lambda_{ij}(\text{Å})}{4861} \frac{\alpha_{\mathrm{eff}}(\mathrm{H}\beta)}{A_{ij}} \frac{N_{\mathrm{e}}}{n_i}, \tag{5.2}$$

where $I(\lambda_{ij})$ is the dereddened flux of the emission line λ_{ij} emitted by ion X^{i+} following the transition from the upper level i to the lower level j, $I(\mathrm{H}\beta)$ the dereddened flux of Hβ, $\alpha_{\mathrm{eff}}(\mathrm{H}\beta)$ the effective recombination coefficient of Hβ, A_{ij} the Einstein spontaneous transition probability of the transition, n_i the fractional population of the upper level i, and N_{e} is the electron density.

Total elemental and ionic abundances of nitrogen, oxygen, neon, sulphur and argon from CELs are presented in Table 5.7. Total elemental abundances are derived from ionic abundances using the ionization correction factors (icf) formulas given by Kingsburgh & Barlow (1994). The total O/H abundance ratio is obtained by simply taking the sum of the $\mathrm{O}^{+}/\mathrm{H}^{+}$ derived from [O II] $\lambda\lambda$3726,3729 doublet, and the $\mathrm{O}^{2+}/\mathrm{H}^{+}$ derived from [O III] $\lambda\lambda$4959,5007 doublet, since He II λ4686 is not present, so $\mathrm{O}^{3+}/\mathrm{H}^{+}$ is negligible. The total N/H abundance ratio was calculated from the $\mathrm{N}^{+}/\mathrm{H}^{+}$ ratio derived from the [N II] $\lambda\lambda$6548,6584 doublet, correcting for the unseen $\mathrm{N}^{2+}/\mathrm{H}^{+}$ using,

$$\frac{\mathrm{N}}{\mathrm{H}} = \left(\frac{\mathrm{N}^{+}}{\mathrm{H}^{+}}\right)\left(\frac{\mathrm{O}}{\mathrm{O}^{+}}\right) \tag{5.3}$$

The $\mathrm{Ne}^{2+}/\mathrm{H}^{+}$ is derived from [Ne III] λ3869 line. Similarly, the unseen $\mathrm{Ne}^{+}/\mathrm{H}^{+}$ is corrected for, using

$$\frac{\mathrm{Ne}}{\mathrm{H}} = \left(\frac{\mathrm{Ne}^{2+}}{\mathrm{H}^{+}}\right)\left(\frac{\mathrm{O}}{\mathrm{O}^{2+}}\right) \tag{5.4}$$

For sulphur, we have $\mathrm{S}^{+}/\mathrm{H}^{+}$ from the [S II] $\lambda\lambda$6716,6731 doublet and $\mathrm{S}^{2+}/\mathrm{H}^{+}$ from the [S III] λ9069 line. The total sulphur abundance is corrected for the unseen stages of ionization using

$$\frac{\mathrm{S}}{\mathrm{H}} = \left(\frac{\mathrm{S}^{+}}{\mathrm{H}^{+}} + \frac{\mathrm{S}^{2+}}{\mathrm{H}^{+}}\right)\left[1 - \left(1 - \frac{\mathrm{O}^{+}}{\mathrm{O}}\right)^{3}\right]^{-1/3} \tag{5.5}$$

The [Ar III] 7136 line is only detected, so we have only $\mathrm{Ar}^{2+}/\mathrm{H}^{+}$. The total argon abundance is obtained by assuming $Ar^{+}/Ar = N^{+}/N$:

$$\frac{\mathrm{Ar}}{\mathrm{H}} = \left(\frac{\mathrm{Ar}^{2+}}{\mathrm{H}^{+}}\right)\left(1 - \frac{\mathrm{N}^{+}}{\mathrm{N}}\right)^{-1} \tag{5.6}$$

As it does not include the unseen Ar^{3+}, so the derived elemental argon may be underestimated.

Fig. 5.4 shows the spatial distribution of ionic abundance ratio He^{+}/H^{+}, N^{+}/H^{+}, O^{2+}/H^{+} and S^{+}/H^{+} derived for given $T_{\rm e} = 10000$ K and $N_{\rm e} = 1000\,{\rm cm}^{-3}$. We notice that both O^{2+}/H^{+} and He^{+}/H^{+} are very high over the shell, whereas N^{+}/H^{+} and S^{+}/H^{+} are seen at the edges of the shell. It shows obvious results of the ionization sequence from the highly inner ionized zones to the outer low ionized regions.

5.5 Photoionization modelling

The 3-D photoionization code MOCASSIN (version 2.02.67; Ercolano et al. 2003a, 2005, 2008) was used to study the best-fitting model for Abell 48. The code has been used to model a number of PNe, for example NGC 3918 (Ercolano et al. 2003b), NGC 7009 (Gonçalves et al. 2006), NGC 6302 (Wright et al. 2011), and SuWt 2 (Danehkar et al. 2013). The modelling procedure consists of defining the density distribution and elemental abundances of the nebula, as well as assigning the ionizing spectrum of the CS. This code uses a Monte Carlo method to solve self-consistently the 3-D radiative transfer of the stellar radiation field in a gaseous nebula with the defined density distribution and chemical abundances. It produces the emission-line spectrum, the thermal structure and the ionization structure of the nebula. It allows us to determine the stellar characteristics and the nebula parameters. The atomic data sets used for the calculation are energy levels, collision strengths and transition probabilities from the CHIANTI data base (version 5.2; Landi et al. 2006), hydrogen and helium free–bound coefficients of Ercolano & Storey (2006), and opacities from Verner et al. (1993)

Table 5.7: Empirical ionic abundances derived from CELs.

Ion	λ(Å)	Mult	Value [a]
N^{+}	6548.10	F1	1.356(−5)
	6583.50	F1	1.486(−5)
	Mean		1.421(−5)
	icf(N)		3.026
N/H			4.299(−5)
O^{+}	3727.43	F1	5.251(−5)
O^{2+}	4958.91	F1	1.024(−4)
	5006.84	F1	1.104(−4)
	Average		1.064(−4)
	icf(O)		1.0
O/H			1.589(−4)
Ne^{2+}	3868.75	F1	4.256(−5)
	icf(Ne)		1.494
Ne/H			6.358(−5)
S^{+}	6716.44	F2	4.058(−7)
	6730.82	F2	3.896(−7)
	Average		3.977(−7)
S^{2+}	9068.60	F1	5.579(−6)
	icf(S)		1.126
S/H			6.732(−6)
Ar^{2+}	7135.80	F1	9.874(−7)
	icf(Ar)		1.494
Ar/H			1.475(−6)

[a] Assuming $T_e = 10\,000\,K$ and $N_e = 1000\,cm^{-3}$.

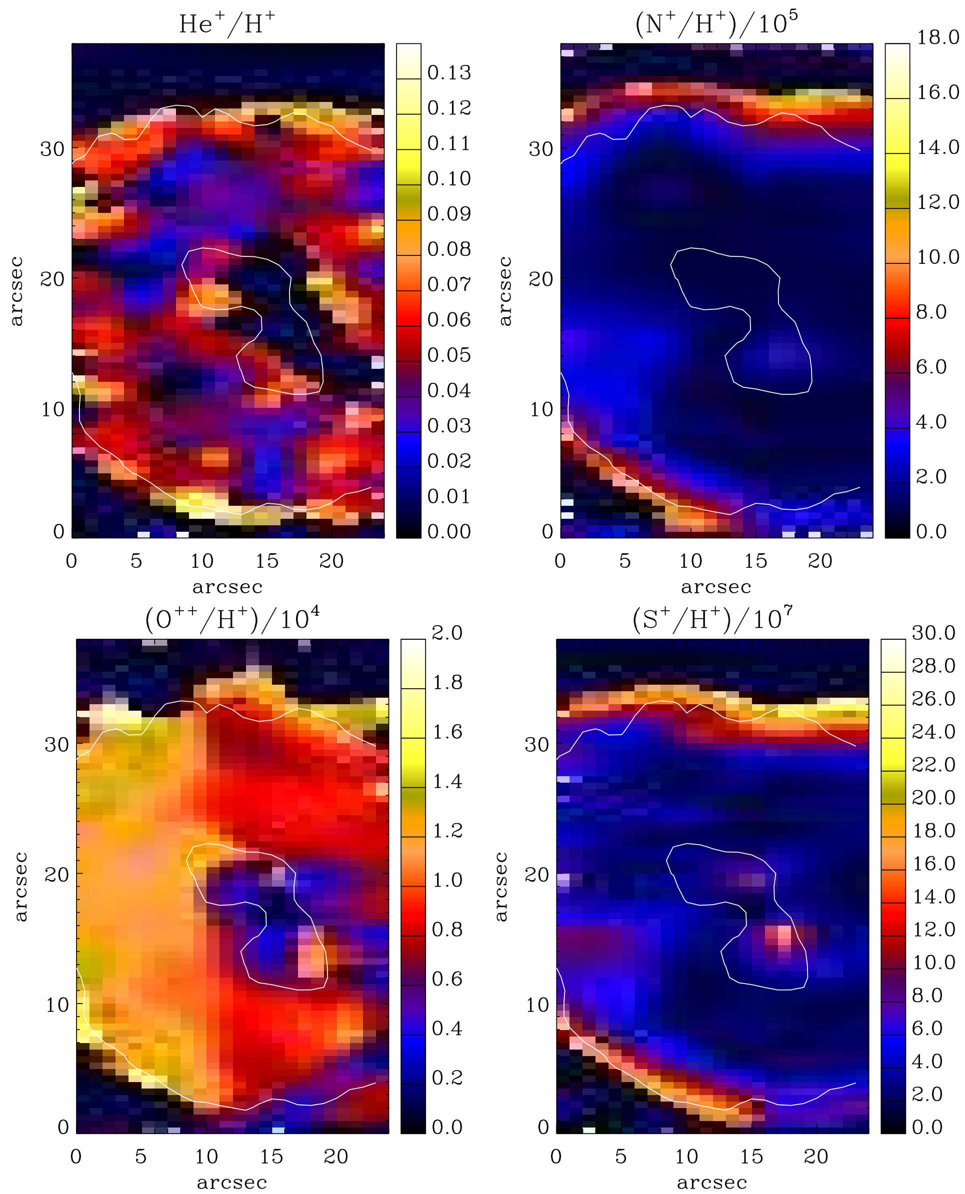

Figure 5.4: Ionic abundance maps of Abell 48. From left to right: spatial distribution maps of singly ionized helium abundance ratio He^{+}/H^{+} from He I ORLs (4472, 5877, 6678); ionic nitrogen abundance ratio N^{+}/H^{+} ($\times 10^{-5}$) from [N II] CELs (5755, 6548, 6584); ionic oxygen abundance ratio O^{2+}/H^{+} ($\times 10^{-4}$) from [O III] CELs (4959, 5007); and ionic sulphur abundance ratio S^{+}/H^{+} ($\times 10^{-7}$) from [S II] CELs (6716, 6731). North is up and east is toward the left-hand side. The white contour lines show the distribution of the narrow-band emission of Hα in arbitrary unit obtained from the SHS.

and Verner & Yakovlev (1995).

The best-fitting model was obtained through an iterative process, involving the comparison of the predicted Hβ luminosity $L_{\mathrm{H}\beta}$(erg s^{-1}), the flux intensities of some important lines, relative to Hβ (such as [O III] λ5007 and [N II] λ6584), with those measured from the observations. The free parameters included distance and nebular parameters. We initially used the stellar luminosity ($L_{\star} = 6000\,\mathrm{L}_{\odot}$) and effective temperature ($T_{\mathrm{eff}} = 70$kK) found by Todt et al. (2013). However, we slightly adjusted the stellar luminosity to match the observed line flux of [O III] emission line. Moreover, we adopted the nebular density and abundances derived from empirical analysis in Section 5.4, but they have been gradually adjusted until the observed nebular emission-line spectrum was reproduced by the model. The best-fitting $L_{\mathrm{H}\beta}$ depends upon the distance and nebula density. The plasma diagnostics yields $N_{\mathrm{e}} = 750$–$1000\,\mathrm{cm}^{-3}$, which can be an indicator of the density range. Based on the kinematic analysis, the distance must be less than 2 kpc, but more than 1.5 kpc due to the large interstellar extinction. We matched the predicted Hβ luminosity $L(\mathrm{H}\beta)$ with the value derived from the observation by adjusting the distance and nebular density. Then, we adjusted abundances to get the best emission-line spectrum.

5.5.1 The ionizing spectrum

The hydrogen-deficient synthetic spectra of Abell 48 was modelled using stellar model atmospheres produced by the Potsdam Wolf–Rayet (PoWR) models for expanding atmospheres (Gräfener et al. 2002; Hamann & Gräfener 2004). It solves the non-local thermodynamic equilibrium (non-LTE) radiative transfer equation in the comoving frame, iteratively with the equations of statistical equilibrium and radiative equilibrium, for an expanding atmosphere under the assumptions of spherical symmetry, stationarity and homogeneity. The result of our model atmosphere is shown in Fig. 5.5. The model atmosphere calculated

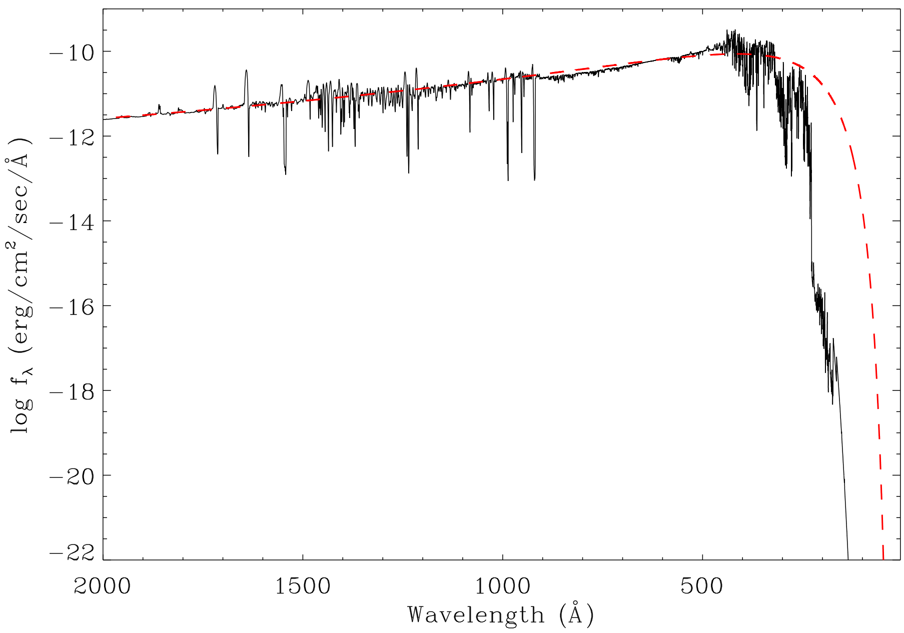

Figure 5.5: Non-LTE model atmosphere flux (solid line) calculated with the PoWR models for the surface abundances H:He:C:N:O = 10:85:0.3:5:0.6 by mass and the stellar temperature $T_{\rm eff} = 70$ kK (Todt et al. 2013), compared with a blackbody (dashed line) at the same temperature.

with the PoWR code is for the stellar surface abundances H:He:C:N:O = 10:85:0.3:5:0.6 by mass, the stellar temperature $T_{\rm eff} = 70$ kK, the transformed radius $R_{\rm t} = 0.54\,{\rm R}_{\odot}$ and the wind terminal velocity $v_{\infty} = 1000$ km s^{-1}. The best photoionization model was obtained with an effective temperature of 70 kK (the same as PoWR model used by Todt et al. 2013) and a stellar luminosity of $L_{\star}/{\rm L}_{\odot} = 5500$, which is close to $L_{\star}/{\rm L}_{\odot} = 6000$ adopted by Todt et al. (2013). This stellar luminosity was found to be consistent with the observed Hβ luminosity and the flux ratio of [O III]/Hβ. A stellar luminosity higher than 5500 L$_{\odot}$ produces inconsistent results for the nebular photoionization modelling. The emission-line spectrum produced by our adopted stellar parameters was found to be consistent with the observations.

5.5.2 The density distribution

We initially used a three-dimensional uniform density distribution, which was developed from our kinematic analysis. However, the interacting stellar winds (ISW) model developed by Kwok et al. (1978) demonstrated that a slow dense superwind from the AGB phase is swept up by a fast tenuous wind during the PN phase, creating a compressed dense shell, which is similar to what we see in Fig. 5.6. Additionally, Kahn & West (1985) extended the ISW model to describe a highly elliptical mass distribution. This extension later became known as the generalized interacting stellar winds theory. There are a number of hydrodynamic simulations, which showed the applications of the ISW theory for bipolar PNe (see e.g. Mellema 1996, 1997). As shown in Fig. 5.6, we adopted a density structure with a toroidal wind mass-loss geometry, similar to the ISW model. In our model, we defined a density distribution in the cylindrical coordinate system, which has the form $N_{\rm H}(r) = N_0[1+(r/r_{\rm in})^{-\alpha}]$, where r is the radial distance from the centre, α the radial density dependence, N_0 the characteristic density, $r_{\rm in} = r_{\rm out} - \delta r$ the inner radius, $r_{\rm out}$ the outer radius and δr the thickness.

The density distribution is usually a complicated input parameter to constrain. However, the values found from our plasma diagnostics ($N_{\rm e} = 750$–1000 cm^{-3}) allowed us to constrain our density model. The outer radius and the height of the cylinder are equal to $r_{\rm out} = 23''$ and the thickness is $\delta r = 13''$. The density model and distance (size) were adjusted in order to reproduce $I({\rm H}\beta) = 1.355 \times 10^{-10}\,{\rm erg\,s^{-1}\,cm^{-2}}$, dereddened using c(H$\beta$) = 3.1 (see Section 5.2). We tested distances, with values ranging from 1.5 to 2.0 kpc. We finally adopted the characteristic density of $N_0 = 600\,{\rm cm^{-3}}$ and the radial density dependence of $\alpha = 1$. The value of 1.90 kpc found here, was chosen, because of the best predicted Hβ luminosity, and it is in excellent agreement with the distance constrained by the synthetic spectral energy distribution (SED) from the PoWR models. Once the density distribution and distance were identified,

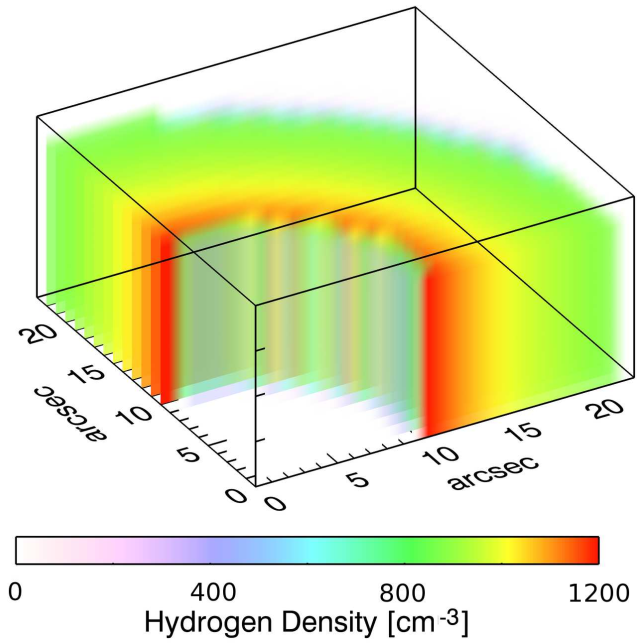

Figure 5.6: The density distribution based on the ISW models adopted for photoionization modelling of Abell 48. The cylinder has outer radius of 23″ and thickness of 13″. Axis units are arcsec, where 1 arcsec is equal to 9.30×10^{-3} pc based on the distance determined by our photoionization models.

the variation of the nebular ionic abundances were explored.

5.5.3 The nebular elemental abundances

Table 5.8 lists the nebular elemental abundances (with respect to H) used for the photoionization model. We used a homogeneous abundance distribution, since we do not have any direct observational evidence for the presence of chemical inhomogeneities. Initially, we used the abundances from empirical analysis as initial values for our modelling (see Section 5.4). They were successively modified to fit the optical emission-line spectrum through an iterative process. We obtain a C/O ratio of 21 for Abell 48, indicating that it is predominantly C-rich. Furthermore, we find a helium abundance of 0.12. This can be an indicator of a large amount of mixing processing in the He-rich lay-

Table 5.8: Input parameters for the MOCASSIN photoionization models.

Stellar and Nebular Parameters		Nebular Abundances	Model	Obs.
$T_{\rm eff}$ (kK)	70	He/H	0.120	0.124
$L_{\star}$ ($L_{\odot}$)	5500	C/H $\times 10^3$	3.00	–
$N_{\rm H}$ (cm^{-3})	800-1200	N/H $\times 10^5$	6.50	4.30
D (kpc)	1.9	O/H $\times 10^4$	1.40	1.59
$r_{\rm out}$ (arcsec)	23	Ne/H $\times 10^5$	6.00	6.36
δr (arcsec)	13	S/H $\times 10^6$	6.00	6.73
h (arcsec)	23	Ar/H $\times 10^6$	1.20	1.48

ers during the He-shell flash leading to an increase carbon abundance. The nebulae around H-deficient CSs typically have larger carbon abundances than those with H-rich CSs (see review by De Marco & Barlow 2001). The O/H we derive for Abell 48 is lower than the solar value (O/H $= 4.57 \times 10^{-4}$; Asplund et al. 2009). This may be due to that the progenitor has a sub-solar metallicity. The enrichment of carbon can be produced in a very intense mixing process in the He-shell flash (Herwig et al. 1997). Other elements seem to be also decreased compared to the solar values, such as sulphur and argon. Sulphur could be depleted on to dust grains (Sofia et al. 1994), but argon cannot have any strong depletion by dust formation (Sofia & Jenkins 1998). We notice that the N/H ratio is about the solar value given by Asplund et al. (2009), but it can be produced by secondary conversion of initial carbon if we assume a sub-solar metallicity progenitor. The combined (C+N+O)/H ratio is by a factor of 3.9 larger than the solar value, which can be produced by multiple dredge-up episodes occurring in the AGB phase.

5.6 Model results

5.6.1 Comparison of the emission-line fluxes

Table 5.9 compares the flux intensities predicted by the best-fitting model with those from the observations. Columns 2 and 3 present the dereddened fluxes of our observations and those from Todt et al. (2013). The predicted emission-line fluxes are given in Column 4, relative to the intrinsic dereddened Hβ flux, on a scale where $I(\mathrm{H}\beta) = 100$. The most emission-line fluxes presented are in reasonable agreement with the observations. However, we notice that the [O II] λ7319 and λ7330 doublets are overestimated by a factor of 3, which can be due to the recombination contribution. Our photoionization code incorporates the recombination term to the statistical equilibrium equations. However, the recombination contribution are less than 30 per cent for the values of T_{e} and N_{e} found from the plasma diagnostics. Therefore, the discrepancy between our model and observed intensities of these lines can be due to inhomogeneous condensations such as clumps and/or colder small-scale structures embedded in the global structure. It can also be due to the measurement errors of these weak lines. The [O II] $\lambda\lambda$3726,3729 doublet predicted by the model is around 25 per cent lower, which can be explained by either the recombination contribution or the flux calibration error. There is a notable discrepancy in the predicted [N II] λ5755 auroral line, being higher by a factor of ~ 3. It can be due to the errors in the flux measurement of the [N II] λ5755 line. The predicted [Ar III] λ7751 line is also 30 per cent lower, while [Ar III] λ7136 is about 20 per cent higher. The [Ar III] λ7751 line usually is blended with the telluric line, so the observed intensity of these line can be overestimated. It is the same for [S III] λ9069, which is typically affected by the atmospheric absorption band.

Table 5.9: Dereddened observed and predicted emission lines fluxes for Abell 48. Uncertain and very uncertain values are followed by ':' and '::', respectively. The symbol '*' denotes blended emission lines.

Line	Observed		Predicted
	D13	T13	
$I(\mathrm{H}\beta)/10^{-10}\,\frac{\mathrm{erg}}{\mathrm{cm}^2\mathrm{s}}$	1.355	–	1.371
Hβ 4861	100.00	100.00	100.00
Hα 6563	286.00	290.60	285.32
Hγ 4340	54.28:	45.10	46.88
Hδ 4102	–	–	25.94
He I 4472	7.42:	–	6.34
He I 5876	18.97	20.60	17.48
He I 6678	5.07	4.80	4.91
He I 7281	0.58::	0.70	0.97
He II 4686	–	–	0.00
C II 6462	0.38	–	0.27
C II 7236	1.63	–	1.90
[N II] 5755	0.43::	0.40	1.20
[N II] 6548	26.09	28.20	26.60
[N II] 6584	87.28	77.00	81.25
[O II] 3726	128.96:	–	59.96
[O II] 3729	*	–	43.54
[O II] 7320	–	0.70	2.16
[O II] 7330	–	0.60	1.76

References: D13 – this work; T13 – Todt et al. (2013).

Table 5.9: (continued)

Line	Observed		Predicted
	D13	T13	
[O III] 4363	–	3.40	2.30
[O III] 4959	99.28	100.50	111.82
[O III] 5007	319.35	316.50	333.66
[Ne III] 3869	38.96	–	39.60
[Ne III] 3967	–	–	11.93
[S II] 4069	–	–	1.52
[S II] 4076	–	–	0.52
[S II] 6717	7.44	5.70	10.30
[S II] 6731	7.99	6.80	10.57
[S III] 6312	0.60::	–	2.22
[S III] 9069	19.08	–	16.37
[Ar III] 7136	10.88	10.20	12.75
[Ar III] 7751	4.00::	–	3.05
[Ar IV] 4712	–	–	0.61
[Ar IV] 4741	–	–	0.51

5.6.2 Ionization and thermal structure

The volume-averaged fractional ionic abundances are listed in Table 5.10. We note that hydrogen and helium are singly-ionized. We see that the O^+/O ratio is higher than the N^+/N ratio by a factor of 1.34, which is dissimilar to what is generally assumed in the *icf* method. However, the O^{2+}/O ratio is nearly a factor of 1.16 larger than the Ne^{2+}/Ne ratio, in agreement with the general assumption for *icf*(Ne). We see that only 19 per cent of the total nitrogen in the nebula is in the form of N^+. However, the total oxygen largely exists as O^{2+} with 70 per cent and then O^+ with 26 per cent.

The elemental abundances we used for the photoionization model returns

Table 5.10: Fractional ionic abundances for Abell 48 obtained from the photoionization models.

	Ion						
Element	I	II	III	IV	V	VI	VII
H	3.84(−2)	9.62(−1)					
He	3.37(−2)	9.66(−1)	1.95(−6)				
C	5.43(−4)	1.73(−1)	8.18(−1)	8.93(−3)	1.64(−15)	1.00(−20)	1.00(−20)
N	1.75(−2)	1.94(−1)	7.79(−1)	8.98(−3)	2.72(−15)	1.00(−20)	1.00(−20)
O	4.32(−2)	2.60(−1)	6.97(−1)	1.18(−7)	3.09(−20)	1.00(−20)	1.00(−20)
Ne	9.94(−3)	3.88(−1)	6.03(−1)	1.12(−13)	1.00(−20)	1.00(−20)	1.00(−20)
S	6.56(−5)	8.67(−2)	6.99(−1)	2.12(−1)	2.42(−3)	1.66(−15)	1.00(−20)
Ar	2.81(−3)	3.74(−2)	8.43(−1)	1.17(−1)	1.02(−13)	1.00(−20)	1.00(−20)

ionic abundances listed in Table 5.11, are comparable to those from the empirical analysis derived in Section 5.4. The ionic abundances derived from the observations do not show major discrepancies in He^{+}/H^{+}, C^{2+}/H^{+}, N^{+}/H^{+}, O^{2+}/H^{+}, Ne^{2+}/H^{+} and Ar^{2+}/H^{+}; differences remain below 18 per cent. However, the predicted and empirical values of O^{+}/H^{+}, S^{+}/H^{+} and S^{2+}/H^{+} have discrepancies of about 45, 31 and 33 per cent, respectively.

Fig. 5.7(bottom) shows plots of the ionization structure of helium, carbon, oxygen, argon (left-hand panel), nitrogen, neon and sulphur (right-hand panel) as a function of radius along the equatorial direction. As seen, ionization layers have a clear ionization sequence from the highly ionized inner parts to the outer regions. Helium is 97 percent singly-ionized over the shell, while oxygen is 26 percent singly ionized and 70 percent doubly ionized. Carbon and nitrogen are about ~ 20 percent singly ionized ~ 80 percent doubly ionized. The distribution of N^{+} is in full agreement with the IFU map, given in Fig 5.4. Comparison between the He^{+}, O^{2+} and S^{+} ionic abundance maps obtained from our IFU observations and the ionic fractions predicted by our photoionization model also show excellent agreement.

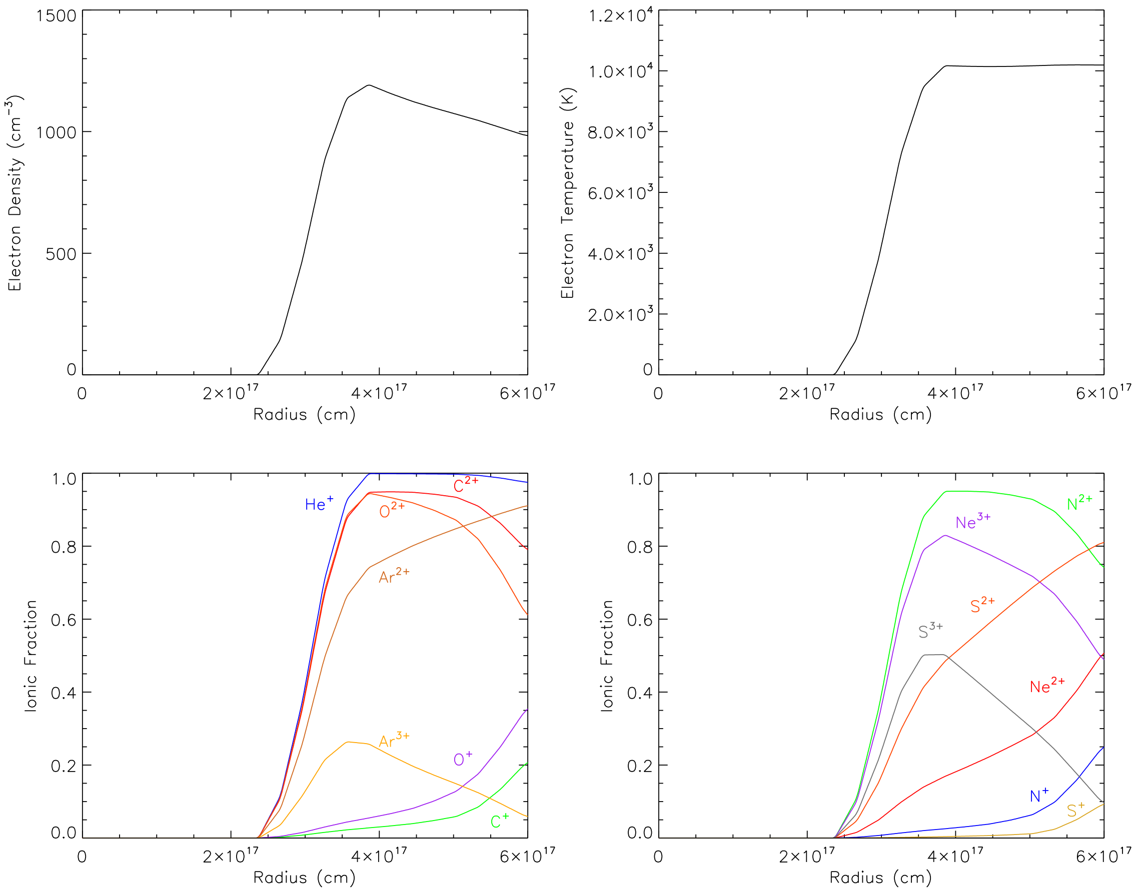

Figure 5.7: Top: electron density and temperature as a function of radius along the equatorial direction. Bottom: ionic stratification of the nebula. Ionization fractions are shown for helium, carbon, oxygen, argon (left-hand panel), nitrogen, neon and sulfur (right-hand panel).

Table 5.12 lists mean temperatures weighted by the ionic abundances. Both [N II] and [O III] doublets, as well as He I lines arise from the same ionization zones, so they should have roughly similar values. The ionic temperatures increasing towards higher ionization stages could also have some implications for the mean temperatures averaged over the entire nebula. However, there is a large discrepancy by a factor of 2 between our model and ORL empirical value of $T_{\rm e}$(He I). This could be due to some temperature fluctuations in the nebula (Peimbert 1967, 1971). The temperature fluctuations lead to overestimating the electron temperature deduced from CELs. This can lead to the discrepancies in abundances determined from CELs and ORLs (see e.g. Liu et al. 2000). Nevertheless, the temperature discrepancy can also be produced by bi-abundance models (Liu 2003; Liu et al. 2004a), containing some cold hydrogen-deficient material, highly enriched in helium and heavy elements, embedded in the diffuse warm nebular gas of normal abundances. The existence and origin of such inclusions are still unknown. It is unclear whether there is any link between the assumed H-poor inclusions in PNe and the H-deficient CSs.

5.6.3 Evolutionary status

Fig. 5.8 compares the position of CSPN Abell 48 in the HertzsprungRussell diagram for helium burning models to the VLTP evolutionary tracks from Blöcker (1995a) (top panel) and Miller Bertolami & Althaus (2006) (bottom panel). The evolutionary model of Blöcker (1995a) implies a stellar mass of 0.62 $M_{\odot}$, corresponding to a progenitor mass of 3 $M_{\odot}$. The model of Miller Bertolami & Althaus (2006) yields a central star with a mass of $\sim$0.52 $M_{\odot}$ and $\log g = 4.8$, corresponding to a progenitor mass of 1 $M_{\odot}$. The nebula size and density correspond to an ionized mass of 0.8 $M_{\odot}$, which is likely consistent with an initial stellar mass about 3 $M_{\odot}$.

The timescales of the VLTP evolutionary tracks (Blöcker 1995a), for a 3 $M_{\odot}$

Table 5.11: Integrated ionic abundance ratios for He, C, N, O, Ne, S and Ar, derived from model ionic fractions and compared to those from the empirical analysis.

Ionic ratio	Observed	Model
He^{+}/H^{+}	0.118	0.116
C^{2+}/H^{+}	2.08(−3)	2.45(−3)
N^{+}/H^{+}	1.42(−5)	1.26(−5)
O^{+}/H^{+}	5.25(−5)	3.63(−5)
O^{2+}/H^{+}	1.06(−4)	9.76(−5)
Ne^{2+}/H^{+}	4.26(−5)	3.62(−5)
S^{+}/H^{+}	3.98(−7)	5.20(−7)
S^{2+}/H^{+}	5.58(−6)	4.19(−6)
Ar^{2+}/H^{+}	9.87(−7)	1.01(−6)

Table 5.12: Mean electron temperatures (K) weighted by ionic species for the whole nebula obtained from the photoionization model.

	Ion						
El.	I	II	III	IV	V	VI	VII
H	9044	10194					
He	9027	10189	10248				
C	9593	9741	10236	10212	10209	10150	10150
N	8598	9911	10243	10212	10209	10150	10150
O	9002	10107	10237	10241	10211	10150	10150
Ne	8672	10065	10229	10225	10150	10150	10150
S	9386	9388	10226	10208	10207	10205	10150
Ar	8294	9101	10193	10216	10205	10150	10150

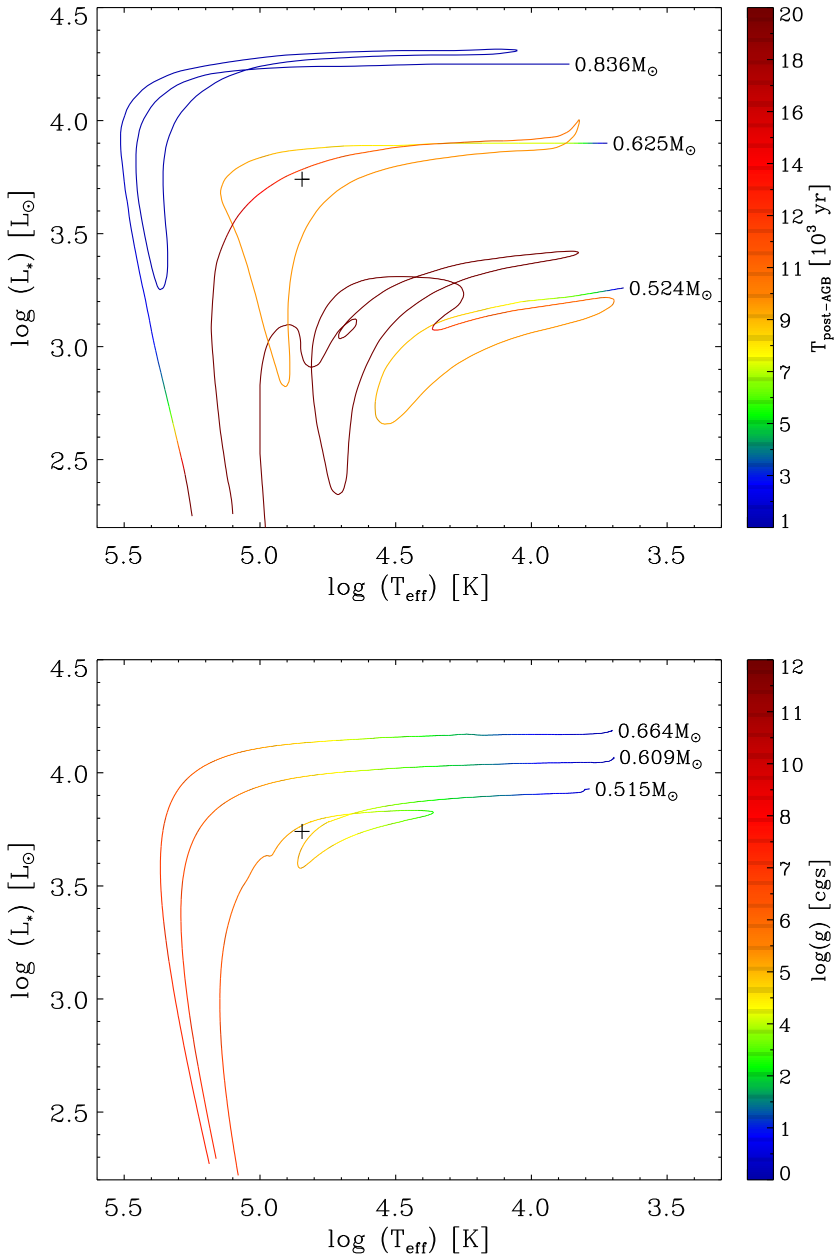

Figure 5.8: Top panel: VLTP evolutionary tracks from Blöcker (1995a) compared to the position of the central star of Abell 48 derived from our photoionization model. The colour scales indicate the post-AGB timescale in units of 10^3 yr. Bottom panel: VLTP evolutionary tracks from Miller Bertolami & Althaus (2006). The color scales indicate the surface gravity $\log g$ in cgs units.

initial mass star corresponds to ∼9000 yrs. Interestingly, the measured expansion velocity of the shell yields a dynamical age of 5900 yr for $D = 1.9\,\mathrm{kpc}$, assuming the constant expansion velocity through the nebula evolution. Following Dopita et al. (1996), we estimated the true age around 1.5 of the dynamical age, so the star left the top of the AGB around 8880 years ago, in good agreement with the VLTP evolutionary timescale. Moreover, the presence of nitrogen (5 per cent by mass) in the stellar atmosphere indicates that the star may experience a VLTP event.

Fig. 5.9 shows the position of Abell 48 among PNe with hydrogen-deficient central stars using the nebular Hβ surface brightness and the V-band surface brightness calculated by the stellar V-band flux instead of the Hβ flux, corrected for interstellar extinction. It indicates that Abell 48 stands among [WCE] PNe. But, the surface abundance pattern depicts a negligible carbon, in contrast to the typical [WC] stars. It implies that its evolutionary path must be completely different from the sequence proposed for [WC] stars: [WCL]→[WCE]→[WC]-PG1159→PG1159 (Werner 2001; Werner & Herwig 2006).

The extreme helium-rich (85 per cent by mass) atmosphere of Abell 48 is mostly aligned with extreme helium (EHe) and R Coronae Borealis (RCB) stars (e.g., see review by Clayton 1996), observed to contain approximately 98 percent He and 1 percent C by mass. Two scenarios have been proposed to explain the RCB stars: final helium shell flash in a single star (Iben et al. 1983a) and the merger of degenerate white dwarfs in a binary (Webbink 1984). A final helium-shell flash while the star is still in its cooling phase can remove the hydrogen outer layer. However, it also leads to extreme carbon-enrichment in the He-rich layers during the He-shell flash (Herwig et al. 1997), so it cannot produce an extreme helium-rich atmosphere. Therefore, the merger of helium and carbon–oxygen white dwarfs in a close binary system leading to an extreme helium-rich atmosphere remains the plausible scenario for the production of RCB and EHe stars (Saio & Jeffery 2002; Jeffery et al. 2011). However, the merger models of

He and CO white dwarfs predict lower nitrogen abundance at the stellar surface (less than 0.2 per cent by mass; Saio & Jeffery 2002).

The merger of two helium white dwarfs can make extremely helium-rich stars (Saio & Jeffery 2000; Han et al. 2002). The hydrodynamic study of the merger process by Zhang & Jeffery (2012) showed that the fast (or hot) He+He mergers make the hot stars with carbon-rich surfaces (carbon 1.26 per cent by mass), while the slow (or cold) He+He mergers make the cooler stars with nitrogen-rich surfaces (nitrogen 1.29 per cent by mass). However, they did not predict any hydrogen abundance at the surface. Moreover, the predicted nitrogen is by a factor of 4 lower than what we found in Abell 48. Therefore, the reason for the residual hydrogen (10 per cent by mass) and the relatively high nitrogen (5 per cent by mass) still remains unclear.

The common envelope (CE) phases can also have some implications for the merger process, which can affect the evolution of these objects (Han et al. 2002, 2003). Transferring energy and angular momentum from the binary system to the CE shrinks the orbital separation that causes the spiral-in process, resulting in a merger. However, the absence of hydrodynamic models of stellar mergers during the CE evolution does not allow us to evaluate them.

The stellar surface abundances of Abell 48 classified as [WN] is more likely related to helium dominated stars rather than [WC] stars. Miszalski et al. (2012) suggested that IC 4463, another PN with [WN] central star can be a progenitor of O(He) star. However, they did not find any residual hydrogen in IC 4663, while it seems that there is a considerable fraction ($\sim$ 10 per cent by mass) of hydrogen in Abell 48. Therefore, its evolution may be somehow different from the evolutionary sequence of RCB$\rightarrow$EHe$\rightarrow$He-sdO$\rightarrow$O(He) (Werner & Herwig 2006). The evolutionary link between helium dominated stars still needs further investigation. But, they are more likely connected to a merging process of two white dwarfs as recently evidenced by observations (Clayton et al. 2007; García-Hernández et al. 2009) and hydrodynamic simulations (Staff

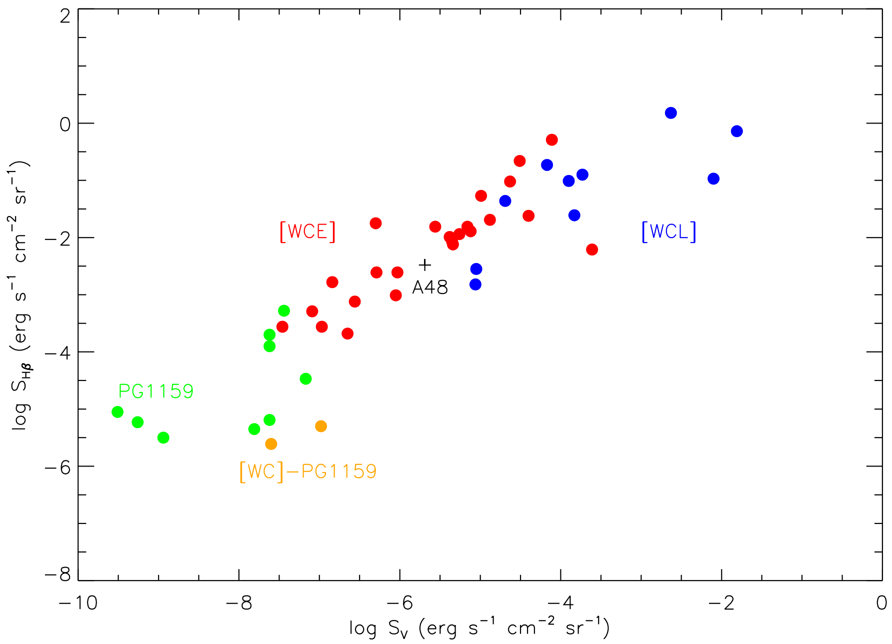

Figure 5.9: The position of Abell 48 among the nebular $S_{H\beta}$ surface brightness and the S_V surface brightness (replacing the Hβ flux with the stellar V-band flux in $S_{H\beta}$) of PNe containing hydrogen-deficient central stars. From Górny & Tylenda (2000). All fluxes were corrected for extinction.

et al. 2012; Zhang & Jeffery 2012; Menon et al. 2013).

5.7 Conclusions

We have constructed a photoionization model for the nebula of Abell 48. This consists of a dense hollow cylinder, assuming homogeneous abundances. The three-dimensional density distribution was interpreted using the morpho-kinematic model determined from spatially resolved kinematic maps and the ISW model. Our aim was to construct a model that can reproduce the nebular emission-line spectra, temperatures and ionization structure determined from the observations. We have used the non-LTE model atmosphere from Todt et al. (2013) as the ionizing source. Using the empirical analysis methods, we have determined the temperatures and the elemental abundances from CELs and ORLs. We notice a discrepancy between temperatures estimated from [O III] CELs and those from the observed He I ORLs. In particular, the abundance ratios derived from empirical analysis could also be susceptible to inaccurate values of electron temperature and density. However, we see that the predicted ionic abundances are in decent agreement with those deduced from the empirical analysis. The emission-line fluxes obtained from the model were in fair agreement with the observations.

We notice large discrepancies between He I electron temperatures derived from the model and the empirical analysis. The existence of clumps and low-ionization structures could solve the problems (Liu et al. 2000). Temperature fluctuations have been also proposed to be responsible for the discrepancies in temperatures determined from CELs and ORLs (Peimbert 1967, 1971). Previously, we also saw large ORL–CEL abundance discrepancies in other PNe with hydrogen-deficient CSs, for example Abell 30 (Ercolano et al. 2003b) and NGC 1501 (Ercolano et al. 2004). A fraction of H-deficient inclusions might produce those discrepancies, which could be ejected from the stellar surface during a very late thermal pulse (VLTP) phase or born-again event (Iben & Renzini 1983). However, the VLTP event is expected to produce a carbon-rich stellar surface abundance (Herwig 2001), whereas in the case of Abell 48 negligible carbon was found at the stellar surface (C/He $= 3.5 \times 10^{-3}$ by mass; Todt et al. 2013). The stellar evolution of Abell 48 still remains unclear and needs to be investigated further. But, its extreme helium-rich atmosphere (85 per cent by mass) is more likely connected to a merging process of two white dwarfs as evidenced for R Cor Bor stars of similar chemical surface composition by observations (Clayton et al. 2007; García-Hernández et al. 2009) and hydrodynamic simulations (Staff et al. 2012; Zhang & Jeffery 2012; Menon et al. 2013).

We derived a nebula ionized mass of ~ 0.8 M$_{\odot}$. The high C/O ratio indicates that it is a predominantly C-rich nebula. The C/H ratio is largely over-abundant compared to the solar value of Asplund et al. (2009), while oxygen, sulphur and argon are under-abundant. Moreover, nitrogen and neon are roughly similar to the solar values. Assuming a sub-solar metallicity progenitor, a 3rd dredge-up must have enriched carbon and nitrogen in AGB-phase. However, extremely high carbon must be produced through mixing processing in the He-rich layers during the He-shell flash. The low N/O ratio implies that the progenitor star never went through the hot bottom burning phase, which occurs in AGB stars with initial masses more than $5\mathrm{M}_{\odot}$ (Karakas & Lattanzio 2007; Karakas et al. 2009). Comparing the stellar parameters found by the model, $T_{\rm eff} = 70$ kK and $L_{\star}/\mathrm{L}_{\odot} = 5500$, with VLTP evolutionary tracks from Blöcker (1995a), we get a current mass of $\sim 0.62\mathrm{M}_{\odot}$, which originated from a progenitor star with an initial mass of $\sim 3\mathrm{M}_{\odot}$. However, the VLTP evolutionary tracks by Miller Bertolami & Althaus (2006) yield a current mass of $\sim 0.52\mathrm{M}_{\odot}$ and a progenitor mass of $\sim 1\mathrm{M}_{\odot}$, which is not consistent with the derived nebula ionized mass. Furthermore, time-scales for VLTP evolutionary track (Blöcker 1995a) imply that the CS has a post-AGB age of about $\sim 9\,000$ yr, in agreement with the nebula's age determined from the kinematic analysis. We therefore conclude that Abell 48 originated from an ~ 3 $\mathrm{M}_{\odot}$ progenitor, which is consistent with the nebula's features.

6

PB 8 with a [WN/WC]-type star

The contents of this chapter are being prepared for publication in the Monthly Notices of the Royal Astronomical Society. The 6.5-m Magellan telescope observation and the emission line fluxes used in this chapter were received from García-Rojas et al. (2009). The non-LTE model atmosphere used in this chapter was determined by Todt et al. (2010).

6.1 Introduction

The planetary nebula PB 8 (PN G292.4+04.1) has been the subject of some recent studies (García-Rojas et al. 2009; Todt et al. 2010; Miller Bertolami et al. 2011). The central star of PB 8 has been classified as [WC 5-6] by Acker & Neiner (2003); but weak emission-line stars (*wels*; Tylenda et al. 1993; Gesicki et al. 2006); [WC]-PG 1159 stars (Parthasarathy et al. 1998); and also [WN/WC] hybrid by Todt et al. (2010). Particularly, it is one of few stars, which has provoked a lot controversy about their stellar evolution (Miller Bertolami et al. 2011). A detailed abundance analysis of the nebula by García-Rojas et al. (2009) showed an abundance discrepancy factor (ADF) of 2.57 for the O^{++} ion, which is in the range of typical ADFs observed in PNe (see review by Liu et al. 2006). The nebular morphology was described as a round elliptical nebula with inner knots or filaments by Stanghellini et al. (1993), and classified as elliptical by Gorny et al. (1997). However, a narrow-band Hα+[N II] image of PB 8 taken by Schwarz et al. (1992) show a roughly spherical nebula with an angular diameter of about 7 arcsec (6.5 arcsec $\times$ 6.6 arcsec reported by Tylenda et al. 2003). The half width at half maximum (HWHM) expansion velocity of 14 ± 2 km s^{-1} measured by García-Rojas et al. (2009) corresponds to a kinematic age of about 5000 yr at the distance of 4.2 kpc determined by Todt et al. (2010). Adopting $v_{\rm exp} = 20$ km s^{-1} reported in this work, it could have a kinematic age of around 3500 yr, i.e. a relatively young PN.

Deep optical spectroscopy of the planetary nebula PB 8 shows the moderate discrepancies between temperatures and ionic abundances measured from ORLs and those from CELs, which may be due to the existence of colder and metal-rich inclusions embedded in the diffuse nebula of normal abundances. In this chapter, we have constructed photoionization models of the planetary nebula PB 8 to be confronted with available optical and infrared observations, constrained by a model atmosphere for the ionizing source calculated to match its central star spectrum. The density distribution for the nebular gas was adopted based on one-dimensional hydrodynamics models computed for different stellar evolutionary tracks. Three different sets of photoionization models were tried, the first being chemically homogeneous models that failed to reproduce the optical recombination lines (ORLs) of heavy elements. To reproduce the observed ORLs, dual abundance models were built by incorporating a small fraction of metal-rich inclusions embedded in the gas envelope with normal abundances. The final bi-abundance model provided a better fit to the most observed heavy element ORLs, whose metal-rich inclusions have a mass of ~ 5 percent of the total ionized mass and nearly twice cooler and denser than the normal composition nebula. Their O/H and N/H abundance ratios are ~ 1.0 and 1.7 dex larger than the diffuse warm nebula, respectively. The model did not predict the thermal spectral energy distribution of the nebula observed with the *Spitzer* infrared spectrograph. Therefore, we aimed to reproduce the thermal infrared emission by including dust grains in the final photoionization model.

The aim of the present chapter is to determine whether a bi-abundance model consists of a chemically homogeneous density distribution containing a small fraction of metal-rich structures can be applied to the abundance dependency problem in the PN PB 8. We present photoionization models of PB 8, for which high quality spectroscopy has now become available (García-Rojas et al. 2009), constrained by a model atmosphere of the central star determined using the Potsdam Wolf-Rayet (PoWR) models for expanding atmospheres (Todt et al. 2010), using the photoionization code MOCASSIN. In addition, we aim to identify the dust properties, which can produce the *Spitzer* infrared continuum of the PN PB 8. The observations and modeling procedure are respectively described in Sections 6.2 and 6.3. In Section 6.4, we present our modeling results, while a discussion of the implications and limitation are given in Section 6.5.

6.2 Observations

The deep optical long-slit spectra of the PN PB 8 were obtained at Las Campanas Observatory, using the 6.5-m Magellan telescope and the double echelle MIKE spectrograph in 2006 May (described in detail by García-Rojas et al. 2009). The standard grating settings used yield wavelength coverage from 3350-5050 Å in the blue and 4950-9400 Å in the red. The mean spectral resolution is 0.15 Å FWHM in the blue and 0.25 Å FWHM in the red. The top and bottom panels of Fig. 6.1 show the blue and red spectra of PB 8 extracted from the 2D MIKE echellograms, normalized such that $F(\mathrm{H}\beta) = 100$. As seen, several recombination lines from heavy element ions have been observed.

The integral field unit (IFU) spectra were obtained at the Siding Spring Observatory in 2010 April, using the 2.3-m ANU telescope and the Wide Field Spectrograph (WiFeS; Dopita et al. 2007, 2010). The gratings used were the

B7000/R7000 grating combination and the RT 560 dichroic, giving wavelength coverage from 4415-5589 Å in the blue and 5222-7070 Å in the red, and mean spectral resolution of 0.83 Å FWHM in the blue and 1.03 Å FWHM in the red. The WiFeS IFU rawdata were reduced using the IRAF pipeline wifes, which consists of bias-subtraction, sky-subtraction, flat-fielding, wavelength calibration using Cu-Ar arc exposures, spatial calibration using wire frames, differential atmospheric refraction correction, and flux calibration using spectrophotometric standard star EG 274 and LTT 3864 (fully described in Chapter 2).

The infrared (IR) spectra of the PN PB 8 were taken in 2008 February with the IR spectrograph on board the *Spitzer* Space Telescope (programme ID 40115, P.I. Giovanni Fazio). The flux calibrated IR spectra used in this chapter have been obtained from the Cornell Atlas of *Spitzer*/Infrared Spectrograph Sources[1] (CASSIS; Lebouteiller et al. 2011). Table 6.3 lists the line fluxes measured from the *Spitzer* IR spectra. The intrinsic line fluxes presented in column 3 are on a scale where $I(\mathrm{H}\beta) = 100$, and the dereddened flux $I(\mathrm{H}\beta) = 16.0 \times 10^{-12}$ $\mathrm{erg\,cm^{-2}\,s^{-1}}$ calculated using the total Hβ flux from Acker et al. (1992) and $E(B-V) = 0.41$ from Todt et al. (2010).

Fig. 6.2 shows the spatially resolved flux intensity and radial velocity maps of PB 8 extracted from the emission line [N II] λ6584 for spaxels across the WiFeS IFU field. The black/white contour lines depict the distribution of the emission of Hα obtained from the SuperCOSMOS Hα Sky Survey (SHS; Parker et al. 2005), which can aid us in distinguishing the nebular borders. The emission line maps were obtained from solutions of the nonlinear least-squares minimization to a Gaussian curve function for each spaxel. The observed velocity $v_{\rm obs}$ was transferred to the local standard of rest (LSR) radial velocity $v_{\rm LSR}$ by correcting for the radial velocities induced by the motions of the Earth and Sun at the time of our observation. As seen in Fig. 6.2, PB 8 may not have a spherical geometry, and its orientation onto the plane of the sky has a position angle

[1]Website: http://cassis.astro.cornell.edu

Table 6.1: IR line fluxes of the PN PB 8.

Lines	$F(\lambda)$	$I(\lambda)$
	10^{-12} erg cm^{-2} s^{-1}	$[I(\mathrm{H}\beta)=100]$
[Ar III] 8.99 μm	2.95	18.44
[Ne II] 12.82 μm	4.80	30.00
[Ne III] 15.55 μm	21.60	135.00
[S III] 18.68 μm	10.80	67.50
[S III] 33.65 μm	5.98	37.38
[Ne III] 36.02 μm	1.45	9.06

of $132^{\circ} \pm 8^{\circ}$ relative to the north equatorial pole towards the east.

We obtained an expansion velocity of $v_{\rm exp} = 20 \pm 4$ km s^{-1} from the HWHM of the [N II] λ6584 flux integrated across the whole nebula in the WiFeS field, which is in agreement with $v_{\rm exp} = 19$ km s^{-1} from [N II] λ6584 line derived by Todt et al. (2010). However, García-Rojas et al. (2009) derived the expansion velocity of $v_{\rm exp} = 14 \pm 2$ km s^{-1} from [O III] λ5007 line. The WiFeS observation also yields a LSR systemic velocity of $v_{\rm sys} = 9.5$ km s^{-1}, which is not quite similar to the value of $v_{\rm sys} = 2.4$ km s^{-1} given by Todt et al. (2010). Moreover, García-Rojas et al. (2009) found $v_{\rm sys} = 1.4$ km s^{-1} from [O III] lines. The MIKE spectrograph resolution of $R \sim 25000$ used by the previous works is more accurate than the WiFeS moderate resolution of $R \sim 7000$. Therefore, our value of the systemic velocity is not quite accurate due to the typical calibration error of 0.1 Å for the WiFeS spectral resolution.

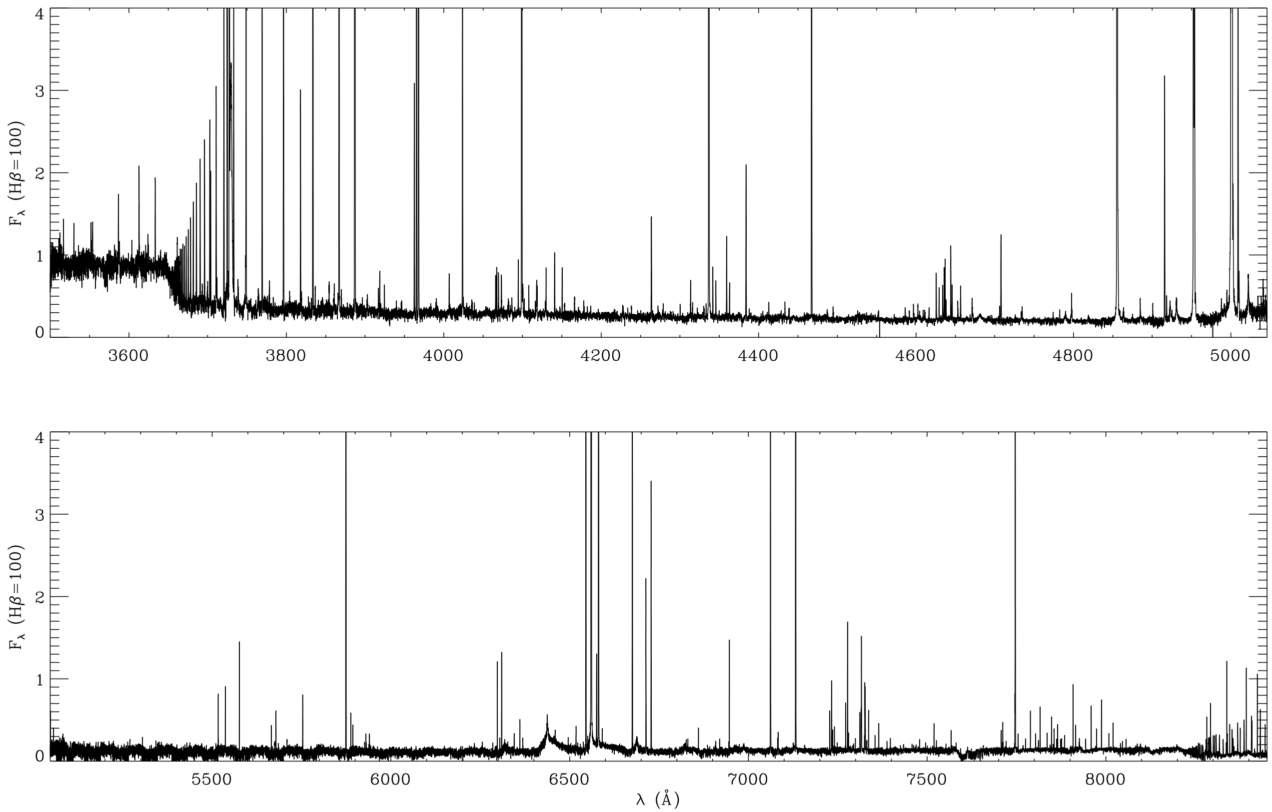

Figure 6.1: The observed optical spectrum of the PN PB 8, covering wavelengths of (top) 3500–5046 Å and (bottom) 5047–8451 Å, and normalized such that $F(\mathrm{H}\beta) = 100$ (García-Rojas et al. 2009).

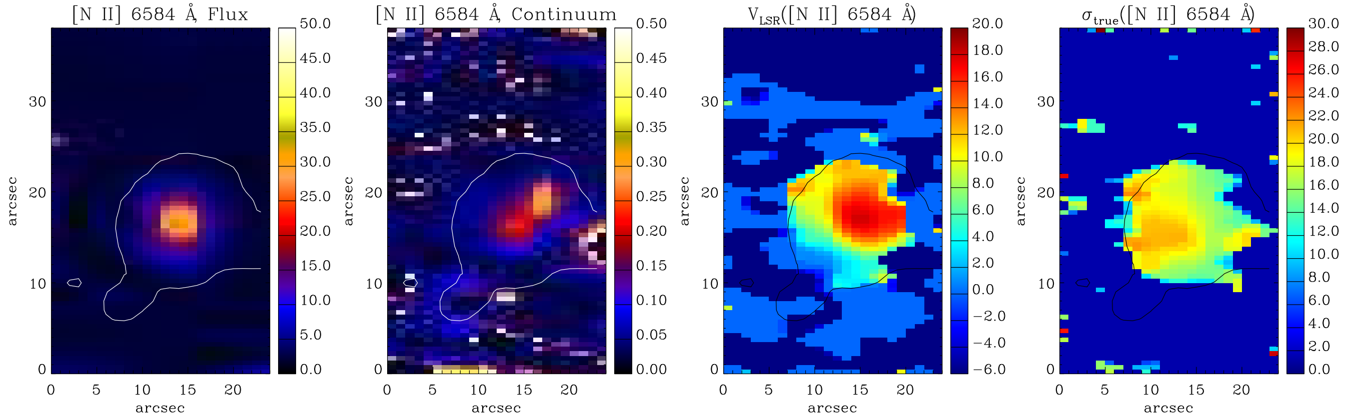

Figure 6.2: Maps of PB 8 in [N II] λ6584 Å from the IFU observation. From left to right: spatial distribution maps of flux intensity, continuum, LSR velocity and velocity dispersion. Flux unit is in 10^{-15} erg s^{-1} cm^{-2} spaxel^{-1}, continuum in 10^{-15} erg s^{-1} cm^{-2} Å^{-1} spaxel^{-1}, and velocities in km s^{-1}. North is up and east is toward the left-hand side. The white/black contour lines show the distribution of the narrow-band emission of Hα in arbitrary unit obtained from the SuperCOSMOS Sky Hα Survey (Parker et al. 2005).

The PPMXL catalog (Roeser et al. 2010) reveals that PB 8 moves with the proper motion of $\mu_l = -3.37\,\mathrm{mas\,yr^{-1}}$, $\mu_b = -8.9\,\mathrm{mas\,yr^{-1}}$, and the magnitude of $\mu = 13.07\,\mathrm{mas\,yr^{-1}}$. This indicates that PB 8 located above the Galactic plane ($b = 4.16$) is moving toward the Galactic disk with a noncircular (peculiar) velocity of $v_\mu = D(\mathrm{kpc})45.1\,\mathrm{km\,s^{-1}}$. It is not possible to get its distance from its proper motion components and radial velocity, since its trigonometric parallax is unknown. The dust maps (Schlegel et al. 1998) implies a mean reddening value of $E(B-V) = 0.39$ at the location of $(l,b) = (292.4, 4.1)$, whereas PB 8 has a reddening of $E(B-V) \simeq 0.41$. Thus, its distance is between 1 and 20 kpc, line-of-sight depth of the Galaxy.

6.3 Photoionization Modeling

The photoionization modeling is performed using the MOCASSIN code (version 2.02.70), described in detail by Ercolano et al. (2003a, 2005, 2008) in which the radiative transfer of the stellar and diffuse field is computed using a Monte Carlo method, allowing completely arbitrary distribution of nebular density and abundances. This code has already been used to study some chemical inhomogeneous models, namely the H-deficient knots of Abell 30 (Ercolano et al. 2003b) and the super-metal-rich knots of NGC 6153 (Yuan et al. 2011). To solve the problem of ORL-CEL abundance dependencies in those PNe, they used a metal-rich component, whose ratio of C, N and O relative to H is higher than the normal component. Interestingly, both PNe have hydrogen-deficient central stars; the central star of Abell 30 was found to be a [WC]-PG1159 star (Parthasarathy et al. 1998), and the stellar spectrum of NGC 6153 was also classified as of [WC]-PG 1159 type by Liu et al. (2000).

To investigate the abundance discrepancies between the ORLs and CELs, we have constructed different photoionization models for PB 8. We run sets of models, but we selected three, which best produced the observations. Our first model (MC1) consists of a chemically homogeneous density distribution constructed in a cubical Cartesian grid. Our second model (MC2) is the same, but it includes some H-poor knots (cells) embedded in the density model of normal abundances. The final model (MC3) includes dust grains to match the *Spitzer* infrared observation. The atomic data sets used for our models include energy levels, collision strengths and transition probabilities from Version 7.0 of the CHIANTI database (Landi et al. 2012, and references therein), hydrogen and helium free–bound coefficients of Ercolano & Storey (2006), and opacities from Verner et al. (1993) and Verner & Yakovlev (1995).

The model parameters, as well as the physical properties for the models, are summarized in Table 6.2, and discussed in more detail in the following sections. The models were run on the high-performance distributed-memory RAIJIN cluster at Australian National University, consisting of 57,472 Intel Sandy Bridge 2.6-GHz cores and 160 TB of memory each. The gas density distribution was constructed in 20^3 cubic grids with the same size. The modeling procedure consists of an iterative process, involving the comparison of the predicted emission line fluxes with the values measured from the observations, and the ionization and thermal structures with the values derived from the empirical analysis. The free parameters used in our models included nebular parameters (gas density and abundances) and stellar parameters (luminosity and effective temperature). The nebular ionization structure depends upon the gas density and stellar temperature. But, we adopted an effective temperature of $T_{\rm eff} = 52\,{\rm kK}$ and a non-local thermodynamic equilibrium (NLTE) model atmosphere determined by Todt et al. (2010). Thus, the first step is to find gas density and stellar luminosity required to produce the nebular total Hβ intrinsic line flux and the relative intensities of the strongest CELs (such as [N II] λ6584 and [O III] λ5007). The distance (size) was varied until the best values of the nebular Hβ intrinsic line flux was produced. It is found that the adopted NLTE model atmosphere with a stellar luminosity of $L_{\star} = 6000{\rm L}_{\odot}$ well produces the best nebula

Table 6.2: Model parameters and physical properties.

	Empirical		Models				
			MC1	MC2		MC3	
Parameter	CEL	ORL		Normal	H-poor	Normal	H-poor
$T_{\rm eff}$ (kK)	52		52	52		52	
$L_\star$ ($L_\odot$)	6000		6000	6000		6000	
$R_{\rm in}$ (10^{17} cm)	–		0.8	0.8		0.8	
$R_{\rm out}$ (10^{17} cm)	–		2.6	2.6		2.6	
Filling factor	–		1.00	1.00	0.056	1.00	0.056
$\langle N({\rm H}^+)\rangle$ (cm^{-3})	–		1950	1957	3300	1957	3300
$\langle N_{\rm e}\rangle$ (cm^{-3})	2550	–	2191	2199	4012	2199	4012
$\rho_{\rm d}/\rho_{\rm H}$	–		–	–		0.01	
M_i ($M_\odot$)	–		0.284	0.269	0.014	0.269	0.014
He/H	–	0.122	0.122	0.122	0.20	0.122	0.20
C/H $\times 10^5$	–	72.25	63.0	63.0	63.0	63.0	63.0
N/H $\times 10^5$	16.22	31.41	11.0	6.1	298.0	6.1	298.0
O/H $\times 10^5$	57.54	146.61	40.0	58.7	551.0	58.7	551.0
Ne/H $\times 10^5$	13.49	19.9	10.0	15.0	15.0	15.0	15.0
S/H $\times 10^7$	204.17	–	300.0	300.0	300.0	300.0	300.0
Cl/H $\times 10^7$	2.0	–	1.2	1.6	1.6	1.6	1.6
Ar/H $\times 10^7$	43.65	–	39.0	45.0	45.0	45.0	45.0

spectrum at a distance of 4.9 kpc. We initially used the elemental abundances determined by García-Rojas et al. (2009), but we adjusted them to match the observed nebular spectrum.

6.3.1 The density distribution

The first nebular model (MC1) to be run was the simplest possible density distribution, a spherical geometry, to reproduce the CELs. The density and abundances were taken to be homogeneous. A first attempt was made by using a homogeneous density distribution of 2500 cm^{-3}, deduced from the [O II], [S II] and [Cl III] (García-Rojas et al. 2009). However, the uniform density distribution did not match the ionization and thermal structures, so we examined different density distributions obtained by means of detailed 1-D radiation-hydrodynamics calculations to make the best fit to the observed CELs.

Fig. 6.3 compares radial number density distributions of hydrogen atom $N_{\rm H}$ for the spherical density models obtained from two hydrodynamical models calculated by the time-dependent 1-D radiation-hydrodynamics code NEBEL (see e.g. Perinotto et al. 2004; Schönberner et al. 2005a,b, 2010; Jacob et al. 2013). The first hydrodynamical model (dashed line in the figure) has an AGB remnant mass of $M = 0.605{\rm M}_{\odot}$, a terminal AGB wind speed of $V_{\rm agb} = 15\,{\rm km\,s^{-1}}$, a post-AGB age of $t_{\rm age} = 3108$ yr, an AGB mass-loss rate of $\dot{M}_{\rm agb} = 10^{-4}\,{\rm M}_{\odot}\,{\rm yr}^{-1}$, an effective temperature of $T_{\rm eff} = 53\,{\rm kK}$, and a stellar luminosity of $L_{\star} = 6145{\rm L}_{\odot}$ (described in detail by Perinotto et al. 2004). The second hydrodynamical model (dotted-dashed line in the figure), which used more "realistic" approaches for describing planetary nebulae, has the parameters $M = 0.605{\rm M}_{\odot}$, $t_{\rm age} = 4212$ yr, $T_{\rm eff} = 50\,{\rm kK}$, and $L_{\star} = 5462{\rm L}_{\odot}$ (the model extensively discussed by Schönberner et al. 2005b). The best ionization and thermal structures were produced by a spherical density distribution (solid line) obtained from the second model calculated by "realistic" 1-D radiation-hydrodynamics, while the density distribution was scaled until the photoionization model MC1 well produces the total Hβ intrinsic line flux, $I({\rm H}\beta) = 16 \times 10^{-12}\,{\rm erg\,cm^{-2}\,s^{-1}}$, and the mean electron density, $\langle N_{\rm e} \rangle = 2550$ cm^{-3}. The distance of $D = 4.9$ kpc found here, was chosen, because of the best predicted Hβ luminosity $L({\rm H}\beta) = 4\pi D^2 I({\rm H}\beta)$, and it is within the range of distances 2.2 and 5.8 kpc (Phillips 2004, and references therein), and 4.2 and 5.15 kpc estimated by Todt et al. (2010). The mean densities obtained from the adopted density model (solid line in Fig. 6.3) were listed in Table 6.2. Once the density geometry and size (distance) were identified, the variation of the nebular ionic abundances were explored.

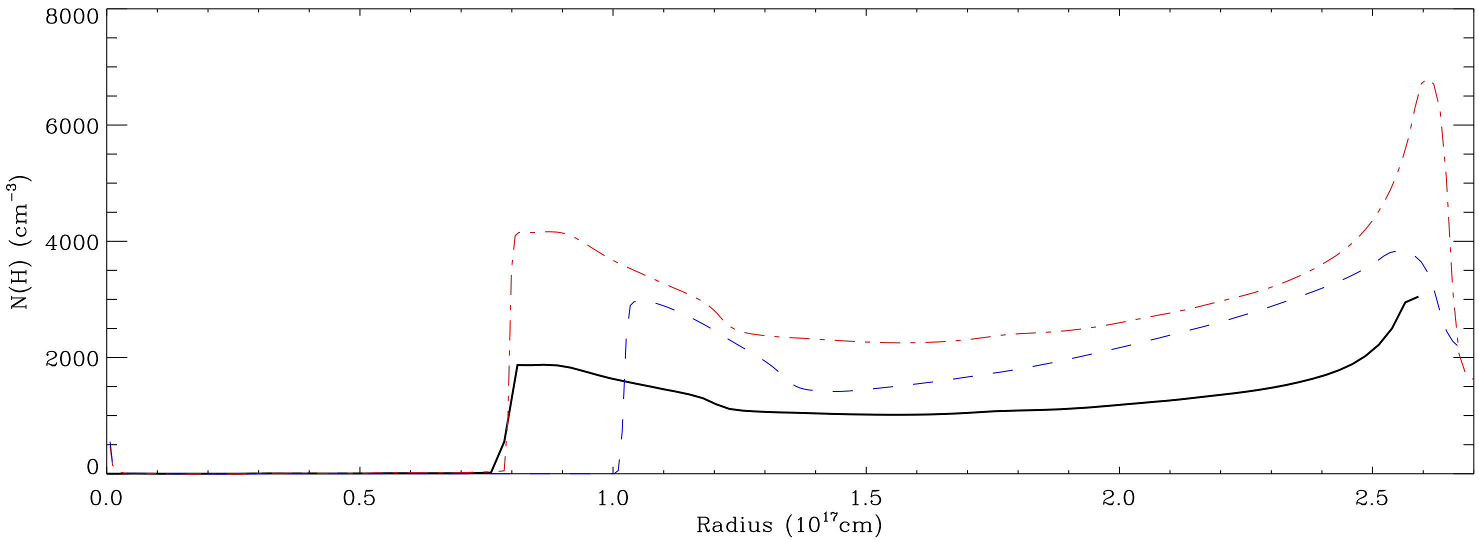

Figure 6.3: Density distributions of hydrogen atom $N_{\rm H}$ as a function of radius for the hydrodynamical model with $M = 0.605{\rm M}_{\odot}$, $V_{\rm agb} = 15\,{\rm km\,s^{-1}}$, $t_{\rm age} = 3108$ yr, $\dot{M}_{\rm agb} = 10^{-4}\,{\rm M}_{\odot}\,{\rm yr}^{-1}$, $T_{\rm eff} = 53\,{\rm kK}$, and $L_{\star} = 6145{\rm L}_{\odot}$ (blue dashed line; Perinotto et al. 2004) and the "realistic" hydrodynamical model with $M = 0.605{\rm M}_{\odot}$, $t_{\rm age} = 4212$ yr, $T_{\rm eff} = 50\,{\rm kK}$, and $L_{\star} = 5462{\rm L}_{\odot}$ (red dotted-dashed line; Schönberner et al. 2005b). The density distribution obtained from the realistic hydrodynamical model scaled to reproduce the total Hβ intrinsic flux and the mean electron density (black solid line).

A second attempt (MC2) was to produce the observed ORLs by introducing a fraction of dense, metal-rich knots into the density distribution used by the first model. The abundance ratios of He, N and O relative to H in the metal-rich component are higher than those in the normal component. The H number density in the metal-rich component is taken to be homogeneous, $N_{\rm H} = 3300\,{\rm cm}^{-3}$, which is higher than the mean H number density, $\langle N_{\rm e} \rangle = 2199\,{\rm cm}^{-3}$in the normal component in the model MC2.

6.3.2 The nebular elemental abundances

We used a homogeneous elemental abundance distribution for the model MC1 consisting of 9 elements, including all the major contributors to the thermal balance of the nebula and those producing the density- and temperature-sensitive CELs. The abundances derived from the empirical analysis (García-Rojas et al. 2009) were chosen as starting values; these were iteratively modified to get a better fit to the CELs. The final abundance values are listed in Table 6.2, where they are given by number with respect to H.

An inhomogeneous elemental abundance distribution was used for the model MC2 that yields a better fit to the ORLs. The initial guesses at the elemental abundances of N and O in the the metal-rich component were taken from the ORL empirical results; they were successively increased to fit the observed N II and O II ORLs. Table 6.2 lists the final elemental abundances (with respect to H) derived for both components, normal and metal-rich. The final model, which provided a better fit to the most observed ORLs, has a total metal-rich mass about 5 percent of the ionized mass of the whole nebula. The O/H and N/H abundance ratios in the metal-rich component are about 1.0 and 1.7 dex larger than those in the normal component, respectively.

6.3.3 The ionizing spectrum

The non-LTE stellar atmosphere used in this work were calculated using the Potsdam Wolf–Rayet (PoWR) models for expanding atmospheres (Gräfener et al. 2002), for H:He:C:N:O = 40:55:1.3:2:1.3 by mass and a central star effective temperature of $T_{\rm eff} = 52$ kK. This non-LTE stellar atmosphere was found to be consistent with the dereddened stellar spectra from FUSE, IUE and MIKE, as well as 2MASS JHK bands (Todt et al. 2010). The stellar luminosity (gravity) of the central star and distance were slightly varied in order to reproduce the nebular emission-line fluxes, under the constraints of our adopted effective temperature of the central star and spherical density distribution. The best results for the photoionization models were obtained with a stellar luminosity of $L_{*} = 6000\,{\rm L}_{\odot}$, which is the same value adopted by Todt et al. (2010).

Fig. 6.4 compares the non-LTE model atmosphere flux of PB 8 with a blackbody flux at the same temperature. At the energies higher than 54 eV (He II ground state), there is a significant difference between the non-LTE model atmosphere and blackbody spectral energy distribution (SED). As seen, a blackbody is not an accurate representation of the ionizing flux (e.g. see Rauch 2003). Moreover, the non-LTE H-deficient model atmosphere has a major departure from the solar model atmosphere at higher energies due to the small opacity from hydrogen. The non-LTE model atmosphere can have a major impact on the predicted line fluxes of the higher ionization stages of ions. Therefore, we used a non-LTE model atmosphere as ionizing inputs in our photoionization model to provide the best fit to the nebular spectrum.

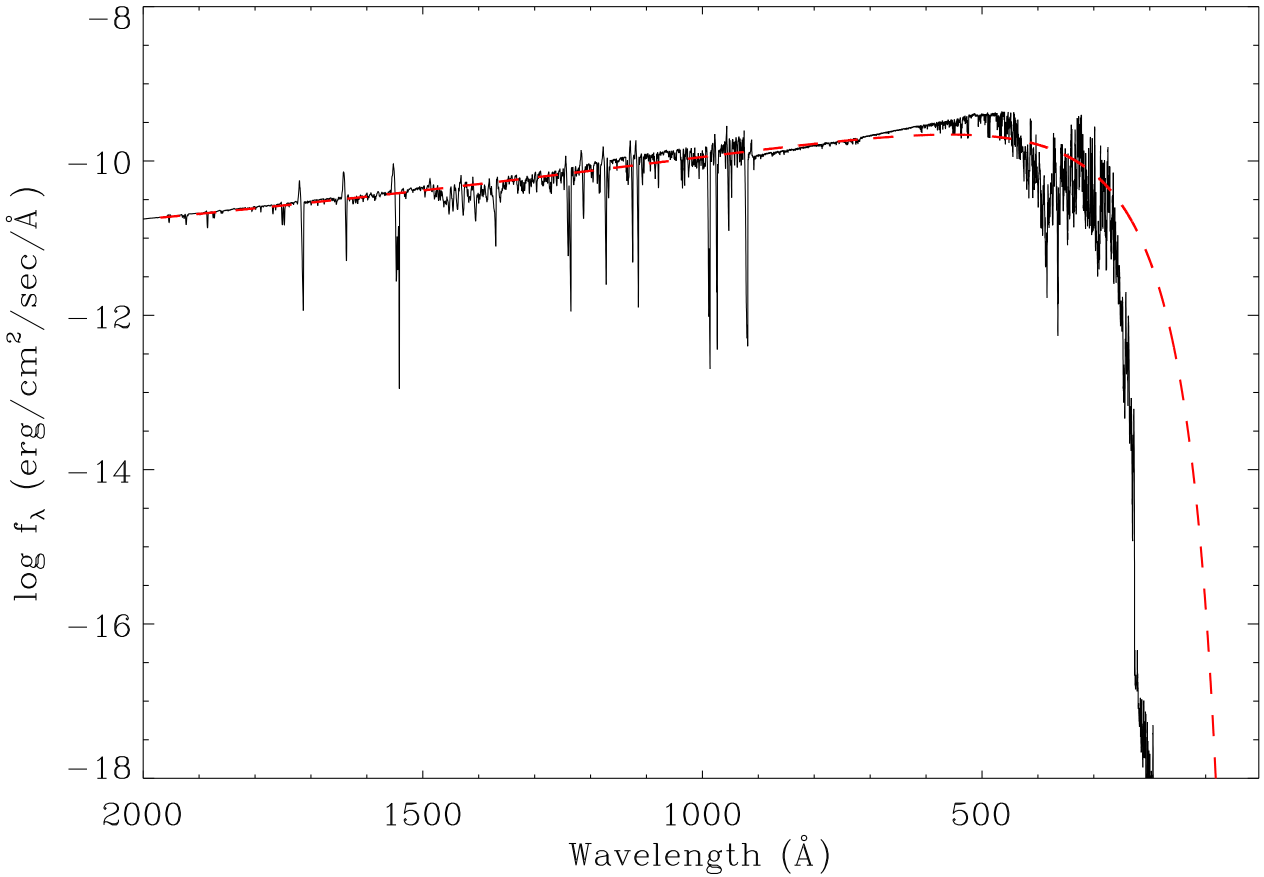

Figure 6.4: Non-LTE model atmosphere flux (grey line) calculated with $T_{\rm eff} = 52\,{\rm kK}$ and chemical abundance ratio of H:He:C:N:O = 40:55:1.3:2:1.3 by mass (Todt et al. 2010), compared with a blackbody (dashed line) at the same temperature.

6.3.4 Dust modeling

The PN PB 8 is known to be very dusty (e.g. Lenzuni et al. 1989; Stasińska & Szczerba 1999), which must influence the radiative process in the nebula. Lenzuni et al. (1989) studied the IRAS measurements (25, 60 and 100 μm fluxes), and derived a dust temperature of $T_{\rm d} = 85 \pm 0.4$ K, an optical depth of $\tau = 0.63$ and a dust-to-gas mass ratio of $\rho_{\rm d}/\rho_{\rm g} = 0.0123$ from a blackbody function fitted to the IRAS data. Similarly, Stasińska & Szczerba (1999) determined $T_{\rm d} = 85$ K, but $\rho_{\rm d}/\rho_{\rm g} = 0.0096$ from the broad band IRAS data. From the comparison of mid-IR emission with a blackbody with 150 K, Todt et al. (2010) suggests it possibly contain a warm dust with different dust compositions. We notice that the first two models cannot provide enough thermal effects to account for the *Spitzer* IR continuum, so a dust component is necessary to produce the thermal spectral energy distribution (SED) of the nebula observed with the IR spectrograph. The third model (MC3) presented here treats dust properties of PB 8 using the dust radiative transfer features included in the MOCASSIN (Ercolano et al. 2005). Discrete grain sizes has been determined according to the radius-dependent grains temperature distributions and the radius range from Mathis et al. (1977). The absence of the 9.7 μm amorphous silicate feature commonly observed in O-rich circumstellar envelopes could imply that PB 8 has a carbon-based dust. However, strong features at 23.5, 27.5, and 33.8 μm are mostly attributed to crystalline silicates (Molster et al. 2002). Features seen at 6.2, 7.7, 8.6, and 11.3 μm are related to polycyclic aromatic hydrocarbons (PAHs) (García-Lario et al. 1999), together with broad features at 21 and 30 μm corresponding to a mixed chemistry having both O-rich and C-rich dust grains. The far-IR emission fluxes at 65 and 90 μm (Yamamura et al. 2010) could be related to relatively warm forsterite grains, which emit at a longer wavelength. The 65 μm emission may be related to a crystalline water-ice structure, although its presence cannot be confirmed at the moment. The 90 μm flux is obscured by

Table 6.3: Input parameters for the dust model of PB 8.

Grain Size	Weight	Radius
a_{min}	50	16.0×10^{-6} cm
a_{max}	1	40.0×10^{-6} cm
Grain Species	**Weight**	**Reference for optical constants**
Amorphous Carbon	1	Hanner (1988)
Crystalline Silicate	1	Jaeger et al. (1994)

the presence of the [O III] emission line at 88.35 μm.

Table 6.3 lists the dust parameters used for the final model of PB 8, the dust-to-hydrogen ratio was given in Table 6.2. The geometry of the dust distribution is the same as the gas density distribution. The thermal IR emission of PB 8 was modelled by adding a mixed dust chemistry to the pure-gas photoionization model described in the previous sections. We explored a number of grain sizes and species, which could provide a best-fitting curve to the *Spitzer* IR continuum, as shown in Fig. 6.4. We also tried to match the far-IR emission flux at 65 μm, since the 90 μm flux could have some contribution from the [O III] emission line, and the 140 μm flux is extremely uncertain. The dust-to-hydrogen mass ratio was varied until the best IR continuum flux was produced; the value of $\rho_{\rm d}/\rho_{\rm H} = 0.01$ found here is in agreement with Lenzuni et al. (1989). The final dust model consists of two different grains, amorphous carbon and crystalline silicate with optical constants taken from Hanner (1988) and Jaeger et al. (1994), respectively. For PB 8, Lenzuni et al. (1989) estimated a grain radius of 1.7×10^{-6} cm from the thermal balance equation under the assumption of the UV absorption efficiency $Q_{\rm UV} = 1$. Stasińska & Szczerba (1999) argued that the method of Lenzuni et al. underestimates the grain radius, and one cannot derive the grain size in such a way. Our photoionization modeling implies that dust grain with a radius of 0.017 μm produces very hot emission, much higher than $T_{\rm d} = 85$ K. As listed in Table 6.2, the final model uses two discrete grain sizes, namely grains radius of 0.16 μm (warm) and 0.40 μm (cool), which can produce the observed thermal infrared SED.

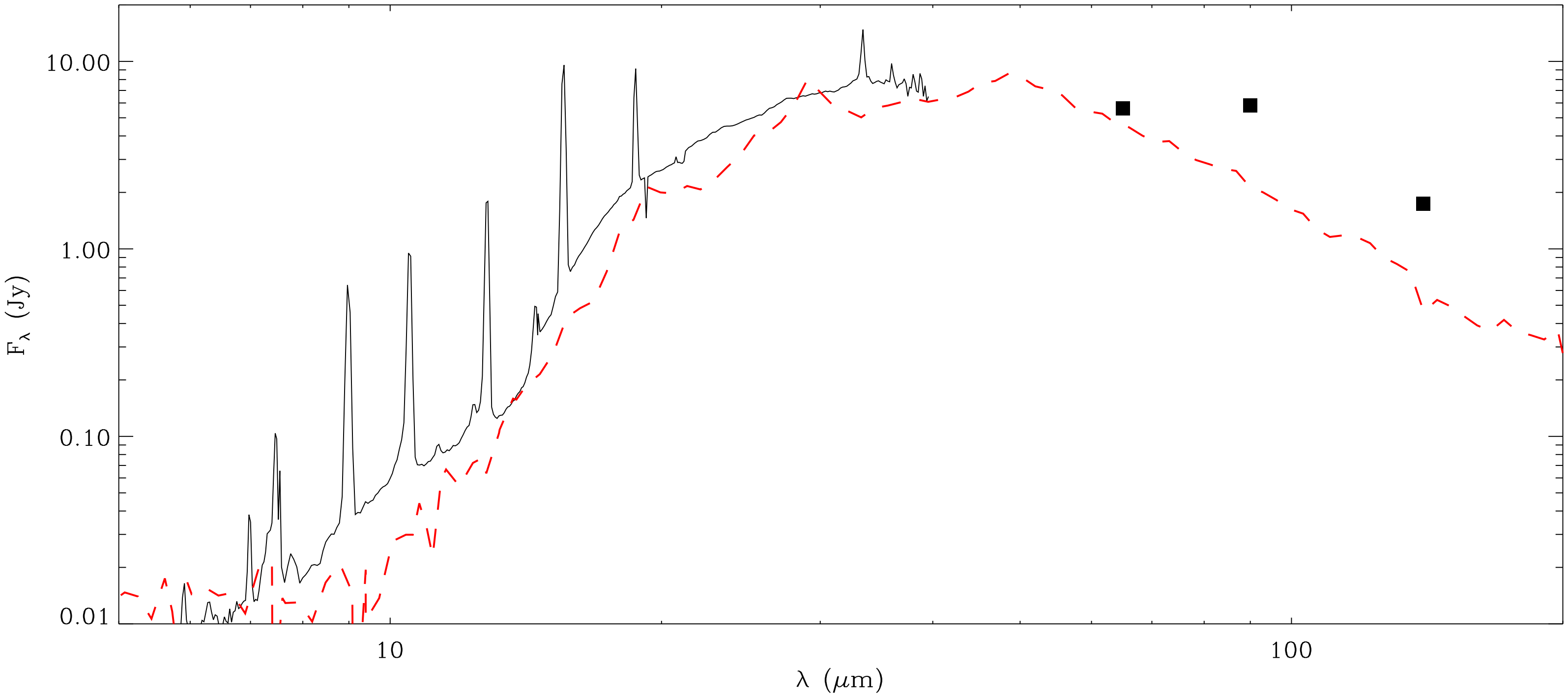

Figure 6.5: Observed *Spitzer* spectrum (black solid line) of PB 8 are compared with the SED predicted by the model (red dashed line). The far-IR measurements (65, 90 and 140 μm; Yamamura et al. 2010) are also shown.

6.4 Results

6.4.1 Comparison of the emission-line fluxes

Table 6.4 lists the observed and predicted nebular emission line fluxes. Column 4 presents the observed, dereddened intensities of PB 8 from García-Rojas et al. (2009), relative to the intrinsic dereddened Hβ flux, on a scale where $I(\mathrm{H}\beta) = 100$. The ratios of predicted over observed values from the best-fitting model MC1 are presented in Column 5. Columns 6–8 present the ratios of predicted over observed values for the normal, H-poor component and total from the best-fitting model MC2. The values obtained from the model MC3 are given in Columns 9–11. The majority of the CEL intensities predicted by model MC1 are in reasonable agreement with the observations. However, there are some large discrepancies between the prediction of model MC1 and the observations for ORLs. These discrepancies could be explained by either temperature fluctuations or colder H-poor inclusions. From the model MC2, it can be seen that the ORL discrepancy between model and observations can be explained by recombination processes of colder H-poor inclusions embedded in the global H-rich environments.

As seen in Table 6.4, the [N II] λ6583 and [O III] λ5007 lines predicted by the model are in excellent agreement with the observations. The H I lines are in good agreement with the observations. The majority of the He I lines are in good agreement with the observations, discrepancies within 10%, apart from the He I λ3889 (30%) and λ7065 (26%). This may be due to line blending or/and measurement errors. Alternatively, inhomogeneous condensations and high density clumps may have some implications. The [O II] λ7319 and λ7330 doublets are underestimated by a factor of 2. Recombination processes can largely enhance to the observed fluxes of these lines. Our photoionization code calculates the recombination contribution in the models, by including recombination and collisional population and depopulation. The discrepancy between model and observation must be attributed to recombination processes from a separate, colder, denser region, which is difficult to evaluate. The predicted [S II] lines are in reasonable agreement (12-22%) with the observations, whereas the predicted [S III] lines are by a factor of near 2 larger than the observations. The predicted [S III] lines could be problematic due to possible errors in the atomic data (see e.g. improved atomic data by Grieve et al. 2014). Alternatively, chemical inhomogeneous, very dense clumps in the inner layers of the nebula could enhance [S III] lines. The predicted [Ar III] λ7136 and λ7751 lines show discrepancies less than 20% with the observations. But, the IR fine-structure [Ar III] 8.99 μm line predicted by the model is about 50% higher than the observed value, which could be attributed to errors in the flux calibration or the fine-structure collision strengths for Ar^{2+} used for the calculations.

Although the [O II] 4363 Å auroral line is perfectly matched by the last two models (MC2 and MC3) and discrepancies remain less than 7%, there is a notable discrepancy in the [N II] 5755 Å auroral line. This may be due to the errors in the flux measurement of this faint line or the flux calibration error. The recombination contribution to [N II] auroral lines can be correctly estimated for low-density uniform nebular media. However, it can be extremely difficult to evaluate it in the present of inhomogeneous condensations. The collisional de-excitation of the very dense clumps in the nebula suppresses the $\lambda\lambda$6548,6584 nebular lines, but not the auroral lines (Viegas & Clegg 1994). Therefore, the discrepancy between the model and observation could be due to inhomogeneous condensations, which is very difficult to qualify.

Table 6.4: Comparison of predictions from the models and the observations. The observed, dereddened intensities are in units such that $I(\mathrm{H}\beta)= 100$. Columns (5)–(8) give the ratios of predicted over observed values in each case.

Line	λ_0(Å)	Mult	I_{obs}	MC1	MC2			MC3		
					Normal	H-poor	Total	Normal	H-poor	Total
				H, He recombination lines						
$\mathrm{H}\beta/10^{-12}$ erg cm^{-2} s^{-1}			16.00	0.934	0.279	0.944	1.223	0.278	0.937	1.215
Hβ	4861.33	H4	100.000	1.000	1.000	1.000	1.000	1.000	1.000	1.000
Hα	6562.82	H3	282.564	1.031	1.037	1.081	1.047	1.037	1.080	1.047
Hγ	4340.47	H5	45.666	1.019	1.016	1.001	1.013	1.017	1.001	1.013
Hδ	4101.74	H6	24.285	1.057	1.053	1.031	1.048	1.054	1.031	1.049
H I	3970.07	H7	14.466	1.089	1.085	1.060	1.080	1.086	1.061	1.080
H I	3835.39	H9	6.784	1.069	1.065	1.043	1.060	1.066	1.043	1.061
He I	3888.65	2	19.892	0.702	0.689	1.029	0.766	0.690	1.030	0.768
He I	7065.28	10	4.265	0.752	0.715	0.885	0.754	0.719	0.888	0.758
He I	5875.64	11	17.127	1.089	1.104	2.072	1.325	1.102	2.067	1.323
He I	4471.47	14	6.476	1.014	1.020	1.802	1.199	1.020	1.799	1.198
He I	4026.21	18	3.116	0.976	0.981	1.603	1.123	0.980	1.604	1.123
He I	7281.35	45	0.815	1.126	1.091	1.484	1.181	1.095	1.488	1.185
He I	6678.15	46	5.233	1.020	1.039	1.891	1.233	1.037	1.889	1.231
He I	4921.93	48	1.737	1.014	1.023	1.761	1.191	1.022	1.760	1.191

Table 6.4: (continued)

Line	λ_0(Å)	Mult	$I_{\rm obs}$	MC1	MC2			MC3		
					Normal	H-poor	Total	Normal	H-poor	Total
				Heavy-element recombination lines						
C II	6578.05	2	0.545	0.575	0.567	0.550	0.563	0.567	0.550	0.563
C II	7231.34	3	0.234	1.088	1.088	1.124	1.096	1.085	1.123	1.094
C II	7236.42	3	0.464	0.988	0.988	1.021	0.995	0.986	1.019	0.993
C II	4267.15	6	0.781	0.857	0.955	0.888	0.868	0.865	0.953	0.885
N II	5666.64	3	0.192	0.114	0.062	2.993	0.731	0.062	2.993	0.732
N II	5676.02	3	0.084	0.116	0.063	3.035	0.741	0.063	3.035	0.743
N II	5679.56	3	0.260	0.157	0.085	4.116	1.006	0.085	4.116	1.007
N II	4601.48	5	0.099	0.073	0.040	1.841	0.451	0.040	1.841	0.452
N II	4607.16	5	0.083	0.070	0.038	1.754	0.429	0.038	1.754	0.430
N II	4613.87	5	0.063	0.069	0.037	1.730	0.424	0.037	1.730	0.424
N II	4621.39	5	0.085	0.068	0.037	1.707	0.418	0.037	1.708	0.419
N II	4630.54	5	0.289	0.075	0.040	1.880	0.460	0.040	1.880	0.461
N II	4643.06	5	0.122	0.059	0.032	1.480	0.362	0.032	1.481	0.363
N II	4994.37	24	0.099	0.066	0.036	1.840	0.448	0.036	1.839	0.449
N II	5931.78	28	0.151	0.045	0.025	1.246	0.303	0.025	1.245	0.304
N II	5941.65	28	0.115	0.110	0.060	3.049	0.743	0.060	3.047	0.743

Table 6.4: (continued)

Line	λ_0(Å)	Mult	I_{obs}	MC1	MC2			MC3		
					Normal	H-poor	Total	Normal	H-poor	Total
O II	4638.86	1	0.206	0.181	0.256	2.307	0.724	0.254	2.304	0.723
O II	4641.81	1	0.380	0.248	0.350	3.155	0.990	0.348	3.151	0.989
O II	4649.13	1	0.458	0.391	0.552	4.978	1.562	0.549	4.972	1.561
O II	4650.84	1	0.221	0.169	0.238	2.150	0.675	0.237	2.148	0.674
O II	4661.63	1	0.222	0.215	0.303	2.735	0.858	0.301	2.731	0.857
O II	4676.24	1	0.184	0.218	0.307	2.772	0.870	0.306	2.769	0.869
O II	4319.63	2	0.081	0.364	0.515	4.676	1.465	0.512	4.670	1.463
O II	4336.83	2	0.054	0.161	0.228	2.068	0.648	0.226	2.065	0.647
O II	4349.43	2	0.197	0.346	0.490	4.452	1.395	0.487	4.447	1.393
O II	3749.48	3	0.281	0.132	0.185	1.645	0.518	0.184	1.643	0.518
O II	4414.90	5	0.036	0.489	0.678	5.588	1.799	0.676	5.587	1.799
O II	4416.97	5	0.090	0.109	0.151	1.241	0.399	0.150	1.240	0.399
O II	4072.15	10	0.265	0.331	0.470	4.324	1.350	0.467	4.319	1.348
O II	4075.86	10	0.275	0.460	0.654	6.020	1.879	0.650	6.012	1.876
O II	4085.11	10	0.086	0.190	0.270	2.488	0.776	0.268	2.485	0.775
O II	4121.46	19	0.163	0.063	0.090	0.837	0.260	0.089	0.836	0.260
O II	4132.80	19	0.202	0.099	0.142	1.319	0.410	0.141	1.317	0.410
O II	4153.30	19	0.250	0.115	0.163	1.523	0.474	0.162	1.521	0.473

Table 6.4: (continued)

Line	λ_0(Å)	Mult	I_{obs}	MC1	MC2			MC3		
					Normal	H-poor	Total	Normal	H-poor	Total
O II	4110.79	20	0.147	0.060	0.086	0.798	0.248	0.085	0.796	0.248
O II	4119.22	20	0.087	0.374	0.533	4.961	1.544	0.529	4.954	1.541
O II	4699.22	25	0.026	0.093	0.133	1.239	0.386	0.132	1.237	0.385
O II	4906.81	28	0.096	0.096	0.136	1.267	0.394	0.135	1.265	0.394
O II	4924.53	28	0.154	0.101	0.144	1.344	0.418	0.143	1.342	0.417
Collisionally excited lines										
[N II]	5754.64	3F	0.346	0.485	0.219	0.121	0.196	0.238	0.128	0.213
[N II]	6548.03	1F	7.667	0.926	0.509	2.685	1.006	0.542	2.757	1.048
[N II]	6583.41	1F	22.318	0.972	0.534	2.817	1.055	0.568	2.892	1.100
[O II]	3726.03	1F	17.103	0.897	1.226	0.269	1.008	1.341	0.285	1.100
[O II]	3728.82	1F	9.450	0.782	1.054	0.193	0.857	1.154	0.204	0.936
[O II]	7318.92	2F	0.227	0.530	0.636	0.033	0.498	0.709	0.036	0.555
[O II]	7319.99	2F	0.811	0.451	0.542	0.028	0.424	0.603	0.030	0.472
[O II]	7329.66	2F	0.387	0.518	0.622	0.033	0.488	0.694	0.035	0.543
[O II]	7330.73	2F	0.471	0.419	0.503	0.026	0.394	0.560	0.028	0.439
[O III]	4363.21	2F	0.528	1.733	1.202	0.032	0.935	1.291	0.035	1.003
[O III]	4958.91	1F	116.957	1.130	1.111	0.599	0.995	1.149	0.623	1.028
[O III]	5006.84	1F	348.532	1.132	1.113	0.600	0.996	1.150	0.624	1.030

Table 6.4: (continued)

Line	λ_0(Å)	Mult	I_{obs}	MC1	MC2			MC3		
					Normal	H-poor	Total	Normal	H-poor	Total
[Ne II]	12.82μm		30.000	0.419	0.733	0.744	0.735	0.754	0.734	0.750
[Ne III]	3868.75	1F	19.164	1.131	1.015	0.026	0.790	1.058	0.027	0.822
[Ne III]	3967.46	1F	5.689	1.147	1.031	0.026	0.801	1.074	0.028	0.835
[Ne III]	15.55μm		135.000	0.824	1.119	0.728	1.030	1.116	0.736	1.029
[Ne III]	36.02μm		9.060	1.036	1.401	0.839	1.272	1.397	0.849	1.272
[S II]	4068.60	1F	0.223	1.004	0.905	0.050	0.710	1.001	0.053	0.784
[S II]	6716.47	2F	0.957	0.978	0.962	0.115	0.769	1.049	0.121	0.837
[S II]	6730.85	2F	1.441	1.010	1.002	0.141	0.805	1.093	0.147	0.877
[S III]	6312.10	3F	0.639	3.617	2.571	0.067	2.000	2.735	0.071	2.126
[S III]	18.68μm		67.500	2.027	2.078	1.399	1.923	2.115	1.402	1.951
[S III]	33.65μm		37.380	1.686	1.709	0.800	1.501	1.740	0.802	1.525
[Cl III]	5517.71	1F	0.366	0.940	0.921	0.060	0.725	0.955	0.062	0.750
[Cl III]	5537.88	1F	0.366	1.054	1.045	0.088	0.826	1.081	0.091	0.855
[Ar III]	7135.78	1F	15.477	1.048	1.004	0.151	0.809	1.032	0.155	0.831
[Ar III]	7751.10	2F	3.493	1.113	1.066	0.160	0.859	1.096	0.164	0.883
[Ar III]	8.99μm		18.440	1.345	1.560	1.247	1.489	1.568	1.247	1.495

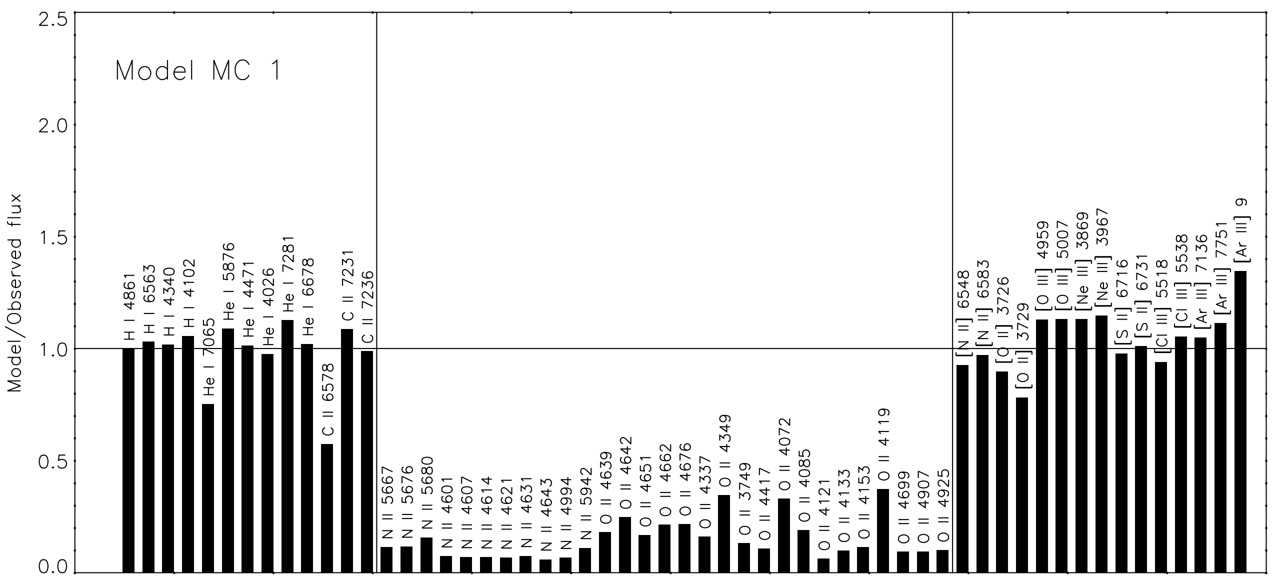

Figure 6.6: The predicted over observed flux ratio for the chemically homogeneous model MC1 (top panel) and the bi-chemistry model MC2 (bottom panel).

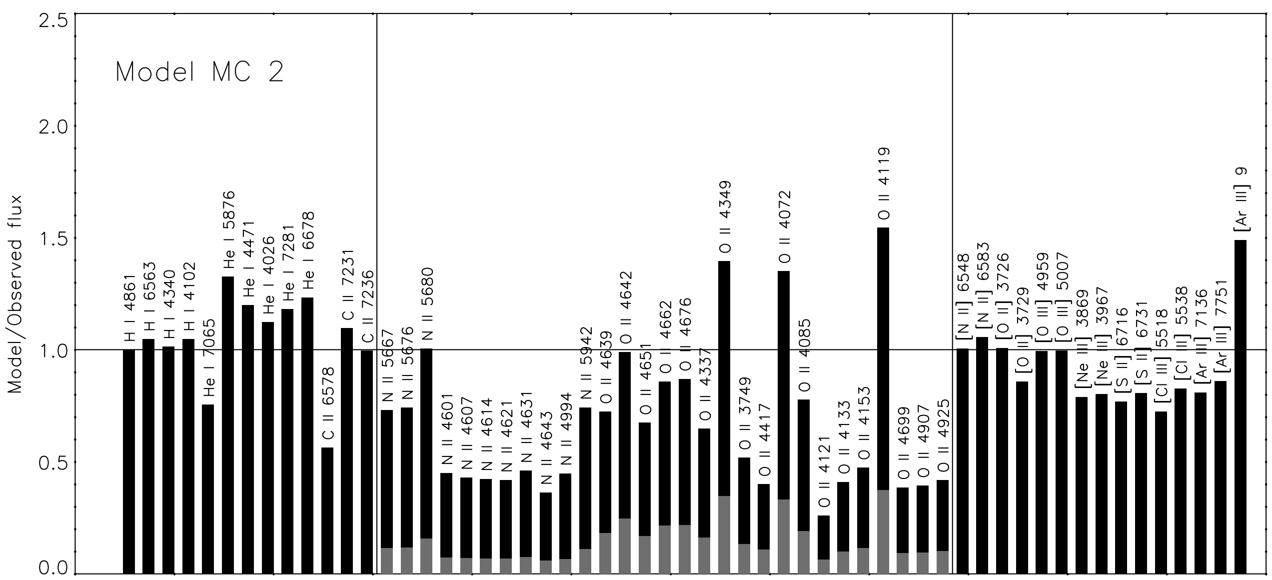

Figure 6.6: (continued)

The ORL and CEL intensities predicted by the model MC2 and MC3, bi-abundance models, are also compared to the observed values in Table 6.4. As shown in Fig. 6.6, the predicted line fluxes compared with the observations in MC1 and MC2, the bi-abundance model can better predict the heavy element ORLs. The agreement between the ORL intensities predicted by the two last models and the observations is better than those derived from the first model (MC1). The C II ORLs show much lower discrepancies within 12%, except C II λ6578 line. The C II λ4267.2 line is very stronger, and it could not be blended with any of nearby O II ORLs. The C II λ6578 line has unreliable measurements and may be blended with nearby lines. The majority of the strong O II lines are in good agreement with the observations, with fits to within 40%, except λ4649.13, λ3749.48, λ4075.86, λ4132.80 and λ4153.30. The well-measured N II λ5666.64, λ5676.02 and λ5679.56 lines are in good agreement with the observations, discrepancies less than 30%. Large discrepancies seen in the faint O II and N II ORLs can be explained by the measurement errors. Moreover, fluorescence excitation has a considerable effect in relatively low ionization or low density regions, so most of the ORLs may also be affected by fluorescence lines (see e.g. Escalante & Morisset 2005; Escalante et al. 2012).

6.4.2 Thermal structure

Mean electron temperatures weighted by ionic species for the three models have been calculated and are listed in Table 6.5. The first entries in each row are for MC1, the chemically homogeneous model; the second entries are for MC2, the chemically inhomogeneous model containing H-poor inclusions; the third entries are for MC3, the dusty chemically inhomogeneous model containing dust grains. The value of $T_{\rm e}$(N II) = 7746 K predicted by the model MC1 is about 1,150 lower than the value of $T_{\rm e}$(N II) = 8900 K empirically derived from CELs by García-Rojas et al. (2009). This could be due to the errors in the flux measurement of this faint line or recombination contribution to the auroral line, as it is too difficult to evaluate in the present of very dense clumps (Viegas & Clegg 1994). Alternatively, it may be explained by errors in the flux measurement of the faint auroral line. The temperature of T_e(O II) = 7746 K predicted by the model MC1 is in agreement with T_e(O II) = 7050 K empirically derived by García-Rojas et al. (2009). However, the temperature corresponding to [O III] (λ4959+λ5007)/λ4363 calculated by the model is 7613 K higher than the empirical result of T_e(O III) = 6900 K. The temperature of T_e(N II) = 6772 K predicted by the model MC2 is about 2,130 lower than the value empirically derived. However, T_e(O II) = 6692 K and T_e(O III) = 6568 K obtained by the model MC2 are in good agreement with T_e(O II) = 7050 K and T_e(O III) = 6900 K empirically derived from CELs by García-Rojas et al. (2009), respectively. Additionally, T_e(He I) = 6584 K calculated by the model MC2 in agreement with the empirical value of T_e(He I) = 6250 K derived by García-Rojas et al. (2009). The temperatures predicted by MC2 is lower than those from MC1, which is because of the cooling effects of the H-poor inclusions. We take no account of the interaction between the two components, namely normal and H-poor, which could also lead to a temperature variation. Moreover, positions of individual H-poor knots can dramatically influence thermal structures. Dust grains could also play a major role in the heating of the nebula through photoelectric emissions. As seen in Table 6.5, T_e(O II) and T_e(O III) predicted by the dusty model MC3 is about 70 and 53 K higher than those calculated by the model MC2. Therefore, dust heating made a smaller thermal contribution to the nebula.

Table 6.6 represents mean electron temperatures weighted by ionic abundances for the different components of MC3. The first entries for each element are for the H-poor inclusion and the second entries are for the normal plasma. It can be seen that the temperatures for the two different components of the nebula are very different. The electron temperatures separately weighted by the ionic species of the H-poor inclusions were much lower than those from

Table 6.5: Mean electron temperatures (K) weighted by ionic species for the whole nebula obtained from the photoionization models. For each element the first row is for MC1, the second row is for MC2 and the third row is for MC3.

	Ion						
El	I	II	III	IV	V	VI	VII
H	7746	7625					
	6647	6584					
	6719	6640					
He	7746	7625	7595				
	6655	6584	6784				
	6726	6640	6843				
C	7829	7741	7621	7468	7431	7625	7625
	6806	6673	6580	6549	6631	6584	6584
	6886	6742	6635	6491	6640	6641	6641
N	7834	7746	7617	7468	7431	7625	7625
	6883	6772	6567	6439	6565	6584	6584
	6959	6840	6622	6414	6580	6641	6641
O	7860	7746	7613	7566	7625	7625	7625
	7176	6692	6568	6618	6584	6584	6584
	7250	6762	6621	6671	6641	6641	6641
Ne	7812	7720	7601	7564	7625	7625	7625
	6602	6599	6579	6764	6584	6584	6584
	6690	6671	6630	6819	6641	6641	6641
S	7855	7783	7685	7541	7411	7390	7625
	6760	6676	6632	6497	6453	6572	6584
	6848	6751	6694	6541	6435	6597	6641
Cl	7836	7748	7635	7503	7467	7625	7625
	6747	6658	6598	6408	6612	6584	6584
	6832	6731	6656	6444	5640	6241	6641
Ar	7846	7766	7659	7535	7490	7625	7625
	6699	6606	6588	6570	6684	6584	6584
	6783	6680	6647	6618	6737	6641	6641

Table 6.6: Mean electron temperatures (K) weighted by ionic species for the whole nebula obtained from the photoionization model MC2. For each element the first row is for the normal component and the second row is for the H-poor component.

	Ion						
El	I	II	III	IV	V	VI	VII
H	7298	7097					
	4341	4309					
He	7307	7097	7054				
	4343	4309	4310				
C	7436	7295	7088	6795	6739	7098	7098
	4361	4342	4307	4252	4253	4309	4309
N	7460	7315	7077	6796	6738	7098	7098
	4363	4344	4306	4257	4258	4309	4309
O	7507	7319	7064	6989	7098	7098	7098
	4364	4346	4302	4302	4309	4309	4309
Ne	7414	7260	7042	6988	7098	7098	7098
	4361	4340	4294	4295	4309	4309	4309
S	7466	7349	7186	6937	6713	6678	7098
	4365	4349	4324	4276	4243	4243	4309
Cl	7444	7302	7113	6875	6720	6721	7098
	4361	4343	4312	4261	4241	4245	4309
Ar	7468	7336	7148	6929	6861	7098	7098
	4366	4349	4317	4267	4267	4309	4309

the normal part. Mean electron temperatures for the total structure of MC3 are presented in Table 6.5. The metal-rich inclusion soften the radiation field, so the entire nebula was cooled down to lower temperatures. From Table 6.6, it is possible to understand the different thermal effects by the cold metal-rich component and the diffuse warm normal component contributed to the nebula.

6.4.3 Fractional ionic abundances

The volume-averaged fractional ionic abundances calculated from the three models are listed in Table 6.7, where, once again, the first entries for each element are for the chemically homogeneous model MC1, the second entries are for the bi-abundance model MC2, and the third entries are the dusty bi-abundance model MC3. We see that hydrogen and helium are both fully singly-ionized and neutrals are less than 0.1% in the three models. It can be seen that the ionization structure in MC2 is in reasonable agreement with MC1. The elemental oxygen largely exists as O^{2+} with 90 percent and then O^{+} with 9 per cent in the model MC1, whereas O^{2+} is about 87 percent and then O^{+} is about 13 per cent in the model MC2. Moreover, The elemental nitrogen largely exists as N^{2+} with 93 percent and then N^{+} with 7 per cent in the model MC1, whereas N^{2+} is about 91 percent and then N^{+} is about 9 per cent in the model MC2. The O^{+}/O ratio is about 1.5 times higher than the N^{+}/N ratio, which is in disagreement with the general assumption of $N/N^{+}=O/O^{+}$ in the ionization correction factor (icf) method, introducing errors to empirically derived elemental abundances. But, the O^{2+}/O ratio is about 1.15 higher than the Ne^{2+}/Ne ratio, in agreement with the assumption for icf(Ne). The S^{+} and S^{2+} ionic fractions predicted by MC2 is 1.3 and 1.01 times the predication of MC1, respectively, while S^{3+} is 0.86 times the predication of MC1. The ionic fraction of Cl and Ar predicted by MC2 are about the values calculated by MC1. The small discrepancies in fractional ionic abundances between MC1 and MC2 can be explained by a small fraction of the metal-rich structures included in MC2.

It can be seen in Table 6.8 that the model MC2 do not predicts very different ionic fractions for the two components of the nebula. The upper entries for each element in the table are for the H-poor component and the lower entries are for the normal component of the nebula. It indicates that the ionization correction factors from CELs may be used to correct the abundances derived from ORLs

Table 6.7: Fractional ionic abundances obtained from the photoionization models. For each element the first row is for MC1, the second row is for MC2 and the third row is for MC3.

	Ion						
Element	I	II	III	IV	V	VI	VII
H	6.88(−4)	9.99(−1)					
	8.23(−4)	9.99(−1)					
	8.59(−4)	9.99(−1)					
He	1.91(−3)	9.98(−1)	1.62(−12)				
	2.39(−3)	9.98(−1)	1.38(−12)				
	2.47(−3)	9.98(−1)	1.39(−12)				
C	1.19(−5)	4.15(−2)	9.56(−1)	2.39(−3)	2.70(−16)	1.00(−20)	1.00(−20)
	1.63(−5)	5.03(−2)	9.48(−1)	1.86(−3)	1.91(−16)	1.00(−20)	1.00(−20)
	1.75(−5)	5.18(−2)	9.46(−1)	1.71(−3)	1.75(−16)	1.00(−20)	1.00(−20)
N	1.60(−5)	6.82(−2)	9.28(−1)	3.40(−3)	6.86(−16)	1.00(−20)	1.00(−20)
	2.51(−5)	8.50(−2)	9.12(−1)	2.92(−3)	5.41(−16)	1.00(−20)	1.00(−20)
	2.69(−5)	8.74(−2)	9.10(−1)	2.80(−3)	5.21(−16)	1.00(−20)	1.00(−20)
O	6.40(−5)	9.40(−2)	9.06(−1)	2.00(−13)	1.00(−20)	1.00(−20)	1.00(−20)
	1.06(−4)	1.31(−1)	8.68(−1)	1.82(−13)	1.00(−20)	1.00(−20)	1.00(−20)
	1.19(−4)	1.36(−1)	8.64(−1)	1.81(−13)	1.00(−20)	1.00(−20)	1.00(−20)
Ne	1.06(−4)	2.02(−1)	7.97(−1)	7.74(−14)	1.00(−20)	1.00(−20)	1.00(−20)
	1.78(−4)	2.61(−1)	7.39(−1)	6.04(−14)	1.00(−20)	1.00(−20)	1.00(−20)
	1.87(−4)	2.65(−1)	7.35(−1)	6.03(−14)	1.00(−20)	1.00(−20)	1.00(−20)
S	3.01(−7)	4.72(−3)	5.81(−1)	4.13(−1)	1.90(−3)	8.26(−16)	1.00(−20)
	4.46(−7)	6.14(−3)	6.36(−1)	3.56(−1)	1.46(−3)	5.63(−16)	1.00(−20)
	4.87(−7)	6.46(−3)	6.42(−1)	3.50(−1)	1.42(−3)	5.48(−16)	1.00(−20)
Cl	2.68(−6)	1.85(−2)	8.91(−1)	9.02(−2)	9.99(−15)	1.00(−20)	1.00(−20)
	3.79(−6)	2.22(−2)	8.97(−1)	8.09(−2)	7.66(−15)	1.00(−20)	1.00(−20)
	4.12(−6)	2.30(−2)	8.96(−1)	8.09(−2)	5.00(−7)	1.47(−19)	1.00(−20)
Ar	4.47(−7)	4.11(−3)	7.21(−1)	2.75(−1)	1.56(−13)	1.00(−20)	1.00(−20)
	7.85(−7)	5.95(−3)	7.72(−1)	2.22(−1)	1.11(−13)	1.00(−20)	1.00(−20)
	8.43(−7)	6.12(−3)	7.72(−1)	2.22(−1)	1.12(−13)	1.00(−20)	1.00(−20)

Table 6.8: Fractional ionic abundances obtained from the photoionization model MC2. For each element the first row is for the normal component and the second row is for the H-poor component.

	Ion						
Element	I	II	III	IV	V	VI	VII
H	7.86(−4)	9.99(−1)					
	1.01(−3)	9.99(−1)					
He	2.28(−3)	9.98(−1)	1.53(−12)				
	2.93(−3)	9.97(−1)	6.49(−13)				
C	1.59(−5)	4.86(−2)	9.49(−1)	2.05(−3)	2.22(−16)	1.00(−20)	1.00(−20)
	1.87(−5)	5.89(−2)	9.40(−1)	9.20(−4)	3.12(−17)	1.00(−20)	1.00(−20)
N	2.49(−5)	8.49(−2)	9.12(−1)	3.06(−3)	6.13(−16)	1.00(−20)	1.00(−20)
	2.60(−5)	8.55(−2)	9.12(−1)	2.20(−3)	1.73(−16)	1.00(−20)	1.00(−20)
O	1.16(−4)	1.27(−1)	8.73(−1)	1.92(−13)	1.00(−20)	1.00(−20)	1.00(−20)
	5.74(−5)	1.55(−1)	8.45(−1)	1.31(−13)	1.00(−20)	1.00(−20)	1.00(−20)
Ne	1.60(−4)	2.47(−1)	7.53(−1)	6.77(−14)	1.00(−20)	1.00(−20)	1.00(−20)
	2.72(−4)	3.32(−1)	6.68(−1)	2.29(−14)	1.00(−20)	1.00(−20)	1.00(−20)
S	4.20(−7)	5.83(−3)	6.29(−1)	3.64(−1)	1.59(−3)	6.56(−16)	1.00(−20)
	5.74(−7)	7.74(−3)	6.75(−1)	3.17(−1)	7.82(−4)	8.85(−17)	1.00(−20)
Cl	3.59(−6)	2.13(−2)	8.97(−1)	8.13(−2)	8.59(−15)	1.00(−20)	1.00(−20)
	4.84(−6)	2.69(−2)	8.94(−1)	7.89(−2)	2.87(−15)	1.00(−20)	1.00(−20)
Ar	7.21(−7)	5.50(−3)	7.60(−1)	2.35(−1)	1.26(−13)	1.00(−20)	1.00(−20)
	1.11(−6)	8.25(−3)	8.37(−1)	1.55(−1)	3.19(−14)	1.00(−20)	1.00(−20)

(as assumed by Wang & Liu 2007). It is seen that abundance discrepancies can only be understood in terms of the distinctive elemental abundances used by the two components. It makes possible to understand the physical properties that contributed to the observed ORLs.

6.5 Conclusion

In this chapter, three photoionization models have been constructed for the planetary nebula PB 8, a chemically homogeneous model, and a bi-abundance model and a dusty model. Our intention was to construct a model that can reproduce the observed emission-lines and thermal structure determined from the plasma diagnostics. The spherical density distribution for the nebular gad was developed from detailed time-dependent 1-D radiation-hydrodynamics calculations for different stellar evolutionary tracks. The density distribution was scaled to produce the total Hβ intrinsic line flux of the nebula, and the mean electron density derived from the plasma diagnostics. We have used the NLTE model atmosphere determined by Todt et al. (2010) with temperature $T_{\rm eff} =$ 52 kK and luminosity $L_{\star} = 6000{\rm L}_{\odot}$. This ionizing source well produced the nebular observed Hβ absolute flux at the distance of 4.9 kpc.

Our initial model produced the majority of CELs and thermal structure, but large discrepancies exist in the observed ORLs from heavy element ions. Furthermore, the temperature corresponding to [O III] line ratio predicted by the model is higher than the value empirically derived. It is found that chemical homogeneities cannot explain the ORLs observed in the nebular spectrum. We therefore intended to address the cause of the heavily underestimated ORLs. Following the hypothesis of the bi-abundance model by Liu et al. (2000), a small fraction of hydrogen-deficient inclusions was introduced into the second model. The ORLs are mainly emitted from the cold 'H-deficient' structures embedded in the dominate diffuse warm plasma of normal abundances. The agreement between the ORL intensities predicted by the model MC2 and the observations is better than the first model (MC1). The metal-rich inclusions have a mass of ~ 5 percent of the total ionized mass and nearly twice cooler and denser than the normal composition nebula. The O/H and N/H abundance ratios in the metal-rich inclusions are ~ 1.0 and 1.7 dex larger than the diffuse warm nebula, respectively. The temperatures predicted by MC2 is lower than those from MC1, which is because of the cooling effects of the H-poor inclusions. The results indicate that the bi-abundance model can naturally explain the heavily underestimated ORLs in the first model. Therefore, the metal-rich inclusions may solve the long-standing problem of ORL/CEL abundance discrepancies. However, the model MC2 cannot explain the thermal SED of the nebula observed with the *Spitzer* spectrograph. In our final model, we have incorporated a dual dust chemistry consisting of two different grains, amorphous carbon and crystalline silicate, and discrete grain radii, 0.16 μm (warm) and 0.40 μm (cool). It is found that a dust-to-hydrogen ratio of 0.01 by mass for the whole nebula can produce the observed IR continuum.

It is unclear whether there is any link between the supposed H-deficient inclusions within the nebula and hydrogen-deficient stars. It has been suggested that a (very-) late thermal pulse is responsible for the formation of H-deficient central stars of planetary nebulae (see e.g. Blöcker 2001; Herwig 2001; Werner 2001; Werner & Herwig 2006). Thermal pulses normally occur during the AGB phase, when the helium-burning shell becomes thermally unstable. The occurrence of the thermal pulse in the post-AGB phase can result in a H-deficient star. The (very-) late thermal pulse occurs when the star moves from the AGB phase towards the white dwarf. It returns the star to the AGB phase and makes a H-deficient stellar surface, so called *born-again* scenario. It is possible that the H-deficient material were ejected during the born-again scenario. Further studies are necessary to trace the origin of the H-deficient inclusions within the nebula.

Part III

Planetary nebulae with PG 1159-type stars

7

SuWt 2 with a PG 1159-type star

The contents of this chapter were published in the Monthly Notices of the Royal Astronomical Society, Vol. 434, Pages 1513–1530, 2013. The authors were A. Danehkar, Q. A. Parker and B. Ercolano. Some small modifications have been made.

7.1 Introduction

The southern planetary nebula SuWt 2 appears as an elliptical ring-like nebula with much fainter bipolar lobes extending perpendicularly to the ring, and with what appears to be an obvious, bright central star. The inside of the ring is apparently empty, but brighter than the nebula's immediate surroundings. An overall view of this ring-shaped structure and its surrounding environment can be seen in the Hα image available from the SuperCOSMOS Hα Sky Survey (SHS; Parker et al. 2005). West (1976) classified SuWt 2 as of intermediate excitation class ($p = 6$–7; Aller & Liller 1968) based on the strength of the He II λ4686 and [O II] λ3728 doublet lines. The line ratio of [N II] λ6584 and Hα illustrated by Smith et al. (2007) showed a nitrogen-rich nebula that most likely originated from post-main-sequence mass-loss of an intermediate-mass progenitor star.

Over a decade ago, Bond (2000) discovered that the apparent central star of SuWt 2 (NSV 19992) is a detached double-lined eclipsing binary consisting of two early A-type stars of nearly identical type. Furthermore, Bond et al. (2002) suggested that this is potentially a triple system consisting of the two A-type stars and a hot, unseen PN central star. However, to date, optical and UV studies have failed to find any signature of the nebula's true ionizing source (e.g. Bond et al. 2002, 2003; Exter et al. 2003, 2010). Hence the putative hot (pre-)white dwarf would have to be in a wider orbit around the close eclipsing pair. Exter et al. (2010) recently derived a period of 4.91 d from time series photometry and spectroscopy of the eclipsing pair, and concluded that the centre-of-mass velocity of the central binary varies with time, based on different systemic velocities measured over the period from 1995 to 2001. This suggests the presence of an unseen third orbiting body, which they concluded is a white dwarf of $\sim 0.7 M_{\odot}$, and is the source of ionizing radiation for the PN shell.

There is also a very bright B1Ib star, SAO 241302 (HD 121228), located 73 arcsec northeast of the nebula. Smith et al. (2007) speculated that this star is the ionizing source for SuWt 2. However, the relative strength of He II λ4686 in our spectra (see later) shows that the ionizing star must be very hot, $T >$ 100,000 K, so the B1 star is definitively ruled out as the ionizing source.

Narrow-band Hα+[N II] and [O III] 5007 images of SuWt 2 obtained by Schwarz et al. (1992) show that the angular dimensions of the bright elliptical ring are about 86.5 arcsec $\times$ 43.4 arcsec at the 10% of maximum surface brightness isophote (Tylenda et al. 2003), and are used throughout this chapter. Smith et al. (2007) used the MOSAIC2 camera on the Cerro Tololo Inter-American Observatory (CTIO) 4-m telescope to obtain a more detailed Hα+[N II] image, which hints that the ring is possibly the inner edge of a swept-up disc. The [N II] image also shows the bright ring structure and much fainter bipolar lobes extending perpendicular to the ring plane. We can see similar structure in the images taken by Bond and Exter in 1995 with the CTIO 1.5 m telescope using an Hα+[N II] filter. Fig. 7.1 shows both narrow-band [N II] 6584 Å and Hα images taken in 1995 with the ESO 3.6 m New Technology Telescope at the La Silla Paranal Observatory using the ESO Multi-Mode Instrument (EMMI). The long-slit emission-line spectra also obtained with the EMMI (programme ID 074.D-0373) in 2005 revealed much more detail of the nebular morphology. The first spatio-kinematical model using the EMMI long-slit data by Jones et al. (2010a) suggested the existence of a bright torus with a systemic heliocentric radial velocity of -25 ± 5 km s^{-1} encircling the waist of an extended bipolar nebular shell.

In this chapter, we aim to uncover the properties of the hidden hot ionizing source in SuWt 2. We aim to do this by applying a self-consistent three-dimensional photoionization model using the MOCASSIN 3D code. We use optical integral-field spectroscopy to study the emission lines of the inner nebula ring. This has enabled us to perform an empirical analysis of the optical collisionally excited lines, together with a fully three-dimensional photoionization modeling. Our empirical results are used to constrain the photoionization models, that determine the evolutionary stage of the responsible ionizing source and its likely progenitor.

This chapter is structured as follows. In Section 7.2, we describe our optical integral field observations as well as the data reduction process and the corrections for interstellar extinction. In Section 7.3, we describe the kinematics. In Section 7.4, we present our derived electron temperature and density, together with our empirical ionic abundances in Section 7.5. In Section 7.6, we present derived ionizing source properties and distance from our self-consistent photoionization models, followed by a conclusion in Section 7.7.

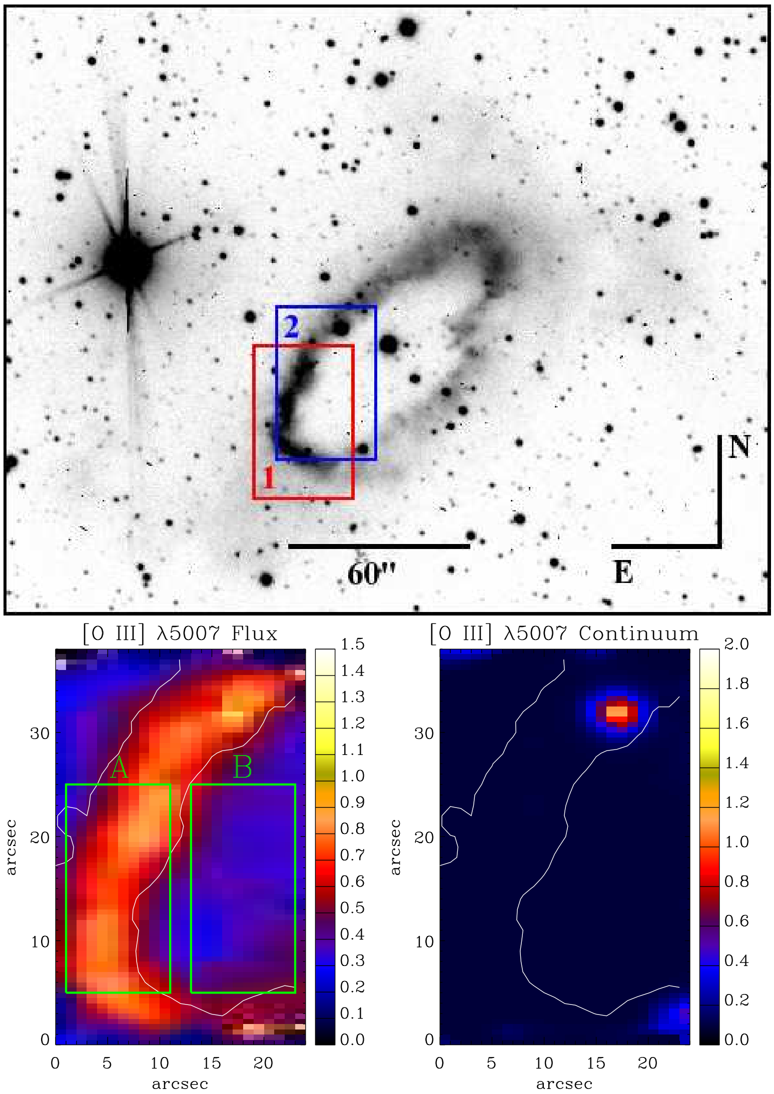

Figure 7.1: Top panel: narrow-band filter image of the PN SuWt 2 on a logarithmic scale in Hα and [N II] 6584 Å taken with the European Southern Observatory (ESO) 3.6-m telescope (programme ID 055.D-0550). The rectangles correspond to the WiFeS fields of view used for our study: 1 (red) and 2 (blue); see Table 7.1 for more details. Bottom panels: Spatial distribution maps of flux intensity and continuum of [O III] λ5007 for field 2 and locations of apertures (10 arcsec $\times$ 20 arcsec) used to integrate fluxes, namely 'A' the ring and 'B' the interior structure. The white contour lines show the distribution of the above narrow-band Hα emission in arbitrary unit. North is up and east is towards the left-hand side.

7.2 Observations and data reduction

Integral-field spectra of SuWt 2 were obtained during two observing runs in 2009 May and 2012 August with the Wide Field Spectrograph (WiFeS; Dopita et al. 2007). WiFeS is an image-slicing Integral Field Unit (IFU) developed and built for the ANU 2.3-m telescope at the Siding Spring Observatory, feeding a double-beam spectrograph. WiFeS samples 0.5 arcsec along each of twenty five $38\,\mathrm{arcsec} \times 1\,\mathrm{arcsec}$ slits, which provides a field-of-view of $25\,\mathrm{arcsec} \times 38\,\mathrm{arcsec}$ and a spatial resolution element of $1.0\,\mathrm{arcsec} \times 0.5\,\mathrm{arcsec}$ (or $1'' \times 1''$ for y-binning=2). The spectrograph uses volume phase holographic gratings to provide a spectral resolution of $R = 3000$ (100 km s^{-1} full width at half-maximum, FWHM), and $R = 7000$ (45 km s^{-1} FWHM) for the red and blue arms, respectively. Each grating has a different wavelength coverage. It can operate two data accumulation modes: classical and nod-and-shuffle (N&S). The N&S accumulates both object and nearby sky-background data in either equal exposures or unequal exposures. The complete performance of the WiFeS has been fully described by Dopita et al. (2007, 2010).

Our observations were carried out with the B3000/R3000 grating combination and the RT 560 dichroic using N&S mode in 2012 August; and the B7000/R7000 grating combination and the RT 560 dichroic using the classical mode in 2009 May. This covers $\lambda\lambda$3300–5900 Å in the blue channel and $\lambda\lambda$5500–9300 Å in the red channel. As summarized in Table 7.1, we took two different WiFeS exposures from different positions of SuWt 2; see Fig. 7.1 (top). The sky field was collected about 1 arcmin away from the object. To reduce and calibrate the data, it is necessary to take the usual bias frames, dome flat-field frames, twilight sky flats, 'wire' frames and arc calibration lamp frames. Although wire, arc, bias and dome flat-field frames were collected during the afternoon prior to observing, arc and bias frames were also taken through the night. Twilight sky flats were taken in the evening. For flux calibration, we also

Table 7.1: Journal of SuWt 2 Observations at the ANU 2.3-m Telescope.

Field	1	2
Instrument	WiFeS	WiFeS
Wavelength Resolution	~ 7000	~ 3000
Wavelength Range (Å)	4415–5589, 5222–7070	3292–5906, 5468–9329
Mode	Classical	N&S
Y-Binning	1	2
Object Exposure (s)	900	1200
Sky Exposure (s)	–	600
Standard Star	LTT 3218	LTT 9491, HD 26169
$v_{\rm LSR}$ correction	-5.51	-25.77
Airmass	1.16	1.45
Position (see Fig. 7.1)	13:55:46.2 −59:22:57.9	13:55:45.5 −59:22:50.3
Date (UTC)	16/05/09	20/08/12

observed some spectrophotometric standard stars.

7.2.1 WiFeS data reduction

The WiFeS data were reduced using the WIFES pipeline (updated on 2011 November 21), which is based on the Gemini IRAF[1] package (version 1.10; IRAF version 2.14.1) developed by the Gemini Observatory for the integral-field spectroscopy.

Each CCD pixel in the WiFeS camera has a slightly different sensitivity, giving pixel-to-pixel variations in the spectral direction. This effect is corrected using the dome flat-field frames taken with a quartz iodine (QI) lamp. Each slitlet is corrected for slit transmission variations using the twilight sky frame taken at the beginning of the night. The wavelength calibration was performed

[1]The Image Reduction and Analysis Facility (IRAF) software is distributed by the National Optical Astronomy Observatory.

using Ne–Ar arc exposures taken at the beginning of the night and throughout the night. For each slitlet the corresponding arc spectrum is extracted, and then wavelength solutions for each slitlet are obtained from the extracted arc lamp spectra using low-order polynomials. The spatial calibration was accomplished by using so called 'wire' frames obtained by diffuse illumination of the coronagraphic aperture with a QI lamp. This procedure locates only the centre of each slitlet, since small spatial distortions by the spectrograph are corrected by the WiFeS cameras. Each wavelength slice was also corrected for the differential atmospheric refraction by relocating each slice in x and y to its correct spatial position.

In the N&S mode, the sky spectra are accumulated in the unused 80 pixel spaces between the adjacent object slices. The sky subtraction is conducted by subtracting the image shifted by 80 pixels from the original image. The cosmic rays and bad pixels were removed from the raw data set prior to sky subtraction using the IRAF task LACOS_IM of the cosmic ray identification procedure of van Dokkum (2001), which is based on a Laplacian edge detection algorithm. However, a few bad pixels and cosmic rays still remained in raw data, and these were manually removed by the IRAF/STSDAS task IMEDIT.

We calibrated the science data to absolute flux units using observations of spectrophotometric standard stars observed in classical mode (no N&S), so sky regions within the object data cube were used for sky subtraction. An integrated flux standard spectrum is created by summing all spectra in a given aperture. After manually removing absorption features, an absolute calibration curve is fitted to the integrated spectrum using third-order polynomials. The flux calibration curve was then applied to the object data to convert to an absolute flux scale. The [O I] λ5577Å night sky line was compared in the sky spectra of the red and blue arms to determine a difference in the flux levels, which was used to scale the blue spectrum of the science data. Our analysis using different spectrophotometric standard stars (LTT 9491 and HD 26169) revealed that the spectra at the extreme blue have an uncertainty of about 30% and are particularly unreliable for faint objects due to the CCD's poor sensitivity in this area.

7.2.2 Nebular spectrum and reddening

Table 7.2 represents a full list of observed lines and their measured fluxes from different apertures (10 arcsec $\times$ 20 arcsec) taken from field 2: (A) the ring and (B) the inside of the shell. Fig. 7.1 (bottom panel) shows the location and area of each aperture in the nebula. The top panel, and the middle and bottom panels of Fig. 7.2 respectively show the extracted blue and red spectra after integration over the aperture located on the ring with the strongest lines truncated so the weaker features can be seen. The emission line identification, laboratory wavelength, multiplet number, the transition with the lower- and upper-spectral terms, are given in columns 1–4 of Table 7.2, respectively. The observed fluxes of the interior and ring, and the fluxes after correction for interstellar extinction are given in columns 5–8. Columns 9 and 10 present the integrated and dereddened fluxes after integration over two apertures (A and B). All fluxes are given relative to Hβ, on a scale where H$\beta = 100$.

For each spatially resolved emission line profile, we extracted flux intensity, central wavelength (or centroid velocity), and FWHM (or velocity dispersion). Each emission line profile for each spaxel is fitted to a single Gaussian curve using the MPFIT routine (Markwardt 2009), an IDL version of the MINPACK-1 FORTRAN code (Moré 1977), which applies the Levenberg–Marquardt technique to the non-linear least-squares problem. Flux intensity maps of key emission lines of field 2 are shown in Fig. 7.3 for [O III] λ5007, Hα λ6563, [N II] λ6584 and [S II] λ6716; the same ring morphology is visible in the [N II] map as seen in Fig. 7.1. White contour lines in the figures depict the distribution of the narrow-band emission of Hα and [N II] taken with the ESO 3.6 m telescope, which can be used to distinguish the borders between the ring structure and the inside region. We excluded the stellar continuum offset from the final flux maps using MPFIT, so spaxels show only the flux intensities of the nebulae.

The Hα and Hβ Balmer emission-line fluxes were used to derive the logarithmic extinction at Hβ, $c(\mathrm{H}\beta) = \log[I(\mathrm{H}\beta)/F(\mathrm{H}\beta)]$, for the theoretical line ratio of the case B recombination ($T_{\rm e} = 10\,000$ K and $N_{\rm e} = 100$ cm^{-3}; Hummer & Storey 1987). Each flux at the central wavelength was corrected for reddening using the logarithmic extinction $c(\mathrm{H}\beta)$ according to

$$I(\lambda) = F(\lambda)\,10^{c(\mathrm{H}\beta)[1+f(\lambda)]}, \tag{7.1}$$

where $F(\lambda)$ and $I(\lambda)$ are the observed and intrinsic line flux, respectively, and $f(\lambda)$ is the standard Galactic extinction law for a total-to-selective extinction ratio of $R_V \equiv A(V)/E(B-V) = 3.1$ (Seaton 1979b,a; Howarth 1983).

Accordingly, we obtained an extinction of $c(\mathrm{H}\beta) = 0.64$ $[E(B-V) = 0.44]$ for the total fluxes (column 9 in Table 7.2). Our derived nebular extinction is in good agreement with the value found by Exter et al. (2010), $E(B-V) = 0.40$ for the central star, though they obtained $E(B-V) = 0.56$ for the nebula. It may point to the fact that all reddening is not due to the interstellar medium (ISM), and there is some dust contribution in the nebula. Adopting a total observed flux value of $\log F(\mathrm{H}\alpha) = -11.69$ erg cm^{-2} s^{-1} for the ring and interior structure (Frew 2008; Frew et al. 2013a, 2014a) and using $c(\mathrm{H}\beta) = 0.64$, lead to the dereddened Hα flux of $\log I(\mathrm{H}\alpha) = -11.25$ erg cm^{-2} s^{-1}.

Table 7.2: Observed and dereddened relative line fluxes, on a scale where Hβ = 100. The integrated observed H(β) flux was dereddened using c(Hβ) to give an integrated dereddened flux. Uncertain (errors of 20%) and very uncertain (errors of 30%) values are follows by ":" and "::", respectively. The symbol '*' denotes doublet emission lines.

Region				Interior		Ring		Total	
Line	$\lambda_{\rm lab}$(Å)	Mult	Transition	$F(\lambda)$	$I(\lambda)$	$F(\lambda)$	$I(\lambda)$	$F(\lambda)$	$I(\lambda)$
(1)	(2)	(3)	(4)	(5)	(6)	(7)	(8)	(9)	(10)
3726 [O II]	3726.03	F1	$2p^3\,{}^4S_{3/2} - 2p^3\,{}^2D_{3/2}$	183 ± 54	307 ± 91	576 ± 172	815 ± 244	479 ± 143	702 ± 209
3729 [O II]	3728.82	F1	$2p^3\,{}^4S_{3/2} - 2p^3\,{}^2D_{5/2}$	*	*	*	*	*	*
3869 [Ne III]	3868.75	F1	$2p^4\,{}^3P_2 - 2p^4\,{}^1D_2$	128.93::	199.42::	144.31::	195.22::	145.82::	204.57::
3967 [Ne III]	3967.46	F1	$2p^4\,{}^3P_1 - 2p^4\,{}^1D_2$	–	–	15.37::	20.26::	–	–
4102 Hδ	4101.74	H6	$2p\,{}^2P - 6d\,{}^2D$	–	–	16.19:	20.55:	16.97:	22.15:
4340 Hγ	4340.47	H5	$2p\,{}^2P - 5d\,{}^2D$	24.47::	31.10::	30.52:	36.04:	31.69:	38.18:
4363 [O III]	4363.21	F2	$2p^2\,{}^1D_2 - 2p^2\,{}^1S_0$	37.02::	46.58::	5.60	6.57	5.15	6.15
4686 He II	4685.68	3-4	$3d\,{}^2D - 4f\,{}^2F$	80.97	87.87	29.98	31.72	41.07	43.76
4861 Hβ	4861.33	H4	$2p\,{}^2P - 4d\,{}^2D$	100.00	100.00	100.00	100.00	100.00	100.00
4959 [O III]	4958.91	F1	$2p^2\,{}^3P_1 - 2p^2\,{}^1D_2$	390.90	373.57	173.63	168.27	224.48	216.72
5007 [O III]	5006.84	F1	$2p^2\,{}^3P_2 - 2p^2\,{}^1D_2$	1347.80	1259.76	587.22	560.37	763.00	724.02
5412 He II	5411.52	4-7	$4f\,{}^2F - 7g\,{}^2G$	19.33	15.01	5.12	4.30	6.90	5.68
5755 [N II]	5754.60	F3	$2p^2\,{}^1D_2 - 2p^2\,{}^1S_0$	7.08:	4.90:	13.69	10.61	10.17	7.64
5876 He I	5875.66	V11	$2p\,{}^3P - 3d\,{}^3D$	–	–	11.51	8.69	8.96	6.54
6548 [N II]	6548.10	F1	$2p^2\,{}^3P_1 - 2p^2\,{}^1D_2$	115.24	63.13	629.36	414.79	513.64	321.94
6563 Hα	6562.77	H3	$2p\,{}^2P - 3d\,{}^2D$	524.16	286.00	435.14	286.00	457.70	286.00

Table 7.2: (continued)

Region				Interior		Ring		Total	
Line	$\lambda_{\rm lab}$(Å)	Mult	Transition	$F(\lambda)$	$I(\lambda)$	$F(\lambda)$	$I(\lambda)$	$F(\lambda)$	$I(\lambda)$
(1)	(2)	(3)	(4)	(5)	(6)	(7)	(8)	(9)	(10)
6584 [N II]	6583.50	F1	$2p^2\,{}^3P_2 - 2p^2\,{}^1D_2$	458.99	249.05	1980.47	1296.67	1642.12	1021.68
6678 He I	6678.16	V46	$2p\,{}^1P_1 - 3d\,{}^1D_2$	–	–	3.30	2.12	2.68	1.63
6716 [S II]	6716.44	F2	$3p^3\,{}^4S_{3/2} - 3p^3\,{}^2D_{5/2}$	60.63	31.77	131.84	84.25	116.21	70.36
6731 [S II]	6730.82	F2	$3p^3\,{}^4S_{3/2} - 3p^3\,{}^2D_{3/2}$	30.08	15.70	90.39	57.61	76.98	46.47
7005 [Ar V]	7005.40	F1	$3p^2\,{}^3P - 3p^2\,{}^1D$	5.46:	2.66:	–	–	–	–
7136 [Ar III]	7135.80	F1	$3p^4\,{}^3P_2 - 3p^4\,{}^1D_2$	31.81	15.03	26.22	15.59	27.75	15.51
7320 [O II]	7319.40	F2	$2p^3\,{}^2D_{5/2} - 2p^3\,{}^2P$	18.84	8.54	9.00	5.20	10.96	5.93
7330 [O II]	7329.90	F2	$2p^3\,{}^2D_{3/2} - 2p^3\,{}^2P$	12.24	5.53	4.50	2.60	6.25	3.37
7751 [Ar III]	7751.43	F1	$3p^4\,{}^3P_1 - 3p^4\,{}^1D_2$	46.88	19.38	10.97	5.95	19.05	9.60
9069 [S III]	9068.60	F1	$3p^2\,{}^3P_1 - 3p^2\,{}^1D_2$	12.32	4.07	13.27	6.16	13.34	5.65
c(Hβ)				–	0.822	–	0.569	–	0.638

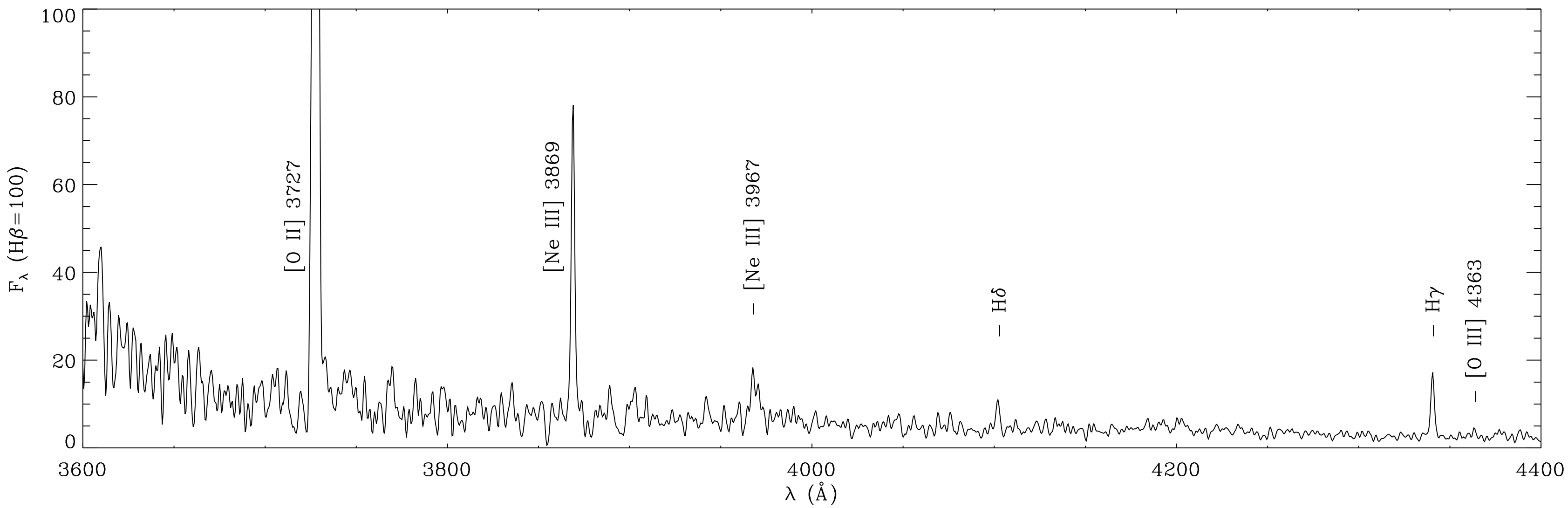

Figure 7.2: The observed optical spectrum from an aperture $10'' \times 20''$ taken from field 2 located on the east ring of the PN SuWt 2 and normalized such that $F(\mathrm{H}\beta) = 100$: blue spectra (top) covers wavelengths 3600–4400 Å and red spectra (middle and bottom) covers 4400–8000 Å.

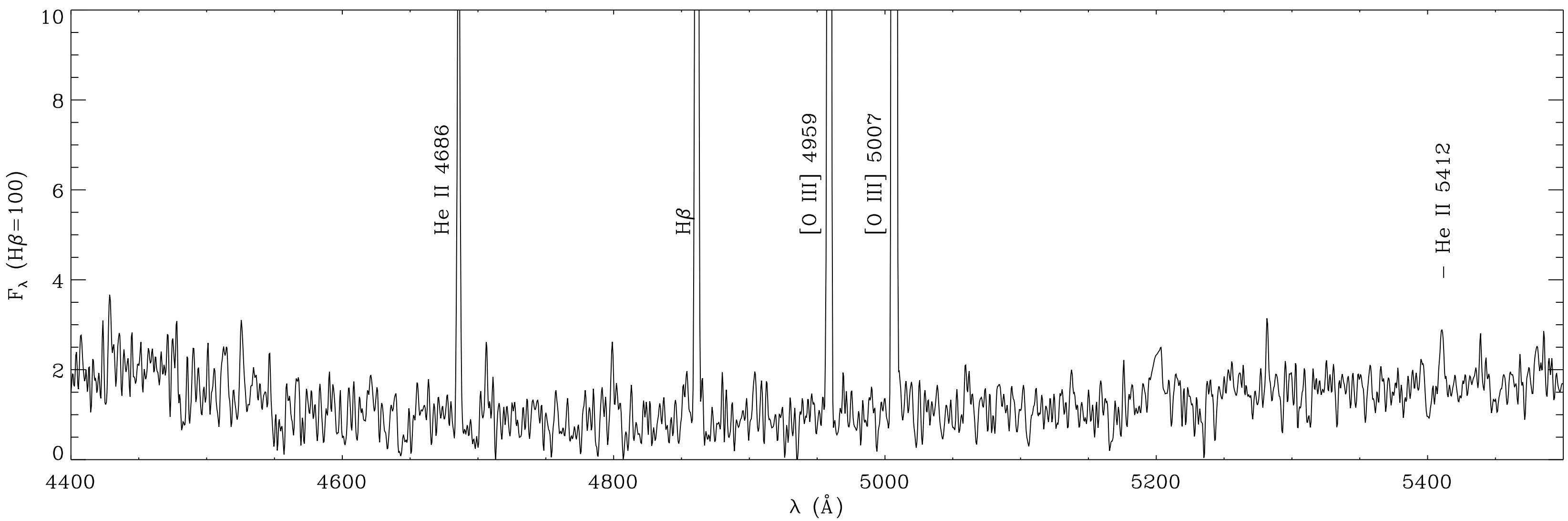

Figure 7.2: (continued)

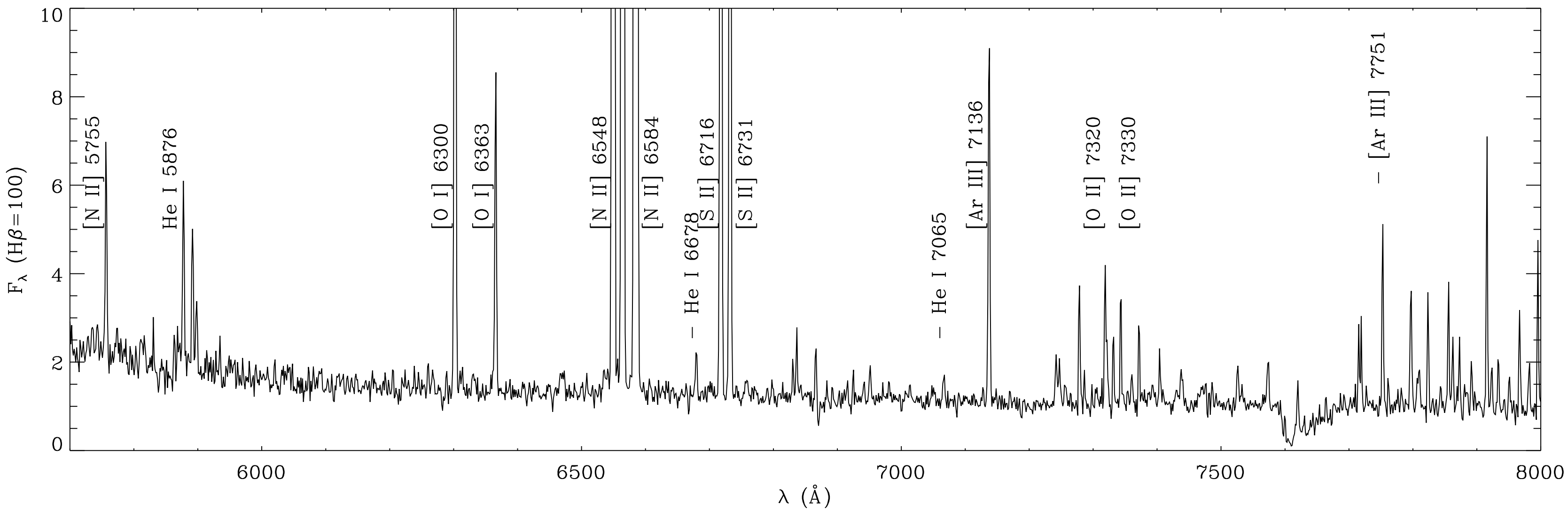

Figure 7.2: (continued)

According to the strength of He II λ4686 relative to Hβ, the PN SuWt 2 is classified as the intermediate excitation class with EC = 6.6 (Dopita & Meatheringham 1990) or EC = 7.8 (Reid & Parker 2010). The EC is an indicator of the central star effective temperature (Dopita & Meatheringham 1991; Reid & Parker 2010). Using the $T_{\rm eff}$–EC relation of Magellanic Cloud PNe found by Dopita & Meatheringham (1991), we estimate $T_{\rm eff} = 143$ kK for EC = 6.6. However, we get $T_{\rm eff} = 177$ kK for EC = 7.8 according to the transformation given by Reid & Parker (2010) for Large Magellanic Cloud PNe.

7.3 Kinematics

Fig. 7.4 presents maps of the flux intensity and the local standard of rest (LSR) radial velocity derived from the Gaussian profile fits for the emission line [N II] λ 6584 Å. We transferred the observed velocity $v_{\rm obs}$ to the LSR radial velocity $v_{\rm lsr}$ by determining the radial velocities induced by the motions of the Earth and Sun using the IRAF/ASTUTIL task RVCORRECT. The emission-line profile is also resolved if its velocity dispersion is wider than the instrumental width $\sigma_{\rm ins}$. The instrumental width can be derived from the [O I] λ5577Å and λ6300Å night sky lines; it is typically $\sigma_{\rm ins} \approx 42\,{\rm km\,s^{-1}}$ for $R \sim 3000$ and $\sigma_{\rm ins} \approx 19\,{\rm km\,s^{-1}}$ for $R \sim 7000$. Fig. 7.4(right) shows the variation of the LSR radial velocity in the south-east side of the nebula. We see that the radial velocity decreases as moving anti-clockwise on the ellipse. It has a low value of about $-70 \pm 30\,{\rm km\,s^{-1}}$ on the west co-vertex of the ellipse, and a high value of $-50 \pm 25\,{\rm km\,s^{-1}}$ on the south vertex. This variation corresponds to the orientation of this nebula, namely the inclination and projected nebula on the plane of the sky. It obviously implies that the east side moves towards us, while the west side escapes from us.

Kinematic information of the ring and the central star is summarized in Table 7.3. Jones et al. (2010a) implemented a morpho-kinematic model using

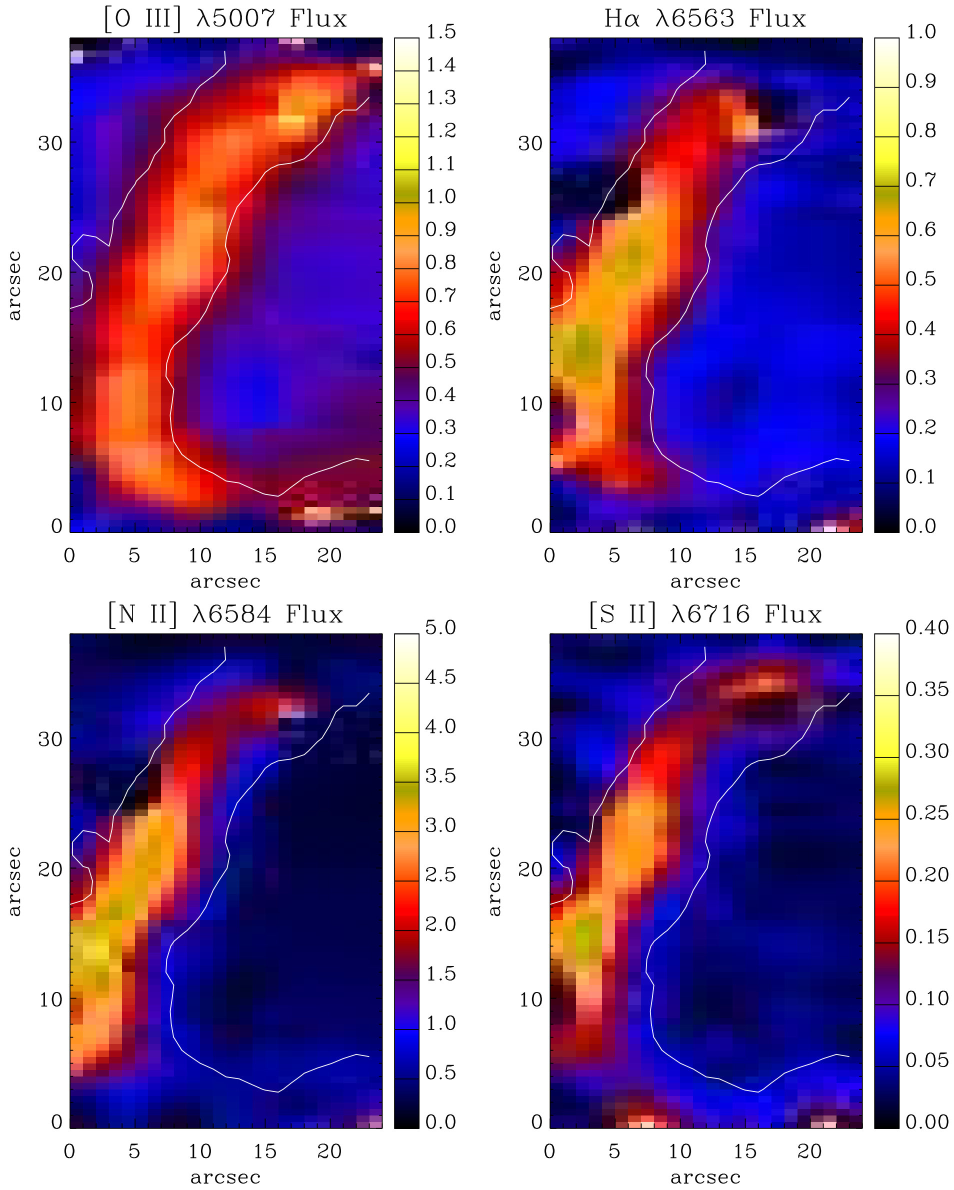

Figure 7.3: Undereddened flux maps for *Field 2* (see Fig. 7.1) of the PN SuWt 2: [O III] λ5007 Å, Hα λ6563 Å, [N II] λ6584 Å and [S II] λ6716 Å. The flux is derived from single Gaussian profile fits to the emission line at each spaxel. White contour lines show the distribution of the narrow-band emission of Hα and [N II] in arbitrary unit taken with the ESO 3.6-m telescope. North is up and east is toward the left-hand side. Flux unit is in 10^{-15} erg s^{-1} cm^{-2} spaxel^{-1}.

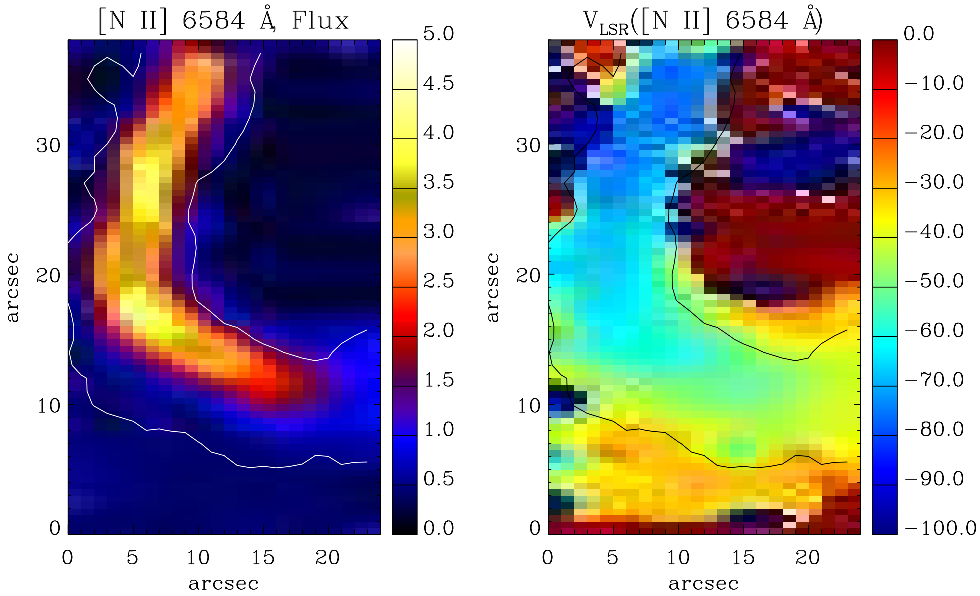

Figure 7.4: Flux intensity and radial velocity ($V_{\rm LSR}$) map in [N II] λ 6584 Å for *Field 1* (see Table 7.1) of the PN SuWt 2. White/black contour lines show the distribution of the narrow-band emission of Hα and [N II] in arbitrary unit taken with the ESO 3.6-m telescope. North is up and east is toward the left-hand side. Units are in km s^{-1}.

the modelling program SHAPE (Steffen & López 2006) based on the long-slit emission-line spectra at the high resolution of $R \sim 40000$, which is much higher than the moderate resolution of $R \sim 3000$ in our observations. They obtained the nebular expansion velocity of $v_{\rm exp} = 28$ km s^{-1} and the LSR systemic velocity of $v_{\rm sys} = -29.5 \pm 5$ at the best-fitting inclination of $i = 68^{\circ} \pm 2^{\circ}$ between the line of sight and the nebular axisymmetry axis. We notice that the nebular axisymmetric axis has a position angle of PA $= 48^{\circ}$ projected on to the plane of the sky, and measured from the north towards the east in the equatorial coordinate system (ECS). Transferring the PA in the ECS to the PA in the Galactic coordinate system yields the Galactic position angle of GPA $= 62^{\circ}16'$, which is the PA of the nebular axisymmetric axis projected on to the plane of the sky, mea-

Table 7.3: Kinematic parameters on the SuWt 2's ring and its central star.

Parameter	Value
$a = r$ (outer radius)	45 ± 4 arcsec
$b = r\cos i$	17 ± 2 arcsec
thickness	13 ± 2 arcsec
PA	$48^\circ \pm 2^\circ$
GPA	$62^\circ 16' \pm 2^\circ$
inclination (i)	$68^\circ \pm 2^\circ$
$v_{\rm sys}$ (LSR)	-29.5 ± 5 km s^{-1}
$v_{\rm exp}$	28 ± 5 km s^{-1}

sured from the North Galactic Pole (NGP; GPA $= 0^\circ$) towards the Galactic east (GPA $= 90^\circ$). We notice an angle of $-27^\circ 44'$ between the nebular axisymmetric axis projected onto the plane of the sky and the Galactic plane. Fig. 7.5 shows the flux ratio map for the [S II] doublet to the Hα recombination line emission. The shock criterion [S II] $\lambda\lambda$6716,6731/H$\alpha \geq 0.5$ indicates the presence of a shock-ionization front in the ring. Therefore, the brightest south-east side of the nebula has a signature of an interaction with ISM.

The PPMXL catalogue[2] (Roeser et al. 2010) reveals that the A-type stars of SuWt 2 move with the proper motion of $v_l = D\mu_l \cos(b) = (-8.09 \pm 8.46)D$ km s^{-1} and $v_b = D\mu_b = (11.79 \pm 8.82)D$ km s^{-1}, where D is its distance in kpc. They correspond to the magnitude of $v_\mu = (14.30 \pm 8.83)D$ km s^{-1}. Assuming a distance of $D = 2.3$ kpc (Exter et al. 2010) and $v_{\rm sys} = -29.5 \pm 5$ km s^{-1} (LSR; Jones et al. 2010a), this PN moves in the Cartesian Galactocentric frame with peculiar (non-circular) velocity components of $(U_s, V_s, W_s) = (35.4 \pm 18.4, 11.0 \pm 13.7, 33.18 \pm 26.4)$ km s^{-1}, where U_s is towards the Galactic centre, V_s in the local direction of Galactic rotation, and W_s towards the NGP (see Reid et al. 2009,

[2]Website: `http://vo.uni-hd.de/ppmxl`

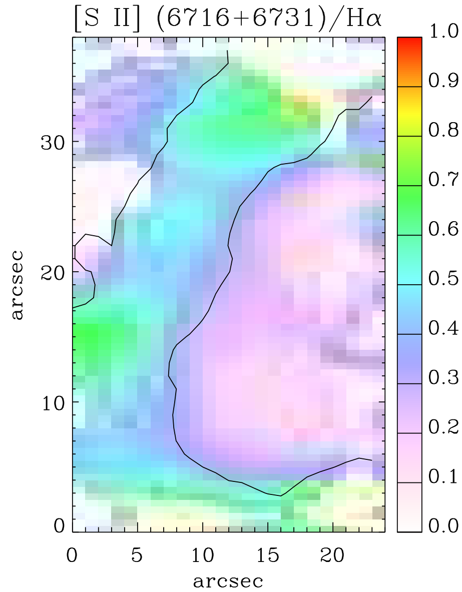

Figure 7.5: Flux ratio maps of the [S II] λ 6716+6731 Å to the Hα recombination line emission.

peculiar motion calculations in appendix). We see that SuWt 2 moves towards the NGP with $W_s = 33.18\,\mathrm{km\,s^{-1}}$, and there is an interaction with ISM in the direction of its motion, i.e., the east-side of the nebula.

We notice a very small peculiar velocity ($V_s = 11$ km s^{-1}) in the local direction of Galactic rotation, so a kinematic distance may also be estimated as the Galactic latitude is a favorable one for such a determination. We used the FORTRAN code for the 'revised' kinematic distance prescribed in Reid et al. (2009), and adopted the IAU standard parameters of the Milky Way, namely the distance to the Galactic centre $R_0 = 8.5$ kpc and a circular rotation speed $\Theta_0 = 220$ km s^{-1} for a flat rotation curve ($\mathrm{d}\Theta/\mathrm{d}R = 0$), and the solar motion of $\mathrm{U}_\odot = 10.30$ km s^{-1}, $\mathrm{V}_\odot = 15.3$ km s^{-1} and $\mathrm{W}_\odot = 7.7$ km s^{-1}. The LSR systemic velocity of -29.5 km s^{-1} (Jones et al. 2010a) gives a kinematic distance of 2.26 kpc, which is in quite good agreement with the distance of 2.3 ± 0.2 kpc found by Exter et al. (2010) based on an analysis of the double-lined eclipsing binary system.

This distance implies that SuWt 2 is in the tangent of the Carina-Sagittarius spiral arm of the Galaxy ($l = 311\overset{\circ}{.}0$, $b = 2\overset{\circ}{.}4$). Our adopted distance of 2.3 kpc means the ellipse's major radius of 45 arcsec corresponds to a ring radius of $r = 0.47 \pm 0.04$ pc. The expansion velocity of the ring then yields a dynamical age of $\tau_{\rm dyn} = r/v_{\rm exp} = 17500 \pm 1560$ yr, which is defined as the radius divided by the constant expansion velocity. Nonetheless, the true age is more than the dynamical age, since the nebula expansion velocity is not constant through the nebula evolution. Dopita et al. (1996) estimated the true age typically around 1.5 of the dynamical age, so we get $\tau_{\rm true} = 26250 \pm 2330$ yr for SuWt 2. If we take the asymptotic giant branch (AGB) expansion velocity of $v_{\rm AGB} = v_{\rm exp}/2$ (Gesicki & Zijlstra 2000), as the starting velocity of the new evolving PN, we also estimate the true age as $\tau_{\rm true} = 2r/(v_{\rm exp} + v_{\rm AGB}) = 23360 \pm 2080$ yr.

7.4 Plasma diagnostics

We derived the nebular electron temperatures $T_{\rm e}$ and densities $N_{\rm e}$ from the intensities of the collisionally excited lines (CELs) by solving the equilibrium equations for an n-level atom ($\geqslant 5$) using EQUIB, a FORTRAN code originally developed by Howarth & Adams (1981). Recently, it has been converted to FORTRAN 90, and combined into simpler routines for NEAT (Wesson et al. 2012). The atomic data sets used for our plasma diagnostics, as well as for the CEL abundance determination in § 7.5, are the same as those used by Wesson et al. (2012).

The diagnostics procedure was as follows: we assumed a representative initial electron temperature of 10 000 K in order to derive $N_{\rm e}$([S II]); then $T_{\rm e}$([N II]) was derived in conjunction with the mean density derived from $N_{\rm e}$([S II]). The calculations were iterated to give self-consistent results for $N_{\rm e}$ and $T_{\rm e}$. The correct choice of electron density and temperature is essential to determine ionic abundances.

Fig. 7.6 shows flux ratio maps for the density-sensitive [S II] doublet. It indicates the electron density $N_{\rm e}$ of about $\lesssim 100$ cm^{-3} in the ring. We see that the interior region has a [S II] $\lambda\lambda$ 6716/6731 flux ratio of more than 1.4, which means the inside of the ring has a very low density ($N_{\rm e} \lesssim 50$ cm^{-3}). Flux ratio maps for the temperature-sensitive [N II] $\lambda\lambda$5755, 6548, 6583 lines indicate that the electron temperature $T_{\rm e}$ varies from 7 000 to 14 000 K. As shown in Fig. 7.6, the brightest part of the ring in [N II] λ 6584 Å has an electron temperature of about 8 000 K. The inside of the ring has a mean electron temperature of about 11 800 K. We notice that Smith et al. (2007) found $N_{\rm e} = 90$ cm^{-3} and $T_{\rm e} = 11\,400$ K using the R-C Spectrograph ($R \sim 6000$) on the CTIO 4-m telescope, though they obtained them from a 0.8 arcsec slit oriented along the major axis of the ring (PA $= 135°$).

Table 7.4 lists the electron density ($N_{\rm e}$) and the electron temperature ($T_{\rm e}$) of the different regions, together with the ionization potential required to create the emitting ions. We see that the east part of the ring has a mean electron density of $N_{\rm e}$([S II]) $\lesssim 100$ cm^{-3} and mean temperatures of $T_{\rm e}$([N II]) $= 8\,140$ K and $T_{\rm e}$([O III]) $= 12\,390$ K, while the less dense region inside the ring shows a high mean temperature of $T_{\rm e}$([N II]) $= 11\,760$ K and $T_{\rm e}$([O III]) less than 20000 K. We point out that the [S II] $\lambda\lambda$6716/6731 line ratio of more than 1.40 is associated with the low-density limit of $N_{\rm e} < 100$ cm^{-3}, and we cannot accurately determine the electron density less than this limit (see e.g. A 39; Jacoby et al. 2001). Furthermore, we cannot resolve the [O II] $\lambda\lambda$3726,3729 doublet with our moderate spectral resolution ($R \sim 3000$). Plasma diagnostics indicates that the interior region is much hotter than the ring region. This implies the presence of a hard ionizing source located at the centre. It is worth to mention that $T_{\rm e}$([N II]) is more appropriate for singly ionized species, while $T_{\rm e}$([O III]) is associated with doubly and more ionized species. Kingsburgh & Barlow (1994) found that $T_{\rm e}$([O III])$/T_{\rm e}$([N II]) $= 1.25$ for medium-excitation PNe and $T_{\rm e}$([O III])$/T_{\rm e}$([N II]) $= 1.15 + 0.0037 I(4686)$ for high-excitation PNe. Here, we no-

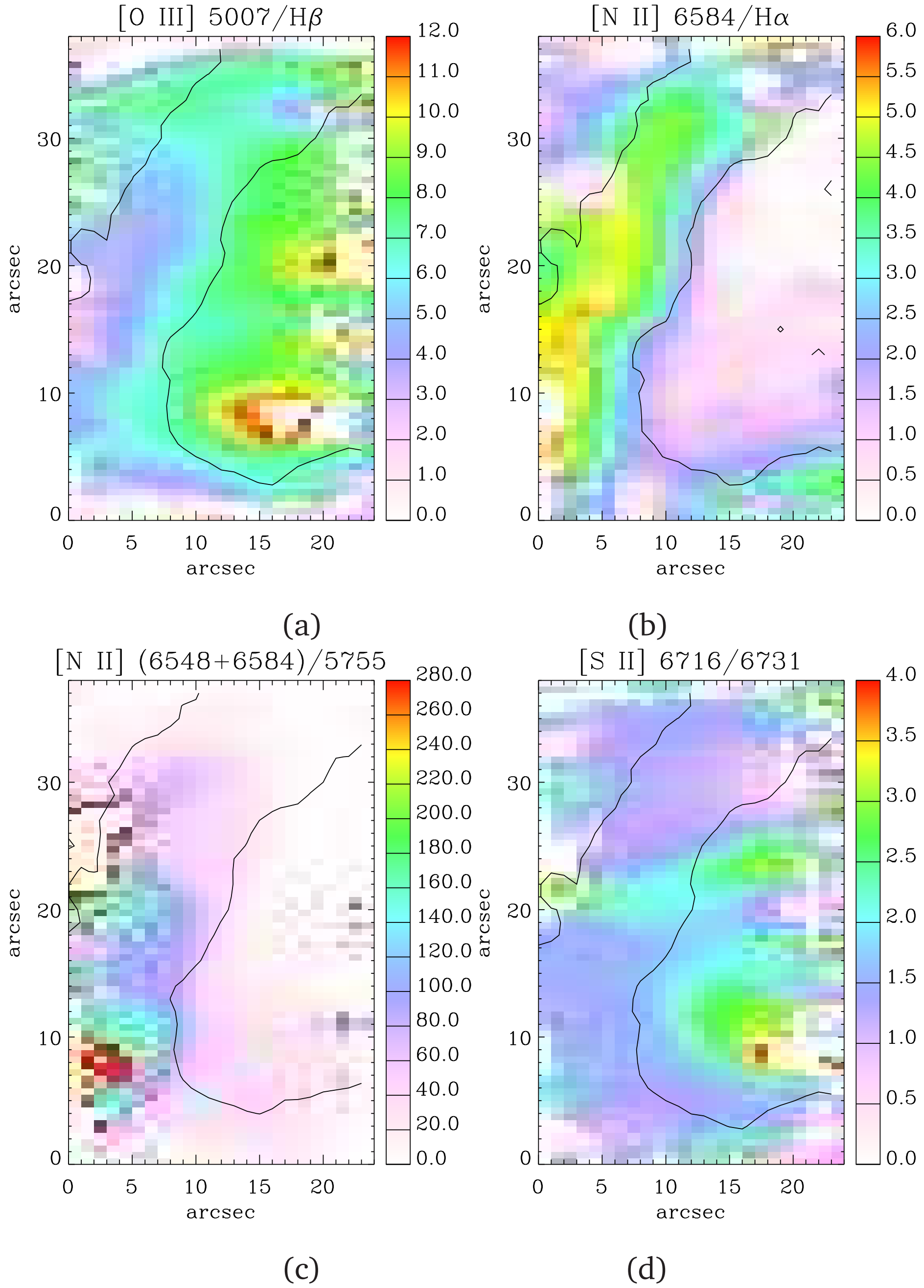

Figure 7.6: Flux ratio maps for *Field 2* (see Fig. 7.1) of the PN SuWt 2. From left to right: (a) flux ratio maps of the [O III] λ 5007 Å to the Hβ recombination line emission, (b) flux ratio map of the [N II] λ 6584 to the Hα recombination line emission, (c) flux ratio map for the temperature-sensitive [N II] $\lambda\lambda$5755, 6548, 6583 lines, and (d) for the density-sensitive [S II] doublet. Black contour lines show the distribution of the narrow-band emission of Hα and [N II] in arbitrary units taken with the ESO 3.6-m telescope observations.

tice that $T_{\rm e}([\mathrm{O\ III}])/T_{\rm e}([\mathrm{N\ II}]) = 1.52$ for the ring and $T_{\rm e}([\mathrm{O\ III}])/T_{\rm e}([\mathrm{N\ II}]) = 1.39$ for the total flux.

7.5 Ionic and total abundances

We derived ionic abundances for SuWt 2 using the observed CELs and the optical recombination lines (ORLs). We determined abundances for ionic species of N, O, Ne, S and Ar from CELs. In our determination, we adopted the mean $T_{\rm e}([\mathrm{O\ III}])$ and the upper limit of $N_{\rm e}([\mathrm{S\ II}])$ obtained from our empirical analysis in Table 7.4. Solving the equilibrium equations, using EQUIB, yields level populations and line sensitivities for given $T_{\rm e}$ and $N_{\rm e}$. Once the level population are solved, the ionic abundances, $\mathrm{X}^{i+}/\mathrm{H}^{+}$, can be derived from the observed line intensities of CELs. We determined ionic abundances for He from the measured intensities of ORLs using the effective recombination coefficients from Storey & Hummer (1995) and Smits (1996). We derived the total abundances from deduced ionic abundances using the ionization correction factor (icf) formulae given by Kingsburgh & Barlow (1994):

$$\frac{\mathrm{He}}{\mathrm{H}} = \left(\frac{\mathrm{He}^{+}}{\mathrm{H}^{+}} + \frac{\mathrm{He}^{2+}}{\mathrm{H}^{+}}\right) \times icf(\mathrm{He}), \quad icf(\mathrm{He}) = 1, \tag{7.2}$$

$$\frac{\mathrm{O}}{\mathrm{H}} = \left(\frac{\mathrm{O}^{+}}{\mathrm{H}^{+}} + \frac{\mathrm{O}^{2+}}{\mathrm{H}^{+}}\right) \times icf(\mathrm{O}), \quad icf(\mathrm{O}) = \left(1 + \frac{\mathrm{He}^{2+}}{\mathrm{He}^{+}}\right)^{2/3}, \tag{7.3}$$

$$\frac{\mathrm{N}}{\mathrm{H}} = \left(\frac{\mathrm{N}^{+}}{\mathrm{H}^{+}}\right) \times icf(\mathrm{N}), \quad icf(\mathrm{N}) = \left(\frac{\mathrm{O}}{\mathrm{O}^{+}}\right), \tag{7.4}$$

$$\frac{\mathrm{Ne}}{\mathrm{H}} = \left(\frac{\mathrm{Ne}^{2+}}{\mathrm{H}^{+}}\right) \times icf(\mathrm{Ne}), \quad icf(\mathrm{Ne}) = \left(\frac{\mathrm{O}}{\mathrm{O}^{2+}}\right), \tag{7.5}$$

$$\frac{\mathrm{S}}{\mathrm{H}} = \left(\frac{\mathrm{S}^{+}}{\mathrm{H}^{+}} + \frac{\mathrm{S}^{2+}}{\mathrm{H}^{+}}\right) \times icf(\mathrm{S}), \tag{7.6}$$

$$icf(\mathrm{S}) = \left[1 - \left(1 - \frac{\mathrm{O}^{+}}{\mathrm{O}}\right)^{3}\right]^{-1/3}, \tag{7.7}$$

$$\frac{\mathrm{Ar}}{\mathrm{H}} = \left(\frac{\mathrm{Ar}^{2+}}{\mathrm{H}^{+}}\right) \times icf(\mathrm{Ar}), \quad icf(\mathrm{Ar}) = \left(1 - \frac{\mathrm{N}^{+}}{\mathrm{N}}\right)^{-1}. \tag{7.8}$$

Table 7.4: Diagnostic ratios for the electron temperature, T_e and the electron density, N_e.

Ion	Diagnostic	I.P.(eV)	Interior		Ring		Total	
			Ratio	$T_e(10^3\mathrm{K})$	Ratio	$T_e(10^3\mathrm{K})$	Ratio	$T_e(10^3\mathrm{K})$
[N II]	$\frac{\lambda 6548+\lambda 6584}{\lambda 5755}$	14.53	63.71:	11.76:	161.33	8.14	175.78	7.92
[O III]	$\frac{\lambda 4959+\lambda 5007}{\lambda 4363}$	35.12	35.41::	$\lesssim$ 20.0::	110.93	12.39	152.49	11.07
			Ratio	$N_e(\mathrm{cm}^{-3})$	Ratio	$N_e(\mathrm{cm}^{-3})$	Ratio	$N_e(\mathrm{cm}^{-3})$
[S II]	$\frac{\lambda 6716}{\lambda 6731}$	10.36	2.02	$\lesssim$ 50.0	1.46	$\lesssim$ 100.0	1.51	$\lesssim$ 100.0

We derived the ionic and total helium abundances from the observed λ5876 and λ6678, and He II λ4686 ORLs. We assumed case B recombination for the singlet He I λ6678 line and case A for other He I λ5876 line (theoretical recombination models of Smits 1996). The He^{+}/H^{+} ionic abundances from the He I lines at λ5876 and λ6678 were averaged with weights of 3:1, roughly the intrinsic intensity ratios of the two lines. The He^{2+}/H^{+} ionic abundances were derived from the He II λ4686 line using theoretical case B recombination rates from Storey & Hummer (1995). For high- and middle-EC PNe (E.C. >4), the total He/H abundance ratio can be obtained by simply taking the sum of singly and doubly ionized helium abundances, and with an icf(He) equal or less than 1.0. For PNe with low levels of ionization it is more than 1.0. SuWt 2 is an intermediate-EC PN (EC $=6.6$; Dopita & Meatheringham 1990), so we can use an icf(He) of 1.0. We determined the O^{+}/H^{+} abundance ratio from the [O II] λ3727 doublet, and the O^{2+}/H^{+} abundance ratio from the [O III] λ4959 and λ5007 lines. In optical spectra, only O^{+} and O^{2+} CELs are seen, so the singly and doubly ionized helium abundances deduced from ORLs are used to include the higher ionization stages of oxygen abundance.

We derived the ionic and total nitrogen abundances from [N II] λ6548 and λ6584 CELs. For optical spectra, it is possible to derive only N^{+}, which mostly comprises only a small fraction ($\sim$ 10-30%) of the total nitrogen abundance. Therefore, the oxygen abundances were used to correct the nitrogen abundances for unseen ionization stages of N^{2+} and N^{3+}. Similarly, the total Ne/H abundance was corrected for undetermined Ne^{3+} by using the oxygen abundances. The $\lambda\lambda$6716,6731 lines usually detectable in PN are preferred to be used for the determination of S^{+}/H^{+}, since the $\lambda\lambda$4069,4076 lines are usually enhanced by recombination contribution, and also blended with O II lines. We notice that the $\lambda\lambda$6716,6731 doublet is affected by shock excitation of the ISM interaction, so the S^{+}/H^{+} ionic abundance must be lower. When the observed S^{+} is not appropriately determined, it is possible to use the expression given by Kingsburgh & Barlow (1994) in the calculation, i.e. $(S^{2+}/S^{+}) = 4.677 + (O^{2+}/O^{+})^{0.433}$.

The total abundances of He, N, O, Ne, S, and Ar derived from our empirical analysis for selected regions of the nebula are given in Table 7.5. From Table 7.5 we see that SuWt 2 is a nitrogen-rich PN, which may be evolved from a massive progenitor ($M \geq 5$). However, the nebula's age (23 400–26 300 yr) cannot be associated with faster evolutionary time-scale of a massive progenitor, since the evolutionary time-scale of $7M_{\odot}$ calculated by Blöcker (1995a) implies a short time-scale (less than 8000 yr) for the effective temperatures and the stellar luminosity (see Table 7.2) that are required to ionize the surrounding nebula. So, another mixing mechanism occurred during AGB nucleosynthesis, which further increased the nitrogen abundances in SuWt 2. Mass transfer to the two A-type companions may explain this typical abundance pattern.

Fig. 7.7 shows the spatial distribution of ionic abundance ratio N^{+}/H^{+}, O^{++}/H^{+} and S^{+}/H^{+} derived for given $T_{e} = 10\,000$ K and $N_{e} = 100\,\mathrm{cm}^{-3}$. We notice that O^{++}/H^{+} ionic abundance is very high in the inside shell; through the assumption of homogeneous electron temperature and density is not correct. The values in Table 7.5 are obtained using the mean T_{e}([O III]) and N_{e}([S II]) listed in Table 7.4. We notice that $O^{2+}/O^{+} = 5.9$ for the interior and $O^{2+}/O^{+} = 0.6$ for the ring. Similarly, $He^{2+}/He^{+} = 2.6$ for the interior and $He^{2+}/He^{+} = 0.4$ for the ring. This means that there are many more ionizing photons in the inner region than in the outer region, which hints at the presence of a hot ionizing source in the centre of the nebula.

7.6 Photoionization model

We used the 3 D photoionization code MOCASSIN (version 2.02.67) to study the ring of the PN SuWt 2. The code, described in detail by Ercolano et al. (2003a, 2005, 2008), applies a Monte Carlo method to solve self-consistently

Table 7.5: Ionic and total abundances deduced from empirical analysis of the observed fluxes across different nebula regions of SuWt 2.

λ(Å)	Abundance	Interior	Ring	Total
5876	He^{+}/H^{+}	–	0.066	0.049
6678	He^{+}/H^{+}	0.031	0.057	0.043
Mean	He^{+}/H^{+}	0.031	0.064	0.048
4686	He^{2+}/H^{+}	0.080	0.027	0.036
	icf(He)	1.0	1.0	1.0
	He/H	0.111	0.091	0.084
6548	N^{+}/H^{+}	7.932(−6)	1.269(−4)	1.284(−4)
6584	N^{+}/H^{+}	1.024(−5)	1.299(−4)	1.334(−4)
Mean	N^{+}/H^{+}	9.086(−6)	1.284(−4)	1.309(−4)
	icf(N)	16.240	2.014	3.022
	N/H	1.476(−4)	2.587(−4)	3.956(−4)
3727	O^{+}/H^{+}	1.109(−5)	1.576(−4)	1.597(−4)
4959	O^{2+}/H^{+}	6.201(−5)	8.881(−5)	1.615(−4)
5007	O^{2+}/H^{+}	6.998(−5)	9.907(−5)	1.808(−4)
Mean	O^{2+}/H^{+}	6.599(−5)	9.394(−5)	1.711(−4)
	icf(O)	2.336	1.262	1.459
	O/H	1.801(−4)	3.175(−4)	4.826(−4)
3869	Ne^{2+}/H^{+}	2.635(−5)	9.608(−5)	1.504(−4)
3968	Ne^{2+}/H^{+}	–	3.306(−5)	–
Mean	Ne^{2+}/H^{+}	2.635(−5)	6.457(−5)	1.504(−4)
	icf(Ne)	2.728	3.380	2.820
	Ne/H	7.191(−5)	2.183(−4)	4.241e(−4)
6716	S^{+}/H^{+}	3.307(−7)	2.034(−6)	2.179(−6)
6731	S^{+}/H^{+}	2.189(−7)	1.834(−6)	1.903(−6)
Mean	S^{+}/H^{+}	2.748(−7)	1.934(−6)	2.041(−6)
6312	S^{2+}/H^{+}	–	3.292(−8)	–
9069	S^{2+}/H^{+}	3.712(−7)	1.198(−6)	1.366(−6)
Mean	S^{2+}/H^{+}	3.712(−7)	6.155(−7)	1.366(−6)
	icf(S)	1.793	1.047	1.126
	S/H	1.158(−6)	2.668(−6)	3.836(−6)

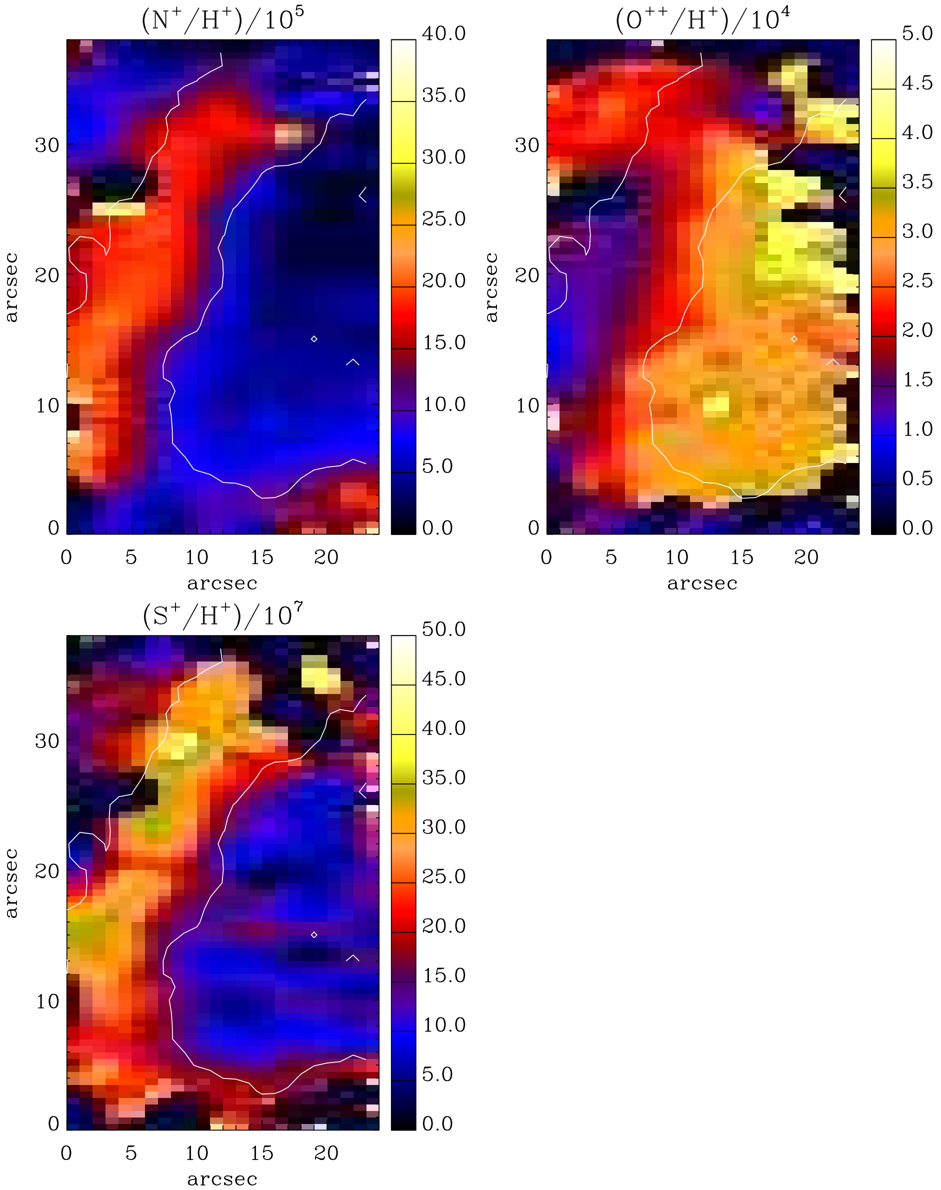

Figure 7.7: Spatial distribution maps of ionic nitrogen abundance ratio N^+/H^+ ($\times 10^{-5}$) from [N II] CELs (6548, 6584); ionic oxygen abundance ratio O^{++}/H^+ ($\times 10^{-4}$) from [O III] CELs (4959, 5007); and ionic sulfur abundance ratio S^+/H^+ ($\times 10^{-7}$) from [S II] CELs (6716, 6731) for $T_e = 10000$ K and $N_e = 100\,\mathrm{cm}^{-3}$. White contour lines show the distribution of the narrow-band emission of Hα and [N II] in arbitrary unit taken with the ESO 3.6-m telescope.

Table 7.5: (continued)

λ(Å)	Abundance	Interior	Ring	Total
7136	Ar^{2+}/H^{+}	3.718(−7)	8.756(−7)	1.111(−6)
4740	Ar^{3+}/H^{+}	–	–	4.747(−7)
7005	Ar^{4+}/H^{+}	3.718(−7)	–	–
	icf(Ar)	1.066	1.986	1.494
	Ar/H	5.230(−7)	1.739(−6)	2.370(−6)

the 3 D radiative transfer of the stellar and diffuse field in a gaseous and/or dusty nebula having asymmetric/symmetric density distribution and inhomogeneous/homogeneous chemical abundances, so it can deal with any structure and morphology. It also allows us to include multiple ionizing sources located in any arbitrary position in the nebula. It produces several outputs that can be compared with observations, namely a nebular emission-line spectrum, projected emission-line maps, temperature structure and fractional ionic abundances. This code has already been used for a number of axisymmetric PNe, such as NGC 3918 (Ercolano et al. 2003b), NGC 7009 (Gonçalves et al. 2006), NGC 6781 (Schwarz & Monteiro 2006), NGC 6302 (Wright et al. 2011) and NGC 40 (Monteiro & Falceta-Gonçalves 2011). To save computational time, we began with the gaseous model of a $22 \times 22 \times 3$ Cartesian grid, with the ionizing source being placed in a corner in order to take advantage of the axisymmetric morphology used. This initial low-resolution grid helped us explore the parameter space of the photoionization models, namely ionizing source, nebula abundances and distance. Once we found the best fitting model, the final simulation was done using a density distribution model constructed in $45 \times 45 \times 7$ cubic grids with the same size, corresponding to 14 175 cubic cells of length 1 arcsec each. Due to computational restrictions on time, we did not run any model with higher number of cubic cells. The atomic data set used for the photoionization modelling, includes the CHIANTI database (version 5.2; Landi

et al. 2006), the improved coefficients of the H I, He I and He II free–bound continuous emission (Ercolano & Storey 2006) and the photoionization cross-sections and ionic ionization energies (Verner et al. 1993; Verner & Yakovlev 1995).

The modelling procedure consists of an iterative process during which the calculated Hβ luminosity $L_{\mathrm{H}\beta}$ (erg s^{-1}), the ionic abundance ratios (i.e. $\mathrm{He}^{2+}/\mathrm{He}^{+}$, $\mathrm{N}^{+}/\mathrm{H}^{+}$, $\mathrm{O}^{2+}/\mathrm{H}^{+}$) and the flux intensities of some important lines, relative to Hβ (such as He II λ4686, [N II] λ6584 and [O III] λ5007) are compared with the observations. We performed a maximum of 20 iterations per simulation and the minimum convergence level achieved was 95%. The free parameters included distance and stellar characteristics, such as luminosity and effective temperature. Although we adopted the density and abundances derived in Sections 7.4 and 7.5, we gradually scaled up/down the abundances in Table 7.5 until the observed emission-line fluxes were reproduced by the model. Due to the lack of infrared data we did not model the dust component of this object. We notice however some variations among the values of $c(\mathrm{H}\beta)$ between the ring and the inner region in Table 7.2. It means that all of the observed reddening may not be due to the ISM. We did not include the outer bipolar lobes in our model, since the geometrical dilution reduces radiation beyond the ring. The faint bipolar lobes projected on the sky are far from the UV radiation field, and are dominated by the photodissociation region (PDR). There is a transition region between the photoionized region and PDR. Since MOCASSIN cannot currently treat a PDR fully, we are unable to model the region beyond the ionization front, i.e. the ring. This low-density PN is extremely faint, and not highly optically thick (i.e. some UV radiations escape from the ring), so it is difficult to estimate a stellar luminosity from the total nebula Hβ intrinsic line flux. The best-fitting model depends upon the effective temperature (T_{eff}) and the stellar luminosity ($L_{\star}$), though both are related to the evolutionary stage of the central star. Therefore, it is necessary to restrict our stellar parameters to the evolutionary tracks of the post-AGB stellar models, e.g., 'late thermal pulse', 'very late thermal pulse' (VLTP), or 'asymptotic giant branch final thermal pulse' (see e.g. Iben & Renzini 1983; Schönberner 1983; Vassiliadis & Wood 1994; Blöcker 1995a; Herwig 2001; Miller Bertolami et al. 2006). To constrain $T_{\rm eff}$ and $L_{\star}$, we employed a set of evolutionary tracks for initial masses between 1 and 7M$_{\odot}$ calculated by Blöcker (1995a, Tables 3-5). Assuming a density model shown in Fig. 7.8, we first estimated the effective temperature and luminosity of the central star by matching the Hβ luminosity $L({\rm H}\beta)$ and the ionic helium abundance ratio ${\rm He}^{2+}/{\rm He}^{+}$ with the values derived from observation and empirical analysis. Then, we scaled up/down abundances to get the best values for ionic abundance ratios and the flux intensities.

7.6.1 Model input parameters

Density distribution

The dense torus used for the ring was developed from the higher spectral resolution kinematic model of Jones et al. (2010a) and our plasma diagnostics (Section 7.4). Although the density cannot be more than the low-density limit of $N_{\rm e} < 100\,{\rm cm}^{-3}$ due to the [S II] $\lambda\lambda$6716/6731 line ratio of $\gtrsim 1.40$, it was slightly adjusted to produce the total Hβ Balmer intrinsic line flux $I({\rm H}\beta)$ derived for the ring and interior structure or the Hβ luminosity $L({\rm H}\beta) = 4\pi D^2 I({\rm H}\beta)$ at the specified distance D. The three-dimensional density distribution used for the torus and interior structure is shown in Fig. 7.8. The central star is located in the centre of the torus. The torus has a radius of 38.1 arcsec from its centre to the centre of the tube (1 arcsec is equal to 1.12×10^{-2} pc based on the best-fitting photoionization models). The radius of the tube of the ring is 6.9 arcsec. The hydrogen number density of the torus is taken to be homogeneous and equal to $N_{\rm H} = 100$ cm^{-3}. Smith et al. (2007) studied similar objects, including SuWt 2, and found that the ring itself can be a swept-up thin disc, and the interior of the ring is filled with a uniform equatorial disc. Therefore, inside the ring, there is a less dense oblate spheroid with a homogeneous density of 50 cm^{-3}, a semimajor axis of 31.2 arcsec and a semiminor axis of 6.9 arcsec. The H number density of the oblate spheroid is chosen to match the total $L(\mathrm{H}\beta)$ and be a reasonable fit for H^{2+}/H^{+} compared to the empirical results. The dimensions of the model were estimated from the kinematic model of Jones et al. (2010a) with an adopted inclination of 68°. The distance was estimated over a range 2.1–2.7 kpc, which corresponds to a reliable range based on the Hα surface brightness–radius relation of Frew & Parker (2006) and Frew (2008). The distance was allowed to vary to find the best-fitting model. The value of 2.3 kpc adopted in this work yielded the best match to the observed Hβ luminosity and it is also in very good agreement with Exter et al. (2010).

Nebular abundances

All major contributors to the thermal balance of the gas were included in our model. We used a homogeneous elemental abundance distribution consisting of eight elements. The initial abundances of He, N, O, Ne, S and Ar were taken from the observed empirically derived total abundances listed in Table 7.5. The abundance of C was a free parameter, typically varying between 5×10^{-5} and 8×10^{-3} in PNe. We initially used the typical value of $\mathrm{C/H}=5.5\times10^{-4}$ (Kingsburgh & Barlow 1994), and adjusted it to preserve the thermal balance of the nebula. We kept the initial abundances fixed while the stellar parameters and distance were being scaled to produce the best fit for the Hβ luminosity and He^{2+}/He^{+} ratio, and then we gradually varied them to obtain the finest match between the predicted and observed emission-line fluxes, as well as ionic abundance ratios from the empirical analysis.

The flux intensity of He II λ4686 Å and the He^{2+}/He^{+} ratio highly depend on the temperature and luminosity of the central star. Increasing either T_{eff} or $L_{\star}$ or both increases the He^{2+}/He^{+} ratio. Our method was to match the He^{2+}/He^{+}

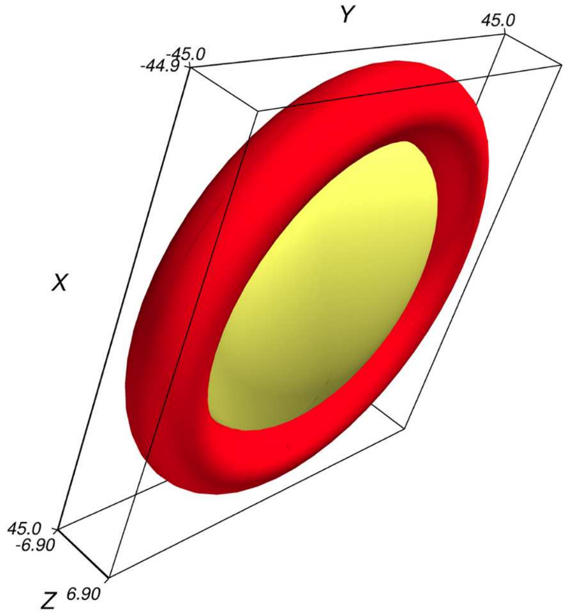

Figure 7.8: 3-D isodensity plot of the dense torus adopted for photoionization modeling of SuWt 2. The torus has a homogeneous density of 100 cm^{-3}, a radius of 38.″1 from its center to the tube center, and a tube radius of 6.″9. The less dense oblate spheroid has a homogeneous density of 50 cm^{-3}, a semi-major axis of 31.″2 and a semi-minor axis of 6.″9. Axis units are arcsec, where one arcsec is equal to 1.12×10^{-2} pc based on the distance determined by our photoionization models.

ratio, and then scale the He/H abundance ratio to produce the observed intensity of He II λ4686 Å.

The abundance ratio of oxygen was adjusted to match the intensities of [O III] $\lambda\lambda$4959,5007 and to a lesser degree [O II] $\lambda\lambda$3726, 3729. In particular, the intensity of the [O II] doublet is unreliable due to the contribution of recombination and the uncertainty of about 30% at the extreme blue of the WiFeS. So we gradually modified the abundance ratio O/H until the best match for [O III] $\lambda\lambda$4959,5007 and O^{2+}/H^{+} was produced. The abundance ratio of nitrogen was adjusted to match the intensities of [N II] $\lambda\lambda$6548,6584 and N^{+}/H^{+}.

Unfortunately, the weak [N II] λ5755 emission line does not have a high S/N ratio in our data.

The abundance ratio of sulphur was adjusted to match the intensities of [S III] λ9069. The intensities of [S II] $\lambda\lambda$6716,6731 and S^{+}/H calculated by our models are about seven and ten times lower than those values derived from observations and empirical analysis, respectively. The intensity of [S II] $\lambda\lambda$6716,6731 is largely increased due to shock-excitation effects.

Finally, the differences between the total abundances from our photoionization model and those derived from our empirical analysis can be explained by the *icf* errors resulting from a non-spherical morphology and properties of the exciting source. Gonçalves et al. (2012) found that additional corrections are necessary compared to those introduced by Kingsburgh & Barlow (1994) due to geometrical effects. Comparison with results from photoionization models shows that the empirical analysis overestimated the neon abundances. The neon abundance must be lower than the value found by the empirical analysis to reproduce the observed intensities of [Ne III] $\lambda\lambda$3869,3967. It means that the *icf*(Ne) of Kingsburgh & Barlow (1994) overestimates the unseen ionization stages. Bohigas (2008) suggested to use an alternative empirical method for correcting unseen ionization stages of neon. It is clear that with the typical $Ne^{2+}/Ne = O^{2+}/O$ assumption of the *icf* method, the neon total abundance is overestimated by the empirical analysis.

Ionizing source

The central ionizing source of SuWt 2 was modelled using different non-local thermodynamic equilibrium (NLTE; Rauch 2003) model atmospheres listed in Table 7.6, as they resulted in the best fit of the nebular emission-line fluxes. Initially, we tested a set of blackbody fluxes with the effective temperature ($T_{\rm eff}$) ranging from 80 000 to 190 000 K, the stellar luminosity compared to that of the Sun ($L_{\star}/L_{\odot}$) ranging from 50-800 and different evolutionary tracks

Table 7.6: Parameters of the two best-fitting photoionization models. The initial mass, final mass, and Post-AGB age are obtained from the evolutionary tracks calculated for hydrogen- and helium-burning models by Blöcker (1995a)

	Nebula abundances		Stellar parameters	
Model 1	He/H	0.090	$T_{\rm eff}$ (kK)	140
	C/H	4.00(−4)	$L_\star$ ($L_\odot$)	700
	N/H	2.44(−4)	log g (cgs)	7.0
	O/H	2.60(−4)	H : He	8 : 2
	Ne/H	1.11(−4)	$M_\star$ ($M_\odot$)	~ 0.605
	S/H	1.57(−6)	$M_{\rm ZAMS}$ ($M_\odot$)	3.0
	Ar/H	1.35(−6)	$\tau_{\rm post-AGB}$ (yr)	7 500
Model 2	He/H	0.090	$T_{\rm eff}$ (kK)	160
	C/H	4.00(−4)	$L_\star$ ($L_\odot$)	600
	N/H	2.31(−4)	log g (cgs)	7.3
	O/H	2.83(−4)	He : C : N : O	33 : 50 : 2 : 15
	Ne/H	1.11(−4)	$M_\star$ ($M_\odot$)	~ 0.64
	S/H	1.57(−6)	$M_{\rm ZAMS}$ ($M_\odot$)	3.0
	Ar/H	1.35(−6)	$\tau_{\rm post-AGB}$ (yr)	25 000
Nebula physical parameters				
$M_i/M_\odot$		0.21	D (pc)	2 300
$N_{\rm torus}$		100 cm^{-3}	$\tau_{\rm true}$ (yr)	23 400–26 300
$N_{\rm spheroid}$		50 cm^{-3}	[Ar/H]	−0.049

(Blöcker 1995a). A blackbody spectrum provides a rough estimate of the ionizing source required to photoionize the PN SuWt 2. The assumption of a blackbody spectral energy distribution (SED) is not quite correct as indicated by Rauch (2003). The strong differences between a blackbody SED and a stellar atmosphere are mostly noticeable at energies higher than 54 eV (He II ground state). We thus successively used the NLTE Tübingen Model-Atmosphere Fluxes

Package[3] (TMAF; Rauch 2003) for hot compact stars. We initially chose the stellar temperature and luminosity (gravity) of the best-fitting blackbody model, and changed them to get the best observed ionization properties of the nebula.

Fig. 7.9 shows the NTLE model atmosphere fluxes used to reproduce the observed nebular emission-line spectrum by our photoionization models. We first used a hydrogen-rich model atmosphere with an abundance ratio of H : He $= 8:2$ by mass, $\log g = 7$ (cgs), and $T_{\rm eff} = 140\,000$ K (Model 1), corresponding to the final stellar mass of $M_{\star} = 0.605\,{\rm M}_{\odot}$ and the zero-age main sequence (ZAMS) mass of $M_{\rm ZAMS} = 3\,{\rm M}_{\odot}$, where ${\rm M}_{\odot}$ is the solar mass. However, its post-AGB age ($\tau_{\rm post-AGB}$) of 7 500 yr, as shown in Fig. 7.11 (left-hand panel), is too short to explain the nebula's age. We therefore moved to a hydrogen-deficient model, which includes Wolf-Rayet central stars ([WC]) and the hotter PG 1159 stars. [WC]-type central stars are mostly associated with carbon-rich nebula (Zijlstra et al. 1994). The evolutionary tracks of the VLTP for H-deficient models, as shown in Fig. 7.11 (right-hand panel), imply a surface gravity of $\log g = 7.2$ for given $T_{\rm eff}$ and $L_{\star}$. From the high temperature and high surface gravity, we decided to use 'typical' PG 1159 model atmosphere fluxes (He : C : N : O = 33 : 50 : 2 : 15) with $T_{\rm eff} = 160\,000$ K and $L_{\star}/{\rm L}_{\odot} = 600$ (Model 2), corresponding to the post-AGB age of about $\tau_{\rm post-AGB} = 25\,000$ yr, $M_{\star} = 0.64\,{\rm M}_{\odot}$ and $M_{\rm ZAMS} = 3\,{\rm M}_{\odot}$. The stellar mass found here is in agreement with the $0.7\,{\rm M}_{\odot}$ estimate of Exter et al. (2010). Fig. 7.9 compares the two model atmosphere fluxes with a blackbody with $T_{\rm eff} = 160\,000$ K.

Table 7.6 lists the parameters used for our final simulations in two different NTLE model atmosphere fluxes. The ionization structure of this nebula was best reproduced using these best two models. Each model has different effective temperature, stellar luminosity and abundances (N/H, O/H and Ne/H). The results of our two models are compared in Tables 7.7–7.10 to those derived from the observation and empirical analysis.

[3]Website: http://astro.uni-tuebingen.de/ rauch/TMAF/TMAF.html

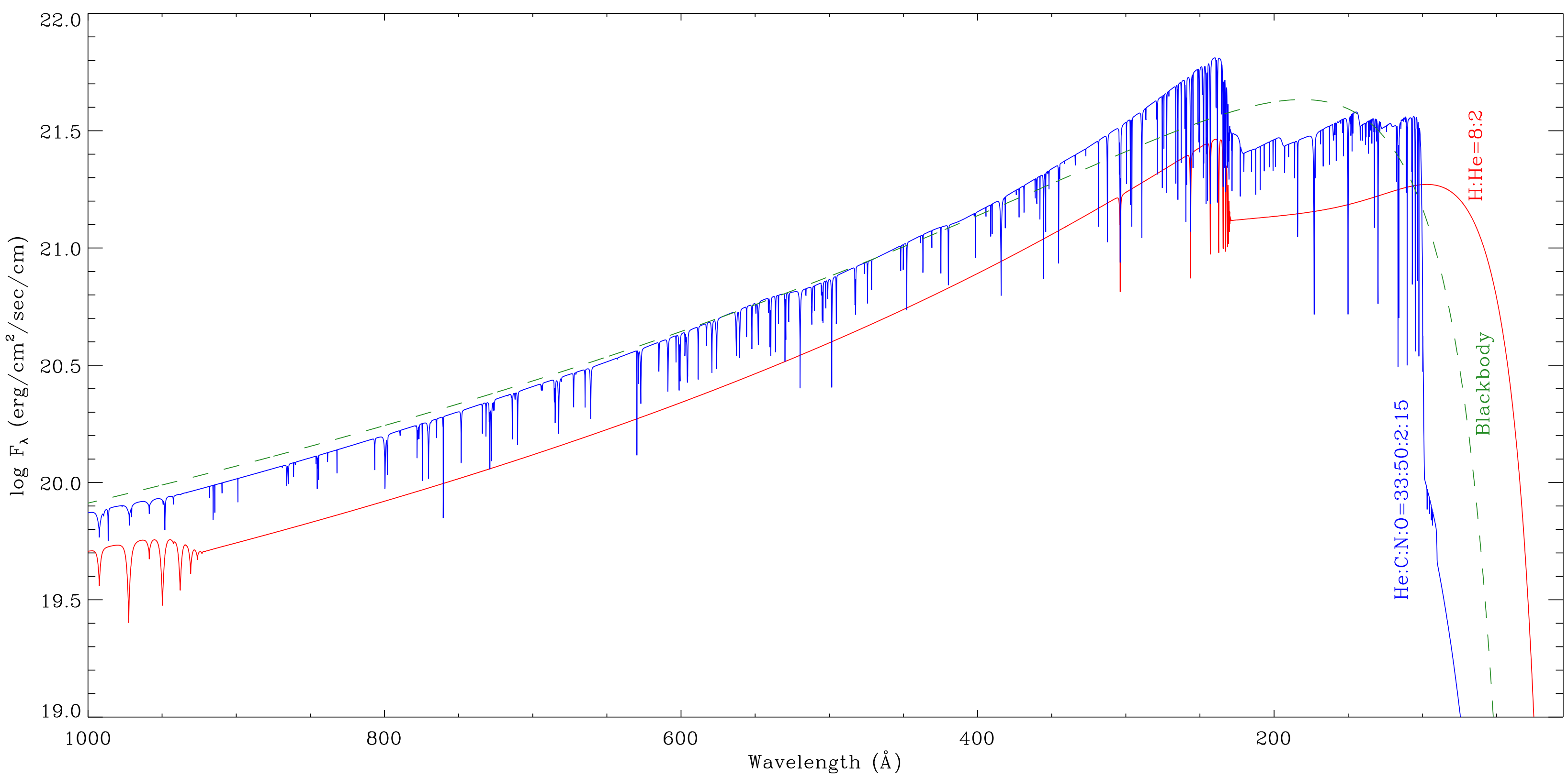

Figure 7.9: Comparison of two NLTE model atmosphere fluxes (Rauch 2003) used as ionizing inputs in our 2 models. Red line: H-rich model with an abundance ratio of H : He = 8 : 2 by mass, $\log g = 7$ (cgs) and $T_{\rm eff} = 140\,000$ K; blue line: PG 1159 model with He : C : N : O = 33 : 50 : 2 : 15, $\log g = 7$ and $T_{\rm eff} = 160\,000$ K; and dashed gray green line: the flux of a blackbody with $T_{\rm eff} = 160\,000$ K.

7.6.2 Model results

Emission-line fluxes

Table 7.7 compares the flux intensities calculated by our models with those from the observations. The fluxes are given relative to Hβ, on a scale where H$\beta = 100$. Most predicted line fluxes from each model are in fairly good agreement with the observed values and the two models produce very similar fluxes for most observed species. There are still some discrepancies in the few lines, e.g. [O II] $\lambda\lambda$3726,3729 and [S II] $\lambda\lambda$6716,6731. The discrepancies in [O II] $\lambda\lambda$3726,3729 can be explained by either recombination contributions or intermediate phase caused by a complex density distribution (see e.g. discussion in Ercolano et al. 2003b). [S II] $\lambda\lambda$6716,6731 was affected by shock-ionization and its true flux intensity is much lower without the shock fronts. Meanwhile, [Ar III] 7751 was enhanced by the telluric line. The recombination line Hδ λ4102 and He II λ5412 were also blended with the O II recombination lines. There are also some recombination contributions in the [O II] $\lambda\lambda$7320,7330 doublet. Furthermore, the discrepancies in the faint auroral line [N II] λ5755 and [O III] λ4363 can be explained by the recombination excitation contribution (see section 3.3 in Liu et al. 2000).

Temperature structure

Table 7.8 represents mean electron temperatures weighted by ionic abundances for Models 1 and 2, as well as the ring region and the inside region of the PN. We also see each ionic temperature corresponding to the temperature-sensitive line ratio of a specified ion. The definition for the mean temperatures was given in Ercolano et al. (2003b); and in detail by Harrington et al. (1982). Our model results for T_e[O III] compare well with the value obtained from the empirical analysis in § 7.4. Fig. 7.10 (top left) shows T_e obtained for Model 2 (adopted best-fitting model) constructed in $45 \times 45 \times 7$ cubic grids, and with the ionizing

Table 7.7: Model line fluxes for SuWt 2.

Line	Observ.	Model 1	Model 2
3726 [O II]	702::	309.42	335.53
3729 [O II]	*	408.89	443.82
3869 [Ne III]	204.57::	208.88	199.96
4069 [S II]	1.71::	1.15	1.25
4076 [S II]	–	0.40	0.43
4102 Hδ	22.15:	26.11	26.10
4267 C II	–	0.27	0.26
4340 Hγ	38.18:	47.12	47.10
4363 [O III]	6.15	10.13	9.55
4686 He II	43.76	42.50	41.38
4740 [Ar IV]	1.94	2.27	2.10
4861 Hβ	100.00	100.00	100.0
4959 [O III]	216.72	243.20	238.65
5007 [O III]	724.02	725.70	712.13
5412 He II	5.68	3.22	3.14
5755 [N II]	7.64	21.99	21.17
5876 He I	6.54	8.01	8.30
6548 [N II]	321.94	335.22	334.67
6563 Hα	286.00	281.83	282.20
6584 [N II]	1021.68	1023.78	1022.09
6678 He I	1.63	2.25	2.33
6716 [S II]*	70.36	9.17	10.21
6731 [S II]*	46.47	6.94	7.72
7065 He I	1.12	1.59	1.63
7136 [Ar III]	15.51	15.90	15.94
7320 [O II]	5.93	10.60	11.17
7330 [O II]	3.37	8.64	9.11
7751 [Ar III]	9.60	3.81	3.82
9069 [S III]	5.65	5.79	5.58
$I(\mathrm{H}\beta)/10^{-12}\,\frac{\mathrm{erg}}{\mathrm{cm^2 s}}$	1.95	2.13	2.12

Note. * The shock-excitation largely enhances the observed [S II] doublet.

source being placed in the corner. It replicates the situation where the inner region has much higher T_e in comparison to the ring T_e as previously found by plasma diagnostics in § 7.4. In particular the mean values of T_e[O III] for the ring (torus of the actual nebula) and the inside (spheroid) regions are around 12 000 and 15 000 K in all two models, respectively. They can be compared to the values of Table 7.4 that is T_e[O III] $= 12\,300$ K (ring) and $\lesssim 20\,000$ K (interior). Although the average temperature of T_e[N II] $\simeq 11\,700$ K over the entire nebula is higher than that given in Table 7.4, the average temperature of T_e[O III] $\simeq 13,000$ K is in decent agreement with that found by our plasma diagnostics.

It can be seen in Table 7.4 that the temperatures for the two main regions of the nebula are very different, although we assumed a homogeneous elemental abundance distribution for the entire nebula relative to hydrogen. The temperature variations in the model can also be seen in Fig. 7.10. The gas density structure and the location of the ionizing source play a major role in heating the central regions, while the outer regions remain cooler as expected. Overall, the average electron temperature of the entire nebula increases by increasing the helium abundance and decreasing the oxygen, carbon and nitrogen abundances, which are efficient coolants. We did not include any dust grains in our simulation, although we note that a large dust-to-gas ratio may play a role in the heating of the nebula via photoelectric emissions from the surface of grains.

Ionization structure

Results for the fractional ionic abundances in the ring (torus) and inner (oblate spheroid) regions of our two models are shown in Table 7.9 and Fig. 7.10. It is clear from the figure and table that the ionization structures from the models vary through the nebula due to the complex density and radiation field distribution in the gas. As shown in Table 7.9 , He^{2+}/He is much higher in the inner regions, while He^{+}/He is larger in the outer regions, as expected. Similarly, we find that the higher ionization stages of each element are larger in the in-

Table 7.8: Mean electron temperatures (K) weighted by ionic species for the whole nebula obtained from the photoionization model. For each element the upper row is for the Model 1 and the lower row is the Model 2. The bottom lines present the mean electron temperatures and electron densities for the torus (ring) and and the oblate spheroid (inside).

	Ion						
Element	I	II	III	IV	V	VI	VII
H	11696	12904					
	11470	12623					
He	11628	12187	13863				
	11405	11944	13567				
C	11494	11922	12644	15061	17155	17236	12840
	11289	11696	12405	14753	16354	16381	12550
N	11365	11864	12911	14822	16192	18315	18610
	11170	11661	12697	14580	15836	17368	17475
O	11463	11941	12951	14949	15932	17384	20497
	11283	11739	12744	14736	15797	17559	19806
Ne	11413	11863	12445	14774	16126	18059	22388
	11196	11631	12215	14651	16166	18439	20488
S	11436	11772	12362	14174	15501	16257	18313
	11239	11557	12133	13958	15204	15884	17281
Ar	11132	11593	12114	13222	14908	15554	16849
	10928	11373	11894	13065	14713	15333	16392

	torus		spheroid	
	T_e[O III]	N_e[S II]	T_e[O III]	N_e[S II]
M.1	12187 K	105 cm^{-3}	15569 K	58 cm^{-3}
M.2	11916 K	103 cm^{-3}	15070 K	58 cm^{-3}

ner regions. From Table 7.9 we see that hydrogen and helium are both fully ionized and neutrals are less than 8% by number in these best-fitting models. Therefore, our assumption of $icf(\mathrm{He}) = 1$ is correct in our empirical method.

Table 7.10 lists the nebular average ionic abundance ratios calculated from the photoionization models. The values that our models predict for the helium ionic ratio are fairly comparable with those from the empirical methods given in § 7.5, though there are a number of significant differences in other ions. The O^{+}/H^{+} ionic abundance ratio is about 33 per cent lower, while O^{2+}/H^{+} is about 60% lower in Model 2 than the empirical observational value. The empirical value of S^{+} differs by a factor of 8 compared to our result in Model 2, explained by the shock-excitation effects on the [S II] $\lambda\lambda$6716,6731 doublet. Additionally, the Ne^{2+}/H^{+} ionic abundance ratio was underestimated by roughly 67% in Model 2 compared to observed results, explained by the properties of the ionizing source. The Ar^{3+}/H^{+} ionic abundance ratio in Model 2 is 56% lower than the empirical results. Other ionic fractions do not show major discrepancies; differences remain below 35%. We note that the N^{+}/N ratio is roughly equal to the O^{+}/O ratio, similar to what is generally assumed in the $icf(\mathrm{N})$ method. However, the Ne^{2+}/Ne ratio is nearly a factor of 2 larger than the O^{2+}/O ratio, in contrast to the general assumption for $icf(\mathrm{Ne})$ (see equation 7.5). It has already been noted by Bohigas (2008) that an alternative ionization correction method is necessary for correcting the unseen ionization stages for the neon abundance.

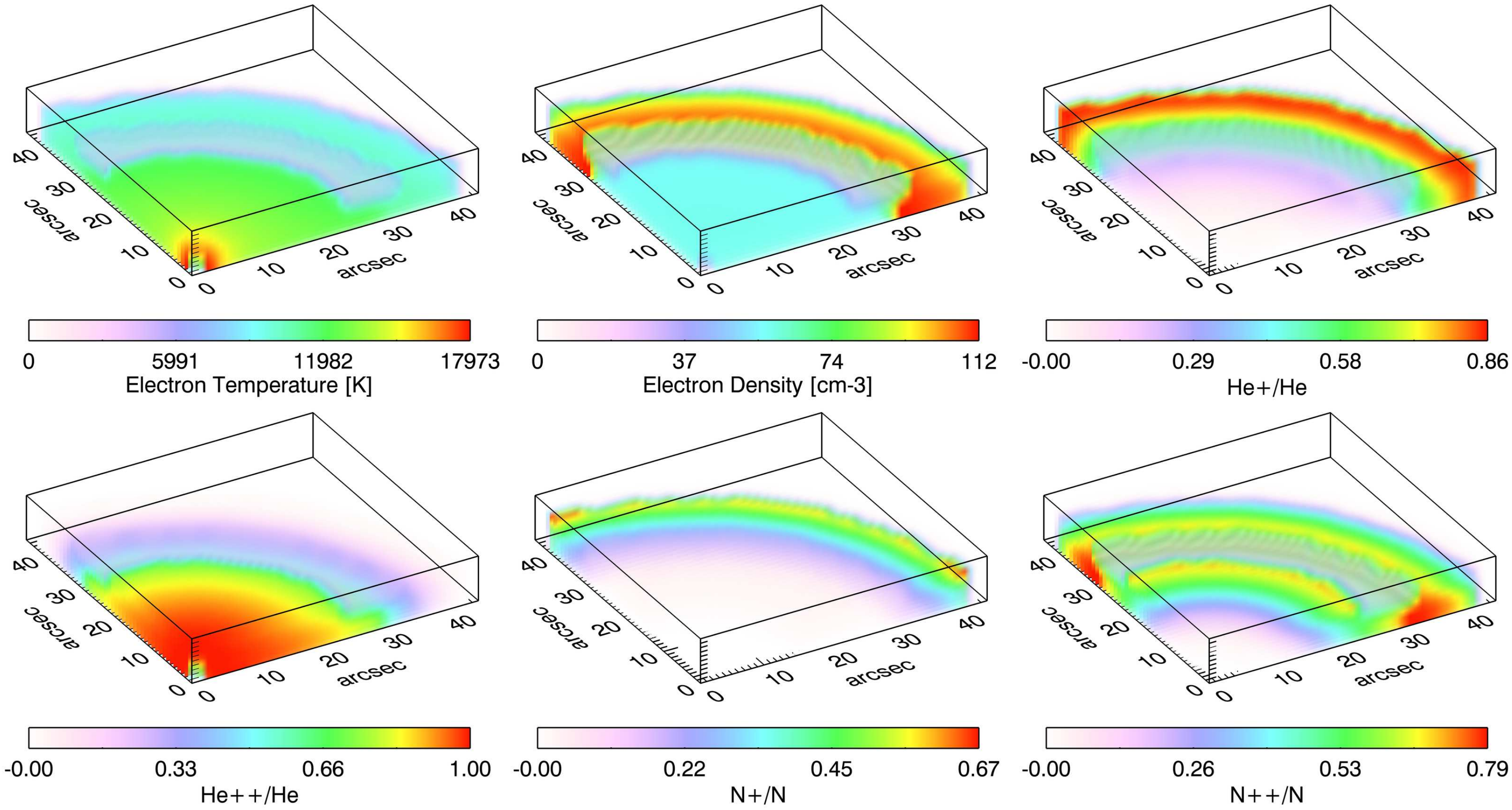

Figure 7.10: The 3-D distributions of electron temperature, electron density and ionic fractions from the adopted the Model 2 constructed in $45 \times 45 \times 7$ cubic grids, and the ionizing source being placed in the corner (0,0,0). Each cubic cell has a length of 1.12×10^{-2} pc, that corresponds to the actual PN ring size.

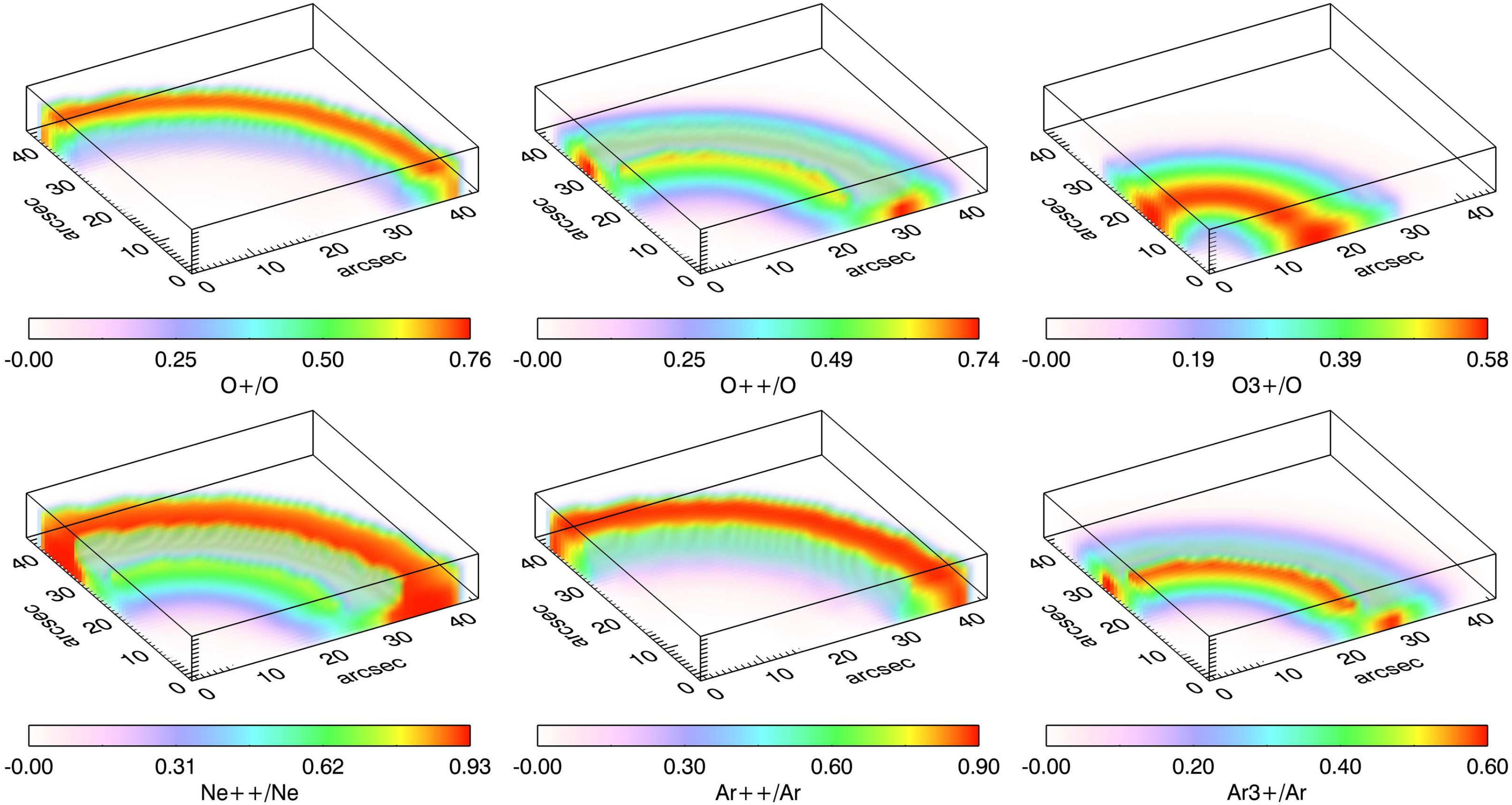

Figure 7.10: (continued)

Table 7.9: Fractional ionic abundances for SuWt 2 obtained from the photoionization models. For each element the upper row is for the torus (ring) and the lower row is for the oblate spheroid (inside).

	Element	Ion						
		I	II	III	IV	V	VI	VII
Model 1	H	6.53(−2)	9.35(−1)					
		3.65(−3)	9.96(−1)					
	He	1.92(−2)	7.08(−1)	2.73(−1)				
		3.05(−4)	1.27(−1)	8.73(−1)				
	C	5.92(−3)	2.94(−1)	6.77(−1)	2.33(−2)	1.86(−4)	7.64(−16)	1.00(−20)
		3.49(−5)	1.97(−2)	3.97(−1)	4.50(−1)	1.33(−1)	1.09(−12)	1.00(−20)
	N	7.32(−3)	4.95(−1)	4.71(−1)	2.62(−2)	4.18(−4)	6.47(−6)	2.76(−17)
		1.02(−5)	1.30(−2)	3.65(−1)	3.97(−1)	1.59(−1)	6.69(−2)	6.89(−13)
	O	6.15(−2)	4.98(−1)	4.21(−1)	1.82(−2)	7.09(−4)	1.34(−5)	7.28(−8)
		6.96(−5)	1.26(−2)	3.31(−1)	4.03(−1)	1.69(−1)	6.00(−2)	2.42(−2)
	Ne	3.46(−4)	6.70(−2)	9.10(−1)	2.26(−2)	3.56(−4)	4.25(−6)	2.11(−9)
		1.39(−6)	3.32(−3)	3.71(−1)	3.51(−1)	2.05(−1)	6.55(−2)	4.49(−3)
	S	1.13(−3)	1.67(−1)	7.75(−1)	5.52(−2)	1.15(−3)	6.20(−5)	8.53(−7)
		3.18(−6)	3.89(−3)	1.73(−1)	3.53(−1)	2.43(−1)	1.57(−1)	6.91(−2)
	Ar	4.19(−4)	3.15(−2)	7.51(−1)	2.10(−1)	5.97(−3)	1.13(−3)	5.81(−5)
		1.12(−7)	2.33(−4)	5.81(−2)	2.83(−1)	1.85(−1)	2.73(−1)	2.01(−1)

Evolutionary tracks

In Fig. 7.11 we compared the values of the effective temperature $T_{\rm eff}$ and luminosity $L_{\star}$ obtained from our two models listed in Table 7.6 to evolutionary tracks of hydrogen-burning and helium-burning models calculated by Blöcker (1995a). We compared the post-AGB age of these different models with the dynamical age of the ring found in § 7.3. The kinematic analysis indicates that the nebula was ejected about 23 400–26 300 yr ago. The post-AGB age of the hydrogen-burning model (top panel in Fig. 7.11) is considerably shorter than the nebula's age, suggesting that the helium-burning model (VLTP; bottom panel in Fig. 7.11) may be favoured to explain the age.

The physical parameters of the two A-type stars also yield a further con-

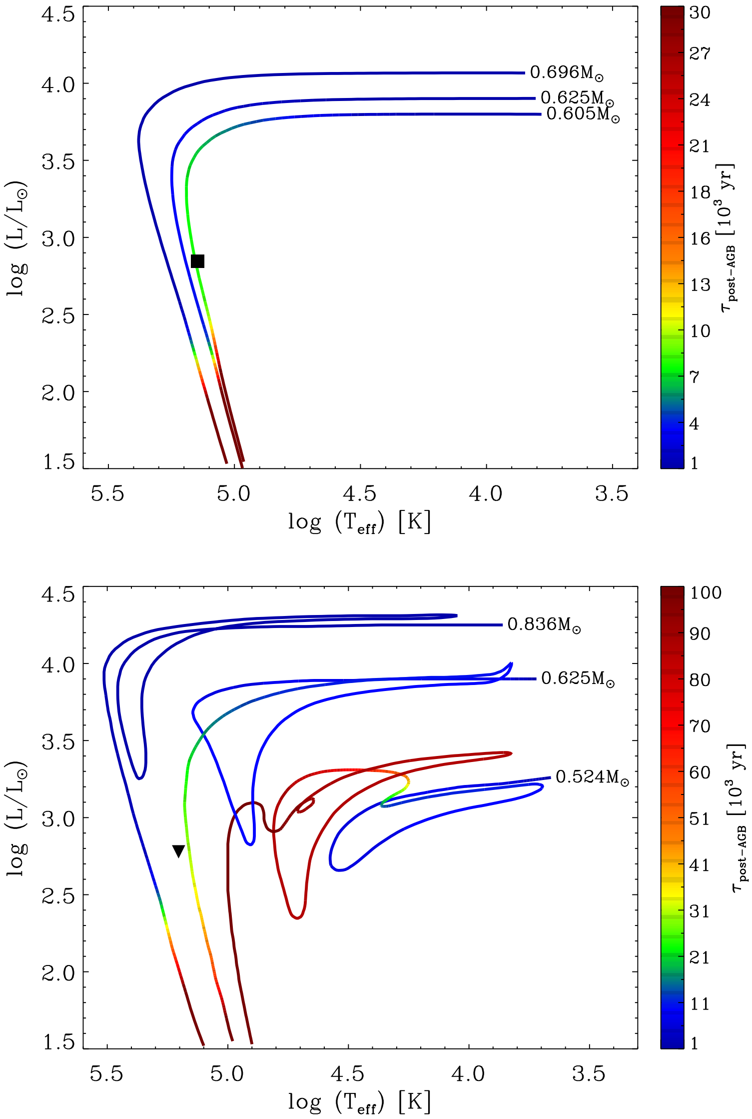

Figure 7.11: Hertzsprung–Russell diagrams for hydrogen-burning models (top panel) with $(M_{\rm ZAMS}, M_\star) = (3{\rm M}_\odot, 0.605{\rm M}_\odot)$, $(3{\rm M}_\odot, 0.625{\rm M}_\odot)$ and $(4{\rm M}_\odot, 0.696{\rm M}_\odot)$, and helium-burning models (bottom panel) with $(M_{\rm ZAMS}, M_\star) = (1{\rm M}_\odot, 0.524{\rm M}_\odot)$, $(3{\rm M}_\odot, 0.625{\rm M}_\odot)$ and $(5{\rm M}_\odot, 0.836{\rm M}_\odot)$ from Blöcker (1995a) compared to the position of the central star of SuWt 2 derived from two different photoionization models, namely Model 1 (denoted by ■) and Model 2 (▼). Bottom panel: the evolutionary tracks contain the first evolutionary phase, the VLTP (born-again scenario), and the second evolutionary phase. The colour scales indicate the post-AGB ages ($\tau_{\rm post-AGB}$) in units of 10^3 yr.

Table 7.9: (continued)

		Ion						
	Element	I	II	III	IV	V	VI	VII
Model 2	H	7.94(−2)	9.21(−1)					
		4.02(−3)	9.96(−1)					
	He	2.34(−2)	7.25(−1)	2.51(−1)				
		3.51(−4)	1.33(−1)	8.67(−1)				
	C	7.97(−3)	3.23(−1)	6.49(−1)	1.93(−2)	1.29(−4)	5.29(−16)	1.00(−20)
		4.45(−5)	2.23(−2)	4.13(−1)	4.41(−1)	1.23(−1)	1.00(−12)	1.00(−20)
	N	1.00(−2)	5.44(−1)	4.24(−1)	2.15(−2)	2.62(−4)	2.20(−6)	9.23(−18)
		1.31(−5)	1.52(−2)	3.84(−1)	4.07(−1)	1.50(−1)	4.40(−2)	4.34(−13)
	O	7.91(−2)	5.29(−1)	3.78(−1)	1.40(−2)	4.27(−4)	2.05(−6)	6.62(−11)
		9.34(−5)	1.50(−2)	3.60(−1)	4.20(−1)	1.75(−1)	2.97(−2)	1.85(−4)
	Ne	4.54(−4)	7.35(−2)	9.09(−1)	1.73(−2)	1.41(−4)	1.94(−8)	2.25(−14)
		1.75(−6)	3.85(−3)	4.19(−1)	3.86(−1)	1.89(−1)	1.73(−3)	6.89(−7)
	S	1.64(−3)	1.95(−1)	7.58(−1)	4.47(−2)	7.84(−4)	3.39(−5)	3.05(−7)
		4.23(−6)	4.86(−3)	1.96(−1)	3.61(−1)	2.39(−1)	1.47(−1)	5.16(−2)
	Ar	7.22(−4)	3.99(−2)	7.74(−1)	1.81(−1)	3.95(−3)	5.62(−4)	1.60(−5)
		1.72(−7)	3.22(−4)	7.30(−2)	3.30(−1)	1.96(−1)	2.62(−1)	1.39(−1)

straint. The stellar evolutionary tracks of the rotating models for solar metallicity calculated by Ekström et al. (2012) imply that the A-type stars, both with masses close to 2.7M$_{\odot}$ and $T_{\rm eff} \simeq 9200\,$K, have ages of $\sim$ 500 Myr. We see that they are in the evolutionary phase of the "blue hook"; a very short-lived phase just before the Hertzsprung gap. Interestingly, the initial mass of 3M$_{\odot}$ found for the ionizing source has the same age. As previously suggested by Exter et al. (2010), the PN progenitor with an initial mass slightly greater than 2.7M$_{\odot}$ can be coeval with the A-type stars, and it recently left the AGB phase. But, they adopted the system age of about 520 Myr according to the Y^2 evolutionary tracks (Yi et al. 2003; Demarque et al. 2004).

The effective temperature and stellar luminosity obtained for both models correspond to the progenitor mass of 3M$_{\odot}$. However, the strong nitrogen enrichment seen in the nebula is inconsistent with this initial mass, so another

Table 7.10: Integrated ionic abundance ratios for the entire nebula obtained from the photoionization models.

		Model 1		Model 2	
Ionic ratio	Empirical	Abundance	Ionic Fraction	Abundance	Ionic Fraction
He^{+}/H^{+}	4.80(−2)	5.308(−2)	58.97%	5.419(−2)	60.21%
He^{2+}/H^{+}	3.60(−2)	3.553(−2)	39.48%	3.415(−2)	37.95%
C^{+}/H^{+}	–	9.597(−5)	23.99%	1.046(−4)	26.16%
C^{2+}/H^{+}	–	2.486(−4)	62.14%	2.415(−4)	60.38%
N^{+}/H^{+}	1.309(−4)	9.781(−5)	40.09%	1.007(−4)	43.58%
N^{2+}/H^{+}	–	1.095(−4)	44.88%	9.670(−5)	41.86%
N^{3+}/H^{+}	–	2.489(−5)	10.20%	2.340(−5)	10.13%
O^{+}/H^{+}	1.597(−4)	1.048(−4)	40.30%	1.201(−4)	42.44%
O^{2+}/H^{+}	1.711(−4)	1.045(−4)	40.20%	1.065(−4)	37.64%
O^{3+}/H^{+}	–	2.526(−5)	9.72%	2.776(−5)	9.81%
Ne^{+}/H^{+}	–	6.069(−6)	5.47%	6.571(−6)	5.92%
Ne^{2+}/H^{+}	1.504(−4)	8.910(−5)	80.27%	9.002(−5)	81.10%
Ne^{3+}/H^{+}	–	1.001(−5)	9.02%	1.040(−5)	9.37%
S^{+}/H^{+} [(a)]	2.041(−6)	2.120(−7)	13.50%	2.430(−7)	15.48%
S^{2+}/H^{+}	1.366(−6)	1.027(−6)	65.44%	1.013(−6)	64.55%
S^{3+}/H^{+}	–	1.841(−5)	11.73%	1.755(−7)	11.18%
Ar^{+}/H^{+}	–	3.429(−8)	2.54%	4.244(−8)	3.14%
Ar^{2+}/H^{+}	1.111(−6)	8.271(−7)	61.26%	8.522(−7)	63.13%
Ar^{3+}/H^{+}	4.747(−7)	3.041(−7)	22.52%	2.885(−7)	21.37%
Ar^{4+}/H^{+}	–	5.791(−8)	4.29%	5.946(−8)	4.40%
Ar^{5+}/H^{+}	–	7.570(−8)	5.61%	7.221(−8)	5.35%

Note. [(a)] Shock-excitation largely enhances the S^{+}/H^{+} ionic abundance ratio.

mixing process rather than the hot-bottom burning (HBB) occurs at substantially lower initial masses than the stellar evolutionary theory suggests for AGB-phase (Herwig 2005; Karakas & Lattanzio 2007; Karakas et al. 2009). The stellar models developed by Karakas & Lattanzio (2007) indicate that HBB occurs in intermediate-mass AGB stars with the initial mass of $\geqslant 5M_{\odot}$ for the metallicity of $Z = 0.02$; and $\geqslant 4M_{\odot}$ for $Z = 0.004$–0.008. However, they found that a low-metallicity AGB star ($Z = 0.0001$) with the progenitor mass of $3M_{\odot}$ can also experience HBB. Our determination of the argon abundance in SuWt 2 (see

Table 7.6) indicates that it does not belong to the low-metallicity stellar population; thus, another non-canonical mixing process made the abundance pattern of this PN.

The stellar evolution also depends on the chemical composition of the progenitor, namely the helium content (Y) and the metallicity (Z), as well as the efficiency of convection (see e.g. Salaris & Cassisi 2005). More helium increases the H-burning efficiency, and more metallicity makes the stellar structure fainter and cooler. Any change in the outer layer convection affects the effective temperature. There are other non-canonical physical processes such as rotation, magnetic field and mass-loss during Roche lobe overflow (RLOF) in a binary system, which significantly affect stellar evolution. Ekström et al. (2012) calculated a grid of stellar evolutionary tracks with rotation, and found that N/H at the surface in rotating models is higher than non-rotating models in the stellar evolutionary tracks until the end of the central hydrogen- and helium-burning phases prior to the AGB stage. The Modules for Experiments in Stellar Astrophysics (MESA) code developed by Paxton et al. (2011, 2013) indicates that an increase in the rotation rate (or angular momentum) enhances the mass-loss rate. The rotationally induced and magnetically induced mixing processes certainly influence the evolution of intermediate-mass stars, which need further studies by MESA. The mass-loss in a binary or even triple system is much more complicated than a single rotating star, and many non-canonical physical parameters are involved (see e.g. BINSTAR code by Siess 2006; Siess et al. 2013). Chen & Han (2002) used the Cambridge stellar evolution (STARS) code developed by Eggleton (1971, 1972, 1973) to study numerically evolution of Population I binaries, and produced surface abundances of helium and negligible hydrogen at the end of RLOF in the Hertzsprung gap. Similarly, Benvenuto & De Vito (2003, 2005) developed a helium white dwarf from a low mass progenitor in a close binary system. A helium enrichment in the our layer can considerably influence other elements through the helium-burning mixing process.

7.7 Conclusion

In this chapter, we have analysed new optical integral-field spectroscopy of the PN SuWt 2 to study detailed ionized gas properties, and to infer the properties of the unobserved hot ionizing source located in the centre of the nebula. The spatially resolved emission-line maps in the light of [N II] λ6584 have described the kinematic structure of the ring. The previous kinematic model (Jones et al. 2010a) allowed us to estimate the nebula's age and large-scale kinematics in the Galaxy. An empirical analysis of the emission line spectrum led to our initial determination of the ionization structure of the nebula. The plasma diagnostics revealed as expected that the inner region is hotter and more excited than the outer regions of the nebula, and is less dense. The ionic abundances of He, N, O, Ne, S and Ar were derived based on the empirical methods and adopted mean electron temperatures estimated from the observed [O III] emission lines and electron densities from the observed [S II] emission lines.

We constructed photoionization models for the ring and interior of SuWt 2. This model consisted of a higher density torus (the ring) surrounding a low-density oblate spheroid (the interior disc). We assumed a homogeneous abundance distribution consisting of eight abundant elements. The initial aim was to find a model that could reproduce the flux intensities, thermal balance structure and ionization structure as derived from by the observations. We incorporated NLTE model atmospheres to model the ionizing flux of the central star. Using a hydrogen-rich model atmosphere, we first fitted all the observed line fluxes, but the time-scale of the evolutionary track was not consistent with the nebula's age. Subsequently, we decided to use hydrogen-deficient stellar atmospheres implying a VLTP (born-again scenario), and longer time-scales were likely to be in better agreement with the dynamical age of the nebula. Although the results obtained by the two models of SuWt 2 are in broad agreement with the observations, each model has slightly different chemical abundances and very different stellar parameters. We found a fairly good fit to a hydrogen-deficient central star with a mass of $\sim 0.64\mathrm{M}_{\odot}$ with an initial (model) mass of $\sim 3\mathrm{M}_{\odot}$. The evolutionary track of Blöcker (1995a) implies that this central star has a post-AGB age of about 25 000 yr. Interestingly, our kinematic analysis (based on v_{exp} from Jones et al. 2010a) implies a nebular true age of about 23 400–26 300 yr.

Table 7.6 lists two best-fitting photoionization models obtained for SuWt 2. The hydrogen-rich model atmosphere (Model 1) has a normal evolutionary path and yields a progenitor mass of $3\mathrm{M}_{\odot}$, a dynamical age of 7,500 yr and nebular $\mathrm{N/O} = 0.939$ (by number). The PG 1159 model atmosphere (Model 2) is the most probable solution, which can be explained by a VLTP phase or born-again scenario: VLTP $\rightarrow$ [WCL] $\rightarrow$ [WCE] $\rightarrow$ [WC]-PG 1159 $\rightarrow$PG 1159 (Blöcker 2001; Herwig 2001; Miller Bertolami & Althaus 2006; Werner & Herwig 2006). The PG 1159 model yields $\mathrm{N/O} = 0.816$ and a stellar temperature of $T_{\mathrm{eff}} = 160$ kK corresponding to the progenitor mass of $3\mathrm{M}_{\odot}$ and much longer evolutionary time-scale. The VLTP can be characterized as the helium-burning model, but this cannot purely explain the fast stellar winds ($V_{\infty} = 2000\,\mathrm{km\,s^{-1}}$) of typical [WCE] stars. It is possible that an external mechanism such as the tidal force of a companion and mass transfer to an accretion disc, or the strong stellar magnetic field of a companion can trigger (late) thermal pulses during post-AGB evolution (e.g. see Hajduk et al. 2007; Frankowski & Soker 2009).

The abundance pattern of SuWt 2 is representative of a nitrogen-rich PN, which is normally considered to be the product of a relatively massive progenitor star (Becker & Iben 1980; Kingsburgh & Barlow 1994). Recent work suggests that HBB, which enhances the helium and nitrogen, and decreases oxygen and carbon, occurs only for initial masses of $\geq 5\,\mathrm{M}_{\odot}$ ($Z = 0.02$; Karakas & Lattanzio 2007; Karakas et al. 2009); hence, the nitrogen enrichment seen in the nebula appears to result from an additional mixing process active in stars down to a mass of $3\mathrm{M}_{\odot}$. Additional physical processes such as rotation increase the mass-loss rate (Paxton et al. 2013) and nitrogen abundance at the stellar surface (end of the core H- and He-burning phases; Ekström et al. 2012). The mass-loss via RLOF in a binary (or triple) system can produce a helium-rich outer layer (Chen & Han 2002; Benvenuto & De Vito 2005), which significantly affects other elements at the surface.

8

Conclusions and Future Work

The research carried out here tried to broaden our understanding of the planetary nebulae (PNe) surrounding hydrogen-deficient WR-type central stars. We used a diverse range of methodologies to interpret our integral field unit (IFU) observations. Our aim in this work was to determine kinematic features, physical conditions and chemical abundances. The capabilities of the IFU observations, coupled with archival imaging, have allowed us to provide the spatially resolved distributions of velocities, temperatures, densities and ionic abundances. In this chapter, I summarize the main results reached, followed by suggestions on how to extend this work, which might solve the long-standing problems in the study of PNe.

8.1 Summary

In Chapter 2, morphological features for a sample of PNe have been determined. The capabilities of the IFU observations, coupled with *HST* or archival imaging, allowed us to identify their three-dimensional morpho-kinematic structures. The 3-D morpho-kinematic modeling program SHAPE was used to study the kinematic structures. The results indicate that these PNe have axisymmetric morphologies, either bipolar or elliptical. Some of them show elliptical shapes with FLIERS (e.g. M 3-30 and Hb 4). This could imply a possible link between PNe and their WR-type nuclei. However, the expansion velocities do not show any strong link with the stellar parameters. The relationship between their morpho-kinematic structures and WR-type nuclei needs to be investigated further.

In Chapter 3, the chemical abundances for a sample of PNe with different WR-type stars have been determined. This might provide clues about the origin of the abundance discrepancy and temperature dichotomy derived from CELs and ORLs. The ORL abundances are found to be several times higher than the CEL abundances, whereas the temperatures derived from the He I recombination lines are typically lower than those measured from the collisionally excited nebular-to-auroral forbidden line ratios. This may point to the existence of cold, hydrogen-deficient materials embedded in the diffuse warm nebula. The abundance discrepancy factors for heavy ions were found to be closely correlated with the temperature dichotomy. It is found that the ADF and temperature dichotomy are correlated with the intrinsic nebular Hβ surface brightness. This suggests that the abundance discrepancy problem must be related to the nebular evolution rather than the stellar parameters. The existence of cold hydrogen-deficient, metal-rich inclusions in the nebula has been proposed to solve the ORL versus CEL problem (Liu et al. 2000; Liu 2003). The origin of such structures is as yet unknown, and their presences in the nebula have not yet been confirmed. The metal-rich materials could be ejected from the stellar surface during the very late thermal pulse (born-again scenario).

In Chapter 4, we constructed a 3D photoionisation model of Hb 4 assuming homogeneous elemental abundances. The nebula is approximated by a density model developed from the kinematic analysis and *HST* imaging. The results indicate that the ionization correction factor method and the electron temperature used for the empirical analysis are mostly responsible for apparent enhanced nitrogen abundance. It is also found that the enhancement of the

[N II] emission in the FLIERs is more attributed to the geometry and density distribution. However, our first photoionization model under-predicted the ORLs. Therefore, we aimed to reproduce the ORLs of Hb 4 by using a bi-abundance photoionization model consisting of a chemically homogeneous torus with normal abundances, surrounding a small fraction of cold, metal-rich inclusions occupying ~ 5 percent of the total volume. The results indicate that the bi-abundance model provides acceptable matches to the ORLs. Moreover, the temperatures of the whole nebula predicted by the bi-abundance model reasonably match the empirical results. We conclude that the presence of the metal-rich inclusions may explain the observed ORLs.

In Chapter 5, a three-dimensional photoionization model of Abell 48 was constructed, constrained by our new IFU spectroscopic data and the three-dimensional density structure model developed from our kinematic analysis, assuming homogeneous elemental abundances. The ionic abundances deduced from our model are in decent agreement with those derived by the empirical analysis. But, we notice obvious discrepancies between electron temperatures derived from the model and the ORL empirical analysis, as overestimated by our model. This may be due to the presence of metal-rich knots, which were not included in our model. The amount of nitrogen (5 per cent by mass) detected in the stellar atmosphere implies that the central star may have undergone a very late thermal pulse (VLTP), but this is inconsistent with the extreme helium-rich (85 per cent by mass) atmosphere of Abell 48, which was probably rather formed by a merging process of two white dwarfs. Nevertheless, the VLTP evolutionary timescale agrees with the nebula's dynamical age, implying that the central star left the asymptotic giant branch about 9 000 years ago. Based on the evolutionary tracks and nebular mass, we also estimated the progenitor mass to be ~ 3 $M_{\odot}$.

In Chapter 6, we have constructed photoionization models of the planetary nebula PB 8 to be confronted with available optical and infrared observations, constrained by a model atmosphere for the ionizing source calculated by Todt et al. (2010) to match its central star spectrum. The density distribution for the nebular gas was adopted based 1-D hydrodynamics models (Perinotto et al. 2004; Schönberner et al. 2005b) computed for different stellar evolutionary tracks. Three different sets of photoionization models were tried, the first being chemically homogeneous models that failed to reproduce the observed ORLs of heavy elements. To reproduce the observed ORLs, bi-abundance models were built by including a small fraction of metal-rich inclusions embedded in the gas envelope with normal abundances. The final bi-abundance model provided a better fit to the most observed heavy element ORLs, whose metal-rich inclusions have a mass of ~ 5 percent of the total ionized mass and nearly twice cooler and denser than the normal composition nebula. Their O/H and N/H abundance ratios are ~ 1.0 and 1.7 dex larger than the diffuse warm nebula, respectively. The model did not predict the thermal spectral energy distribution of the nebula observed with the *Spitzer* infrared spectrograph. Therefore, we aimed to produce the thermal infrared emission by including dust grains in the final photoionization model. It is found that the photoelectric emission from dust grains with a dust-to-hydrogen ratio of 0.01 by mass for the whole nebula is sufficient to match the dust temperatures and emergent spectral energy distribution.

In Chapter 7, we used optical integral-field spectroscopy to study the emission lines of the inner nebula ring of SuWt 2. It is an unusual object with a prominent, inclined central emission ellipse and faint bipolar extensions. It has two A-type stars in a proven binary system at the center. However, the radiation from these two central stars is too soft to ionize the surrounding material leading to a so far fruitless search for the responsible ionizing source. Moreover, the ejected nebula is nitrogen-rich which raises question about the mass-loss process from a likely intermediate-mass progenitor. We performed an empirical analysis of CELs, together with a fully 3-D photoionization modeling. The time-scale for the evolutionary track of a hydrogen-rich model atmosphere is inconsistent with the dynamical age obtained for the ring. This suggests that the central star has undergone a very late thermal pulse (VLTP). We conclude that the ionizing star could be hydrogen-deficient and compatible with what is known as a PG 1159-type star. The evolutionary tracks for the very late thermal pulse models imply a central star mass of $\sim 0.64\mathrm{M}_{\odot}$, which originated from a $\sim 3\mathrm{M}_{\odot}$ progenitor. The evolutionary time-scales suggest that the central star left the asymptotic giant branch about 25,000 years ago, which is consistent with the nebula's age.

8.2 Future Work

The kinematic analysis for a sample of PNe with WR stars carried out in Chapter 2 showed these PNe have axisymmetric morphologies, either bipolar or elliptical. However, the open questions remain unanswered. It is unclear which physical mechanism produces axisymmetric morphologies and how the density and velocity of FLIERs contrast sharply with the main body of the nebula. Much work can be done in the future on deep imaging and kinematic observations of PNe with WR-type stars to provide more accurate kinematic structures. Deeper spectroscopy of central stars can develop a better understanding of the mechanisms, which shape their aspherical morphologies. The presence of binary companions should be examined to unravel the puzzle of their morphologies. The recent X-Ray observation (e.g. Montez et al. 2005; Kastner et al. 2008) shows diffuse X-ray sources and hot bubbles in some PNe with [WR] stars. The "hard X-ray" emission could be an indicator of a binary companion, whereas soft, diffuse X-ray emission is probably produced by the interaction of the mass loss from the central star and the nebular material (Kastner et al. 2012). More X-ray observations of [WR] PNe will provide clues about their origin.

Our detailed abundance analysis of PNe with WR-type stars done in Chapter 3 correlated the abundance discrepancy problem with the nebula evolution. It is found that the ADF is larger in old evolved nebulae. But, it has no dependence on the stellar parameters. Previously, Liu et al. (2000) suggested the bi-abundance models, containing cold metal-rich inclusions inside the diffuse warm nebula. Most PNe follow the relation $T_{\rm e}({\rm CELs}) > T_{\rm e}({\rm He\,\textsc{i}}) > T_{\rm e}({\rm O\,\textsc{ii}\ ORLs})$, in agreement with the bi-abundance model (Wesson et al. 2005). The feasibility of the bi-chemistry model has been examined in photoionization models of Hb 4 (see Chapter 4) and PB 8 (see Chapter 6), Abell 30 (Ercolano et al. 2003b) and NGC 6153 (Yuan et al. 2011). Although cold metal-rich inclusions have been proposed to solve the problems, the origin of such structures is as yet unknown. A born-again event can result in stripped off the stellar surface, but it is still unclear whether it occurs. Liu (2003) suggested that they could be also produced by the evaporation and destruction of the planetary system of the progenitor star. Further work is required to investigate any link between then and their H-deficient stars. However, Nicholls et al. (2012, 2013) recently proposed κ-distributed electrons to solve the problem. Zhang et al. (2014) found that observations of 4 PNe with extremely large ADFs are in favor of both the scenarios, bi-abundance models and κ-distributed electrons. It is possible that chemically inhomogeneous medium also introduces κ-distributed electrons to the nebula. The relations between both the scenarios should be investigated. More deeper high-resolution spectroscopy and further investigation are required to gain a better understanding of the ORL versus CEL problem.

In Chapter 5, the observed nebular spectrum was best produced by using a hydrogen-deficient [WN] model atmosphere, which corresponds to a relatively low-mass progenitor star rather than a massive Pop I star. The amount of nitrogen (5 per cent by mass) detected in the stellar atmosphere implies that the central star may have undergone a very late thermal pulse, but this is inconsistent with the extreme helium-rich (85 per cent by mass) atmosphere. Its typical abundance pattern puts it among helium dominated stars, namely RCB, EHe, He-sdO and O(He) stars, rather than [WC] stars. A merger of white dwarfs is the plausible scenario, which can explain typical surface abundances of these stars. However, residual hydrogen seen in Abell 48 is still a problem, which cannot be explained by the merger models. The common envelope evolution may also have some impacts. The stellar evolution still remain unclear and need to be investigated further.

In Chapter 6, the thermal mid-infrared continuum of PB 8 was best produced by using a dual-dust chemistry with discrete grain sizes and different grain species, amorphous carbon and crystalline silicate. We still do know which physical process makes dual-dust chemistry in PNe with WR-type nuclei. There are a number of scenarios proposed to explain dual-dust chemistry (see Cohen et al. 1999). One scenario is that a recent thermal pulse converted formerly O-rich outflows into C-rich. Another scenario is that one of the grain components more likely silicates existed before the current AGB outflows. Binarity is an alternative scenario suggested by De Marco & Soker (2002) to explain the dual dust chemistry phenomenon. Recently, Górny et al. (2010) found more PNe with dual-dust chemistry in the Galactic bulge, and speculated that the simultaneous presence of O-rich and C-rich dust is more likely related to the stellar evolution in a close binary system.

The photoionization models of SuWt 2 constructed in Chapter 7 suggested the existence of a hot ionizing source with $T_{\rm eff} \sim 150$ kK and $L_{\star} \sim 600 {\rm L}_{\odot}$. This PN has two A-type stars in a proven binary system at the centre, whose radiation is too soft to produce the surrounding nebula. The observed temporal variation of the centre-of-mass velocity of the two A-type stars by Exter et al. (2010) also suggested the presence of an unseen third orbiting body with $\sim 0.7 {\rm M}_{\odot}$. The future measurement of the orbital radial-velocity variation with time will yield a better constraint on the mass of the unseen star. Furthermore, deeper UV spectroscopy with IUE and *HST* observations might directly detect a hot body.

References

Abell, G. O. 1955. Globular Clusters and Planetary Nebulae Discovered on the National Geographic Society-Palomar Observatory Sky Survey. PASP, 67, 258

Abell, G. O. & Goldreich, P. 1966. On the Origin of Planetary Nebulae. PASP, 78, 232

Acker, A. 1976. Cinematique, age, et binarite des noyaux de nebuleuses planetaires. Publication de l'Observatoire de Strasbourg, 4, 1

Acker, A., Gesicki, K., Grosdidier, Y., & Durand, S. 2002. Turbulent planetary nebulae around [WC]-type stars. A&A, 384, 620

Acker, A., Marcout, J., Ochsenbein, F., et al. 1992, The Strasbourg-ESO Catalogue of Galactic Planetary Nebulae. Parts I, II., ed. Acker, A., Marcout, J., Ochsenbein, F., Stenholm, B., Tylenda, R., & Schohn, C.

Acker, A. & Neiner, C. 2003. Quantitative classification of WR nuclei of planetary nebulae. A&A, 403, 659

Acker, A., Raytchev, B., Koeppen, J., & Stenholm, B. 1991a. An estimation study of planetary nebulae in the galactic bulge. I - Spectrophotometric data. A&AS, 89, 237

Acker, A., Raytchev, B., Stenholm, B., & Tylenda, R. 1991b. The absolute H-beta fluxes for galactic planetary nebulae. A&AS, 90, 89

Acker, A., Stenholm, B., & Tylenda, R. 1989. The absolute H-beta fluxes for southern planetary nebulae. A&AS, 77, 487

Akras, S. & López, J. A. 2012. Three-dimensional modelling of the collimated bipolar outflows of compact planetary nebulae with Wolf-Rayet-type central stars. MNRAS, 425, 2197

Aller, L. H. & Czyzak, S. J. 1983. Chemical compositions of planetary nebulae. ApJS, 51, 211

Aller, L. H. & Keyes, C. D. 1985. A survey of the central-star characteristics of mostly faint planetary nebulae. PASP, 97, 1142

Aller, L. H. & Keyes, C. D. 1987. A spectroscopic survey of 51 planetary nebulae. ApJS, 65, 405

Aller, L. H., Keyes, C. D., & Feibelman, W. A. 1986. Spectrum and chemical analysis of the double-ring planetary nebula IC 1297. ApJ, 311, 930

Aller, L. H. & Liller, W. 1968, Planetary Nebulae, ed. B. M. Middlehurst & L. H. Aller, Planetary Nebulae (the University of Chicago Press), 483

Aller, L. H. & Menzel, D. H. 1945. Physical Processes in Gaseous Nebulae. XVIII. The Chemical Composition of the Planetary Nebulae. ApJ, 102, 239

Anders, E. & Grevesse, N. 1989. Abundances of the elements - Meteoritic and solar. Geochim. Cosmochim. Acta, 53, 197

Asplund, M., Grevesse, N., & Sauval, A. J. 2005, The Solar Chemical Composition, in Astronomical Society of the Pacific Conference Series, Vol. 336, Cosmic Abundances as Records of Stellar Evolution and Nucleosynthesis, ed. T. G. Barnes, III & F. N. Bash, 25

Asplund, M., Grevesse, N., Sauval, A. J., & Scott, P. 2009. The Chemical Composition of the Sun. ARA&A, 47, 481

Balick, B. 1987. The evolution of planetary nebulae. I - Structures, ionizations, and morphological sequences. AJ, 94, 671

Balick, B., Alexander, J., Hajian, A. R., et al. 1998. FLIERs and Other Microstructures in Planetary Nebulae. IV. Images of Elliptical PNs from the Hubble Space Telescope. AJ, 116, 360

Balick, B. & Frank, A. 2002. Shapes and Shaping of Planetary Nebulae. ARA&A, 40, 439

Balick, B., Perinotto, M., Maccioni, A., Terzian, Y., & Hajian, A. 1994. FLIERs and other microstructures in planetary nebulae, 2. ApJ, 424, 800

Balick, B., Rugers, M., Terzian, Y., & Chengalur, J. N. 1993. Fast, low-ionization emission regions and other microstructures in planetary nebulae. ApJ, 411, 778

Barlow, M. J. & Hummer, D. G. 1982, The WO Wolf-Rayet stars, in IAU Symposium, Vol. 99, Wolf-Rayet Stars: Observations, Physics, Evolution, ed. C. W. H. De Loore & A. J. Willis, 387–392

Beals, C. S. 1938, , in IAU Trans., Vol. 6, , 248

Becker, S. A. & Iben, Jr., I. 1979. The asymptotic giant branch evolution of intermediate-mass stars as a function of mass and composition. I - Through the second dredge-up phase. ApJ, 232, 831

Becker, S. A. & Iben, Jr., I. 1980. The asymptotic giant branch evolution of intermediate-mass stars as a function of mass and composition. II - Through the first major thermal pulse and the consequences of convective dredge-up. ApJ, 237, 111

Bell, K. L., Hibbert, A., & Stafford, R. P. 1995. Transition probabilities for some spectral lines of singly ionised nitrogen. Phys. Scr., 52, 240

Benjamin, R. A., Skillman, E. D., & Smits, D. P. 1999. Improving Predictions for Helium Emission Lines. ApJ, 514, 307

Benvenuto, O. G. & De Vito, M. A. 2003. A code for stellar binary evolution and its application to the formation of helium white dwarfs. MNRAS, 342, 50

Benvenuto, O. G. & De Vito, M. A. 2005. The formation of helium white dwarfs in close binary systems - II. MNRAS, 362, 891

Biemont, E. & Bromage, G. E. 1983. Transition probabilities for forbidden lines - The silicon isoelectronic sequence from S III to SN XXXVII. MNRAS, 205, 1085

Biémont, E. & Hansen, J. E. 1986. Forbidden Transitions in $3p^4$ and $4p^4$ Configurations. Phys. Scr., 34, 116

Biermann, P. L. & Cassinelli, J. P. 1993. Cosmic rays. II. Evidence for a magnetic rotator Wolf-Rayet star origin. A&A, 277, 691

Blöcker, T. 1995a. Stellar evolution of low- and intermediate-mass stars. II. Post-AGB evolution. A&A, 299, 755

Blöcker, T. 1995b. Stellar evolution of low and intermediate-mass stars. I. Mass loss on the AGB and its consequences for stellar evolution. A&A, 297, 727

Blöcker, T. 2001. Evolution on the AGB and beyond: on the formation of H-deficient post-AGB stars. Ap&SS, 275, 1

Bohigas, J. 2008. Photoionization Models Applied to Planetary Nebulae. ApJ, 674, 954

Bond, H. E. 2000, Binarity of Central Stars of Planetary Nebulae, in Astronomical Society of the Pacific Conference Series, Vol. 199, Asymmetrical Planetary Nebulae II: From Origins to Microstructures, ed. J. H. Kastner, N. Soker, & S. Rappaport, 115

Bond, H. E., O'Brien, M. S., Sion, E. M., et al. 2002, V471 Tauri and SuWt 2: The Exotic Descendants of Triple Systems?, in Astronomical Society of the Pacific Conference Series, Vol. 279, Exotic Stars as Challenges to Evolution, ed. C. A. Tout & W. van Hamme, 239

Bond, H. E., Pollacco, D. L., & Webbink, R. F. 2003. WeBo 1: A Young Barium Star Surrounded by a Ringlike Planetary Nebula. AJ, 125, 260

Boothroyd, A. I., Sackmann, I.-J., & Ahern, S. C. 1993. Prevention of High-Luminosity Carbon Stars by Hot Bottom Burning. ApJ, 416, 762

Bowen, I. S. 1927a. The Origin of the Chief Nebular Lines. PASP, 39, 295

Bowen, I. S. 1927b. The Origin of the Nebulium Spectrum. Nature, 120, 473

Bowen, I. S. 1928. The origin of the nebular lines and the structure of the planetary nebulae. ApJ, 67, 1

Brocklehurst, M. 1971. Calculations of level populations for the low levels of hydrogenic ions in gaseous nebulae. MNRAS, 153, 471

Brown, J. C., Cassinelli, J. P., Li, Q., Kholtygin, A. F., & Ignace, R. 2004. Optically thick clumps - not the solution to the Wolf-Rayet wind momentum problem? A&A, 426, 323

Busso, M., Gallino, R., & Wasserburg, G. J. 1999. Nucleosynthesis in Asymptotic Giant Branch Stars: Relevance for Galactic Enrichment and Solar System Formation. ARA&A, 37, 239

Butler, K. & Zeippen, C. J. 1989. Effective collision strengths for fine-structure forbidden transitions in the 3p3 configuration of Cl(III). A&A, 208, 337

Cahn, J. H., Kaler, J. B., & Stanghellini, L. 1992. A catalogue of absolute fluxes and distances of planetary nebulae. A&AS, 94, 399

Cameron, A. G. W. & Fowler, W. A. 1971. Lithium and the s-PROCESS in Red-Giant Stars. ApJ, 164, 111

Cassinelli, J. P. 1991, Wolf-Rayet Stellar Wind Theory (review), in IAU Symposium, Vol. 143, Wolf-Rayet Stars and Interrelations with Other Massive Stars in Galaxies, ed. K. A. van der Hucht & B. Hidayat, 289

Charbonnel, C. & Lagarde, N. 2010. Thermohaline instability and rotation-induced mixing. I. Low- and intermediate-mass solar metallicity stars up to the end of the AGB. A&A, 522, A10

Chen, X. & Han, Z. 2002. Low- and intermediate-mass close binary evolution and the initial-final mass relation - II. Non-conservative case with convective overshooting. MNRAS, 335, 948

Chesneau, O., Collioud, A., De Marco, O., et al. 2006. A close look into the carbon disk at the core of the planetary nebula CPD-56deg8032. A&A, 455, 1009

Chiappini, C., Górny, S. K., Stasińska, G., & Barbuy, B. 2009. Abundances in the Galactic bulge: results from planetary nebulae and giant stars. A&A, 494, 591

Ciardullo, R., Bond, H. E., Sipior, M. S., et al. 1999. A HUBBLE SPACE TELESCOPE Survey for Resolved Companions of Planetary Nebula Nuclei. AJ, 118, 488

Clark, D. M., López, J. A., Steffen, W., & Richer, M. G. 2013. A Detailed Spatiokinematic Model of the Conical Outflow of the Multipolar Planetary Nebula NGC 7026. AJ, 145, 57

Clayton, G. C. 1996. The R Coronae Borealis Stars. PASP, 108, 225

Clayton, G. C., Geballe, T. R., Herwig, F., Fryer, C., & Asplund, M. 2007. Very Large Excesses of ^{18}O in Hydrogen-deficient Carbon and R Coronae Borealis Stars: Evidence for White Dwarf Mergers. ApJ, 662, 1220

Clegg, R. E. S., Miller, S., Storey, P. J., & Kisielius, R. 1999. Recombination line intensities for hydrogenic ions: The fine-structure components of H I and He Ii. A&AS, 135, 359

Cohen, M., Barlow, M. J., Liu, X.-W., & Jones, A. F. 2002. The dual dust chemistries of planetary nebulae with [WCL] central stars. MNRAS, 332, 879

Cohen, M., Barlow, M. J., Sylvester, R. J., et al. 1999. Water Ice, Silicate, and Polycyclic Aromatic Hydrocarbon Emission Featuresin the Infrared Space Observatory Spectrum of the Carbon-richPlanetary Nebula CPD -56 deg8032. ApJ, 513, L135

Condon, J. J. & Kaplan, D. L. 1998. Planetary Nebulae in the NRAO VLA Sky Survey. ApJS, 117, 361

Condon, J. J., Kaplan, D. L., & Terzian, Y. 1999. Infrared Planetary Nebulae in the NRAO VLA Sky Survey. ApJS, 123, 219

Corradi, R. L. M., Manso, R., Mampaso, A., & Schwarz, H. E. 1996. Unveiling low-ionization microstructures in planetary nebulae. A&A, 313, 913

Corradi, R. L. M. & Schwarz, H. E. 1995. Morphological populations of planetary nebulae: which progenitors? I. Comparative properties of bipolar nebulae. A&A, 293, 871

Costa, R. D. D., de Freitas Pacheco, J. A., & De Franca, Jr., J. A. 1996. Abundances in type I planetary nebulae: is the galactic disk presently oxygen deficient? A&A, 313, 924

Crowther, P. A., De Marco, O., & Barlow, M. J. 1998. Quantitative classification of WC and WO stars. MNRAS, 296, 367

Crowther, P. A., Hillier, D. J., & Smith, L. J. 1995. Fundamental parameters of Wolf-Rayet stars. I. Ofpe/WN9 stars. A&A, 293, 172

Curtis, H. D. 1918. The planetary nebulae. Publications of Lick Observatory, 13, 55

Danehkar, A., Parker, Q. A., & Ercolano, B. 2013. Observations and three-dimensional ionization structure of the planetary nebula SuWt 2. MNRAS, 434, 1513

Danehkar, A., Todt, H., Ercolano, B., & Kniazev, A. Y. 2014. Observations and three-dimensional photoionization modelling of the Wolf-Rayet planetary nebula Abell 48. MNRAS, 439, 3605

Davey, A. R., Storey, P. J., & Kisielius, R. 2000. Recombination coefficients for C II lines. A&AS, 142, 85

De Marco, O. 2009. The Origin and Shaping of Planetary Nebulae: Putting the Binary Hypothesis to the Test. PASP, 121, 316

De Marco, O. & Barlow, M. J. 2001. Abundances of [WC] central stars and their planetary nebulae. Ap&SS, 275, 53

De Marco, O., Barlow, M. J., & Cohen, M. 2002. Discovery of an Edge-on Dust Disk around the [WC10] Central Star CPD -56deg8032. ApJ, 574, L83

De Marco, O., Barlow, M. J., & Storey, P. J. 1997. The WC10 central stars CPD-56 deg 8032 and He 2-113. I - Distances and nebular parameters. MNRAS, 292, 86

De Marco, O. & Crowther, P. A. 1998. The WC10 central stars CPD-56 deg8032 and He2-113 - II. Model analysis and comparison with nebular properties. MNRAS, 296, 419

De Marco, O. & Soker, N. 2002. A New Look at the Evolution of Wolf-Rayet Central Stars of Planetary Nebulae. PASP, 114, 602

De Marco, O., Storey, P. J., & Barlow, M. J. 1998. The WC10 central stars CPD-56 deg8032 and He2-113 -III. Wind electron temperatures and abundances. MNRAS, 297, 999

Demarque, P., Woo, J.-H., Kim, Y.-C., & Yi, S. K. 2004. Y^2 Isochrones with an Improved Core Overshoot Treatment. ApJS, 155, 667

Depew, K., Parker, Q. A., Miszalski, B., et al. 2011. Newly discovered Wolf-Rayet and weak emission-line central stars of planetary nebulae. MNRAS, 414, 2812

Dinerstein, H. L., Richter, M. J., Lacy, J. H., & Sellgren, K. 2003. Observations of [S IV] 10.5 μm and [Ne II] 12.8 μm in Two Halo Planetary Nebulae: Implications for Chemical Self-Enrichment. AJ, 125, 265

Dopita, M., Hart, J., McGregor, P., et al. 2007. The Wide Field Spectrograph (WiFeS). Ap&SS, 310, 255

Dopita, M., Rhee, J., Farage, C., et al. 2010. The Wide Field Spectrograph (WiFeS): performance and data reduction. Ap&SS, 327, 245

Dopita, M. A., Ford, H. C., Bohlin, R., Evans, I. N., & Meatheringham, S. J. 1993. Hubble Space Telescope Observations of Planetary Nebulae in the Magellanic Clouds. I. The Extreme Type I SMP 83/WS 35. ApJ, 418, 804

Dopita, M. A., Lawrence, C. J., Ford, H. C., & Webster, B. L. 1985. The kinematics and internal dynamics of planetary nebulae in the small Magellanic Cloud. ApJ, 296, 390

Dopita, M. A. & Meatheringham, S. J. 1990. The evolutionary sequence of planetary nebulae. ApJ, 357, 140

Dopita, M. A. & Meatheringham, S. J. 1991. Photoionization modeling of Magellanic Cloud planetary nebulae. II. ApJ, 377, 480

Dopita, M. A., Meatheringham, S. J., Webster, B. L., & Ford, H. C. 1988. The internal dynamics of the planetary nebulae in the Large Magellanic Cloud. ApJ, 327, 639

Dopita, M. A., Sutherland, R. S., Nicholls, D. C., Kewley, L. J., & Vogt, F. P. A. 2013. New Strong-line Abundance Diagnostics for H II Regions: Effects of κ-distributed Electron Energies and New Atomic Data. ApJS, 208, 10

Dopita, M. A., Vassiliadis, E., Meatheringham, S. J., et al. 1996. Hubble Space Telescope Observations of Planetary Nebulae in the Magellanic Clouds. IV. [O iii] Images and Evolutionary Ages. ApJ, 460, 320

Dos Santos, L. C., Jatenco-Pereira, V., & Opher, R. 1993. Mass loss from Wolf-Rayet stars due to radiation pressure and Alfven waves. ApJ, 410, 732

Dreizler, S. & Werner, K. 1996, Spectral analysis of hot helium-rich white dwarfs, in Astronomical Society of the Pacific Conference Series, Vol. 96, Hydrogen Deficient Stars, ed. C. S. Jeffery & U. Heber, 281

Driver, S. P., Popescu, C. C., Tuffs, R. J., et al. 2007. The Millennium Galaxy Catalogue: the B-band attenuation of bulge and disc light and the implied cosmic dust and stellar mass densities. MNRAS, 379, 1022

Durand, S., Acker, A., & Zijlstra, A. 1998. The kinematics of 867 galactic planetary nebulae. A&AS, 132, 13

Eggleton, P. P. 1971. The evolution of low mass stars. MNRAS, 151, 351

Eggleton, P. P. 1972. Composition changes during stellar evolution. MNRAS, 156, 361

Eggleton, P. P. 1973. A numerical treatment of double shell source stars. MNRAS, 163, 279

Ekström, S., Georgy, C., Eggenberger, P., et al. 2012. Grids of stellar models with rotation. I. Models from 0.8 to 120 $\mathrm{M}_{\&sun;}$ at solar metallicity (Z = 0.014). A&A, 537, A146

Ercolano, B., Barlow, M. J., & Storey, P. J. 2005. The dusty MOCASSIN: fully self-consistent 3D photoionization and dust radiative transfer models. MNRAS, 362, 1038

Ercolano, B., Barlow, M. J., Storey, P. J., & Liu, X.-W. 2003a. MOCASSIN: a fully three-dimensional Monte Carlo photoionization code. MNRAS, 340, 1136

Ercolano, B., Barlow, M. J., Storey, P. J., et al. 2003b. Three-dimensional photoionization modelling of the hydrogen-deficient knots in the planetary nebula Abell 30. MNRAS, 344, 1145

Ercolano, B., Morisset, C., Barlow, M. J., Storey, P. J., & Liu, X.-W. 2003b.

Three-dimensional photoionization modelling of the planetary nebula NGC 3918. MNRAS, 340, 1153

Ercolano, B. & Storey, P. J. 2006. Theoretical calculations of the HI, HeI and HeII free-bound continuous emission spectra. MNRAS, 372, 1875

Ercolano, B., Wesson, R., Zhang, Y., et al. 2004. Observations and three-dimensional photoionization modelling of the Wolf-Rayet planetary nebula NGC 1501. MNRAS, 354, 558

Ercolano, B., Young, P. R., Drake, J. J., & Raymond, J. C. 2008. X-Ray Enabled MOCASSIN: A Three-dimensional Code for Photoionized Media. ApJS, 175, 534

Escalante, V. & Morisset, C. 2005. The NII spectrum of the Orion nebula. MNRAS, 361, 813

Escalante, V., Morisset, C., & Georgiev, L. 2012. Excitation of emission lines by fluorescence and recombination in IC 418. MNRAS, 426, 2318

Escalante, V. & Victor, G. A. 1990. Effective recombination coefficients of neutral carbon and singly ionized nitrogen. ApJS, 73, 513

Exter, K., Bond, H., Pollacco, D., & Dufton, P. 2003, The Bizarre Central Star of SuWt2, in IAU Symposium, Vol. 209, Planetary Nebulae: Their Evolution and Role in the Universe, ed. S. Kwok, M. Dopita, & R. Sutherland, 234

Exter, K., Bond, H. E., Stassun, K. G., et al. 2010. The Exotic Eclipsing Nucleus of the Ring Planetary Nebula SuWt 2. AJ, 140, 1414

Fang, X. & Liu, X.-W. 2013. Very deep spectroscopy of the bright Saturn nebula NGC 7009 - II. Analysis of the rich optical recombination spectrum. MNRAS, 429, 2791

Ferland, G. J. 1992. N III line emission in planetary nebulae - Continuum fluorescence. ApJ, 389, L63

Frank, A. & Blackman, E. G. 2004. Application of Magnetohydrodynamic Disk Wind Solutions to Planetary and Protoplanetary Nebulae. ApJ, 614, 737

Frankowski, A. & Soker, N. 2009. Very late thermal pulses influenced by accretion in planetary nebulae. New Astro., 14, 654

Frew, D. J. 2008, Planetary Nebulae in the Solar Neighbourhood: Statistics, Distance Scale and Luminosity Function. PhD thesis, Department of Physics, Macquarie University, NSW 2109, Australia

Frew, D. J., Bojičić, I. S., & Parker, Q. A. 2013a. A catalogue of integrated Hα fluxes for 1258 Galactic planetary nebulae. MNRAS, 431, 2

Frew, D. J., Bojičić, I. S., Parker, Q. A., et al. 2014a. Flux calibration of the AAO/UKST SuperCOSMOS Hα Survey. MNRAS, 440, 1080

Frew, D. J., Bojičić, I. S., Parker, Q. A., et al. 2014b. The planetary nebula Abell 48 and its [WN] nucleus. MNRAS, 440, 1345

Frew, D. J. & Parker, Q. A. 2006, Towards a New Distance Scale and Luminosity Function for Nearby Planetary Nebulae, in IAU Symposium, Vol. 234, Planetary Nebulae in our Galaxy and Beyond, ed. M. J. Barlow & R. H. Méndez, 49–54

Galavis, M. E., Mendoza, C., & Zeippen, C. J. 1995. Atomic data from the IRON Project. X. Effective collision strengths for infrared transitions in silicon- and sulphur-like ions. A&AS, 111, 347

García-Díaz, M. T., Clark, D. M., López, J. A., Steffen, W., & Richer, M. G. 2009. The Outflows and Three-Dimensional Structure of NGC 6337: A Planetary Nebula with a Close Binary Nucleus. ApJ, 699, 1633

García-Hernández, D. A., Hinkle, K. H., Lambert, D. L., & Eriksson, K. 2009. CNO Abundances of Hydrogen-Deficient Carbon and R Coronae Borealis Stars: A View of the Nucleosynthesis in a White Dwarf Merger. ApJ, 696, 1733

García-Lario, P., Manchado, A., Ulla, A., & Manteiga, M. 1999. Infrared Space Observatory Observations of IRAS 16594-4656: A New Proto-Planetary Nebula with a Strong 21 Micron Dust Feature. ApJ, 513, 941

García-Rojas, J., Esteban, C., Peimbert, A., et al. 2005. Deep echelle spectrophotometry of S 311, a Galactic HII region located outside the solar circle. MNRAS, 362, 301

García-Rojas, J., Esteban, C., Peimbert, A., et al. 2007. The chemical composition of the Galactic H II regions M8 and M17. A revision based on deep VLT echelle spectrophotometry. RMxAA, 43, 3

García-Rojas, J., Esteban, C., Peimbert, M., et al. 2006. Faint emission lines in the Galactic HII regions M16, M20 and NGC 3603*. MNRAS, 368, 253

García-Rojas, J., Peña, M., Morisset, C., et al. 2013. Analysis of chemical abundances in planetary nebulae with [WC] central stars. II. Chemical abundances and the abundance discrepancy factor. A&A, 558, A122

García-Rojas, J., Peña, M., Morisset, C., Mesa-Delgado, A., & Ruiz, M. T. 2012. Analysis of chemical abundances in planetary nebulae with [WC] central stars. I. Line intensities and physical conditions. A&A, 538, A54

García-Rojas, J., Peña, M., & Peimbert, A. 2009. Faint recombination lines in Galactic PNe with a [WC] nucleus. A&A, 496, 139

García-Segura, G. 1997. Three-dimensional Magnetohydrodynamical Modeling of Planetary Nebulae: The Formation of Jets, Ansae, and Point-symmetric Nebulae via Magnetic Collimation. ApJ, 489, L189

García-Segura, G., Langer, N., Różyczka, M., & Franco, J. 1999. Shaping Bipolar and Elliptical Planetary Nebulae: Effects of Stellar Rotation, Photoionization Heating, and Magnetic Fields. ApJ, 517, 767

García-Segura, G. & López, J. A. 2000. Three-dimensional Magnetohydrodynamic Modeling of Planetary Nebulae. II. The Formation of Bipolar and Elliptical Nebulae with Point-symmetric Structures and Collimated Outflows. ApJ, 544, 336

Garnett, D. R. 1992. Electron temperature variations and the measurement of nebular abundances. AJ, 103, 1330

Gesicki, K. & Acker, A. 1996. Velocity field in nebulae around [WC] stars. Ap&SS, 238, 101

Gesicki, K. & Zijlstra, A. A. 2000. Expansion velocities and dynamical ages of planetary nebulae. A&A, 358, 1058

Gesicki, K. & Zijlstra, A. A. 2007. White dwarf masses derived from planetary nebula modelling. A&A, 467, L29

Gesicki, K., Zijlstra, A. A., Acker, A., et al. 2006. Planetary nebulae with emission-line central stars. A&A, 451, 925

Girard, P., Köppen, J., & Acker, A. 2007. Chemical compositions and plasma parameters of planetary nebulae with Wolf-Rayet and wels type central stars. A&A, 463, 265

Gleizes, F., Acker, A., & Stenholm, B. 1989. Zanstra temperatures of the central stars of southern planetary nebulae. A&A, 222, 237

Gonçalves, D. R., Corradi, R. L. M., & Mampaso, A. 2001. Low-Ionization Structures in Planetary Nebulae: Confronting Models with Observations. ApJ, 547, 302

Gonçalves, D. R., Corradi, R. L. M., Mampaso, A., & Perinotto, M. 2003. The Physical Parameters, Excitation, and Chemistry of the Rim, Jets, and Knots of the Planetary Nebula NGC 7009. ApJ, 597, 975

Gonçalves, D. R., Ercolano, B., Carnero, A., Mampaso, A., & Corradi, R. L. M. 2006. On the nitrogen abundance of fast, low-ionization emission regions: the outer knots of the planetary nebula NGC 7009. MNRAS, 365, 1039

Gonçalves, D. R., Mampaso, A., Corradi, R. L. M., & Quireza, C. 2009. Low-ionization pairs of knots in planetary nebulae: physical properties and excitation. MNRAS, 398, 2166

Gonçalves, D. R., Wesson, R., Morisset, C., Barlow, M., & Ercolano, B. 2012, When shape matters: Correcting the ICFs to derive the chemical abundances of bipolar and elliptical PNe, in IAU Symposium, Vol. 283, IAU Symposium, 144–147

Górny, S. K., Chiappini, C., Stasińska, G., & Cuisinier, F. 2009. Planetary nebulae in the direction of the Galactic bulge: on nebulae with emission-line central stars. A&A, 500, 1089

Górny, S. K., Perea-Calderón, J. V., García-Hernández, D. A., García-Lario, P., & Szczerba, R. 2010. New groups of planetary nebulae with peculiar dust chemistry towards the Galactic bulge. A&A, 516, A39

Górny, S. K., Schwarz, H. E., Corradi, R. L. M., & Van Winckel, H. 1999. An atlas of images of Planetary Nebulae. A&AS, 136, 145

Górny, S. K., Stasińska, G., Escudero, A. V., & Costa, R. D. D. 2004. The populations of planetary nebulae in the direction of the Galactic bulge. Chemical abundances and Wolf-Rayet central stars. A&A, 427, 231

Gorny, S. K., Stasińska, G., & Tylenda, R. 1997. Planetary nebulae morphologies, central star masses and nebular properties. A&A, 318, 256

Górny, S. K. & Tylenda, R. 2000. Evolutionary status of hydrogen-deficient central stars of planetary nebulae. A&A, 362, 1008

Gräfener, G., Koesterke, L., & Hamann, W.-R. 2002. Line-blanketed model atmospheres for WR stars. A&A, 387, 244

Grieve, M. F. R., Ramsbottom, C. A., Hudson, C. E., & Keenan, F. P. 2014. Electron-impact Excitation Collision Strengths and Theoretical Line Intensities for Transitions in S III. ApJ, 780, 110

Hajduk, M., Zijlstra, A. A., van Hoof, P. A. M., et al. 2007. The enigma of the oldest ‘nova’: the central star and nebula of CK Vul. MNRAS, 378, 1298

Hajian, A. R., Balick, B., Terzian, Y., & Perinotto, M. 1997. FLIERs and Other Microstructures in Planetary Nebulae. III. ApJ, 487, 304

Hamann, W.-R. 1996, Wolf-Rayet stars of high and low mass, in Astronomical Society of the Pacific Conference Series, Vol. 96, Hydrogen Deficient Stars, ed. C. S. Jeffery & U. Heber, 127

Hamann, W.-R. & Gräfener, G. 2004. Grids of model spectra for WN stars, ready for use. A&A, 427, 697

Hamann, W.-R., Peña, M., Gräfener, G., & Ruiz, M. T. 2003. The central star of the planetary nebula N 66 in the Large Magellanic Cloud: A detailed analysis of its dramatic evolution 1983-2000. A&A, 409, 969

Han, Z., Podsiadlowski, P., Maxted, P. F. L., & Marsh, T. R. 2003. The origin of subdwarf B stars - II. MNRAS, 341, 669

Han, Z., Podsiadlowski, P., Maxted, P. F. L., Marsh, T. R., & Ivanova, N. 2002. The origin of subdwarf B stars - I. The formation channels. MNRAS, 336, 449

Hanner, M. S. 1988, Grain optical properties, in NASA Conf. Pub., Vol. 3004, Infrared Observations of Comets Halley and Wilson and Properties of the Grains, 22–49

Harrington, J. P., Seaton, M. J., Adams, S., & Lutz, J. H. 1982. Ultraviolet spectra of planetary nebulae. VI - NGC 7662. MNRAS, 199, 517

Heap, S. R. 1982, Subluminous Wolf-Rayet stars - Observations, in IAU Symposium, Vol. 99, Wolf-Rayet Stars: Observations, Physics, Evolution, ed. C. W. H. De Loore & A. J. Willis, 423–445

Henry, R. B. C. 1990. Abundance patterns in planetary nebulae. ApJ, 356, 229

Henry, R. B. C., Kwitter, K. B., & Balick, B. 2004. Sulfur, Chlorine, and Argon Abundances in Planetary Nebulae. IV. Synthesis and the Sulfur Anomaly. AJ, 127, 2284

Henry, R. B. C., Kwitter, K. B., & Howard, J. W. 1996. A New Look at Carbon Abundances in Planetary Nebulae. I. PB 6, HU 2–1, K648, and H4–1. ApJ, 458, 215

Herschel, W. 1791. On Nebulous Stars, Properly So Called. By William Herschel, LL.D. F. R. S. Royal Society of London Philosophical Transactions Series I, 81, 71

Herwig, F. 2001. Internal mixing and surface abundance of [WC]-CSPN. Ap&SS, 275, 15

Herwig, F. 2005. Evolution of Asymptotic Giant Branch Stars. ARA&A, 43, 435

Herwig, F., Bloecker, T., Schoenberner, D., & El Eid, M. 1997. Stellar evolution of low and intermediate-mass stars. IV. Hydrodynamically-based overshoot and nucleosynthesis in AGB stars. A&A, 324, L81

Hillier, D. J. 1991. The effects of electron scattering and wind clumping for early emission line stars. A&A, 247, 455

Hiltner, W. A. & Schild, R. E. 1966. Spectral Classification of Wolf-Rayet Stars. ApJ, 143, 770

Hollenbach, D. J. & Tielens, A. G. G. M. 1997. Dense Photodissociation Regions (PDRs). ARA&A, 35, 179

Howarth, I. D. 1983. LMC and galactic extinction. MNRAS, 203, 301

Howarth, I. D. & Adams, S. 1981, Program EQUIB. University College London, (Wesson R., 2009, Converted to FORTRAN 90)

Huang, K.-N. 1985. Energy-Level Scheme and Transition Probabilities of Si-like Ions. Atomic Data and Nuclear Data Tables, 32, 503

Hubble, E. P. 1922. The source of luminosity in galactic nebulae. ApJ, 56, 400

Huckvale, L., Prouse, B., Jones, D., et al. 2013. Spatio-kinematic modelling of Abell 65, a double-shelled planetary nebula with a binary central star. MNRAS, 434, 1505

Huggins, W. & Miller, W. A. 1864. On the Spectra of Some of the Nebulae. By William Huggins, F.R.A.S. A Supplement to the Paper ”On the Spectra of Some of the Fixed Stars William Huggins F.R.A.S., and W. A. Miller, M.D., LL.D., Treas. and V.P.P.S.”. Royal Society of London Philosophical Transactions Series I, 154, 437

Hummer, D. G. & Storey, P. J. 1987. Recombination-line intensities for hydrogenic ions. I - Case B calculations for H I and He II. MNRAS, 224, 801

Husfeld, D., Kudritzki, R. P., Simon, K. P., & Clegg, R. E. S. 1984. Non-LTE model atmospheres of hot central stars close to the Eddington limit - The Zanstra discrepancy and the occurrence of an emission edge at 228 A. A&A, 134, 139

Iben, Jr., I. 1973. On the Abundance of Lithium in Red Giants of Intermediate Mass. ApJ, 185, 209

Iben, Jr., I. 1975. Thermal pulses; p-capture, alpha-capture, s-process nucleosynthesis; and convective mixing in a star of intermediate mass. ApJ, 196, 525

Iben, Jr., I. 1995. Planetary nebulae and their central stars - origin and evolution. Phys. Rep., 250, 2

Iben, Jr., I., Kaler, J. B., Truran, J. W., & Renzini, A. 1983a. On the evolution of those nuclei of planetary nebulae that experience a final helium shell flash. ApJ, 264, 605

Iben, Jr., I., Kaler, J. B., Truran, J. W., & Renzini, A. 1983b. On the evolution of those nuclei of planetary nebulae that experience a final helium shell flash. ApJ, 264, 605

Iben, Jr., I. & Renzini, A. 1983. Asymptotic giant branch evolution and beyond. ARA&A, 21, 271

Jacob, R., Schönberner, D., & Steffen, M. 2013. The evolution of planetary nebulae. VIII. True expansion rates and visibility times. A&A, 558, A78

Jacoby, G. H., Ferland, G. J., & Korista, K. T. 2001. The Planetary Nebula A39: An Observational Benchmark for Numerical Modeling of Photoionized Plasmas. ApJ, 560, 272

Jaeger, C., Mutschke, H., Begemann, B., Dorschner, J., & Henning, T. 1994. Steps toward interstellar silicate mineralogy. 1: Laboratory results of a silicate glass of mean cosmic composition. A&A, 292, 641

Jeffery, C. S., Karakas, A. I., & Saio, H. 2011. Double white dwarf mergers and elemental surface abundances in extreme helium and R Coronae Borealis stars. MNRAS, 414, 3599

Jewitt, D. C., Danielson, G. E., & Kupferman, P. N. 1986. Halos around planetary nebulae. ApJ, 302, 727

Jones, D., Lloyd, M., Mitchell, D. L., et al. 2010a. Kinematics of the ring-like nebula SuWt 2. MNRAS, 401, 405

Jones, D., Lloyd, M., Santander-García, M., et al. 2010b. Abell 41: shaping of a planetary nebula by a binary central star. MNRAS, 408, 2312

Jones, D., Mitchell, D. L., Lloyd, M., et al. 2012. The morphology and kinematics of the Fine Ring Nebula, planetary nebula Sp 1, and the shaping influence of its binary central star. MNRAS, 420, 2271

Kahn, F. D. & West, K. A. 1985. Shapes of planetary nebulae. MNRAS, 212, 837

Kaler, J. B. 1986. Electron temperatures in planetary nebulae. ApJ, 308, 322

Kaler, J. B. & Shaw, R. A. 1984. The O VI nucleus of the planetary nebula M3-30. ApJ, 278, 195

Kaler, J. B., Shaw, R. A., Feibelman, W. A., & Imhoff, C. L. 1991. PB 6 and its central star. PASP, 103, 67

Karakas, A. & Lattanzio, J. C. 2007. Stellar Models and Yields of Asymptotic Giant Branch Stars. PASA, 24, 103

Karakas, A. I. 2010. Updated stellar yields from asymptotic giant branch models. MNRAS, 403, 1413

Karakas, A. I., Campbell, S. W., & Stancliffe, R. J. 2010. Is Extra Mixing Really Needed in Asymptotic Giant Branch Stars? ApJ, 713, 374

Karakas, A. I., García-Hernández, D. A., & Lugaro, M. 2012. Heavy Element Nucleosynthesis in the Brightest Galactic Asymptotic Giant Branch Stars. ApJ, 751, 8

Karakas, A. I. & Lattanzio, J. C. 2003. AGB Stars and the Observed Abundance of Neon in Planetary Nebulae. PASA, 20, 393

Karakas, A. I., Lattanzio, J. C., & Pols, O. R. 2002. Parameterising the Third Dredge-up in Asymptotic Giant Branch Stars. PASA, 19, 515

Karakas, A. I. & Lugaro, M. 2010. Heavy Element Abundances in Planetary Nebulae: A Theorist's Perspective. PASA, 27, 227

Karakas, A. I., van Raai, M. A., Lugaro, M., Sterling, N. C., & Dinerstein, H. L. 2009. Nucleosynthesis Predictions for Intermediate-Mass Asymptotic Giant Branch Stars: Comparison to Observations of Type I Planetary Nebulae. ApJ, 690, 1130

Kastner, J. H., Montez, Jr., R., Balick, B., & De Marco, O. 2008. Serendipitous Chandra X-Ray Detection of a Hot Bubble within the Planetary Nebula NGC

5315. ApJ, 672, 957

Kastner, J. H., Montez, Jr., R., Balick, B., et al. 2012. The Chandra X-Ray Survey of Planetary Nebulae (CHANPLANS): Probing Binarity, Magnetic Fields, and Wind Collisions. AJ, 144, 58

Kingdon, J. B. & Ferland, G. J. 1995. Temperature Fluctuations in Photoionized Nebulae. ApJ, 450, 691

Kingsburgh, R. L. & Barlow, M. J. 1994. Elemental abundances for a sample of southern galctic planetary nebulae. MNRAS, 271, 257

Kingsburgh, R. L., Barlow, M. J., & Storey, P. J. 1995. Properties of the WO Wolf-Rayet stars. A&A, 295, 75

Kisielius, R., Storey, P. J., Ferland, G. J., & Keenan, F. P. 2009. Electron-impact excitation of OII fine-structure levels. MNRAS, 397, 903

Koeppen, J., Acker, A., & Stenholm, B. 1991. Spectrophotometric survey of southern planetary nebulae. II - Chemical compositions. A&A, 248, 197

Koesterke, L. 2001. Spectral analyses of WR-type central stars of planetary nebulae. Ap&SS, 275, 41

Koesterke, L. & Hamann, W.-R. 1997. Spectral analyses of central stars of planetary nebulae of early WC-type NGC 6751 and Sanduleak 3. A&A, 320, 91

Kohoutek, L. 1977. New southern planetary nebulae. A&A, 59, 137

Kurucz, R. L. 1991, New Lines, New Models, New Colors, in Precision Photometry: Astrophysics of the Galaxy, ed. A. G. D. Philip, A. R. Upgren, & K. A. Janes, 27

Kwitter, K. B. & Henry, R. B. C. 2001. Sulfur, Chlorine, and Argon in Planetary Nebulae. I. Observations and Abundances in a Northern Sample. ApJ, 562, 804

Kwitter, K. B., Henry, R. B. C., & Milingo, J. B. 2003. Sulfur, Chlorine, and Argon Abundances in Planetary Nebulae. III. Observations and Results for a Final Sample. PASP, 115, 80

Kwok, S. 2010. Morphological Structures of Planetary Nebulae. PASA, 27, 174

Kwok, S., Purton, C. R., & Fitzgerald, P. M. 1978. On the origin of planetary nebulae. ApJ, 219, L125

Lagadec, E., Chesneau, O., Matsuura, M., et al. 2006. New insights on the complex planetary nebula Hen 2-113. A&A, 448, 203

Landi, E. & Bhatia, A. K. 2005. Atomic data and spectral line intensities for Ne III. Atomic Data and Nuclear Data Tables, 89, 195

Landi, E., Del Zanna, G., Young, P. R., Dere, K. P., & Mason, H. E. 2012. CHIANTI–An Atomic Database for Emission Lines. XII. Version 7 of the Database. ApJ, 744, 99

Landi, E., Del Zanna, G., Young, P. R., et al. 2006. CHIANTI-An Atomic Database for Emission Lines. VII. New Data for X-Rays and Other Improvements. ApJS, 162, 261

Lasker, B. M., Lattanzi, M. G., McLean, B. J., et al. 2008. The Second-Generation Guide Star Catalog: Description and Properties. AJ, 136, 735

Lattanzio, J. C. 1986. The asymptotic giant branch evolution of 1.0-3.0 solar mass stars as a function of mass and composition. ApJ, 311, 708

Lebouteiller, V., Barry, D. J., Spoon, H. W. W., et al. 2011. CASSIS: The Cornell Atlas of Spitzer/Infrared Spectrograph Sources. ApJS, 196, 8

Lennon, D. J. & Burke, V. M. 1994. Atomic data from the IRON project. II. Effective collision strength S for infrared transitions in carbon-like ions. A&AS, 103, 273

Lenzuni, P., Natta, A., & Panagia, N. 1989. Properties and evolution of dust grains in planetary nebulae. ApJ, 345, 306

Leuenhagen, U. & Hamann, W.-R. 1994. V 348 Sagittarii: Analysis of the (WC 12) stellar spectrum. A&A, 283, 567

Leuenhagen, U. & Hamann, W.-R. 1998. Spectral analyses of late-type [WC] central stars of planetary nebulae: more empirical constraints for their evolutionary status. A&A, 330, 265

Leuenhagen, U., Hamann, W.-R., & Jeffery, C. S. 1996. Spectral analyses of late-type WC central stars of planetary nebulae. A&A, 312, 167

Liu, X.-W. 2003, Probing the Dark Secrets of PNe with ORLs (invited review), in IAU Symposium, Vol. 209, Planetary Nebulae: Their Evolution and Role in the Universe, ed. S. Kwok, M. Dopita, & R. Sutherland, 339

Liu, X.-W., Barlow, M. J., Zhang, Y., Bastin, R. J., & Storey, P. J. 2006. Chemical abundances for Hf 2-2, a planetary nebula with the strongest-known heavy-element recombination lines. MNRAS, 368, 1959

Liu, X.-W. & Danziger, J. 1993. Electron temperature determination from nebular continuum emission in planetary nebulae and the importance of temperature fluctuations. MNRAS, 263, 256

Liu, X.-W., Luo, S.-G., Barlow, M. J., Danziger, I. J., & Storey, P. J. 2001. Chemical abundances of planetary nebulae from optical recombination lines - III. The Galactic bulge PN M 1-42 and M 2-36. MNRAS, 327, 141

Liu, X.-W., Storey, P. J., Barlow, M. J., & Clegg, R. E. S. 1995. The rich O II recombination spectrum of the planetary nebula NGC 7009: new observations and atomic data. MNRAS, 272, 369

Liu, X.-W., Storey, P. J., Barlow, M. J., et al. 2000. NGC 6153: a super-metal-rich planetary nebula? MNRAS, 312, 585

Liu, Y., Liu, X.-W., Barlow, M. J., & Luo, S.-G. 2004a. Chemical abundances of planetary nebulae from optical recombination lines - II. Abundances derived from collisionally excited lines and optical recombination lines. MNRAS, 353, 1251

Liu, Y., Liu, X.-W., Luo, S.-G., & Barlow, M. J. 2004b. Chemical abundances of planetary nebulae from optical recombination lines - I. Observations and plasma diagnostics. MNRAS, 353, 1231

López, J. A., García-Díaz, M. T., Steffen, W., Riesgo, H., & Richer, M. G. 2012. Morpho-kinematic Analysis of the Point-symmetric, Bipolar Planetary Nebulae Hb 5 and K 3-17, A Pathway to Poly-polarity. ApJ, 750, 131

López, J. A., Richer, M. G., García-Díaz, M. T., et al. 2012. The SPM Kinematic Catalogue of Galactic Planetary Nebulae. RMxAA, 48, 3

Lopez, J. A., Steffen, W., & Meaburn, J. 1997. Bipolar, Collimated Outbursts in the Planetary Nebula HB 4. ApJ, 485, 697

López-Sánchez, Á. R., Esteban, C., García-Rojas, J., Peimbert, M., & Rodríguez, M. 2007. The Localized Chemical Pollution in NGC 5253 Revisited: Results from Deep Echelle Spectrophotometry. ApJ, 656, 168

Lucy, L. B. & Abbott, D. C. 1993. Multiline transfer and the dynamics of Wolf-Rayet winds. ApJ, 405, 738

Luo, S.-G., Liu, X.-W., & Barlow, M. J. 2001. Chemical abundances of planetary nebulae from optical recombination lines - II. The neon abundance of NGC 7009. MNRAS, 326, 1049

Maciel, W. J. & Dutra, C. M. 1992. Kinematics of disk planetary nebulae. A&A, 262, 271

Marigo, P. 2002. Asymptotic Giant Branch evolution at varying surface C/O ratio: effects of changes in molecular opacities. A&A, 387, 507

Markwardt, C. B. 2009, Non-linear Least-squares Fitting in IDL with MPFIT, in Astronomical Society of the Pacific Conference Series, Vol. 411, Astronomical Data Analysis Software and Systems XVIII, ed. D. A. Bohlender, D. Durand, & P. Dowler, 251

Massey, P., DeGioia-Eastwood, K., & Waterhouse, E. 2001. The Progenitor Masses of Wolf-Rayet Stars and Luminous Blue Variables Determined from Cluster Turnoffs. II. Results from 12 Galactic Clusters and OB Associations. AJ, 121, 1050

Mathis, J. S., Rumpl, W., & Nordsieck, K. H. 1977. The size distribution of interstellar grains. ApJ, 217, 425

McCook, G. P. & Sion, E. M. 1999. A Catalog of Spectroscopically Identified White Dwarfs. ApJS, 121, 1

McKenna, F. C., Keenan, F. P., Kaler, J. B., et al. 1996. [N II] and [O III] Mean Electron Temperatures in Planetary Nebulae. PASP, 108, 610

McLaughlin, B. M. & Bell, K. L. 2000. Electron collisional excitation of Ne III: ($1s^2 2s^2 2p^4$ $^3P_{2,1,0}$,$^1D_2$,$^1S_0$) fine-structure transitions. Journal of Physics B Atomic Molecular Physics, 33, 597

McNabb, I. A., Fang, X., Liu, X.-W., Bastin, R. J., & Storey, P. J. 2013. Plasma diagnostics for planetary nebulae and H ii regions using the N ii and O ii optical recombination lines. MNRAS, 428, 3443

Meatheringham, S. J. & Dopita, M. A. 1991. Optical spectroscopy of Magellanic Cloud planetary nebulae. ApJS, 75, 407

Meatheringham, S. J., Wood, P. R., & Faulkner, D. J. 1988. A study of some southern planetary nebulae. ApJ, 334, 862

Medina, S., Peña, M., Morisset, C., & Stasińska, G. 2006. Galactic Planetary Nebulae with Wolf-Rayet Nuclei III. Kinematical Analysis of a Large Sample of Nebulae. RMxAA, 42, 53

Mellema, G. 1996. Hydrodynamic Models of Planetary Nebulae. Ap&SS, 245, 239

Mellema, G. 1997. The formation of bipolar planetary nebulae. A&A, 321, L29

Méndez, R. H. 1991, Photospheric Abundances in Central Stars of Planeteray Nebulae, and Evolutionary Implications, in IAU Symposium, Vol. 145, Evolution of Stars: the Photospheric Abundance Connection, ed. G. Michaud & A. V. Tutukov, 375

Méndez, R. H. & Niemela, V. S. 1982, A reclassification of WC and 'O VI' central stars of planetary nebulae, and comparison with population I WC stars, in IAU Symposium, Vol. 99, Wolf-Rayet Stars: Observations, Physics, Evolution, ed. C. W. H. De Loore & A. J. Willis, 457–460

Mendoza, C. & Zeippen, C. J. 1982. Transition probabilities for forbidden lines in the 3p3 configuration. MNRAS, 198, 127

Menon, A., Herwig, F., Denissenkov, P. A., et al. 2013. Reproducing the Observed Abundances in RCB and HdC Stars with Post-double-degenerate Merger Models–Constraints on Merger and Post-merger Simulations and Physics Processes. ApJ, 772, 59

Menzel, D. H. 1926. The Planetary Nebulae. PASP, 38, 295

Messier, C. 1781, Catalogue des Nébuleuses & des amas d'Étoiles (Catalog of Nebulae and Star Clusters). Tech. rep.

Milingo, J. B., Kwitter, K. B., Henry, R. B. C., & Cohen, R. E. 2002. Sulfur, Chlorine, and Argon in Planetary Nebulae. IIA. Observations of a Southern Sample. ApJS, 138, 279

Miller Bertolami, M. M. & Althaus, L. G. 2006. Full evolutionary models for PG 1159 stars. Implications for the helium-rich O(He) stars. A&A, 454, 845

Miller Bertolami, M. M., Althaus, L. G., Olano, C., & Jiménez, N. 2011. The diffusion-induced nova scenario: CK Vul and PB8 as possible observational counterparts. MNRAS, 415, 1396

Miller Bertolami, M. M., Althaus, L. G., Serenelli, A. M., & Panei, J. A. 2006. New evolutionary calculations for the born again scenario. A&A, 449, 313

Milne, D. K. & Aller, L. H. 1975. Radio observations at 5 GHz of southern planetary nebulae. A&A, 38, 183

Miszalski, B., Acker, A., Moffat, A. F. J., Parker, Q. A., & Udalski, A. 2009a. Binary planetary nebulae nuclei towards the Galactic bulge. I. Sample discovery, period distribution, and binary fraction. A&A, 496, 813

Miszalski, B., Acker, A., Parker, Q. A., & Moffat, A. F. J. 2009b. Binary planetary nebulae nuclei towards the Galactic bulge. II. A penchant for bipolarity and low-ionisation structures. A&A, 505, 249

Miszalski, B., Crowther, P. A., De Marco, O., et al. 2012. IC 4663: the first unambiguous [WN] Wolf-Rayet central star of a planetary nebula. MNRAS, 423, 934

Mitchell, D. L., Pollacco, D., O'Brien, T. J., et al. 2007. Proof of polar ejection from the close-binary core of the planetary nebula Abell 63. MNRAS, 374, 1404

Molster, F. J., Waters, L. B. F. M., Tielens, A. G. G. M., & Barlow, M. J. 2002. Crystalline silicate dust around evolved stars. I. The sample stars. A&A, 382, 184

Monk, D. J., Barlow, M. J., & Clegg, R. E. S. 1988. An optical spectrophotometric survey of abundances in Magellanic Cloud planetary nebulae. MNRAS, 234, 583

Monteiro, H. & Falceta-Gonçalves, D. 2011. Three-dimensional Photoionization Structure and Distances of Planetary Nebulae. IV. NGC 40. ApJ, 738, 174

Montez, Jr., R., Kastner, J. H., De Marco, O., & Soker, N. 2005. X-Ray Imaging of Planetary Nebulae with Wolf-Rayet-type Central Stars: Detection of the Hot Bubble in NGC 40. ApJ, 635, 381

Moré, J. 1977, The Levenberg-Marquardt Algorithm: Implementation and Theory, in Numerical Analysis, ed. G. A. Watson, Vol. vol. 630 (Springer-Verlag: Berlin), 105

Morgan, D. H., Parker, Q. A., & Cohen, M. 2003. A unique Galactic planetary nebula with a [WN] central star. MNRAS, 346, 719

Morgan, W. W., Keenan, P. C., & Kellman, E. 1943, An atlas of stellar spectra, with an outline of spectral classification

Morisset, C., Schaerer, D., Bouret, J.-C., & Martins, F. 2004. Mid-IR observations of Galactic H II regions: Constraining ionizing spectra of massive stars and the nature of the observed excitation sequences. A&A, 415, 577

Mowlavi, N. & Meynet, G. 2000. Aluminum 26 production in asymptotic giant branch stars. A&A, 361, 959

Napiwotzki, R. 1999. Spectroscopic investigation of old planetaries. IV. Model atmosphere analysis. A&A, 350, 101

Napiwotzki, R. & Schoenberner, D. 1991. Spectroscopic investigation of old planetaries. II - Detection of a 'hybrid' central star. A&A, 249, L16

Napiwotzki, R. & Schoenberner, D. 1995. Spectroscopic investigation of old planetaries. III. Spectral types, magnitudes, and distances. A&A, 301, 545

Nicholls, D. C., Dopita, M. A., & Sutherland, R. S. 2012. Resolving the Electron Temperature Discrepancies in H II Regions and Planetary Nebulae: κ-distributed Electrons. ApJ, 752, 148

Nicholls, D. C., Dopita, M. A., Sutherland, R. S., Kewley, L. J., & Palay, E. 2013. Measuring Nebular Temperatures: The Effect of New Collision Strengths with Equilibrium and κ-distributed Electron Energies. ApJS, 207, 21

Nordhaus, J. & Blackman, E. G. 2006. Low-mass binary-induced outflows from asymptotic giant branch stars. MNRAS, 370, 2004

Nordhaus, J., Blackman, E. G., & Frank, A. 2007. Isolated versus common envelope dynamos in planetary nebula progenitors. MNRAS, 376, 599

Nordhaus, J., Spiegel, D. S., Ibgui, L., Goodman, J., & Burrows, A. 2010. Tides and tidal engulfment in post-main-sequence binaries: period gaps for planets and brown dwarfs around white dwarfs. MNRAS, 408, 631

Nugis, T. & Lamers, H. J. G. L. M. 2000. Mass-loss rates of Wolf-Rayet stars as a function of stellar parameters. A&A, 360, 227

O'Dell, C. R. 1962. A Distance Scale for Planetary Nebulae Based on Emission-Line Fluxes. ApJ, 135, 371

Osterbrock, D. E. & Ferland, G. J. 2006, Astrophysics of gaseous nebulae and active galactic nuclei, ed. Osterbrock, D. E. & Ferland, G. J.

Paczyński, B. 1971. Evolution of Single Stars. VI. Model Nuclei of Planetary Nebulae. Acta Astronomica, 21, 417

Paczynski, B. 1976, Common Envelope Binaries, in IAU Symposium, Vol. 73, Structure and Evolution of Close Binary Systems, ed. P. Eggleton, S. Mitton, & J. Whelan, 75

Parker, Q. A., Phillipps, S., Pierce, M., & et al. 2005. The AAO/UKST SuperCOSMOS Hα survey. MNRAS, 362, 689

Parthasarathy, M., Acker, A., & Stenholm, B. 1998. Weak emission line [WELS] central stars of planetary nebulae are [WC]-PG1159 stars. A&A, 329, L9

Pauldrach, A., Puls, J., Kudritzki, R. P., Méndez, R. H., & Heap, S. R. 1988. Radiation-driven winds of hot stars. V - Wind models for central stars of planetary nebulae. A&A, 207, 123

Paxton, B., Bildsten, L., Dotter, A., et al. 2011. Modules for Experiments in Stellar Astrophysics (MESA). ApJS, 192, 3

Paxton, B., Cantiello, M., Arras, P., et al. 2013. Modules for Experiments in Stellar Astrophysics (MESA): Planets, Oscillations, Rotation, and Massive Stars. ApJS, 208, 4

Peña, M. 1995, New Results in Planetary Nebulae with WR Nuclei. The Evolution of LMC-N66 (Invited paper), in Revista Mexicana de Astronomia y Astrofisica Conference Series, Vol. 3, Revista Mexicana de Astronomia y Astrofisica Conference Series, ed. M. Pena & S. Kurtz, 215

Peña, M., Hamann, W.-R., Ruiz, M. T., Peimbert, A., & Peimbert, M. 2004. A high resolution spectroscopic study of the extraordinary planetary nebula LMC-N66. A&A, 419, 583

Peña, M. & Ruiz, M. T. 1988. A spectrophotometric study of the planetary nebula N66 in the Large Magellanic Cloud. RMxAA, 16, 55

Peña, M., Stasińska, G., Esteban, C., et al. 1998. Galactic planetary nebulae with Wolf-Rayet nuclei. I. Objects with [WC]-early type stars. A&A, 337, 866

Peña, M., Stasińska, G., & Medina, S. 2001. Galactic planetary nebulae with Wolf-Rayet nuclei. II. A consistent observational data set. A&A, 367, 983

Peña, M., Torres-Peimbert, S., Peimbert, M., Ruiz, M. T., & Maza, J. 1994. A thermal pulse in progress in the nucleus of the LMC planetary nebula N66. ApJ, 428, L9

Peña-Guerrero, M. A., Peimbert, A., Peimbert, M., & Ruiz, M. T. 2012. Analysis of Two Small Magellanic Cloud H II Regions Considering Thermal Inhomogeneities: Implications for the Determinations of Extragalactic Chemical Abundances. ApJ, 746, 115

Peimbert, A., Peimbert, M., & Ruiz, M. T. 2005. Chemical Composition of Two H II Regions in NGC 6822 Based on VLT Spectroscopy. ApJ, 634, 1056

Peimbert, M. 1967. Temperature Determinations of H II Regions. ApJ, 150, 825

Peimbert, M. 1971. Planetary Nebulae II. Electron Temperatures and Electron

Densities. Boletin de los Observatorios Tonantzintla y Tacubaya, 6, 29

Peimbert, M., Peimbert, A., Ruiz, M. T., & Esteban, C. 2004. Physical Conditions of the Planetary Nebula NGC 5315 Derived from VLT Echelle Observations and the t^2 Problem. ApJS, 150, 431

Peimbert, M. & Torres-Peimbert, S. 1983, Type I planetary nebulae, in IAU Symposium, Vol. 103, Planetary Nebulae, ed. D. R. Flower, 233–241

Pequignot, D., Petitjean, P., & Boisson, C. 1991. Total and effective radiative recombination coefficients. A&A, 251, 680

Péquignot, D., Walsh, J. R., Zijlstra, A. A., & Dudziak, G. 2000. Third-dredge-up oxygen in planetary nebulae. A&A, 361, L1

Perinotto, M., Schönberner, D., Steffen, M., & Calonaci, C. 2004. The evolution of planetary nebulae. I. A radiation-hydrodynamics parameter study. A&A, 414, 993

Phillips, J. P. 2004. Planetary nebula distances re-examined: an improved statistical scale. MNRAS, 353, 589

Piliugin, L. S. & Khromov, G. S. 1979. Evolution of planetary nebulae and their nuclei - Temperatures of nebular nuclei. Soviet Ast., 23, 425

Poe, C. H., Friend, D. B., & Cassinelli, J. P. 1989. A rotating, magnetic, radiation-driven wind model for Wolf-Rayet stars. ApJ, 337, 888

Porter, R. L., Ferland, G. J., Storey, P. J., & Detisch, M. J. 2012. Improved He I emissivities in the case B approximation. MNRAS, 425, L28

Porter, R. L., Ferland, G. J., Storey, P. J., & Detisch, M. J. 2013. Erratum: 'Improved He I emissivities in the Case B approximation'. MNRAS, 433, L89

Pottasch, S. R. & Bernard-Salas, J. 2006. Planetary nebulae abundances and stellar evolution. A&A, 457, 189

Pottasch, S. R., Surendiranath, R., & Bernard-Salas, J. 2011. Abundances in planetary nebulae: NGC 1535, NGC 6629, He2-108, and Tc1. A&A, 531, A23

Pradhan, A. K., Montenegro, M., Nahar, S. N., & Eissner, W. 2006. [OII] line ratios. MNRAS, 366, L6

Preite-Martinez, A., Acker, A., Koeppen, J., & Stenholm, B. 1989. The Energy-Balance temperature of central stars of galactic planetary nebulae. A&AS, 81, 309

Preite-Martinez, A., Acker, A., Koeppen, J., & Stenholm, B. 1991. The energy-balance temperature of central stars of galactic planetary nebulae. II. A&AS, 88, 121

Preite-Martinez, A. & Pottasch, S. R. 1983. The temperature of central stars of planetary nebulae - The energy-balance method. A&A, 126, 31

Purton, C. R., Feldman, P. A., Marsh, K. A., Allen, D. A., & Wright, A. E. 1982. Radio observations of early-type emission-line stars and related objects. MNRAS, 198, 321

Quirion, P.-O., Fontaine, G., & Brassard, P. 2005. The nature of the driving mechanism in the pulsating hybrid PG 1159 star Abell 43. A&A, 441, 231

Ramsbottom, C. A., Bell, K. L., & Keenan, F. P. 1997. Effective collision strengths for fine-structure forbidden transitions among the 3s^23p^3 levels of AR IV. MNRAS, 284, 754

Ramsbottom, C. A., Bell, K. L., & Stafford, R. P. 1996. Effective Collision Strengths for Electron Impact Excitation of Singly Ionized Sulfur. Atomic Data and Nuclear Data Tables, 63, 57

Ratag, M. A., Pottasch, S. R., Dennefeld, M., & Menzies, J. 1997. Abundances in planetary nebulae near the galactic centre. I. Abundance determinations. A&AS, 126, 297

Rauch, T. 2003. A grid of synthetic ionizing spectra for very hot compact stars from NLTE model atmospheres. A&A, 403, 709

Reid, M. J., Menten, K. M., Zheng, X. W., et al. 2009. Trigonometric Parallaxes of Massive Star-Forming Regions. VI. Galactic Structure, Fundamental Parameters, and Noncircular Motions. ApJ, 700, 137

Reid, W. A. & Parker, Q. A. 2010. An Evaluation of the Excitation-Class Parameter for the Central Stars of Planetary Nebulae. PASA, 27, 187

Richer, M. G., Báez, S.-H., López, J. A., Riesgo, H., & García-Díaz, M. T. 2009. What Can We Learn About the Kinematics of Bright Extragalactic Planetary Nebulae? RMxAA, 45, 239

Robinson, G. J., Reay, N. K., & Atherton, P. D. 1982. Measurements of expansion velocities in planetary nebulae. MNRAS, 199, 649

Roeser, S., Demleitner, M., & Schilbach, E. 2010. The PPMXL Catalog of Positions and Proper Motions on the ICRS. Combining USNO-B1.0 and the Two

Micron All Sky Survey (2MASS). AJ, 139, 2440

Rola, C. & Stasińska, G. 1994. The carbon abundance problem in planetary nebulae. A&A, 282, 199

Rubin, R. H., Bhatt, N. J., Dufour, R. J., et al. 2002. Temperature variations from Hubble Space Telescope imagery and spectroscopy of NGC 7009. MNRAS, 334, 777

Russell, H. N., Dugan, R. S., Stewart, J. Q., & Young, C. A. 1926, Astronomy; a revision of Young's Manual of astronomy

Sackmann, I.-J., Smith, R. L., & Despain, K. H. 1974. Carbon and eruptive stars: surface enrichment of lithium, carbon, nitrogen, and ^{13}C by deep mixing. ApJ, 187, 555

Sahai, R., Morris, M. R., & Villar, G. G. 2011. Young Planetary Nebulae: Hubble Space Telescope Imaging and a New Morphological Classification System. AJ, 141, 134

Sahai, R. & Trauger, J. T. 1998. Multipolar Bubbles and Jets in Low-Excitation Planetary Nebulae: Toward a New Understanding of the Formation and Shaping of Planetary Nebulae. AJ, 116, 1357

Saio, H. & Jeffery, C. S. 2000. The evolution of a rapidly accreting helium white dwarf to become a low-luminosity helium star. MNRAS, 313, 671

Saio, H. & Jeffery, C. S. 2002. Merged binary white dwarf evolution: rapidly accreting carbon-oxygen white dwarfs and the progeny of extreme helium stars. MNRAS, 333, 121

Salaris, M. & Cassisi, S. 2005, Evolution of Stars and Stellar Populations

Sawey, P. M. J. & Berrington, K. A. 1993. Collision Strengths from a 29-State R-Matrix Calculation on Electron Excitation in Helium. Atomic Data and Nuclear Data Tables, 55, 81

Scalo, J. M., Despain, K. H., & Ulrich, R. K. 1975. Studies of evolved stars. V - Nucleosynthesis in hot-bottom convective envelopes. ApJ, 196, 805

Schlegel, D. J., Finkbeiner, D. P., & Davis, M. 1998. Maps of Dust Infrared Emission for Use in Estimation of Reddening and Cosmic Microwave Background Radiation Foregrounds. ApJ, 500, 525

Schneider, S. E., Terzian, Y., Purgathofer, A., & Perinotto, M. 1983. Radial velocities of planetary nebulae. ApJS, 52, 399

Schönberner, D. 1981. Late stages of stellar evolution - Central stars of planetary nebulae. A&A, 103, 119

Schönberner, D. 1983. Late stages of stellar evolution. II - Mass loss and the transition of asymptotic giant branch stars into hot remnants. ApJ, 272, 708

Schönberner, D., Jacob, R., Sandin, C., & Steffen, M. 2010. The evolution of planetary nebulae. VII. Modelling planetary nebulae of distant stellar systems. A&A, 523, A86

Schönberner, D., Jacob, R., & Steffen, M. 2005b. The evolution of planetary nebulae. III. Internal kinematics and expansion parallaxes. A&A, 441, 573

Schönberner, D., Jacob, R., Steffen, M., et al. 2005a. The evolution of planetary nebulae. II. Circumstellar environment and expansion properties. A&A, 431, 963

Schwarz, H. E., Corradi, R. L. M., & Melnick, J. 1992. A catalogue of narrow band images of planetary nebulae. A&AS, 96, 23

Schwarz, H. E. & Monteiro, H. 2006. Three-Dimensional Photoionization Structure and Distances of Planetary Nebulae. III. NGC 6781. ApJ, 648, 430

Schwarzschild, M. & Härm, R. 1965. Thermal Instability in Non-Degenerate Stars. ApJ, 142, 855

Seaton, M. J. 1979a. Extinction of NGC 7027. MNRAS, 187, 785

Seaton, M. J. 1979b. Interstellar extinction in the UV. MNRAS, 187, 73P

Secchi, A. 1867. Spectral Studies on Some of the Planetary Nebulæ. Astronomical register, 5, 40

Shaw, R. A. & Dufour, R. J. 1995. Software for the Analysis of Emission Line Nebulae. PASP, 107, 896

Shaw, R. A. & Kaler, J. B. 1989. Apparent magnitudes of luminous planetary nebula nuclei. II - A survey of southern hemisphere planetary nebulae. ApJS, 69, 495

Shklovsky, I. S. 1956. Astr. Zh., 33, 315

Siess, L. 2006. Evolution of massive AGB stars. I. Carbon burning phase. A&A, 448, 717

Siess, L., Izzard, R. G., Davis, P. J., & Deschamps, R. 2013. BINSTAR: a new binary stellar evolution code. Tidal interactions. A&A, 550, A100

Sion, E. M., Liebert, J., & Starrfield, S. G. 1985. Discovery of oxygen in the PG 1159 degenerate stars - A direct evolutionary link to O VI planetary nebula nuclei and confirmation of pulsation theory. ApJ, 292, 471

Smith, L. F. 1968. A revised spectral classification system and a new catalogue for galactic Wolf-Rayet stars. MNRAS, 138, 109

Smith, L. F. & Aller, L. H. 1969. On the Classification of Emission-Line Spectra of Planetary Nuclei. ApJ, 157, 1245

Smith, L. F., Shara, M. M., & Moffat, A. F. J. 1990. Distances of Galactic WC stars from emission-line fluxes and a quantification of the WC classification. ApJ, 358, 229

Smith, L. F., Shara, M. M., & Moffat, A. F. J. 1996. A three-dimensional classification for WN stars. MNRAS, 281, 163

Smith, L. J., Crowther, P. A., & Prinja, R. K. 1994. A study of the luminous blue variable candidate He 3-519 and its surrounding nebula. A&A, 281, 833

Smith, N., Bally, J., & Walawender, J. 2007. And in the Darkness Bind Them: Equatorial Rings, B[e] Supergiants, and the Waists of Bipolar Nebulae. AJ, 134, 846

Smits, D. P. 1996. Theoretical HeI line intensities in low-density plasmas. MNRAS, 278, 683

Sofia, U. J., Cardelli, J. A., & Savage, B. D. 1994. The abundant elements in interstellar dust. ApJ, 430, 650

Sofia, U. J. & Jenkins, E. B. 1998. Interstellar Medium Absorption Profile Spectrograph Observations of Interstellar Neutral Argon and the Implications for Partially Ionized Gas. ApJ, 499, 951

Soker, N. 1990. On the formation of ansae in planetary nebulae. AJ, 99, 1869

Soker, N. 2006. Why Magnetic Fields Cannot Be the Main Agent Shaping Planetary Nebulae. PASP, 118, 260

Soker, N. & Harpaz, A. 1992. Can a single AGB star form an axially symmetric planetary nebula? PASP, 104, 923

Soker, N. & Livio, M. 1994. Disks and jets in planetary nebulae. ApJ, 421, 219

Springmann, U. 1994. Multiple resonance line scattering and the 'momentum problem' in Wolf-Rayet star winds. A&A, 289, 505

Staff, J. E., Menon, A., Herwig, F., et al. 2012. Do R Coronae Borealis Stars Form from Double White Dwarf Mergers? ApJ, 757, 76

Stafford, R. P., Bell, K. L., Hibbert, A., & Wijesundera, W. P. 1994. Electron Impact Excitation of NII - Fine Structure Collision Strengths and Maxwellian-Averaged Rate Coefficients. MNRAS, 268, 816

Stancliffe, R. J. & Jeffery, C. S. 2007. Mass loss and yield uncertainty in low-mass asymptotic giant branch stars. MNRAS, 375, 1280

Stanghellini, L., Corradi, R. L. M., & Schwarz, H. E. 1993. The correlations between planetary nebula morphology and central star evolution. A&A, 279, 521

Stanghellini, L. & Haywood, M. 2010. The Galactic Structure and Chemical Evolution Traced by the Population of Planetary Nebulae. ApJ, 714, 1096

Stanghellini, L., Shaw, R. A., Balick, B., et al. 2003. Space Telescope Imaging Spectrograph Slitless Observations of Small Magellanic Cloud Planetary Nebulae: A Study on Morphology, Emission-Line Intensity, and Evolution. ApJ, 596, 997

Stanghellini, L., Shaw, R. A., Mutchler, M., et al. 2002. Optical Slitless Spectroscopy of Large Magellanic Cloud Planetary Nebulae: A Study of the Emission Lines and Morphology. ApJ, 575, 178

Stanghellini, L., Shaw, R. A., & Villaver, E. 2008. The Magellanic Cloud Calibration of the Galactic Planetary Nebula Distance Scale. ApJ, 689, 194

Stasińska, G. 2005. Biases in abundance derivations for metal-rich nebulae. A&A, 434, 507

Stasińska, G., Peña, M., Bresolin, F., & Tsamis, Y. G. 2013. Planetary nebulae and H ii regions in the spiral galaxy NGC 300. Clues on the evolution of abundance gradients and on AGB nucleosynthesis. A&A, 552, A12

Stasińska, G., Richer, M. G., & McCall, M. L. 1998. The planetary nebulae populations in five galaxies: abundance patterns and evolution. A&A, 336, 667

Stasińska, G. & Szczerba, R. 1999. The dust content of planetary nebulae: a reappraisal. A&A, 352, 297

Stasińska, G. & Tylenda, R. 1990. On the relation between the nitrogen enhancement in planetary nebulae and the mass of the central stars. A&A, 240, 467

Steffen, W., García-Segura, G., & Koning, N. 2009. Hydrodynamical Velocity Fields in Planetary Nebulae. ApJ, 691, 696

Steffen, W., Koning, N., Wenger, S., Morisset, C., & Magnor, M. 2011. Shape: A 3D Modeling Tool for Astrophysics. IEEE Transactions on Visualization and Computer Graphics, 17, 454

Steffen, W. & López, J. A. 2006. Morpho-Kinematic Modeling of Gaseous Nebulae with SHAPE. RMxAA, 42, 99

Storey, P. J. 1994. Recombination coefficients for O II lines at nebular temperatures and densities. A&A, 282, 999

Storey, P. J. & Hummer, D. G. 1995. Recombination line intensities for hydrogenic ions-IV. Total recombination coefficients and machine-readable tables for Z=1 to 8. MNRAS, 272, 41

Storey, P. J. & Sochi, T. 2013. Electron temperatures and free-electron energy distributions of nebulae from C II dielectronic recombination lines. MNRAS, 430, 599

Storey, P. J. & Zeippen, C. J. 2000. Theoretical values for the [Oiii] 5007/4959 line-intensity ratio and homologous cases. MNRAS, 312, 813

Straniero, O., Chieffi, A., Limongi, M., et al. 1997. Evolution and Nucleosynthesis in Low-Mass Asymptotic Giant Branch Stars. I. Formation of Population I Carbon Stars. ApJ, 478, 332

Tajitsu, A. & Tamura, S. 1998. A New Distance Indicator to Galactic Planetary Nebulae Based upon IRAS Fluxes. AJ, 115, 1989

Tayal, S. S. & Gupta, G. P. 1999. Collision Strengths for Electron Collision Excitation of Fine-Structure Levels in S III. ApJ, 526, 544

Todt, H., Kniazev, A. Y., Gvaramadze, V. V., et al. 2013. Abell 48 - a rare WN-type central star of a planetary nebula. MNRAS, 430, 2302

Todt, H., Peña, M., Hamann, W.-R., & Gräfener, G. 2010. The central star of the planetary nebula PB 8: a Wolf-Rayet-type wind of an unusual WN/WC chemical composition. A&A, 515, A83

Torres, A. V., Conti, P. S., & Massey, P. 1986. Spectroscopic studies of Wolf-Rayet stars. III - The WC subclass. ApJ, 300, 379

Torres-Peimbert, S. & Peimbert, M. 1977. Photoelectric photometry and physical conditions of planetary nebulae. RMxAA, 2, 181

Torres-Peimbert, S., Peimbert, M., & Daltabuit, E. 1980. IUE and visual observations of the Orion Nebula and IC 418 - The carbon abundance. ApJ, 238, 133

Torres-Peimbert, S., Peimbert, M., Ruiz, M. T., & Pena, M. 1993, Spectrophotometry of Selected Planetary Nebulae of Type I in the Magellanic Clouds, in IAU Symposium, Vol. 155, Planetary Nebulae, ed. R. Weinberger & A. Acker, 584

Tsamis, Y. G., Barlow, M. J., Liu, X.-W., Danziger, I. J., & Storey, P. J. 2003a. A deep survey of heavy element lines in planetary nebulae - I. Observations and forbidden-line densities, temperatures and abundances. MNRAS, 345, 186

Tsamis, Y. G., Barlow, M. J., Liu, X.-W., Danziger, I. J., & Storey, P. J. 2003b. Heavy elements in Galactic and Magellanic Cloud HII regions: recombination-line versus forbidden-line abundances. MNRAS, 338, 687

Tsamis, Y. G., Barlow, M. J., Liu, X.-W., Storey, P. J., & Danziger, I. J. 2004. A deep survey of heavy element lines in planetary nebulae - II. Recombination-line abundances and evidence for cold plasma. MNRAS, 353, 953

Tsamis, Y. G. & Péquignot, D. 2005. A photoionization-modelling study of 30 Doradus: the case for small-scale chemical inhomogeneity. MNRAS, 364, 687

Tsamis, Y. G., Walsh, J. R., Péquignot, D., et al. 2008. Integral field spectroscopy of planetary nebulae: mapping the line diagnostics and hydrogen-poor zones with VLT FLAMES. MNRAS, 386, 22

Tylenda, R., Acker, A., Raytchev, B., Stenholm, B., & Gleizes, F. 1991. The B and V magnitudes of the central stars of planetary nebulae. A&AS, 89, 77

Tylenda, R., Acker, A., & Stenholm, B. 1993. Wolf-Rayet Nuclei of Planetary Nebulae - Observations and Classification. A&AS, 102, 595

Tylenda, R., Siódmiak, N., Górny, S. K., Corradi, R. L. M., & Schwarz, H. E. 2003. Angular dimensions of planetary nebulae. A&A, 405, 627

Tyndall, A. A., Jones, D., Lloyd, M., O'Brien, T. J., & Pollacco, D. 2012. A study of the kinematics and binary-induced shaping of the planetary nebula HaTr 4. MNRAS, 422, 1804

Vacca, W. D., Garmany, C. D., & Shull, J. M. 1996. The Lyman-Continuum Fluxes and Stellar Parameters of O and Early B-Type Stars. ApJ, 460, 914

van der Hucht, K. A. 2001. The VIIth catalogue of galactic Wolf-Rayet stars.

New Astro. Rev., 45, 135

van der Hucht, K. A., Conti, P. S., Lundstrom, I., & Stenholm, B. 1981. The Sixth Catalogue of galactic Wolf-Rayet stars, their past and present. Space Sci. Rev., 28, 227

van Dokkum, P. G. 2001. Cosmic-Ray Rejection by Laplacian Edge Detection. PASP, 113, 1420

van Hoof, P. A. M. & van de Steene, G. C. 1999. Photoionization modelling of planetary nebulae - II. Galactic bulge nebulae, a comparison with literature results. MNRAS, 308, 623

Vassiliadis, E. & Wood, P. R. 1993. Evolution of low- and intermediate-mass stars to the end of the asymptotic giant branch with mass loss. ApJ, 413, 641

Vassiliadis, E. & Wood, P. R. 1994. Post-asymptotic giant branch evolution of low- to intermediate-mass stars. ApJS, 92, 125

Ventura, P. & D'Antona, F. 2005. Full computation of massive AGB evolution. I. The large impact of convection on nucleosynthesis. A&A, 431, 279

Ventura, P., Di Criscienzo, M., Carini, R., & D'Antona, F. 2013. Yields of AGB and SAGB models with chemistry of low- and high-metallicity globular clusters. MNRAS, 431, 3642

Verner, D. A. & Yakovlev, D. G. 1995. Analytic FITS for partial photoionization cross sections. A&AS, 109, 125

Verner, D. A., Yakovlev, D. G., Band, I. M., & Trzhaskovskaya, M. B. 1993. Subshell Photoionization Cross Sections and Ionization Energies of Atoms and Ions from He to Zn. Atomic Data and Nuclear Data Tables, 55, 233

Viegas, S. M. & Clegg, R. E. S. 1994. Density Condensations in Planetary Nebulae and the Electron Temperature. MNRAS, 271, 993

Wachter, S., Mauerhan, J. C., Van Dyk, S. D., et al. 2010. A Hidden Population of Massive Stars with Circumstellar Shells Discovered with the Spitzer Space Telescope. AJ, 139, 2330

Wang, W. & Liu, X.-W. 2007. Elemental abundances of Galactic bulge planetary nebulae from optical recombination lines. MNRAS, 381, 669

Wang, W., Liu, X.-W., Zhang, Y., & Barlow, M. J. 2004. A reexamination of electron density diagnostics for ionized gaseous nebulae. A&A, 427, 873

Webbink, R. F. 1984. Double white dwarfs as progenitors of R Coronae Borealis stars and Type I supernovae. ApJ, 277, 355

Webster, B. L. 1975. A survey of planetary nebulae towards the galactic bulge. MNRAS, 173, 437

Webster, B. L. 1988. The abundances and mass distribution of planetary nebulae in the galactic bulge. MNRAS, 230, 377

Webster, B. L. & Glass, I. S. 1974. The coolest Wolf-Rayet stars. MNRAS, 166, 491

Weidmann, W. A., Gamen, R., Díaz, R. J., & Niemela, V. S. 2008. Discovery of a [WO] central star in the planetary nebula Th 2-A. A&A, 488, 245

Weinberger, R. 1989. A catalogue of expansion velocities of Galactic planetary nebulae. A&AS, 78, 301

Werner, K. 2001. Properties of atmospheres and winds of H-deficient central stars and related objects. Ap&SS, 275, 27

Werner, K. & Herwig, F. 2006. The Elemental Abundances in Bare Planetary Nebula Central Stars and the Shell Burning in AGB Stars. PASP, 118, 183

Wesemael, F., Greenstein, J. L., Liebert, J., et al. 1993. An atlas of optical spectra of white-dwarf stars. PASP, 105, 761

Wesson, R., Barlow, M. J., Liu, X.-W., et al. 2008. The hydrogen-deficient knot of the 'born-again' planetary nebula Abell 58 (V605 Aql). MNRAS, 383, 1639

Wesson, R. & Liu, X.-W. 2004. Physical conditions in the planetary nebula NGC 6543. MNRAS, 351, 1026

Wesson, R., Liu, X.-W., & Barlow, M. J. 2003. Physical conditions in the planetary nebula Abell 30. MNRAS, 340, 253

Wesson, R., Liu, X.-W., & Barlow, M. J. 2005. The abundance discrepancy - recombination line versus forbidden line abundances for a northern sample of galactic planetary nebulae. MNRAS, 362, 424

Wesson, R., Stock, D. J., & Scicluna, P. 2012. Understanding and reducing statistical uncertainties in nebular abundance determinations. MNRAS, 422, 3516

West, R. M. 1976. Three southern planetary nebulae. PASP, 88, 896

Wright, N. J., Barlow, M. J., Ercolano, B., & Rauch, T. 2011. A 3D photoionization model of the extreme planetary nebula NGC 6302. MNRAS, 418, 370

Wyse, A. B. 1942. The Spectra of Ten Gaseous Nebulae. ApJ, 95, 356

Yamamura, I., Makiuti, S., Ikeda, N., et al. 2010. AKARI/FIS All-Sky Survey Point Source Catalogues (ISAS/JAXA, 2010). VizieR Online Data Catalog, 2298, 0

Yi, S. K., Kim, Y.-C., & Demarque, P. 2003. The Y^2 Stellar Evolutionary Tracks. ApJS, 144, 259

Yuan, H.-B., Liu, X.-W., Péquignot, D., et al. 2011. Three-dimensional chemically homogeneous and bi-abundance photoionization models of the 'super-metal-rich' planetary nebula NGC 6153. MNRAS, 411, 1035

Zanstra, H. 1927. An Application of the Quantum Theory to the Luminosity of Diffuse Nebulae. ApJ, 65, 50

Zeippen, C. J. 1987. Improved radiative transition probabilities for O II forbidden lines. A&A, 173, 410

Zhang, C. Y. 1995. A statistical distance scale for Galactic planetary nebulae. ApJS, 98, 659

Zhang, C. Y. & Kwok, S. 1993. Trace of planetary nebula evolution by distance-independent parameters. ApJS, 88, 137

Zhang, X. & Jeffery, C. S. 2012. Evolutionary models for double helium white dwarf mergers and the formation of helium-rich hot subdwarfs. MNRAS, 419, 452

Zhang, Y. & Liu, X.-W. 2003. Optical spectrum of the planetary nebula M 2-24. A&A, 404, 545

Zhang, Y., Liu, X.-W., Liu, Y., & Rubin, R. H. 2005. Helium recombination spectra as temperature diagnostics for planetary nebulae. MNRAS, 358, 457

Zhang, Y., Liu, X.-W., Wesson, R., et al. 2004. Electron temperatures and densities of planetary nebulae determined from the nebular hydrogen recombination spectrum and temperature and density variations. MNRAS, 351, 935

Zhang, Y., Liu, X.-W., & Zhang, B. 2014. H I Free-Bound Emission of Planetary Nebulae with Large Abundance Discrepancies: Two-component Models versus κ-distributed Electrons. ApJ, 780, 93

Zijlstra, A. A., van Hoof, P. A. M., Chapman, J. M., & Loup, C. 1994. Radio and infrared emission from a [WC]-type planetary nebula in the LMC. A&A, 290, 228

Zuckerman, B. & Aller, L. H. 1986. Origin of planetary nebulae - Morphology, carbon-to-oxygen abundance ratios, and central star multiplicity. ApJ, 301, 772

Part IV

Appendices

Appendix A

Kinematic maps and Spatio-kinematical Models

This appendix contains spatial-resolved kinematic maps for all nebulae analyzed in Chapter 2. Based on observations made with the ANU 2.3-m Telescope at the Siding Spring Observatory.

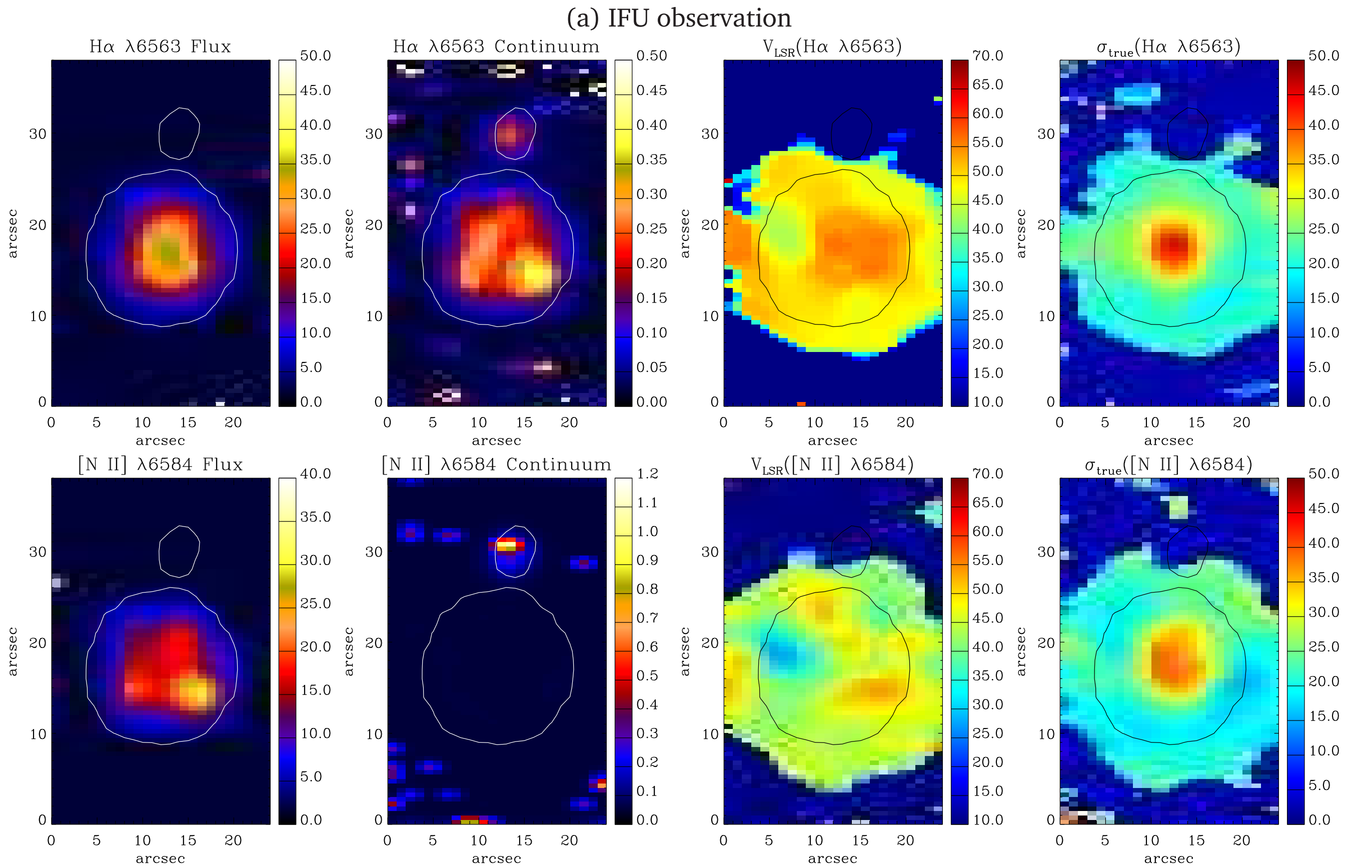

Figure A.1: (a) Kinematic maps of PB 6 in Hα λ6563 Å (top) and [N II] λ6584 Å (bottom). From left to right: spatial distribution maps of flux intensity, continuum, LSR velocity and velocity dispersion. Flux unit is in 10^{-15} erg s^{-1} cm^{-2} spaxel^{-1}, continuum in 10^{-15} erg s^{-1} cm^{-2} Å^{-1} spaxel^{-1}, and velocity unit in km s^{-1}. North is up and east is toward the left-hand side. White/black contour lines show the distribution of the narrow-band emission of Hα in arbitrary unit obtained from the SHS. (b) The STIS/MIRVIS filter image taken by the Hubble Space Telescope (*HST*; Observing program 12600; PI. Dufour, 2012).

(b) *HST* image

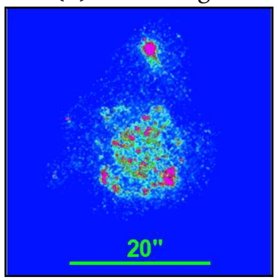

Figure A.1: (continued)

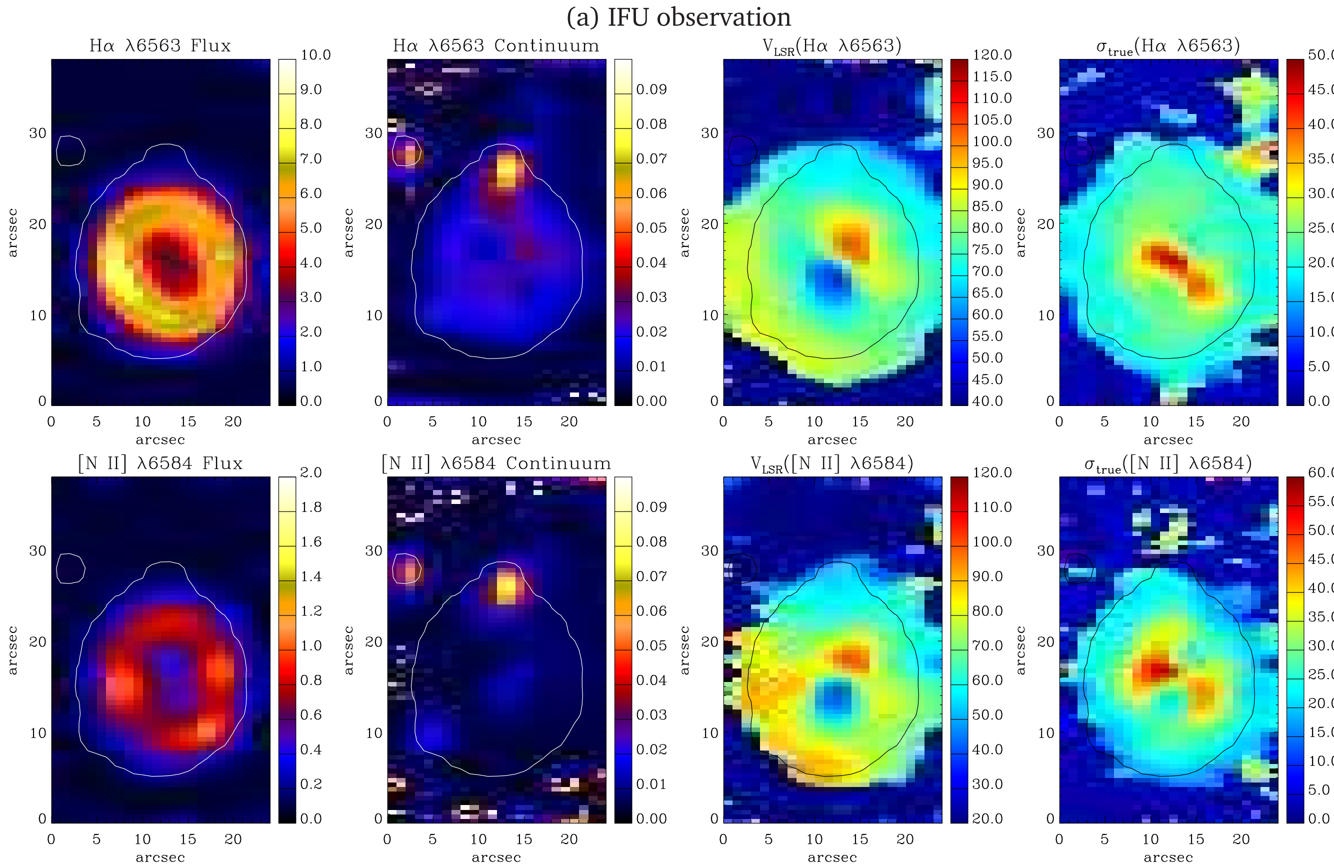

Figure A.2: (a) As Figure A.1 but for M 3-30. (b) The SHAPE mesh model before rendering at the best-fitting inclination, two different orientations (inclination: 90° and 0°, respectively), and corresponding rendered model. (c) The Hα+[N II] narrow band image from Schwarz et al. (1992). (d) The normalized synthetic intensity and radial velocity maps produced by the model.

(b) SHAPE mesh model

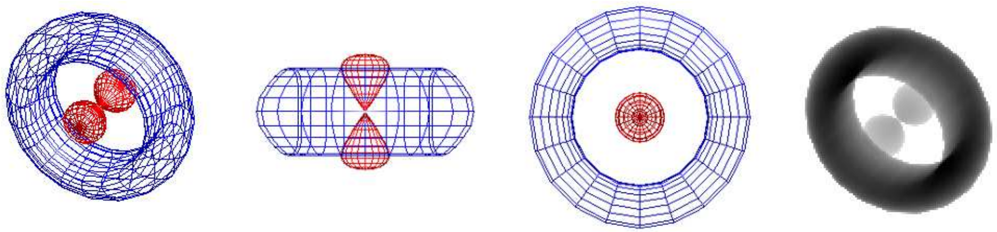

(c) Hα+[N II] narrow band image

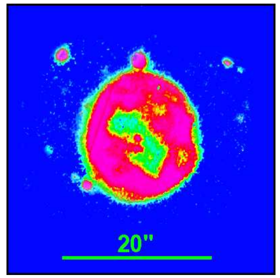

(d) SHAPE model results

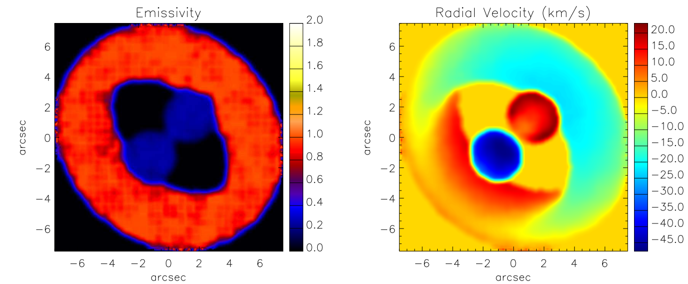

Figure A.2: (continued)

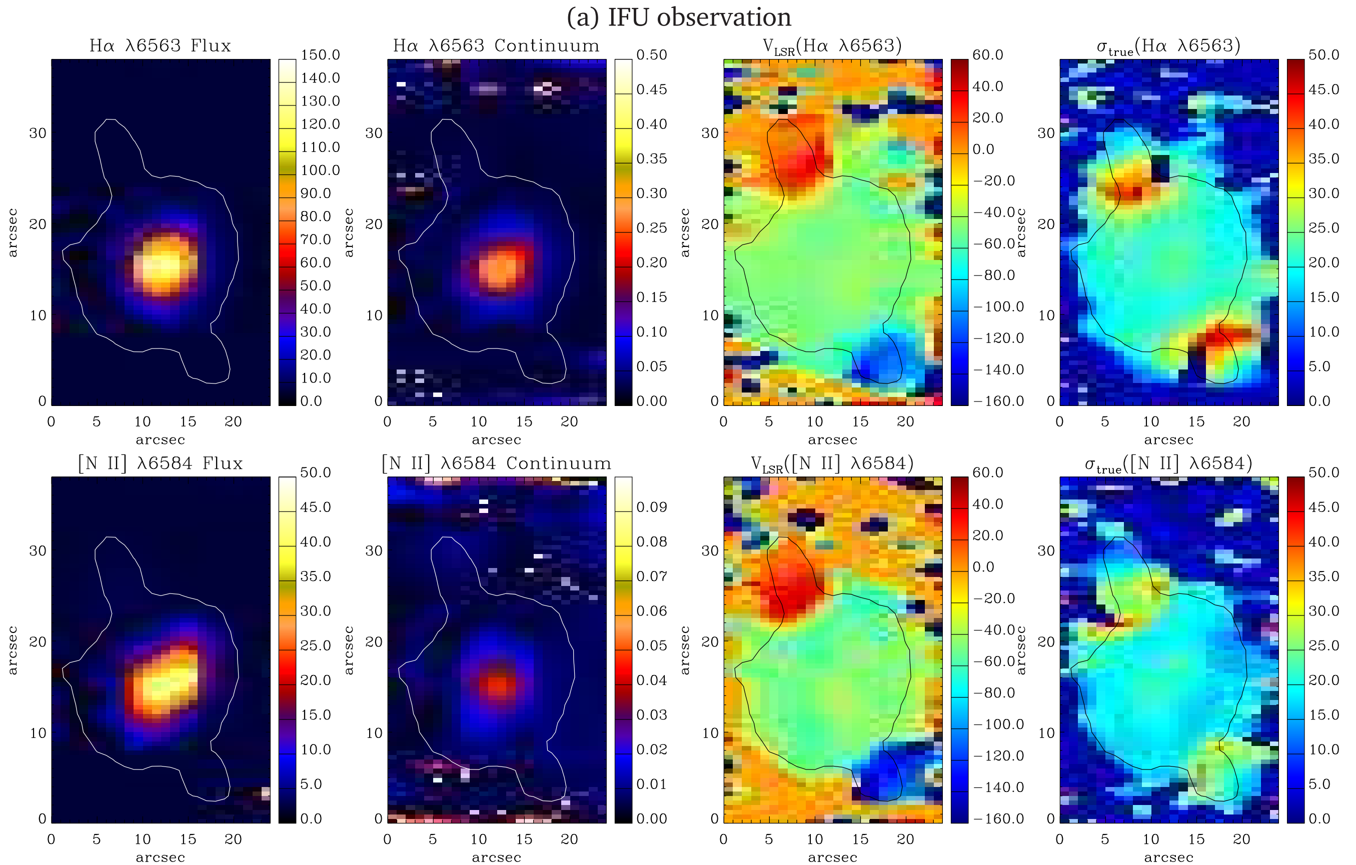

Figure A.3: (a) As Figure A.1 but for Hb 4. (b) The SHAPE mesh model before rendering at the best-fitting inclination, two different orientations (inclination: 90° and 0°, respectively), and corresponding rendered model. (c) The *HST* images taken by F658N filters (Observing program 6347; PI. Borkowski, 1996). (d) The normalized synthetic intensity and radial velocity maps produced by the model.

(b) SHAPE mesh model

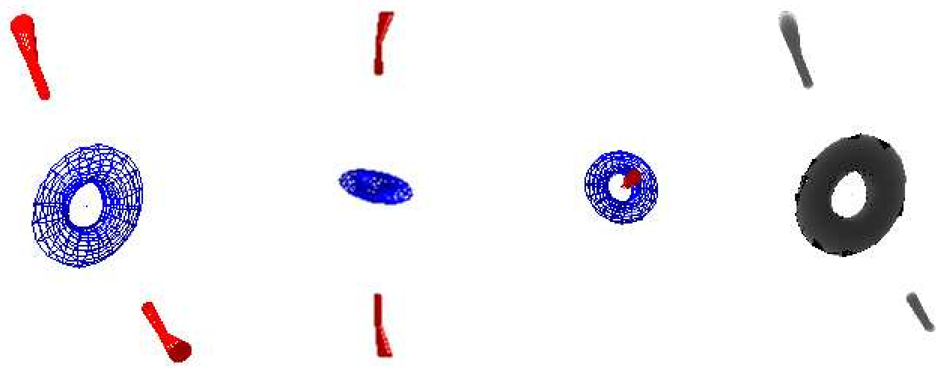

(c) *HST* image

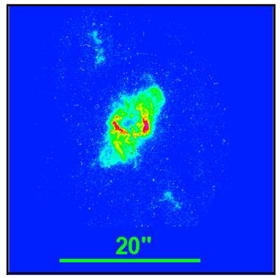

(d) SHAPE model results

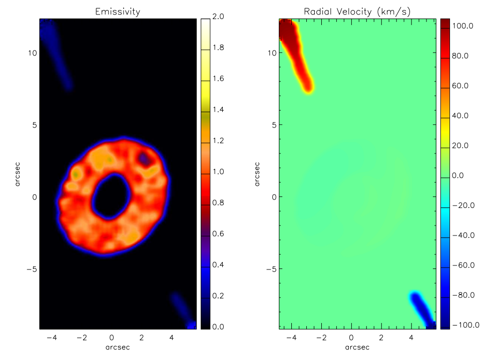

Figure A.3: (continued)

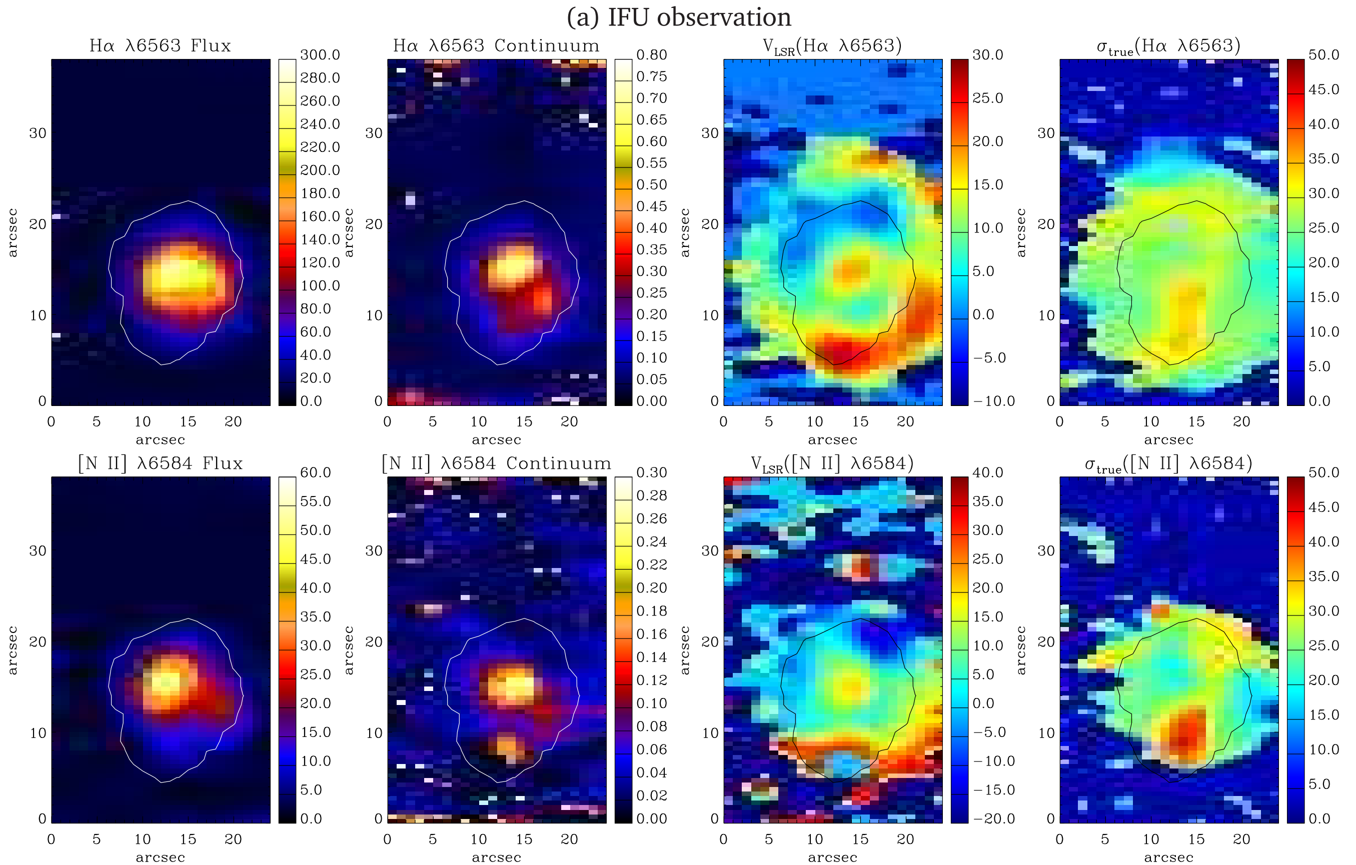

Figure A.4: (a) As Figure A.1 but for IC 1297. (b) The SHAPE mesh model before rendering at the best-fitting inclination, two different orientations (inclination: 90° and 0°, respectively), and corresponding rendered model. (c) The Hα+[N II] narrow band image from Schwarz et al. (1992). (d) The normalized synthetic intensity and radial velocity maps produced by the model.

(b) SHAPE mesh model

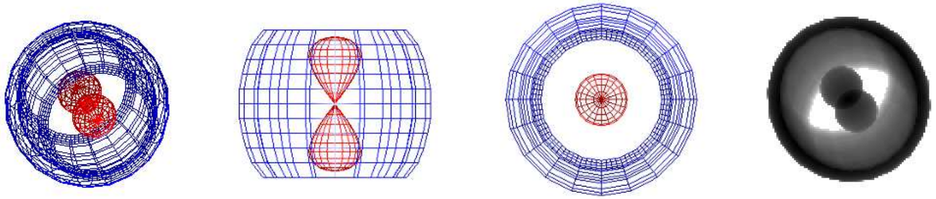

(c) Hα+[N II] narrow band image

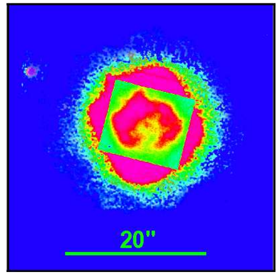

(d) SHAPE model results

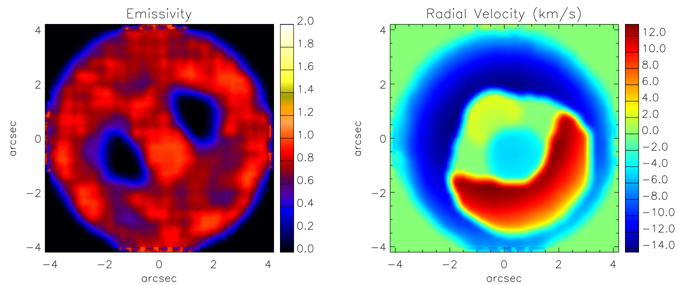

Figure A.4: (continued)

(a) IFU observation

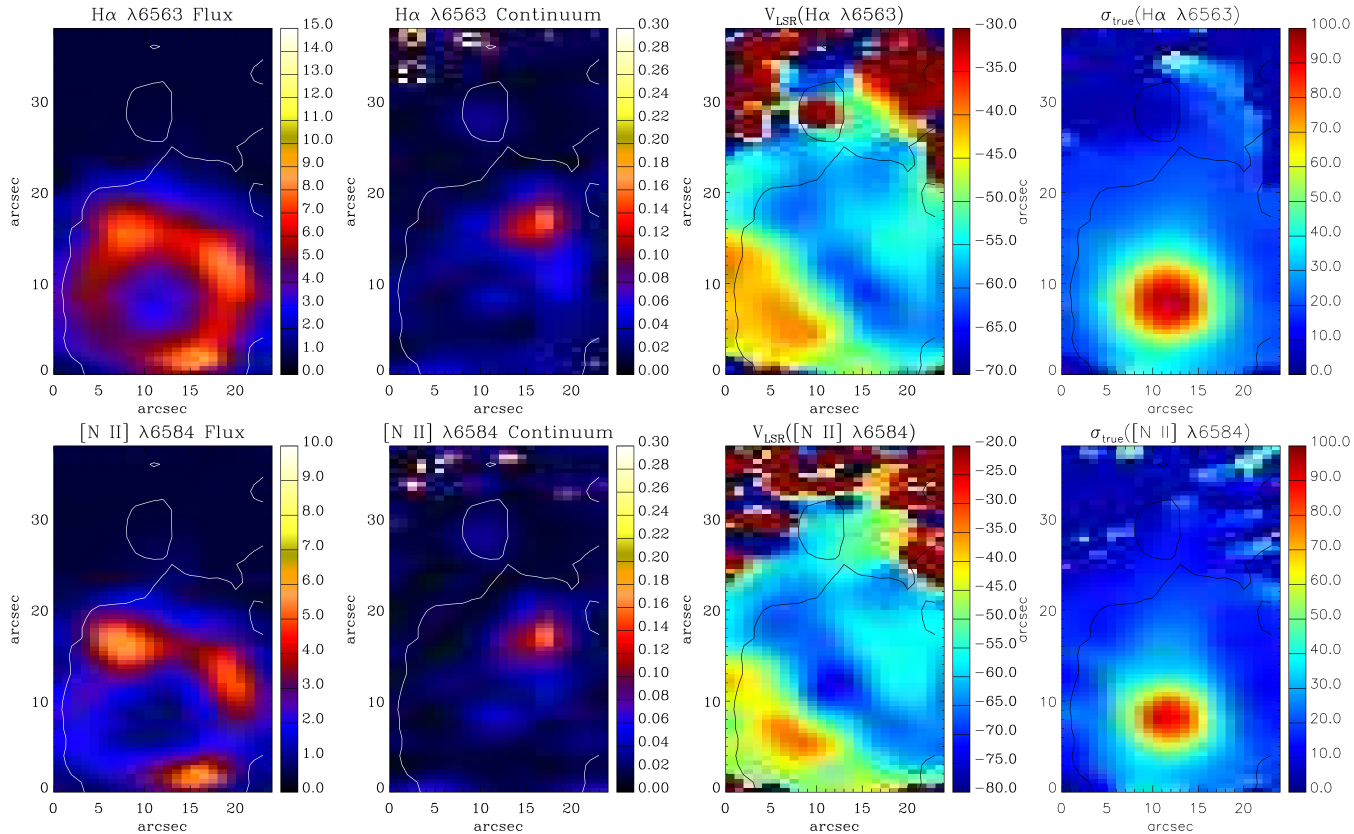

Figure A.5: (a) As Figure A.1 but for Th 2-A. (b) The SHAPE mesh model before rendering at the best-fitting inclination, two different orientations (inclination: 90° and 0°, respectively), and corresponding rendered model. (c) The Hα narrow band image from Górny et al. (1999). (d) The normalized synthetic intensity and radial velocity maps produced by the model.

(b) SHAPE mesh model

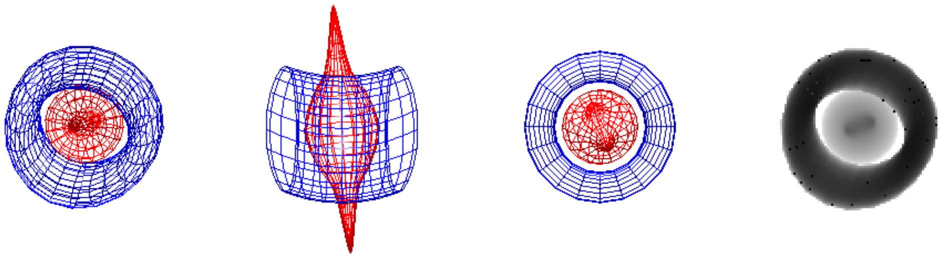

(c) Hα narrow band image

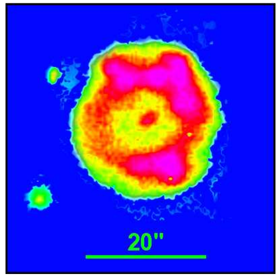

(d) SHAPE model results

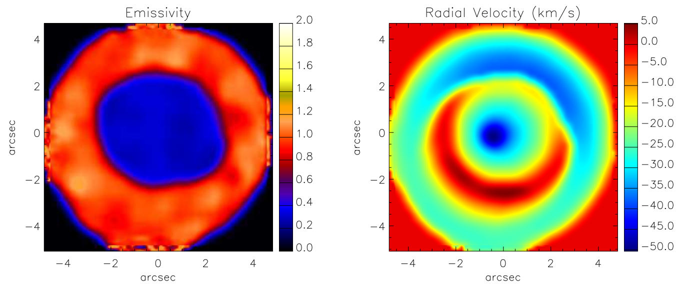

Figure A.5: (continued)

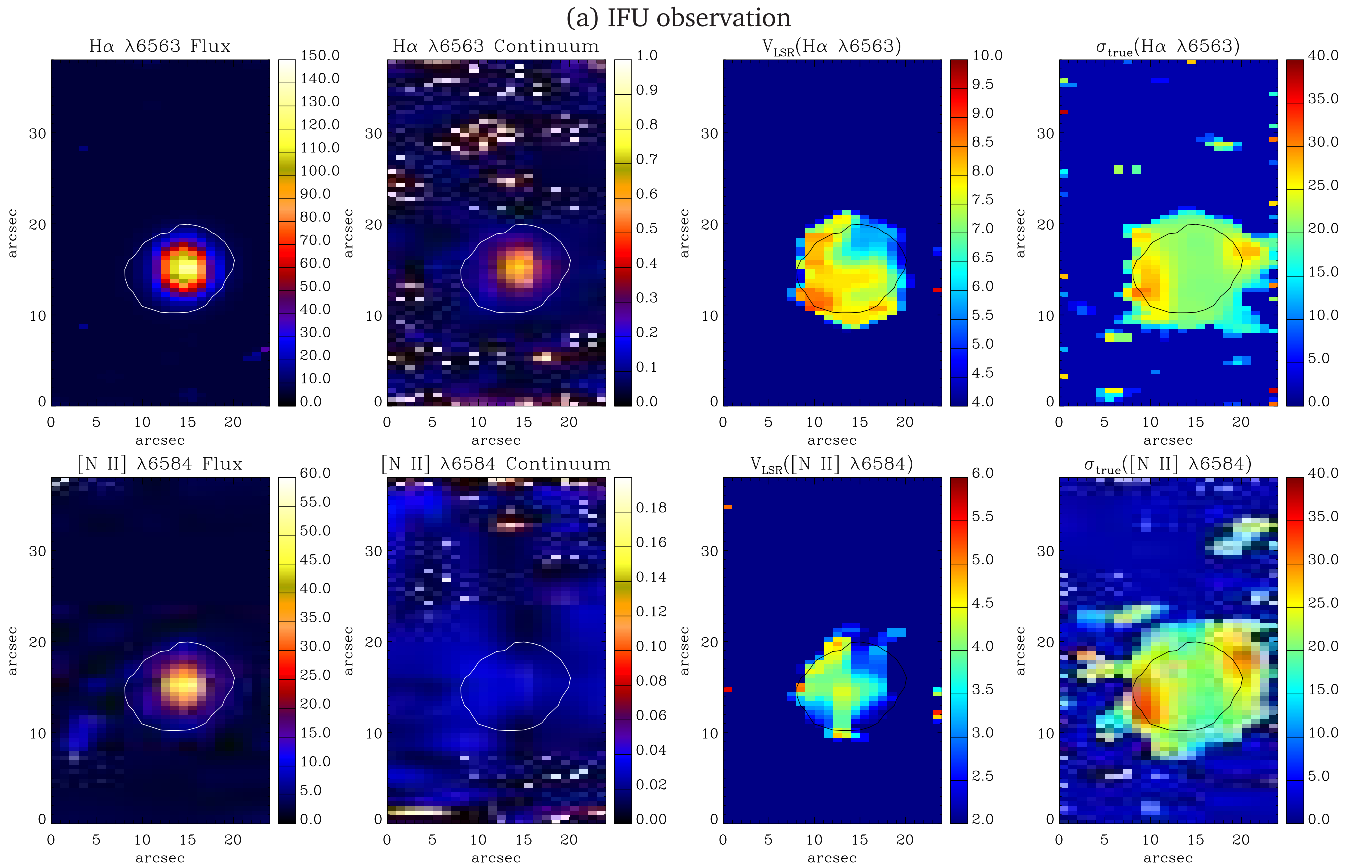

Figure A.6: (a) As Figure A.1 but for Pe 1-1. (b) The SHAPE mesh model before rendering at the best-fitting inclination, two different orientations (inclination: 90° and 0°, respectively), and corresponding rendered model. (c) The *HST* image taken by F350LP filters (Observing program 11657; PI. Stanghellini, 2009).

(b) SHAPE mesh model

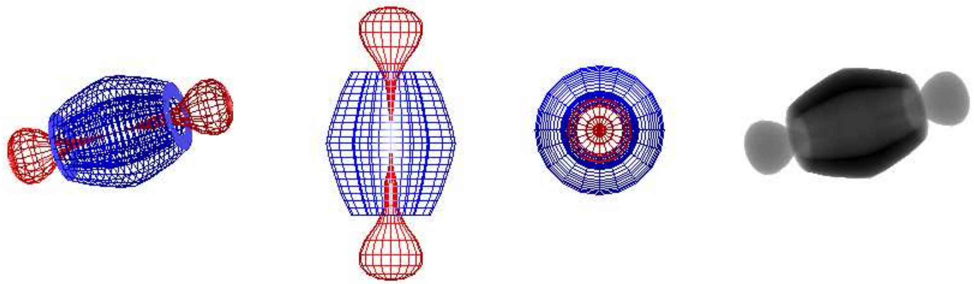

(c) *HST* image

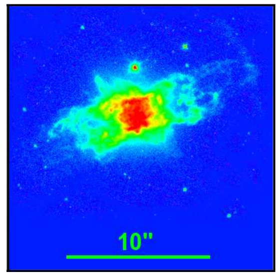

Figure A.6: (continued)

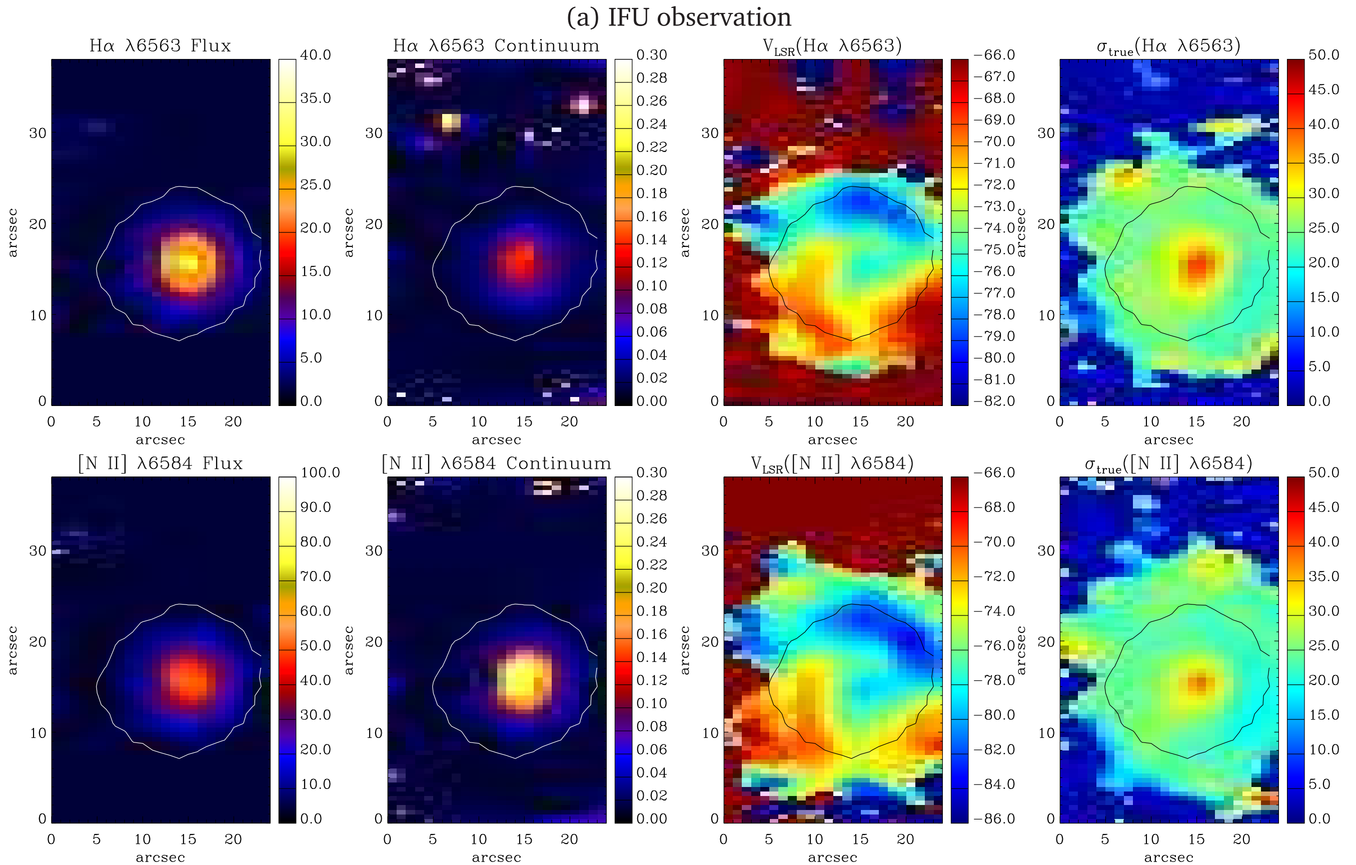

Figure A.7: (a) As Figure A.1 but for M 1-32. (b) The SHAPE mesh model before rendering at the best-fitting inclination, two different orientations (inclination: 90° and 0°, respectively), and corresponding rendered model. (c) The Hα+[N II] narrow band image from Schwarz et al. (1992). (d) The normalized synthetic intensity and radial velocity maps produced by the model.

(b) SHAPE mesh model

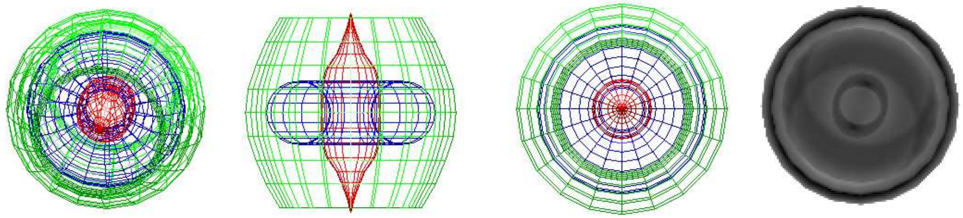

(c) Hα+[N II] narrow band image

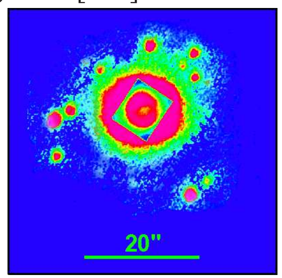

(d) SHAPE model results

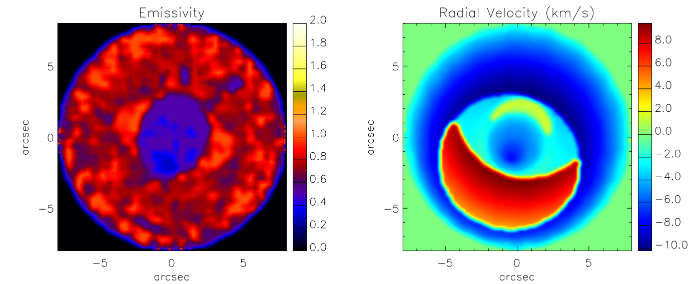

Figure A.7: (continued)

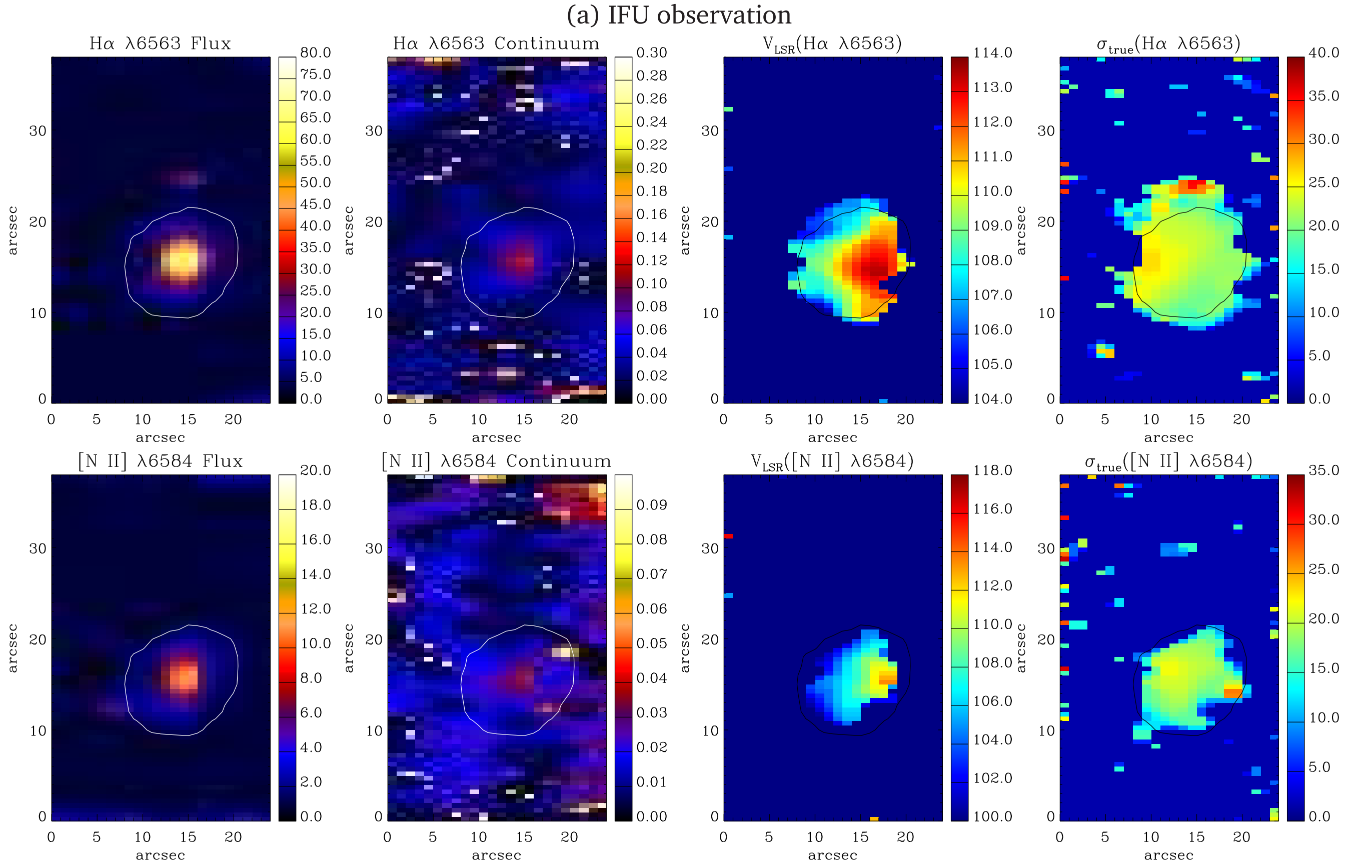

Figure A.8: (a) As Figure A.1 but for M 3-15. (b) The SHAPE mesh model before rendering at the best-fitting inclination, two different orientations (inclination: 90° and 0°, respectively), and corresponding rendered model. (c) The *HST* image taken by F656N filters (Observing program 9356; PI. Zijlstra, 2002).

(b) SHAPE mesh model

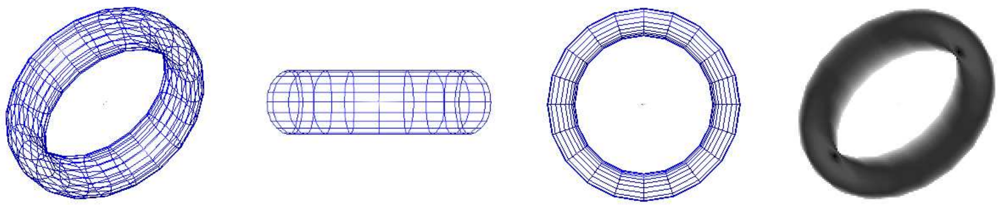

(c) *HST* image

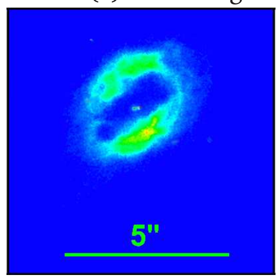

Figure A.8: (continued)

(a) IFU observation

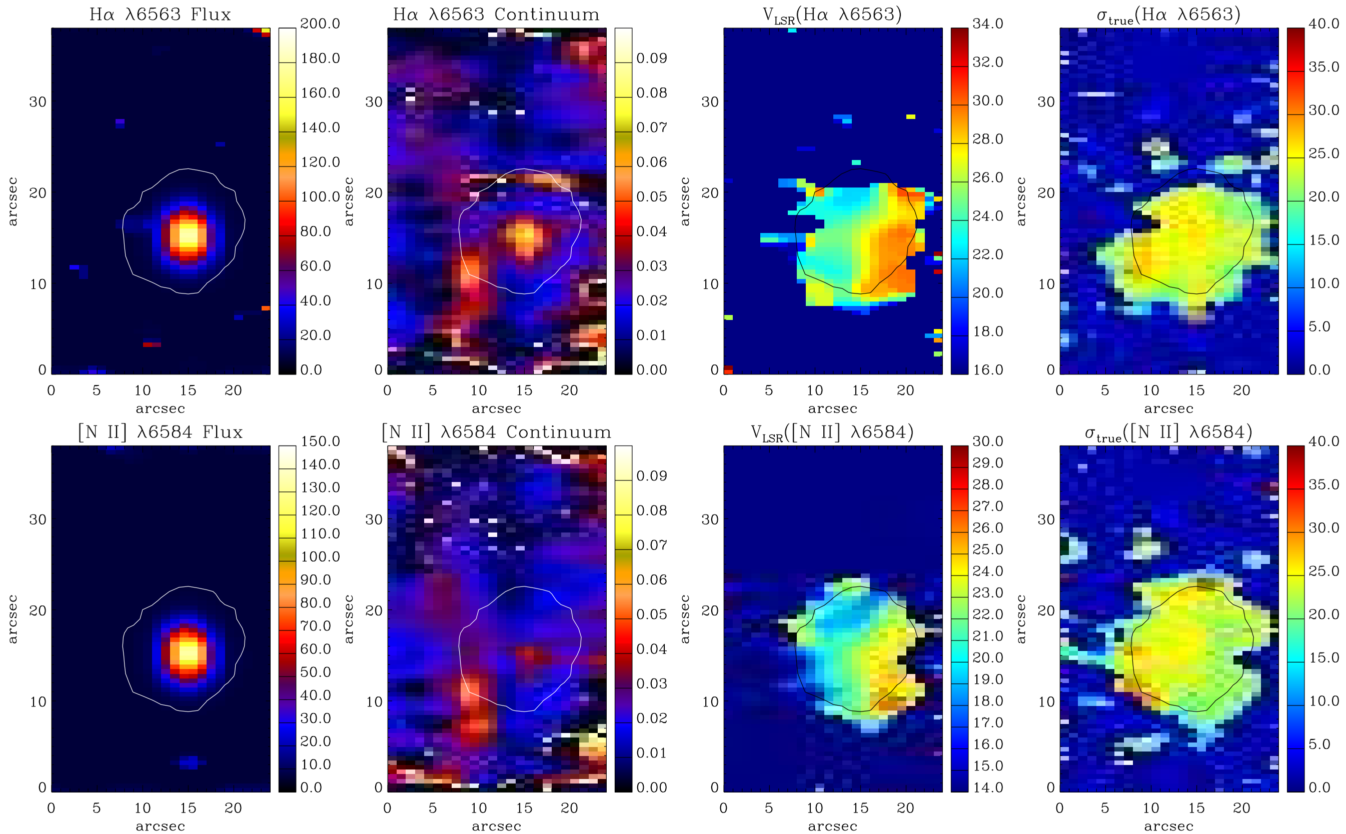

Figure A.9: (a) As Figure A.1 but for M 1-25. (b) The SHAPE mesh model before rendering at the best-fitting inclination, two different orientations (inclination: 90° and 0°, respectively), and corresponding rendered model. (c) The *HST* images taken by F656N filter (Observing program 8345; PI. Sahai, 2001).

(b) SHAPE mesh model

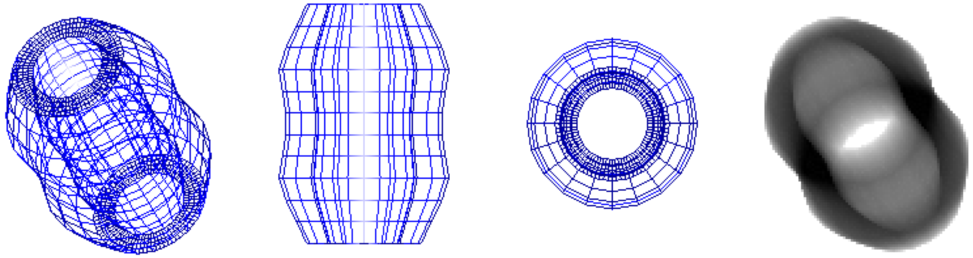

(c) *HST* image

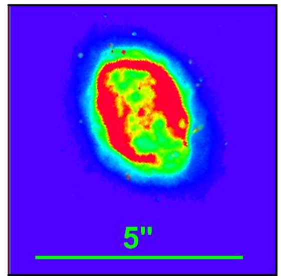

Figure A.9: (continued)

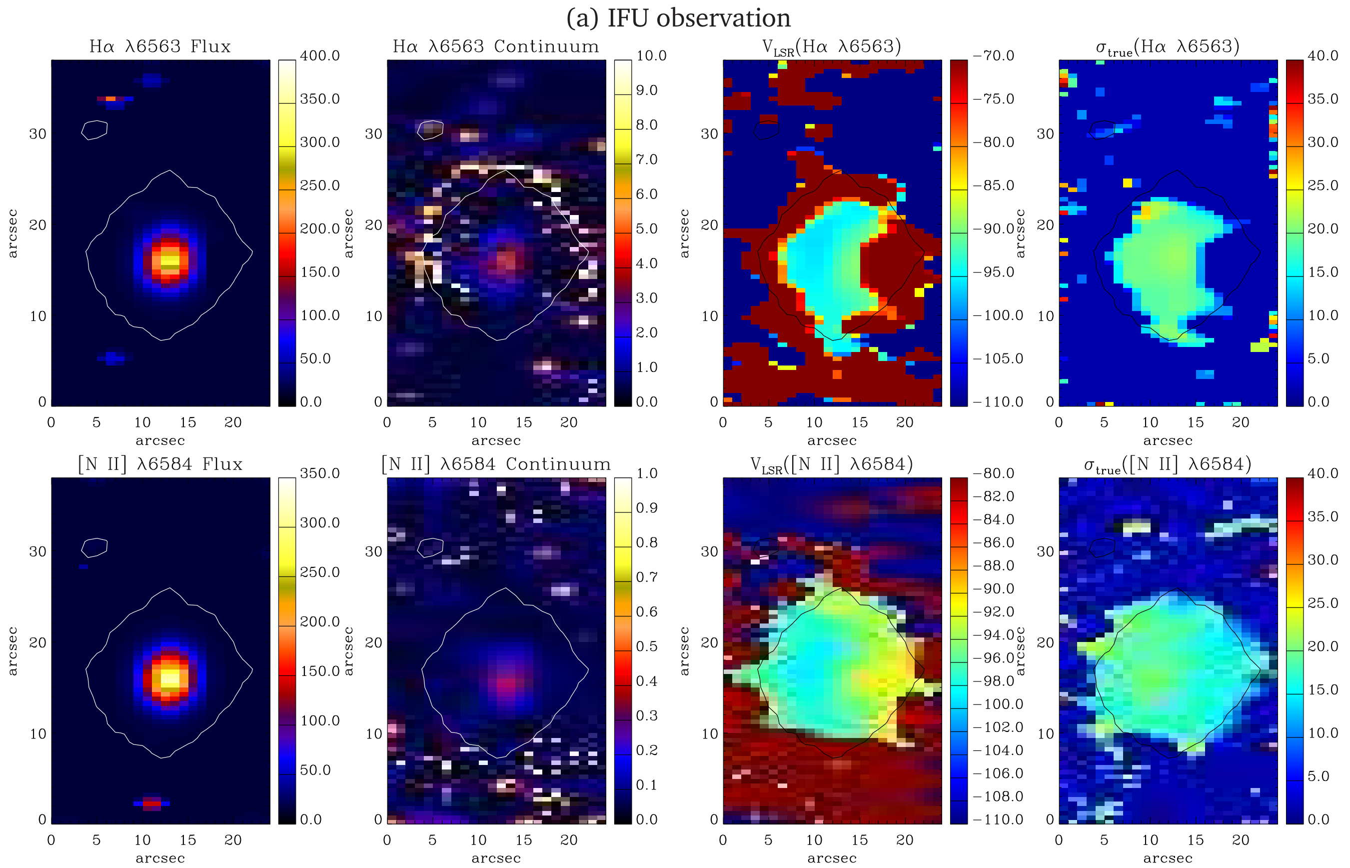

Figure A.10: (a) As Figure A.1 but for Hen 2-142. (b) The SHAPE mesh model before rendering at the best-fitting inclination, two different orientations (inclination: 90° and 0°, respectively), and corresponding rendered model. (c) The *HST* image taken by F656N filter (Observing program 6353; PI. Sahai, 1996).

(b) SHAPE mesh model

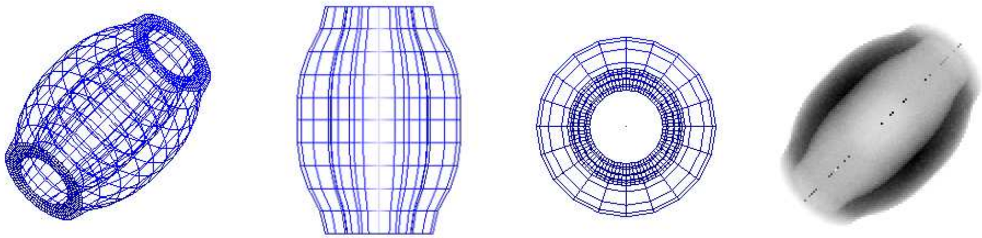

(c) *HST* image

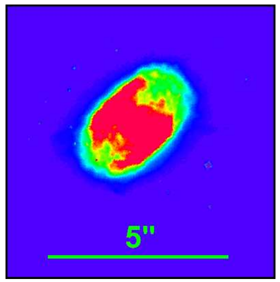

Figure A.10: (continued)

(a) IFU observation

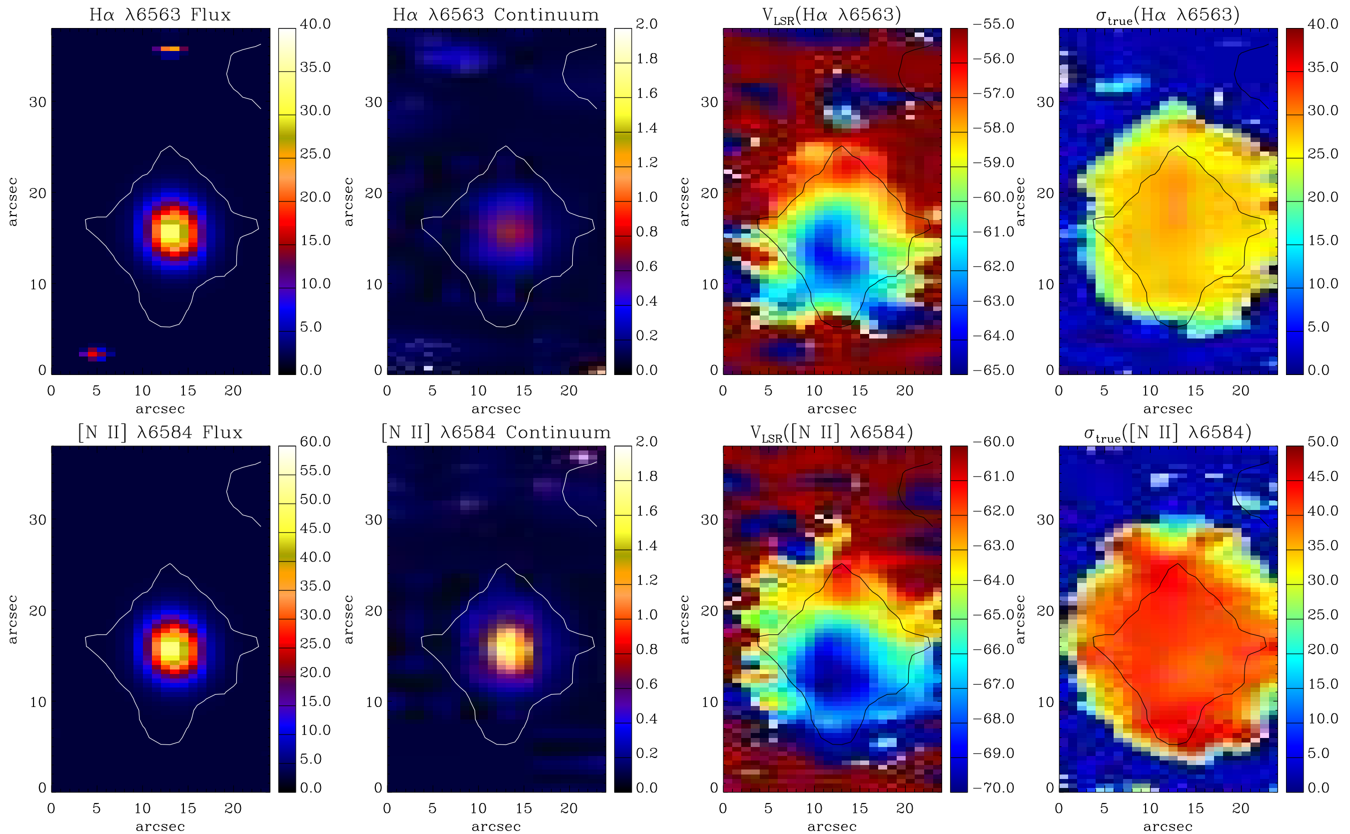

Figure A.11: (a) As Figure A.1 but for Hen 3-1333. (b) The *HST* image taken by the F606W filter (Observing program 9463; PI. Sahai, 2002).

(b) *HST* image

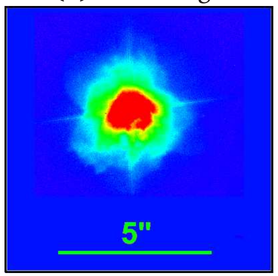

Figure A.11: (continued)

(a) IFU observation

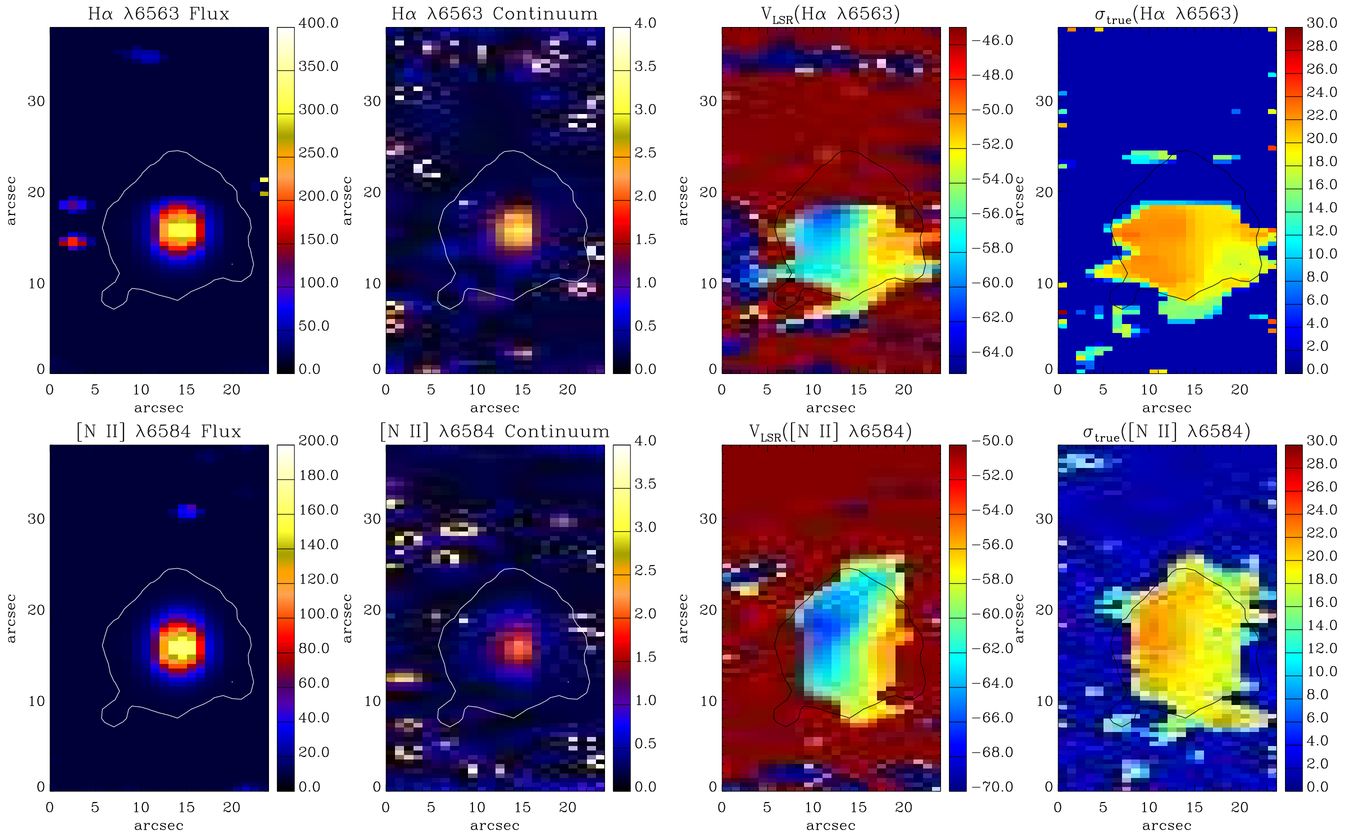

Figure A.12: (a) As Figure A.1 but for Hen 2-113. (b) The *HST* image taken by the F606W filter (Observing program 9463; PI. Sahai, 2003).

(b) *HST* image

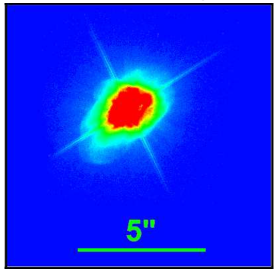

Figure A.12: (continued)

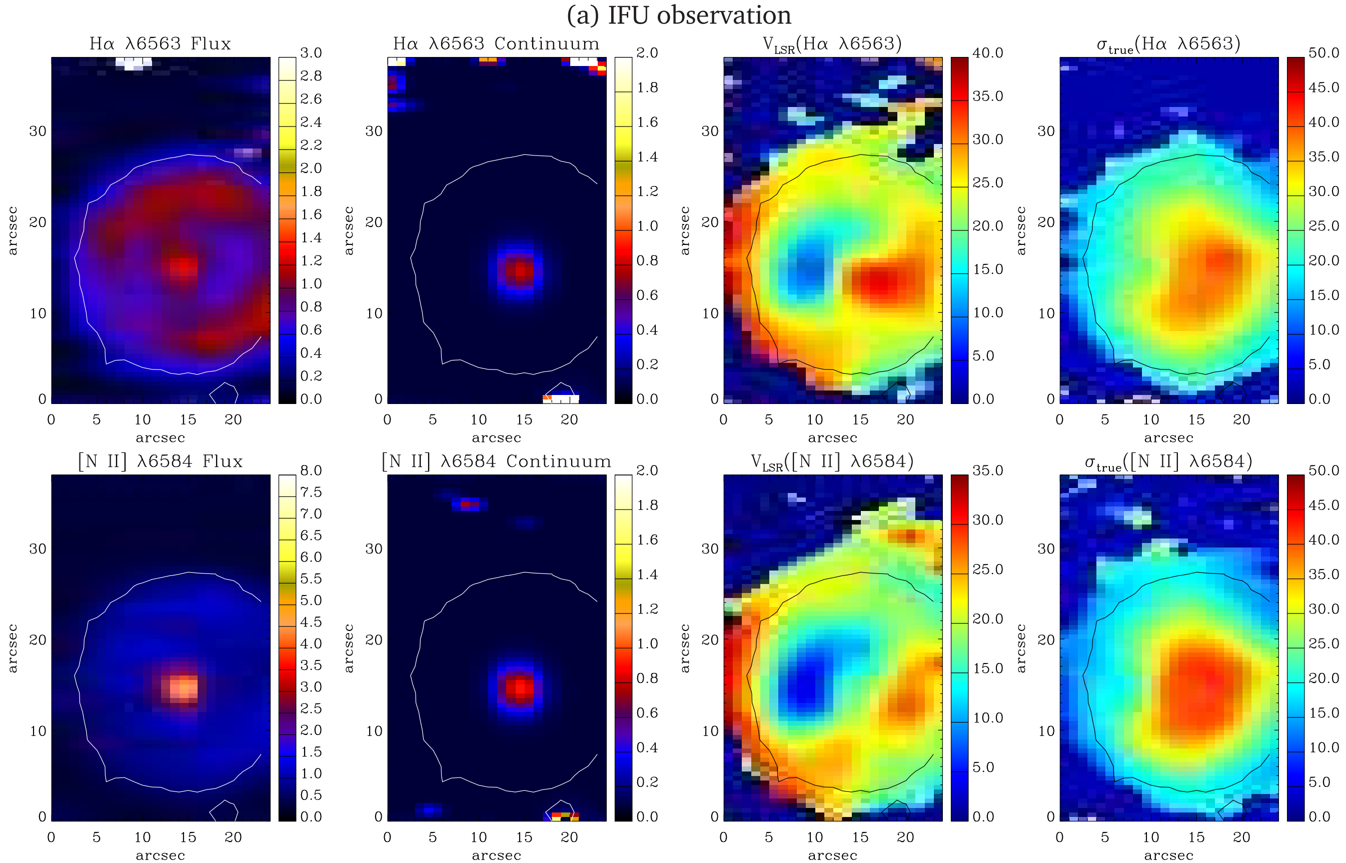

Figure A.13: (a) As Figure A.1 but for K 2-16. (b) The SHAPE mesh model before rendering at the best-fitting inclination, two different orientations (inclination: 90° and 0°, respectively), and corresponding rendered model. (c) The Hα+[N II] narrow band image from Schwarz et al. (1992). (d) The normalized synthetic intensity and radial velocity maps produced by the model.

(b) SHAPE mesh model

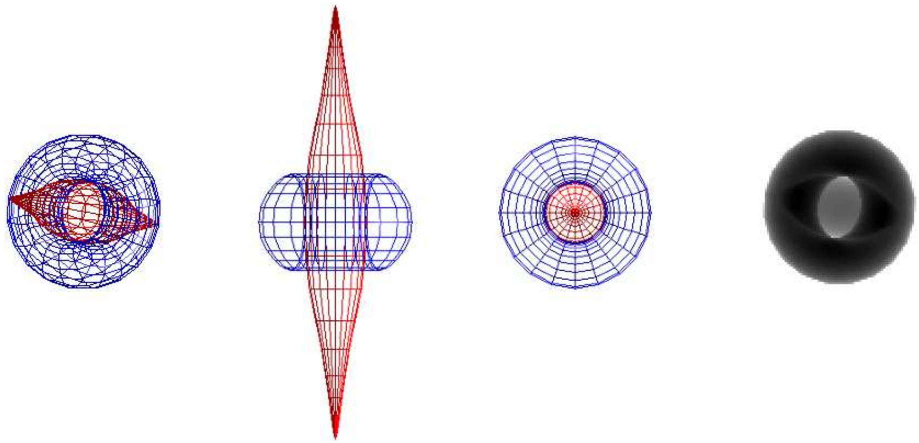

(c) Hα+[N II] narrow band image

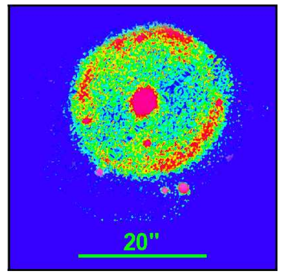

(d) SHAPE model results

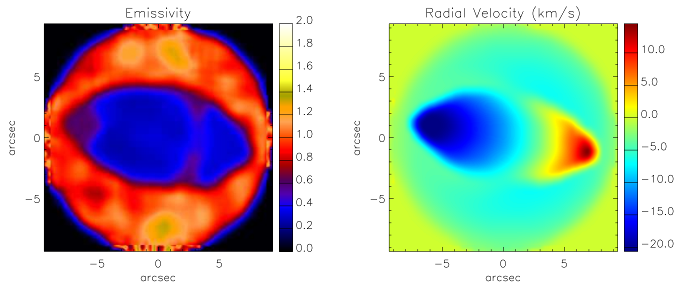

Figure A.13: (continued)

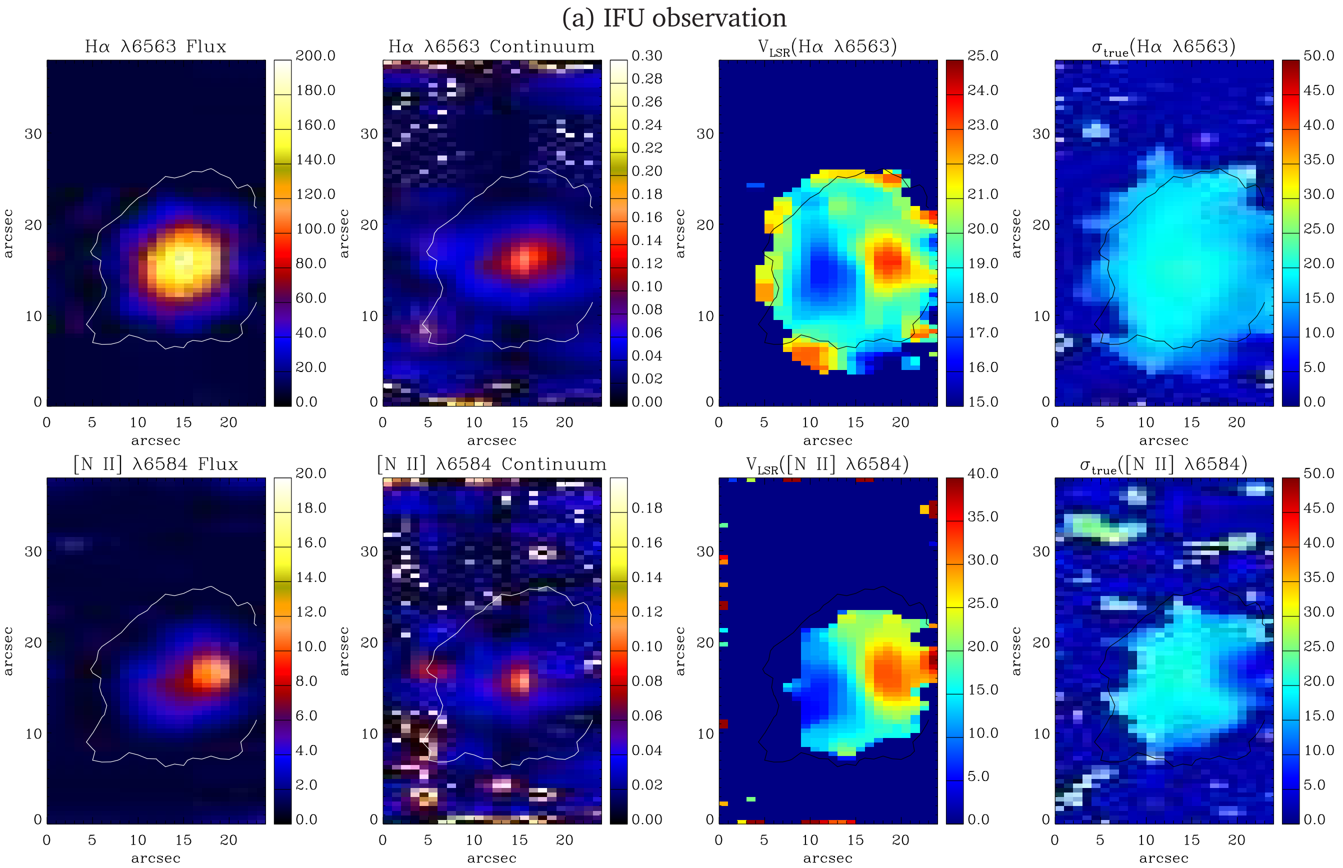

Figure A.14: (a) As Figure A.1 but for NGC 6578. (b) The SHAPE mesh model before rendering at the best-fitting inclination, two different orientations (inclination: 90° and 0°, respectively), and corresponding rendered model. (c) The *HST* image taken by the F502N filter (Observing program 11122; PI. Balick, 2008).

(b) SHAPE mesh model

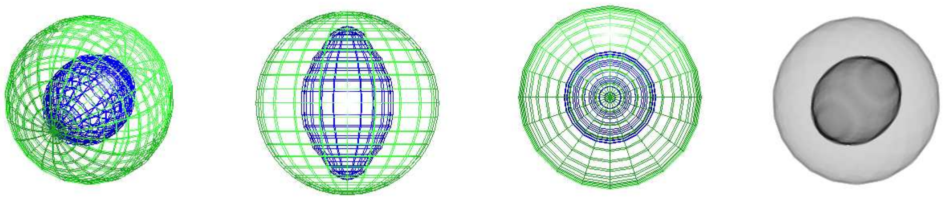

(c) *HST* image

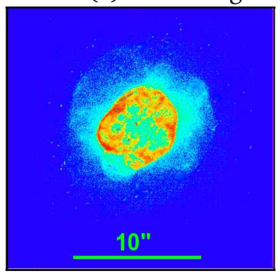

Figure A.14: (continued)

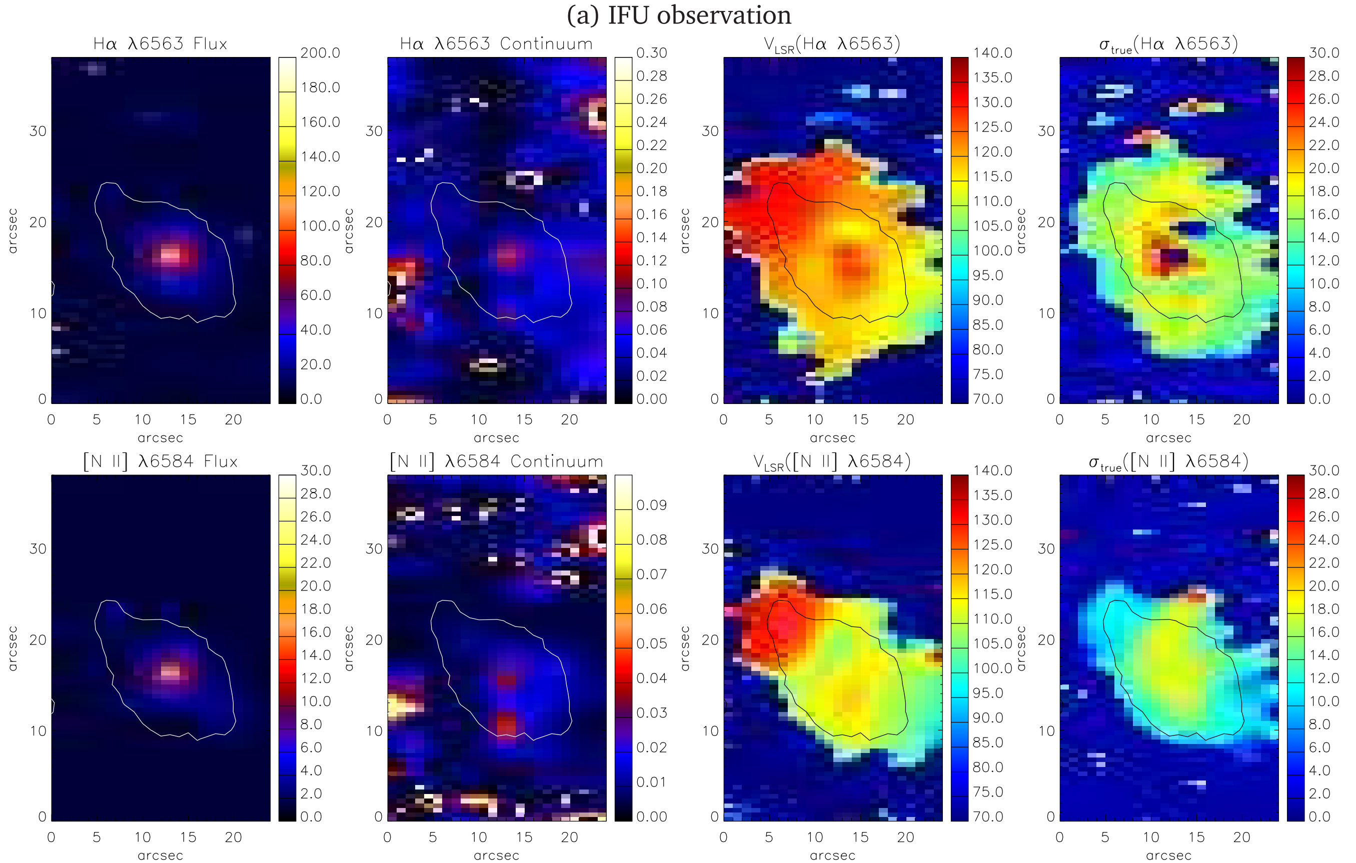

Figure A.15: (a) As Figure A.1 but for M 2-42. (b) The SHAPE mesh model before rendering at the best-fitting inclination, two different orientations (inclination: 90° and 0°, respectively), and corresponding rendered model. (c) The Hα image obtained from the SuperCOSMOS Hα Sky Survey (SHS; Parker et al. 2005). (d) The normalized synthetic intensity and radial velocity maps produced by the model.

(b) SHAPE mesh model

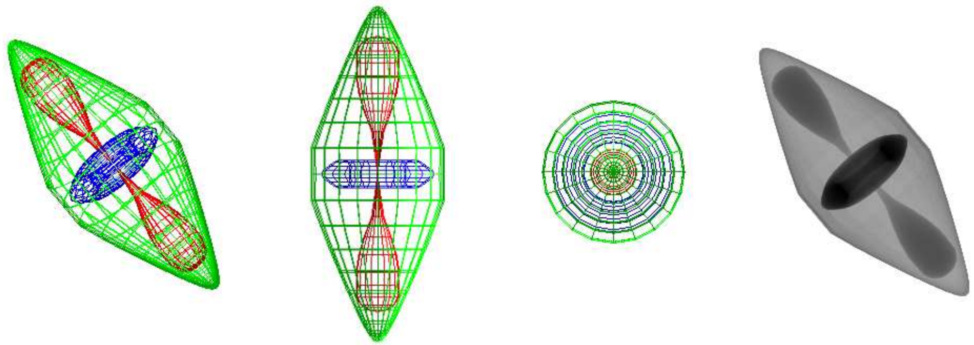

(c) SHS Hα image

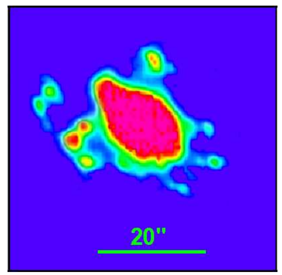

(d) SHAPE model results

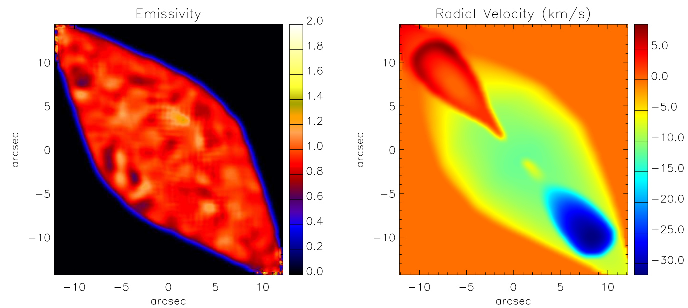

Figure A.15: (continued)

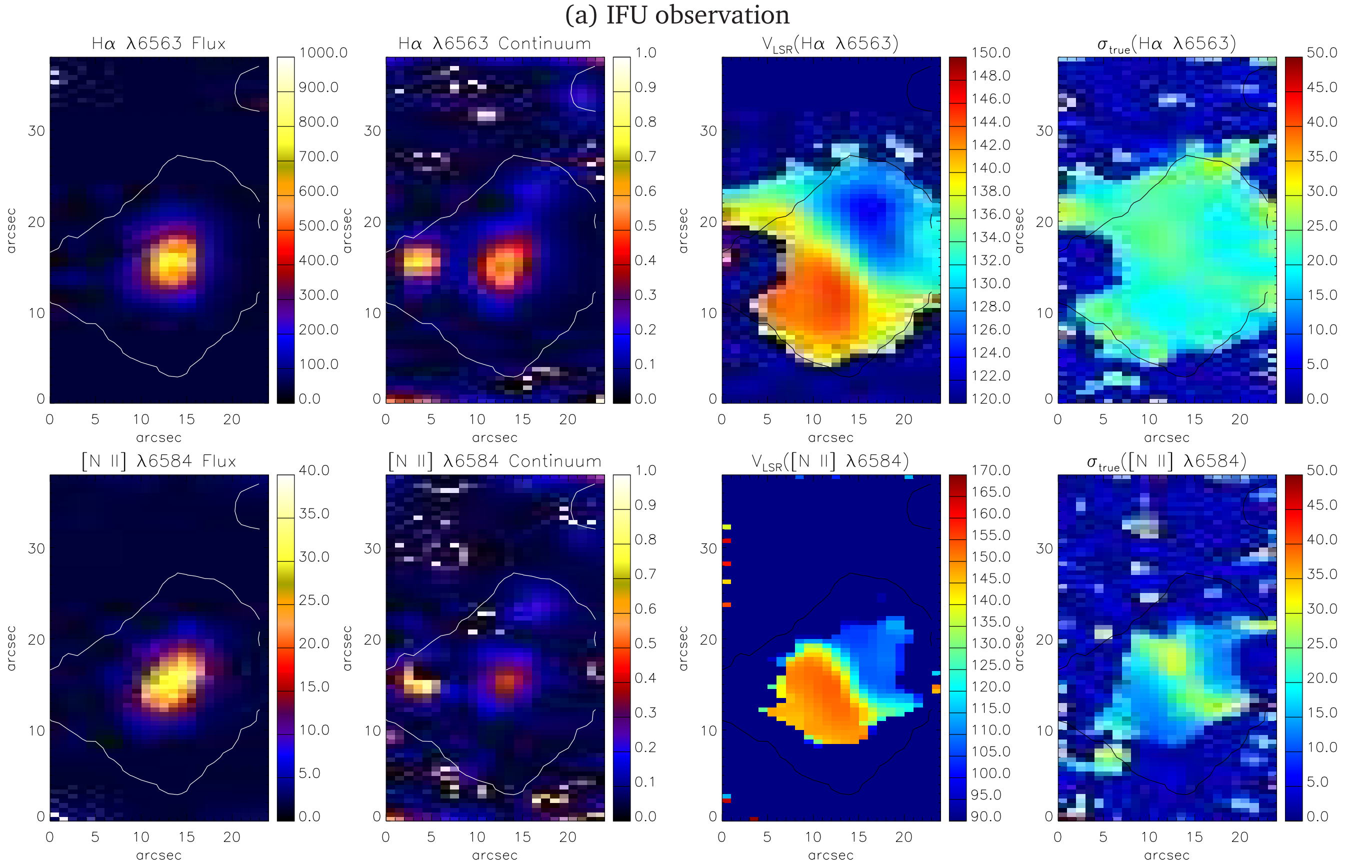

Figure A.16: (a) As Figure A.1 but for NGC 6567. (b) The SHAPE mesh model before rendering at the best-fitting inclination, two different orientations (inclination: 90° and 0°, respectively), and corresponding rendered model. (c) The *HST* image taken by the F108N filter (Observing program 7837; PI. Pottasch, 1998).

(b) SHAPE mesh model

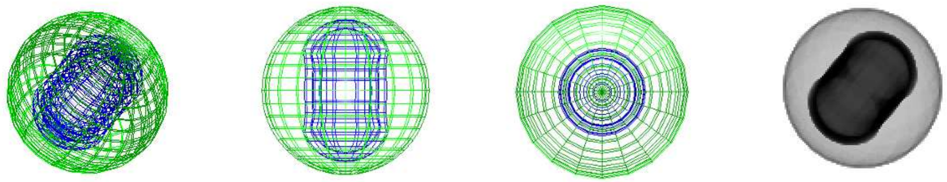

(c) *HST* image

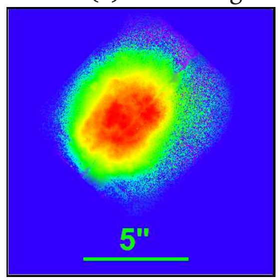

Figure A.16: (continued)

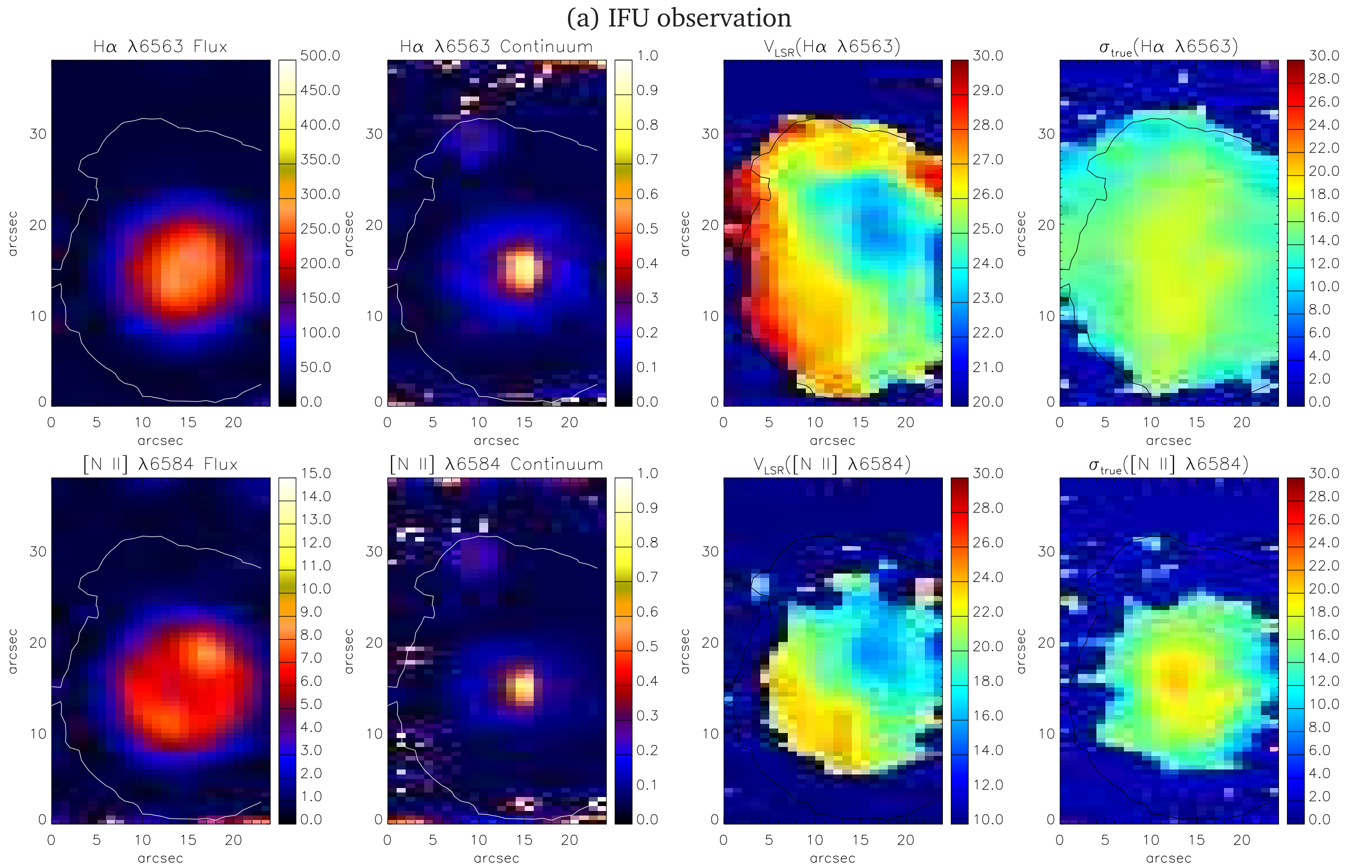

Figure A.17: (a) As Figure A.1 but for NGC 6629. (b) The SHAPE mesh model before rendering at the best-fitting inclination, two different orientations (inclination: 90° and 0°, respectively), and corresponding rendered model. (c) The *HST* image taken by the F555W filter (Observing program 6119; PI. Bond, 1995).

(b) SHAPE mesh model (c) *HST* image

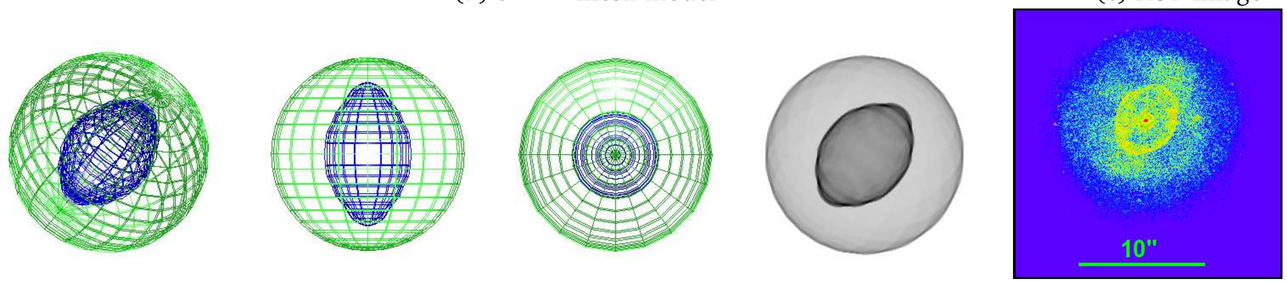

Figure A.17: (continued)

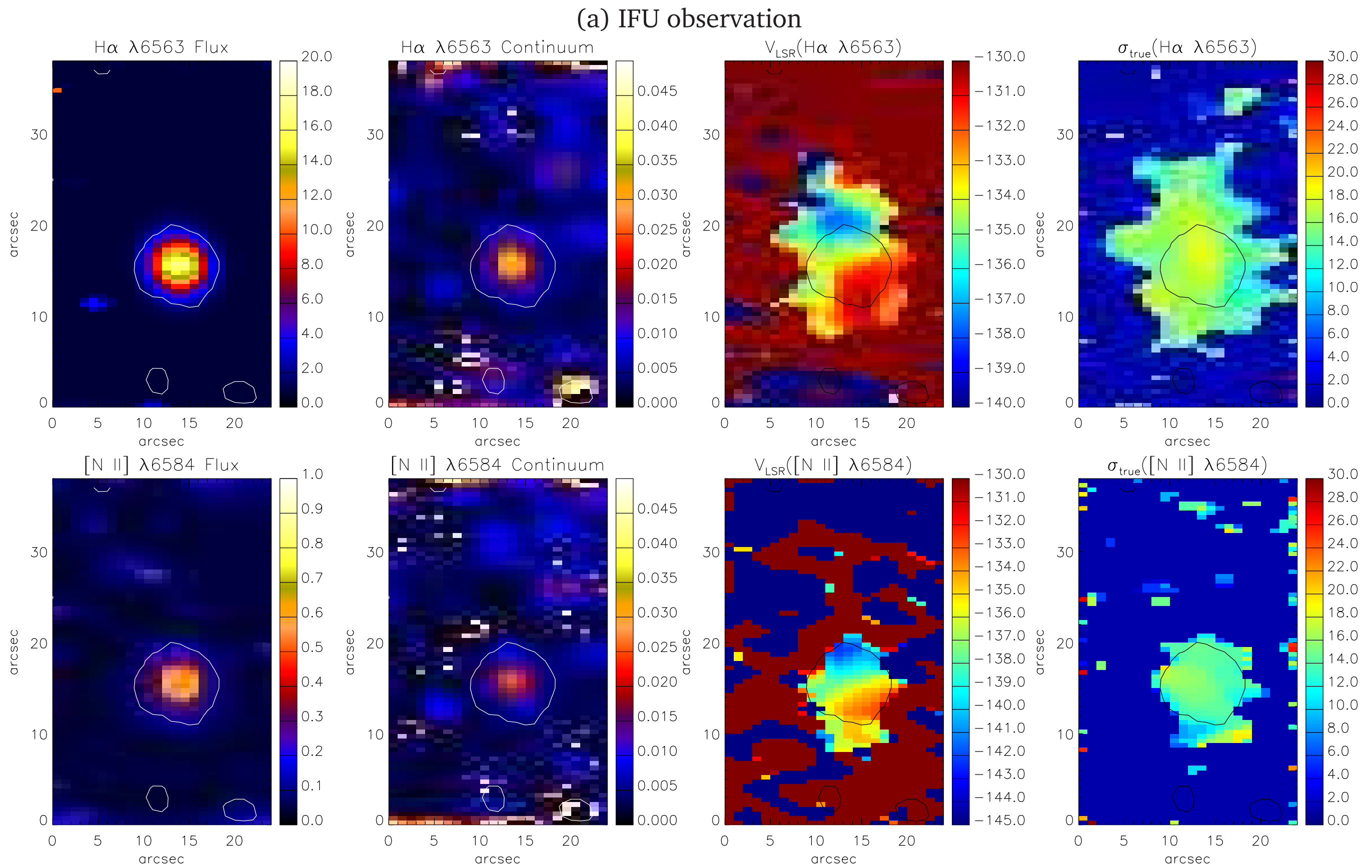

Figure A.18: (a) As Figure A.1 but for Sa 3-107. (b) The Hα image obtained from the SuperCOSMOS Hα Sky Survey (SHS; Parker et al. 2005).

(b) SHS Hα image

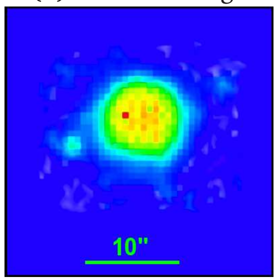

Figure A.18: (continued)

Appendix B

Measured nebular line fluxes

This appendix contains complete emission line lists for all nebulae analyzed in Chapter 3. Tables contain the optical emission lines measured from the WiFeS observations made with the ANU 2.3-m Telescope at the Siding Spring Observatory, while the uncovered emission lines have been adopted from the references given in the footnotes.

Table B.1: OObserved and dereddened line fluxes of PB 6, on a scale relative to Hβ, where H$\beta = 100$. Observed fluxes are denoted by $F(\lambda)$ and dereddened fluxes by $I(\lambda)$. Uncertain (errors of 50 per cent) and very uncertain (greater than a factor of 2) values are followed by ':' and '::', respectively. The symbol '*' indicates that the listed line is blended with the above listed line.

			PB 6		
			$c(\mathrm{H}\beta) = 0.60$		
λ_0(Å)	ID	Mult	$F(\lambda)$	$I(\lambda)$	Err(%)
3726.03	[O II] [a]	F1	50.70	72.41	...
3728.82	[O II] [a]	F1	*	*	...
3868.75	[Ne III] [a]	F1	84.00	115.75	...
3889.05	H I 8-2 [a]	H8	11.50	15.76	...
3967.46	[Ne III] [a]	F1	30.80	41.28	...
4026.21	He I [a]	V18	2.50	3.29	...
4068.60	[S II] [a]	F1	3.20	4.16	...
4076.35	[S II] [a]	F1	*	*	...
4101.74	H I 6-2 [a]	H6	22.50	28.97	...
4340.47	H I 5-2 [a]	H5	44.20	52.72	...
4363.21	[O III] [a]	F2	17.10	20.25	...
4471.50	He I	V14	2.06	2.35	5.1
4541.59	He II	4.9	5.80	6.47	...
4624.92	[Ar V]		0.10	0.11	5.6
4685.68	He II	3.4	132.35	140.55	5.0
4711.37	[Ar IV]	F1	9.70	10.21	5.9
4724.15	[Ne IV]	F1	3.08	3.23	7.2
4740.17	[Ar IV]	F1	8.62	8.98	5.0
4861.33	H I 4-2	H4	100.00	100.00	5.2
4881.11	[Fe III]	F2	0.07	0.07	5.3
4921.93	He I	V48	0.56	0.55	5.2
4958.91	[O III]	F1	394.77	381.83	5.2
5006.84	[O III]	F1	1308.84	1245.43	5.8
5199.84	[N I]	F1	2.13	1.90	11.3
5411.52	He II	4.7	12.86	10.68	5.1
5452.08	N II	V29	0.08	0.07	9.2
5517.66	[Cl III]	F1	0.87	0.70	5.3
5537.60	[Cl III]	F1	0.93	0.75	5.4
5754.60	[N III]	F3	6.01	4.59	5.1
5875.66	He I	V11	9.36	6.94	5.1
5931.78	N II	V28	0.25	0.18	6.3
5940.24	N II	V28	0.24	0.18	5.3
6036.70	He II	5.21	0.29	0.21	5.2
6074.10	He II	5.20	0.30	0.21	5.2
6101.83	[K IV]	F1	0.59	0.42	5.1
6118.20	He II	5.19	0.40	0.28	5.1
6233.80	He II	5.17	0.56	0.38	5.2
6300.30	[O I]	F1	5.74	3.88	5.7
6312.10	[S III]	F3	4.70	3.17	6.0
6363.77	[O I]	F1	1.95	1.30	5.5
6406.30	He II	5.15	0.94	0.62	5.1
6434.73	[Ar V]	F1	2.73	1.79	5.0
6461.95	C II	V17.04	0.07	0.05	5.2
6527.11	He II	5.14	1.19	0.77	5.1
6548.10	[N III]	F1	111.21	71.45	5.3
6562.77	H I 3-2	H3	442.53	283.49	5.7
6583.50	[N III]	F1	344.27	219.64	5.9
6678.16	He I	V46	2.62	1.64	10.9
6716.44	[S II]	F2	9.56	5.94	5.2
6730.82	[S II]	F2	12.85	7.97	5.2
6890.88	He I	5.12	1.59	0.96	5.2
7005.40	[Ar V] [a]	V10	10.20	6.01	...
7135.80	[Ar III] [a]	F1	19.70	11.35	...
7319.40	[O II] [a]	F2	10.00	5.58	...
7329.90	[O II] [a]	F2	*	*	...

[a] Fluxes adopted from Kaler et al. (1991).

Table B.2: As Table B.1 but for M 3-30.

M 3-30					
$c(\mathrm{H}\beta)=0.96$					
λ_0(Å)	ID	Mult	$F(\lambda)$	$I(\lambda)$	Err(%)
3726.03	[O II] [a]	F1	6.60	11.66	...
3728.82	[O II] [a]	F1	8.67	15.30	...
3868.75	[Ne III] [a]	F1	34.47	57.45	...
4363.21	[O III] [a]	F2	3.20	4.19	...
4471.50	He I	V14	2.94	3.63	5.3
4634.14	N III	V2	1.08	1.22	6.3
4640.64	N III	V2	3.06	3.45	8.0
4649.13	O II	V1	1.49	1.67	6.4
4661.63	O II	V1	0.46	0.51	5.4
4676.23	O II	V1	0.26	0.29	5.8
4685.68	He II	3.4	76.13	83.78	5.0
4711.37	[Ar IV]	F1	1.86	2.02	5.4
4724.15	[Ne IV]	F1	0.25	0.27	10.6
4740.17	[Ar IV]	F1	1.42	1.52	5.2
4861.33	H I 4-2	H4	100.00	100.00	5.1
4906.83	O II	V28	0.13	0.13	7.3
4921.93	He I	V48	0.83	0.80	6.2
4958.91	[O III]	F1	187.89	178.18	5.1
5006.84	[O III]	F1	578.74	534.72	5.1
5199.84	[N I]	F1	0.35	0.29	11.7
5411.52	He II	4.7	8.07	6.00	5.5
5517.66	[Cl III]	F1	1.01	0.72	6.6
5537.60	[Cl III]	F1	0.73	0.51	6.7
5666.63	N II	V3	0.13	0.09	6.2
5754.60	[N III]	F3	0.58	0.38	5.6
5875.66	He I	V11	20.45	12.71	5.0
6036.70	He II	5.21	0.16	0.09	6.4
6074.10	He II	5.20	0.21	0.12	5.8
6118.20	He II	5.19	0.16	0.09	5.6
6233.80	He II	5.17	0.61	0.33	8.9
6312.10	[S III]	F3	2.49	1.33	6.1
6461.95	C II	V17.04	0.41	0.21	5.8
6527.11	He II	5.14	0.72	0.36	5.7
6548.10	[N III]	F1	21.82	10.78	5.2
6562.77	H I 3-2	H3	586.87	288.69	5.1
6583.50	[N III]	F1	69.54	33.99	5.1
6678.16	He I	V46	7.34	3.48	5.6
6716.44	[S II]	F2	12.89	6.05	5.0
6730.82	[S II]	F2	11.39	5.32	17.9
6890.88	He I	5.12	1.09	0.49	5.6
7135.80	[Ar III] [b]	F1	33.60	13.96	...

[a] Fluxes adopted from Peña et al. (2001).

[b] Fluxes adopted from Girard et al. (2007).

Table B.3: As Table B.1 but for Hb 4.

		Hb 4 (shell) $c(\mathrm{H}\beta) = 1.86$			
λ_0(Å)	ID	Mult	$F(\lambda)$	$I(\lambda)$	Err(%)
3726.03	[O II] [a]	F1	5.93	17.81	10.0
3728.82	[O II] [a]	F1	2.74	8.21	10.0
3868.75	[Ne III] [a]	F1	41.08	110.26	9.0
3967.46	[Ne III] [a]	F1	13.86	34.16	8.0
4068.60	[S II] [a]	F1	1.03	2.31	9.0
4076.35	[S II] [a]	F1	0.55	1.23	11.0
4340.47	H I 5-2 [a]	H5	28.90	49.75	7.0
4363.21	[O III] [a]	F2	4.39	7.38	7.0
4471.50	He I	V14	3.24	4.88	5.1
4609.44	O II	V92a	0.03	0.04	6.4
4649.13	O II	V1	0.52	0.65	16.9
4685.68	He II	3.4	11.95	14.38	5.0
4711.37	[Ar IV]	F1	1.72	2.01	6.2
4740.17	[Ar IV]	F1	2.29	2.60	5.1
4861.33	H I 4-2	H4	100.00	100.00	5.0
4921.93	He I	V48	1.22	1.14	5.2
4958.91	[O III]	F1	438.84	396.05	5.0
5006.84	[O III]	F1	1375.95	1180.83	5.0
5411.52	He II	4.7	1.82	1.03	5.2
5517.66	[Cl III]	F1	1.08	0.56	5.7
5537.60	[Cl III]	F1	1.79	0.91	5.5
5679.56	N II	V3	0.21	0.10	5.6
5754.60	[N III]	F3	4.24	1.84	5.1
5875.66	He I	V11	40.04	15.97	5.0
5931.78	N II	V28	0.08	0.03	7.2
5940.24	N II	V28	0.04	0.02	5.8
6074.10	He II	5.20	0.05	0.02	5.6
6101.83	[K IV]	F1	0.41	0.14	5.6
6118.20	He II	5.19	0.10	0.03	8.6
6300.30	[O I]	F1	16.87	5.05	5.1
6312.10	[S III]	F3	8.21	2.44	5.0
6363.77	[O I]	F1	5.94	1.71	5.1
6406.30	He II	5.15	0.24	0.07	6.0
6434.73	[Ar V]	F1	0.07	0.02	5.6
6461.95	C II	V17.04	0.16	0.04	6.0
6482.05	N II	V8	0.05	0.01	5.2
6527.11	He II	5.14	0.34	0.09	5.7
6548.10	[N III]	F1	131.32	33.62	5.1
6562.77	H I 3-2	H3	1124.52	285.37	5.0
6583.50	[N III]	F1	418.58	104.89	5.0
6641.05	O II	V4	0.03	0.01	5.1
6678.16	He I	V46	17.96	4.25	5.0
6716.44	[S II]	F2	25.90	5.99	5.0
6730.82	[S II]	F2	45.62	10.47	5.2
7005.40	[Ar V]	V10	0.21	0.04	6.0
7135.80	[Ar III] [a]	F1	119.03	21.80	14.0
7281.35	He I [a]	V45	3.94	0.67	14.0
7319.40	[O II] [a]	F2	17.56	2.92	14.0
7329.90	[O II] [a]	F2	15.06	2.50	14.0
7751.43	[Ar III] [a]	F1	37.38	5.06	15.0
9068.60	[S III] [a]	F1	486.39	39.74	20.0

[a] Fluxes adopted from García-Rojas et al. (2012).

Table B.3: (continued)

Hb 4 (N-knot) $c(\mathrm{H}\beta) = 2.07$					
λ_0(Å)	ID	Mult	$F(\lambda)$	$I(\lambda)$	Err(%)
4861.33	H I 4-2	H4	100.00	100.00	6.1
4958.91	[O III]	F1	356.06	317.60	5.6
5006.84	[O III]	F1	1134.72	956.98	5.6
5754.60	[N III]	F3	11.83	4.68	8.5
5875.66	He I	V11	31.97	11.48	6.3
6300.30	[O I]	F1	21.95	5.72	9.7
6363.77	[O I]	F1	6.60	1.64	16.3
6548.10	[N III]	F1	334.37	73.30	5.2
6562.77	H I 3-2	H3	1317.70	286.00	5.4
6583.50	[N III]	F1	1102.44	235.94	5.2
6678.16	He I	V46	10.26	2.06	12.0
6716.44	[S II]	F2	97.51	19.10	5.6
6730.82	[S II]	F2	103.42	20.07	14.9

Hb 4 (S-knot) $c(\mathrm{H}\beta) = 1.91$					
λ_0(Å)	ID	Mult	$F(\lambda)$	$I(\lambda)$	Err(%)
4861.33	H I 4-2	H4	100.00	100.00	6.5
4958.91	[O III]	F1	270.46	243.44	5.3
5006.84	[O III]	F1	935.68	799.84	5.1
5875.66	He I	V11	25.52	9.94	8.7
6300.30	[O I]	F1	44.71	12.97	10.1
6363.77	[O I]	F1	16.78	4.67	52.2
6548.10	[N III]	F1	274.17	67.78	9.4
6562.77	H I 3-2	H3	1167.54	286.00	5.3
6583.50	[N III]	F1	962.34	232.71	5.2
6678.16	He I	V46	6.75	1.54	11.3
6716.44	[S II]	F2	83.80	18.68	5.5
6730.82	[S II]	F2	91.44	20.21	5.4

Table B.4: As Table B.1 but for IC 1297.

		IC 1297			
		$c(\mathrm{H}\beta) = 0.23$			
λ_0(Å)	ID	Mult	$F(\lambda)$	$I(\lambda)$	Err(%)
3726.03	[O II] [a]	F1	49.10	56.22	…
3728.82	[O II] [a]	F1	*	*	…
3868.75	[Ne III] [a]	F1	109.00	123.11	…
3889.05	H I 8-2 [a]	H8	19.20	21.64	…
3967.46	[Ne III] [a]	F1	50.70	56.66	…
4026.21	He I [a]	V18	2.10	2.33	…
4068.60	[S II] [a]	F1	2.80	3.09	…
4076.35	[S II] [a]	F1	*	*	…
4101.74	H I 6-2 [a]	H6	26.00	28.62	…
4340.47	H I 5-2 [a]	H5	45.70	48.87	…
4363.21	[O III] [a]	F2	9.30	9.92	…
4471.50	He I	V14	3.92	4.12	5.1
4491.23	O II	V86a	0.04	0.04	5.1
4552.53	N II	V58a	0.04	0.04	5.9
4609.44	O II	V92a	0.04	0.04	5.7
4640.64	N III	V2	1.77	1.82	8.7
4649.13	O II	V1	0.66	0.68	15.4
4676.23	O II	V1	0.07	0.07	5.0
4685.68	He II	3.4	36.89	37.74	5.0
4711.37	[Ar IV]	F1	1.95	1.99	5.6
4740.17	[Ar IV]	F1	1.80	1.83	5.2
4861.33	H I 4-2	H4	100.00	100.00	5.1
4921.93	He I	V48	1.01	1.00	5.4
4958.91	[O III]	F1	457.90	452.14	5.0
5006.84	[O III]	F1	1317.25	1292.64	5.1
5060.00	C II		0.01	0.01	5.9
5199.84	[N I]	F1	0.16	0.15	17.4
5411.52	He II	4.7	3.02	2.81	5.1
5517.66	[Cl III]	F1	0.71	0.65	6.0
5537.60	[Cl III]	F1	0.73	0.67	5.8
5679.56	N II	V3	0.05	0.05	5.2
5754.60	[N III]	F3	0.71	0.64	5.5
5875.66	He I	V11	14.49	12.94	5.1
5931.78	N II	V28	0.05	0.04	7.3
6074.10	He II	5.20	0.05	0.04	6.3
6101.83	[K IV]	F1	0.12	0.11	5.6
6151.43	C II	V16.04	0.03	0.03	5.1
6233.80	He II	5.17	0.15	0.13	5.4
6300.30	[O I]	F1	1.89	1.63	5.1
6312.10	[S III]	F3	2.67	2.30	5.2
6363.77	[O I]	F1	0.63	0.54	5.6
6406.30	He II	5.15	0.16	0.14	6.5
6434.73	[Ar V]	F1	0.10	0.09	8.7
6461.95	C II	V17.04	0.06	0.05	5.1
6527.11	He II	5.14	0.24	0.20	6.7
6548.10	[N III]	F1	17.14	14.49	5.2
6562.77	H I 3-2	H3	339.40	286.60	5.0
6583.50	[N III]	F1	53.70	45.27	5.2
6678.16	He I	V46	4.25	3.56	5.2
6716.44	[S II]	F2	5.64	4.71	5.2
6730.82	[S II]	F2	7.79	6.50	11.9
6890.88	He I	5.12	0.31	0.26	6.1
7065.20	He I	V10	4.70	3.83	…
7135.80	[Ar III] [a]	F1	18.00	14.60	…
7281.35	He I [a]	V45	0.60	0.48	…
7319.40	[O II] [a]	F2	5.00	4.00	…
7329.90	[O II] [a]	F2	*	*	…
7751.43	[Ar III] [a]	F1	3.80	2.97	…
9068.60	[S III] [a]	F1	32.60	23.94	…

[a] Fluxes adopted from Milingo et al. (2002).

Table B.5: As Table B.1 but for Th 2-A.

		Th 2-A			
		$c(\mathrm{H}\beta) = 1.11$			
λ_0(Å)	ID	Mult	$F(\lambda)$	$I(\lambda)$	Err(%)
3728.82	[O II] [a]	F1	59.01	113.61	...
3868.75	[Ne III] [a]	F1	112.74	203.21	...
3889.05	H I 8-2 [a]	H8	8.64	15.41	...
3967.46	[Ne III] [a]	F1	33.75	57.81	...
4101.74	H I 6-2 [a]	H6	14.57	23.18	...
4068.60	[S II] [a]	F1	3.09	5.01	50.0
4076.35	[S II] [a]	F1	2.70	4.36	50.0
4340.47	H I 5-2 [a]	H5	29.26	40.46	...
4363.21	[O III] [a]	F2	13.35	18.21	...
4471.50	He I	V14	2.41	3.08	5.2
4685.68	He II	3.4	52.04	58.12	5.1
4711.37	[Ar IV]	F1	2.61	2.87	5.2
4740.17	[Ar IV]	F1	2.08	2.24	5.1
4788.13	N II	V20	0.15	0.16	5.1
4861.33	H I 4-2	H4	100.00	100.00	5.2
4881.11	[Fe III]	F2	0.86	0.85	5.7
4906.83	O II	V28	0.22	0.21	5.4
4958.91	[O III]	F1	548.64	516.06	5.1
5006.84	[O III]	F1	1693.86	1546.13	5.1
5199.84	[N I]	F1	2.08	1.68	10.0
5411.52	He II	4.7	5.65	4.02	5.4
5754.60	[N III]	F3	3.44	2.09	5.3
5875.66	He I	V11	18.35	10.60	5.1
6300.30	[O I]	F1	10.96	5.34	6.2
6312.10	[S III]	F3	4.48	2.17	5.3
6363.77	[O I]	F1	3.54	1.68	5.6
6461.95	C II	V17.04	0.29	0.13	5.1
6527.11	He II	5.14	0.32	0.14	5.4
6548.10	[N III]	F1	97.49	43.24	5.1
6562.77	H I 3-2	H3	648.17	285.96	5.2
6583.50	[N III]	F1	307.20	134.51	5.0
6678.16	He I	V46	6.49	2.75	5.1
6716.44	[S II]	F2	14.87	6.21	5.1
6730.82	[S II]	F2	18.63	7.74	7.6
7135.80	[Ar III] [b]	F1	64.00	23.24	...
7751.43	[Ar III] [b]	F1	14.90	4.52	...
9068.60	[S III] [b]	F1	98.90	22.19	25.0

[a] Fluxes adopted from Kingsburgh & Barlow (1994).

[b] Fluxes adopted from Milingo et al. (2002).

Table B.6: As Table B.1 but for Pe 1-1.

		Pe 1-1			
		$c(\mathrm{H}\beta) = 1.96$			
λ_0(Å)	ID	Mult	$F(\lambda)$	$I(\lambda)$	Err(%)
3726.03	[O II] [a]	F1	13.15	41.80	7.0
3728.82	[O II] [a]	F1	5.21	16.53	7.0
3868.75	[Ne III] [a]	F1	31.05	87.69	7.0
3889.05	H I 8-2 [a]	H8	7.50	20.80	7.0
3967.46	[Ne III] [a]	F1	9.52	24.58	7.0
4068.60	[S II] [a]	F1	1.60	3.75	7.0
4076.35	[S II] [a]	F1	0.64	1.49	8.0
4101.74	H I 6-2 [a]	H6	12.15	27.54	6.0
4340.47	H I 5-2 [a]	H5	29.13	51.57	6.0
4363.21	[O III] [a]	F2	4.31	7.45	6.0
4471.50	He I	V14	3.55	5.46	5.9
4649.13	O II	V1	0.22	0.28	5.6
4711.37	[Ar IV]	F1	0.04	0.05	39.0
4740.17	[Ar IV]	F1	0.16	0.18	18.0
4861.33	H I 4-2	H4	100.00	100.00	5.0
4906.83	O II	V28	0.10	0.10	29.4
4921.93	He I	V48	0.35	0.33	7.4
4958.91	[O III]	F1	374.08	335.82	5.0
5006.84	[O III]	F1	1190.96	1014.04	5.0
5495.67	N II	V29	0.11	0.06	5.3
5517.66	[Cl III]	F1	0.45	0.23	8.0
5537.60	[Cl III]	F1	1.27	0.63	6.0
5679.56	N II	V3	0.09	0.04	5.4
5754.60	[N III]	F3	6.36	2.65	5.3
5875.66	He I	V11	42.55	16.18	5.0
5931.78	N II	V28	0.11	0.04	7.1
5941.65	N II	V28	0.03	0.01	6.1
6151.43	C II	V16.04	0.10	0.03	5.2
6300.30	[O I]	F1	33.48	9.42	5.0
6312.10	[S III]	F3	5.81	1.62	5.5
6363.77	[O I]	F1	10.44	2.81	5.2
6461.95	C II	V17.04	0.40	0.10	5.2
6548.10	[N III]	F1	151.82	36.24	5.0
6562.77	H I 3-2	H3	1205.41	285.00	5.0
6583.50	[N III]	F1	496.28	115.79	5.0
6678.16	He I	V46	19.21	4.22	5.1
6716.44	[S II]	F2	10.74	2.31	5.2
6730.82	[S II]	F2	22.86	4.86	9.6
7135.80	[Ar III] [a]	F1	113.03	18.96	10.0
7281.35	He I [a]	V45	5.35	0.83	10.0
7319.40	[O II] [a]	F2	78.99	11.99	10.0
7329.90	[O II] [a]	F2	64.22	9.70	10.0
7751.43	[Ar III] [a]	F1	35.47	4.33	11.0
9068.60	[S III] [a]	F1	337.70	24.25	14.0

[a] Fluxes adopted from García-Rojas et al. (2012).

Table B.7: As Table B.1 but for M 1-32.

		M 1-32			
		$c(\mathrm{H}\beta) = 1.40$			
λ_0(Å)	ID	Mult	$F(\lambda)$	$I(\lambda)$	Err(%)
3726.03	[O II] [a]	F1	34.29	78.22	9.0
3728.82	[O II] [a]	F1	15.48	35.26	9.0
3868.75	[Ne III] [a]	F1	5.77	12.10	8.0
3889.05	H I 8-2 [a]	H8	10.33	21.38	8.0
3967.46	[Ne III] [a]	F1	2.08	4.09	8.0
4068.60	[S II] [a]	F1	4.84	8.88	7.0
4076.35	[S II] [a]	F1	1.70	3.10	8.0
4101.74	H I 6-2 [a]	H6	13.48	24.16	7.0
4363.21	[O III] [a]	F2	1.64	2.42	7.0
4471.50	He I	V14	4.01	5.45	5.3
4740.17	[Ar IV]	F1	0.08	0.08	9.0
4861.33	H I 4-2	H4	100.00	100.00	5.2
4921.93	He I	V48	1.75	1.67	5.9
4958.91	[O III]	F1	168.15	155.70	5.2
5006.84	[O III]	F1	521.80	465.27	5.2
5199.84	[N I]	F1	3.57	2.74	17.4
5517.66	[Cl III]	F1	0.83	0.51	9.0
5537.60	[Cl III]	F1	1.74	1.05	7.0
5710.77	N II	V3	0.11	0.06	7.0
5754.60	[N III]	F3	11.22	6.01	5.4
5875.66	He I	V11	37.60	18.87	5.5
6101.83	[K IV]	F1	0.03	0.01	5.6
6170.17	N II	V36	0.06	0.03	6.1
6300.30	[O I]	F1	22.64	9.16	5.4
6312.10	[S III]	F3	6.43	2.59	5.5
6363.77	[O I]	F1	7.38	2.90	5.4
6461.95	C II	V17.04	0.50	0.19	13.8
6527.11	He II	5.14	0.17	0.06	6.1
6548.10	[N III]	F1	457.38	164.66	5.4
6562.77	H I 3-2	H3	806.57	288.42	5.3
6583.50	[N III]	F1	1439.48	509.90	5.4
6678.16	He I	V46	15.22	5.17	5.5
6716.44	[S II]	F2	35.24	11.76	8.2
6730.82	[S II]	F2	68.34	22.66	5.3
7135.80	[Ar III] [a]	F1	103.46	28.97	13.0
7281.35	He I [a]	V45	3.62	0.96	13.0
7319.40	[O II] [a]	F2	50.06	13.05	13.0
7329.90	[O II] [a]	F2	40.82	10.60	13.0
7751.43	[Ar III] [a]	F1	29.49	6.59	14.0
9068.60	[S III] [a]	F1	444.65	67.98	19.0

[a] Fluxes adopted from García-Rojas et al. (2012).

Table B.8: As Table B.1 but for M 3-15.

		M 3-15			
		$c(\mathrm{H}\beta) = 2.27$			
λ_0(Å)	ID	Mult	$F(\lambda)$	$I(\lambda)$	Err(%)
3726.03	[O II] [a]	F1	3.30	12.62	10.0
3728.82	[O II] [a]	F1	1.41	5.39	13.0
3868.75	[Ne III] [a]	F1	18.60	61.98	8.0
3967.46	[Ne III] [a]	F1	3.66	10.99	9.0
4068.60	[S II] [a]	F1	0.48	1.29	21.0
4076.35	[S II] [a]	F1	0.29	0.77	30.0
4101.74	H I 6-2 [a]	H6	9.72	25.10	7.0
4340.47	H I 5-2 [a]	H5	24.48	47.46	6.0
4363.21	[O III] [a]	F2	1.74	3.28	10.0
4471.50	He I	V14	3.71	6.11	7.0
4650.84	O II	V1	0.74	0.97	22.2
4711.37	[Ar IV]	F1	0.60	0.73	23.4
4740.17	[Ar IV]	F1	0.80	0.93	15.0
4861.33	H I 4-2	H4	100.00	100.00	5.0
4958.91	[O III]	F1	366.72	323.60	5.0
5006.84	[O III]	F1	1195.19	991.90	5.0
5517.66	[Cl III]	F1	0.79	0.35	9.0
5537.60	[Cl III]	F1	1.39	0.61	8.0
5666.63	N II	V3	0.10	0.04	7.4
5679.56	N II	V3	0.23	0.09	7.5
5754.60	[N III]	F3	1.19	0.43	7.8
5875.66	He I	V11	50.56	16.49	5.2
6151.43	C II	V16.04	0.14	0.04	20.0
6300.30	[O I]	F1	10.64	2.44	5.4
6312.10	[S III]	F3	5.11	1.16	6.2
6461.95	C II	V17.04	0.34	0.07	15.0
6548.10	[N III]	F1	88.07	16.73	5.0
6562.77	H I 3-2	H3	1543.23	289.96	5.0
6583.50	[N III]	F1	277.00	51.25	5.0
6678.16	He I	V46	22.80	3.94	5.2
6716.44	[S II]	F2	15.63	2.63	15.6
6730.82	[S II]	F2	29.28	4.87	9.5
7135.80	[Ar III] [a]	F1	115.62	14.60	13.0
7281.35	He I [a]	V45	6.44	0.74	13.0
7319.40	[O II] [a]	F2	16.74	1.88	13.0
7329.90	[O II] [a]	F2	13.72	1.53	13.0
7751.43	[Ar III] [a]	F1	36.88	3.22	14.0
9068.60	[S III] [a]	F1	532.32	25.12	19.0

[a] Fluxes adopted from García-Rojas et al. (2012).

Table B.9: As Table B.1 but for M 1-25.

M 1-25 $c(\mathrm{H}\beta) = 1.60$					
λ_0(Å)	ID	Mult	$F(\lambda)$	$I(\lambda)$	Err(%)
3726.03	[O II] [a]	F1	22.58	58.19	7.0
3728.82	[O II] [a]	F1	9.71	24.98	7.0
3868.75	[Ne III] [a]	F1	5.03	11.77	7.0
3967.46	[Ne III] [a]	F1	1.11	2.41	7.0
4068.60	[S II] [a]	F1	1.87	3.75	7.0
4076.35	[S II] [a]	F1	0.75	1.50	8.0
4101.74	H I 6-2 [a]	H6	14.17	27.69	6.0
4340.47	H I 5-2 [a]	H5	32.37	51.66	6.0
4363.21	[O III] [a]	F2	0.84	1.32	7.0
4471.50	He I	V14	3.99	5.67	5.3
4491.23	O II	V86a	0.02	0.03	6.0
4649.13	O II	V1	0.38	0.46	5.8
4861.33	H I 4-2	H4	100.00	100.00	5.0
4906.83	O II	V28	0.07	0.07	9.5
4921.93	He I	V48	0.78	0.74	6.5
4958.91	[O III]	F1	173.87	159.17	5.0
5006.84	[O III]	F1	548.77	481.08	5.0
5517.66	[Cl III]	F1	0.65	0.37	6.0
5537.60	[Cl III]	F1	1.39	0.78	6.0
5666.63	N II	V3	0.22	0.11	5.6
5679.56	N II	V3	0.33	0.17	5.4
5686.21	N II	V3	0.05	0.03	6.8
5710.77	N II	V3	0.06	0.03	5.4
5754.60	[N III]	F3	4.06	1.98	5.5
5875.66	He I	V11	41.10	18.63	7.0
6300.30	[O I]	F1	6.21	2.20	5.3
6312.10	[S III]	F3	4.62	1.62	5.4
6363.77	[O I]	F1	1.73	0.59	6.2
6461.95	C II	V17.04	0.20	0.06	5.1
6482.05	N II	V8	0.50	0.16	9.3
6548.10	[N III]	F1	226.23	70.02	5.0
6562.77	H I 3-2	H3	944.38	290.04	5.0
6583.50	[N III]	F1	717.23	217.90	5.0
6678.16	He I	V46	18.49	5.35	5.0
6716.44	[S II]	F2	19.12	5.43	5.0
6730.82	[S II]	F2	34.99	9.86	10.2
7135.80	[Ar III] [a]	F1	91.63	21.25	10.0
7281.35	He I [a]	V45	3.43	0.75	10.0
7319.40	[O II] [a]	F2	23.24	4.97	10.0
7329.90	[O II] [a]	F2	18.99	4.04	10.0
7751.43	[Ar III] [a]	F1	26.07	4.66	11.0
9068.60	[S III] [a]	F1	361.98	41.91	14.0

[a] Fluxes adopted from García-Rojas et al. (2012).

Table B.10: As Table B.1 but for Hen 2-142.

		Hen 2-142			
		$c(\mathrm{H}\beta) = 1.55$			
λ_0(Å)	ID	Mult	$F(\lambda)$	$I(\lambda)$	Err(%)
3726.03	[O II] [a]	F1	45.50	113.46	...
3728.82	[O II] [a]	F1	*	*	...
4101.74	H I 6-2 [a]	H6	20.10	38.42	...
4340.47	H I 5-2 [a]	H5	46.80	73.55	...
4471.50	He I	V14	0.74	1.04	6.2
4774.24	N II	V20	0.04	0.04	9.4
4861.33	H I 4-2	H4	100.00	100.00	5.0
4958.91	[O III]	F1	1.54	1.41	5.5
5006.84	[O III]	F1	6.05	5.33	5.3
5754.60	[N III]	F3	9.72	4.86	5.0
6233.80	He II	5.17	0.20	0.08	11.9
6300.30	[O I]	F1	10.22	3.74	5.1
6312.10	[S III]	F3	1.69	0.62	5.5
6363.77	[O I]	F1	3.26	1.15	5.3
6527.11	He II	5.14	0.23	0.07	7.4
6548.10	[N III]	F1	286.08	92.04	5.0
6562.77	H I 3-2	H3	901.90	288.00	5.0
6583.50	[N III]	F1	896.23	283.20	5.0
6678.16	He I	V46	3.37	1.02	5.2
6716.44	[S II]	F2	7.58	2.24	5.6
6730.82	[S II]	F2	17.50	5.14	5.1
7319.40	[O II] [a]	F2	129.00	29.01	...
7329.90	[O II] [a]	F2	109.00	24.41	...

[a] Fluxes adopted from Girard et al. (2007).

Table B.11: As Table B.1 but for Hen 3-1333.

		Hen 3-1333 $c(H\beta) = 1.04$			
λ_0(Å)	ID	Mult	$F(\lambda)$	$I(\lambda)$	Err(%)
3726.03	[O II] [a]	F1	45.60	85.41	20.0
3728.82	[O II] [a]	F1	*	*	...
4861.33	H I 4-2	H4	100.00	100.00	5.1
5754.60	[N III]	F3	12.93	8.03	5.1
6300.30	[O I]	F1	90.87	45.59	5.1
6363.77	[O I]	F1	35.35	17.33	5.3
6548.10	[N III]	F1	208.28	95.59	5.0
6562.77	H I 3-2	H3	629.43	287.40	5.1
6583.50	[N III]	F1	981.57	444.97	6.3
6716.44	[S II]	F2	29.01	12.57	10.1
6730.82	[S II]	F2	100.94	43.52	6.1
7319.40	[O II] [a]	F2	71.65	25.72	15.0
7329.90	[O II] [a]	F2	36.18	12.95	15.0
9068.60	[S III] [a]	F1	8.70	2.08	15.0

[a] Fluxes adopted from De Marco et al. (1997).

Table B.12: As Table B.1 but for Hen 2-113.

		Hen 2-113			
		$c(\mathrm{H}\beta) = 1.31$			
λ_0(Å)	ID	Mult	$F(\lambda)$	$I(\lambda)$	Err(%)
3726.03	[O II] [a]	F1	6.41	13.94	20.0
3728.82	[O II] [a]	F1	6.29	13.66	20.0
4861.33	H I 4-2	H4	100.00	100.00	5.1
5754.60	[N III]	F3	9.61	5.34	5.0
6300.30	[O I]	F1	12.17	5.19	5.0
6312.10	[S III]	F3	1.10	0.47	5.2
6363.77	[O I]	F1	4.78	1.98	5.1
6461.95	C II	V17.04	19.28	7.65	5.4
6548.10	[N III]	F1	118.10	45.11	5.0
6562.77	H I 3-2	H3	760.28	288.60	5.0
6583.50	[N III]	F1	401.30	150.98	5.2
6716.44	[S II]	F2	6.08	2.16	7.0
6730.82	[S II]	F2	22.05	7.80	5.9
7319.40	[O II] [a]	F2	65.92	18.58	15.0
7329.90	[O II] [a]	F2	58.06	16.31	15.0
9068.60	[S III] [a]	F1	47.19	8.05	30.0

[a] Fluxes adopted from De Marco et al. (1997).

Table B.13: As Table B.1 but for K 2-16.

			K 2-16		
			$c(\mathrm{H}\beta) = 0.56$		
λ_0(Å)	ID	Mult	$F(\lambda)$	$I(\lambda)$	Err(%)
3726.03	[O II] [a]	F1	96.33	134.19	...
3728.82	[O II] [a]	F1	128.71	179.19	...
4861.33	H I 4-2	H4	100.00	100.00	5.2
4958.91	[O III]	F1	40.57	39.33	5.3
5006.84	[O III]	F1	144.22	137.72	5.9
5754.60	[N III]	F3	4.49	3.49	5.0
6300.30	[O I]	F1	6.07	4.22	5.1
6548.10	[N III]	F1	97.46	64.64	5.1
6562.77	H I 3-2	H3	432.40	286.00	5.1
6583.50	[N III]	F1	446.89	294.46	6.5
6716.44	[S II]	F2	90.75	58.38	5.8
6730.82	[S II]	F2	67.18	43.11	5.6

[a] Fluxes adopted from Peña et al. (2001).

Table B.14: As Table B.1 but for NGC 6578.

		NGC 6578			
		$c(\mathrm{H}\beta) = 1.53$			
λ_{lab}(Å)	ID	Mult	$F(\lambda)$	$I(\lambda)$	Err(%)
3726.03	[O II] [a]	F1	7.50	18.57	...
3728.82	[O II] [a]	F1	*	*	...
3868.75	[Ne III] [a]	F1	30.40	68.59	...
3889.05	H I 8-2 [a]	H8	10.00	22.25	...
3967.46	[Ne III] [a]	F1	18.80	39.54	...
4068.60	[S II] [a]	F1	0.90	1.75	50.0
4076.35	[S II] [a]	F1	*	*	...
4101.74	H I 6-2 [a]	H6	15.30	29.06	...
4340.47	H I 5-2 [a]	H5	32.90	51.47	...
4363.21	[O III] [a]	F2	1.60	2.46	...
4471.50	He I	V14	4.00	5.60	5.3
4649.13	O II	V1	0.56	0.67	7.2
4661.63	O II	V1	0.20	0.24	6.8
4685.68	He II	3.4	0.47	0.55	6.7
4711.37	[Ar IV]	F1	0.90	1.03	15.0
4740.17	[Ar IV]	F1	1.00	1.11	15.0
4861.33	H I 4-2	H4	100.00	100.00	5.0
4890.86	O II	V28	0.05	0.05	7.3
4921.93	He I	V48	0.58	0.55	5.5
4958.91	[O III]	F1	277.43	254.93	5.0
5006.84	[O III]	F1	865.69	763.17	5.0
5411.52	He II	4.7	0.20	0.12	12.3
5517.66	[Cl III]	F1	0.60	0.35	...
5537.60	[Cl III]	F1	0.80	0.46	...
5754.60	[N III]	F3	0.41	0.21	15.8
5875.66	He I	V11	37.06	17.37	5.0
6300.30	[O I]	F1	0.28	0.10	7.1
6312.10	[S III]	F3	2.06	0.76	5.5
6461.95	C II	V17.04	0.37	0.13	6.7
6548.10	[N III]	F1	12.34	4.01	5.1
6562.77	H I 3-2	H3	884.24	285.56	5.0
6583.50	[N III]	F1	40.21	12.85	5.1
6678.16	He I	V46	15.56	4.75	5.0
6716.44	[S II]	F2	2.53	0.76	5.3
6730.82	[S II]	F2	4.58	1.36	5.2
7135.80	[Ar III] [a]	F1	63.60	15.70	...
7281.35	He I [a]	V45	2.90	0.67	...
7319.40	[O II] [a]	F2	9.80	2.23	...
7329.90	[O II] [a]	F2	*	*	...
7751.43	[Ar III] [a]	F1	17.70	3.41	...
9068.60	[S III] [a]	F1	158.00	20.05	...

[a] Fluxes adopted from Kwitter et al. (2003).

Table B.15: As Table B.1 but for M 2-42.

		M 2-42			
		$c(\mathrm{H}\beta) = 0.99$			
$\lambda_{\rm lab}$(Å)	ID	Mult	$F(\lambda)$	$I(\lambda)$	Err(%)
3726.03	[O II] [a]	F1	19.37	34.72	...
3728.82	[O II] [a]	F1	*	*	...
3868.75	[Ne III] [a]	F1	29.09	49.17	...
3889.05	H I 8-2 [a]	H8	9.74	16.31	...
3967.46	[Ne III] [a]	F1	5.69	9.19	...
3970.07	H I 7-2 [a]	H7	7.04	11.36	...
4068.60	[S II] [a]	F1	1.30	2.00	...
4076.35	[S II] [a]	F1	0.72	1.10	...
4101.74	H I 6-2 [a]	H6	15.30	23.14	...
4340.47	H I 5-2 [a]	H5	34.77	46.41	...
4363.21	[O III] [a]	F2	2.05	2.70	...
4471.50	He I	V14	4.61	5.73	5.0
4609.44	O II	V92a	0.04	0.05	5.6
4634.14	N III	V2	0.13	0.15	5.5
4649.13	O II	V1	0.34	0.38	7.6
4676.23	O II	V1	0.08	0.09	5.5
4685.68	He II	3.4	0.30	0.33	5.5
4711.37	[Ar IV]	F1	0.90	0.98	...
4740.17	[Ar IV]	F1	1.00	1.07	5.2
4861.33	H I 4-2	H4	100.00	100.00	5.0
4906.83	O II	V28	0.04	0.04	5.7
4921.93	He I	V48	1.44	1.39	5.3
4958.91	[O III]	F1	227.97	215.87	5.1
5006.84	[O III]	F1	725.69	669.03	6.1
5041.98	O II		0.08	0.07	5.7
5517.66	[Cl III]	F1	0.73	0.51	...
5537.60	[Cl III]	F1	0.85	0.59	...
5666.63	N II	V3	0.06	0.04	6.2
5679.56	N II	V3	0.11	0.07	5.8
5754.60	[N III]	F3	1.01	0.65	5.1
5875.66	He I	V11	24.33	14.93	5.0
6101.83	[K IV]	F1	0.04	0.02	5.2
6300.30	[O I]	F1	4.51	2.38	5.5
6312.10	[S III]	F3	2.20	1.15	5.0
6363.77	[O I]	F1	1.56	0.80	5.4
6461.95	C II	V17.04	0.12	0.06	5.4
6548.10	[N III]	F1	26.01	12.61	5.0
6562.77	H I 3-2	H3	593.30	286.21	7.1
6583.50	[N III]	F1	80.05	38.36	5.0
6678.16	He I	V46	8.53	3.97	5.0
6716.44	[S II]	F2	8.11	3.73	5.0
6730.82	[S II]	F2	12.82	5.86	5.0
7065.20	He I [a]	V10	7.13	2.95	...
7135.80	[Ar III] [a]	F1	23.47	9.52	...
7281.35	He I [a]	V45	1.17	0.45	...
7319.40	[O II] [a]	F2	5.22	2.01	...
7329.90	[O II] [a]	F2	4.22	1.62	...

[a] Fluxes adopted from Wang & Liu (2007).

Table B.16: As Table B.1 but for NGC 6567.

		NGC 6567 $c(\mathrm{H}\beta) = 0.78$			
λ_{lab}(Å)	ID	Mult	$F(\lambda)$	$I(\lambda)$	Err(%)
3726.03	[O II] [a]	F1	15.60	24.75	...
3728.82	[O II] [a]	F1	*	*	...
3868.75	[Ne III] [a]	F1	43.50	65.87	...
3889.05	H I 8-2 [a]	H8	10.20	15.34	...
3967.46	[Ne III] [a]	F1	17.10	24.98	...
4068.60	[S II] [a]	F1	0.90	1.26	50.0
4076.35	[S II] [a]	F1	*	*	...
4101.74	H I 6-2 [a]	H6	15.30	21.22	...
4340.47	H I 5-2 [a]	H5	36.60	45.99	...
4363.21	[O III] [a]	F2	7.60	9.46	...
4471.50	He I	V14	4.35	5.17	5.0
4609.44	O II	V92a	0.02	0.02	5.1
4640.64	N III	V2	0.35	0.39	7.0
4649.13	O II	V1	0.40	0.44	18.9
4661.63	O II	V1	0.03	0.03	5.7
4676.23	O II	V1	0.03	0.03	5.1
4685.68	He II	3.4	0.77	0.83	5.2
4711.37	[Ar IV]	F1	0.80	0.85	15.0
4740.17	[Ar IV]	F1	1.00	1.06	15.0
4803.29	N II	V20	0.02	0.02	5.5
4861.33	H I 4-2	H4	100.00	100.00	5.0
4906.83	O II	V28	0.01	0.01	5.5
4921.93	He I	V48	1.20	1.17	5.2
4958.91	[O III]	F1	326.76	312.97	5.0
5006.84	[O III]	F1	1006.28	943.63	5.1
5517.66	[Cl III]	F1	0.40	0.30	15.0
5537.60	[Cl III]	F1	0.60	0.45	15.0
5679.56	N II	V3	0.02	0.01	5.0
5754.60	[N III]	F3	0.47	0.33	5.6
5875.66	He I	V11	22.76	15.47	5.0
5927.81	N II	V28	0.02	0.01	5.8
6101.83	[K IV]	F1	0.08	0.05	5.3
6118.20	He II	5.19	0.02	0.01	5.1
6151.43	C II	V16.04	0.08	0.05	5.0
6300.30	[O I]	F1	3.32	2.00	7.0
6312.10	[S III]	F3	1.28	0.77	5.2
6363.77	[O I]	F1	1.18	0.70	6.7
6406.30	He II	5.15	0.03	0.02	5.2
6461.95	C II	V17.04	0.22	0.13	5.0
6548.10	[N III]	F1	8.37	4.72	5.8
6562.77	H I 3-2	H3	503.90	283.15	5.0
6583.50	[N III]	F1	25.89	14.47	6.0
6678.16	He I	V46	7.34	4.01	5.0
6716.44	[S II]	F2	1.18	0.64	5.7
6730.82	[S II]	F2	2.25	1.21	6.0
7065.20	He I [a]	V10	14.70	7.32	...
7135.80	[Ar III] [a]	F1	11.30	5.54	...
7281.35	He I [a]	V45	1.70	0.81	...
7319.40	[O II] [a]	F2	10.60	4.98	...
7329.90	[O II] [a]	F2	*	*	...
7751.43	[Ar III] [a]	F1	2.80	1.21	...
9068.60	[S III] [a]	F1	20.60	7.19	...

[a] Fluxes adopted from Kwitter et al. (2003).

Table B.17: As Table B.1 but for NGC 6629.

NGC 6629					
$c(\mathrm{H}\beta) = 0.98$					
λ_{lab}(Å)	ID	Mult	$F(\lambda)$	$I(\lambda)$	Err(%)
3726.03	[O II] [a]	F1	21.20	37.77	...
3728.82	[O II] [a]	F1	*	*	...
3868.75	[Ne III] [a]	F1	25.70	43.21	...
3889.05	H I 8-2 [a]	H8	12.20	20.33	...
3967.46	[Ne III] [a]	F1	18.50	29.74	...
4101.74	H I 6-2 [a]	H6	17.60	26.51	...
4340.47	H I 5-2 [a]	H5	36.90	49.11	...
4363.21	[O III] [a]	F2	2.10	2.76	...
4471.50	He I	V14	3.92	4.86	5.1
4491.23	O II	V86a	0.02	0.02	5.0
4649.13	O II	V1	0.28	0.31	5.7
4676.23	O II	V1	0.05	0.06	5.0
4685.68	He II	3.4	0.41	0.45	7.9
4740.17	[Ar IV]	F1	0.20	0.21	5.3
4803.29	N II	V20	0.06	0.06	5.0
4861.33	H I 4-2	H4	100.00	100.00	5.0
4890.86	O II	V28	0.05	0.05	5.0
4906.83	O II	V28	0.08	0.08	5.0
4921.93	He I	V48	1.33	1.29	5.2
4958.91	[O III]	F1	233.63	221.35	5.1
5006.84	[O III]	F1	713.86	658.67	5.1
5517.66	[Cl III]	F1	0.45	0.32	15.0
5537.60	[Cl III]	F1	0.50	0.35	15.0
5679.56	N II	V3	0.09	0.06	5.0
5710.77	N II	V3	0.01	0.01	5.0
5754.60	[N III]	F3	0.14	0.09	5.2
5875.66	He I	V11	23.75	14.64	5.0
5931.78	N II	V28	0.02	0.01	5.0
6312.10	[S III]	F3	1.02	0.54	5.2
6461.95	C II	V17.04	0.12	0.06	5.0
6548.10	[N III]	F1	5.38	2.63	5.1
6562.77	H I 3-2	H3	594.29	288.82	5.0
6583.50	[N III]	F1	17.39	8.40	5.2
6678.16	He I	V46	8.67	4.06	5.0
6716.44	[S II]	F2	0.91	0.42	5.1
6730.82	[S II]	F2	1.42	0.65	5.1
7065.20	He I [a]	V10	9.70	4.05	...
7135.80	[Ar III] [a]	F1	29.10	11.91	...
7281.35	He I [a]	V45	2.00	0.79	...
7319.40	[O II] [a]	F2	4.50	1.75	...
7329.90	[O II] [a]	F2	*	*	...
9068.60	[S III] [a]	F1	33.60	9.00	...

[a] Fluxes adopted from Milingo et al. (2002).

Table B.18: As Table B.1 but for Sa 3-107.

		Sa 3-107			
		$c(\mathrm{H}\beta) = 1.61$			
λ_{lab} (Å)	ID	Mult	$F(\lambda)$	$I(\lambda)$	Err(%)
4471.50	He I	V14	4.15	5.91	5.2
4640.64	N III	V2	0.37	0.45	5.6
4685.68	He II	3.4	1.83	2.15	12.9
4861.33	H I 4-2	H4	100.00	100.00	5.0
4890.86	O II	V28	0.09	0.09	5.7
4906.83	O II	V28	0.08	0.08	5.6
4958.91	[O III]	F1	112.68	103.09	5.0
5006.84	[O III]	F1	353.70	309.78	5.0
5710.77	N II	V3	0.14	0.07	5.6
5754.60	[N III]	F3	0.41	0.20	5.2
5875.66	He I	V11	41.56	18.73	5.0
5931.78	N II	V28	0.17	0.08	5.4
6312.10	[S III]	F3	1.08	0.38	5.2
6461.95	C II	V17.04	0.22	0.07	5.3
6548.10	[N III]	F1	11.08	3.40	5.2
6562.77	H I 3-2	H3	935.55	284.88	5.0
6583.50	[N III]	F1	38.00	11.44	5.2
6678.16	He I	V46	17.79	5.10	5.0
6716.44	[S II]	F2	1.95	0.55	5.2
6730.82	[S II]	F2	2.86	0.80	5.1

Appendix C

Nebular Spectra

This appendix contains nebular spectra for all nebulae analyzed in Chapter 3. Based on observations made with the ANU 2.3-m Telescope at the Siding Spring Observatory.

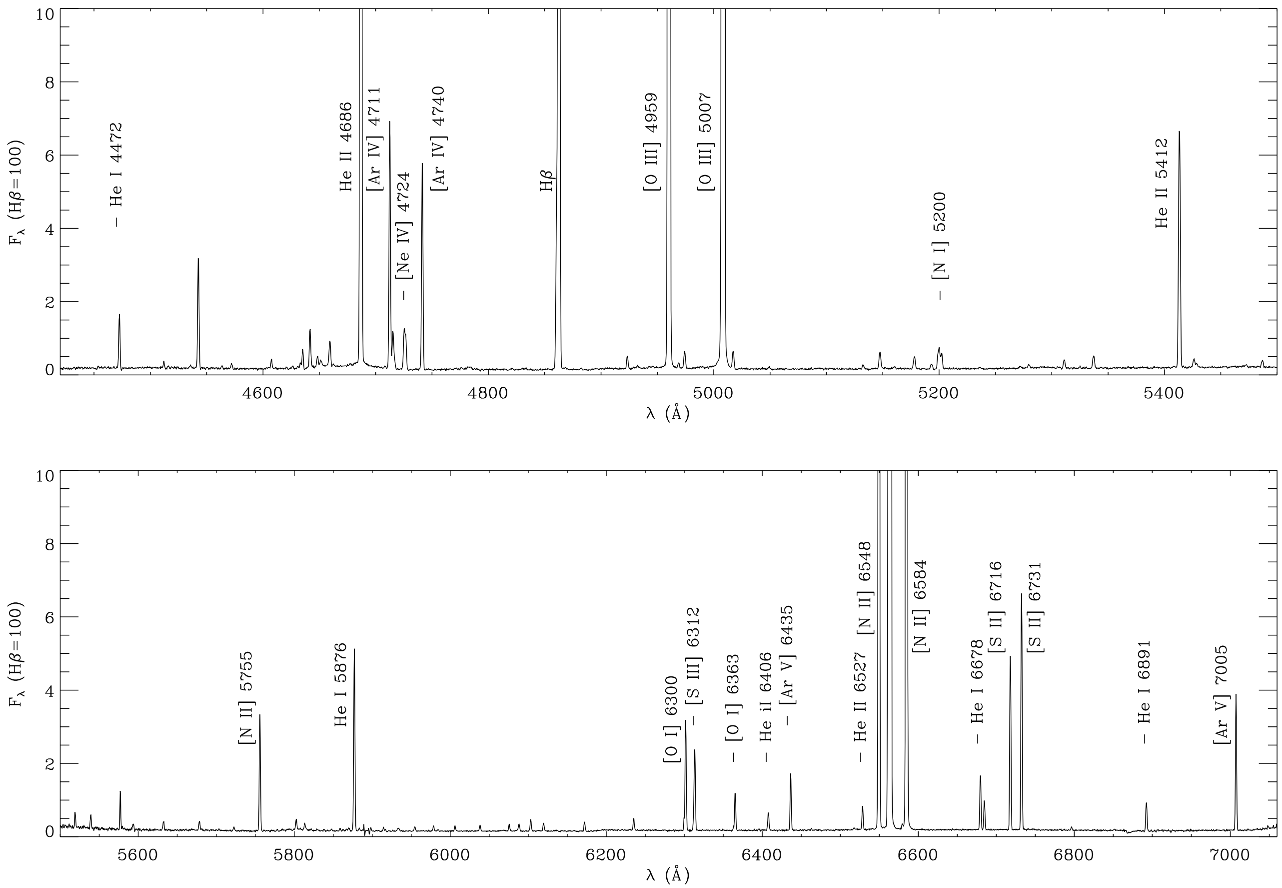

Figure C.1: The observed optical spectra of PB 6 and normalized such that $F(\mathrm{H}\beta) = 100$: grating B7000 (top) covers wavelengths 4415–5500 Å and R7000 (bottom) covers 5500–7060 Å.

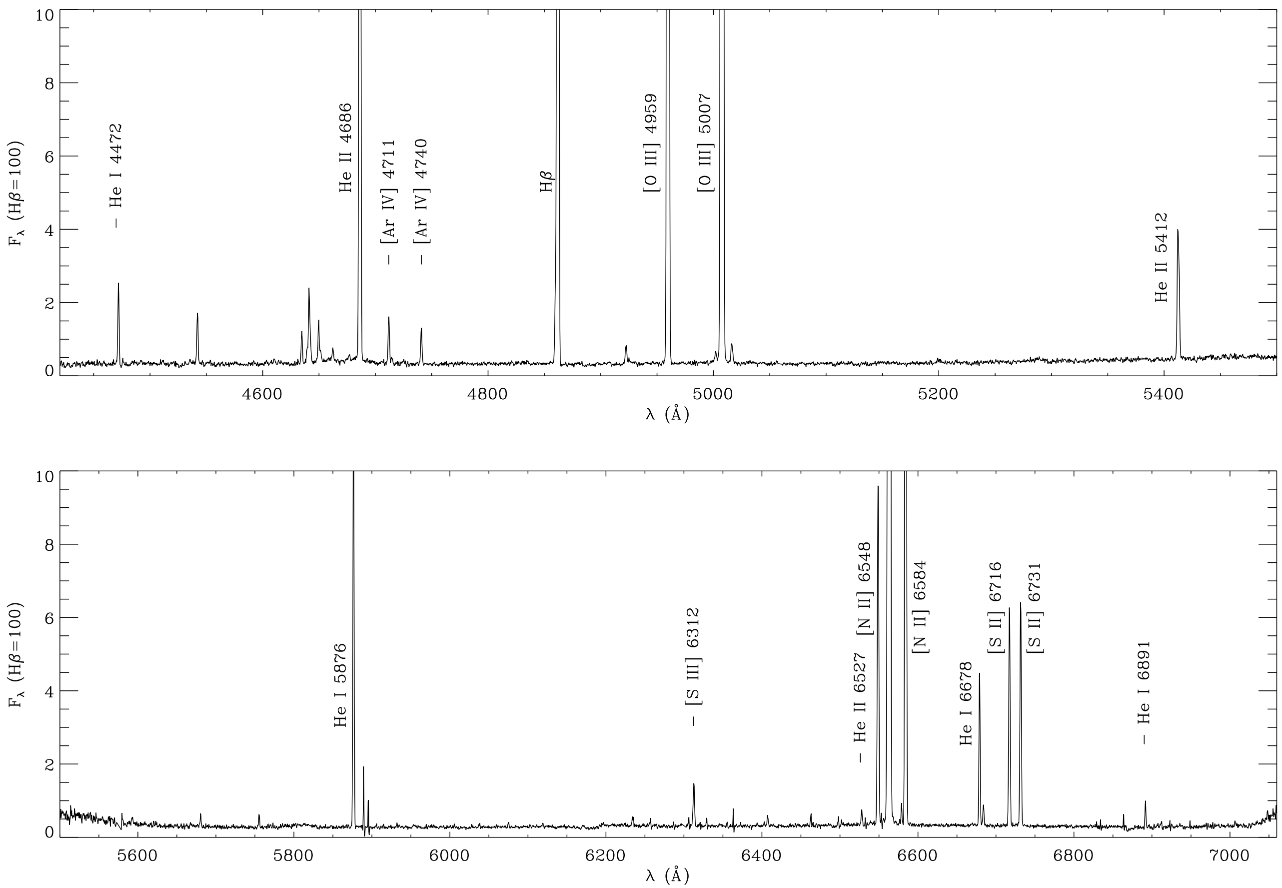

Figure C.2: As Figure C.1 but for M 3-30.

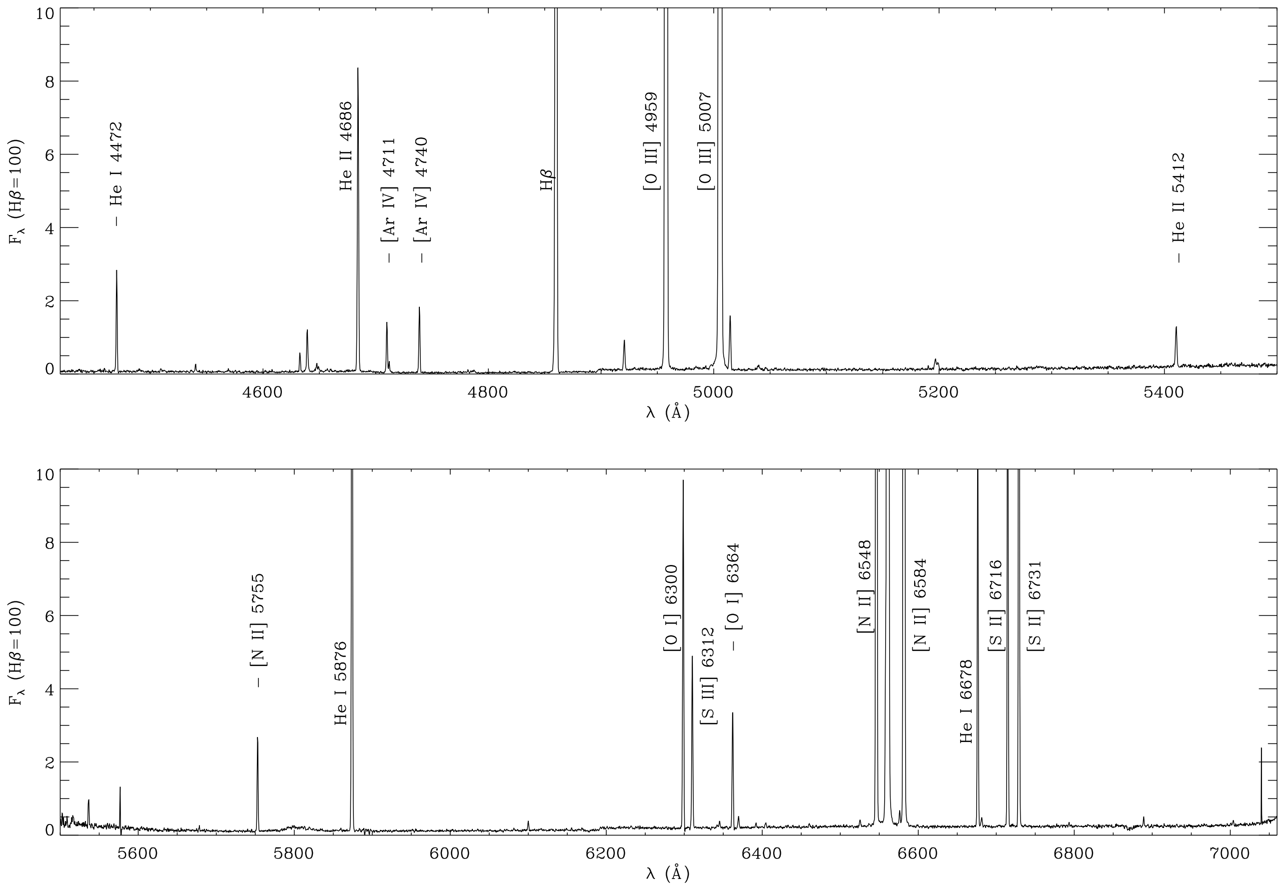

Figure C.3: As Figure C.1 but for Hb 4.

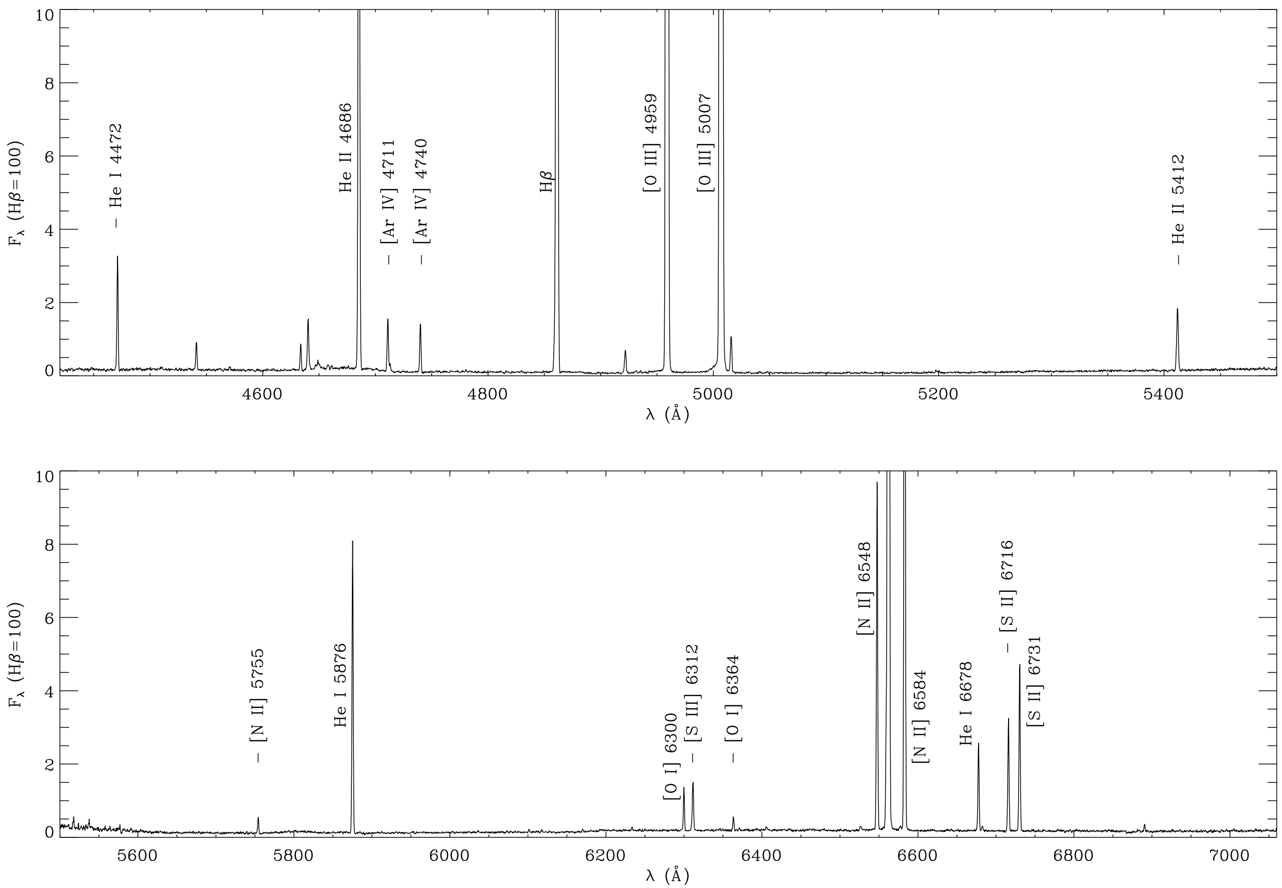

Figure C.4: As Figure C.1 but for IC 1297.

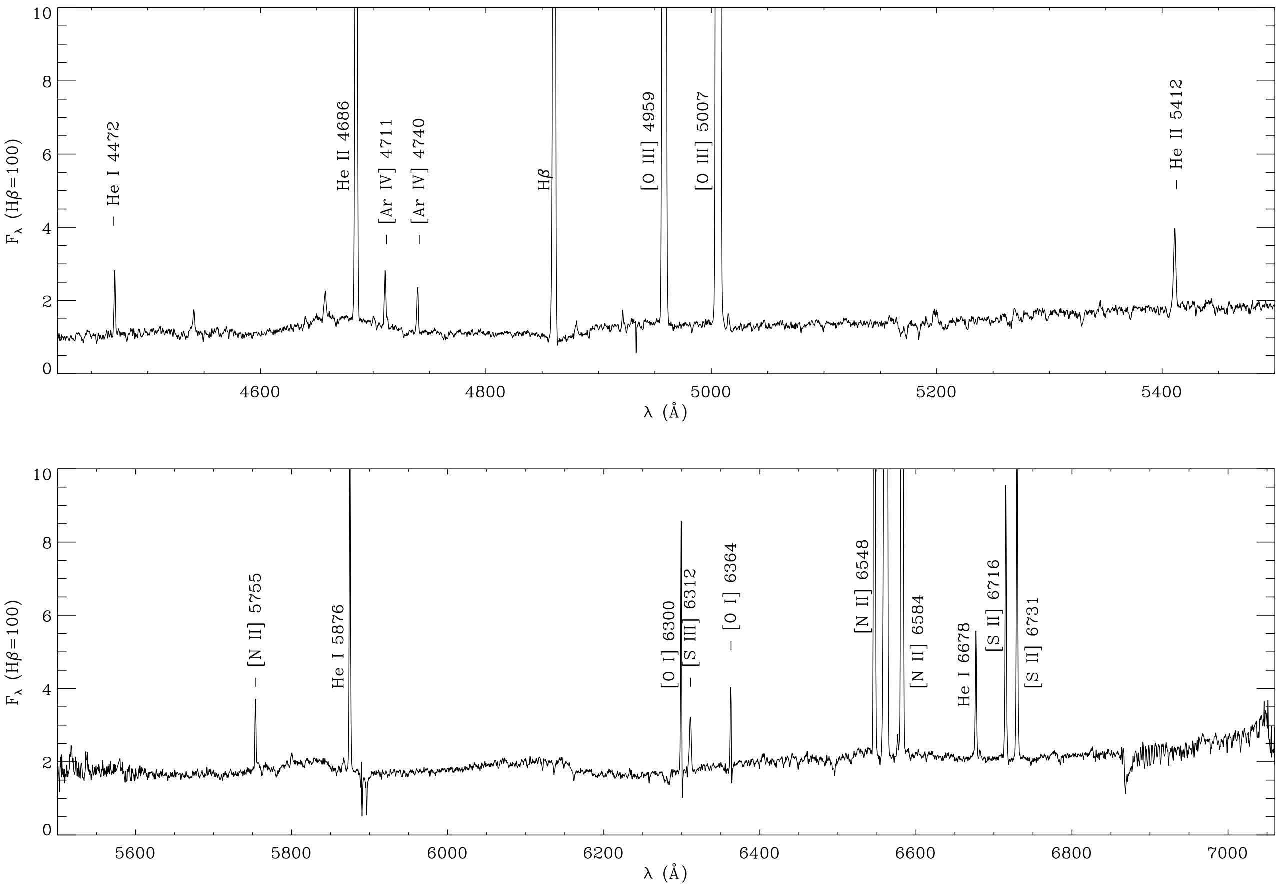

Figure C.5: As Figure C.1 but for Th 2-A.

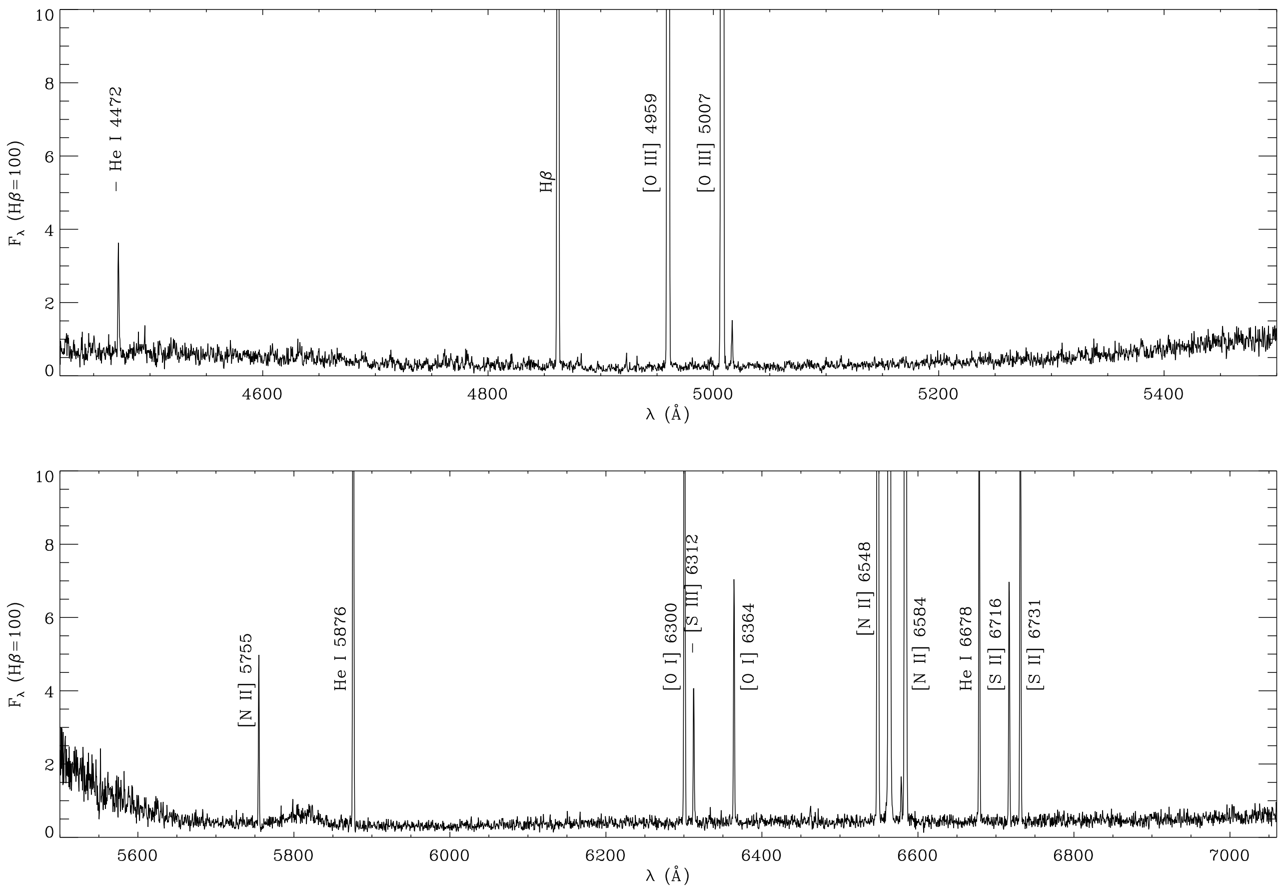

Figure C.6: As Figure C.1 but for Pe 1-1.

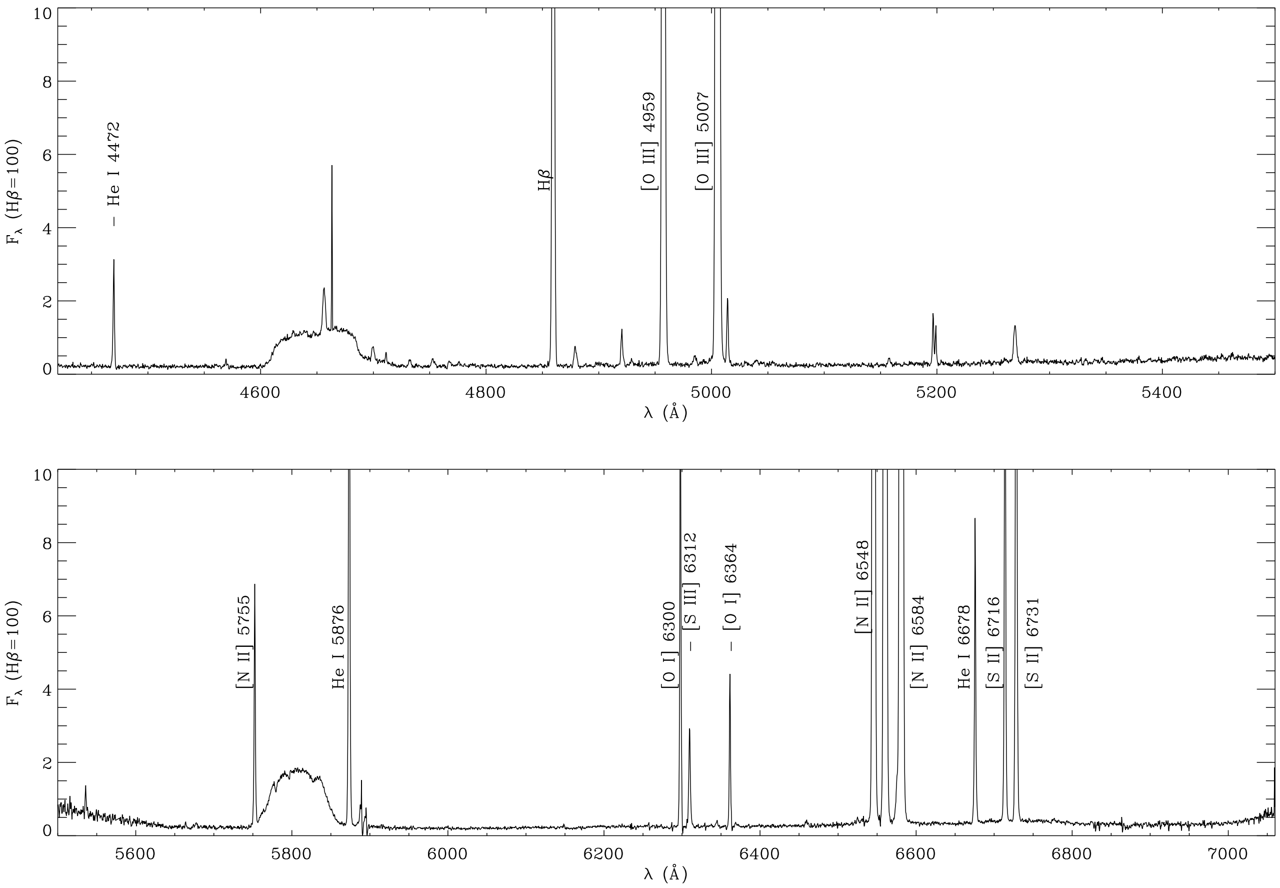

Figure C.7: As Figure C.1 but for M 1-32.

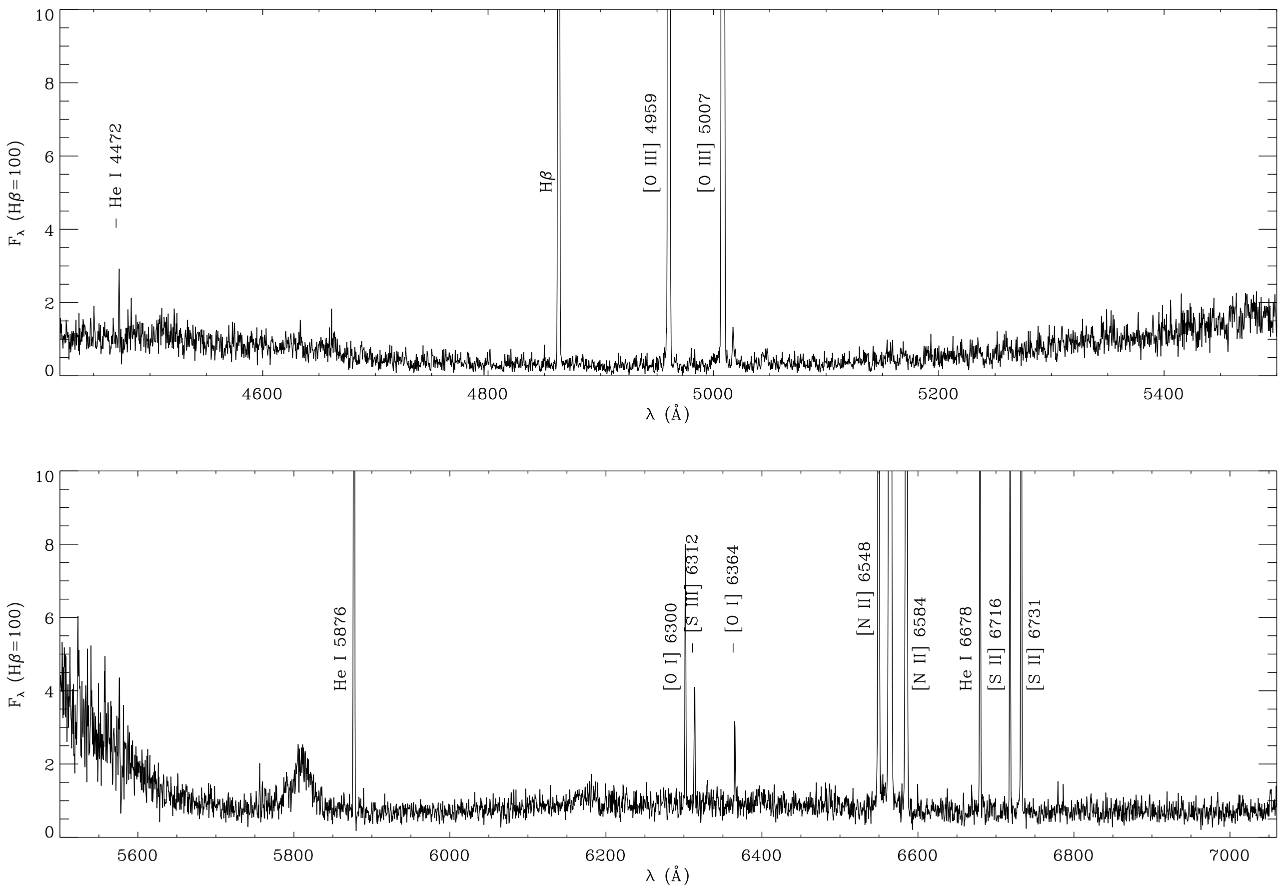

Figure C.8: As Figure C.1 but for M 3-15.

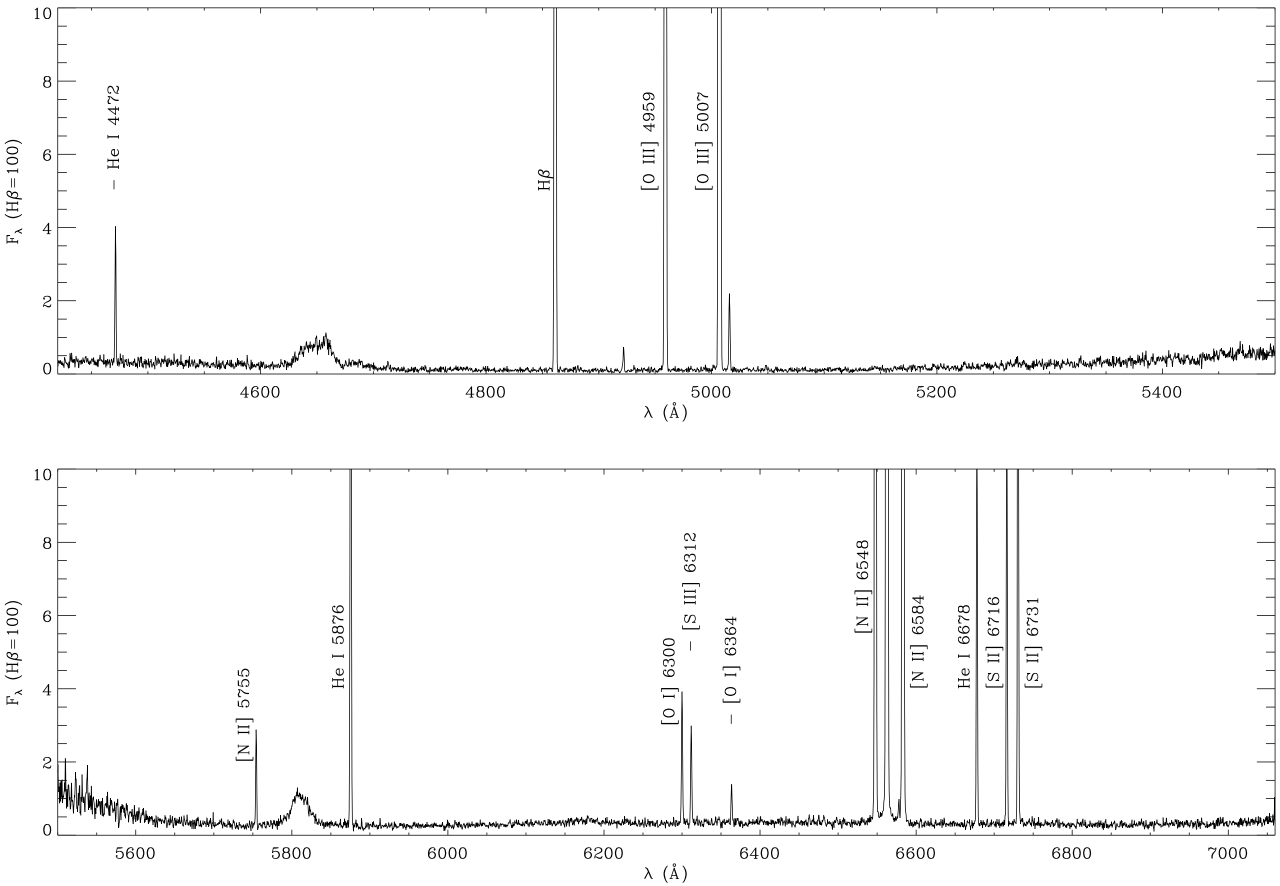

Figure C.9: As Figure C.1 but for M 1-25.

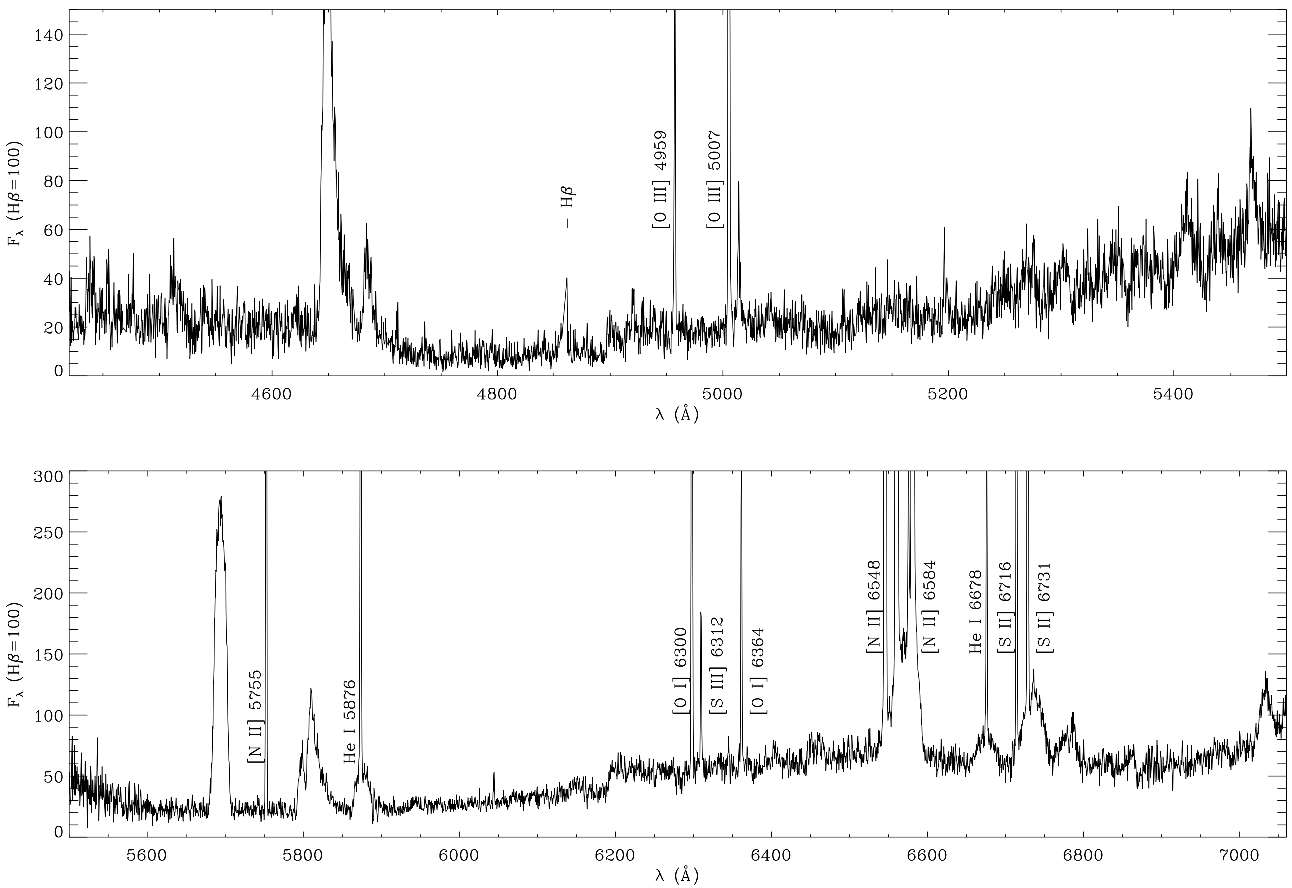

Figure C.10: As Figure C.1 but for Hen 2-142.

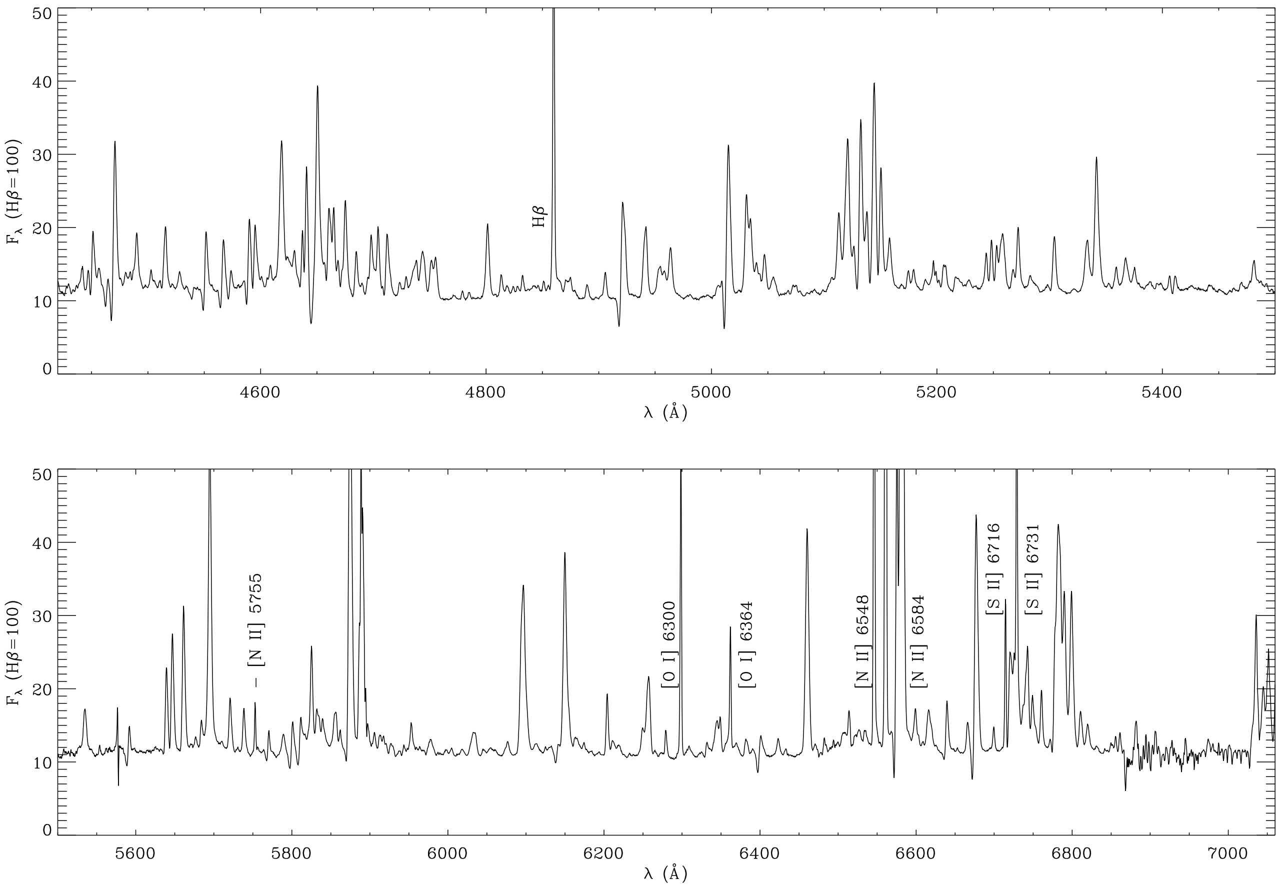

Figure C.11: As Figure C.1 but for Hen 3-1333.

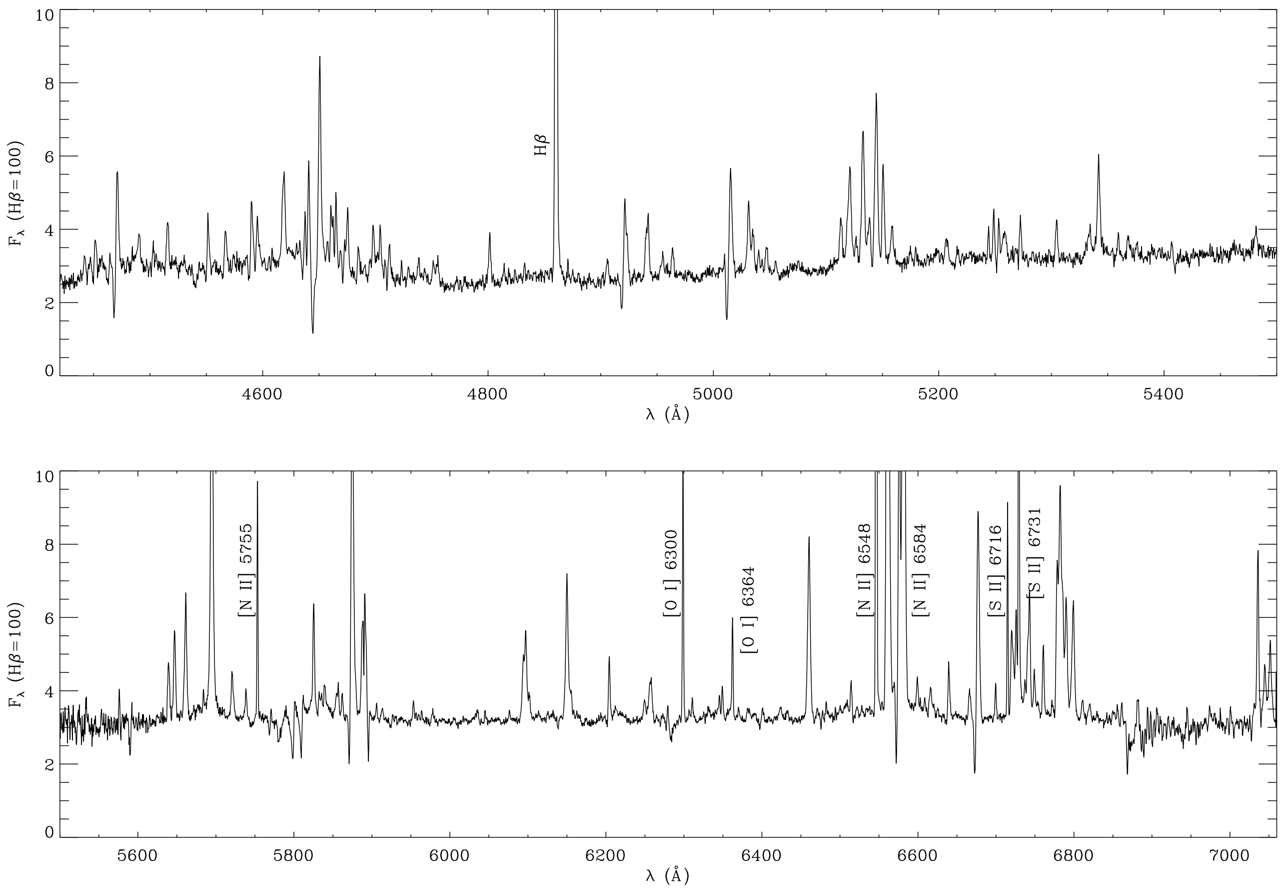

Figure C.12: As Figure C.1 but for Hen 2-113.

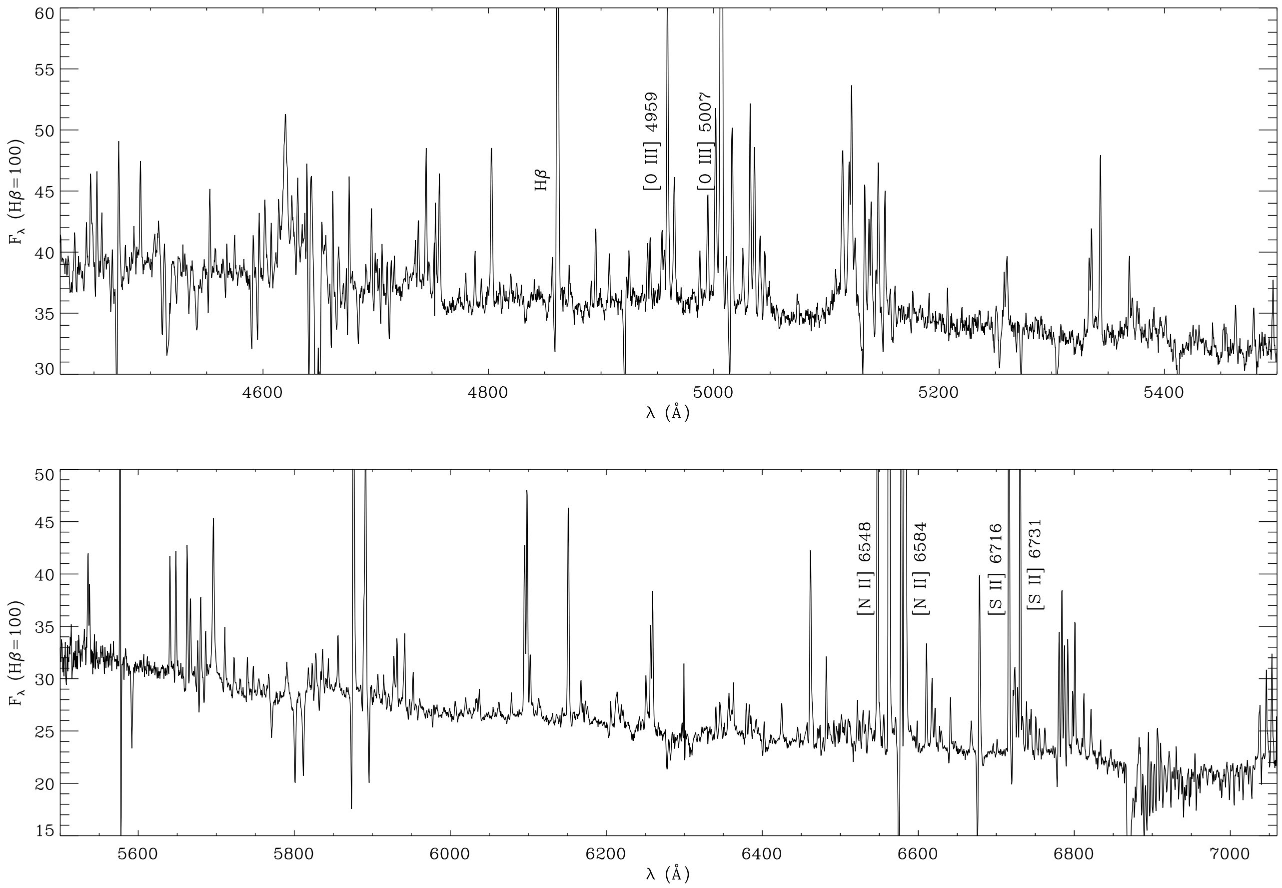

Figure C.13: As Figure C.1 but for K 2-16.

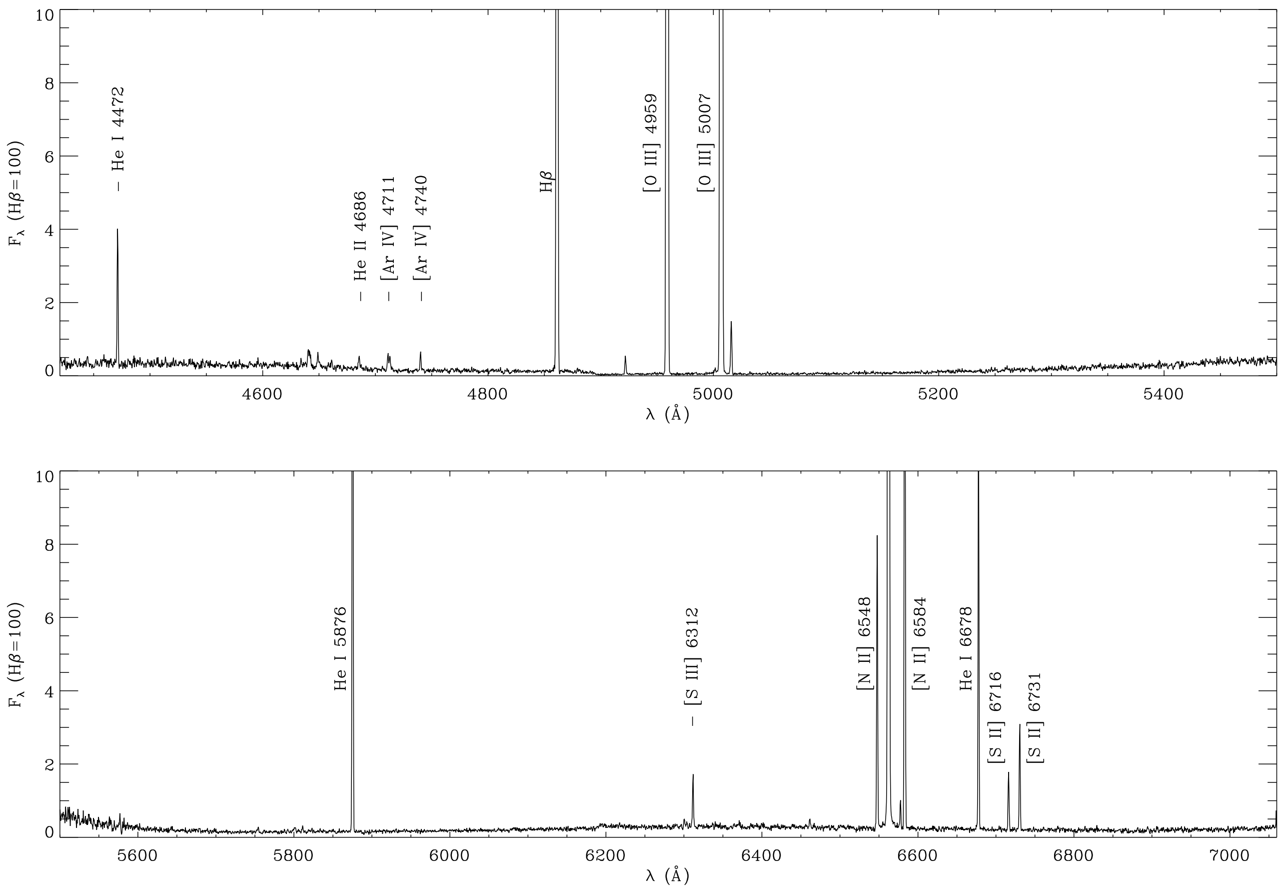

Figure C.14: As Figure C.1 but for NGC 6578.

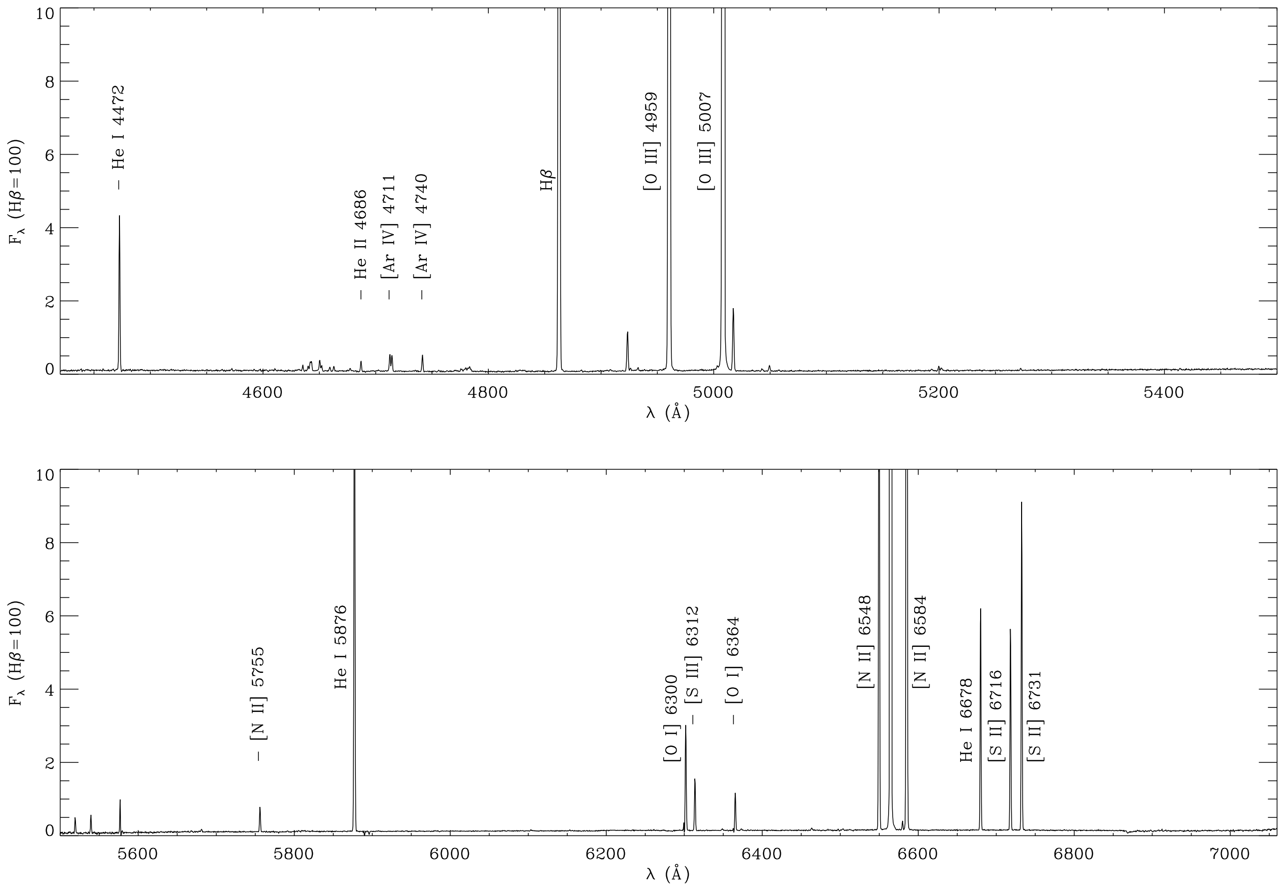

Figure C.15: As Figure C.1 but for M 2-42.

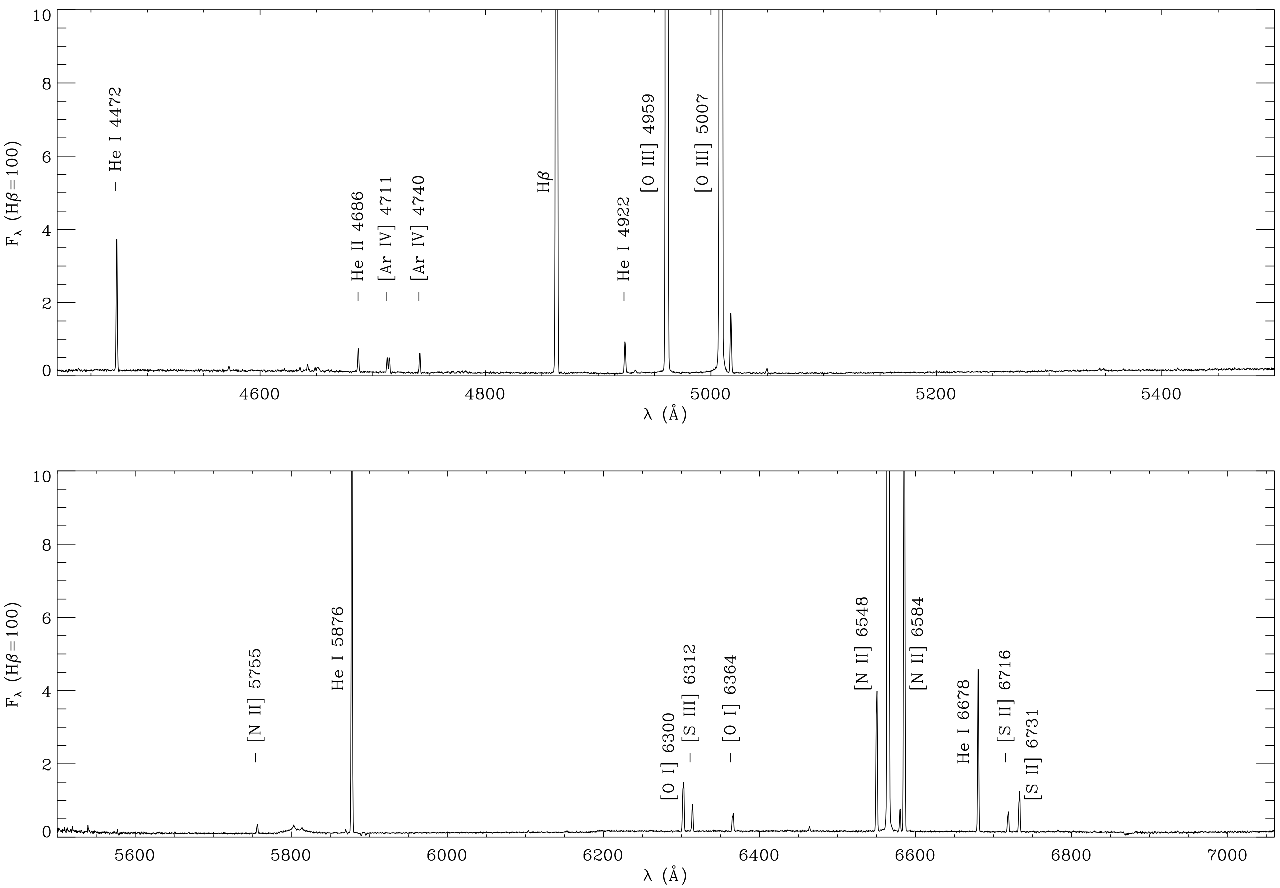

Figure C.16: As Figure C.1 but for NGC 6567.

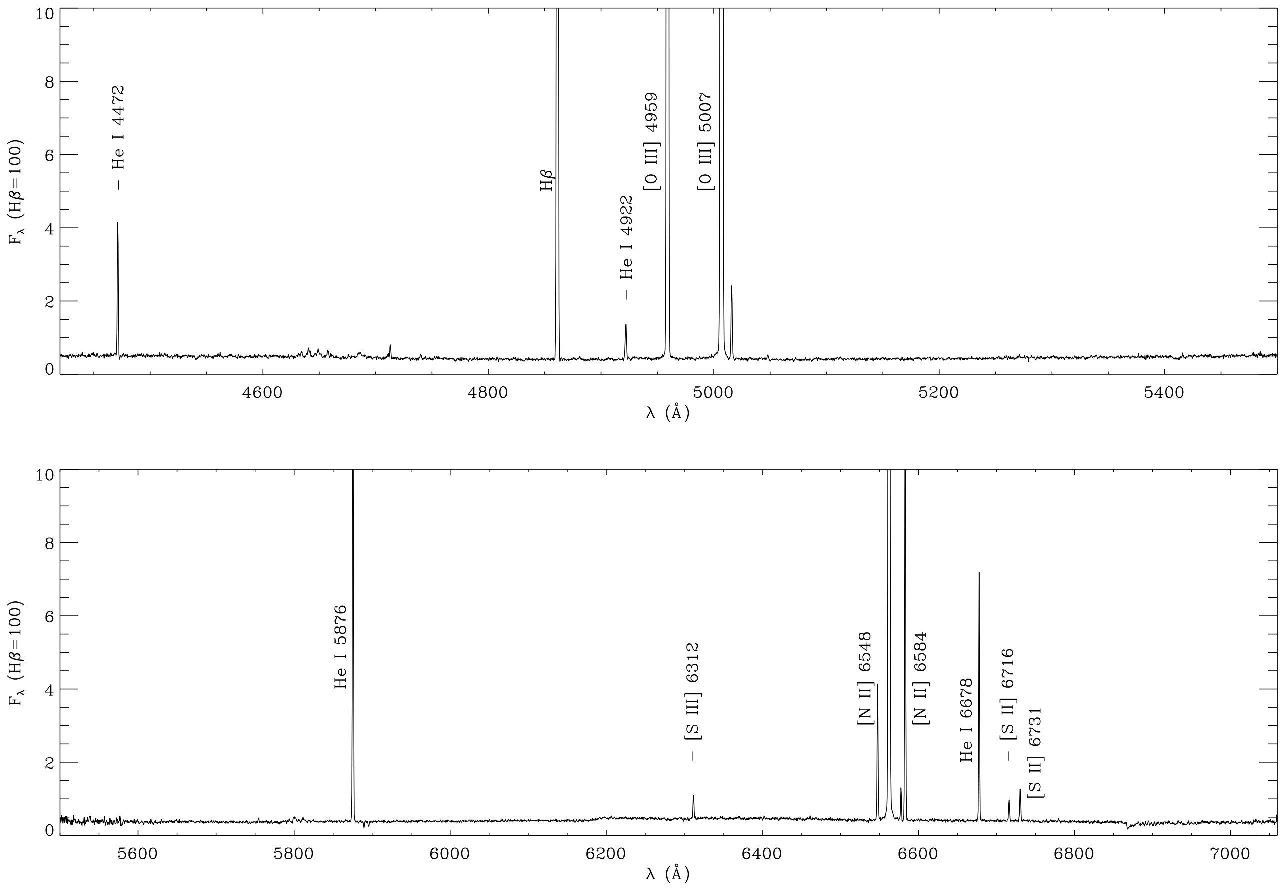

Figure C.17: As Figure C.1 but for NGC 6629.

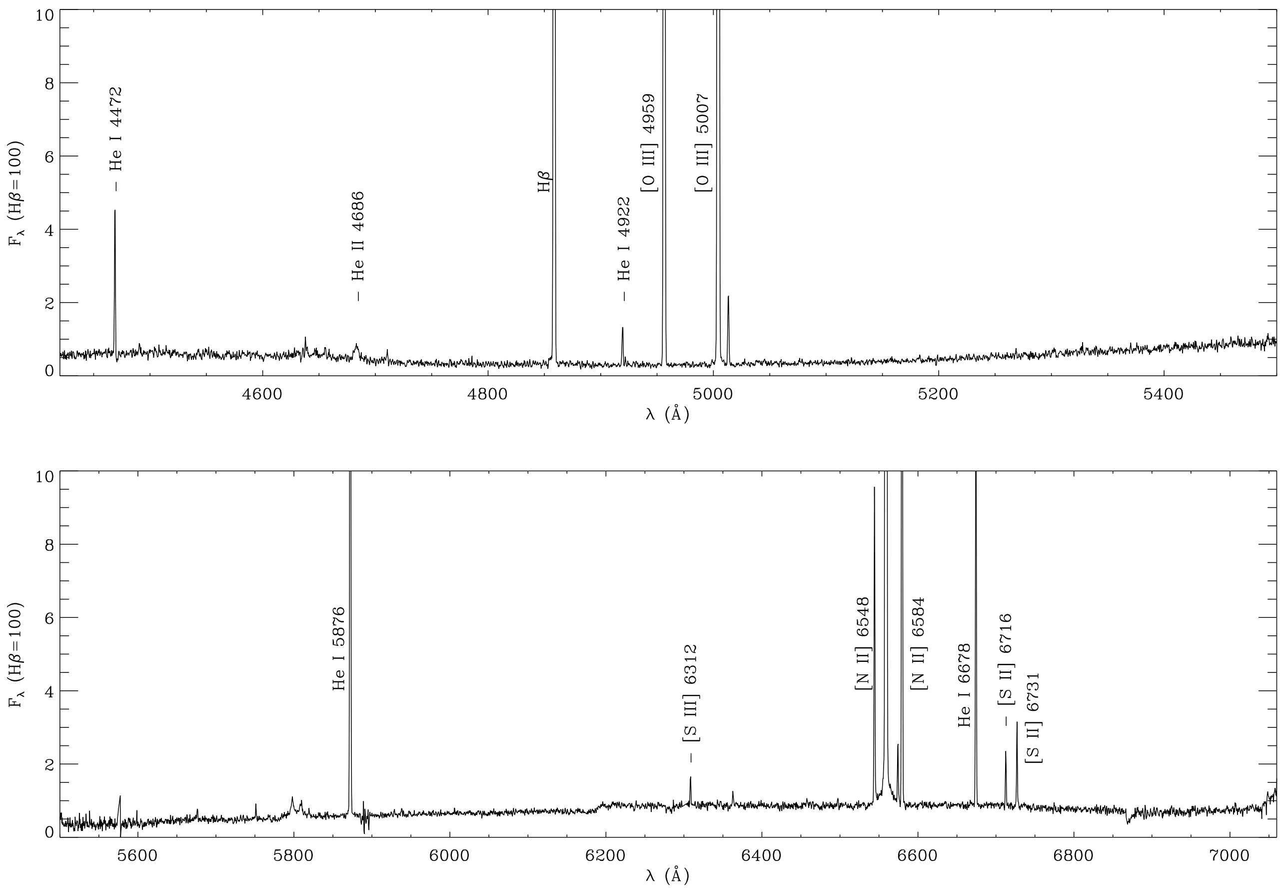

Figure C.18: As Figure C.1 but for Sa 3-107.

Appendix D

Ionic abundance maps

This appendix contains spatial-resolved maps of extinction, temperature, density and ionic abundances for all nebulae analyzed in Chapter 3. Based on observations made with the ANU 2.3-m Telescope at the Siding Spring Observatory.

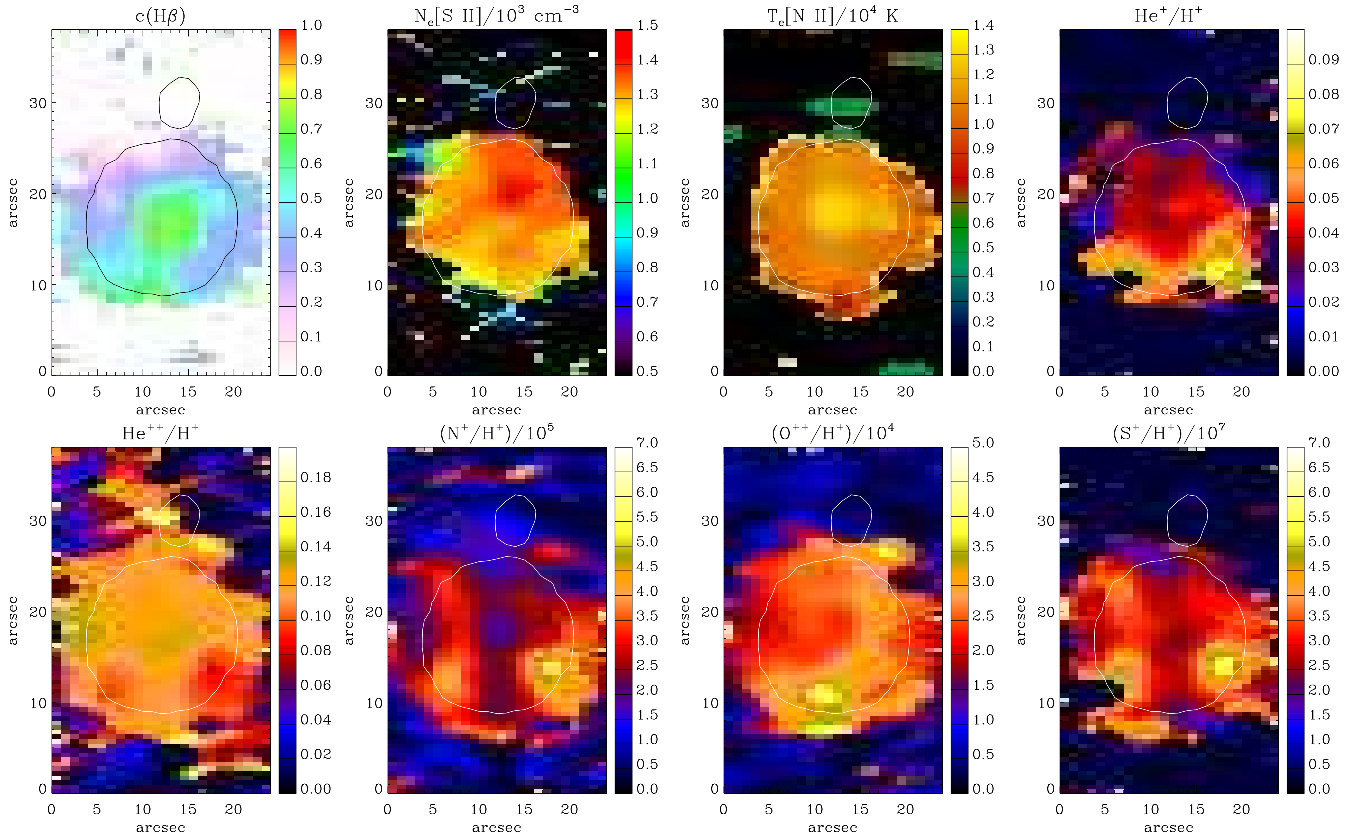

Figure D.1: Empirical maps of PB 6. From left to right, and top to bottom: spatial distribution maps of extinction c(Hα) from the flux ratio Hα/Hβ; electron density $N_e/10^3$ (cm^{-3}) from the flux ratio [S II] 6717/6731; electron temperature $T_e/10^4$ (K) from the flux ratio [N II] (6548+6584)/5755; singly ionized Helium abundance ratio He^+/H^+ from He I ORLs (4472, 5877, 6678); doubly ionized helium abundance ratio H^{++}/H^+ from H II 4686 emission line; ionic nitrogen abundance ratio N^+/H^+ ($\times 10^{-5}$) from [N II] CELs (5755, 6548, 6584); ionic oxygen abundance ratio O^{++}/H^+ ($\times 10^{-4}$) from [O III] CELs (4959, 5007); ionic sulfur abundance ratio S^+/H^+ ($\times 10^{-7}$) from [S II] CELs (6716, 6731); ionic sulfur abundance ratio S^{++}/H^+ ($\times 10^{-7}$) from [S III] 6312 emission line; ionic argon abundance ratio Ar^{++}/H^+ ($\times 10^{-5}$) from [Ar III] 5192 emission line; ionic argon abundance ratio Ar^{+3}/H^+ ($\times 10^{-6}$) from [Ar IV] CELs (4711, 4740); ionic argon abundance ratio Ar^{+4}/H^+ ($\times 10^{-7}$) from [Ar V] CELs (6435, 7005); and ionic chlorine abundance ratio Cl^{++}/H^+ ($\times 10^{-8}$) from [Cl III] CELs (5518, 5538). North is up and east is toward the left-hand side. White/black contour lines show the distribution of the narrow-band emission of Hα in arbitrary unit obtained from the SHS.

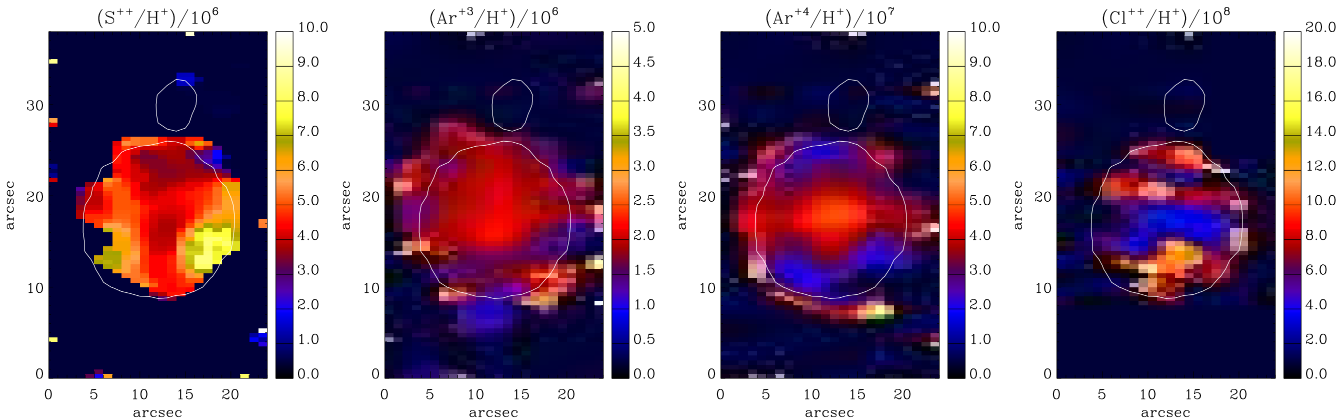

Figure D.1: (continued)

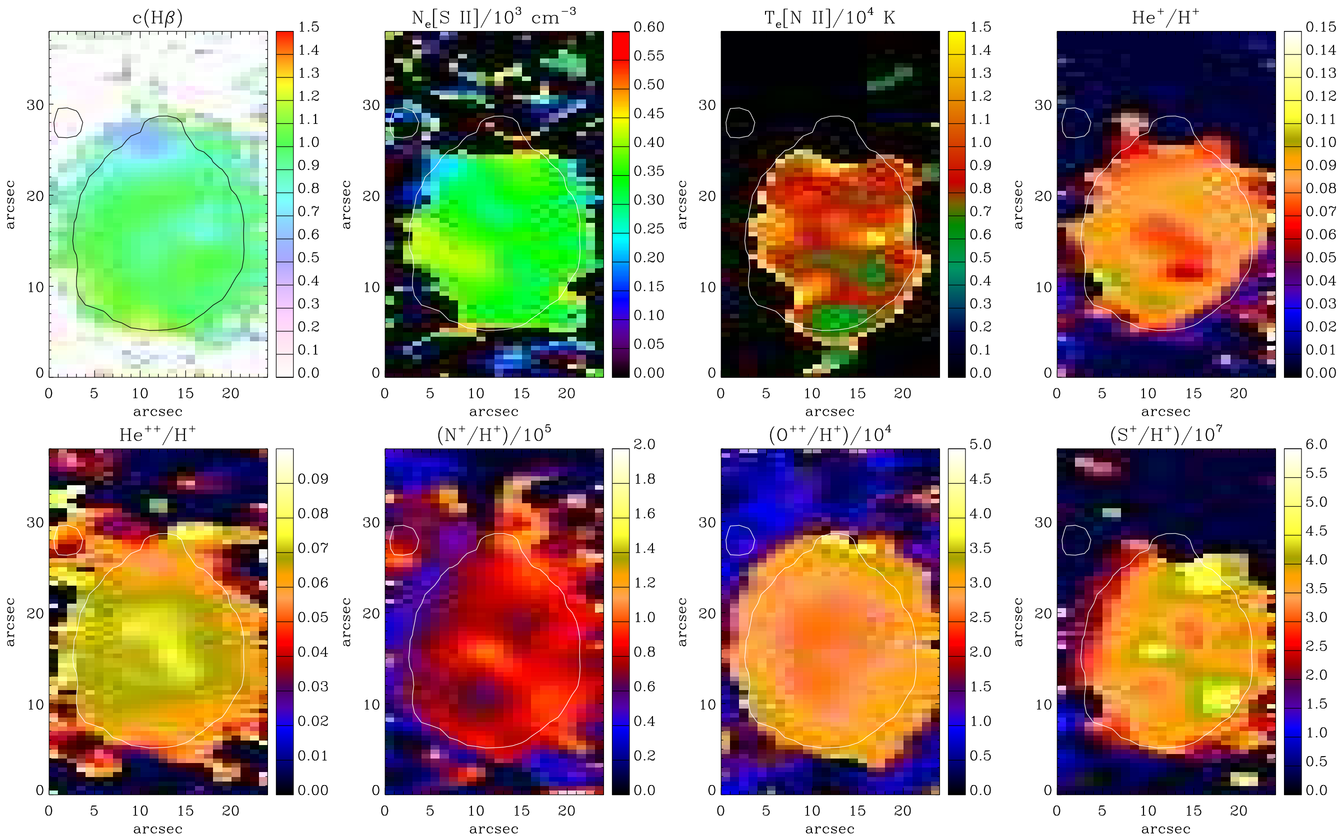

Figure D.2: As Figure D.1 but for M 3-30.

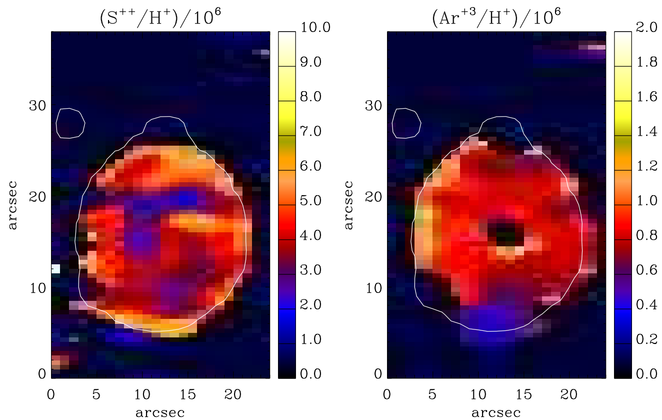

Figure D.2: (continued)

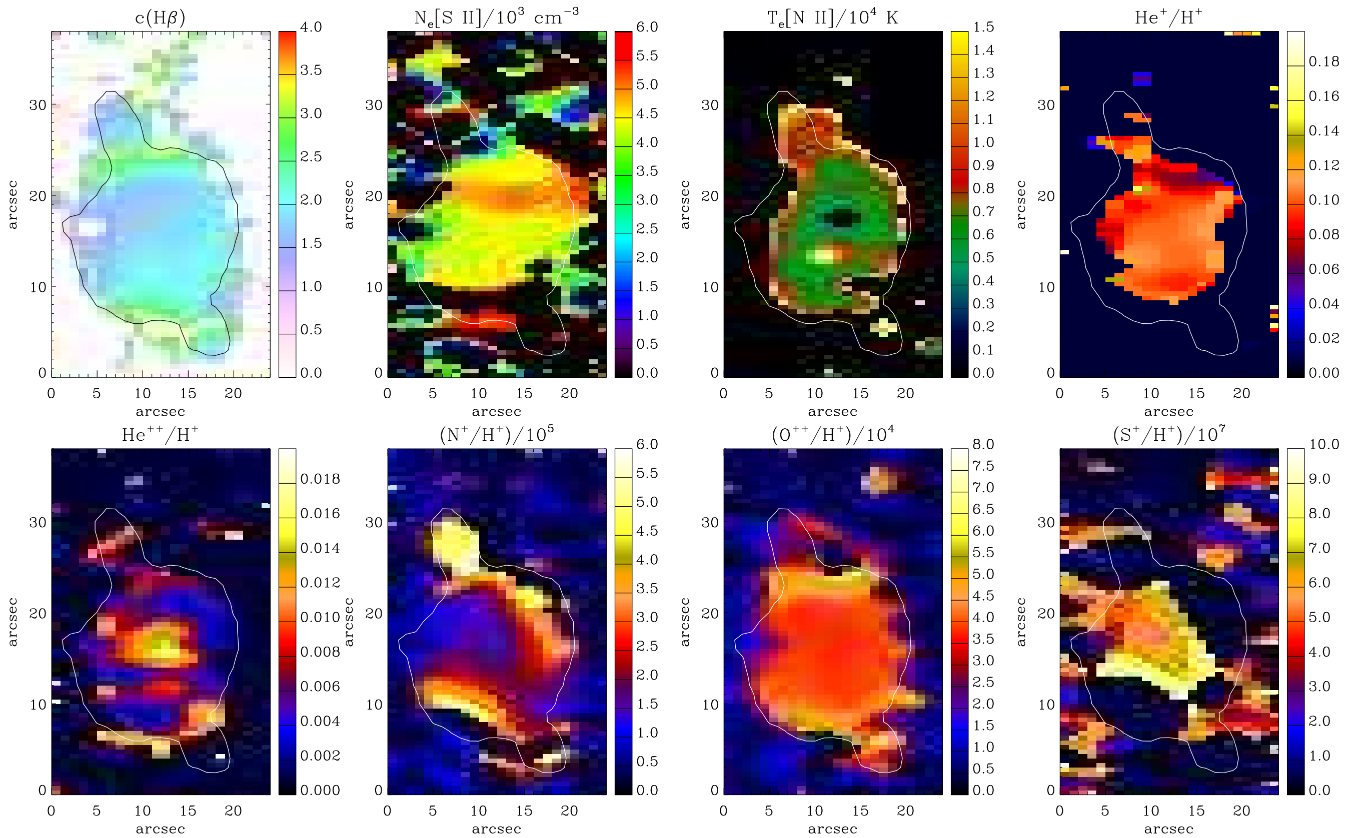

Figure D.3: As Figure D.1 but for Hb 4.

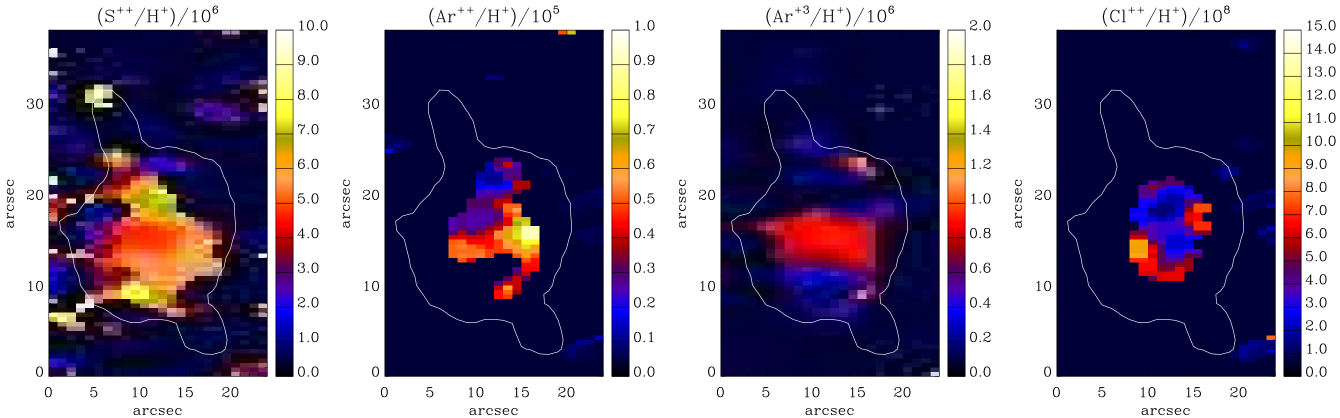

Figure D.3: (continued)

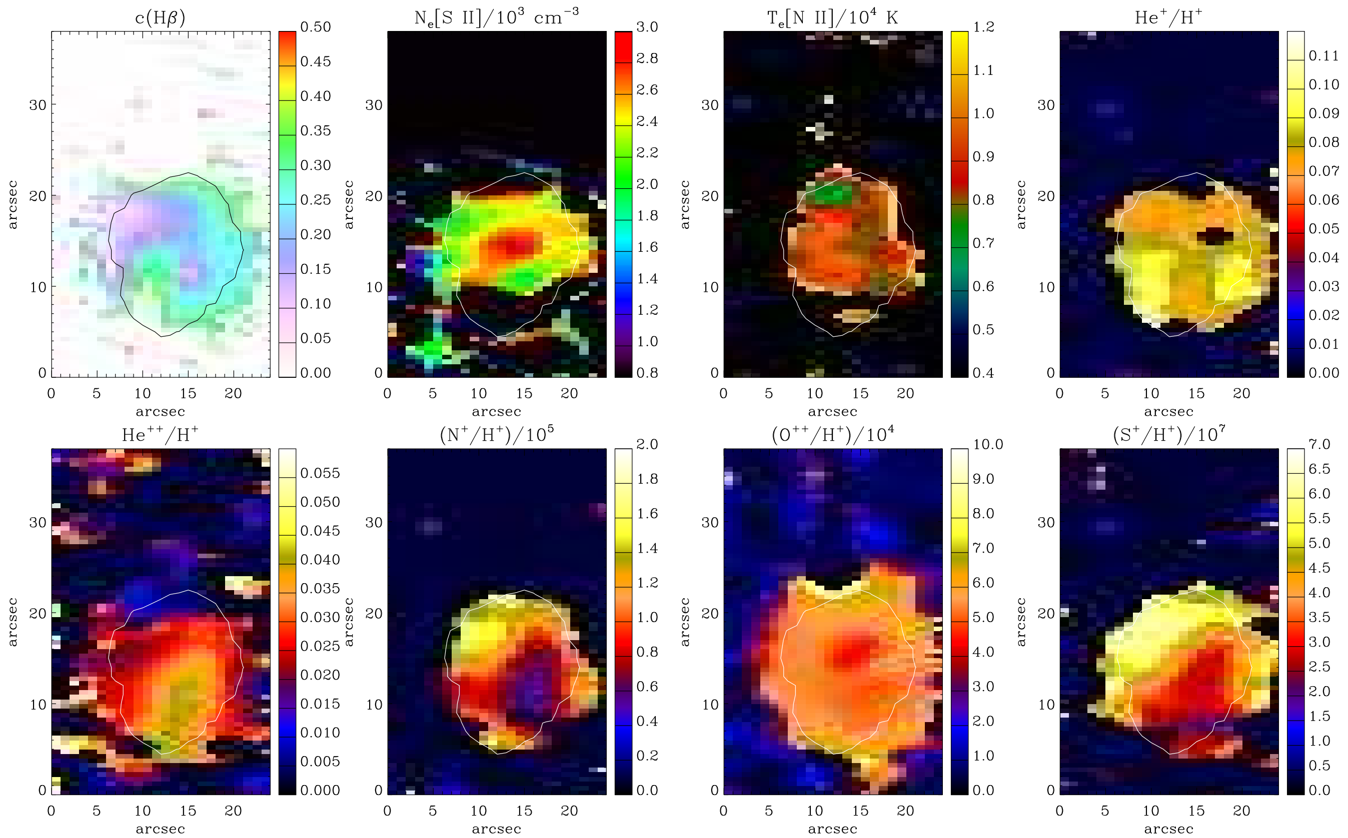

Figure D.4: As Figure D.1 but for IC 1297.

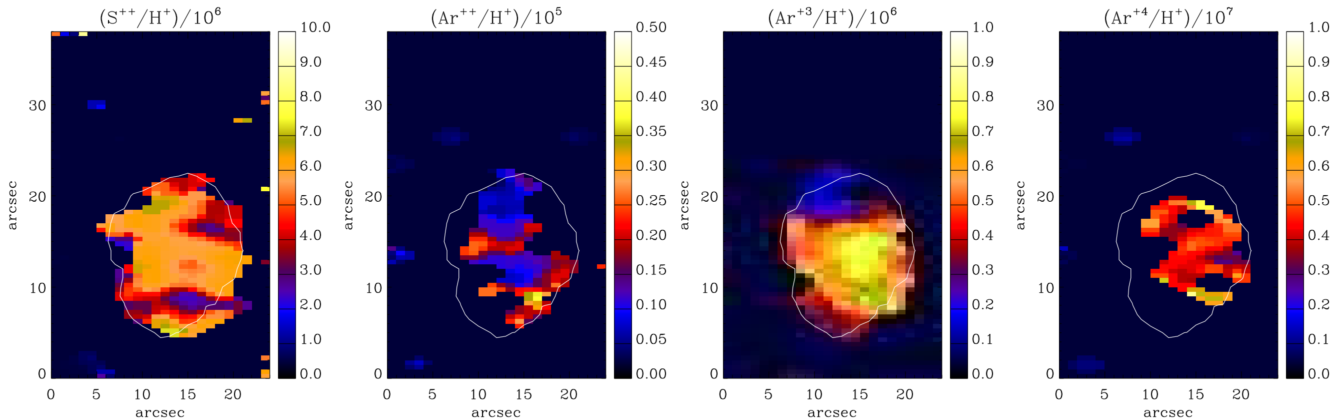

Figure D.4: (continued)

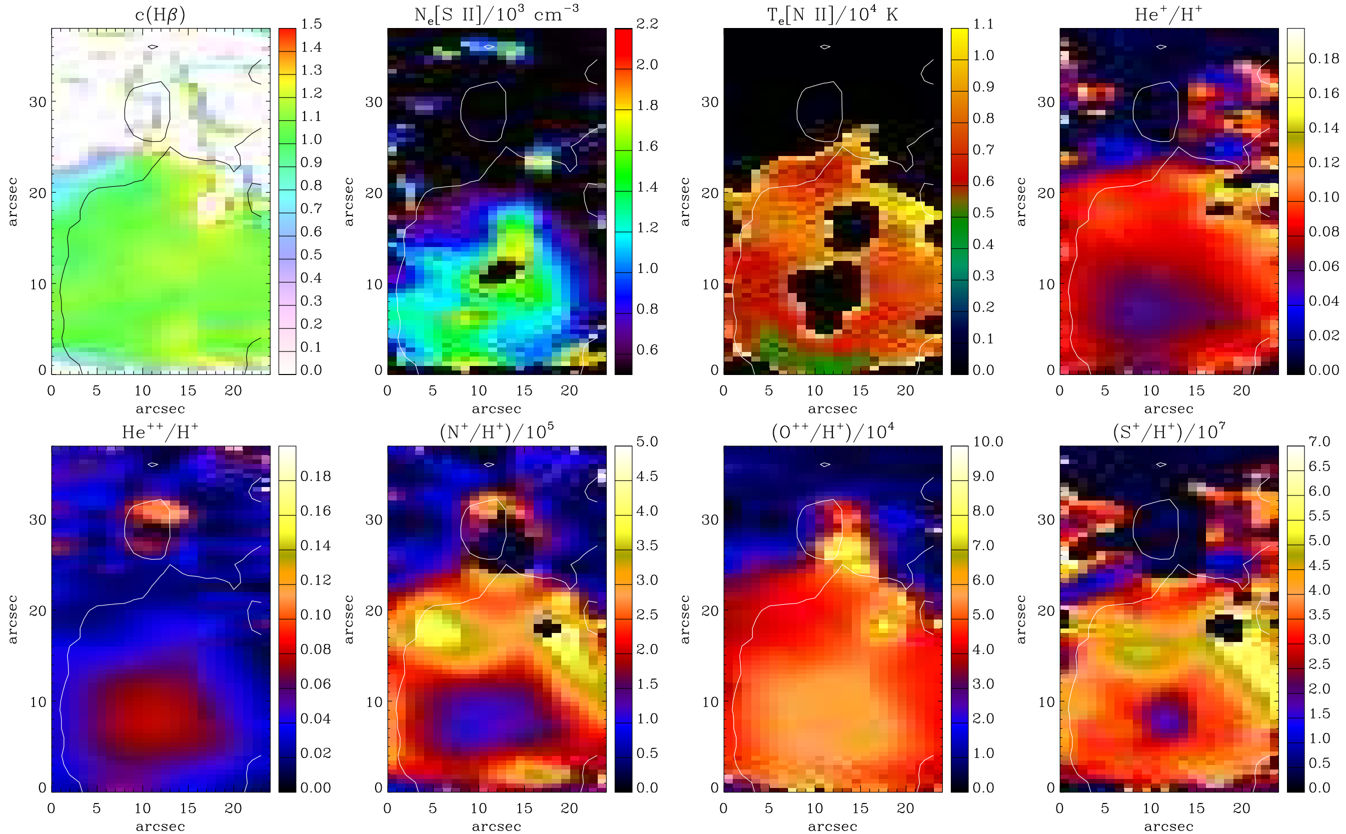

Figure D.5: As Figure D.1 but for Th 2-A.

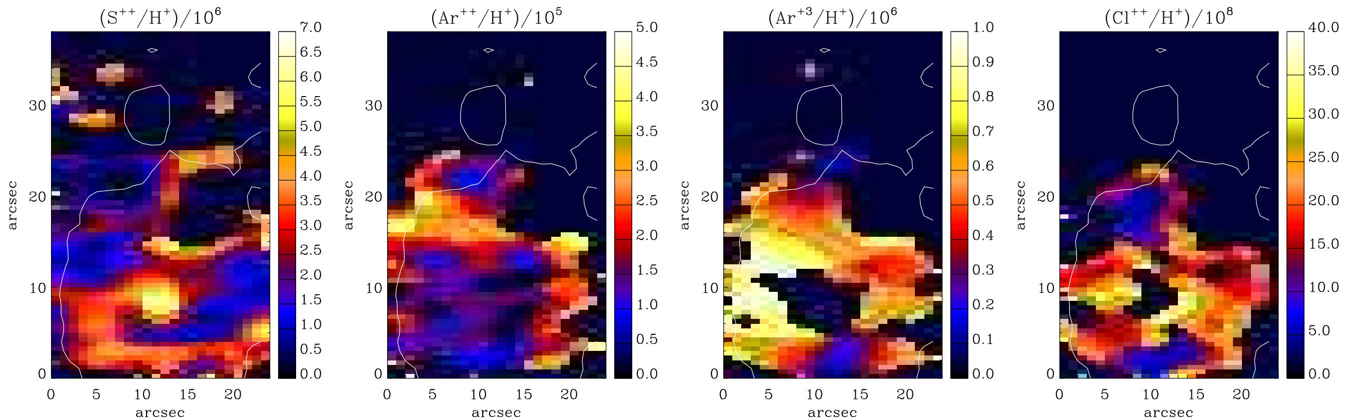

Figure D.5: (continued)

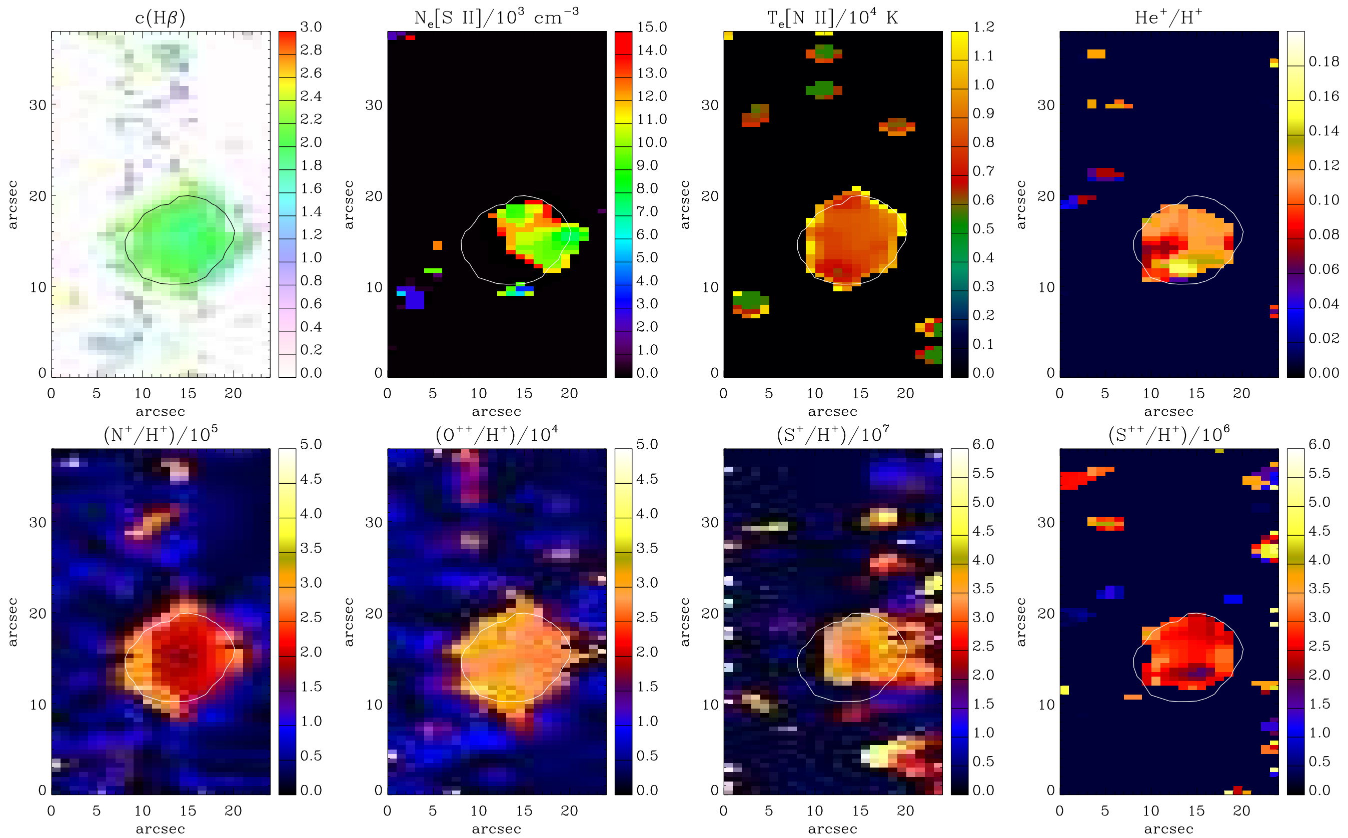

Figure D.6: As Figure D.1 but for Pe 1-1.

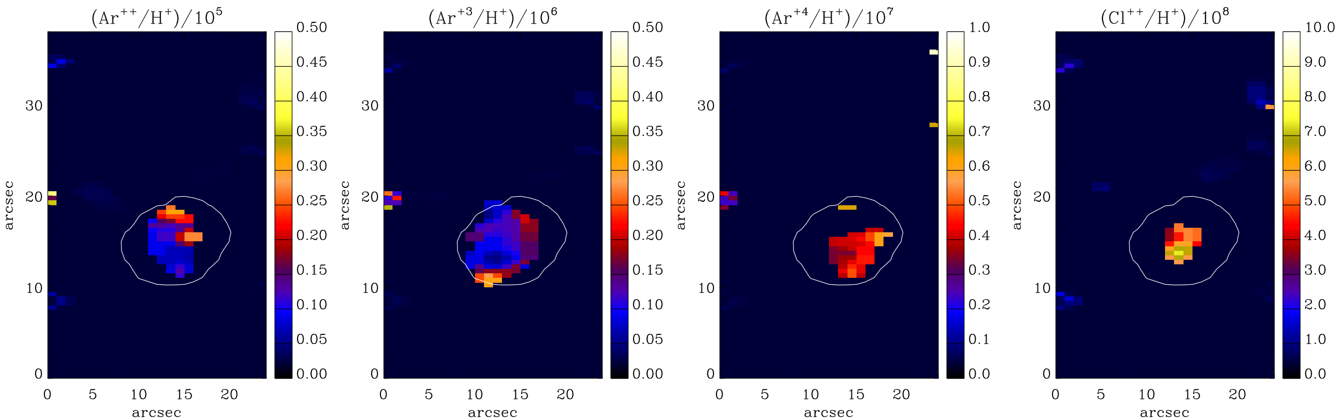

Figure D.6: (continued)

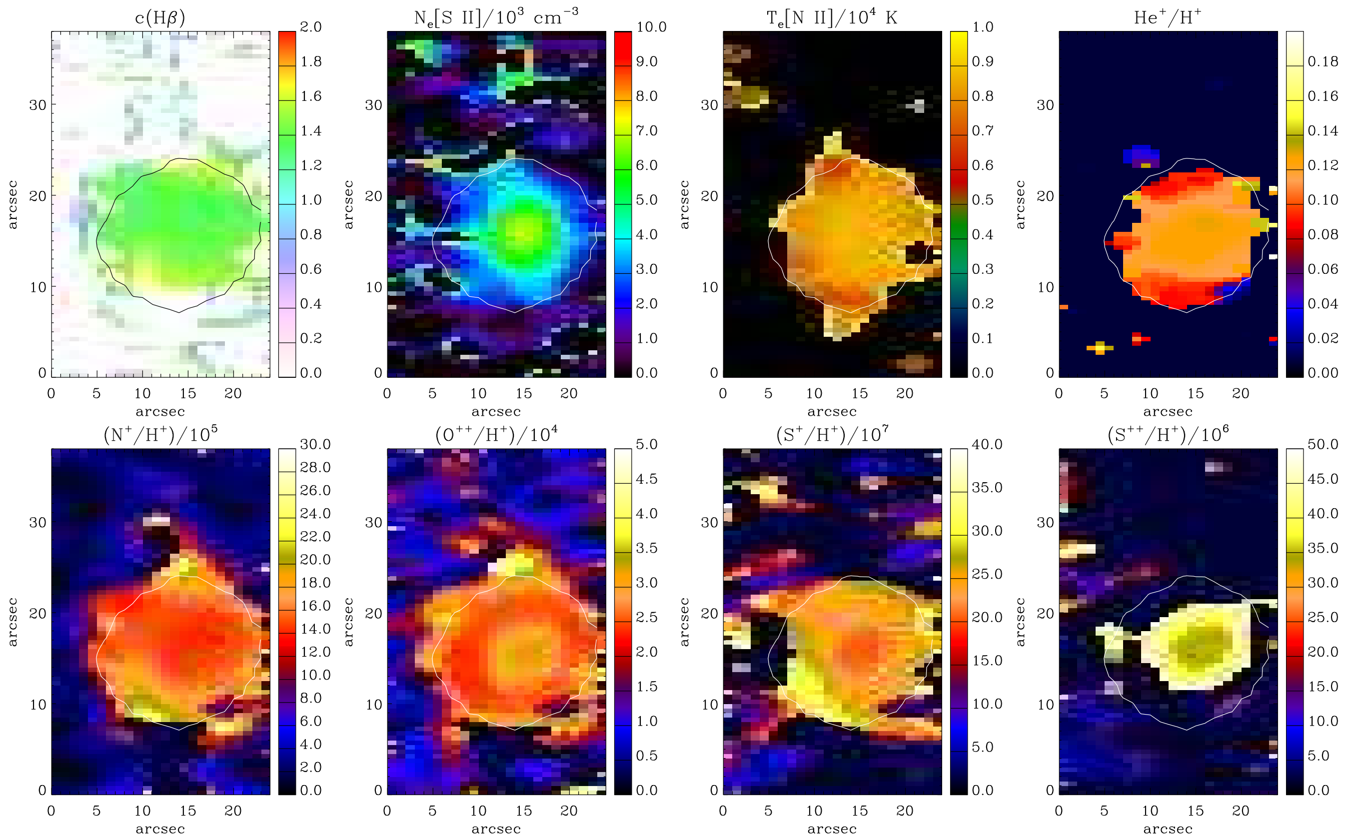

Figure D.7: As Figure D.1 but for M 1-32.

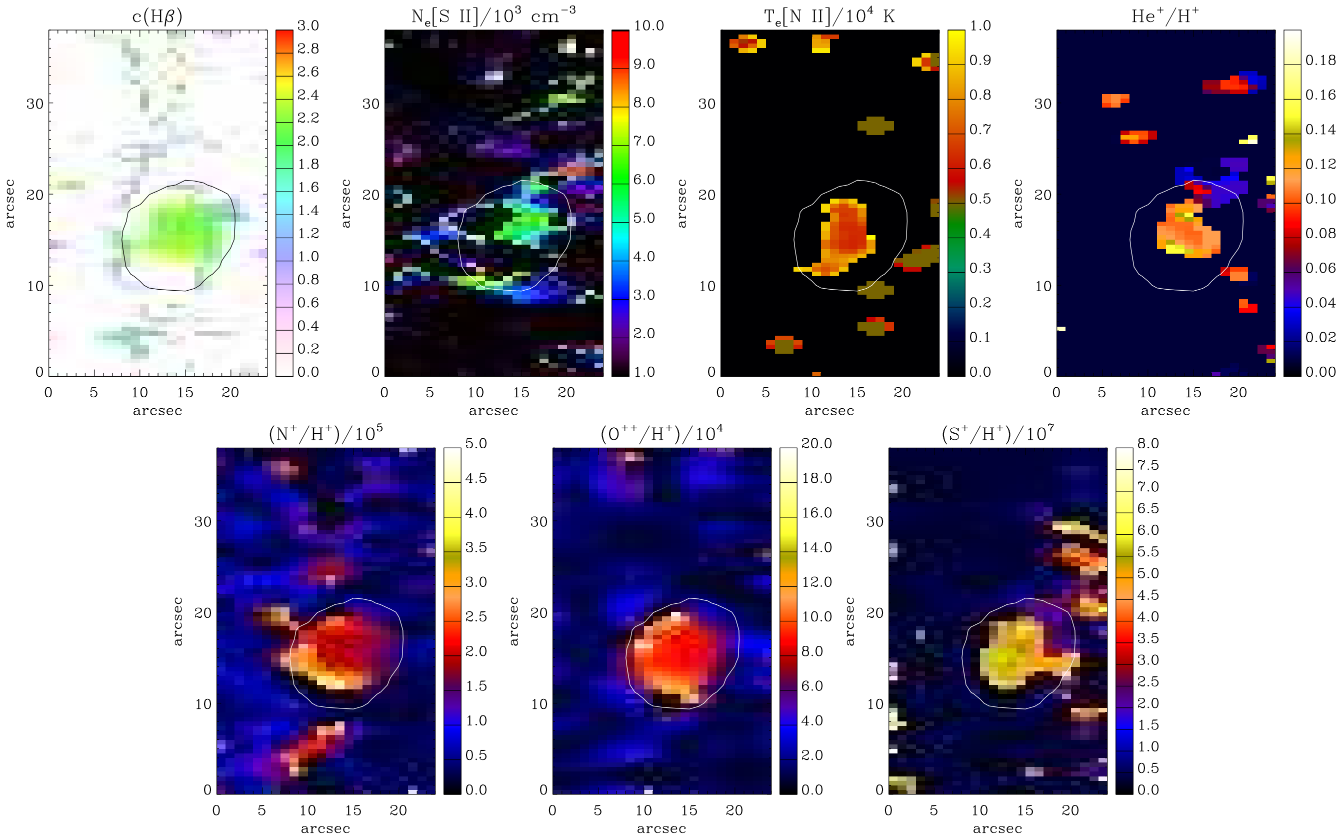

Figure D.8: As Figure D.1 but for M 3-15.

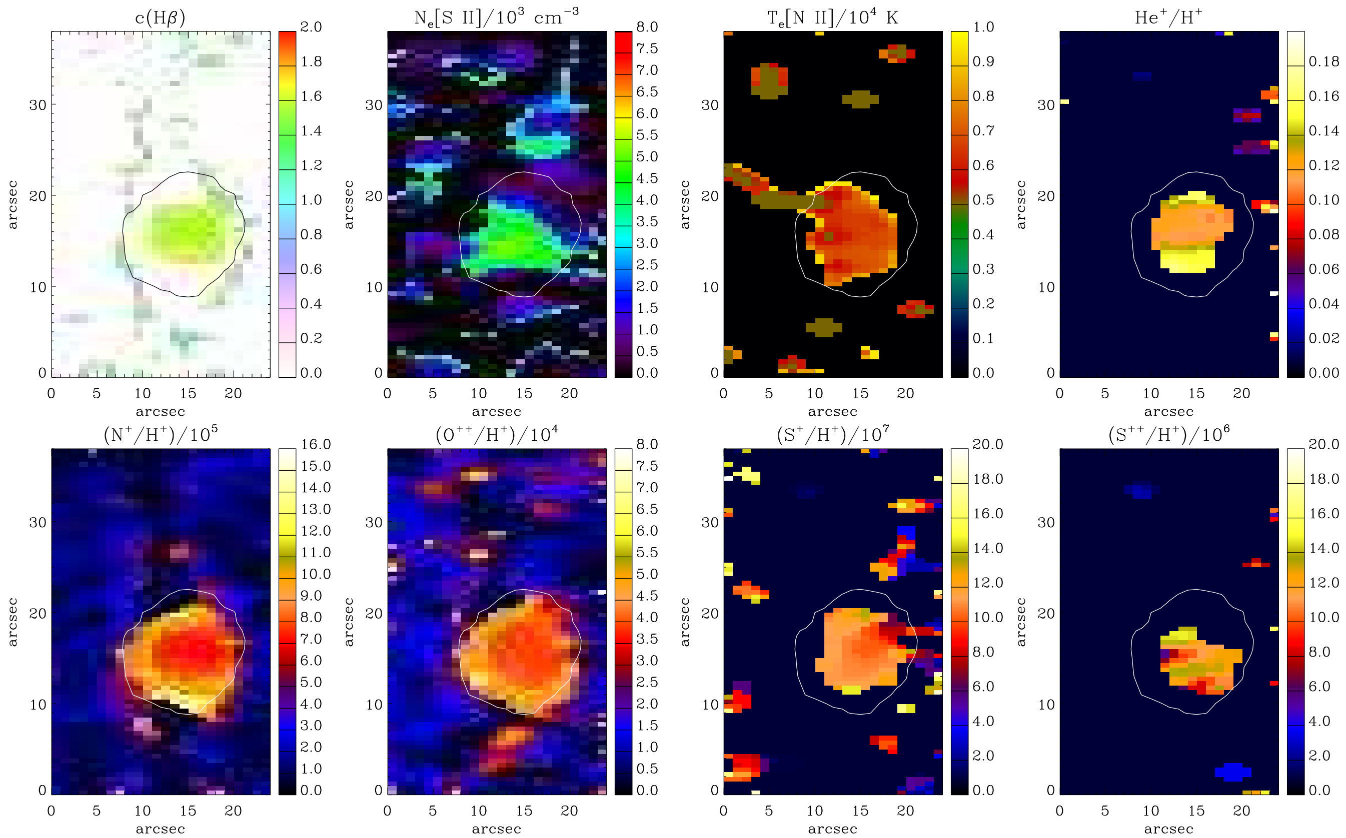

Figure D.9: As Figure D.1 but for M 1-25.

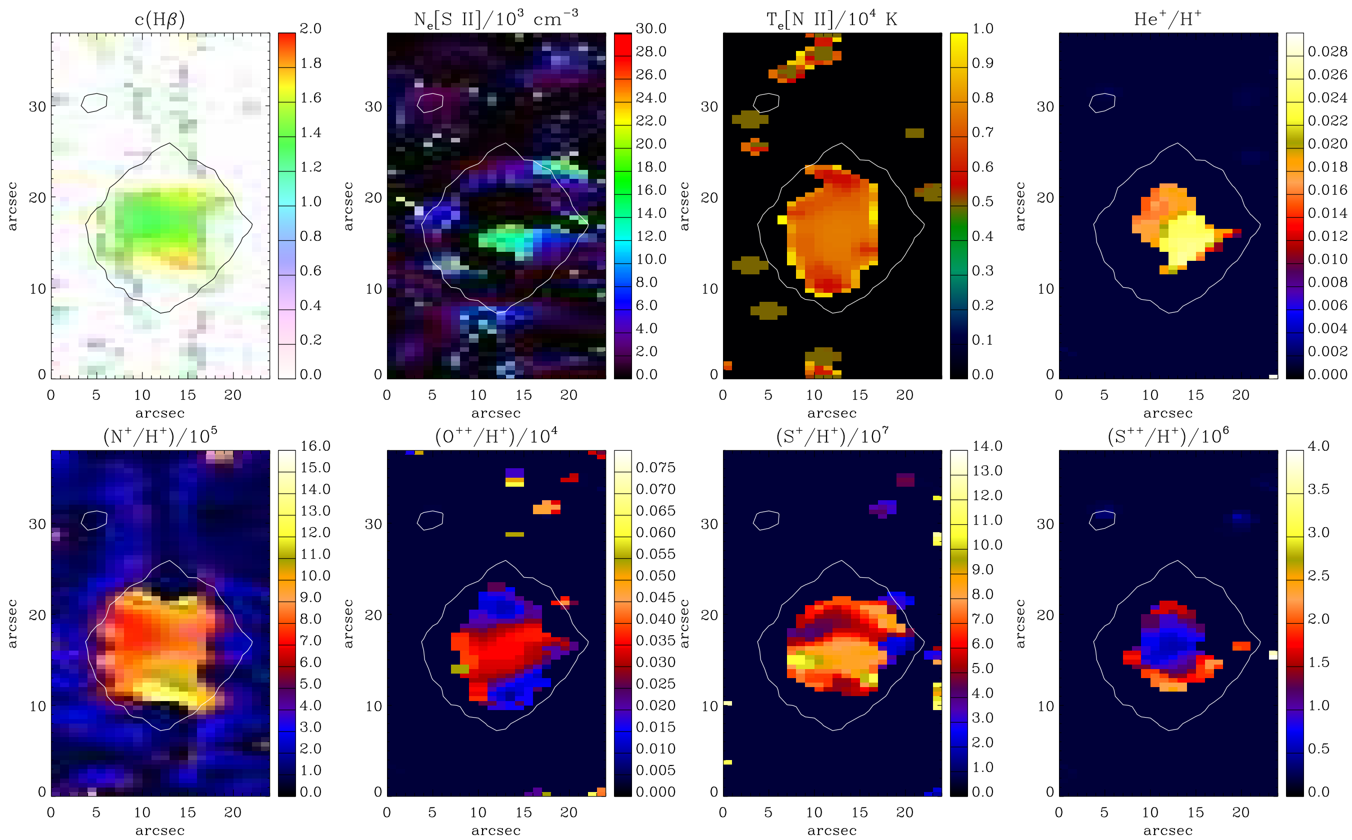

Figure D.10: As Figure D.1 but for Hen 2-142.

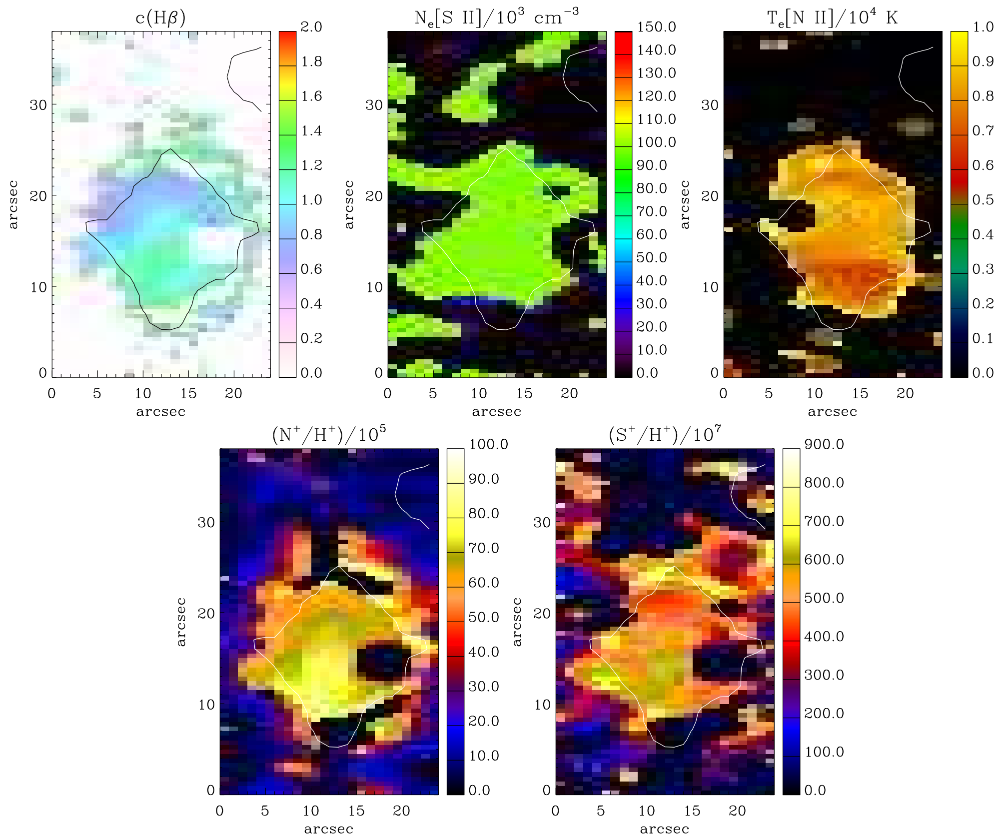

Figure D.11: As Figure D.1 but for Hen 3-1333.

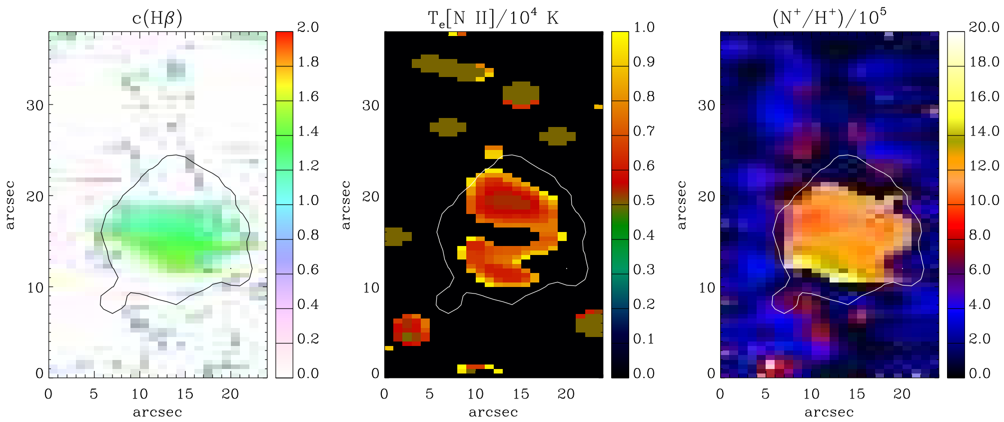

Figure D.12: As Figure D.1 but for Hen 2-113.

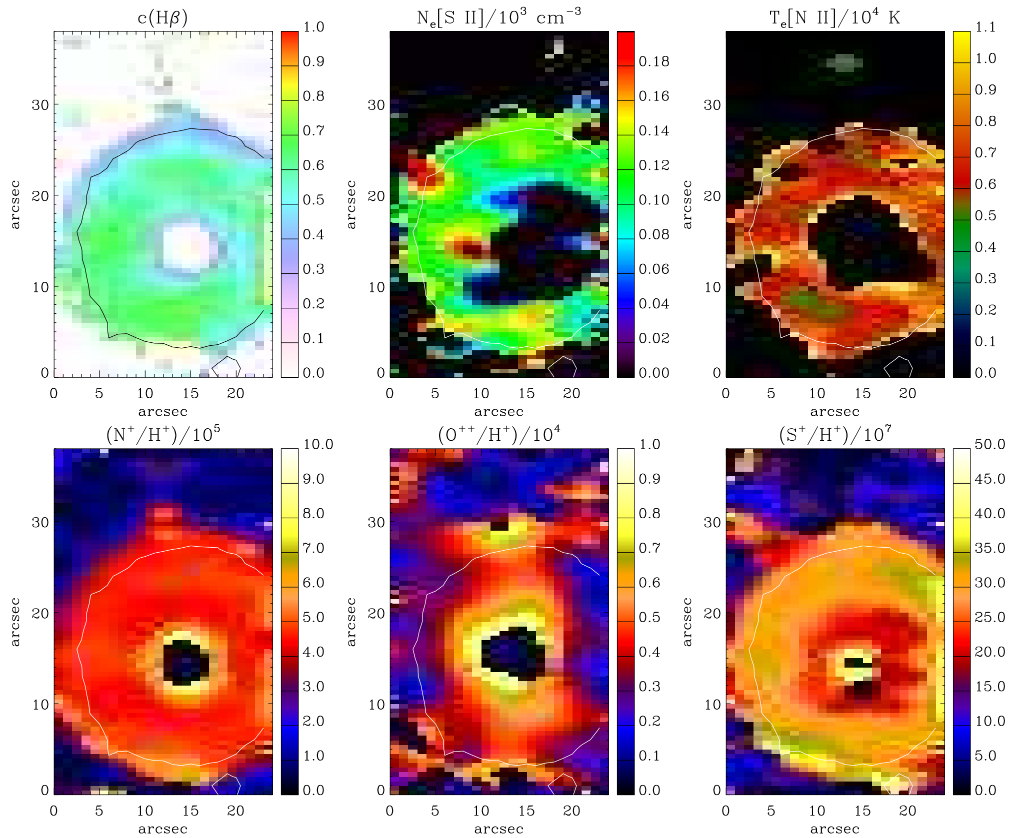

Figure D.13: As Figure D.1 but for K 2-16.

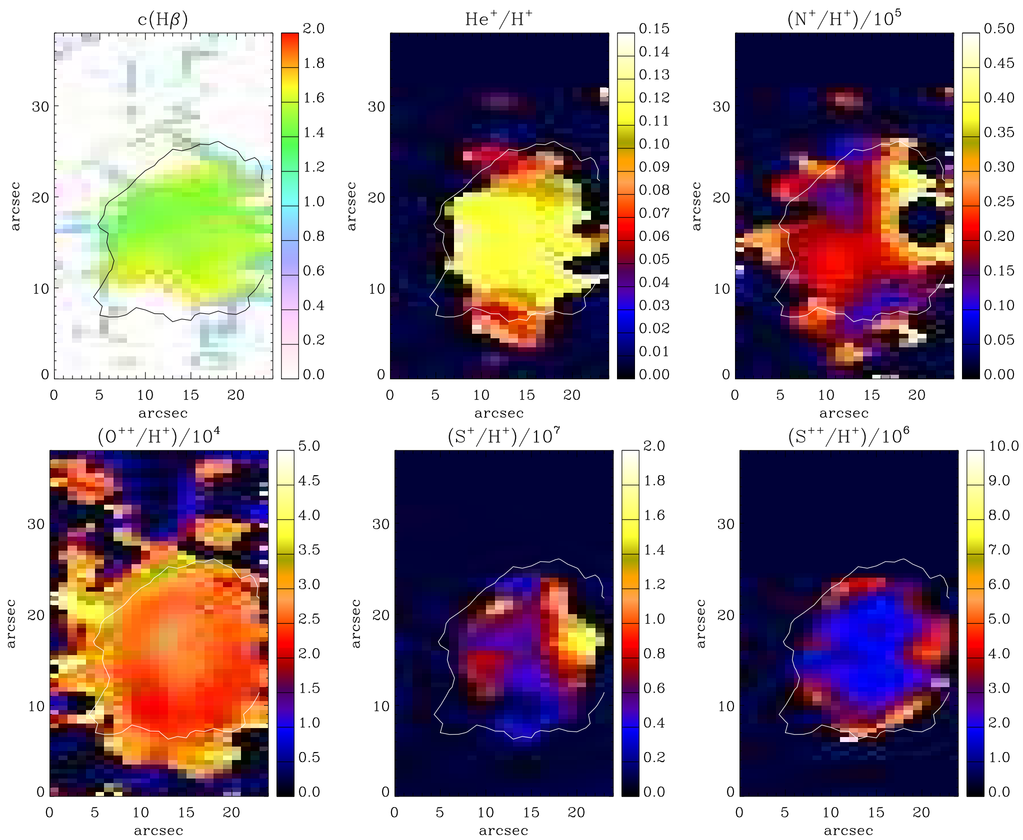

Figure D.14: As Figure D.1 but for NGC 6578.

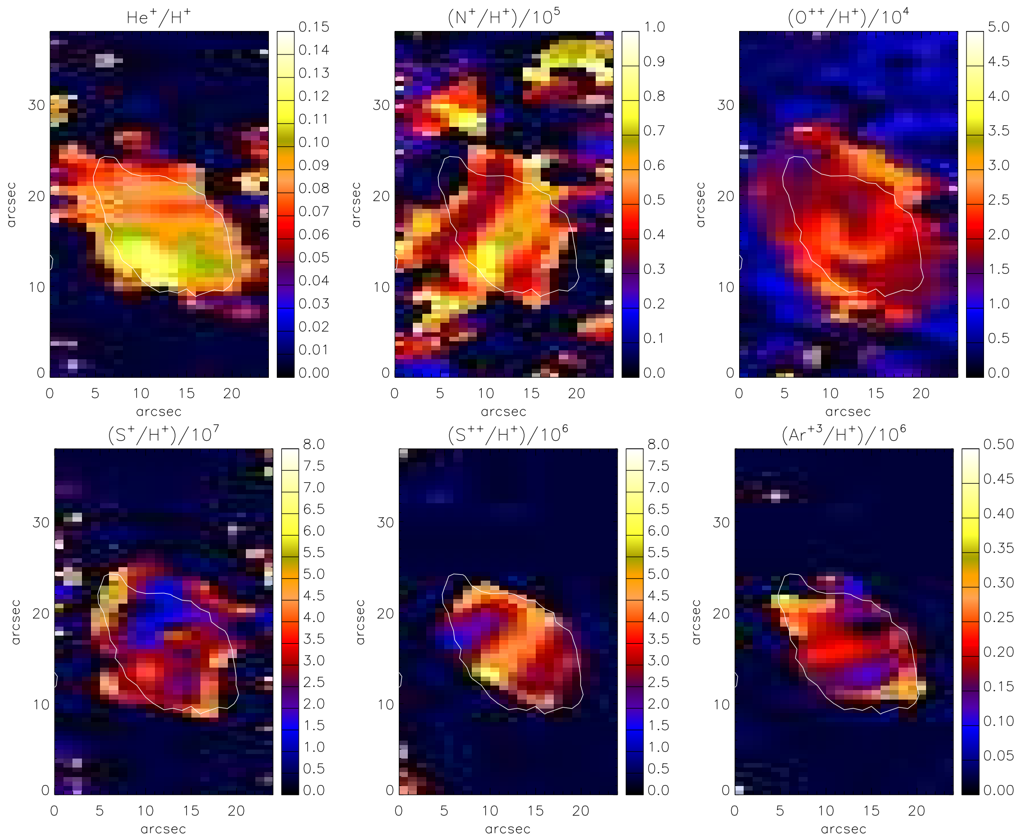

Figure D.15: As Figure D.1 but for M 2-42.

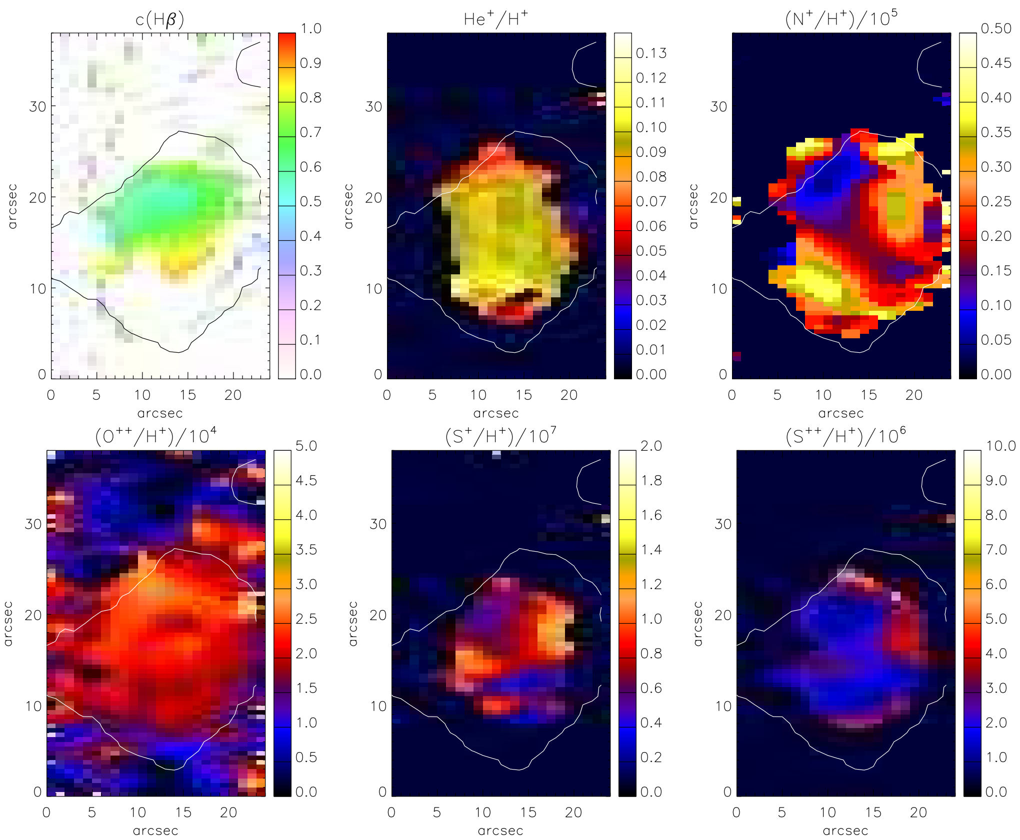

Figure D.16: As Figure D.1 but for NGC 6567.

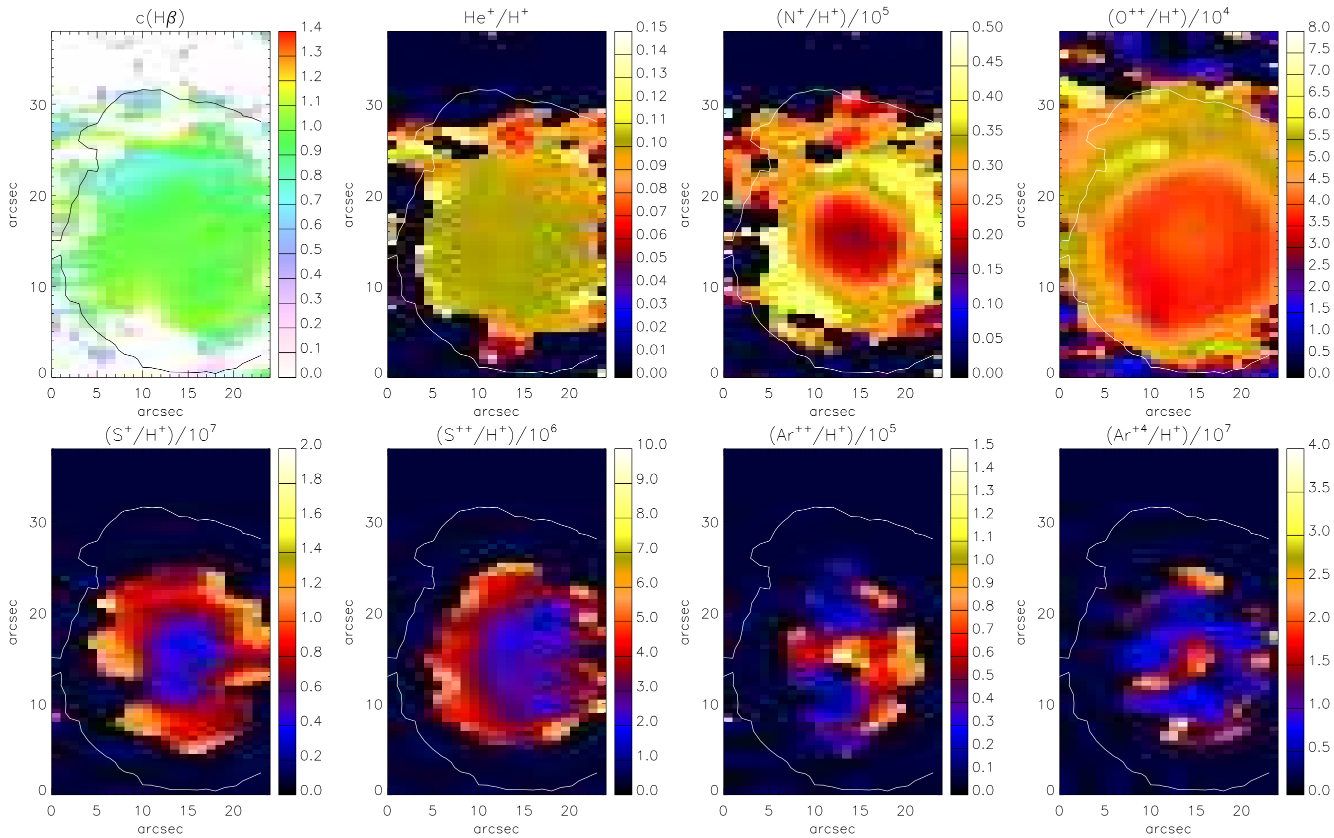

Figure D.17: As Figure D.1 but for NGC 6629.

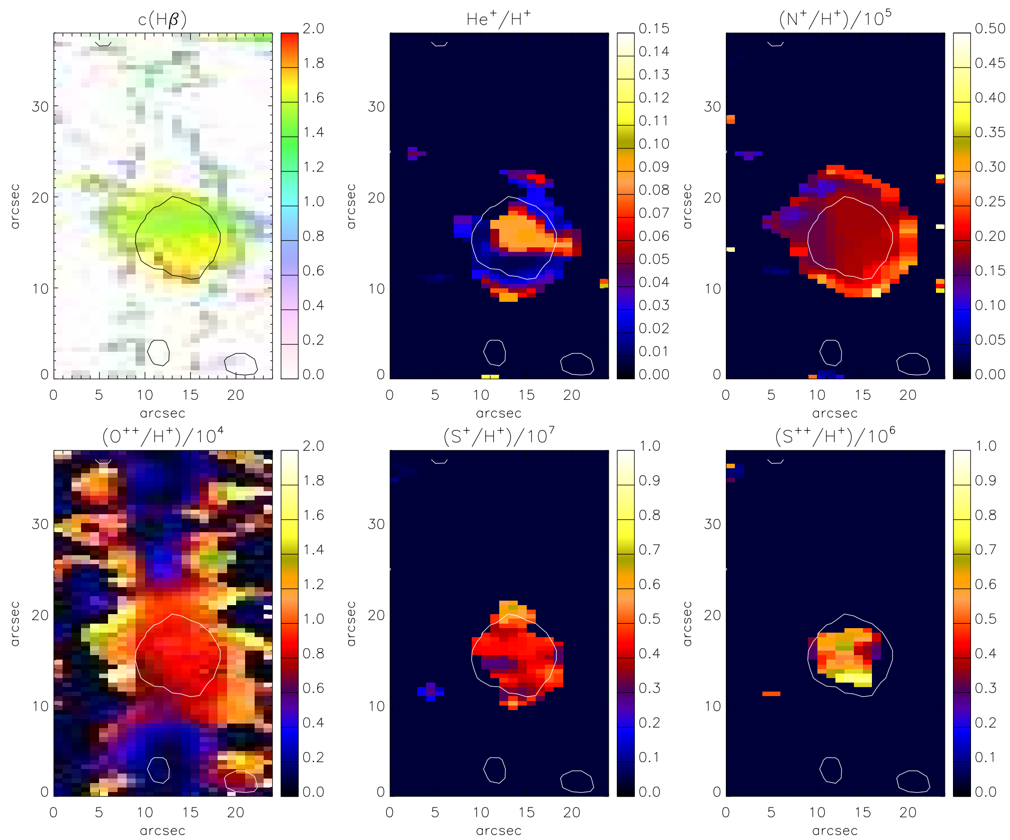

Figure D.18: As Figure D.1 but for Sa 3-107.

Appendix E

Stellar Spectra

This appendix shows central star spectra for all nebulae analyzed in Chapters 2 and 3. Based on observations made with the ANU 2.3-m Telescope at the Siding Spring Observatory.

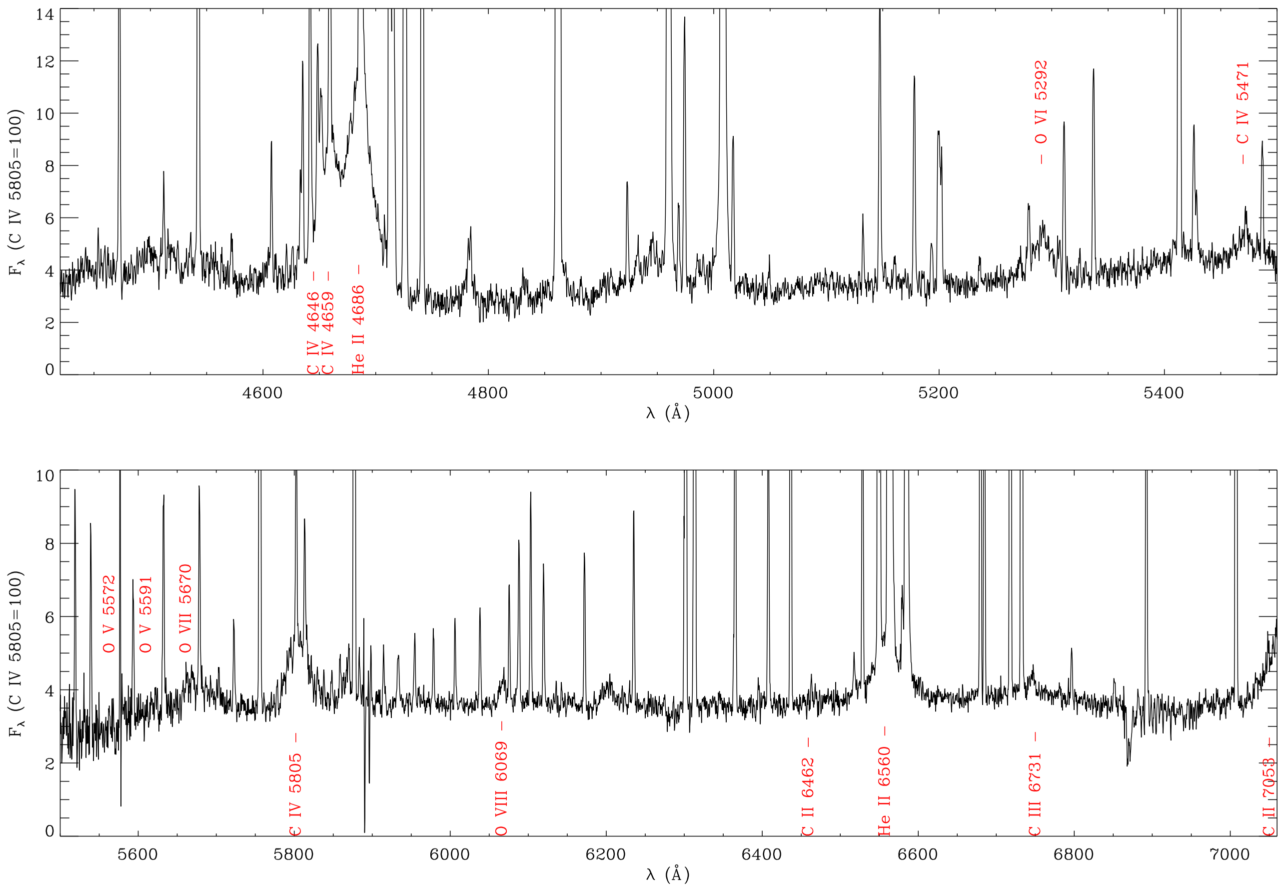

Figure E.1: The observed optical spectra of the CSPN PB 6 and normalized such that $F(\mathrm{CIV}5805) = 100$: grating B7000 (top) covers wavelengths 4415–5500 Å and R7000 (bottom) covers 5500–7060 Å.

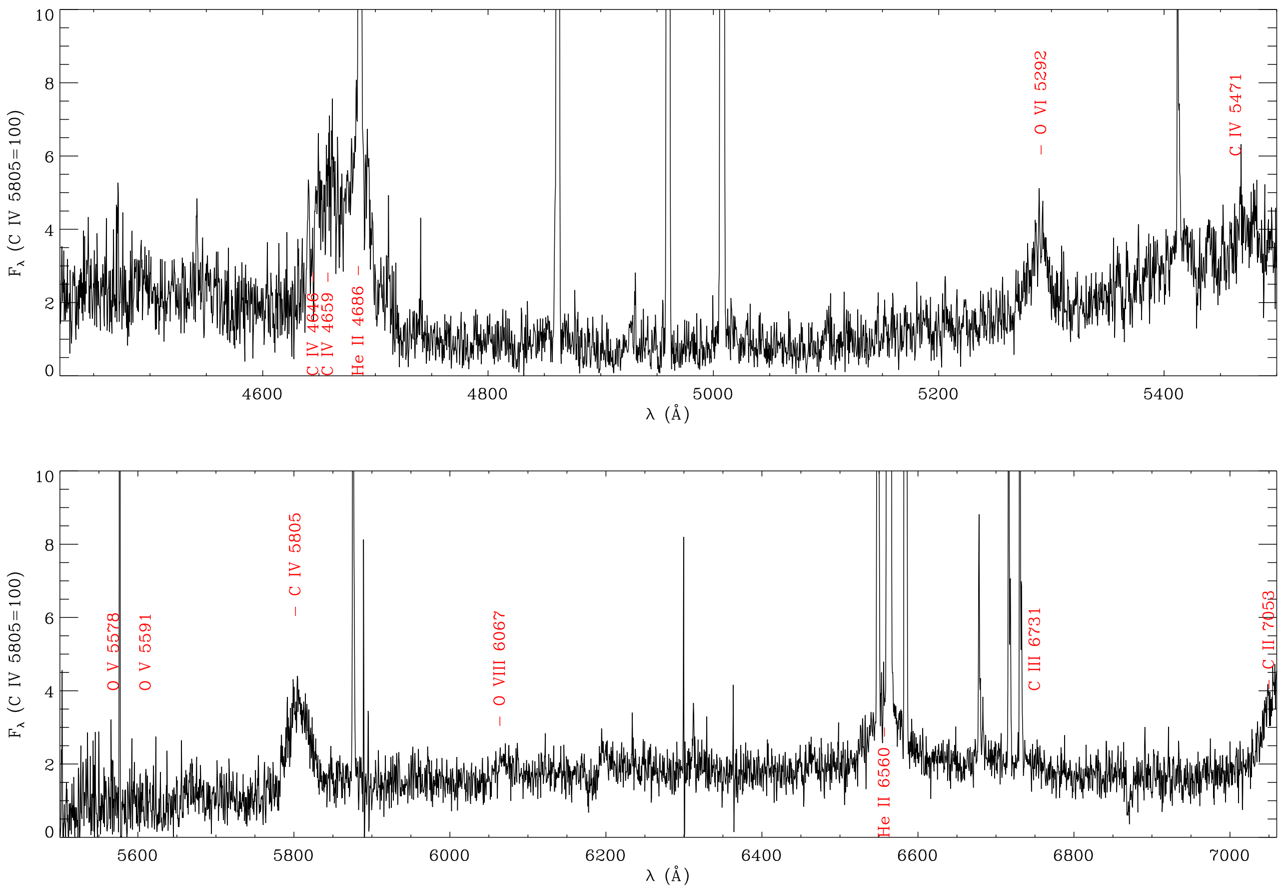

Figure E.2: As Figure E.1 but for the CSPN M3-30.

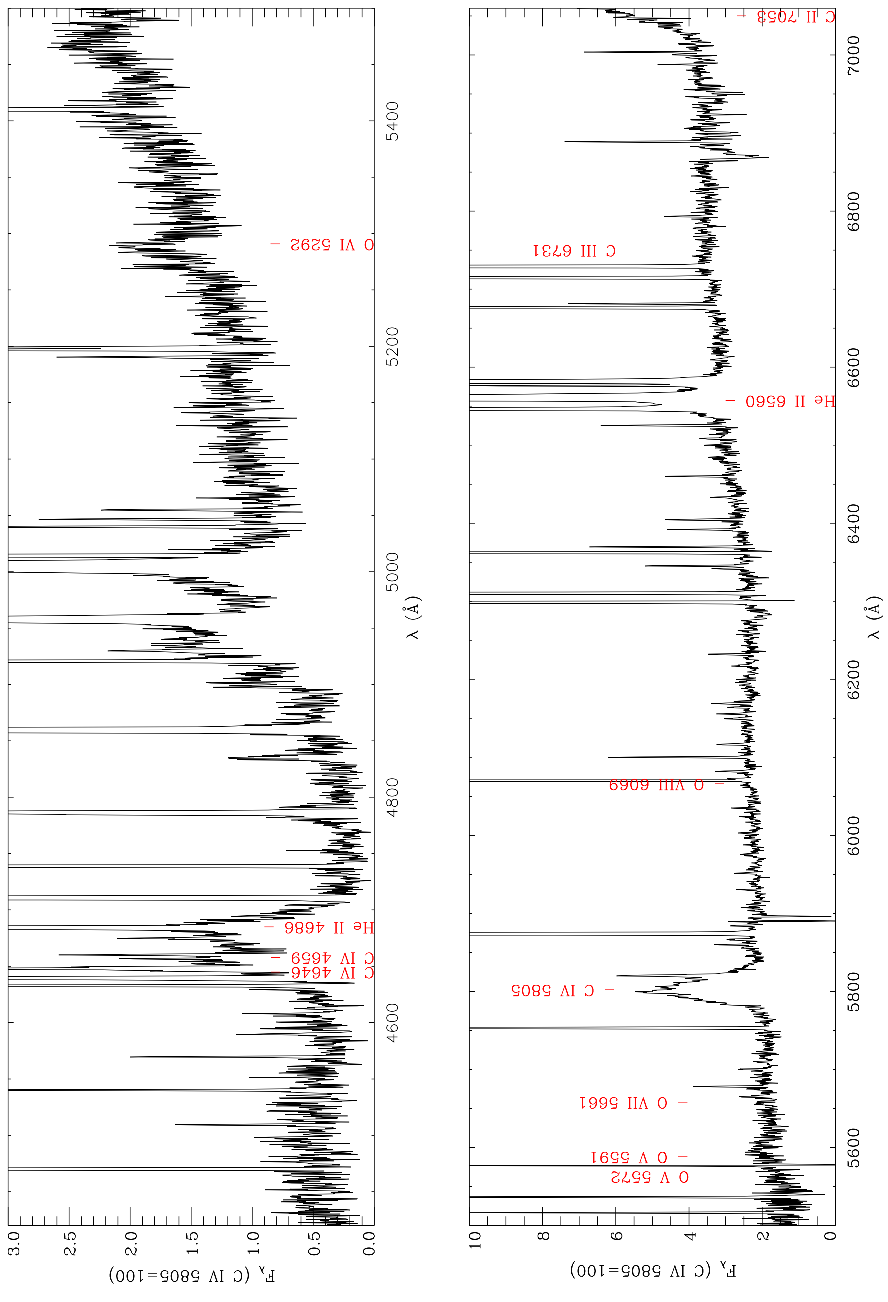

Figure E.3: As Figure E.1 but for the CSPN Hb 4.

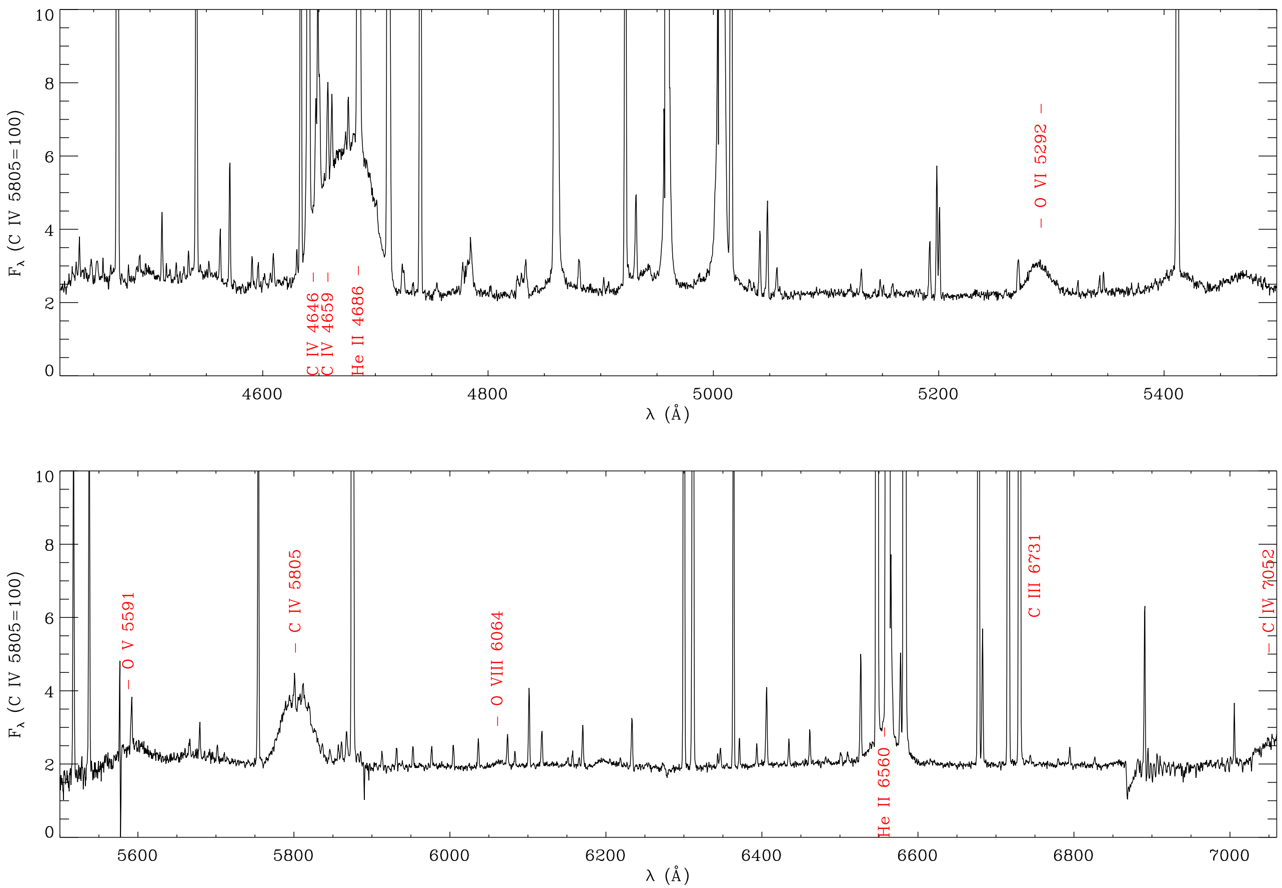

Figure E.4: As Figure E.1 but for the CSPN IC 1297.

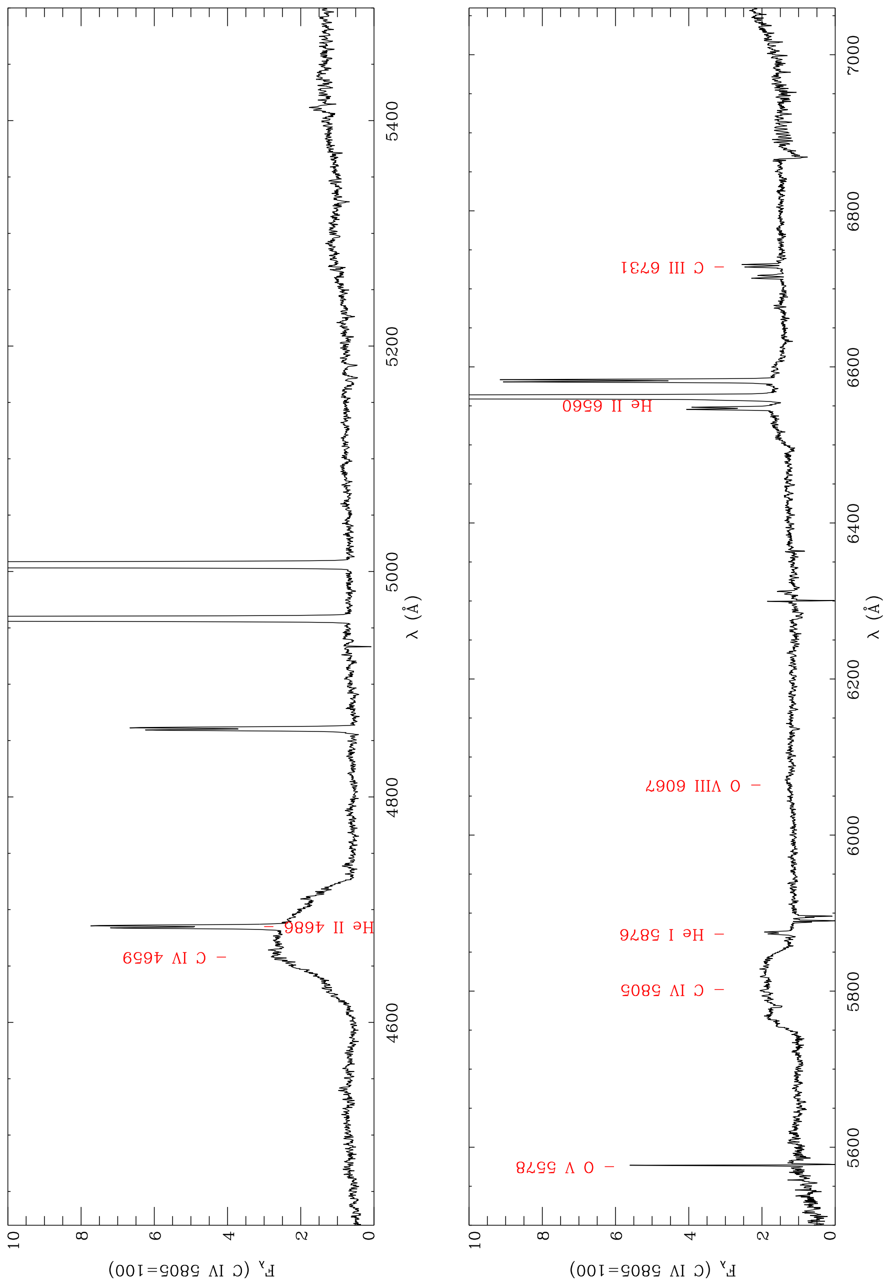

Figure E.5: As Figure E.1 but for the CSPN Th 2-A.

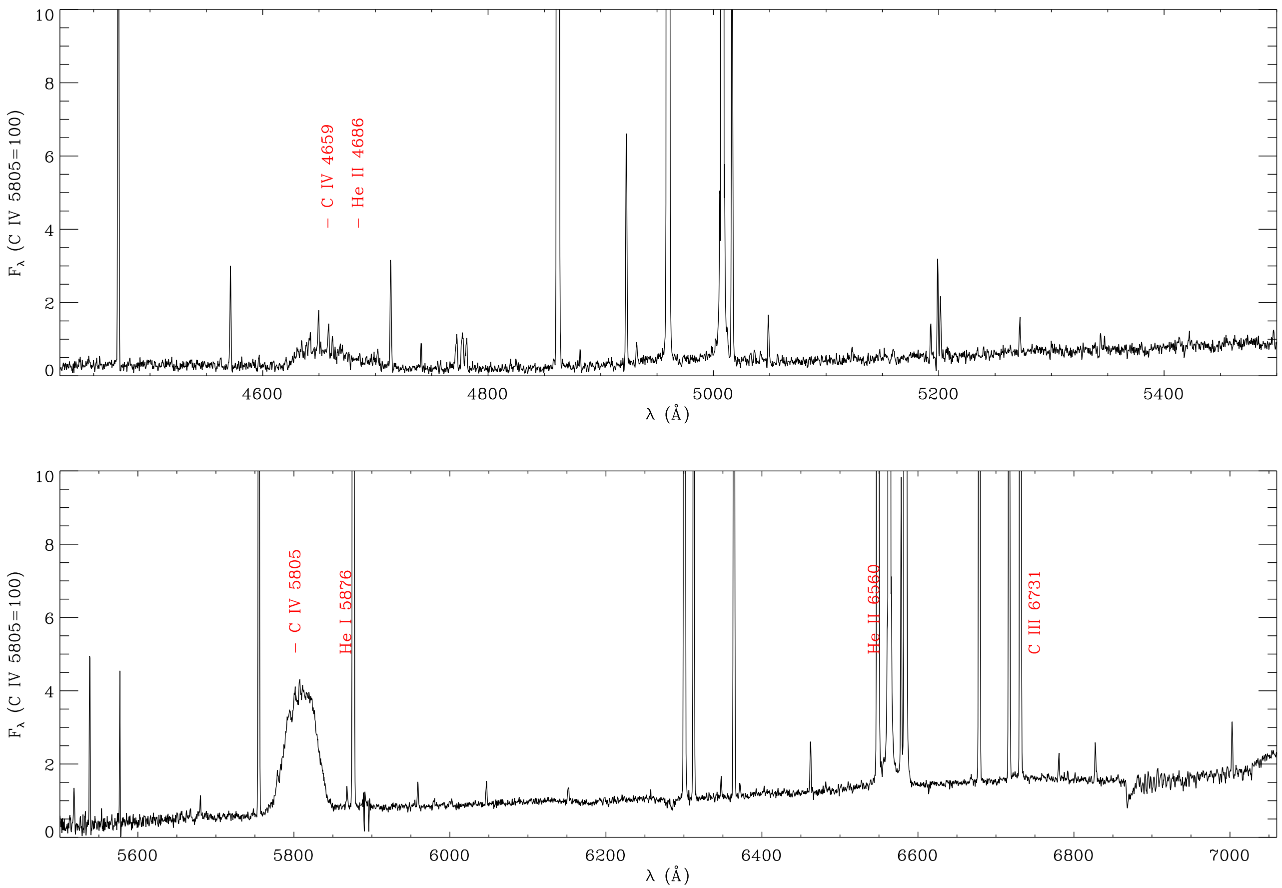

Figure E.6: As Figure E.1 but for the CSPN Pe 1-1.

Figure E.7: As Figure E.1 but for the CSPN M 1-32.

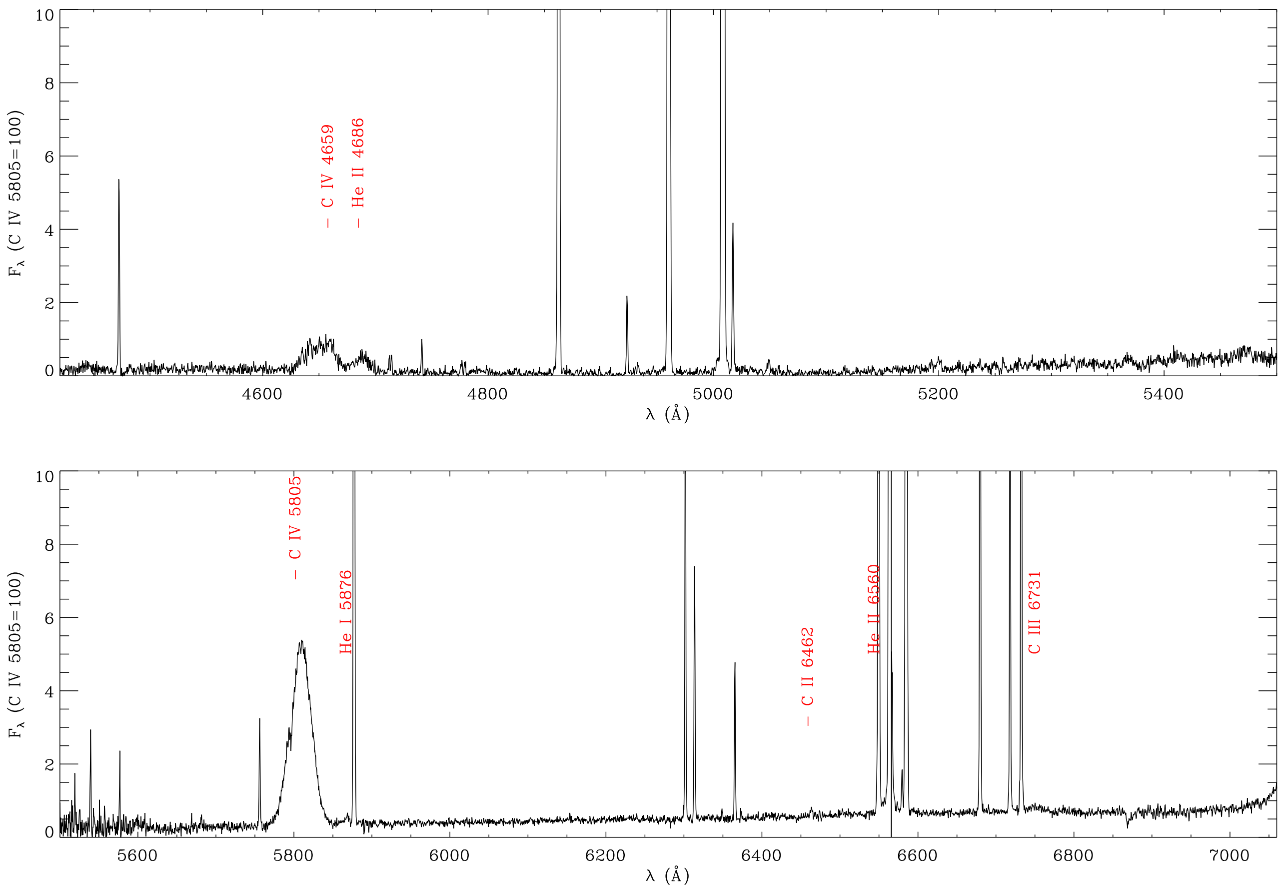

Figure E.8: As Figure E.1 but for the CSPN M 3-15.

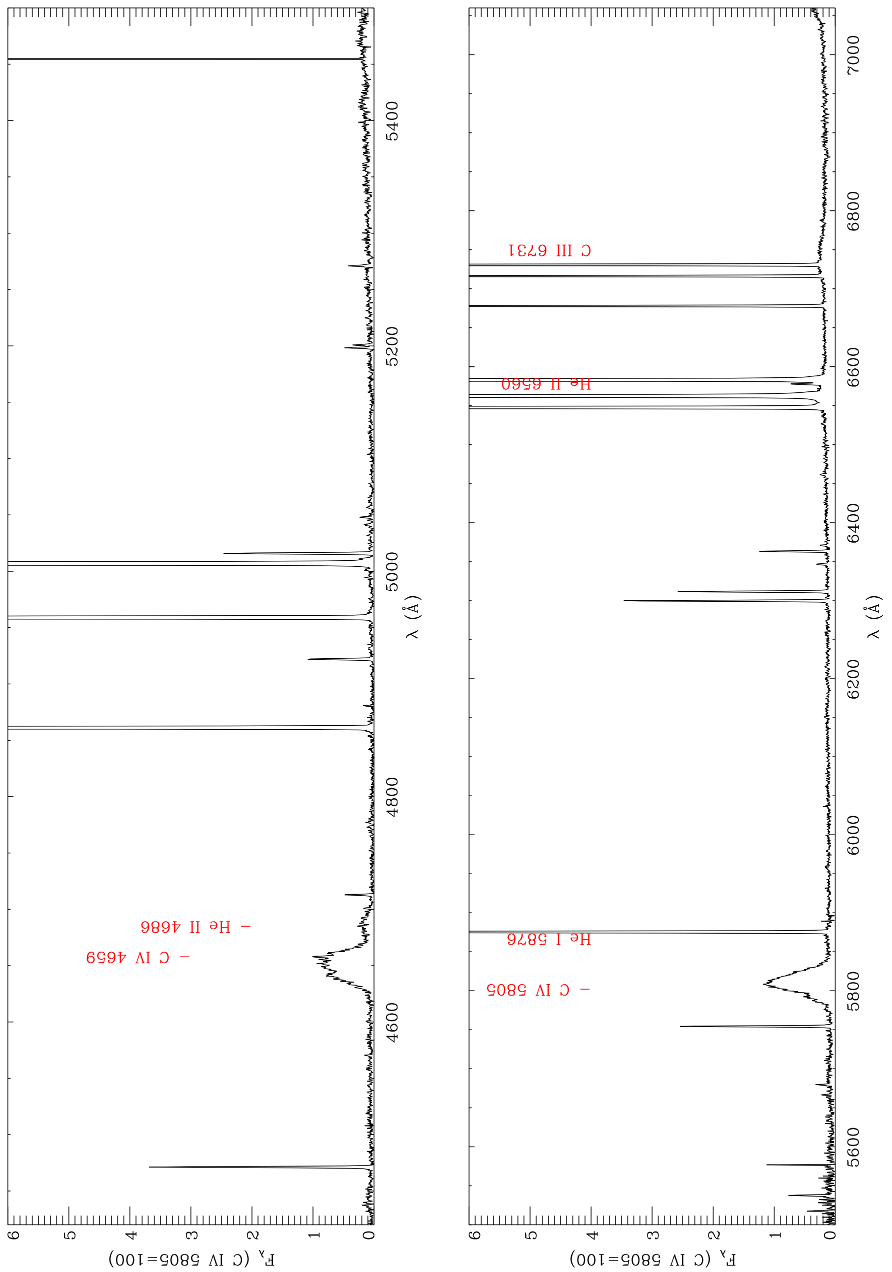

Figure E.9: As Figure E.1 but for the CSPN M 1-25.

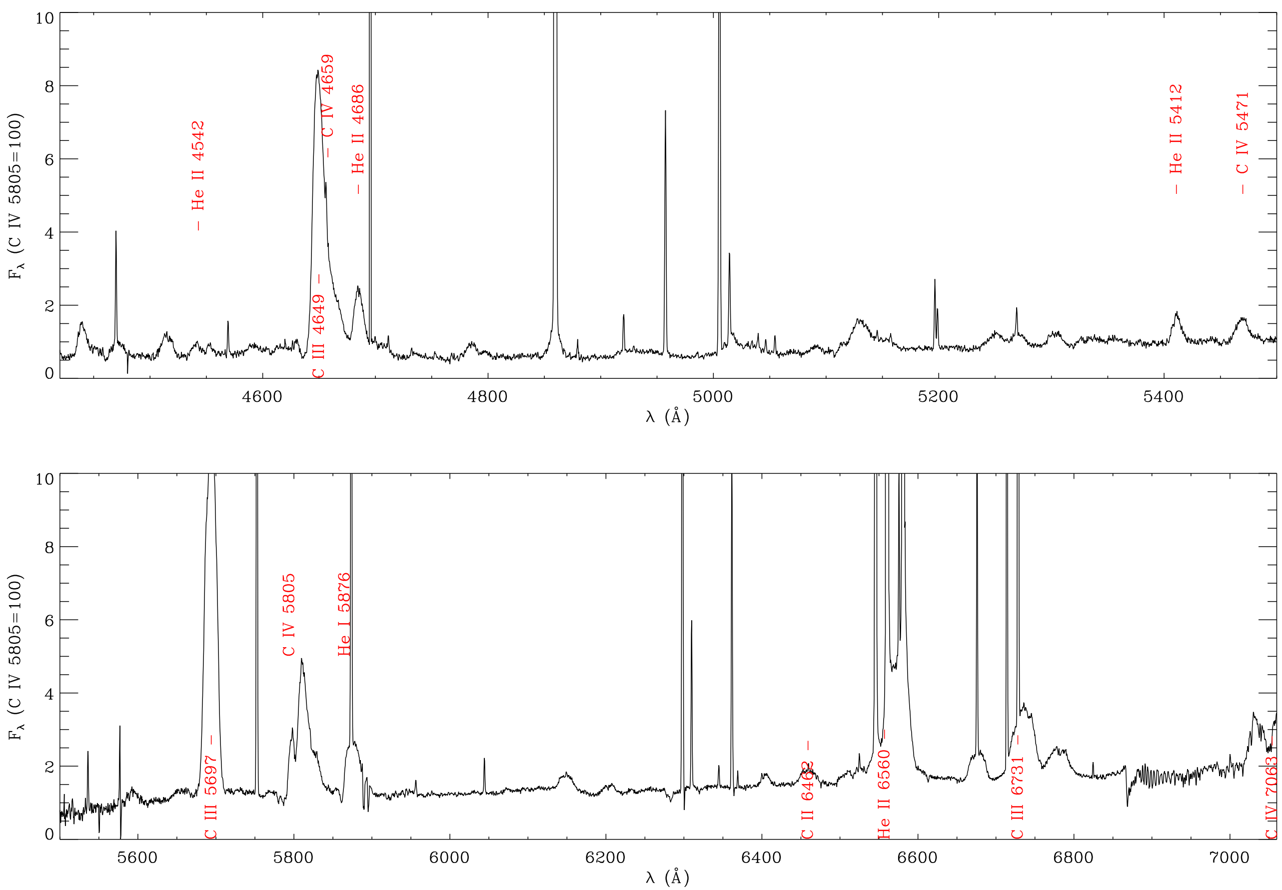

Figure E.10: As Figure E.1 but for the CSPN Hen 2-142.

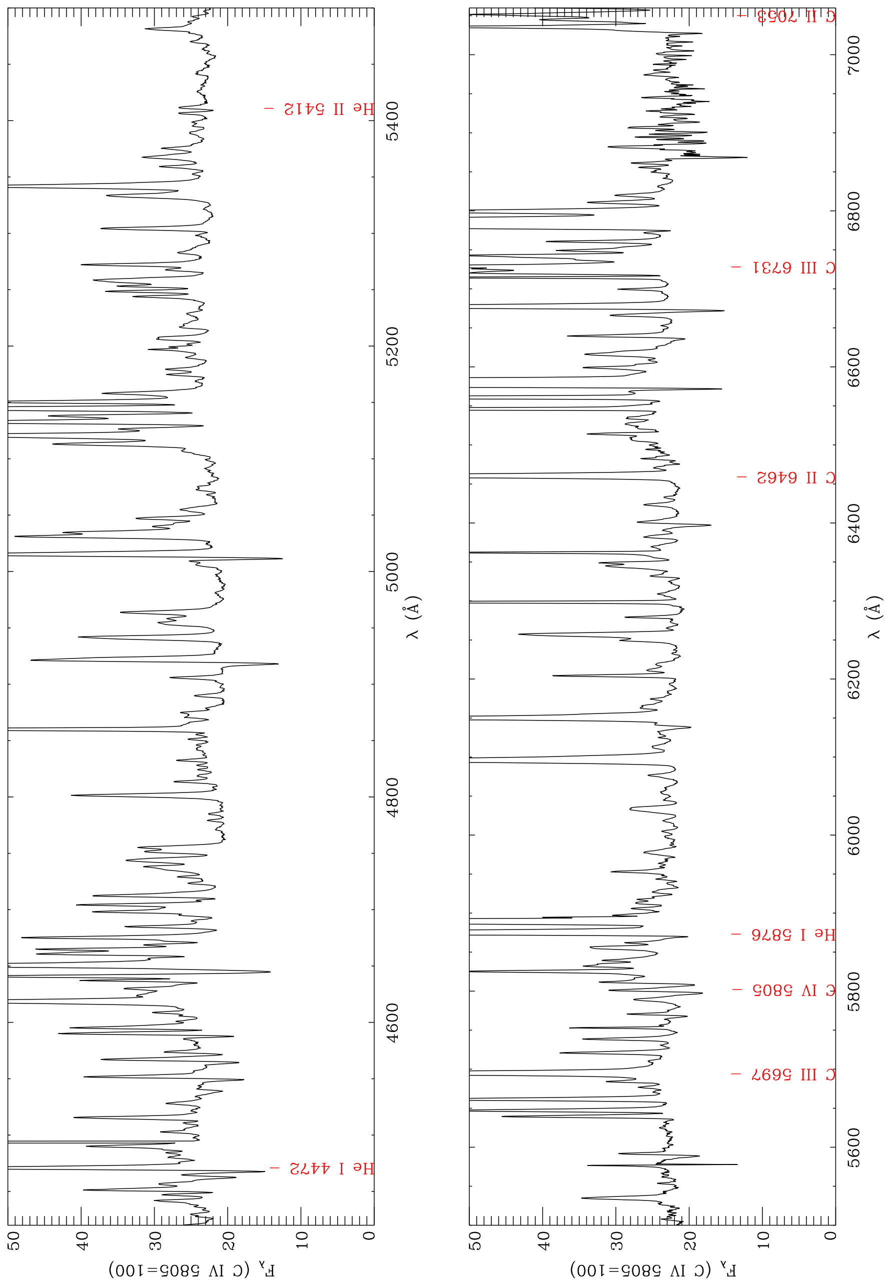

Figure E.11: As Figure E.1 but for the CSPN Hen 3-1333.

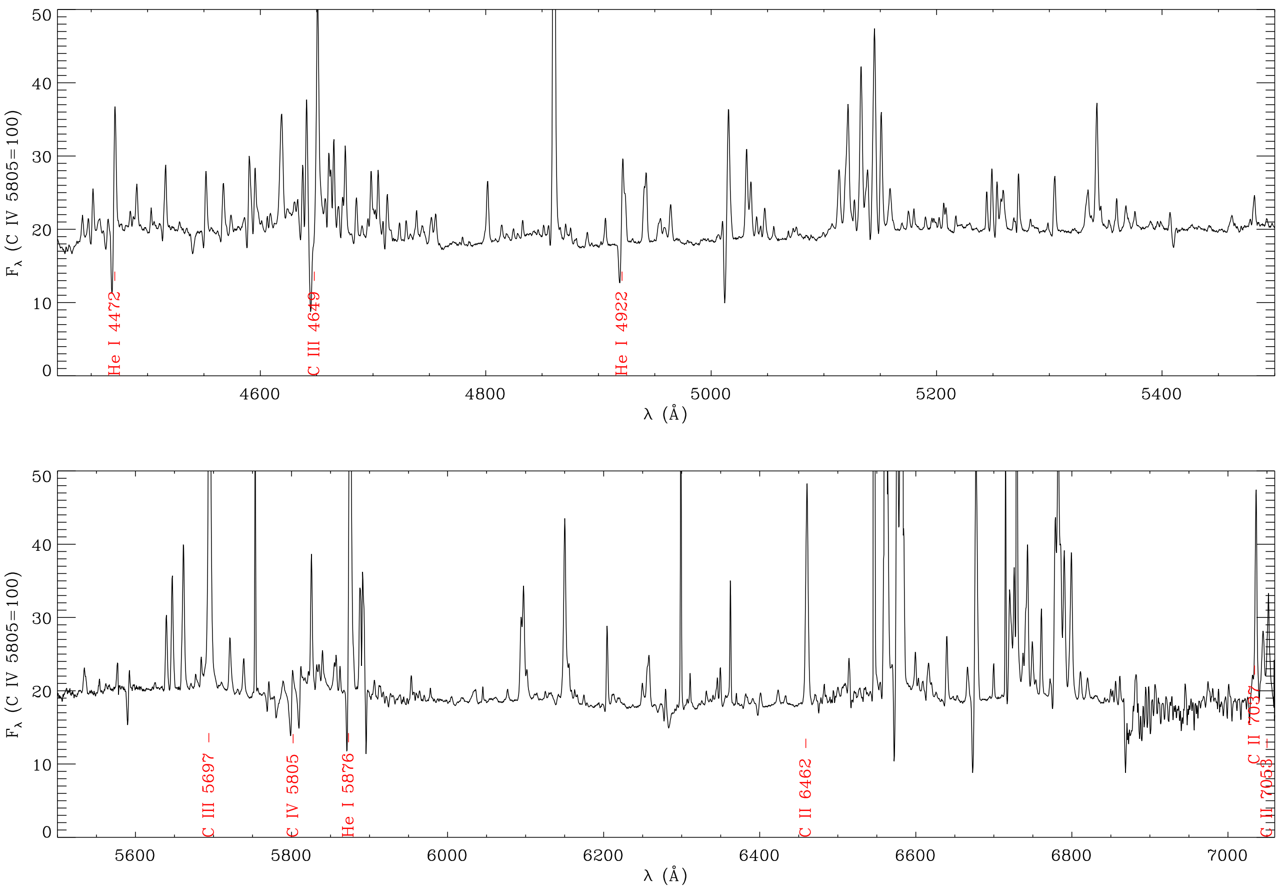

Figure E.12: As Figure E.1 but for the CSPN Hen 2-113.

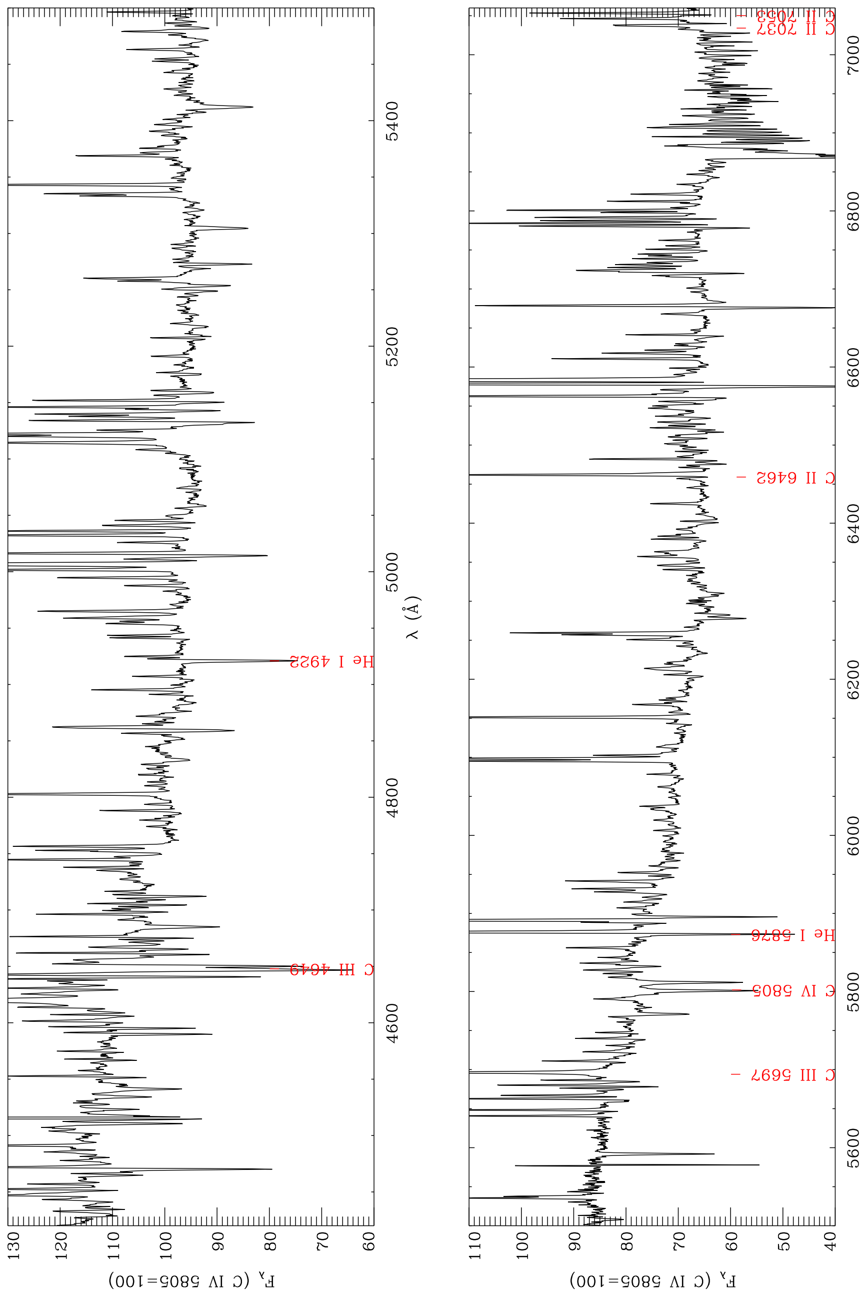

Figure E.13: As Figure E.1 but for the CSPN K 2-16.

Appendix F

Published Papers

1. ***Title:*** Observations and three-dimensional ionization structure of the planetary nebula SuWt 2

   Authors: **Danehkar, A.**, Parker, Q. A., & Ercolano, B.

   Reference: MNRAS, 434, 1513–1530 (2013)

   Abstract: The planetary nebula SuWt 2 (PN G311.0+02.4), is an unusual object with a prominent, inclined central emission ellipse and faint bipolar extensions. It has two A-type stars in a proven binary system at the centre. However, the radiation from these two central stars is too soft to ionize the surrounding material leading to a so far fruitless search for the responsible ionizing source. Such a source is clearly required and has already been inferred to exist via an observed temporal variation of the centre-of-mass velocity of the A-type stars. Moreover, the ejected nebula is nitrogen-rich which raises question about the mass-loss process from a likely intermediate-mass progenitor. We use optical integral-field spectroscopy to study the emission lines of the inner nebula ring. This has enabled us to perform an empirical analysis of the optical collisionally excited lines, together with a fully three-dimensional photoionization modelling. Our empirical results are used to constrain the photoionization models, which determine the evolutionary stage of the responsible ionizing source and its likely progenitor. The time-scale for the evolutionary track of a hydrogen-rich model atmosphere is inconsistent with the dynamical age obtained for the ring. This suggests that the central star has undergone a very late thermal pulse. We conclude that the ionizing star could be hydrogen-deficient and compatible with what is known as a PG 1159-type star. The evolutionary tracks for the very late thermal pulse models imply a central star mass of $\sim 0.64 M_{\odot}$, which originated from a $\sim 3 M_{\odot}$ progenitor. The evolutionary time-scales suggest that the central star left the asymptotic giant branch about 25,000 years ago, which is consistent with the nebula's age.

2. ***Title:*** Observations and three-dimensional photoionization modelling of the Wolf–Rayet planetary nebula Abell 48

   Authors: **Danehkar, A.**, Todt, H., Ercolano, B., & Kniazev, A. Y.

   Reference: MNRAS, 439, 3605–3615 (2014)

   Abstract: Recent observations reveal that the central star of the planetary nebula Abell 48 exhibits spectral features similar to massive nitrogen-sequence Wolf–Rayet stars. This raises a pertinent question, whether it is still a planetary nebula or rather a ring nebula of a massive star. In this study, we have constructed a three-dimensional photoionization model of Abell 48, constrained by our new optical integral field spectroscopy. An analysis of the spatially resolved velocity distributions allowed us to constrain the geometry of Abell 48. We used the collisionally excited lines to obtain the nebular physical conditions and ionic abundances of nitrogen, oxygen, neon, sulphur and argon, relative to hydrogen. We also determined helium temperatures and ionic abundances of helium and carbon from the optical recombination lines. We obtained a good fit to the observations for most of the emission-line fluxes in our photoionization model. The ionic abundances deduced from our model are in decent agreement with those derived by the empirical analysis. However, we notice obvious discrepancies between helium temperatures derived from the model and the empirical analysis, as overestimated by our model. This could be due to the presence of a small fraction of cold metal-rich structures, which were not included in our model. It is found that the observed nebular line fluxes were best reproduced by using a hydrogen-deficient expanding model atmosphere as the ionizing source with an effective temperature of $T_{\rm eff} = 70\,{\rm kK}$ and a stellar luminosity of $L_{\star} = 5500\,{\rm L}_{\odot}$, which corresponds to a relatively low-mass progenitor star (~ 3 $M_{\odot}$) rather than a massive Pop I star.

3. ***Title:*** The planetary nebula Abell 48 and its [WN] nucleus
   Authors: Frew, D. J., Bojicic, I S., Parker, Q. A., Stupar, M., Wachter, S., DePew, K., **Danehkar, A.**, Fitzgerald, M. T., & Douchin, D.
   Reference: MNRAS, 440, 1345–1364 (2014)
   Abstract: We have conducted a detailed multi-wavelength study of the peculiar nebula Abell 48 and its central star. We classify the nucleus as a helium-rich, hydrogen-deficient star of type [WN4–5]. The evidence for either a massive WN or a low-mass [WN] interpretation is critically examined, and we firmly conclude that Abell 48 is a planetary nebula (PN) around an evolved low-mass star, rather than a Population I ejecta nebula. Importantly, the surrounding nebula has a morphology typical of PNe, and is not enriched in nitrogen, and thus not the 'peeled atmosphere' of a massive star. We estimate a distance of 1.6 kpc and a reddening, $E(BV) = 1.90$ mag, the latter value clearly showing the nebula lies on the near side of the Galactic bar, and cannot be a massive WN star. The ionized mass ($\sim 0.3 M_{\odot}$) and electron density (700 cm^{-3}) are typical of middle-aged PNe. The observed stellar spectrum was compared to a grid of models from the Potsdam Wolf-Rayet (PoWR) grid. The best fit temperature is

71 kK, and the atmospheric composition is dominated by helium with an upper limit on the hydrogen abundance of 10 per cent. Our results are in very good agreement with the recent study of Todt et al., who determined a hydrogen fraction of 10 per cent and an unusually large nitrogen fraction of ~ 5 per cent. This fraction is higher than any other low-mass H-deficient star, and is not readily explained by current post-AGB models. We give a discussion of the implications of this discovery for the late-stage evolution of intermediate-mass stars. There is now tentative evidence for two distinct helium-dominated post-AGB lineages, separate to the helium and carbon dominated surface compositions produced by a late thermal pulse. Further theoretical work is needed to explain these recent discoveries.

4. ***Title:*** Three-dimensional photoionization modeling of the Wolf–Rayet planetary nebula Hb 4

   Authors: **Danehkar, A.**, Ercolano, B., Wesson, R., Steffen, W., Parker, Q. A.

   Reference: MNRAS, submitted

   Abstract: Optical integral field spectroscopy of the planetary nebula Hb 4 with a Wolf-Rayet [WO3] central star revealed that its outer pair of the fast, low-ionization emission regions (FLIERs) show an apparent over-abundance of nitrogen. The aim of the present work is to examine whether ionization effects provide a better physical explanation for this problem. We constructed a 3D photoionisation model of Hb 4 assuming homogeneous elemental abundances. The nebula is approximated by a density model developed from the kinematic analysis and *HST* imaging, which consists of a dense toroidal shell, two point-symmetric knots, and outer tenuous halo. The results indicate that the ionization correction factor method and the electron temperature used for the empirical analysis are mostly responsible for apparent enhanced nitrogen abundance. It is also found that the enhancement of the [N II] emission in the FLIERs is more attributed to the geometry and density distribution. Our first photoionization model under-predicted the ORLs. Therefore, we aimed to reproduce the ORLs of Hb 4 by using a bi-abundance photoionization model consisting of a chemically homogeneous torus with normal abundances, surrounding a small fraction of cold, metal-rich inclusions occupying ~ 5 percent of the total volume. The nebular emission line spectrum was best reproduced using a stellar model atmosphere with temperature $T_{\rm eff} = 90\,$kK and luminosity $L_{\star} = 4950\,{\rm L}_{\odot}$. The results indicate that the bi-abundance model provides acceptable matches to the ORLs. Moreover, the temperatures of the whole nebula predicted by the bi-abundance model reasonably match the empirical results. We conclude that the presence of the metal-rich inclusions may explain the observed ORLs.

5. ***Title:*** Photoionization modeling of the WolfRayet planetary nebula PB 8
   Authors: Danehkar, A., et al.
   Reference: MNRAS, in preparation
   Abstract: We have constructed photoionization models of the planetary nebula PB 8 to be confronted with available optical and infrared observations, constrained by a model atmosphere for the ionizing source calculated to match its central star spectrum. The density distribution for the nebular gas was adopted based on one-dimensional hydrodynamics models computed for different stellar evolutionary tracks. Three different sets of photoionization models were tried, the first being chemically homogeneous models that failed to reproduce the optical recombination lines (ORLs) of heavy elements. To reproduce the observed ORLs, dual abundance models were built by incorporating a small fraction of metal-rich inclusions embedded in the gas envelope with normal abundances. The

final bi-abundance model provided a better fit to the most observed heavy element ORLs, whose metal-rich inclusions have a mass of ~ 5 percent of the total ionized mass and nearly twice cooler and denser than the normal composition nebula. Their O/H and N/H abundance ratios are ~ 1.0 and 1.7 dex larger than the diffuse warm nebula, respectively. The model did not predict the thermal spectral energy distribution of the nebula observed with the *Spitzer* infrared spectrograph. Therefore, we aimed to reproduce the thermal infrared emission by including dust grains in the final photoionization model. It is found that the photoelectric emission from dust grains with a dust-to-hydrogen ratio of 0.01 by mass for the whole nebula is sufficient to match the dust temperatures and emergent spectral energy distribution. We conclude that the presence of metal-rich inclusions is necessary to explain the heavy element ORLs, while a dual-dust chemistry with different grain species and sizes in the nebula likely produces the observed infrared continuum.

6. ***Title:*** Physical conditions and chemical abundances for a sample of Galactic planetary nebulae with WR-type central stars

   Authors: Danehkar, A., et al.

   Reference: MNRAS, in preparation

   Abstract: We present optical integral field spectroscopic measurements of emission lines for 13 Galactic PNe with Wolf-Rayet (WR) stars and 5 Galactic planetary nebulae (PNe) with weak emission-line stars (*wels*) made with the Wide Field Spectrograph (WiFeS). The spectra, combined with archival spectra from the literature, have been used to carry out plasma diagnostics and abundance analysis using both collisionally excited lines (CELs) and optical recombination lines (ORLs). Nebular thermal and density structures have been derived using a variety of plasma diagnostics of CELs. The weak temperature dependence of ORLs has also been used to determine the temperature structure where adequate recombination lines were available. The plasma diagnostic results are used to derive ionic and elemental abundances within the nebula from both CELs and ORLs. It is found that the ORL abundances are several times higher than the CEL abundances, whereas the temperatures derived from the He I recombination lines are typically lower than those measured from the collisionally excited nebular-to-auroral forbidden line ratios. This may point to the existence of cold, hydrogen-deficient materials embedded in the diffuse warm nebula. The abundance discrepancy factors (ADFs) for doubly-ionized N and O are within a range from 2 to 49, which are closely correlated with the dichotomy between temperatures derived from forbidden lines and those from He I recombination lines. The results show that the ADF and temperature dichotomy are correlated with the intrinsic nebular surface brightness, suggesting that the abundance discrepancy problem must be related to the nebular evolution. The theoretical predictions of the AGB stellar models suggest that the elemental abundances deduced from CELs could be descendants of progenitors with initial masses of ~ 2–$4\mathrm{M}_{\odot}$, although the abundances derived from ORLs are unlikely to be explained by the models. However, two Type I PNe in our sample show extremely C-rich in contrast to the theoretical model predictions, so alternative mixing processes must evolve them into Type I PNe. We conclude that the discrepancy between abundances derived from CELs and ORLs must be closely related to the nebular evolution rather than the stellar characteristics, and it is higher in old evolved nebulae.

7. ***Title:*** Spatially resolved kinematics of planetary nebulae with WR nuclei
   Authors: Danehkar, A., et al.
   Reference: in preparation
   Abstract: We present new integral field unit (IFU) spectroscopic observa-

tions of a sample of Galactic planetary nebulae (PNe) surrounding Wolf-Rayet (WR) central stars. The Hα and [N II] emission features were used to determine the spatially resolved velocity distributions. Based on the spatially resolved kinematics combined with archival imaging, we determined their three dimensional structures. Comparing the observed velocity maps provided by the IFU observations with those predicted by morpho-kinematic models allowed us to exclude the projection effect from the nebula's appearance and identify the morphology of most PNe, apart from the compact objects. Our results indicate that these PNe have axisymmetric morphologies, either bipolar or elliptical. In many cases the associated kinematic maps for these PNe around hot WR central stars also reveal the presence of so-called fast low-ionization emission regions (FLIERs). The relationship between their morpho-kinematic structures and WR-type nuclei needs to be investigated further.

Appendix G

Glossary

AAO	Australian Astronomical Observatory
ADF(s)	Abundance Discrepancy Factor(s)
ANU	Australian National University
(E/TP-)AGB	(Early/Thermally Pulsing) Asymptotic Giant Branch
CCD	Charge-Coupled Device
CE(s)	Common Envelope(s)
CEL(s)	Collisionally Excited Line(s)
CTIO	Cerro Tololo Inter-American Observatory
CS(s)	Central Star(s)
CSPN(e)	Central Stars of Planetary Nebula(e)
EC/E.C.	Excitation Class
ECS	Equatorial Coordinate System
EMMI	ESO Multi-Mode Instrument
ESO	European Southern Observatory
FDU	First Dredge-Up
FGB	First Giant Branch
FLIER(s)	Fast, Low-Ionization Emission Region(s)
FITS	Flexible Image Transport System
FOV	Field-Of-View

FWHM	Full Width at Half-Maximum
GCS	Galactic Coordinate System
GPA	Galactic Position Angle
HBB	Hot-Bottom Burning
HB	Horizontal Branch
HR	Hertzsprung–Russell
HST	*Hubble Space Telescope*
HWHM	Half Width at Half Maximum
***icf*/ICF**	Ionization Correction Factor
IFU	Integral Field Unit
IFS	Integral Field Spectroscopy
INT	Isaac Newton Telescope
IR	Infrared
IRAF	Image Reduction and Analysis Facility
ISM	Interstellar Medium
(G)ISW	(Generalized) Interacting Stellar Winds
LIS(s)	Low-Ionization Structure(s)
LSR	Local Standard of Rest
LTP	Late Thermal Pulse
MES	Manchester Échelle Spectrometer
MESA	Modules for Experiments in Stellar Astrophysics
MIKE	Magellan Inamori Kyocera Echelle
MOCASSIN	MOnte CArlo SimulationS of Ionized Nebulae
(pre-)MS	(pre-)Main Sequence
MSSSO	Mount Stromlo and Siding Spring Observatories
NGP	North Galactic Pole
NLTE/non-LTE	Non-Local Thermodynamic Equilibrium
N&S	Nod-and-Shuffle

NTT	New Technology Telescope
ORL(s)	Optical Recombination Line(s)
PA	Position Angle
PDR	photodissociation region
P-V	Position-Velocity
PN(e)	Planetary Nebula(e)
PPN(e)	Proto-Planetary Nebula(e)
Pop I	Population I
PoWR	Potsdam Wolf–Rayet models
PSF	Point Spread Function
QI	Quartz Iodine
RG	Red Giant
RGB	Red Giant Branch
RLOF	Roche Lobe Overflow
SDU	Second Dredge-Up
SED	Spectral Energy Distribution
SHS	SuperCOSMOS Hα Sky Survey
“S/N”	Signal to Noise Ratio
SN(e)	Supernova(e)
SNR	Signal to Noise Ratio
SSO	Siding Spring Observatory
SSS	SuperCOSMOS Sky Survey
SPM	San Pedro Martír Observatory
TDU	Third Dredge-Up
TP(s)	Thermal Pulse(s)
UV	Ultraviolet
UVES	Ultraviolet and Visual Echelle Spectrograph
VLTP	Very Late Thermal Pulse

WD	White Dwarf
***wels*/WELS**	Weak Emission Line Star
WiFeS	Wide Field Spectrograph
WC	Carbon sequence of Wolf-Rayet
[WC]	Carbon sequence of PN Wolf-Rayet
WCE	Early-type Carbon sequence of Wolf-Rayet
[WCE]	Early-type Carbon sequence of PN Wolf-Rayet
WCL	Late-type Carbon sequence of Wolf-Rayet
[WCL]	Late-type Carbon sequence of PN Wolf-Rayet
WO	Oxygen sequence of Wolf-Rayet
[WO]	Oxygen sequence of PN Wolf-Rayet
WN	Nitrogen sequence of Wolf-Rayet
[WN]	Nitrogen sequence of PN Wolf-Rayet
WR	Wolf-Rayet
[WR]	PN Wolf-Rayet

Appendix H

Journal Abbreviations

A&A	Astronomy and Astrophysics
A&A Rev.	Astronomy and Astrophysics Review
A&AS	Astronomy and Astrophysics Supplement Series
Acta Astronomica	Acta Astronomica
AJ	Astronomical Journal
ApJ	Astrophysical Journal
ApJS	Astrophysical Journal Supplement Series
Ap&SS	Astrophysics and Space Science
ApJ	Astrophysical Letters
ARA&A	Annual Reviews of Astronomy and Astrophysics
AZh	Astronomicheskii Zhurnal
BAAS	Bulletin of the American Astronomical Society
JKAS	Journal of the Korean Astronomical Society
JRASC	Journal of the Royal Astronomical Society of Canada
LicOB	Lick Observatory Bulletin
MNRAS	Monthly Notices of the Royal Astronomical Society
MmRAS	Memoirs of the Royal Astronomical Society
New Astro.	New Astronomy

New Astro. Rev.	New Astronomy Reviews
PASA	Publications of the Astronomical Society of Australia
PASJ	Publications of the Astronomical Society of Japan
PASP	Publications of the Astronomical Society of the Pacific
Phys. Rep.	Physics Reports
Phys. Scr.	Physica Scripta
PLicO	Publications of the Lick Observatory
QJRAS	Quarterly Journal of the Royal Astronomical Society
RPPhys	Reports on Progress in Physics
RvMPhys	Reviews of Modern Physics
RMxAA	Revista Mexicana de Astronomia y Astrofisica
Space Sci. Rev.	Space Science Reviews
ZAp	Zeitschrift für Astrophysik